Wind, Water and Walls: Developing Luminescence and Geoarchaeological Methods for Ancient Landscape Features

LISA MARIE SNAPE

Wind, Water and Walls: Developing Luminescence and Geoarchaeological Methods for Ancient Landscape Features

Lisa Marie Snape

A thesis submitted for the degree of

DOCTOR OF PHILOSOPHY

Department of Archaeology
Durham University
2018

Abstract

The Sasanian Empire (224 - 624 AD) covered a vast geographical area, which expanded from Mesopotamia and Southern Iran into Central Asia, the Caucasus and the Arabian Peninsula. Its highly organised socio-political and military system enabled the foundation of new urban centres, intensification of agricultural land and expansion of trade networks into farfetched regions such as India and China. One impressive aspect of the Sasanian Empire was its ability to construct and maintain complex large-scale irrigation systems, which required a significant labour force to construct. Recent investigations of the northern and southern frontiers by the *Persia and its Neighbours Project* have identified a wealth of evidence for Sasanian landscape investment. Irrigation systems such as surface canals and channels, and underground aqueducts (qanats) were the most prominent features identified in the lowland regions, while in the uplands, agricultural terraces and field systems dominated.

The aim of this thesis was to draw upon landscape survey methodologies, combining luminescence and geoarchaeological techniques, to gain a better understanding of the timing of construction, maintenance and abandonment of key landscape features. The main methodological issues raised during this research were the complex taphonomy and landscape alterations that occur in many research areas, thus requiring intensive landscape survey, small-scale excavation and testing of samples to identify sites with the best potential for further investigation.

The results of the combined luminescence and geoarchaeological methodology have demonstrated the complex formation histories of Sasanian irrigation systems. The cleaning and maintenance events identified in upcast mounds, revealed important indicators for human-environment interactions at the frontiers. The demise of the Sasanian Empire did not result in the abandonment and collapse of these irrigation systems. Alternatively, canals were maintained into the Early Islamic period, suggesting 'continuity' rather than 'collapse' of key elements of Sasanian society.

Aknowledgements

This thesis took a long time to complete and has been challenging in all manner of ways. I could not have completed it without the support from so many people.

Firstly, I would like to thank Ian Bailiff for his patience, guidance and invaluable expert advice over the last four years. Many thanks also to Graham Philip for generously taking over as second supervisor after Tony Wilkinson passed away, and for the advice and comments at the writing-up stage of this thesis. Thanks to Eberhard Sauer for the opportunity to join this project, for his generosity and kindness. I would also like to thank Kristen Hopper and Dan Lawrence for their tremendous help and support during this time. This project could not have been achieved without the generous funding from the European Research Council (ERC).

Thanks to the many members of the *Persia and its Neighbours Project*: Eve McDonald, Seth Priestman, Graeme Erskine, Ana Gabunia, Lana Chologauri, and Dato Naskidashvilli. I would also like to thank Andrea Ricci for all his help in the field and for organising the shipment of my samples.

I would like to thank the various members of the OSL lab past and present: Helen Drinkall, Nathan Jankowski and Lily Bossin. I would also like to thank Steve Robinson for the technical help in the laboratory. Thanks also to Julie Boreham at Earthslides for making my thin sections.

There are a number of friends in the archaeology department I would like to thank: Steph Piper, Andrew Tibbs, Lucie Johnson, Ann Jacobsen, Claire Hodson, Giorgia Marchiori, Israel Hinojosa-Baliño , Edward Caswell, Elina Petersone-Gordina, Kendra Quinn, Samantha Tipper, Floor Huisman, Mocen Li (Sylvia), Christopher Davis, David Gonzalez-Alvarez, Marco Nebbia, Maria de Falco, Martina Massimino, Kori Lea Filipek-Ogden, Emily Hanscam, Brian Buchanan, Ellen and Ross Kendall.

Thanks also to some of my close friends for all their support and encouragement: Liz Bridge, Stephen Clifford, Nick House, and Ben Saunders. I would also like to thank my housemates at number 1 Brierville past and present: Agni Prijatelj, John Sommerill, and Spike.

I would like to thank my family for their love and support. Most of all, thanks to my grandad who passed away, I dedicate this thesis to you.

Lastly, I would like to thank Jorge for all the happiness, love and support you have given me.

Contents

List of Tables

List of Figures

Chapter 1
Introduction

1.1 *Persia and its Neighbours Project*

The overarching aim of the *Persia and its Neighbours Project* was to explore the scale and extent of Sasanian landscape development, with a specific focus on the military and agricultural investment within the northern, western and southern frontier regions (Fig. 1.1) (Sauer *et al.* 2013; 2015; Lawrence & Wilkinson 2017; Sauer 2017). In order to further understand how the empire adapted to the varying socio-political and environmental conditions, four case studies were investigated (Fig. 1.1). This involved a detailed investigation of the frontiers through a combination of archaeological excavation and landscape survey, to provide new insights into the role of the Sasanian Empire at the frontiers. In the following section, the broader geographical context of the project and the main findings will be introduced. A summary of the regional chronologies will also be provided to permit comparisons of the various evidence found in the different geographical regions explored in this research.

1.1.1 Geographical context

The Caucasus formed a natural defensive boundary and travel route connecting the Eurasia Steppe with Transcaucasia and the Near and Middle East. Dariali Fort, a military outpost strategically positioned in the Dariali Gorge, modern Georgia, was established to defend the mountain pass during Late Antiquity, and was maintained into the Middle Ages (Sauer *et al.* 2015) (Zone 1 in Fig. 1.1). This key site has revealed that the nature and duration of Sasanian control was intermittent and complex in the more remote and risky environments of the northern frontiers. The heterogeneous environments occupied by the empire, suggests that the uplands were utilised differently to the lowlands (Christensen 1993; 19). The lowland areas of the Lesser Caucasus (Zone 2 in Fig. 1.1), the Kura-Araz river basin, located in modern Azerbaijan, were used intensively for irrigation and agriculture during the Sasanian period (Alizadeh *et al.* 2004; Alizadeh & Ur 2007; Alizadeh 2011; Lawrence & Wilkinson 2017). Along the

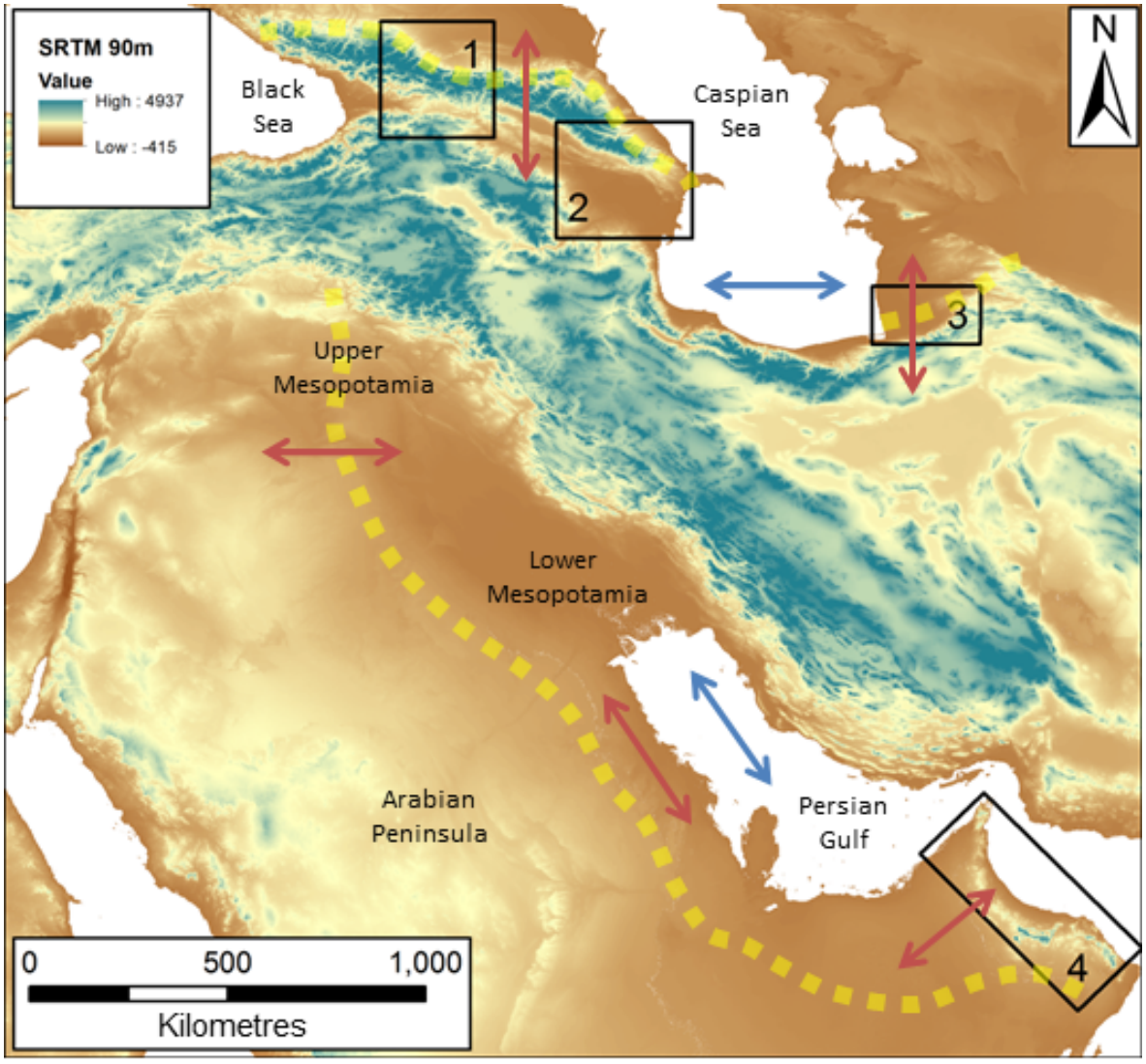

Figure 1.1. Map showing the location of each case study explored in this research. 1) Caspian Gates Project, Georgia; 2) Mil Steppe Survey, Azerbaijan, 3) The Gorgān Wall Project, Northeast Iran, 4) Fulayj Fort and the Rustaq-Batinah Coast surveys, Oman. Yellow dotted line indicates the extent of the Sasanian Empire. Blue arrows indicate maritime trade, and red arrows indicate overland trade. Background SRTM elevation data courtesy of the U.S. Geological Survey.

ancient canals used to irrigate the plains, several fortified cities, that formed a network of defenses between the Caspian and Black Seas, have been identified using remote sensing methods (Lawrence & Wilkinson 2017).

To protect and control seafaring traffic across the Caspian Sea, along with inland routes and trade networks in the open plains of Gorgān in Northeast Iran, significant

investment into military defensive infrastructure was required. The Gorgān Wall was erected along with numerous fortifications, watchtowers and defensive ditches (Zone 3, Fig. 1.1) (Nokandeh *et al.* 2006; Rekavandi *et al.* 2007; 2008; Sauer *et al.* 2013). Several canals were also constructed, but unlike those found in modern Azerbaijan, they were not only used for irrigation, but also for defending extensive agricultural lands, and as a way for navigating through extensive lowland areas. More recent investigations have shown that irrigation infrastructure was also constructed to supply water to large urban centres, suggesting that settlement expansion took place during periods of socio-political stability in the northern frontiers (Alizadeh 2011; Sauer *et al.* 2013; Lawrence & Wilkinson 2017).

Until recently, very little evidence for Sasanian occupation was found, suggesting that the 3rd to the 7th centuries AD was a period of decline (Kennet 2007). Sasanian military and economic investment on the Arabian Peninsula now appears to have been relatively small-scale and ephemeral, compared to the highly militarise landscapes of the Gorgān Plain. Fulayj Fort, located on the Batinah Coast of Oman, is a site that forms part of network of small forts strategically positioned along the coast and inland (Zone 4, Fig. 1.1). This site along with many others appear to have been established in order to enhance maritime trade, control overland trade and networks and maintain regular access to raw materials such as stone and metals (Mouton 2009). Recent archaeological investigations have demonstrated that the Sasanians were involved (either directly or indirectly) with maintaining these overland trade links *ibid.* In the arid regions of southeastern Arabia, the types of irrigation and landscape infrastructure found differs to those found in semi-arid environments of Transcaucasia, where dry-farming is more prevalent.

1.1.2 Chronological framework

The *Persia and its Neighbours Project* covers many geographical regions (Fig. 1.1) each with varying regional chronologies. Due to the complexity in terminologies applied in different regions covered by the project, cultural periods are based on those defined for Mesopotamia (upper and lower Mesopotamia combined) (Adams 1981; Ehrich 1992; Wilkinson 2003), Levant/Eastern Mediterranean (Ehrich 1992; Cameron 2015), Southern Arabia (Ehrich 1992; Potts 1992), Central Asia and the Lesser Caucasus (Kohl *et al.* 1984; Sinor 1990; Johnson 2012), and the Greater Caucasus (Reinhold & Korobov 2007). Fig. 1.2 provides a summary of the regional chronologies, including major climate trends covering the Late ('2k' events) (Büntgen *et al.* 2011; 2016; Xoplaki *et al.* 2016) and Mid-Holocene (summarised in Cullen *et al.* 2000; Roberts *et al.* 2011) and periods of major demographic change linked to wars, famine and disease.

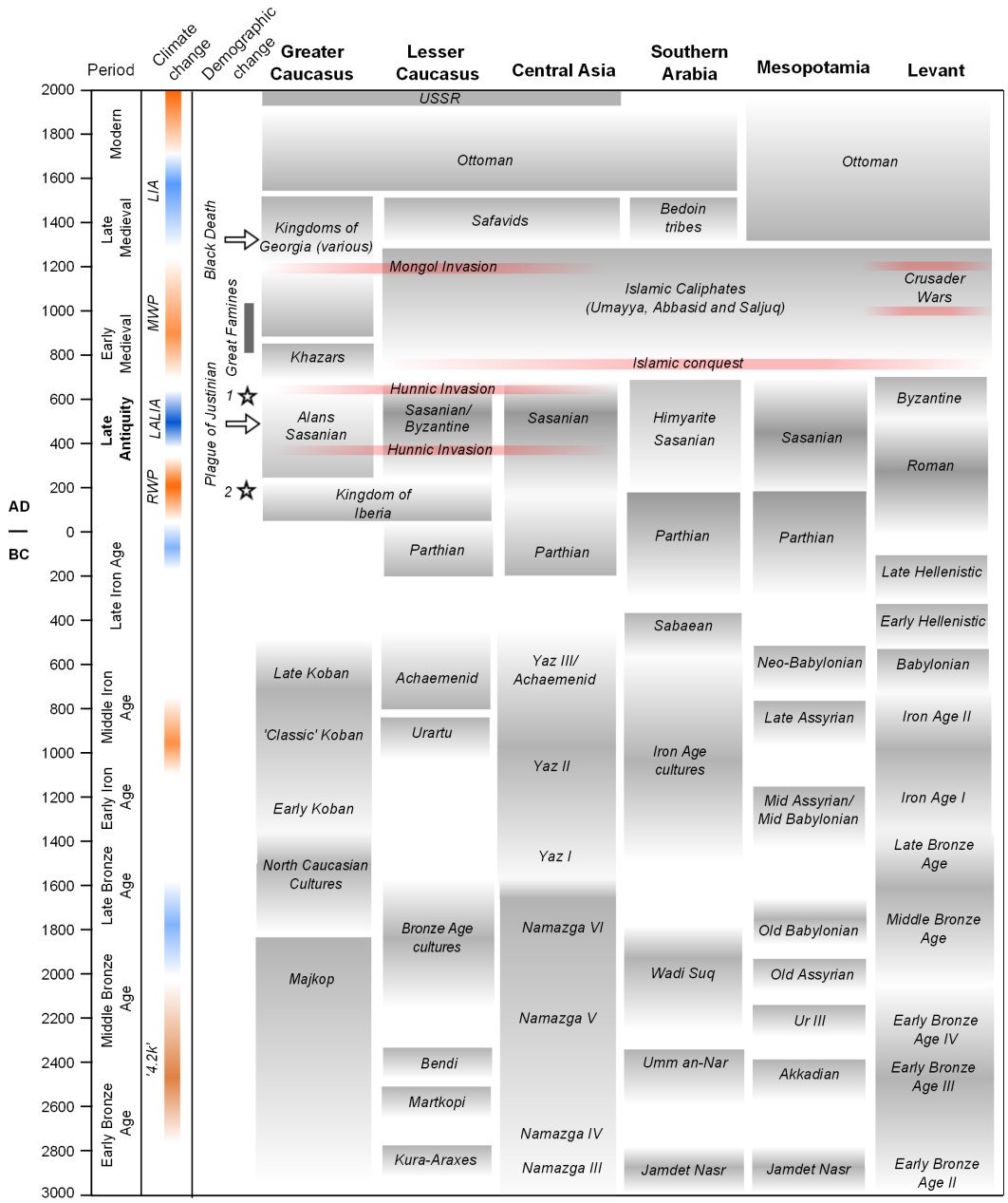

Figure 1.2. Summary chart illustrating the regional chronology, major climate events and periods of demographic variability in the regions occupied by the Sasanian Empire and other powerful polities and states covering the last 5000 years. Stars indicate: 1) Parthian-Sasanian wars, 2) Sasanian-Roman wars. **2k climate change:** orange indicates dry conditions and blue indicates cold/wet conditions. RWP = Roman Warm Period, LALIA = Late Antique Little Ice Age, MWP = Medieval Warm Period, LIA = Little Ice Age. **Geography:** Greater Caucasus = North Georgia, Dagestan, and southern Russia; Lesser Caucasus = Azerbaijan, Armenia and southern Georgia; Central Asia = Northeast Iran, Dehistan, Turkmenistan, and Uzbekistan; Southern Arabia = UAE, Oman and Yemen; Mesopotamia = Iraq, Iran, Syria and Turkey; Levant = Lebanon, Jordan, Israel, Palestine and Syria.

1.2 Thesis structure

- ***Introduction*:** Chapter 1 provides a broad overview of the Sasanian Empire covering aspects of the social organisation, economy, military and religious ideology. This is followed by the aims and objectives and the methodological approaches employed in this research.

- ***Review*:** As this thesis focuses on irrigation and landscape management within the Sasanian frontiers, Chapter 2 provides a review of the various irrigation and water-control features commonly found in the research areas covered by the *Persia and its Neighbours Project*. Examples of the various dating methods, both relative and absolute, applied to different landscape features such as canals, channels, qanats and also fields and terraces, are reviewed summarising the advantages and disadvantages of the various approaches available.

- ***Methodological background*:** Chapter 3 provides the overarching methodological approach to the study of irrigation systems investigated as part of this research. To combine both archaeological and environmental evidence, a multi-method geoarchaeological approach is applied.

- ***Case studies*:** Due to the broad nature of the project which covers many different environments and geographical regions, the physical and environmental background combined with a geoarchaeological assessment of the deposits sampled for dating is provided for each case study in Chapter 4. This was necessary to inform the approaches and techniques applied in the dating procedure.

- ***Luminescence dating background*:** Chapter 5 provides the luminescence background and methodology employed in this research.

- ***Applications*:** The results of the luminescence characterisation and the OSL dates obtained for the archaeological contexts with suitable characteristics are provided in Chapter 6.

- ***Discussion*:** Chapter 7 discusses the results of the luminescence characteristics of quartz recovered from the archaeological contexts sampled from different landscape features. The OSL dates are discussed within the wider archaeological context of the Sasanian frontiers. Based on the outcome of the results, areas of further research are proposed.

- ***Conclusions*:** A summary of the main findings of this research are presented in Chapter 8.

1.3 The Sasanian Empire (224 - 624 AD)

The Sasanian Empire was the last political entity in Iran before the advent of Islam. The empire covered vast territories encompassing the Near and Middle East, Central Asia, Arabia and the Caucasus (Fig. 1.1). Military expansion resulted in frequent confrontations with the neighbouring, powerful Roman Empire and the many semi-nomadic societies that occupied the Caucasus, Central Asia and the Arabian Peninsula. The Sasanians were also renowned for constructing large and elaborate irrigation systems that effectively controlled and navigated water from rivers to agricultural fields (Christensen 1993;29). Only through centralised control of these vast areas was it possible to build such major infrastructure. The following section will introduce the socio-political, economic and ideological background of the Sasanians that enabled the successful control and utilisation of vast geographical areas.

1.3.1 Social organisation

A newly unified Sasanian Empire was founded by King Ardašīr I (220 - 241 AD) after the demise of the Parthian Empire and the defeat of its last king, Artabanus V in the 3rd century AD (Daryaee 2009; Daryaee & Rezakhani 2016). The new empire had a complex and highly stratified hierarchical society dictated by religious ideologies (Christensen 1993; 27; Canepa 2010; Howard-Johnston 2010). Zoroastrianism was the state religion that formed the foundations of the Sasanian Empire. The religion focused power within the royal family, with the king (also known as the 'King of Kings') who was of direct descendant of the spiritual dynasty (Payne 2014; 284). In addition, several regional kings exercised total power and control of vast territories during the expansion (Payne 2013). Below the regional kings were the priests and several ranks of clergymen, scribes, physicians and astronomers, employed by the government to collect information, tax and register financial data (Karimian 2015; Payne 2017). The military system consisted of cavalrymen and foot soldiers that were carefully graded and organised according to importance. Significant investment into the military system was essential to ensure the security and protection of borders and installations (irrigation and religious buildings) (Howard-Johnston 1995). Craftsmen, farmers and villagers formed the largest proportion of Sasanian society, and were directly involved in the establishment of centres for preparing, manufacturing and distributing of goods between major urban centres (Karimian 2015). Agricultural production took place on the peripheries of settlements to provide food for both the agricultural and non-agricultural population. Agrarian society closely resembled that of the medieval feudal system, where local elites and wealthy landowners had direct control of the agricultural areas (Frye 1987). This complex socio-political system was organised and unified under a centralised government. Land and poll tax were collected from the villagers to fund settlement, trade and

agricultural expansion (Adams 2006; 23).

1.3.2 Sasanian settlement and urban expansion

The highly fertile landscape of Mesopotamia and Khuzestan formed the foundations for the newly unified empire (Fig. 1.1). Military control ensured the mobilisation of large populations, the expansion of new settlements and the establishment of new urban centres, including Ctēsiphōn, the Sasanian capital (Wenke 1987; Morony 1994). Settlement expansion was also made possible through the construction of large irrigation networks to provide a regular and reliable water supply and food for a growing population (Christensen 1993; 247; Howard-Johnston 2006; 199). Collapse or failure of these irrigation networks has been shown to have caused extensive shifts in settlement patterns (Adams 1981) and rural depopulation (Wenke 1987; 256).

Ideas of Sasanian settlement expansion, based on examples found in Mesopotamia, were originally defined as settlements that were strongly fortified and positioned at strategic river crossings for transport and trade (Jacobsen 1958; Adams 1965). However, intensive surveys undertaken in the 1960s and 70s showed chronological uncertainties associated with their dating, caused by the misidentification of ceramic assemblages recovered during landscape survey (Adams 1970; 114; Wenke 1975; 54; Adams 1981). The cause of this may be linked to landscape taphonomy (Schiffer 1987; Banning 2002; Wilkinson 2003), which would have led to the partial or, in places, the complete removal of ceramics from the archaeological record. Due to these uncertainties, it is assumed that settlement patterns devised for the Parthian, Sasanian and Early Islamic periods based on early ceramic sequences are likely to be inaccurate, as demonstrated by Simpson (1996). As a result, further investigation through systematic excavation of sites identified in these early surveys is required to redefine the ceramic assemblages used to date this broad time period. Nowadays, access to these sites is no longer possible; however, new areas of research have opened up in the frontier regions. In this way, systematic survey and excavation of sites in Turkmenistan, Northeast Iran and Oman, with long periods of occupation, has significantly improved our understanding of Sasanian ceramic assemblages (e.g. Kennet 2004; Puschnigg 2010; Sauer *et al.* 2013), enabling the successful identification of Sasanian sites in landscape surveys.

Furthermore, the position, size and intensity of occupation was not only influenced by the socio-political demands within the various regions occupied, but also related to the physical and environmental conditions. Sasanian settlements can be found as isolated small compound homesteads (Neely & Wright 1994; Neely 2016) large fortifications with lower towns (Alizadeh 2011; Wilkinson *et al.* 2013), small fortified coastal settlements and ports (Whitehouse 1971; Kennet 1997; Benoist *et al.* 2003), and large inland trading centres (Simpson 2014). The ancient city of Merv, located in the Marghab Oasis in Turkmenistan, remains one of the most important and intensively studied examples

of Sasanian settlement expansion (Herrmann 1997; Williams & Wordsworth 2010) Despite its size and complexity, no monumental urban architecture, defensive structures or temples have been uncovered (Simpson 2000). Instead, it mainly consisted of rectilinear street grids, mud brick architecture, workshops and wide open streets (Simpson 2014), resembling that of an inland market town. Inland trading centres such as this, located on the peripheries of the empire, formed important meeting points for trade and exchange between different polities.

1.3.3 Sasanian frontiers

To ensure effective control and stability on the frontiers covering vast geographical areas, direct control and unification were essential (for internal stability). It was under the rule of King Khushrau I (531-579 AD), that it was finally possible to successfully gain military control of the frontier regions, and to expand settled areas to unify local polities through its social, political and religious ideologies (Christensen 1993; 67; Payne 2013). Colonisation accounts recorded by Muslim historians such as Al-Tabari, Mas'udi and others in the 9th and 10th centuries AD, provide details of the lives and exploits of the Sasanian Kings as they conquered expansive areas of Central Asia, Afghanistan, Transcaucasia, Mesopotamia and parts of Arabia by the 7th century AD (Frye 1983). Although the extensive historical sources are chronologically disconnected, in many of these regions, evidence for the Sasanian expansion and colonisation has been confirmed archaeologically (Kennet 1997; Alizadeh & Ur 2007; Lecomte 2007; Alizadeh 2011; Ulrich 2011; Sauer *et al.* 2013; Simpson 2014). Increasing external threats and internal instability triggered the construction of vast defensive and military infrastructure such as, defensive ditches, fortifications and linear walls, to ensure the protection of the empire and control the movement of people and trade (Nokandeh *et al.* 2006; Rekavandi *et al.* 2007; 2008; Sauer *et al.* 2013).

The rapid construction of large military installations could be achieved through greater capital investment and increased expenditure on a large labour force consisting of slaves and war captives that were mobilised by the military garrison (Lieu 1986). If it is considered that these linear barriers demarcated the edges of the empire, the limits of socio-political control went beyond the frontiers defined by them (Boucharlat & Lecomte 1987; Lecomte 2007), forming a zone of cultural interaction. Alternatively, the frontiers may not have been firm territorial boundaries as traditionally percieved, but may have been defined by the location of cities, trading centres, and natural resources positioned between two powerful political polities (Lightfoot & Martinez 1995; Smith 2005) that were already predetermined prior to settlement and military expansion (Payne 2017; 194), and therefore the limits of the empire become less clear and difficult to define.

1.3.4 Agricultural intensification

The foundation of Sasanian society was the religious ideology of Zoroastrianism that encouraged agriculture and sustainable water management (Payne 2013). Religious and military expansion resulted in the construction of complex large-scale irrigation systems and ditches, requiring a large labour force to excavate and construct numerous tunnels, embankments and foundations. Several examples of large-scale irrigation systems have now been reported in the Northern Frontier regions (e.g. Alizadeh & Ur 2007), suggesting that centralised control of the rural landscape was also implemented on the peripheries of the empire. The dependence on water management infrastructure required administrative control, which involved both the state and the irrigation community (Hunt 1988). Thus, a centralised authority was in charge of managing the surplus output to provide sufficient resources for both rural and urban populations. Centralisation was also required to ensure that resources could be effectively intensified according to the wider demands of the empire Payne 2017. The organisation of the rural landscape would have involved a large labour resource, land planning and engineering to transform the natural environment and hydrological system, implemented by a centralised political-military strategy (Hunt & Hunt 1976; Kelly 1983; Hunt 1988; Adams 2006; Wilkinson & Rayne 2010). Farmers and villagers were actively involved in the maintenance of the agricultural landscapes that consisted of orchards, oases, gardens, alluvial soils, weirs, and several canals, qanats and storage pools (Adams 1965; Neely 1974; Wenke 1987; Neely & Wright 1994; Wilkinson 2003; 92).

Crops would have required expansive cultivatable lands and large-scale irrigation works to manage and control water in order to maximise crops and to prolong agricultural production with winter crops, such as wheat and barley (Christensen 1993; 71). The maintenance and upkeep of these irrigation systems were also essential, as they remained vulnerable to ecological instabilities (flooding, soil salinisation, and insect infestations) (Downing & Gibson 1974; 5; Christensen 1993; 215). With increasing pressures on the landscape, irrigation systems were often self-destructive if not managed sustainably, resulting in flooding and salinisation. Environmental degradation as a result of agricultural intensification triggered further expansion into new geographical regions that were composed of very different climates and environmental conditions compared to those commonly found in Mesopotamia (Christensen 1993; 117). This would have required adaptation of the agricultural regime to suit the local conditions encountered (Downing & Gibson 1974). Therefore, diversification of the agricultural economy combined with multi-cropping cycles was most likely implemented (Watson 1981; Marcus & Stanish 2006; Decker 2009). Increasing evidence for agricultural diversification has been confirmed through the recovery of environmental remains from archaeological contexts (Kennet 1997; Neer *et al.* 2013; Sauer *et al.* 2013; Simpson 2014) and regional palaeoenvironmental records (Connor *et al.* 2007; De Klerk *et al.* 2009; Djamali *et al.* 2009; 2010;

Shumilovskikh *et al.* 2016). Pollen cores, in particular, have revealed that the Sasanian Empire had a direct effect on the wider landscape and vegetation by introducing fruit trees and cotton, which required significant landscape modification. This expansion of the rural landscape in Late Antiquity has also been observed in neighbouring regions of Anatolia that was occupied by the eastern Roman Empire, and is widely referred to as the Beyşehir Occupation Phase (BOP) (Eastwood *et al.* 1998; Izdebski *et al.* 2016). Unfortunately, the exact scale and duration of rural expansion during Sasanian rule in the frontiers is hampered by the disparate and limited number of paleoenvironmental records, along with chronological uncertainties of the records available. This would require further palaeoenvironmental investigations to fully understand the impacts of Sasanian landscape change in the various geographical regions discussed.

1.3.5 Trade and exchange

Military and agricultural expansion into the fertile lands of the northern frontiers of Transcaucasia which encompass Azerbaijan, North Iran, Dehistan and Turkmenistan, that provided new opportunities to expand and diversify the economy further (Kohl 1988; Christensen 1993). On the other hand, it brought tensions to these newly formed frontiers, which had to be resolved in order to maintain important trade networks (Honeychurch 2014). Agricultural intensification was not only driven by the necessity for consumable crops, but also for cash crops required for trade. The recovery of charred cotton seeds dated to the 4th century AD from Sasanian occupation levels at Merv (Simpson 2014) suggests that production of cotton on the frontiers was already in place prior to the Islamic 'cotton boom' (Bulliet 2009). Unlike other luxury goods such as spices, preserved foodstuffs and gemstones that were widely circulated during this period (Simpson 2000), textiles could be traded to reach a much wider economic market and were in demand by all parts of society (Bulliet 2009; 11). One other benefit of cotton was that it flourished in hot climates, particularly during periods of enhanced aridity (Büntgen *et al.* 2011). Dry periods would have created ideal conditions for cotton as it requires long growing seasons (Bouchaud *et al.* 2011). Furthermore, cotton was generally less complicated to process than silk, flax and wool, and was relatively light in weight. This made it easy to transport using land (via camels/caravans), rivers and canals, and maritime routes (Simpson 2000; Daryaee 2010). Increasing demands for cotton required further landscape investment, particularly military protection of major irrigation works in order to produce a sufficient surplus to trade.

The economy was diversified further in the 5th and 6th centuries AD, as new maritime trade links flourished (Whitehouse & Williamson 1973). Coinage, ceramics and other portable artefacts with Sasanian stylistic attributes, which may be used as proxies for contact and exchange during this period of economic success, have been found at many sites and coastal ports in Mesopotamia, Central Asia, India, Arabia and even as far as

China (Simpson 2000). It was in the urban centres that artisans produced luxury goods (precious stones, silver coins, textiles, seals, pottery, glassware and metal objects) (*ibid.*), which were organised and distributed from these central nodes within and beyond the regions of Sasanian control (Daryaee 2003) (Fig. 1.1). The sourcing of raw materials for the production of luxury objects would have also triggered further expansion into new territories. The Arabian Peninsula is an example of a region with rich natural resources (copper, lime and salt), that were exploited to diversify the economy and expand the frontiers (Costa & Wilkinson 1987; Daryaee 2003; Morony 2004; Mouton 2009). Although such materials would have been bulky and labour intensive to source, requiring a large and reliable labour force, new opportunities to diversify the economy meant that less pressure was placed on agriculture in increasingly fragile environments (Downing & Gibson 1974). Economic diversity, therefore, reduced socio-political risks associated with agricultural intensification.

Trade and exchange also took place within the decentralised parts of society, particularly within villages and oases on the margins that provided opportunities for small-scale exchange networks to develop between sedentary farmers, nomadic communities and the military (Howard-Johnston 2006). Nomadic societies were also important allies for the Sasanian economy (*ibid.*), an idea which is supported by the evidence for nomadic seasonal settlements that have been found in the northern frontiers (Alizadeh & Ur 2007; Stride *et al.* 2009; Wilkinson *et al.* 2013). Contact with nomadic groups would have provided the empire with livestock (horses), crafts and luxury goods such as furs and wool, and additional labour when required in exchange for access to services e.g. pastureland and a regular supply of water for livestock (Honeychurch 2014). Further pressures for the maintenance of agricultural and irrigation networks were required to ensure balance and peace between sedentary and nomadic societies.

1.3.6 Sasanian demise

Socio - political instability

The rise and fall of many powerful polities occurred during Late Antiquity (3^{rd} - 7^{th} centuries AD) (Diamond 2005; Butzer 2012). A number of societal and environmental factors were most likely at play during this period and would have had a direct and indirect effect on societies that had sophisticated economic, military and political links. As the economy and trade networks became increasingly diverse, increased external pressures from neighbouring polities in 5^{th} and 6^{th} centuries AD caused internal socio-political instability. It has been widely reported that the Sasanians were frequently at war with neighbouring powerful empires and polities (Bosworth 1999), including the Byzantines and the Romans to the West, the Alans, the Khazars and the Huns to the North, and the Kushans, the Hephthalites (White Huns) and the Türks to the

East (Christensen 1993; Howard-Johnston 1995; Masson 1996; Dignas & Winter 2007). Although many of the textual sources are often biased, incomplete, or exaggerated the scale of battles in favour of Sasanian success. Despite this, these accounts provide a useful insight into the socio-political complexity at the time. The exact conditions (scale, duration and intensity) of socio-political change that took place over the *longue durée* remains unclear. However, it is likely that pressures from external polities were not the only factors that caused increased socio-political instability during this period. Historical sources have reported that the last Sasanian king, Yazdgard III (633 - 651 AD), took refuge at the ancient city of Merv in Turkmenistan where he was later murdered during the Arab invasion (Simpson 2014), marking the end of the Sasanian Empire (Howard-Johnston 2010). During the gradual decline in Sasanian control, the unification of the Arab kingdoms of Arabia formed a newly unified political power that eventually took control of the vast territories of the empire and beyond in the 7^{th} - 10^{th} centuries AD (Kennedy 2007; Hourani 2013; Decker 2017) (Fig. 1.1). Furthermore, this transition appears to have been a gradual rather than a sudden switch in political power (Choksy 1987).

Health deterioration

Increasing evidence for disease (e.g. 'Plague of Justinian'), famine and mass migrations and their effects on the demographics of the Byzantine and Roman Empires have been widely reported (Stathakopoulos 2017; 101). Food and health crises reported in other neighbouring empires most likely occurred in Sasanian society, resulting in significant shifts and displacement of populations over vast areas. Unfortunately, very few textual sources mention health and disease in everyday society. However, with increased urban expansion, a deterioration in human health most likely occurred; for example, the spread of parasites, water contamination and pollution had a detrimental effect on urban populations (McMichael 2012). In the rural landscape, the construction of irrigation and water storage facilities would have also increased the risk of malaria within settlements located close to marshes and irrigated lands (Sallares 2002; 32). Bioarchaeological analysis of human remains obtained from excavations of cemeteries would provide direct evidence for the health conditions during the Sasanian period.

Natural disasters

Natural disasters such as flooding, earthquakes and volcanic eruptions had a dramatic effect on the immediate environment and landscape during Late Antiquity (Butzer 2012). Periods of enhanced volcanism have been detected in many regions during this period (Fei *et al.* 2007; Sigl *et al.* 2015; Fuks *et al.* 2017), however, the exact effects of these events remains poorly understood. Initially, volcanic events can cause devastating ef-

fects on human and animal populations and the disruption or collapse of socio-political networks (Grattan 2006), but regions that are volcanically active form attractive environments with highly fertile soils (*ibid.*). Although very few historical sources report natural disasters during the Sasanian period, active seismic zones surrounding the Caspian Sea and the volcanically active Caucasus mountain range would have made societies susceptible to natural disasters (Boroffka 2010; Butzer 2012). Earthquakes in particular can change the natural hydrological regime resulting in flooding and the destruction of irrigation systems such as canals and qanats (Boroffka 2010). It has been shown that the failure of irrigation systems resulted, directly, in crop failure, collapse in trade networks and famine (Banaji 2002; 16).

Climate and environmental change

The role of climate fluctuations in the rise and fall of societies has been widely reported in the Mediterranean, Anatolia, the Near East and Asia (Büntgen *et al.* 2011; McCormick *et al.* 2012; Büntgen & Di Cosmo 2016; Büntgen *et al.* 2016; Sadori *et al.* 2016; Xoplaki *et al.* 2016; Fuks *et al.* 2017). Proxy records - microfossils (e.g. pollen and diatoms), speleothems, tree-rings, and lake and ocean sedimentary sequences, and global temperature records - vary in time-scales and chronological resolution. Considering the variability in proxy records available, two major climate events have been identified that are directly relevant to the chronological time-frame of the Sasanians. These are the 'Roman Warm Period' (RWP) and the Late Antique Little Ice Age (LALIA) (Büntgen *et al.* 2011) (Fig. 1.2).

Major warming and cooling events caused significant societal impacts during this period, however, the scale and intensity of these fluctuations within the various regions occupied by the Sasanian Empire remains unknown. As discussed in Sec. 1.3.5, the limited number of palaeoenvironmental records available for this vast geographical region makes it difficult to assess the direct impacts of climate change on society. Further integration of datasets that reflect environmental variability on the 'human-scale' is required to understand more specific questions regarding the influence of local environmental change on individual populations. Local records can also be obtained from geoarchaeological archives (e.g. buried soils and alluvium) that contain environmental remains useful for reconstructing human-environmental relations in the past (Wilkinson 1997; Alizadeh *et al.* 2004; Heyvaert *et al.* 2012). Further analysis of human and environmental remains recovered from archaeological deposits (e.g. anthropogenic shell middens) can also be used as short-term climate records (e.g. Wang *et al.* 2013).

In summary, to fully understand the climate and environmental change and its impact on Sasanian society, further integration of the various records available is required to improve our understanding of human-environment interactions in the various regions occupied during Late Antiquity.

1.4 Summary

As Late Antiquity is a highly dynamic and culturally fluid period of history, different scales of analysis are required to understand the impacts of climate and environmental change on the different socio-political systems that were intricately connected during this period. By the 6th century AD, the Sasanian Empire finally ended, and the reasons for this are most likely linked not just to a single, but to many social and environmental factors. A dependence on large-scale irrigation and agriculture introduced additional risk and uncertainty into the social, political and economic system of the empire. The collapse of agricultural infrastructure and economy due to soil salinisation, crop blights and insect infestations was an additional trigger for the expansion into the frontier regions, which introduced further pressures on the empire as a whole. Whether the demise of the Sasanian Empire can be defined as 'collapse' or simply a 'continuation' of Sasanian society into the Early Islamic period in the 7th century AD, needs to be clarified through further archaeological research during this period of socio-political complexity. This thesis aims to contribute to the debate by developing geoarchaeological and chronological methods applied to landscape features found in a wide range of environments such as lowland, highlands and coastal settings that were occupied by the Sasanian Empire.

1.5 Aims and objectives

1.5.1 Introduction

The overarching aim of this thesis is to understand the human-environmental dynamics of the Sasanian Empire within three contrasting environmental settings: 1) lowland semiarid floodplains, 2) temperate uplands, and 3) lowland arid coastal plains. The landscape features and their chronology will be used to discuss the socio-political and economic variability found within the contrasting environments exploited, and to contribute to the wider debate in understanding how the Sasanian Empire eventually ended prior to the rise of Islam.

In order to achieve this, optically stimulated luminescence (OSL) dating will be employed combined with geoarchaeological techniques to directly date archaeological contexts. This method is invaluable for landscape features where organic remains that can be radiocarbon dated are absent or have been reworked from their primary context. Types of landscape features that have been reliably dating using OSL include small surface canals (Berger *et al.* 2009; Huckleberry & Rittenour 2014; Desruelles *et al.* 2016), qanat mounds (Fattahi *et al.* 2011; Bailiff *et al.* 2015; Fattahi 2015) and fills of agricultural terraces (Davidovich *et al.* 2012; Avni *et al.* 2013; Kinnaird *et al.* 2017). A vast number of these features have also been identified in many landscapes investigated

in four case study regions. The two most common relative dating approaches applied in landscape archaeology are based on surface pottery and 'dating by association' to sites of known age. Although these approaches provide a broad and rapid characterisation of the chronological periods present in the field, they can only provide broad date ranges that may be inaccurate. OSL dating can provide a potential solution for resolving such chronological inaccuracies.

1.5.2 Aims and objectives

Four specific aims of this research are outlined below in order of the staged approach taken:

1. To identify landscape features with well-preserved contexts within the frontier regions.

   This will be achieved by undertaking small-scale excavation and sampling of landscape features, which includes: canals, channels, and field systems, located within close proximity to Sasanian settlements. This is necessary to test whether 'dating by association' can be a reliable method for rapidly identifying different phases of landscape investment within the four case study regions that includes Georgia, Azerbaijan, Iran and Oman.

2. To characterise the sediments sampled in order to place the OSL dates within their stratigraphic context.

   Due to the variability in contexts likely to be encountered in the four regions, a multi-method geoarchaeological approach will be employed. Cathodoluminescence will be applied to mineral extracts to identify the source of sediments that form the deposits sampled. Bulk sedimentary techniques (organic content, magnetic susceptibility, and particle-size analysis), will be applied to vertically stratified deposits such as those uncovered in field systems. This is necessary to identify subtle variations with depth to detect site-formation processes. Combined with this, micromorphology will be used as a means to characterise sediments and soils *in situ*, and identify components that may affect the external variability between OSL samples, which may be caused by:

   a. Frequency and distribution of coarse grains of quartz within an individual context.

   b. Post-depositional mixing and bioturbation and the movement of grains from their original stratigraphic position.

c. Post-depositional chemical alterations caused by alternating wetting and drying cycles.

d. The presence of relevant components that may cause localised variability in uranium (U), thorium (Th) and potassium (K), which may have a direct effect on the evaluation of sample dose-rate.

3. To determine the suitability of coarse-grained quartz recovered from the sampled contexts, and to determine the success of the conventional single aliquot regenerative (SAR) dating procedure in order to develop a chronostratigraphic sequence.

   Scanning electron microscope coupled with energy dispersive x-ray spectrometry will be used as a means to rapidly determine the purity of the refined quartz sample after chemical and physical separation. A consideration of the natural signal intensities and signal characteristics will be routinely employed as part of the SAR procedure to obtain a reliable estimate of equivalent dose (D_e). To ensure that appropriate age models will be applied, results of the geoarchaeological assessment will be carefully considered in the analysis of D_e distributions, particularly in contexts affected by bioturbation and mixing.

4. The OSL dates will then be considered within the wider regional chronological context of the *Persia and its Neighbours Project* in order to further understand the scale and extent of Sasanian landscape investment in the different environments occupied between the 3rd to the 7th centuries AD.

Chapter 2
A dating framework for ancient landscape features: a review

2.1 Introduction

The aim of the following chapter is to introduce the types of landscape features that have been identified in the four case studies introduced in Chapter 1. A review of the various approaches applied to date landscape features investigated as part of this research, including canals, channels, field systems and qanats will be given. In landscape archaeology, relative dating methods are frequently used in order to characterise the landscape and identify the main phases of occupation, this can be done using diagnostic artefacts such as pottery and brick found on the ground surface, association of features to sites of known age, textural and epigraphic sources, and typologies of stone and their arrangement that may reflect cultural styles. The common use of these approaches is due to the fact that they are rapid and provide insights into the broad trends in different periods present in the landscape. Although these methods have proven to be very useful, it is necessary to have more accurate techniques in order to better date the different types of features present in the landscape. Radiocarbon dating of organic material and luminescence dating (OSL) are two techniques that are now widely employed.

2.2 Irrigation systems

2.2.1 Canals and irrigation channels

Large-scale canals and small surface channels are constructed according to the climate, flow system and scale of agricultural intensity required by a society. As mentioned in Chapter 1, the large-scale canal systems found in the extensive alluvial floodplains found in the Near and Middle East and Central Asia, are usually associated with highly organised empires and states. Large-scale canals are clearly visible in satellite imagery

(CORONA) (see Sec. 3.2.1 for further details) taken prior to the construction of modern irrigation systems that have resulted in the widespread destruction of archaeological sites and landscape features in many regions (Wilkinson 2003). Canals in particular are easily identified in satellite images, as they appear as dark and light linear features that define the fill and associated upcast banks (Fig. 2.1). Remote sensing methods are widely applied to identify major irrigation networks in the Near and Middle East, Central Asia and East Asia (Alizadeh & Ur 2007; Stride *et al.* 2009; Hritz 2010; Ur 2013; Wilkinson *et al.* 2013; Hu *et al.* 2017). These methods also enable sites and features to be targeted in the field as they can cover vast areas of the alluvial plains (Wilkinson *et al.* 2006). Canal systems are often found in association with settlements - regionally referred to as tell in the Near East or qal'eh in Central Asia - that appear as distinct circular or rectilinear features in satellite imagery (Fig. 2.1). Canals are often dated 'by association' with settlements of known age and from surface pottery (Adams 1965; Neely 1974; Wilkinson 1998; Nokandeh *et al.* 2006; Lecomte 2007; Rekavandi *et al.* 2007). However, drawbacks of this approach is that additional chronological uncertainties can be introduced due to the successive reoccupation of these fertile plains that can partially or completely destroy former landscapes (Wilkinson 2003; Alizadeh & Ur 2007). In the lowland plains it is usually the most recent periods of settlement activity that dominate the archaeological record.

Chronology and stratigraphy of canals

Excavation of canals identified in satellite images can provide stratigraphic control to improve the reliability of the dating evidence available. Radiocarbon dating of bone (Clarke *et al.* 2005; Malatesta *et al.* 2012), charcoal (Schiffer 1986; Bishop *et al.* 2004; Gillmore *et al.* 2009; Kühn *et al.* 2010b), seeds (Hu *et al.* 2017), and the recovery of diagnostic artefacts such as pottery and fired brick (Newson *et al.* 2007; Wilkinson *et al.* 2013), have been used to date the fill of canals. Unfortunately this approach can be problematic, as artefacts and residual organic remains are likely to be reworked prior to redeposition within the fluvial deposits that fill the canal after abandonment. Charcoal recovered from canals may also be affected by the 'old wood' effect (Bishop *et al.* 2004).

One of the major complications with investigating canals is their sheer scale, thus requiring large-scale excavation to completely uncover both the bank and canal fill deposits. In unique cases, natural river exposures through canal deposits enables further investigation of the stratigraphy without labour intensive and time-consuming excavation (Wilkinson 1998). As part of this research, excavations of a canal system in Azerbaijan and a moat in Northeast Iran provided a unique insight into the formation and evolution of large-scale irrigation systems (see Chapter 4). As illustrated in Fig. 2.2; b, a canal fill can consist of thick units of fine-grained alluvium (silt and clay), and the full extent of these deposits can be difficult to define from excavation alone, requiring

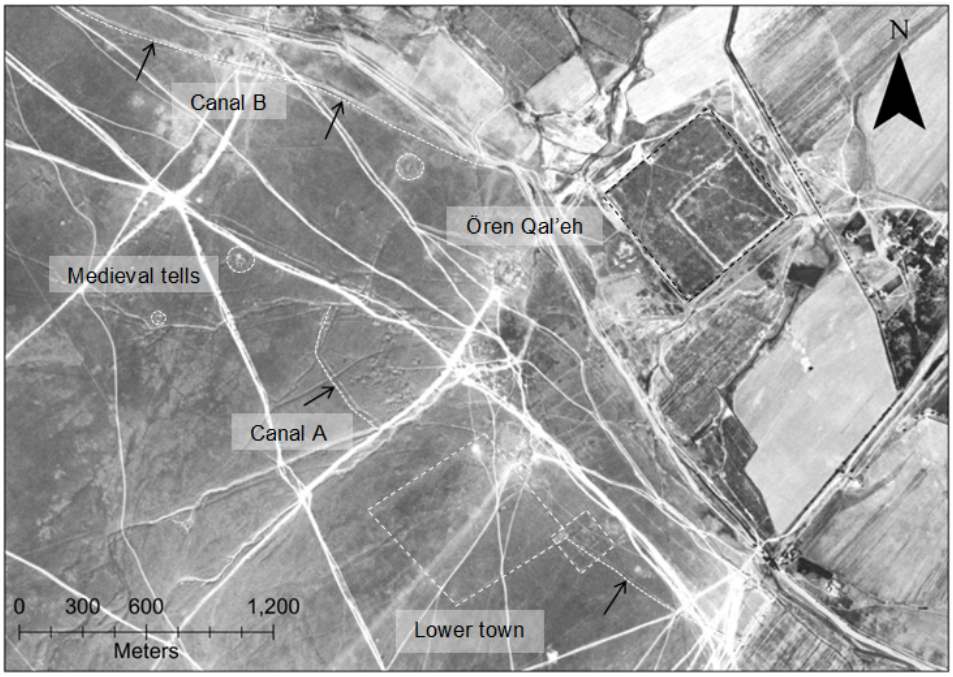

Figure 2.1. A CORONA satellite image of a region in the Mil Steppe, Azerbaijan (courtesy of the U.S. Geological Survey) showing the location of Ören Qal'eh Fort, lower town and its extensive irrigation canal system (canal A and B as indicated by arrows). Small medieval tells were also identified on the imagery.

further coring to penetrate deeper depths (Sanderson *et al.* 2003; 2007; Gilliland *et al.* 2013). Sanderson *et al.* (2003; 2007) used coring techniques to sample the lowermost fill for OSL dating, however, the results obtained revealed significant mixing and disturbance. Small-scale channels, particularly those constructed in prehistory, are sometimes preserved beneath thick units of natural or anthropogenic sediment (e.g. Gillmore *et al.* 2009). Due to their small scale, the full extent of these channels can be easily exposed in an archaeological excavation, however, fills are generally shallow and lack upcast banks (Fig. 2.2; a). Small channels, however, provide better opportunities for OSL sampling where boundaries and areas of disturbance can be easily avoided. OSL dates obtained from the fills of channels from small systems can only provide a *terminus ante quem* (Berger *et al.* 2004; 2009; Huckleberry & Rittenour 2014). However, ^{14}C of 'old' carbon, e.g. eroded from the sides of river or canal banks, can be carried downstream and incorporated into the sediments.

Alternatively, the excavation of canal upcast banks that are well-preserved for large-scale systems have provided opportunities to test the OSL dating method applied to banks (Wilkinson *et al.* 2013; 77) and bunds (Gilliland *et al.* 2013) in Iran and Sri Lanka respectively. To provide a *terminus post quem*, the transition from the old ground surface (OGS) and the initial construction deposits would theoretically provide the closest date to the construction event. However, the OSL dates obtained from a preliminary investigation gave ages that were significantly older than the age of the bank (Schwenninger & Fattahi 2013; 444), suggesting incomplete exposure of the sediments to light when deposited to form the banks. Building on this early work, this research aims to understand not only the timing of canal abandonment, but also the construction and maintenance events that created substantial banks. As illustrated in Fig. 2.2; b, large upcast banks can be highly complex requiring a detailed stratigraphic investigation that will be employed to ensure that the most suitable deposits are sampled for OSL dating.

2.2.2 Agricultural fields

Many different varieties of agricultural fields have been identified in the lowland and highland regions of the Mediterranean, Near and Middle East, the Caucasus, and Southern Arabia (French & Whitelaw 1999; Frederick & Krahtopoulou 2000; Grove & Rackham 2001; Wilkinson 2003; Barker *et al.* 2007; Reinhold & Korobov 2007; Harrower 2008; Bruins & Ore 2009; Bevan & Conolly 2011; Haiman 2012; Beckers *et al.* 2013; Korobov & Borisov 2013). They were constructed in order to deepen soils, increase surface area, enhance moisture and nutrients, and reduce surface erosion. The location, size and shape of a field system is dictated by a range of physical variables such as; aspect slope, precipitation and site-formation processes (Wilkinson 2003). In the highlands of Yemen, the shape of fields was mainly determined by the slope angle, steep slopes create narrow 'contour' terraces, while gentle slopes formed 'broad field' terraces (Gibson & Wilkinson

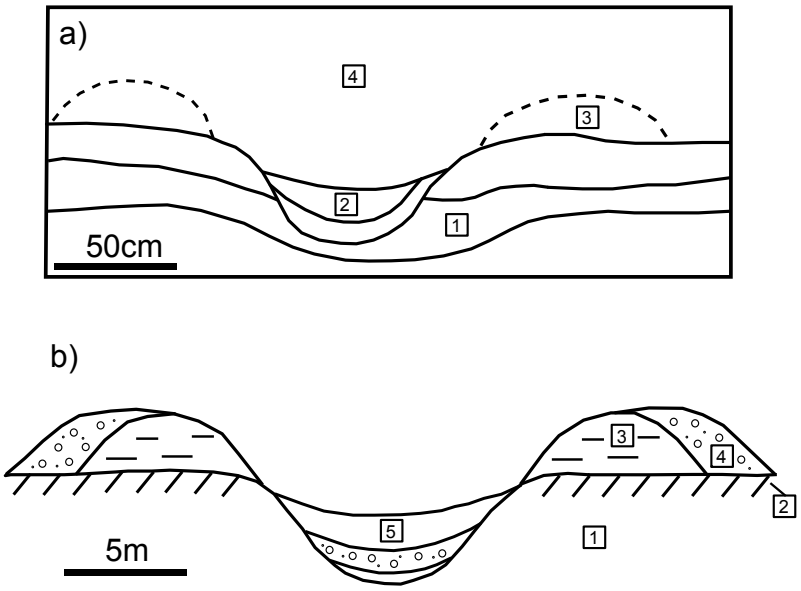

Figure 2.2. Schematic diagrams to illustrate the main sediment deposit types associated with small earthen channels and canals. a) Channel: 1 - alluvial silts, 2 - channel fill (structured silts and clays), 3 - eroded upcast bank, 4 - alluvial silts. b) Canal: 1 - alluvial silts, 2 - old ground surface, 3 - construction upcast, 4 - maintenance upcast, 5 - canal fill (structured silts and clays).

1995). Lowland regions that were relatively flat or gently sloping, formed fields that were sub-angular in shape (*ibid.*). The full extent of a field in lowland areas are often difficult to define unless demarcated by boundary walls. Furthermore, middening processes often result in the accumulation of diagnostic artefacts, such as ceramics that become incorporated into the field deposits, are widely used to define a field and can be used for relative dating (Wilkinson 1982; Costa & Wilkinson 1987; Bintliff & Snodgrass 1988).

Anthropogenic landscape alterations and colluvial processes in upland regions can affect site visibility and artefact recovery, that can lead to misidentification of the scale and extent of landscape features such as terraces (e.g. Bevan *et al.* 2013). Furthermore, in temperate climates, dense vegetation cover hinders ground-based landscape surveys as surface artefacts go undetected (Banning 2002). In upland regions, walls were often constructed to capture sediment to form a levelled surface, also referred to as the riser (Frederick & Krahtopoulou 2000), to deepen soils on slopes and also to reduce erosion. The formation of terraces occurs as a result of gradual sediment accumulation that buries and preserves an old ground surface (*ibid.*). As the terrace aggrade over time, diagnostic artefacts and organic remains become incorporated into the fills, and during periods of landscape stability, soil horizons can form within the sediment (Holliday 2004). Different terrace systems and soil formation may vary according to the position on a slope. A model based on the fieldwork undertaken in the Dariali Gorge, Georgia, is presented

here to illustrate the variability in terrace formation on a slope (Fig. 2.3).

On a slope with an angle of 18° sediments can accumulate relatively slowly under stable conditions (Fig. 2.3; A). In most cases, no terrace wall is required to level the ground to form a riser, as sediments can aggrade naturally. The terrace sequence can exhibit a reversing of the natural stratigraphy where components from the natural A horizon that become incorporated into the basal deposits followed by the reworking of B and C horizons. Similarly, on unstable slopes formed by extensive colluvial deposits, aggradation can take place relatively rapidly (Fig. 2.3; C). A similar reversing in stratigraphy may also be observed. At points on a slope where the natural soil is shallow on small undulating outcrops, extensive terrace walls (2.5 m high) may be constructed to aid the formation of the riser (Fig. 2.3; B). The complexity of site-formation processes that can occur at different points on a slope has implications for relative and absolute dating methods.

Diagnostic artefacts are a useful indicator for identifying the main phases of settlement activity within the immediate area of a field system, and is a widely used method for dating fields and terrace systems (Frederick & Krahtopoulou 2000), however, they are often redeposited within the fill during natural aggradation processes and can be an inaccurate method for dating terraces and field systems. Alternatively, ^{14}C dating of organic remains, such as charcoal, and bulk soil organic matter, is widely used to date buried soils (Harrower 2008; Acabado 2009; Korobov & Borisov 2013). However, bulk soil carbon often gives significantly older ages as carbon can originate from older soil formation phases that are reworked within colluvial slope deposits (Kühn *et al.* 2017). In regions where OSL dating has been used in conjunction with ^{14}C for dating colluvium and buried soils, a reversed chronostratigraphy was found in the ^{14}C ages (Lang & Nolte 1999; Lang & Hönscheidt 1999). OSL ages confirmed that old organic matter was redeposited by colluvial processes (Lang & Hönscheidt 1999). In many arid regions, organic remains are often absent, and OSL dating is often the primary means of absolute dating.

In the Negev Highlands of Israel and neighbouring regions of Jordan, in such arid areas where vegetation cover is sparse, surface pottery has been widely used to date terrace systems (Barker *et al.* 2007; Bruins 2012). However, a number of studies have employed OSL for dating terraces due to the bright luminescence properties of aeolian quartz widely deposited in the region (Avni *et al.* 2012; Davidovich *et al.* 2012; Avni *et al.* 2013). The OSL dates presented in some of these papers suggested that these terraces were constructed in the Late Byzantine/Early Islamic period and then abandoned in the 10th - 11th centuries AD (Davidovich *et al.* 2012), indicating that older pottery and charcoal had been significantly reworked when incorporated into the terrace fills.

Considering the advantages of the OSL dating procedure for sediments from this region, particularly for identifying deposits that had been redeposited - thus enabling pottery and other diagnostic artefacts to be excluded from the analysis - such land-

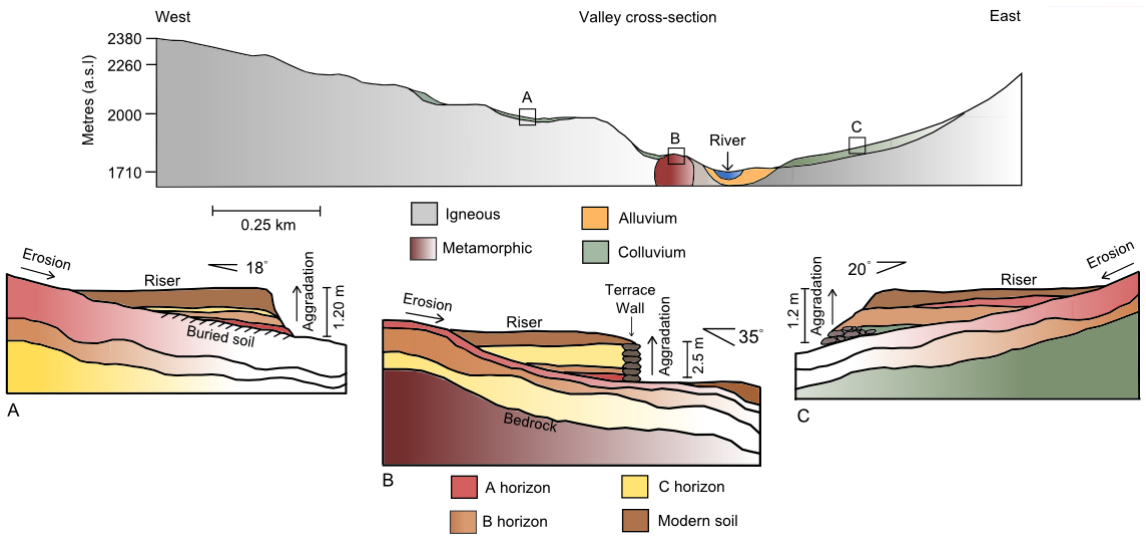

Figure 2.3. A model to show the different agricultural terrace systems that can be found at various positions on a slope. An earthen terrace formed by natural aggradation processes (A); a stone-walled terrace formed by natural aggradation with intermittent anthropogenic deposition (B); and a terrace formed on top of substantial colluvial deposits formed by rapid natural aggradation (C).

scape features are often affected by disturbance of the sediment stratigraphy. In such cases, the incorporation of 'young' quartz can occur which can lead to significant age underestimation (Davidovich *et al.* 2012). Systematic stratigraphic investigations and geoarchaeological approaches are widely used in the study of field systems and terraces (French & Whitelaw 1999; Krahtopoulou & Frederick 2008). However, there remains to be a methodological gap between OSL dating and geoarchaeological analysis of sediments to quantify bioturbation, in order to improve the resolution of the OSL dating procedure where quartz characteristics are suitable. This emphasises the importance of undertaking detailed stratigraphic analysis of deposits prior to sampling to ensure that only the most secure contexts are sampled.

2.2.3 Qanats

The qanat is a subterranean aqueduct that has enabled the permanent occupation of many arid and semi-arid regions (English 1968). They are widespread in many regions, and in each of them they receive a different name. The *qanat* in the Middle and Near East (Beaumont *et al.* 1989; Lightfoot 1997), *falaj* in Arabian Peninsula (Wilkinson 1977; Magee 2005), *karrez* in North Africa (Morocco, Tunisia, Egypt) (Beaumont *et al.* 1989), *galleria* in Spain (Glick 1970; 70) and *puquios* in South America (Lane 2016; 465). This technology has also been found in areas as far as China and Mongolia (Abudu *et al.* 2011; Hu *et al.* 2012). The general model used to describe the qanat system consists of

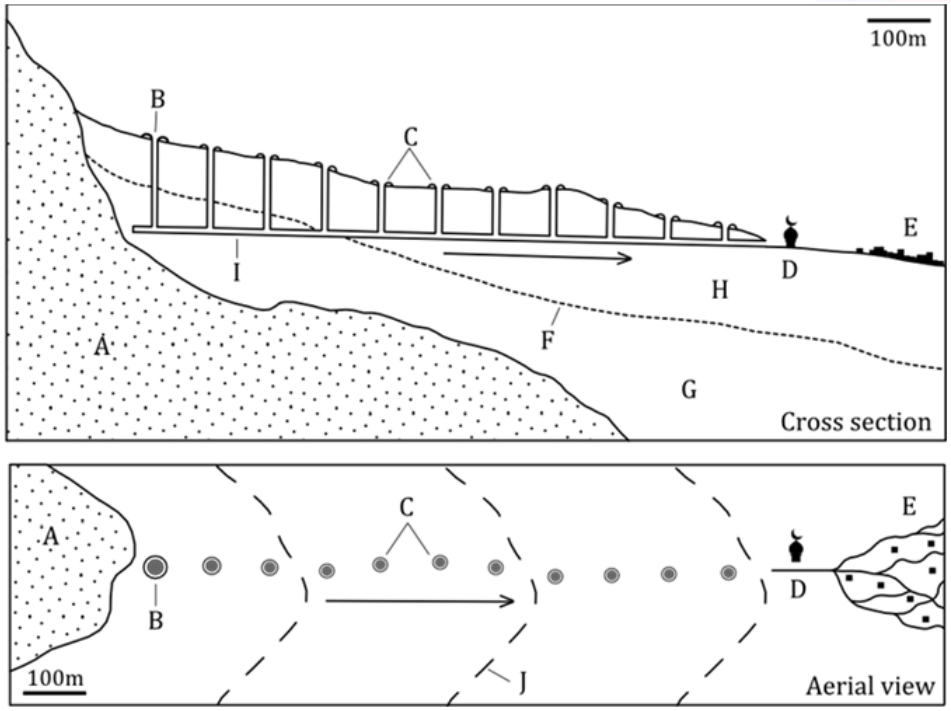

Figure 2.4. Schematic diagram of a qanat system showing the cross-section of the internal layout (top) and the aerial view (bottom) (after Beaumont 1971). The arrow indicates the direction of flow downslope. The topography is shown by the arbitrary contour lines labelled as J in the aerial view. Different features shown in the figure include: A) bedrock, e.g. limestone, B) motherwell, C) qanat shafts, D) mosque, E) village and small gardens/fields/oasis, F) water table, G) fine-grained alluvium, H) coarse-grained sand and gravel, and I) adit.

a primary well (motherwell) located on the hillside (Beaumont 1971). Several vertical shafts were then excavated and connected by a horizontal channel or adit to navigate water to irrigate fields in the dry open plain and to villages and mosques (Fig. 2.4).

Chronology and climate

The origins and spread of qanat technology have been widely debated (Lightfoot 2000; Magee 2005; Wilkinson *et al.* 2012). Traditionally, they were thought to have originated in northwest Iran, and spread by the Achaemenid Empire (Laessøe 1951), however, as mentioned above, these facts are now under debate, and it seems that climate factors such as dry periods could have had a main role in their spread. One of the earliest qanats found in Iran was dated to 2000 BC using luminescence (OSL) dating techniques (Fattahi 2015). This date corresponded to the Assyrian Empire and a major aridity event in the region (Cullen *et al.* 2000; Roberts *et al.* 2011). On the other hand, by

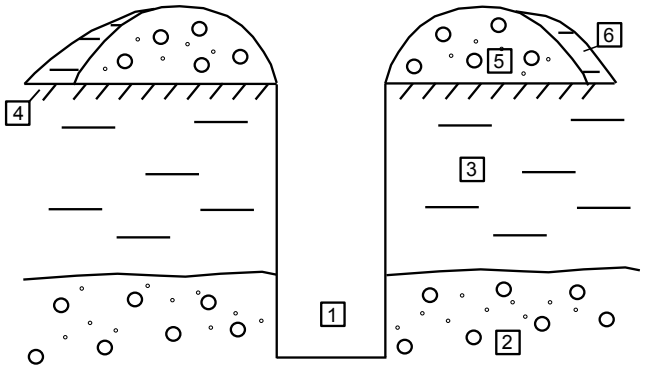

Figure 2.5. Schematic diagram showing the main components of a qanat and associated upcast deposits. 1) Vertical shaft, 2) fluvial sands and gravels, 3) fluvial silts and sands (alluvium), 4) old ground surface, 5) construction upcast, and 6) clean-out upcast.

the Seleucid and Parthian periods, there was little imperial interest in qanat technology, most likely due to enhanced precipitation rates during this period (Büntgen *et al.* 2011), requiring a different irrigation regime to manage surface water. Although limited, this evidence suggests that the construction and spread of qanats appears to relate more specifically to local environmental conditions rather than to imperial policy (Wilkinson *et al.* 2012). It is likely that during later periods of occupation, there was a renewed interest in the old qanat systems, particularly during the Roman and Sasanian periods in the Middle and Near East (Kamash 2012), when periods of enhanced aridity occurred (Büntgen *et al.* 2011), resulting in further demands on groundwater.

To fully understand the origins and spread of qanat technology, improved chronological resolution of these systems is required. Until recently, qanats have mainly been dated in association with Islamic (Wilkinson 1977; Lightfoot 1996), and Iron Age settlements (Costa 1983; Magee 1998; Al-Tikriti 2002; Magee 2005) or from surface artefacts (Costa & Wilkinson 1987). Overall, these approaches can provide a broad indication of the periods represented in the landscape, and that irrigation is likely to relate to periods of major settlement activity. Our understanding of the origins and maintenance of qanats remain unknown due to the limited dating evidence available. A recent study by Bailiff *et al.* (2015) demonstrated that luminescence dating (OSL) could be successfully used to illustrate the chronological complexity both within an individual mound and between different mounds within the same chain of qanats. This study raised the importance of understanding the deposits that comprise the upcast mounds (Fig. 2.5), which are similar to those found in canal upcast banks, but on a much smaller scale. To do this, small-scale excavation is required to assess the preservation, disturbance and repair, and how this may impact on the successful dating of these systems.

2.3 Summary

This review demonstrates the many complexities of many different landscape features found in the archaeological record in the Near East and surrounding regions. Although these various features have been discussed separately in this chapter, each component should be considered as part of a complete landscape. One particular problem is the issue of landscape palimpsest and archaeological visibility, as not all of these components survive in the archaeological record. Chronological uncertainties related to unstratified pottery and reworked organic remains in many of these contexts make it difficult to establish the relationship between irrigation and agriculture infrastructure to settlements. Radiocarbon dating is one method which is now routinely used for dating organic remains, and is the most suitable method for dating short lived material that remains in its primary context. However, when applied to canal fills or any other fluvial or colluvial deposit, organic material is affected by both sediment reworking and the recycling of 'old' carbon material. The latter is particularly problematic in arid regions where there is generally a lack of wood required for construction, resulting in the re-use of old wood in later periods. OSL dating methods are now becoming more widely applied in regions with suitable geologies and mineralogy. However, a greater understanding of irrigation and agricultural field systems requires excavation and geoarchaeological analysis to identify the various elements of construction, particularly for obtaining samples from secure and undisturbed contexts. This thesis aims to develop OSL dating further by placing the dates within their stratigraphic contexts, taking into account additional complications arising from post-depositional alterations of sediments that are commonly associated with anthropogenic contexts. The following chapter will introduce the broader geoarchaeological approach employed in this study.

Chapter 3
Geoarchaelogical background and methods

3.1 Introduction

Geoarchaeology is a subdiscipline of environmental archaeology, which brings together a wide range of evidence from archaeological landscapes, soils and sediments with the aim of understanding how societies in the past interacted with their environment (Brown 1997; Canti 2001; French 2003; Goldberg & Macphail 2006; Rapp & Hill 2006; Butzer 2008). Firstly, soils form as a result of the various interactions between different variables: climate, organisms, relief, parent material, and time, and are the final outcome of *in situ* weathering of the parent material (Holliday 2004; 102). Sediments, however, are deposited via aeolian, colluvial, fluvial (Allen 2012), and can be modified by a range of anthropogenic processes (Courty *et al.* 1989). The determination of the natural and anthropogenic processes that form an archaeological site or landscape can be complex, as they occur on various spatial and temporal scales (Butzer 1982; Schiffer 1987; Wilkinson 2003).

3.1.1 Scales of analysis

There are two main approaches employed in geoarchaological research. Firstly, the microstratigraphic approach, which involves the identification of site-formation processes and the local environmental conditions of a site or landscape feature (Matthews *et al.* 1997; French & Whitelaw 1999; Purdue *et al.* 2010). Secondly, 'off-site' landscape approaches, employ a macroscale approach, which utilises regional climate, environment and sedimentary archives to better characterise human-environment interactions in the past (Wilkinson 1997; Boyer *et al.* 2006; Berger *et al.* 2012; Heyvaert *et al.* 2012). Despite these contrasting approaches, and the various scales of data that that can obtained, a multiscale-multidisciplinary approach is the most useful, as it can provide a more holis-

tic understanding of the physical conditions that influenced how societies manipulated their environment in the past (Butzer 1982). The following sections will outline the methodological approach employed in this study, followed by the field and laboratory methods used to characterise the sediments and soils sampled in the field.

3.1.2 Methodological approach

The multiscale approach employed by the *Persia and its Neighbours Project*, enabled targeted investigations within relatively small and well-defined regions with clear evidence for Sasanian landscape investment (see Chapter 1). However, the lack of excavation and the chronological uncertainties associated with relative dating methods employed in the field (see Chapter 2) required further investigation of the landscape features identified using remote sensing and landscape survey methods. Therefore, this thesis aims to employ luminescence and geoarchaeological methods in order to better understand the chronology of landscape features identified in the case studies introduced in Sec. 1.1.1. of the various landscape features introduced in Chapter 2. Sediment mixing and disturbance is highly probable in regions that have been intensively utilised and is problematic for many dating techniques. Radiocarbon dating of charcoal and mobile short-lived material such as seeds, can be easily eroded form their original depositional contexts, and then transported and redistributed by various physical processes. Luminescence dating techniques (OSL), however, employs mineral grains as the chronometer. Disturbance can influence the overall precision, requiring a careful assessment of the OSL data (see Chapter 5). Therefore, the success of these techniques requires an assessment of the stratigraphy and site-formation processes prior to sampling in the field. This is to ensure that only secure archaeological contexts are sampled for dating. This can only be achieved using a combined luminescence and geoarchaeological methodology, which this thesis aims to develop.

3.2 Fieldwork methodology

3.2.1 Site identification

As part of the *Persia and its Neighbours Project*, the landscape analysis involved the acquisition and processing of CORONA satellite imagery (declassified spy imagery acquired in the 60s and 70s) (following Galiatsatos 2009, topographic data provided by the Shuttle Radar Topographic Mission (SRTM) at 30 and 90m resolution, historical maps and textual references to sites, and site location data obtained in the field recorded by Ground Positioning Systems (GPS), all of which were managed within a Geographical Information System (GIS). High-resolution Google Earth^{TM} (GE) images are freely

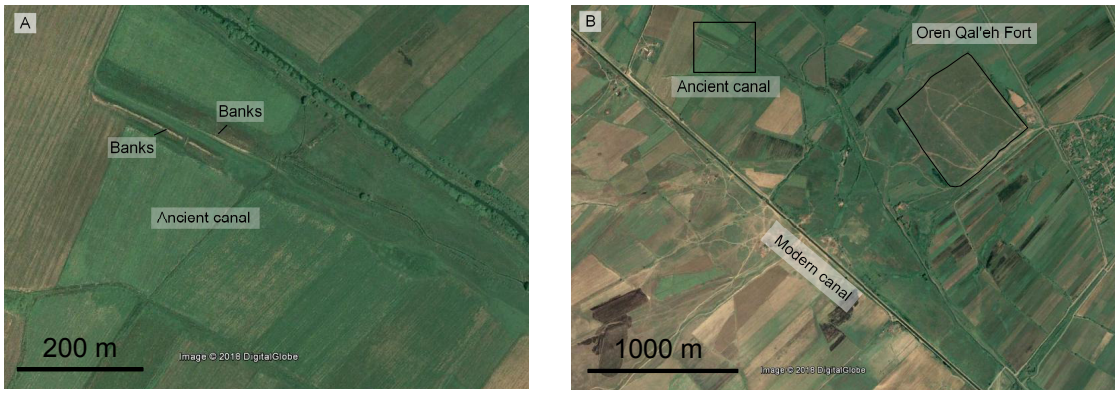

Figure 3.1. Examples of Google Earth^{TM} satellite imagery showing large-scale canals in the Mil Steppe, Azerbaijan. A) The area investigated showing the fort ancient canal in the modern irrigated landscape. B) A close-up image of the only surviving section of the ancient canal with preserved upcast banks. (Accessed 08/12/17) (© DigitalGlobe)

available (http://earth.google.com), and were used to assess the impacts of modern agricultural intensification for the detection of ancient irrigation and field systems prior to fieldwork.

Intensive modern agriculture has had a significant impact on the archaeological landscapes in the Caucasus and Central Asia, as illustrated in Fig. 3.1. GE is a useful tool for determining site preservation before entering the field.

3.2.2 Excavation

The excavation method was adapted according to the location, depth of deposits and time limits in each of the regions investigated. Small-scale excavation was employed in the Caucasus and Oman; only in situations where deposits were too deep to hand excavate, JCB excavation was employed. Large-scale canals and moat systems in Azerbaijan and Iran were machine excavated and step-trenched to provide safe access. The location of each trench was recorded using a hand-held GPS. Each case study was given a unique reference number (e.g. 412), and each stratigraphic section within each region was numbered accordingly (e.g. 412-9, 412-15). In situations where deposits were too deep to machine or hand excavate, coring using a gauge auger was employed. Further details of the excavation methodology are provided for each case study in Chapter 4.

3.2.3 Stratigraphic descriptions

Stratigraphic sections were first cleaned and photographed. Each deposit was given a unique context number, with which artefacts could be easily related. The stratigraphy was described using a combination of a lithostratigraphic approach similar to that outlined in Jones *et al.* (1999), soil characterisation (USDA 1975), and the single-context recording system (MoLAS 1994). Each archaeological context (sedimentary deposit) was described, which included: munsell colour (Munsell 1954), texture (proportions of sand-silt-clay) and other sub-classes, e.g. sandy silt, sorting, frequency of coarse-inclusions and their roundness and shape (Powers 1953), and boundary type (sharp or diffuse) (USDA 1975). Evidence for secondary mineralisation, e.g. carbonates, silicates and iron oxides, was also noted. Although the sedimentary descriptions were qualitative, they provided a basic assessment of the site-formation processes in the field. Deposits were defined as contexts in order to relate artefacts within their stratigraphic position for relative dating purposes.

3.2.4 Sampling strategy

The type of sampling strategy employed varied according to the variability in deposits found and the scale of features investigated. For the field and terrace systems, a systematic sampling strategy was employed. Sampling at regular intervals through the vertical profiles enabled the detection of subtle variations between the contexts that were not clearly visible in the field sections. A targeted sampling strategy was employed for occupation deposits, channels and canals due to the lateral and vertical variability of the deposits uncovered.

3.2.5 Sample collection

OSL sampling

OSL sampling methods followed Duller (2008b), which involved inserting a black plastic (PVC) pipe into the stratigraphic section to sample contexts for dating, taking care to avoid boundaries and areas of disturbance. For thick deposits, a standard OSL tube sample size was employed; ca. 20 cm long by 4 cm wide, that was inserted into the deposit. In relatively shallow deposits, a small tube was used (ca. 20 cm long by 1.5 cm wide). The ends of the tube were sealed with black duct-tape to avoid light exposure, labelled and marked on the section drawing. Each sample was photographed prior to removal. An additional sediment sample was taken from deposits above and below the context for environmental dosimetry analysis.

Micromorphology sampling

Micromorphology blocks were taken from key contexts in conjunction with OSL samples. The method followed similar procedures outlined in Goldberg & Macphail (2003). This involved carefully excavating a block usually of various sizes depending on the thickness of the deposit, most blocks were between 10 to 15 cm in length, 10 cm wide and between 8 to 10 cm thick, this was to ensure that enough material was extracted for micromorphology and OSL analysis where necessary. Prior to removal, each block was recorded on the section drawing and then photographed. Each block was encapsulated with plaster-of-paris and then carefully removed when fully dried. Each block was carefully wrapped, labelled (site name, section number, sample number) and packaged for transportation.

Bulk sediment sampling

Bulk sediment samples were taken from contexts that were vertically deposited in order to detect changes with depth. Sampling involved removing approximately 30 g of sediment from the deposit and packed in self-sealed bags and appropriately labelled (site name, section number, sample number, context number and date). In vertical profiles, bulk samples were taken at every 5 cm intervals through the profile.

3.3 Bulk sedimentary techniques

Bulk sedimentary techniques are widely employed in geoarchaeological studies, as variations in grain size, magnetic susceptibility, bulk geochemistry, and organic content within a stratigraphic profile, are useful proxies for pedogenesis, anthropogenic disturbance, and palaeoenvironmental change (Chapter 16 in Goldberg & Macphail 2006). The following sections will provide the methodology for magnetic susceptibility, loss-on-ignition and particle-size analysis.

3.3.1 Magnetic susceptibility

Magnetic susceptibility can be simply defined as a measure of the degree to which a sediment or soil can be magnetised (Evans & Heller 2003). As this technique is relatively rapid and inexpensive, the presence and quantity of ferromagnetic minerals are used as a proxy for quantifying soil development and for detecting fire and burning in the archaeological record (Tite & Mullins 1971; Mullins 1977; Peters *et al.* 2001; Oldfield & Crowther 2007). It is also used as a paleoclimate indicator, particularly for windblown loess and palaeosols (Pye 1995; Maher *et al.* 2002; Lisa *et al.* 2012). Fine superparam-

agnetic (SPM) particles are formed by some of these processes, and these particles can be detected using low and high frequency dependent susceptibilities (Dearing 1994).

Methodology

Samples were first dried at room temperature and then ground to a fine powder and sieved using a 2 mm mesh to remove large particles to avoid influencing the magnetic properties of the sample (Dearing 1994). Cylindrical pots (10 ml by volume) were weighted before and after the soil samples were added and the nature and concentration of magnetic grains were measured under low (0.47 kHz) and high (4.7 kHz) operation frequencies using a Bartington MS2B susceptibility bridge producing a 0.1 mT alternating magnetic field (*ibid.*). Mass-specific susceptibility (χ^{in}) ($10^{-8}m^3kg^{-1}$) and frequency dependent susceptibility (κ^{fd}) (%) values were calculated following Dearing (1994). Mass specific susceptibility (χ^{in}) was calculated as follows:

$$\chi^{in} = \frac{\chi^{lf}}{SM}/10 \tag{3.1}$$

where χ^{lf} is the average low frequency value and SM is sample mass in grams (g). Frequency dependent susceptibility (κ^{fd}) was calculated as follows:

$$\kappa^{fd} = \frac{\chi^{lf} - \chi^{hf}}{\chi^{lf}} \times 100 \tag{3.2}$$

Where κ^{fd} is susceptibility, χ^{lf} is the average low frequency and χ^{hf} is the average high frequency.

3.3.2 Loss-on-ignition (organic matter %)

Organic matter is the most important soil component which influences both the physical and chemical properties of a soil. Loss-on-ignition (LOI) is used to determine the percentage of organic matter, and is a relatively simple procedure (Ball 1964; Heiri *et al.* 2001; Beaudoin 2003). It is a useful measure for quantifying soil development and sediment accretion rates, and also the identification of unconformities and hiatus events within a continuous stratigraphic sequence (Goldberg & Macphail 2006). The LOI samples were processed in the Sedimentology Laboratory in the Department of Geography, Durham University. The full methodology is provided in Appendix A.

3.3.3 Particle-size analysis

Grain-size is used as a proxy for determining the scale and intensity of depositional processes, particularly in fluvial environments (Allen 2012). Particle-size analysis is a

quantitative measure of the proportions of sand, silt and clay present within a sediment sub-sample (*ibid.*). Various methods are available with varying precisions and accuracies (Lewis & McConchie 1994; Kroetsch & Wang 2008). A laser granulometer was employed in this study (Blott & Kenneth 2006). Measurements were made using a Beckman and Coulter LS230/13320 laser granulometer using laser diffraction with polarization intensity differential scattering (PIDS) based in the Geography Sedimentology Laboratory, Durham University, following procedures outlined in Coulter (1994).

3.4 Microstratigraphic analysis

3.4.1 Micromorphology

Micromorphology enables analysis of undisturbed samples at various magnifications. The method was first established by Kubiëna, which then evolved into a routine technique for soil science (Kubiëna 1948; 1953) and is now widely applied to archaeological contexts since the development of standardised description methods (Bullock *et al.* 1985; Courty *et al.* 1989; Stoops 2003). Ethnographic and experimental data has made significant improvements in the identification of features that can be directly related to agency processes in the archaeological record (e.g. Milek 2012; Banerjea *et al.* 2015; Deák *et al.* 2017). Furthermore, an understanding of the chemical processes in soils and archaeological sediments is useful for identifying post-depositional alterations and secondary mineralisation, which may include calcium carbonate, silicates (e.g. microcrystalline authigenic quartz), sulphates (e.g. gypsum), and iron oxides (e.g. geothite) (Stoops *et al.* 2010). The archaeological contexts sampled from various features in the four case studies, includes:

- Occupational deposits with middens and trampling layers.
- Anthropogenic dumping and mound construction.
- Alluvial, colluvial and aeolian deposits.

As there has been no previous micromorphological examination of similar features found in the four regions investigated, comparisons had to be made with those found in different regions.

Methodology

Micromorphology block samples were dried at room temperature and impregnated with resin to produce a cured block (75 x 50 x 3 mm). A representative thick section ($\sim$ 1 cm

Stage 1	Field descriptions	See Sec. 3.2.3
Stage 2	Thin section examination (X1 magnification)	Scanning, identification of macrostructure, level of heterogeneity, thickness, colour, boundary types.
Stage 3	Observations and descriptions (X4, X25, X40, X100, X200/400)	Microstructure: type, size, shape of aggregates, frequency (%).
		Groundmass: c/f ratio and related distribution, coarse components (organic, mineral and anthropogenic), micromass (colour, b-fabric, limpidity).
		Pedofeatures: type (depletion, crystalline, coating, aggregates), frequency (%), texture, distribution.
Stage 4	Interpretation	Identification of deposit type (DT) and their frequency of occurrence in thin sections, relate micro-analysis with macroscale observations.

Table 3.1. Stages of thin-section analysis.

thick) from this cured block was prepared into a thin section (30 μm thick), which was achieved using precision machinery, involving various stages of cutting, slicing, grinding and polishing to produce a finished thin section by Julie Boreham at Earthslides, following similar procedures outlined in Murphy (1986). A high-resolution flatbed colourscan at 900 dpi was obtained using an Epson Perfection V350 photo scanner. Thin-sections were examined in the DARC Laboratory using a Nikon Eclipse LV100 polarised microscope attached with a Nikon DS Fi1 digital camera. Observations were made under plane polarised light (PPL), cross polarised light (XPL), oblique incident light (OIL), between X4, 40, 100 and 200 magnification. Photomicrographs of key features were taken using Leica software V4.3. Slide descriptions followed the protocol similar to that outlined in Goldberg & Macphail (2008; 354-356), and following standardised criteria outlined in Bullock *et al.* (1985), Courty *et al.* (1989) and Stoops (2003) (outlined in Table 3.1). Frequency class for the coarse and fine material in a representative area and pedofeatures present follow Bullock *et al.* (1985).

Results

The results of the micromorphological analysis will be provided as part of the geoarchaeological assessment for each case study in Chapter 4. The quantification tables for features and inclusions identified in each deposit type for the contexts sampled are provided Appendix F.

3.5 Chemical characterisation

3.5.1 Mineralogy

Some of the main mineralogical components commonly found in sediments include major minerals such as quartz, plagioclase and potassic feldspar (K-feldspar), and clay and mica (muscovite and biotite) minerals (Allen 2012). Sediments also contain a range of heavy minerals (>2.75 g cm^3) that can vary in abundance: zircon, tourmaline, rutile, amphiboles, pyroxenes, garnet, epidote, olivine; and also iron oxides (hematite and magnetite) (Mange & Maurer 2012). Their relative abundance can vary with location and distance from the source rock, making them useful indicators of provenance (*ibid.*). Many of these minerals can be identified in micromorphological thin-sections, however, the frequency of minerals is affected by weathering, diagenesis and soil formation processes (Stoops *et al.* 2010), making them difficult to identify in archaeological deposits. In order to undertake a thorough assessment of the frequency of heavy minerals present, a prior knowledge of the local mineralogy and accessibility to control samples for comparison is required (Andó *et al.* 2012). A full mineralogical assessment was beyond the scope of this research, however, the identification and relative abundance of minerals present, along with roundness, surface textures and fabric analysis of quartz, was carried out in order to determine source and sediment history (e.g. mature or immature) (Powers 1953; Seyedolali *et al.* 1997; Vos *et al.* 2014) (outlined in Secs. 3.6.1 and 3.6.2). The following section will provide the physical and chemical background for the two major mineral types, quartz and feldspar, that are the most widely used chronometers in luminescence dating techniques (Aitken 1998).

3.5.2 Physical and chemical background of major minerals

Quartz

The chemical structure of quartz, silicon dioxide $Si0_2$, is tetrahedrally bonded $Si{+}0_2$ (Nesse 2009; 128) (Fig. 3.2). Quartz tetrahedra can be arranged in many ways, depending on temperature and pressure during formation of crystals (Dietrich & Skinner 1979; 32; Bøtter-Jensen *et al.* 2003b; 119; Preusser *et al.* 2009). There are two main types of quartz, α and β, which have different densities. β-quartz, also known as *high* quartz is formed at high pressure and temperature. When cooled down below 575°C, it transforms to α-quartz or *low* quartz, due to a change in the arrangement of the silica tetrahedra that form its structure (Dietrich & Skinner 1979; 32), as illustrated in Fig. 3.2; B. If this transition is fast the crystal maintains its shape (see Fig. 3.2; A). Trace elements can also replace Si within the tetrahedra structure, which can include: Ca, Fe, Ge, Mg, Mn, and Ti. The occurrence of these trace elements are diagnostic of specific

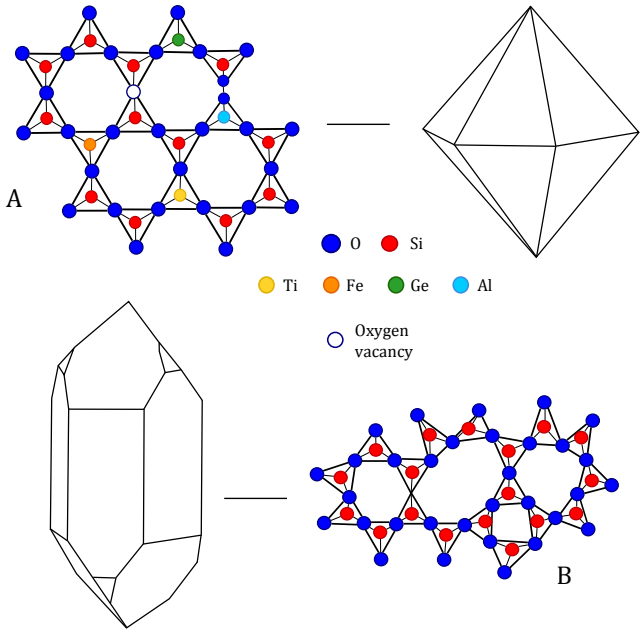

Figure 3.2. α and β quartz crystal structure. A: α-quartz crystal structure and form, including the main defects. B: β-quartz crystal structure and form. Adapted from Dietrich and Skinner (1979; 32).

source rocks e.g. volcanic, plutonic or hydrothermal (Preusser *et al.* 2009). As quartz crystal structure is constructed from SiO_4 tetrahedra, missing or replaced atoms, and the distortion of the structure, create specific defects, which influence the luminescence emissions observed in quartz (Götze *et al.* 2001) (Sec. 3.6.2).

Feldspar

The classification of feldspars depends on the chemical composition and the process of crystallisation. Feldspars are framework alumina-silicates with a chemical structure composed of SiO_4 and $Al0_4$. Feldspar chemical compositional ranges between $Na(AlSi_3O_8)$, $K(AlSi_3O_8)$, and $Ca(AlSi_3O_8)$ (Nesse 2009; 134) (Fig. 3.3). Feldspars vary between low-temperature and high-temperature phases. Feldspars formed at high temperatures cool rapidly (or quenched) preserving its high-temperature form, whereas low-temperature feldspars are formed slowly by slow cooling rates during crystallisation (*ibid.*). Where aluminium atoms replace silicon atoms, potassium (K), sodium (Na) and calcium (Ca) cations are inserted into the lattice. The variability in chemical and physical structure of feldspars is defined using a ternary diagram (Fig. 3.3). The ternary diagram is defined by the end members of albite-orthoclase (Ab-Or), which are high-temperature alkali phase feldspars. Albine-anorthite (Ab-An) are classified as low-temperature plagioclase feldspars. Feldspars can have ordered and disordered structures, for example,

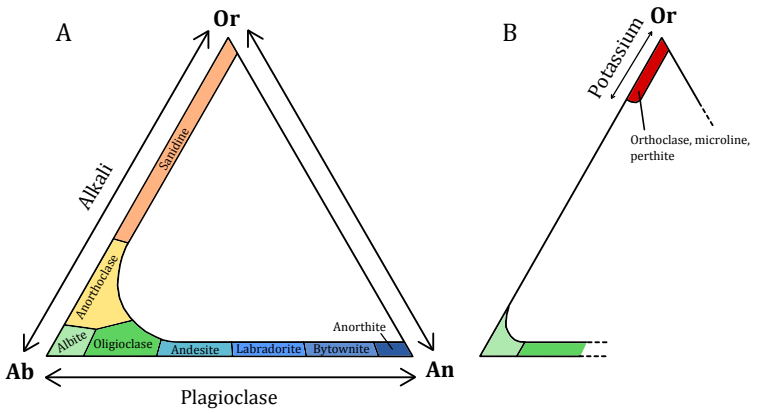

Figure 3.3. Feldspar ternary diagram showing the proportion of K, Na and C found in different phases. A: High-temperature feldspars, B: Intermediate and low-temperature feldspars. Adapted from Deer *et al.* (1963).

potassic-rich feldspars, also referred to as K-feldspars, tend to be ordered and triclinic (e.g. albite and oligoclase). High-temperature alkali feldspars that cool rapidly tend to be disordered and have monoclinic crystal structures (Finch & Klein 1999).

3.6 Analytical techniques

Characterisation of the mineral extracts - mainly quartz and feldspar - recovered from the archaeological contexts sampled, was undertaken to assess their suitability for further OSL analysis. Three analytical methods were employed: scanning electron microscopy (SEM) coupled with an energy dispersive x-ray spectrometer (EDS), and cathodoluminescence (CL). The following section outlines the methods used for the initial characterisation, which includes:

3.6.1 Scanning Electron Microscope (SEM) energy dispersive x-ray spectrometer (EDS)

Hydroflorically (HF) etched grains (200-355 μm) were hand-picked and mounted onto SEM stubs, carbon coated, and analysed using a Hitachi TM3000 scanning electron microscope fitted with a SwiftED2000 energy dispersive x-ray spectrometer (EDS) based in the archaeomaterials laboratory, Durham University. The compositional analysis of individual grains was obtained using SwiftED software, with standardless matrix corrections. Qualitative spectral details were obtained and compared with published spectra

available for common rock-forming minerals (Severin 2004). This technique enabled rapid identification and examination of the surface and morphology of grains after chemical treatment prior to OSL analysis.

3.6.2 Cathodoluminescence (CL)

Introduction

Cathodoluminescence (CL) is widely used in geology and the earth sciences to determine the formation histories and provenance of minerals relevant to sedimentology (Boggs & Krinsley 2006). Its applications to archaeological questions mainly cover the geological sourcing and provenance of raw materials used to manufacture artefacts (*ibid.*), and is used in the characterisation of heated quartz used in OSL dating of ceramics (Roque *et al.* 2004). CL analysis has also been used to check the purity of chemically-etched quartz extracts with poor luminescence characteristics (Steffen *et al.* 2009).

Luminescence in quartz and feldspar can be examined using four different excitation mechanisms, which include: optical and infrared stimulated luminescence and photo luminescence (OSL, IRSL, PL), thermal stimulation (thermal luminescence, TL), electron beam (cathodoluminescence, CL) and by β particles, e.g. radioluminescence (RL) (Bøtter-Jensen *et al.* 2003b). The emission spectra measured using these various forms of luminescence can provide important information related to the traps and defects associated with the production of luminescence in different minerals (Huntley *et al.* 1991; Clarke *et al.* 1997; Duller & Bøtter-Jensen 1997; Krbetschek *et al.* 1997; Rendell & Clarke 1997; Clark & Bailiff 1998; Götze *et al.* 2001). In this research, CL measurements were undertaken to provide insights into the provenance of quartz recovered from archaeological sediments in Georgia, Azerbaijan, Iran, and Oman.

CL colour of quartz has been widely used in provenance studies (Zinkernagel 1978; Matter & Ramseyer 1985; Götze *et al.* 2001), however, Zinkernagel (1978), was the first to identify a general increase in CL intensity with high temperature formation histories. The application of CL for identifying defects and traps related to trace elements present in quartz have been widely reported (Ramseyer & Mullis 1990; Kalceff & Phillips 1995; Götze & Zimmerle 2000; Götze *et al.* 2001; 2004; 2005). As for feldspars, which are much more complicated in terms of geochemistry and formation history, the spectral information varies according to the variations in K, Na, Ca and $Fe_3{}^+$ impurities (Finch & Klein 1999; Götze *et al.* 2000)

Methodology

Firstly, a plastic stub was drilled with a 4 mm hole, and a small amount of epoxy resin and untreated grains (200-355 μm) were mixed together and then left to set. Each stub

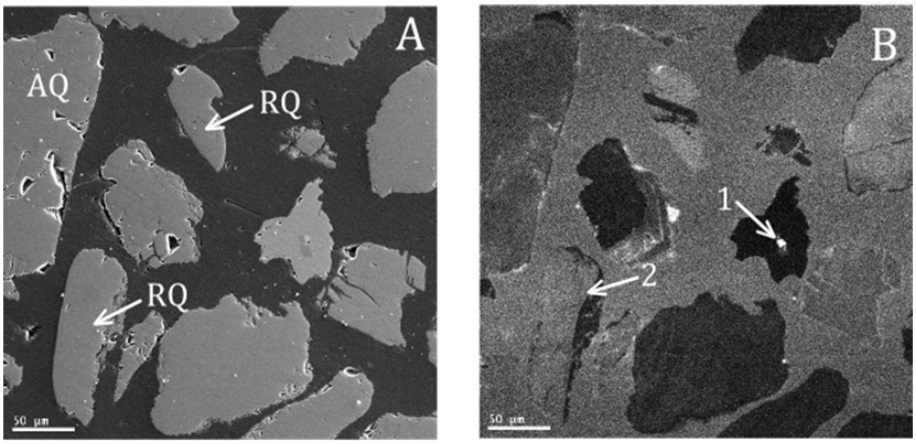

Figure 3.4. SEM backscatter and panchromatic images of quartz. A: SEM backscatter image within a 350 μm area showing multiple grains clearly showing differences in roundness, shape and size, rounded quartz (RQ), and angular quartz (AQ). B: Panchromatic image showing the variability in CL emissions between grains, 1 indicates brightly luminescent inclusion within a dim grain, and 2 indicates a coating on the quartz grain (Location: Azerbaijan).

was polished to a flat levelled surface in the rock thin section facilities in the Earth Science department at Durham University. Each stub was uniformly coated with carbon to remove change build up and prevent damage during electron bombardment. Analysis was undertaken using a Hitachi SU-70 FEG SEM based in the Department of Physics, Durham University. High-resolution images were taken using an SEM to obtain images of surface features using secondary electron and backscatter electron modes (Fig. 3.4). Detailed CL spectra was determined using Gatan MonoCL3 (Oxford Instruments) and a monochromator (Hamamatsu R374) by using a series of three colour filters (red >600 nm; Green 520-580 nm; Blue 400-480 nm) to identify different components with individual minerals in panchromatic view at 10 kV. Spectra were collected using a dwell time set at 3.0 s with a range between 400-500 nm (depending on the dominant component) and the step size was set at 2 nm.

Red-Green-Blue (RGB) false colour coded digital images were produced for visualisation purposes (Fig. 3.5). The intensity of the three primary colours were ranked from 0 to 4, 0 being absent and 4 being dominant and high in luminescence intensity. RGB combined with SEM images enabled the identification of the crystal fabric (Table 3.2); combined with this, emission spectra were obtained from a few grains emitting sufficient luminescence. Individual heterogeneous emissions and the optimal measurement conditions were obtained by concentrating the beam in small area within the grain surface (Fig. 3.6).

The assessment of CL colour is highly subjective, as the observed colours can fade or change after repeated electron bombardment. The common CL colours found in quartz

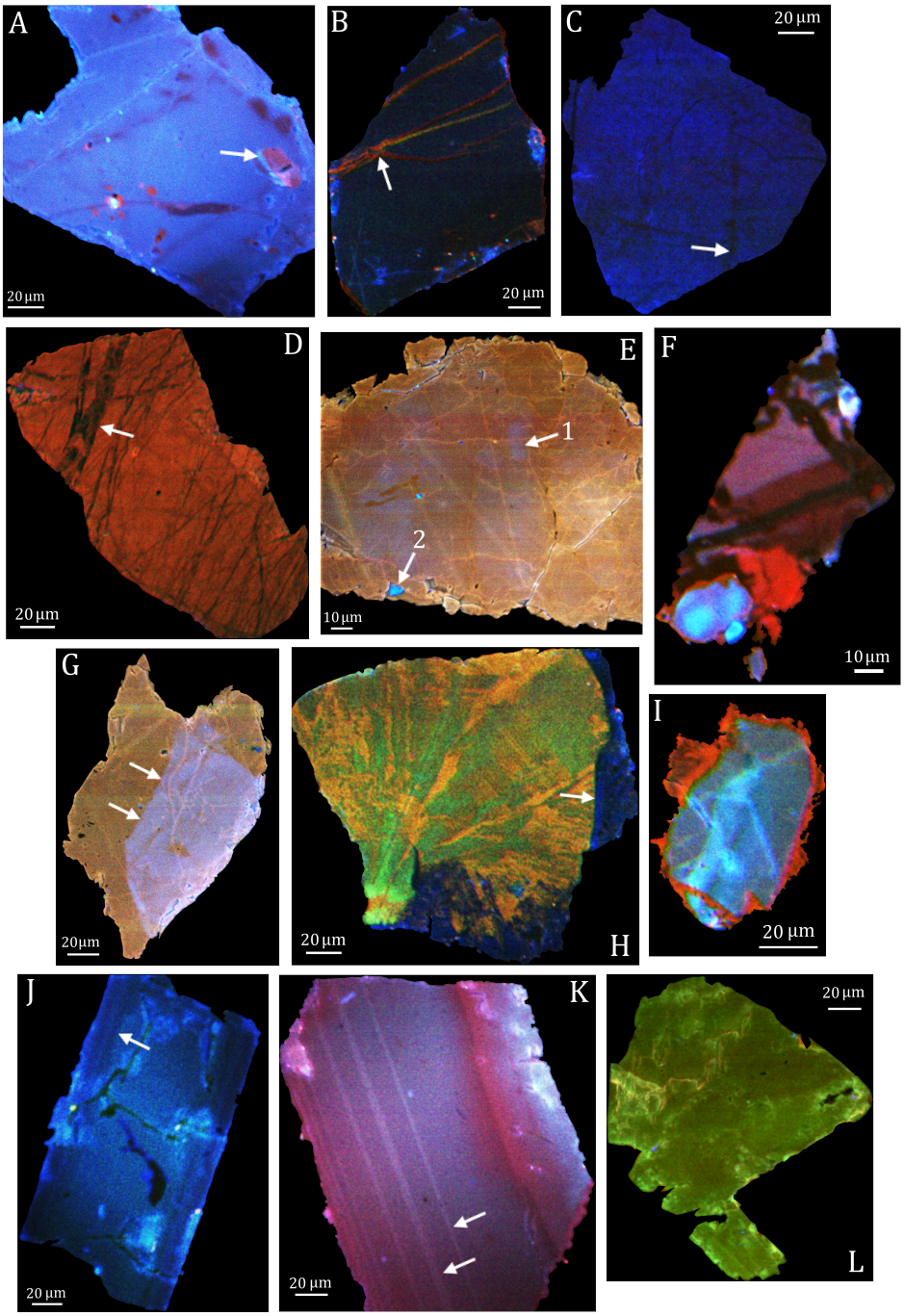

Figure 3.5. Cathodoluminescence images of quartz (A-I), and feldspar (J-L). Arrow indicates: A: feldspar inclusions, B-D: veins, E: 1 shows mottling of faint blue emission, 2: blue emitting overgrowth, G: reformed quartz (polycrystalline), H: hydrothermal quartz with a coating, J-K: feldspar internal structure.

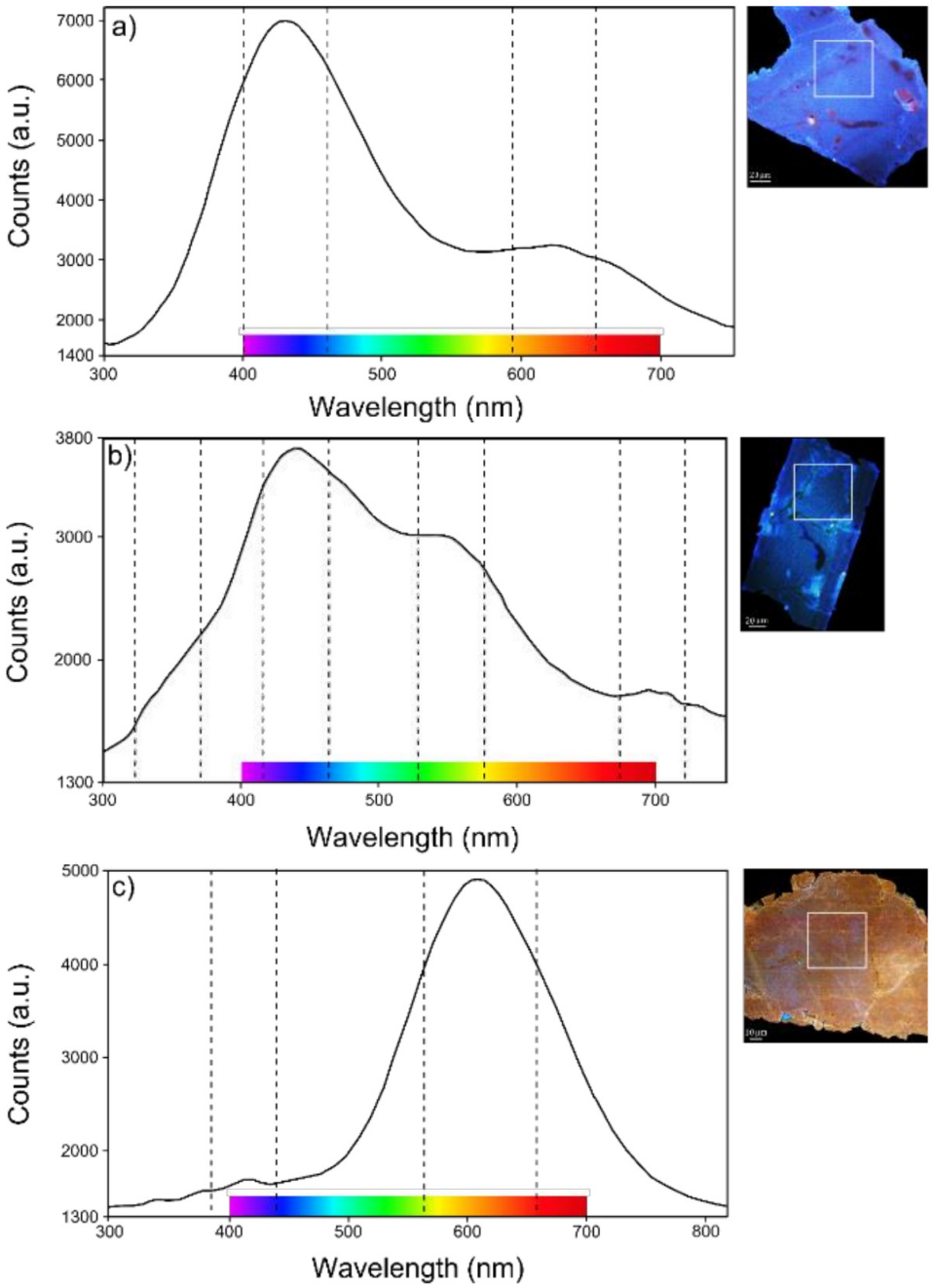

Figure 3.6. Examples of emission spectra obtained from three grains from Georgia. The white boxes on the cathodoluminescence images show the location of measurement. a) Quartz showing one dominant and one minor peak in the ultraviolet/blue and red regions of the light spectrum, b) potassic feldspar showing a broad emission spectra with peaks in the UV, blue, green and red regions, and c) quartz with a dominant peak within the orange region and a minor peak in the ultraviolet region.

summarised in Augustsson & Reker (2012) combined with the fabric analysis approach using SEM/CL combined as outlined in Seyedolali *et al.* (1997) and Boggs & Krinsley (2006), were used to aid the interpretation of the quartz and residual feldspars found in the archaeological samples. As defined by Seyedolali *et al.* (1997), fabric analysis enables a better method for identification of different quartz types, and these are defined as follows: 1) volcanic quartz typically displays zoning, 2) plutonic quartz often consists of patchy CL colour and dark veins or 'spiders' which are healed fractures, and sometimes this type of quartz can have a dark CL, 3) metamorphic quartz can contain closely spaced open fractures, also referred to a 'shocked quartz' and often has mottled CL, no CL can also be a common trait. The fourth type was hydrothermal quartz which tends to have complex zoning and has yellow-green CL (Götze *et al.* 2015).

The data gathered enabled a basic assessment of the provenance and formation history of the quartz in order to aid the OSL analysis, and the results and interpretation of CL colour and fabric found are presented in Table 3.2.

Sample	Grain number	Zoning	Polycristalline	Healed fractures	Open fractures	Spiders'	Mottling	Overgrowths	Coating	Homogeneous	Observed colour (RGB mix) See Fig. 3.5	Interpretation
412-9.1	1			•			•				Orange	3
412-9.1	2			•							Yellowish green	3
412-9.1	3				•						Pale blue	3
412-15.1.1	1			•	•		•	•			Light orange with patches of blue (**E**)	3
412-15.1.1	2		•	•				•			Light orange and pale blue (**G**)	3
412-15.1.1	3			•		•				•	Orange with black veins	3
412-15.1.1	4			•	•					•	Yellowish orange	2
412-15.1.1	5				•		•	•			Yellow with patches of blue	3
412-17.2	1			•							Orange	3
412-17.2	2			•			•				Blue with purple patches (**A**)	2
413-1.6.1	1			•			•				Yellowish green	2
413-1.6.1	2				•	•	•				Light orange with patches of blue	2
413-1.6.1	3	•			•			•			Orange	1
413-1.6.1	4			•					•		Colourless with red zones	3
413-1.6.1	5			•	•						Dark blue with red veins (**B**)	2
413-1.6.1	6				•						Light blue with patches of red	3
413-3.8	1			•		•					Red with black veins (**D**)	2
413-3.8	2			•	•	•	•				Light orange	3
413-3.8	3			•	•		•				Brown	3
413-3.8	4						•				Light brown	3
426-3.6	1			•	•	•	•				Patchy red	3
426-3.6	2			•	•		•				Patchy red	2
426-3.5	1			•	•	•	•		•		Pale blue with red coating (**I**)	3
426-3.5	2	•		•			•		•		Green and orange with blue coating (**H**)	4
426-3.5	3			•	•	•			•		Dark blue	2
426-3.5	4									•	Reddish brown	2
426-3.5	5			•	•						Yellowish green	2
426-3.5	6			•	•						Orange	2
426-3.5	7		•	•	•	•			•		Blue and red (**F**)	2
418-1.4	1				•				•		Pale blue	3
418-1.4	2				•						Colourless	3
418-1.4	3				•						Colourless	3

Table 3.2. Results of the cathodoluminescence analysis of coarse-grained quartz extracts. Interpretation: 1 = volcanic, 2 = plutonic, 3 = metamorphic, 4 = hydrothermal. Notes: 412 (Georgia), 413 (Azerbaijan), 426 (Oman) and 418 (Iran).

Chapter 4
Case studies

This chapter will provide the background for each case study region introduced in Sec. 1.1.1 and will provide the fieldwork results and geoarchaeological assessment of the contexts sampled for OSL dating.

4.1 Case study 1: The Dariali Gorge, Georgia

4.1.1 Introduction

The focus of the archaeological investigations in the Dariali Gorge, Georgia, was at Dariali Fort, a Sasanian military stronghold, located on the modern Georgia-Russian border (Fig. 4.1). The site has long been recognised for its strategic significance in the Caucasus from the late 4th century AD to modern times (Sauer *et al.* 2015). Excavation was undertaken at two main trenches (Trench F and Q) and several exploratory trenches surrounding the main site. The site produced a rich assemblage of artefacts and environmental remains, which enabled insights into the role of the fort and its connections with the southern Russian Steppe (*ibid.*). Considering the fort was located in a marginal and hostile environment, environmental remains and isotopic signatures from burials revealed that the occupants sourced raw materials and consumables that originated from warmer climates (*ibid.*), suggesting that people were mobile. Trade networks were also well connected between the lowlands and the highland regions of the Caucasus and the Dariali Gorge would have enabled the control and movement of trade.

4.1.2 Chronology and phasing

Numerous ^{14}C dates were obtained from multiple phases of occupation deposits uncovered in Trench F (Appendix B, Fig. B.1) (summarised in Table 4.1), providing a chronostratigraphic framework to test the OSL dating method. The positions of ^{14}C samples collected during excavation were located using a total station, but were not

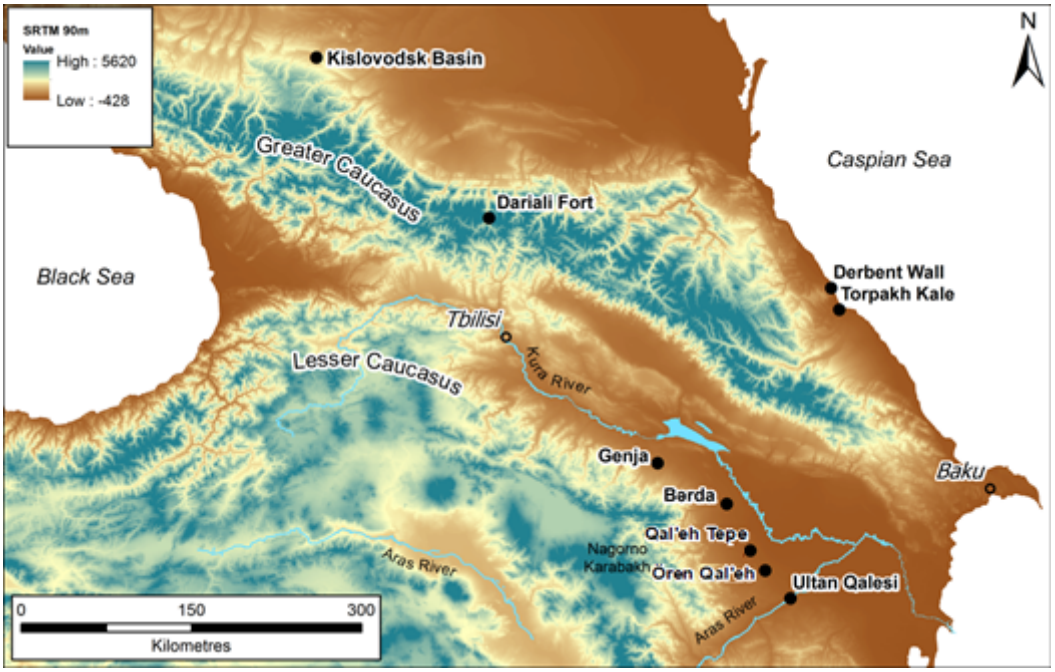

Figure 4.1. Map showing the location of Georgia and the main archaeological sites in the Caucasus.

sampled from the exact same positions as the other two methods employed. Archaeomagnetic samples were collected from the same locations as the OSL samples (Fig. 4.2), which include two burnt horizons (F.129) and (F.096), providing an opportunity to compare the three dating techniques. The radiocarbon results revealed that occupation of the fort was most intensive from the 4th to the 8th centuries AD, the site appears to have undergone multiple abandonment and reoccupation phases. Meanwhile, the wider landscape appears to have been more intensively occupied from the 15th to the 19th centuries AD (Hopper *et al.* in prep.) [1]. To gain a better understanding of the relationship between landscape features (terraces and field systems) and settlements, two sites, Tsdo and Kobi, were investigated further to test the application of the combined OSL dating and geoarchaeological methodology. The following sections will provide the physical and environmental background of the Dariali Gorge, combined with the fieldwork results and geoarchaeological assessment. The results of the OSL dating for Dariali Fort and the field systems will be presented separately (see Chapter 6).

[1]The results from the Caucasus are currently in preparation for publication as a chapter entitled 'Landscapes of the Dariali Gorge' for the Caspian Gates project monograph.

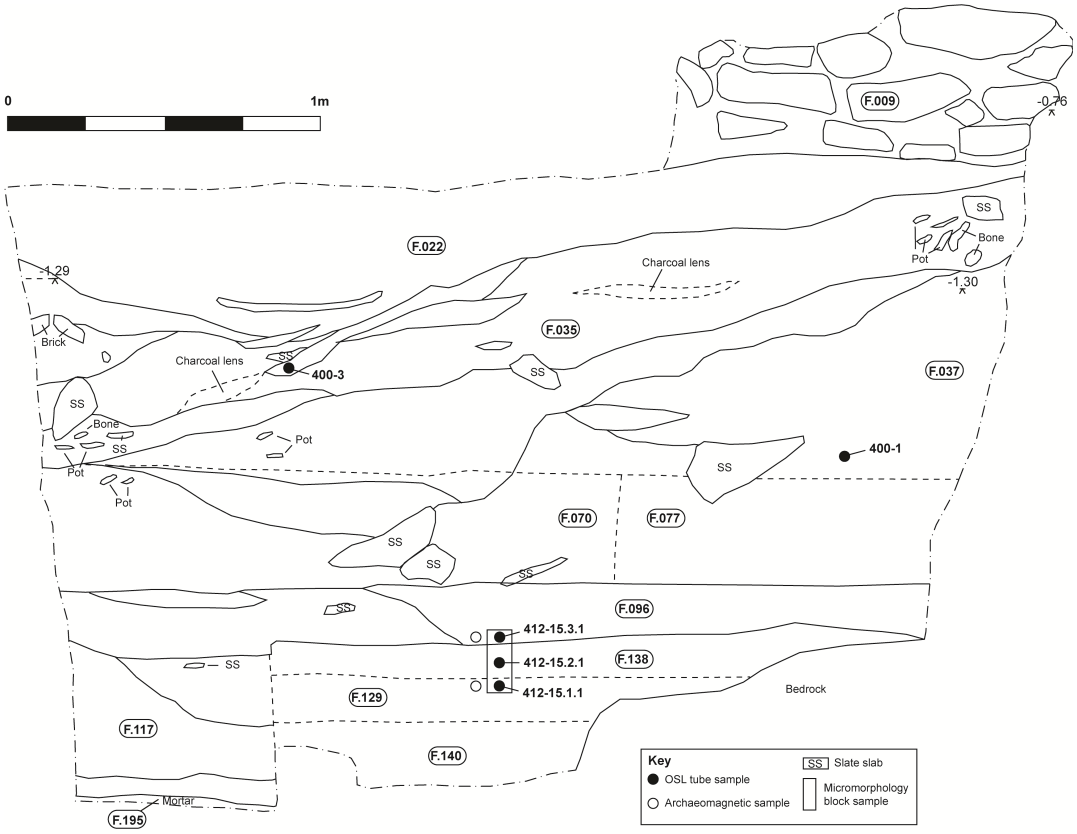

Figure 4.2. South facing section through archaeologicaloccupation deposits uncovered in the sondage from Trench F, showing the location of OSL tube samples (labelled 400-3 and 400-1) and block samples (labelled 412-15.3.1, 412-15.2.1, and 412-15.1.1), including the archaeomagnetic sample locations, obtained from archaeological contexts (labelled F.140 etc).

Phase	Period	Chronology
7	Post-Medieval/Modern	15^{th}-21^{st} centuries AD
6	Late-Medieval	11^{th}-15^{th} centuries AD
5	Early-Medieval	7^{th}-11^{th} centuries AD
4	Early-Medieval	7^{th}-8^{th} centuries AD
3	Late Antiquity	Late 4^{th}-7^{th} centuries AD
2	Prehistoric/Iron Age/Late Antiquity	$<4^{th}$ centuries AD
1	Natural	Geological

Table 4.1. Occupation phases (Trench F)

Figure 4.3. North facing view of the Dariali Gorge and the Tergi River.

4.1.3 Physical background

Dariali Gorge is located in the Kazbegi District in the Mtskheta-Mtianeti region of Georgia that borders Russia, with Stepantsminda being the largest village in the gorge (Fig. 4.1). The most prominent feature is Mount Kazbeg, which reaches an altitude of 5,033 m above sea level (a.s.l). Collisions of the Eurasian, Turkish, Iranian and Arabian plates exposed metamorphic, plutonic and volcanic rock and carboniferous shales, siltstones, and gravels of Jurassic age (Volodicheva 2002). The u-shaped gorge was formed by erosion of the underlying geology and sedimentary deposits during the last glaciation (Solomina *et al.* 2016). The gorge was later infilled by extensive colluvial fan deposits formed by landslides, rockfalls and avalanches, which were later dissected by the anastomosing Tergi River (Fig. 4.3). The region is also renowned for its springs and travertine deposits (calcareous tufa) (Lavrushin *et al.* 2006), which provide an additional source of water for occupants of the gorge.

Climate and environment

North Georgia receives up to 1500 mm of annual rainfall and temperatures range between -8°C and -4°C in the winter, and summers tend to be dry and relatively hot with temperatures between 16.5°C and 32°C (Connor & Kvavadze 2009), resulting in very short growing seasons for consumable crops. Pollen records revealed that the landscape was dominated by coniferous forests and high mountain grasslands during the Mid-

Late Holocene (*ibid.*). Local environmental indicators such as macrocharcoal, recovered from Trench F, included pine, pomegranate, walnut, lime and willow, suggesting that firewood was sourced from a range of environments beyond those found in the gorge (Poole 2014) Today, the vegetation is mainly dominated by herbs, shrubs and grasses, that are typical for Alpine regions (Nakhutsrishvili 2012), and the land is predominantly used for grazing and occasional small garden plots (Hanauer *et al.* 2017). Georgia has a variety of soil types within a small area due to significant vertical zoning, ranging from leptosols, cambisols, gleysols, umbisols, andisols, and histosols (Urushadze 1999). The Dariali Gorge is mainly dominated by humic mountain-meadow soil (umbrisols) (*ibid.*). Modern systematic soil survey of the region clearly showed that uplands areas dominated by mountain-meadow soils were classified as poor to very poor/unusable soils, and only small patches of land on recently occupied thick colluvial fans provide moderate to good quality soil for agriculture (*ibid.*). Therefore, these soils would have required significant improvements of the soil in the past (see Sec.2.2.2).

4.1.4 Fieldwork methodology

Landscape survey

The landscape survey ran approximately ca. 20 km south of the main excavations at Darial Fort. Extensive areas of well-preserved terraces and field systems were identified in the field using a remote sensing guided survey. Very little pottery was retrieved due to dense vegetation, which also hampered the visibility and access to sites. Each site found in the survey was given survey numbers (e.g. Darial Pass Survey - Site 8 = DPS-8) and recorded using a handheld GPS, described, photographed, and given individual waypoint (WP) numbers. The most abundant features preserved in the landscape were agricultural terraces, preserved on rock outcrops that overlooked the valley. The chronological relationship of the field systems to Dariali Fort was unclear on the ground. However, textual sources, which only become available after the landscape survey was conducted, suggested that some of the sites identified (DPS-6 and DPS-8) were established in the Late and Post-Medieval period (Itonishvili 1953; 135). These sources provide a broad indication of the period when the settlements and surrounding fields were occupied.

Excavation and sampling methodology

After site identification using remote sensing and field survey, terrace and field systems were 'ground truthed' to identify those with the best potential. Excavations took place in areas least affected by modern disturbance. At each site, slightly different excavation methodologies were employed, this included a combination of hand excavation, cleaning of naturally eroded sections, and machine excavation. Each trench (ca. 1 x 3 m) was

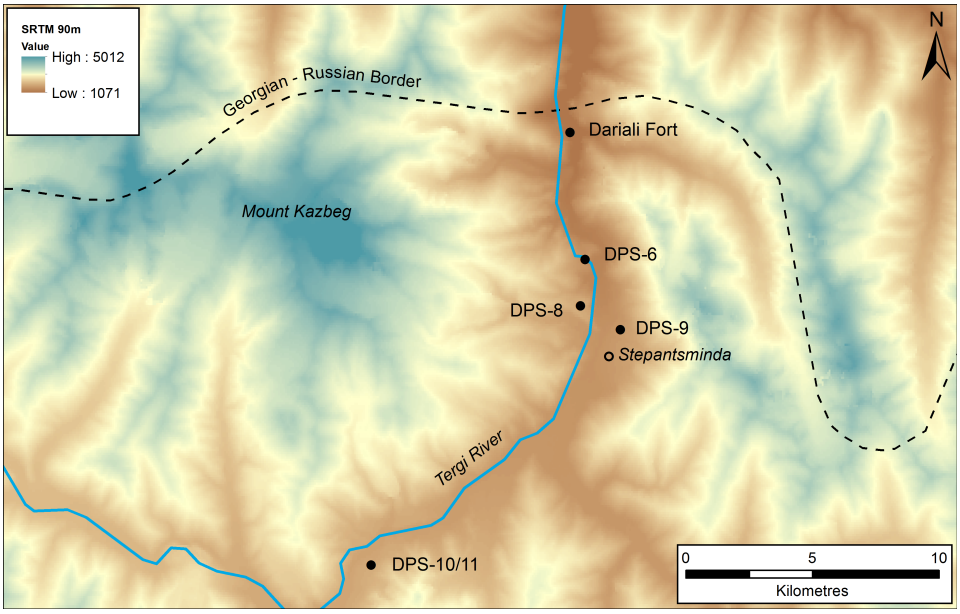

Figure 4.4. Map of Dariali Gorge showing the location of Dariali Fort, the modern village of Stepantsminda and other key sites identified in the landscape survey.

excavated perpendicular to the edge of the terrace and then down to the lowest accessible fill. At certain sites, the terraces were naturally eroding from the section undercut by the River Tergi. This meant that each section could be easily cleaned, recorded and sampled without full excavation. Each section was recorded at 1:20 scale on permatrace to show the thickness and extent of each context, including the location of samples taken. Each context was described using the description methods outlined in Sec. 3.2.3.

Part A: Terraces and field systems

Excavations of field and terrace systems identified in the landscape were undertaken at DPS-6, DPS-8, DPS-9, DPS-10 and DPS-11 (Fig. 4.4). The excavation results for each site are provided in the following sections.

4.1.5 Excavation results

Site DPS-6. The modern village of Tsdo is located on top of a high plateau at 1990 m a.s.l. and faced northeast (Fig. 4.5). Located next to the village was an extensive fortified settlement and a series of large stone-walled agricultural terraces. This settlement was suggested to have been occupied in the 15th century AD (Itonishvili 1971; 135-136), however, many of the architectural features of the fortified settlement resembled those

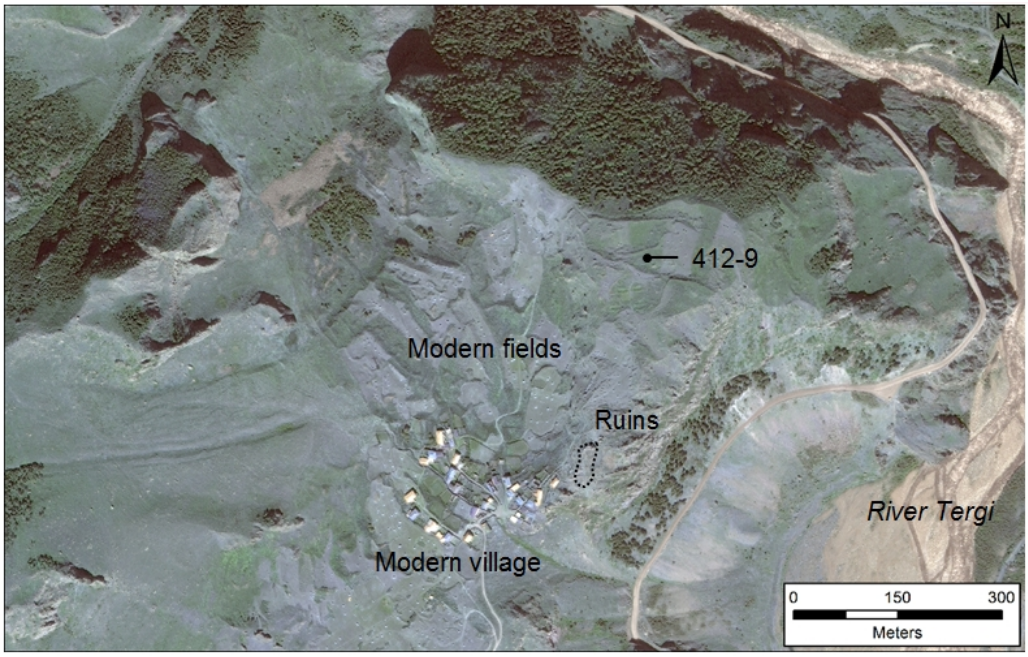

Figure 4.5. Site DPS-6 (Tsdo): Location of the terrace excavated and sampled (412-9).

found at Dariali Fort, suggesting that the site and surrounding terrace systems could have been much earlier in date. Due to their large scale and dense vegetation, the full extent of some of the terraces was not clearly visible on the ground. All terraces located at this site had large stone walls to support the riser. Due to the scale of the terraces, and accessibility issues, only one section was excavated (412-9) (Fig. 4.5).

The field descriptions of the contexts uncovered are provided in Table 4.2, and Fig. 4.6 illustrates the thickness and extent of each context found. The wall was constructed from unworked stone arranged to to enable the formation of deep soils. The terrace sequence formed on top of a volcanic (andisol) soil with preserved ash lenses, which had been later modified to form deep hortisols. After the wall construction, slope wash infilled behind the terrace wall to form a silty clay deposit (context 4). The abundance of highly abraded pottery and occasional fragments of charcoal, which may indicate middening processes. The pottery sherds recovered ranged from the 8^{th} to the 10^{th} and from the 15^{th} to the 17^{th} centuries AD and were similar to the assemblages found at Dariali Fort, providing relative dating evidence for the period of activity in the area. Charcoal fragments collected from this section were not processed as the samples were too small and fragmented. This particular terrace was most likely utilised to increase pastureland on the steep slopes of the rock outcrop.

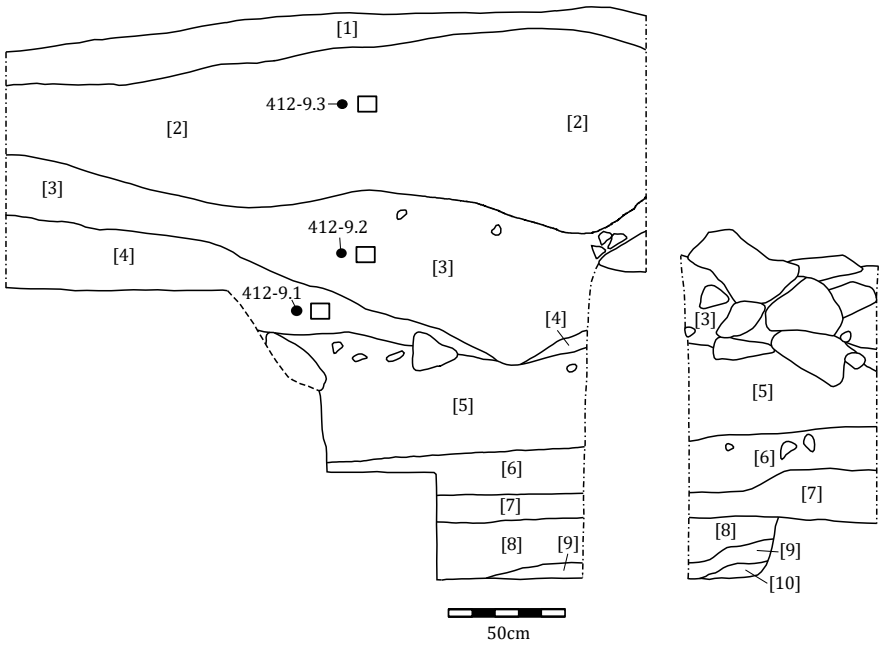

Figure 4.6. Site DPS-6 (Tsdo): Section drawing of deposits found in section 412-9 showing the location of OSL samples (412-9.1, 412-9.2 and 412-9.3) and micromorphology blocks (M1, M2 and M3).

Site DPS-8. The terraces at this site (Qobi) were located on another high basal plateau in the valley of the gorge located at c. 2032 m a.s.l. positioned facing to the East. This site consisted of an abandoned settlement, numerous field clearance cairns and extensive earthen terraces built on steep slopes (Fig. 4.7). Two terraces were excavated at this site, and both had deep humic mountain-meadow soils. Very little disturbance and reworking was found in section 412-17 (Fig. 4.8, Table 4.4), however, in section 412-16, remains of a collapsed wall was uncovered (Fig. 4.9). The sediments and soils preserved in these terraces were similar, a loose loamy silt located above a clay-rich deposit, which appeared to have been deposited by natural sediment aggradation (Table 4.3). Only one pottery sherd recovered; it came from context 5 in 412-16, and was from the 16th century AD. Compared to section 412-9, this terrace systems appears to have been used for the stabilisation of slopes, as very little anthropogenic material was recovered.

Site DPS-9. This area of terracing was located on an extensive colluvial deposit dissected by the Tergi River, positioned at ca. 1876 m a.s.l. The area had been extensively disturbed to make way for a modern gas pipeline and so investigations were restricted to the features found further upslope (Fig. 4.10). The area today is used for small garden plots and pasture (Fig. 4.11). The area also appeared to have been affected by

Harris Matrix

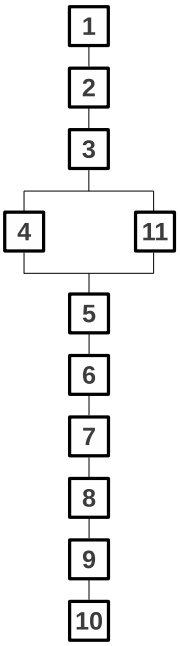

Context number	Depth (cm) (BGL)	Munsell soil colour	Description
1	0 - 13	Very dark greyish brown (10YR3/2)	Moderately compact, sandy silt with occasional gravel inclusions, moderately sorted, frequent roots, gradual boundary.
2	13 - 75	Light yellowish brown (10YR6/4)	Loose sandy silt, poorly sorted, occasional stone and pebble inclusions, some flecks of charcoal and carbonate, abundant pottery, gradual boundary.
3	75 - 127	Greyish brown (10YR5/2)	Loose and crumbly sandy silt, poorly sorted, occasional stones and pottery fragments, and frequent carbonate nodules occurred, sharp boundary.
4	127 - 145	Dark olive grey (5Y3/2)	Compact silty clay with occasional stones, moderately sorted, sharp boundary.
5	145 - 193	Dark yellowish brown (10YR4/4)	Compact sandy silt, poorly sorted, occasional stones and rock, one potsherd, sharp boundary.
6	193 - 211	Light olive brown (2.5Y5/4)	Compact silty loam, well sorted, occasional grit inclusions, sharp boundary.
7	211 - 222	Olive yellow (2.5Y6/6)	"
8	222 - 244	Grey (7.5Y6/1)	"
9	244 - 251	Olive yellow (2.5Y6/6)	"
10	> 244	Grey (7.5Y6/1)	Compact silty loam, well sorted, occasional grit inclusions, lowest boundary not fully excavated.
11	94 - 162	Wall	N/A

Table 4.2. Sedimentary descriptions for section 412-9 (DPS-6).

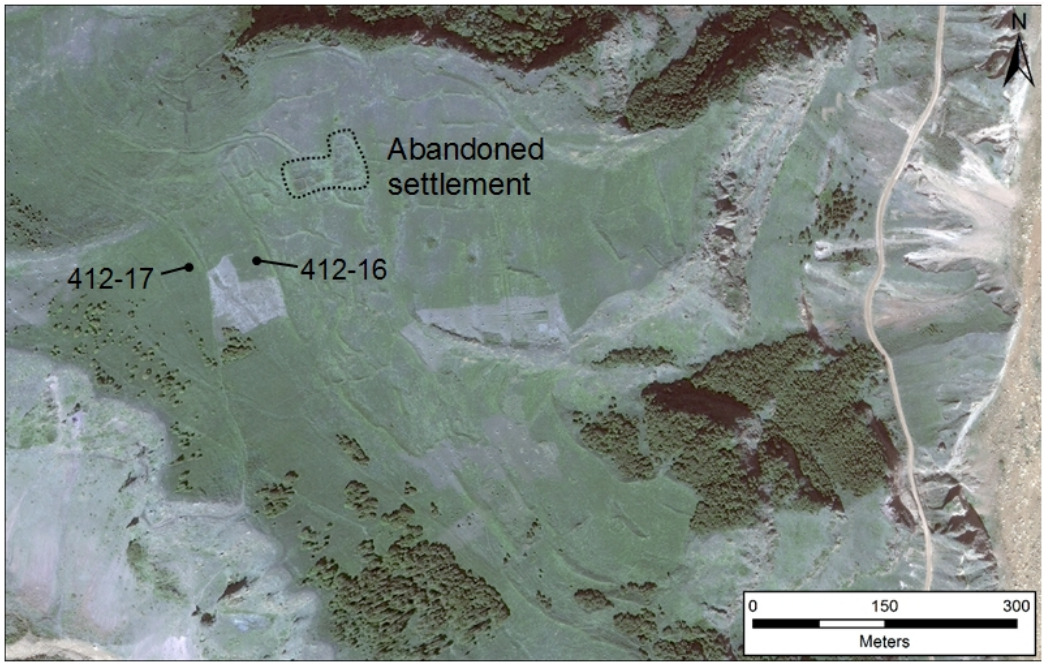

Figure 4.7. Site DPS-8 (Qobi): Location of terraces excavated and sampled (412-16 and 412-17).

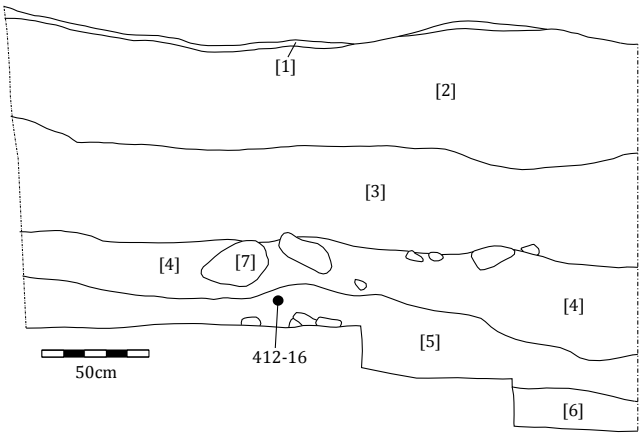

Figure 4.8. Site DPS-8 (Qobi): Section drawing of deposits found in section 412-16.

Harris Matrix

Context number	Depth (cm) (BGL)	Munsell soil colour	Description
1	0 - 5	Yellowish brown (10YR5/4)	Compact, sandy silt with occasional grit inclusions, moderately sorted,frequent roots, gradual boundary.
2	5 - 69	Very dark brown (10YR2/2)	Loose, loamy silt, moderately sorted, organic with frequent rootlets, frequent grit inclusions, gradual boundary.
3	69 - 118	Very dark greyish brown (10YR3/2)	Loose, loamy silt, moderately sorted, organic with rootlets, frequent grit inclusions, gradual boundary.
4	118 - 161	Very dark greyish brown (10YR3/2)	Loose sandy silt with pebbles and grit, poorly sorted, sharp boundary.
5	161 - 194	Dark greyish brown (10YR4/2)	Compact sandy clay, moderately sorted, occasional stones and grit inclusions, one potsherd, sharp boundary.
6	>194	Yellowish brown (10YR5/4)	Compact silty clay, well sorted, occasional grit inclusions, frequent calcareous nodules, lowest boundary not excavated.
7	159 - 179	N/A	Collapsed wall

Table 4.3. Sedimentary descriptions for section 412-16 (DPS-8).

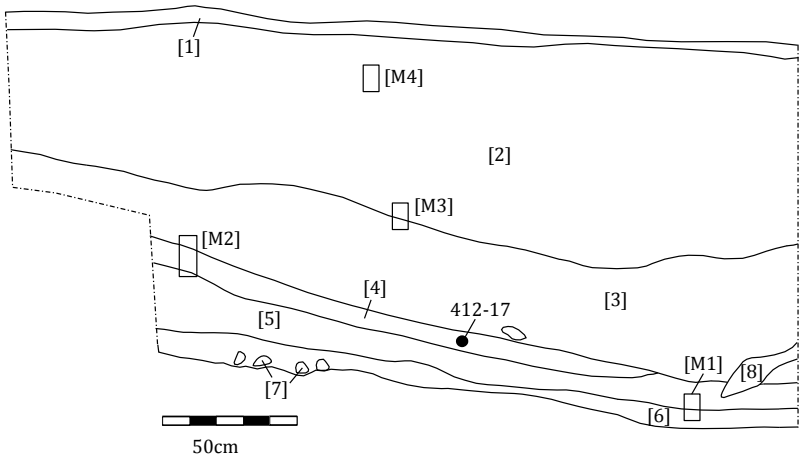

Figure 4.9. Site DPS-8 (Qobi): Section drawing of deposits found in section 412-17 showing the location of OSL samples (412-17.1 and 412-17.2) and micromorphology blocks (M1, M2, M3 and M4).

landslides and rock falls in the past, with extensive scree deposits that accumulated at the base of slopes. Two sections, 412-10 and 412-11, were hand excavated and two were machine excavated. The two machine excavated sections were not suitable for sampling, as the terraces were mainly composed of clearance stones. Both sections had very similar stratigraphy, which was thick, poorly sorted and stony (Fig. 4.12 and 4.13, Tables 4.5 and 4.6). The soils were broadly characterised as weakly developed regosols, of very poor soil quality and contained little organic material. Terraces appear to have been constructed for erosion control and was most likely used as rough pasture, similar to the land use commonly found in the region today.

Sites DPS-10 and DPS-11. Two sites, DPS-10 and DPS-11, are part of one terrace system located on an extensive colluvial fan (Fig. 4.14). Survey and excavation was focused at DPS-10 as it was the least disturbed by modern activity and slope erosion. The terraced fields gently descended East-West and were constructed on top of an extensive unit of glacial-fluvial terraces positioned at ca. 1966 m a.s.l. Most of the terrace risers were between 1-1.5 m high and were partially eroded by the Tergi River, exposing sections through the terrace fills. Three sections were recorded and sampled from natural exposures, 412-4, 412-7, and 412-8. The stratigraphic sections for the three terraces are illustrated in Figs. 4.15 - 4.17, and the descriptions are provided in Tables 4.7 - 4.9.

The terraces uncovered at this site mainly contained a thin layer of poor quality cambic umbrisols that formed above a thick unit of glacial-fluvial terrace deposits. One of the terraces excavated (412-7) had been reinforced with stones and rubble, which was not visible on the surface, reinforcing the need for small-scale excavation to confirm field

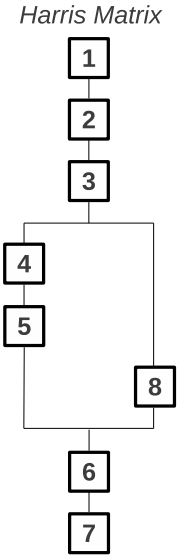

Context number	Depth (cm) (BGL)	Munsell soil colour	Description
1	0 - 5	Yellowish brown (10YR5/4)	Compact, sandy silt with occasional grit inclusions, moderately sorted, frequent roots, gradual boundary.
2	5 - 85	Dark greyish brown (10YR4/2)	Loose, loamy silt with frequent flecks of charcoal, pebbles and large stones, moderately sorted, gradual boundary.
3	85 - 118	Very dark brown (10YR2/2)	Moderately compact, sandy silt, moderately sorted, organic with rootlets, frequent grit inclusions, gradual boundary.
4	118 - 127	Very dark greyish (10YR3/2)	Compact sandy silt, frequent grit inclusions, moderately sorted, sharp boundary.
5	127 - 137	Dark greyish brown (10YR4/2)	Compact sandy clay, moderately sorted occasional stones and grit inclusions, sharp boundary.
6	>137	Yellowish brown (10YR5/4)	Compact silty clay, well sorted, occasional grit inclusions, lowest boundary not excavated.
7	>116	N/A	Compact stone layer, sub-angular in shape, 5cm in size, only exposed on the West side of the trench, continued beyond the limit of excavation.
8	116 - 129	N/A	Collapsed wall

Table 4.4. Sedimentary descriptions for section 412-17 (DPS-8).

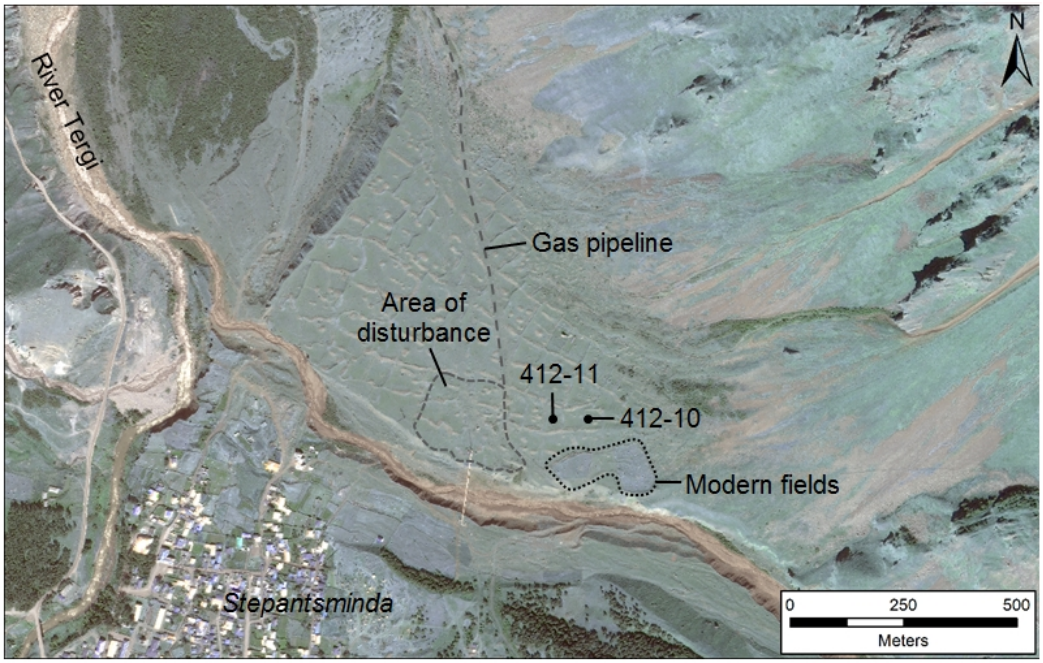

Figure 4.10. Site DPS-9: Location of terraces excavated and sampled.

Figure 4.11. Site DPS-9: View of the area of terracing (East facing).

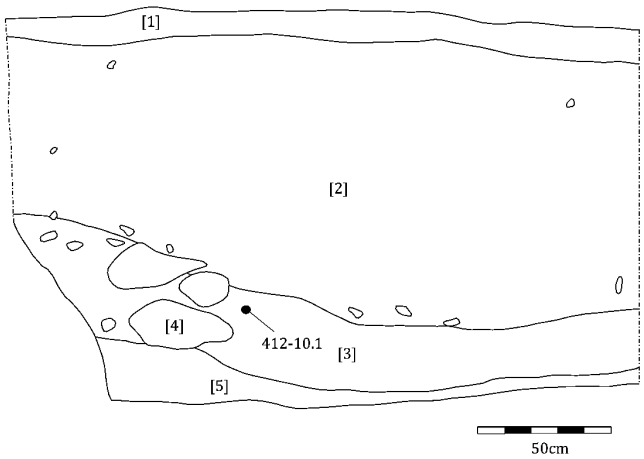

Figure 4.12. Site DPS-9: Section drawing through terrace sequence (412-10) showing contexts uncovered and the location of OSL test sample.

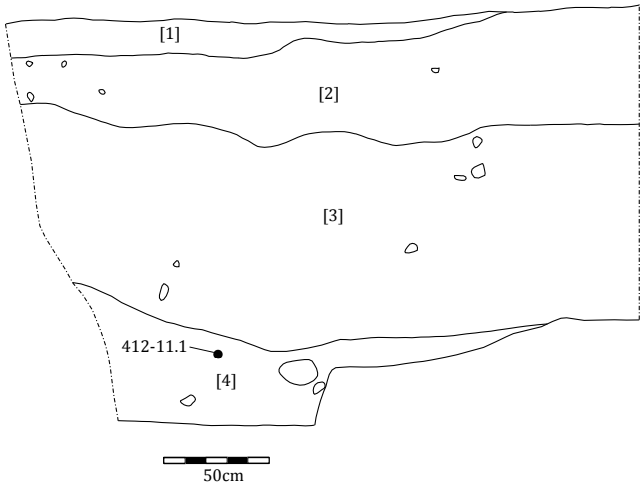

Figure 4.13. Site DPS-9: Section drawing through terrace sequence (412-11) showing contexts uncovered and the location of OSL test sample.

Harris Matrix

Context number	Depth (cm) (BGL)	Munsell soil colour	Description
1	0 - 8	Very dark greyish brown (5Y3/2)	Compact, silty clay with occasional gravel inclusions, frequent roots, gradual boundary.
2	8 - 105	Dark olive grey (5Y3/2)	Compact silty clay loam, poorly sorted, frequent pebble inclusions, gradual boundary.
3	105 - 137	Dark olive grey (5Y3/2)	Moderately compact sandy silt, frequent stones (slate), pebbles and pottery fragments, gradual boundary.
4	Collapsed wall	N/A	N/A
5	$>$ 137	Dark olive grey (5Y3/2)	Compact, silty clay, frequent pebble inclusions lowest boundary not excavated.

Table 4.5. Sedimentary descriptions for section 412-10 (DPS-9).

Harris Matrix

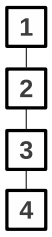

Context number	Depth (cm) (BGL)	Munsell soil colour	Description
1	0 - 16	Very dark greyish brown (5Y3/2)	Moderately compact, sandy silt with occasional gravel inclusions,moderately sorted, frequent roots, gradual boundary.
2	16 - 49	Dark olive grey (5Y3/2)	Compact sandy silt, poorly sorted, frequent pebble inclusions, gradual boundary
3	49 - 146	Dark olive grey (5Y3/2)	Compact silty clay, frequent stones and poorly sorted, gradual boundary.
4	146 - 191	Dark olive grey (5Y3/2)	Compact sandy silt with occasional large stones and frequent pebbles, poorly sorted, underlying boundary not excavated.

Table 4.6. Sedimentary descriptions for section 412-11 (DPS-9).

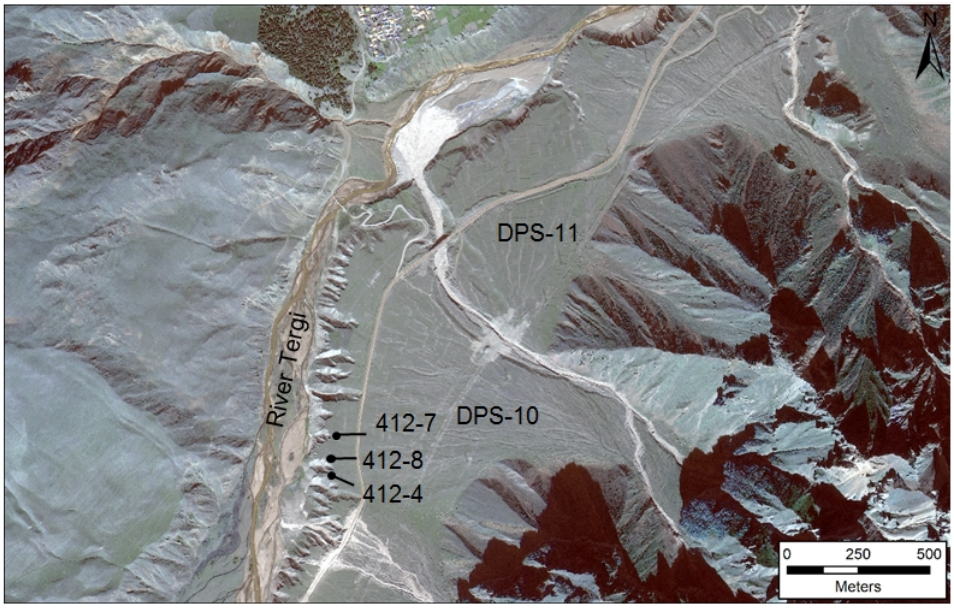

Figure 4.14. Sites DPS-10 and 11: Location of samples collected indicated in the satellite image.

survey results. Two buried soils were also noted in section 412-7 and section 412-4. No relative dating evidence was found on the surface of the field or from the terrace fills. Similar to those found at DPS-9, these terraces were most likely constructed for erosion control and stabilisation of the ground for rough pastureland.

Summary of the results

The excavations and field descriptions provided an insight into the variability in terrace and field formation in the Darial Gorge. The location and preservation of field systems found is related to a number of physical variables,such as location to proximity to a reliable water source and soil type (Table 4.10). The sampled locations with the most potential for obtaining well-preserved sediment stratigraphy were from thick terrace sequences located on top of high plateau sites (DPS-6 and DPS-8), located in areas currently occupied or that had been occupied in the past. Interestingly, the main function of terraces in this region was erosion control. This suggests that the landscape was prone to frequent landslides in the past that were triggered either by anthropogenic (deforestation and over grazing) or by natural gravitational slope processes. The accumulation of colluvium has implications for the preservation of landscape features that pre-date the post medieval/modern period, which appears to be the most dominant period of occupation in the gorge (Hopper et al., in prep), and a number of terraces appeared to have been rebuild. The rebuilding of terraces was most likely a response to increasing demands for pastureland in the region where soil quality is generally poor.

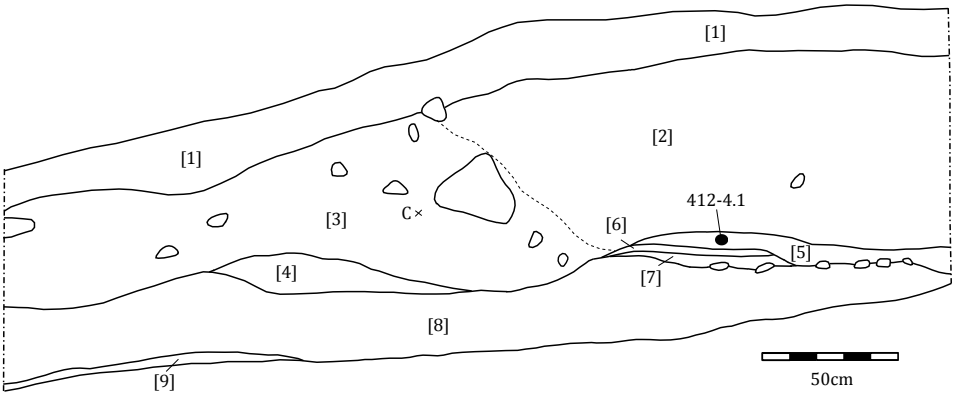

Figure 4.15. Site DPS-10: Terrace section 412-4 showing the location of charcoal (labelled C) and OSL test sample.

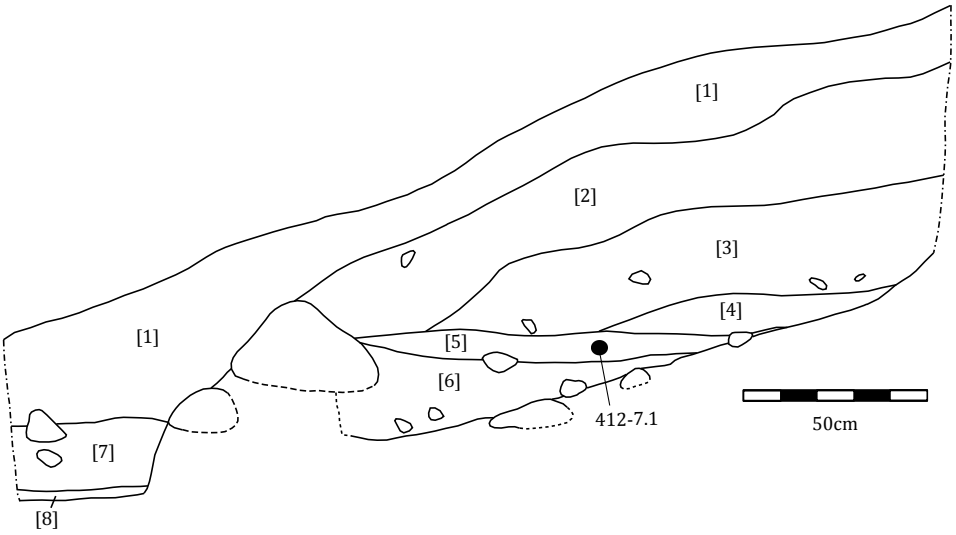

Figure 4.16. Site DPS-10: Terrace section 412-7 showing the location of OSL test sample.

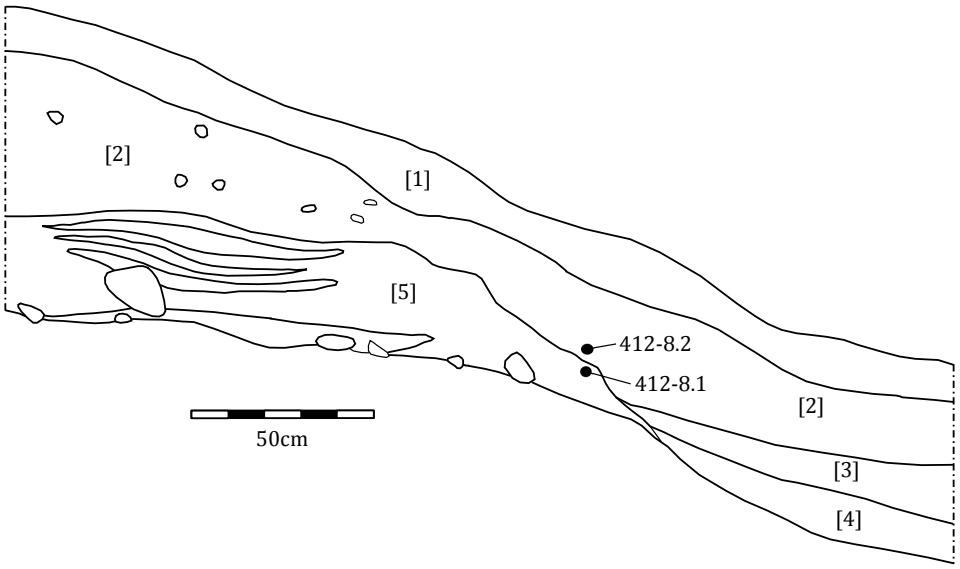

Figure 4.17. Site DPS-10: Terrace section 412-8 showing the location of OSL test samples.

Site number	OSL sections and samples	Archaeological features	Geomorphology	Water source
DPS-6	412-9-(1, 2, 3) (Terrace 4)	Terraces, settlement, underground tunnels, walls, fort	High basalt plateau (Andosol soil)	Slope runoff/ snowmelt
DPS-8	412-16 (Terrace 10), 412-17-(1, 2) (Terrace 18)	Field systems, settlement, trackways, possible irrigation channel and garden plots, animal pens	High basalt plateau (Mountain meadow soil)	Slope runoff/ snowmelt, spring water
DPS-9	412-10-(1), 412-11-(1)	Field systems, Post-Medieval-Modern church and field plots	Colluvial fan (mudstone, gravels and clay)	Slope runoff/ snowmelt
DPS-10	412-4-(1), 412-7-(1) and 412-8-(1,2)	Field systems, walls	Fluvial terraces (coarse sands and mountain meadow soil)	Slope runoff/ snowmelt, riverand spring water

Table 4.10. Summary of the sites and archaeological features mapped and surveyed, and the OSL samples collected.

Harris Matrix

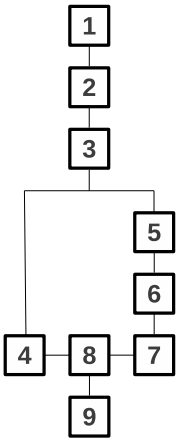

Context number	Depth (cm) (BGL)	Munsell soil colour	Description
1	0 - 17	Dusky red (2.5Y3/2)	Loose poorly sorted, frequent pebble inclusions, frequent roots,and gradual boundary.
2	17 - 68	Dark reddish brown (2.5Y3/3)	Soft and loose loamy sand, with visible silicate minerals, moderately well-sorted occasional granules, gradual boundary.
3	20 - 70	Dark reddish brown (2.5Y3/3)	Loose loamy sand, frequent pebbles and large stones, occasional charcoal, gradual boundary.
4	54 - 67	Dark reddish brown (2.5Y3/3)	Loose poorly sorted coarse sand and gravel deposit, gradual boundary.
5	68 - 74	Dark reddish brown (2.5Y3/3)	Compact, moderately sorted loamy silt, organic, sharp boundary.
6	74 - 77	Dark reddish brown (2.5Y3/3)	Compact silty clay deposit with occasional grit inclusions, gradual boundary.
7	77 - 90	Dark reddish brown (2.5Y3/3)	Compact silty clay deposit with occasional grit inclusions, sharp boundary.
8	90 - 121	Dark yellowish brown (10YR3/6)	Loose and poorly sorted coarse sand and gravel deposit, sharp boundary.
9	>85	Reddish brown (2.5Y4/3)	Compact, moderately sorted, fine and coarse sand, calcium carbonate present, lower boundary not excavated.

Table 4.7. Sedimentary descriptions for section 412-4 (DPS-10).

Context number	Depth (cm) (BGL)	Munsell soil colour	Description
1	0 - 13	Dusky red (2.5Y3/2)	Compact, loam silt with occasional gravel inclusions, frequent roots, gradual boundary.
2	13 - 43	Reddish brown (2.5Y4/4)	Soft and loose loamy sand, with visible silicate minerals, moderately well sorted with occasional granules, gradual boundary.
3	64 - 76	Reddish brown (2.5Y4/4)	Loose poorly sorted coarse sand and gravel deposit, gradual boundary.
4	43 - 50	Dark reddish brown (2.5Y3/3)	Compact, moderately sorted sands, sharp boundary.
5	50 - 74	Dark reddish brown (2.5Y3/3)	Compact, moderately well sorted loamy silt, occasional organic material and grit inclusions, sharp boundary.
6	>50	Reddish brown (2.5Y4/4)	Moderately compact, poorly sorted sand and gravel deposit. Lowest boundary not excavated.

Harris Matrix

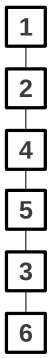

Table 4.8. Sedimentary descriptions for section 412-7 (DPS-10).

Harris Matrix

Context number	Depth (cm) (BGL)	Munsell soil colour	Description
1	0 -12	Dusky red (2.5Y3/2)	Compact, loam silt with occasional gravel inclusions, frequent roots, gradual boundary.
2	12 - 42	Reddish brown (2.5Y4/4)	Loose sandy silt loam, poorly sorted, frequent pebble inclusions, gradual boundary.
3	31 - 41	Olive brown (5Y5/3)	Moderately sorted sandy silt, gradual boundary.
4	41 - 53	Olive brown (5Y5/3)	Loose, poorly sorted sandy silt, gradual boundary.
5	42 - 72	Olive brown (5Y5/3)	Moderately compact, well sorted coarse laminated sands, lowest boundary not excavated.

Table 4.9. Sedimentary descriptions for section 412-8 (DPS-10).

4.1.6 Geoarchaeological assessment

The landscape survey and 'ground truthing' of terraces and fields enabled the best examples to be targeted for further analysis. A number of OSL test samples were obtained in order to be characterised and to identify those with the most suitable characteristics. The results of this analysis is provided in Chapter 6, Sec. 6.1.1. Based on this analysis, of the four sites investigated, two stratigraphic sections from DPS-6 and DPS-8 were investigated further. In order to place the OSL dates within their stratigraphic context, as assessment of the sedimentary characteristics was necessary to understand the site-formation processes and any the identification of post-depositional alterations, which may affect the evaluation of dose-rate for individual OSL samples. Magnetic susceptibility, organic matter and moisture content (%) measurements were made on subsamples taken at regular intervals (ca. 5 cm) through the vertical profiles to identify the site-formation processes. Combined with this macroscale analysis, a close examination of the micromorphological thin-sections were carried out to identify post-depositional processes and coarse inclusions relevant for OSL dating.

Bulk sedimentary results

The three bulk sedimentary characteristics will be discussed together to identify different site-formation processes within the two stratigraphic sections (summarised in Fig. 4.18).

Section 412-9. Organic matter, moisture content, magnetic susceptibility and particle-size analysis correspond relatively well with the contexts identified in the stratigraphy. Clear differences in the soil colour, texture and sorting enabled the boundaries between contexts to be easily defined (Fig. 4.18). The top three contexts (1, 2 and 3) correspond to the O and A soil horizons. These were generally dark greyish brown in colour with a sandy silt texture and loose to moderate compaction. The organic content showed a gradual decrease from the top down to ca. 60 cm below ground level (BGL) to 2% before increasing and then decreasing again at ca. 140 cm BGL. This context also contained abundant charcoal fragments and highly abraded pottery, which may relate to middening and ploughing activities. Contexts 2 and 3 had relatively stable χ^{in} values, which varied between 1.8 and 2 (10^{-8} m^3 kg^{-1}), and very little change was observed in the frequency dependent susceptibility measurements ranging from 3.8 to 4.2% with depth. The natural soil contains iron oxides of haematite and geothite which have shown to correlate with variability in climate, e.g. prolonged wetting and drying periods (Maher *et al.* 2002; 2003). A sudden drop in organic matter (OM) at ca. 140 cm BGL correlated with a spike in moisture content which increases from 12 to 14%, before decreasing back to 11%. This sudden increase marks the transition from the B horizon to the C horizon. The C horizon was recorded archaeologically as context 4, a dark olive grey silty clay deposit with sharp upper boundaries. The shift from the B to C horizon also revealed a drop in χ^{in} and κ^{fd} % values. This drop suggests an increase in coarse-grained diamagnetic minerals such as quartz within the matrix at 160 cm BGL. Below this deposit were multiple layers of yellow and grey silty clay deposits. These were clearly defined as volcanic ash deposits as they contained frequent glassy inclusions mixed with volcanic basalt and tuff. OM and χ^{in} fluctuated within these contexts, suggesting multiple short periods of deposition of volcanic material with variable geochemical characteristics. A general increase in κ^{fd} % and the occurrence of superparamagnetic (SP) grains also showed an increase with depth, suggesting a correlation between SP grains, volcanic ash deposits and also grain-size (increased silt %).

Section 412-17. This section was ca. 140 cm thick, and the limit of excavation defined by a stone and clay layer (context 7) (Fig. 4.18). The bulk analysis revealed an additional boundary not identified in the field, located at ca. 48 cm BGL within context 2. Unlike the topsoil, which was a compact yellowish brown sand silt, context 2 was a loose sandy silt loam soil with frequent flecks of charcoal and gravel inclusions. However, no obvious boundary could be identified in the field. At ca. 48 cm a sudden increase in moisture content was observed from 11 to 18%. From this depth to approximately 100 cm BGL, there was a gradual decrease in organic matter, also χ^{in} increased and the κ^{fd} values showed fluctuation. The latter suggests a period of instability of the soil surface; the presence of small flecks of charcoal may suggests local or regional burning. At 120

cm BGL, a second spike in organic matter was identified which correlated with context 4, a very dark greyish brown sandy silt deposit with frequent grit inclusions. Below this was context 5, which was also dark in colour but was a sandy clay deposit. This may correlate with the slight increase in organic matter found at 132 cm BGL. From ca. 88 to 132 cm BGL, κ^{fd} % increased before suddenly decreasing again from 5.8 to 3.8 %. Overall there was a general increase in the proportion of the sand with depth until 125 cm BGL until it became increasingly dominated by silty clay. This lowermost deposit was context 7, a yellowish brown compact deposit with frequent stones. This was the natural C horizon formed by colluvial slope processes.

Summary. The results of the bulk sedimentary analysis confirmed that both sequences were affected by different depositional processes. Section 412-9 appears to have been disturbed by either natural or anthropogenic processes at various stages in its formation, as confirmed by an increase in fine silts and clays within the first 50 cm of the stratigraphic profile. Underlying the terrace deposits was a substantial unit of volcanic deposits. Volcanic events would have caused significant impacts on the landscape stability, but after a period of stability, they formed highly productive soils that would have been intensively exploited in the past (Grattan 2006). Section 412-17 resembles a stratigraphic sequence that had formed by natural slope processes, as indicated by the gradual decrease in particle-size and magnetic susceptibility signatures from the base of the profile to the surface. The bulk techniques were able to confirm boundaries between different contexts, but also identified subtle variations in the stratigraphic profile that were not obvious in the field. The following section provides a summary of the micromorphological assessment of key phases of the two stratigraphic section.

Micromorphology assessment

In total, three deposit types were recorded from sequence 412-9, and four deposits were identified in 412-17. The following section will present the main characteristics identified in each deposit.

Section 412-9. Context 4 was a sandy silt dominated by a vughy microstructure (Fig. 4.19; A), with frequent channel voids and a porphyric related distribution. The coarse component was randomly orientated with an unrelated distribution and was relatively heterogeneous. It contained frequent sub-rounded charcoal inclusions, amorphous organic material and occasional shell fragments. The quartz:feldspar ratio was 80:20, and quartz appeared within all major size classes. Frequent large polycrystalline quartz grains were also found in the largest grain size range (>200 μm), which appeared to be weakly weathered, along with plagioclase and orthoclase feldspars, which also appeared to have been partially weathered. Zircons were present within the deposit, but formed

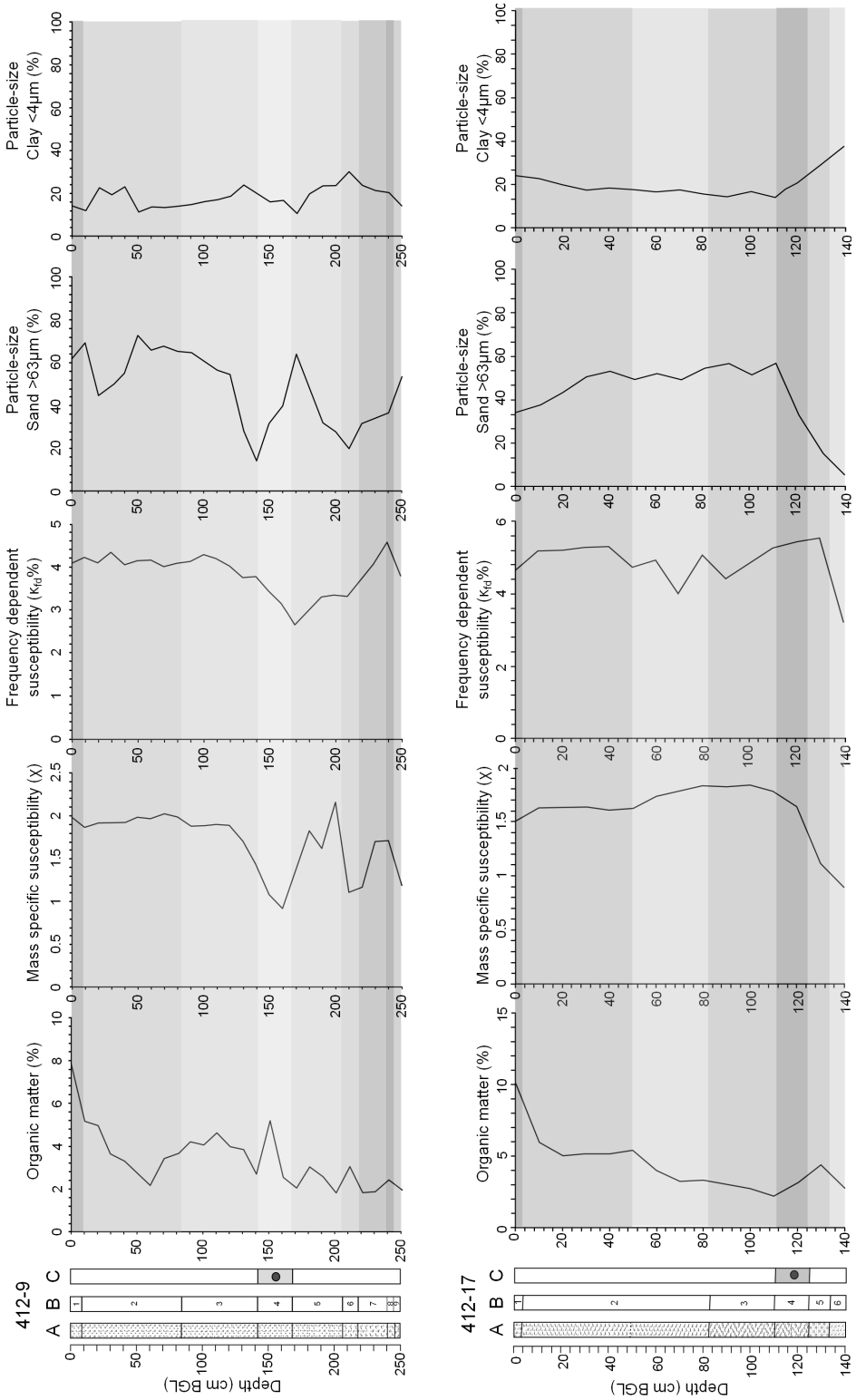

Figure 4.18. Bulk sedimentary data showing the vertical variation of moisture, organic content and magnetic susceptibility in sections 412-9 (top) and 412-17 (bottom). Column A: Sedimentary logs, B: Context number related to section drawings, C: location of OSL sample

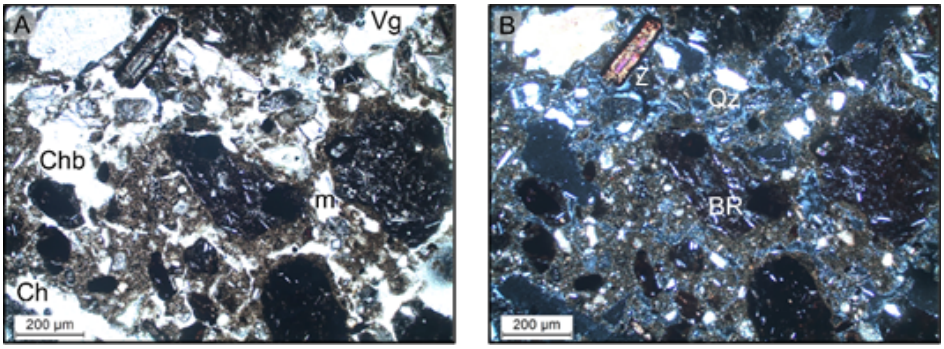

Figure 4.19. Photomicrographs showing coarse mineral and rock inclusions and silt micromass coatings found in context 2. A) Different voids showing vughs (Vg), channels (Ch) and chamber (Chb), and silt micromass coatings (m) (PPL), B) coarse components showing zircon (Z), quartz (Qz) and basalt rock (BR) (XPL). Section 412-9, micromorphological sample M1, context 2.

only a minor component (Fig. 4.19; B). Basalt glass was the main mineralogical component found, reflecting the background geology of the deposits. The main pedofeatures found includes reworked soil aggregates, frequent Mn and Fe nodules and fragmented limpid clay coatings (Fig. 4.20; B and D). A mineralised root (rhizolith) was also found in the A horizon, which may indicate alternating soil moisture conditions and 'liming' used to improve soils (Klappa 1980) was the main source of $CaCO_3$, as found in soils in other regions of the Caucasus (Khokhlova *et al.* 2001; 2009). The two overlying contexts 3 and 2 were similar in composition but both were moderately organic. The proportion of feldspar inclusions become more prevalent, and the frequency of basalt rock and charcoal fragments increase.

Interpretation. The overall interpretation of these deposits suggests that the complex mixture of coarse components occurred as a result of local erosion and sediment reworking of the immediate areas in order to construct substantial terraces. The presence of well-formed minerals, particularly zircons, and polycrystalline quartz, suggests that some of the material incorporated into the context was recently weathered from bedrock that reflects an immature sediment history. Pedogenic features such as clay coatings, suggests disturbance of the land surface, e.g. removal of vegetation for fodder. The presence of rhizoliths may have formed from natural soil carbonate or as a byproduct of the addition of domestic waste and/or lime added to improve the soil.

Implications for OSL dating. The results of the bulk sedimentary and micromorphological analysis enabled an important insight into the variability of the deposits uncovered. The rich mineralogical assemblage also has implications for the OSL analysis, as feldspars and heavy minerals originating from metamorphic, plutonic and volcanic

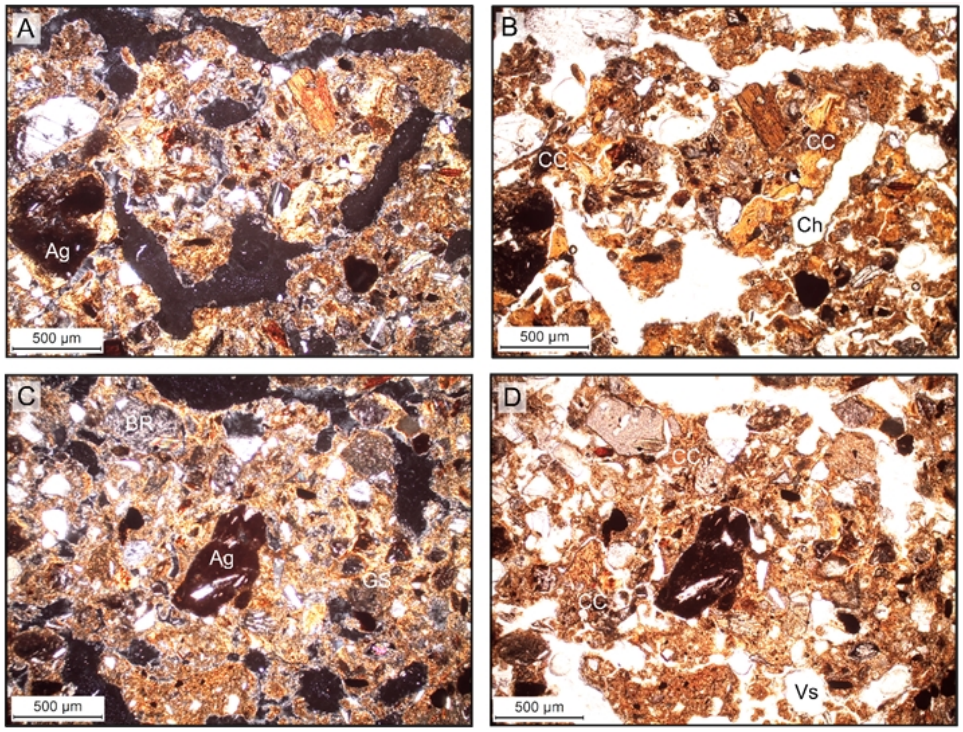

Figure 4.20. Photomicrographs showing the coarse mineral and rock inclusions, voids, chambered microstructure and clay coatings found context 2. A and B) Soil aggregates (Ag), quartz and feldspar in channel microstructure (ch) with fragmented clay coating (cc) (PPL and XPL), C and D) soil aggregates, basalt rock, quartz and feldspar showing granostriated b-fabric (GS) within a chambered microstructure (ch) with vesicles (Vs) and vughs and clay coating (cc) (XPL and PPL). Section 412-9, micromorphological sample M3, context 2.

sources can introduce heterogeneity of the natural radioactivity of the sediments and soils. The presence of modified voids suggests that the soils had also been reworked by earthworms. Clay-coatings were also abundant in the thin-section (M1) obtained from context 2 (A horizon), the frequency of these features decreases with depth. Micromorphological analysis has shown that these sediments have been affected by disturbance and mixing, and the presence of certain minerals may introduce dose rate heterogeneity. These characteristics will be carefully considered in the OSL analysis presented in Chapter 6.

Section 412-17 Context 6 was a silty clay deposit that had a spongy microstructure, and the fine component had a porphyric distribution with a stipple-speckled b-fabric. Vughs, channels and chambered voids were also present. The mineralogical component was mainly dominated by basalt rock inclusions, but quartz was relatively abundant, followed by frequent feldspars. The microstructure of context 5 was dominated by a

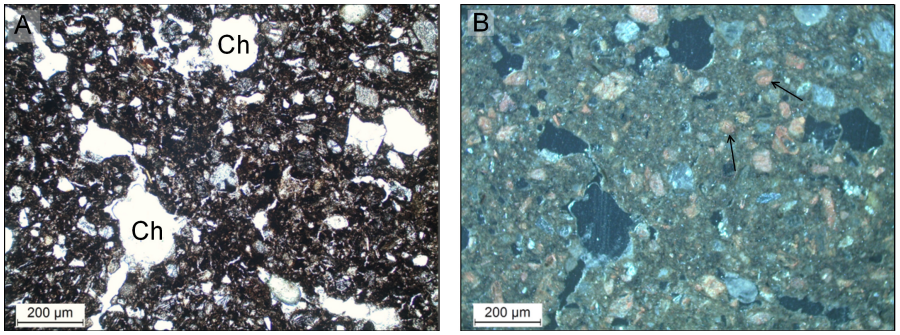

Figure 4.21. Photomicrographs showing the channel and vughy microstructure with compound mineral grains with dense organic amorphous mater found in context 2. A) Dense organic matter (PPL), B) moderately well-sorted coarse minerals and rock inclusions in silt matrix (OIL). Arrows indicate basalt rock inclusions. Section 412-17, micromorphological sample M4, context 2.

vesicular microstructure (Fig. 4.21; A and B), and the fine component was the same as context 6. The frequency of quartz and feldspar was relatively similar to the underlying deposits, however, abundant limpid clay coatings were found along with large pumice inclusions (Fig. 4.22; A), which were mainly concentrated between contexts 6 and 5. Overlying this was context 4, which was the third deposit type identified in the thin sections. It was a sandy silt deposit dominated by a vughy microstructure with an undifferentiated b-fabric. Charcoal was frequent and amorphous organic material was the most dominant component (Fig. 4.21; A). The mineralogical component consisted of frequent Fe and Mn aggregates, but appeared to be relatively well-sorted and evenly distributed (Fig. 4.21; B). Quartz was also relatively common, particularly grains ranging from 90-150 μm and occasional large polycrystalline quartz (>200 μm) was found. Context 2 had a similar microstructure and frequency of quartz, feldspar and rock inclusions, but amorphous organic matter dominated the groundmass along with frequent *in situ* roots.

Interpretation. The interpretation of the stratigraphic sequence based on the micromorphological analysis, revealed three different modes of deposition. Slope processes, e.g. surface runoff, formed the lowermost context. Overlying this was a unit of pumice fragments, rapidly deposited by air fall, as indicated by the vesicular microstructure (Bullock *et al.* 1985). The deposits immediately overlying this layer appeared to be relatively heterogeneous suggesting that the slopes had been destabilised resulting in the influx of allochthonous material into the sequence. The deposits overlying this then returned to more stable conditions to form a thick uniform unit of soil. The presence of clay coatings in contexts 4 to 6 most likely occurred due to localised weathering of pumice and basalt material, as observed in similar volcanic soils in Central Mexico (Sedov *et al.* 2003).

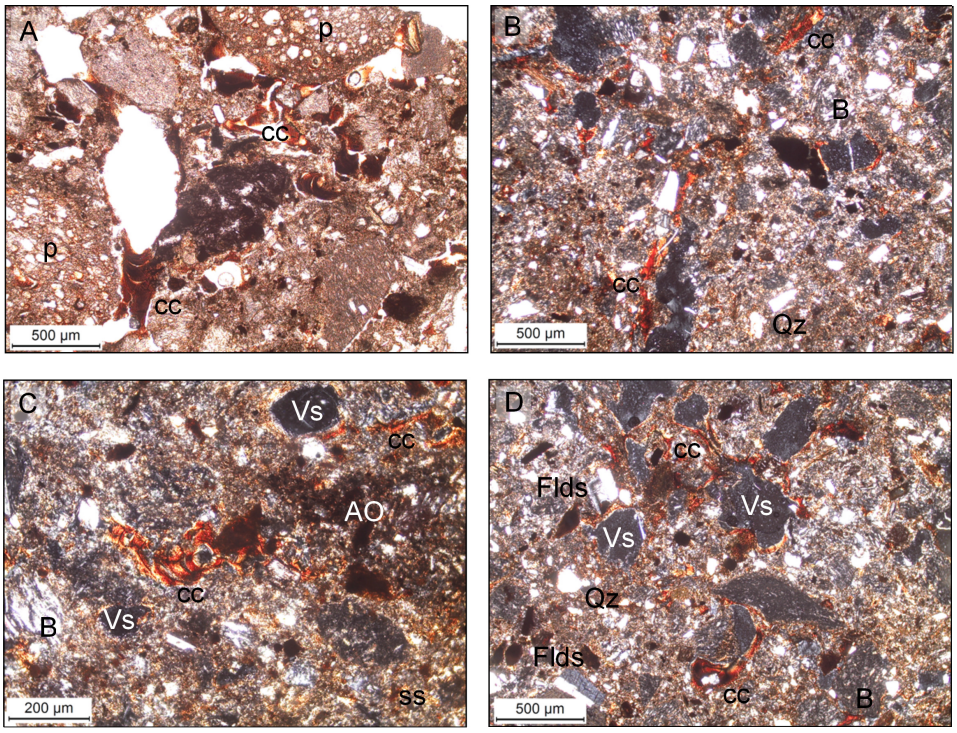

Figure 4.22. Photomicrographs showing the vesicular and vughy microstructure with abundant clay coatings. A) Clay coatings (cc) within voids and surrounding pumice fragments (p) (PPL), B) clay coatings (cc) surrounding channel voids within a poorly sorted deposit containing abundant basalt rock (B) fragments (XPL), C) clay coatings (cc), vesicular voids (Vs), basalt rock fragments (B) and amorphous organic (AO) material (XPL), D) clay coatings (cc) surrounding quartz (Qz) and feldspar (Flds) minerals and basalt rock fragments (B) and vesicular voids (Vs) (XPL). Section 412-17, micromorphological sample M2, transition from contexts 5 to 4.

Implications for OSL dating. The application of micromorphology to this stratigraphic section significantly enhanced the geoarchaeological analysis. Bulk techniques were unable to detect subtle variations in particle-size, particularly the detection of illuvial clay coatings. Furthermore, the presence of OM and Fe-bearing rocks and inclusions suggests uranium remobilisation (Cumberland *et al.* 2016) during repeated wetting and drying phases, which may have concentrated uranium within clay-coatings of various voids. Although *in situ* geochemical quantification of these components was not carried out as part of this research, these features will be carefully considered when interpreting the OSL data.

Part B: Dariali Fort (Trench F)

This section will provide the geoarchaeological assessment of samples obtained from Dariali Fort, Trench F (Fig. 4.2).

4.1.7 Excavation results

The main contexts uncovered in the sondage were composed of thick midden deposits, which includes contexts F.129, F.096, F.037, F.035 and F.022. The very basal deposit was context F.140. This was a moderately compact dark grey brown sandy silt deposit with occasional gravel and charcoal inclusions. Overlying this was F.129, an orange-brown poorly sorted deposit with lenses of charcoal and ash, this was covered by a possible packing layer F.096, a moderately sorted dark grey brown deposit with patches of reddened soil with frequent pebble inclusions, which become more finely layered towards the top of the deposit. A large unit of dumped sediment mixed with collapsed construction material and large stones covered these deposits. This context (F.037), was a loose mottled grey brown sandy silt with abundant artefact inclusions. Above this deposit was a complex unit of finely stratified ash and charcoal lenses mixed with loose sandy silt midden material (F.035). Overlying the whole sequence directly beneath wall (F.009) was a mid-grey poorly sorted deposit with frequent pebble inclusions (F.022).

Five samples in total were collected from a continuous section through the sondage (Fig. 4.2). Samples 400-3 and 400-1 were taken as tube samples in 2013. Samples 412-15.3.1, 2.1 and 1.1 were extracted as block samples due to their heterogeneous and friable nature and were later sub-sampled in the laboratory under subdued red light conditions.

4.1.8 Micromorphological assessment

The micromorphological assessment was focused on contexts F.096, F.138, and F.129, which were also sampled for OSL and archaeomagnetic dating. Ideally, a complete assessment of the full stratigraphic profile would have provided detailed insights into the site-formation processes at play across the site. However, this was beyond the scope of this research, and so only deposits that were from Sasanian phases were sampled. The following section will describe the six deposit types that were identified in the three thin-sections analysed.

The microstructure of deposit type 1 (DT1) was subangular blocky with vughs. Organic remains were abundant, which included charcoal, seeds and straw fragments and frequent phytoliths (Fig. 4.25; 2 and 3). Only occasional coarse mineral inclusions were identified. This deposit was interpreted as hearth rake out which was reworked and incorporated into the second deposits type (DT2). The microstructure of DT2 was

granular with frequent vughs. Coarse inclusions were variable, ranging from reworked soil aggregates, and frequent inclusions of basalt, slate and carbonate material, and occasional organic remains were identified. This was interpreted as an occupation surface containing degraded building material, e.g. lime mortar and rock, to form a compact layer. Deposit type 3 (DT3) had a channel and vughy microstructure with frequent organic remains, consisting of coarse and fine particles of charcoal, and frequent Fe and Mn nodules. This was interpreted as a burnt soil deposit that had been partially fragmented and reworked in the lowermost heated context F.129, while the overlying heated context F.096 was *in situ* (Fig. 4.23; 3). The fourth deposit type identified (DT4) was similar to DT2, but contained frequent vughs and vesicles, and abundant slate fragments, suggesting rapid deposition and collapse of an old roof (Fig. 4.24; 1). Overlying DT3 was deposit type five (DT5), the microstructure was dominated by fissures, channels, and planes. The coarse inclusions were arranged parallel to the boundary which was sharp. Coarse inclusions consisted of frequent quartz and occasional heavy minerals and rock aggregates. Organic remains were also abundant, which includes charcoal, egg shell, and ashes and also occasional Fe/Mn nodules and reworked earthworm granules (Fig. 4.23; 4). This deposits was interpreted as a trampling layer, as coarse inclusions such as shell, showed parallel arrangement and fissures and parallel planes are indicative of trampling (Banerjea *et al.* 2015). Deposit type six (DT6) had a subangular blocky microstructure with frequent vughs, occasional coarse mineral inclusions were identified. Fine organic particles were frequent and Fe/Mn minerals were found. The deposit was also rich in carbonates and contained fine amorphous yellow phosphate that infilled voids. This deposit was interpreted as a floor and was covered with charcoal-rich trampling deposits.

Implications for OSL dating. The thin section analysis enabled the identification of different deposit types which include trampling, burning and levelling deposits that were not visible in the field. The sediments also showed significant disturbance and sediment remobilisation, which has important implications for relative and absolute dating methods. For absolute dating, disturbance would enable small mobile short-lived material such as seeds to migrate through the profile. For OSL dating, individual sand grains can travel through fissures and voids and can contaminate surrounding deposits. This is particularly problematic in anthropogenic contexts where heated and unheated grains that have been heavily mixed and can be accidentally sampled (Rhodes *et al.* 2003). This emphasises the need for thorough micromorphological investigation of deeply stratified archaeological contexts prior to sampling for dating.

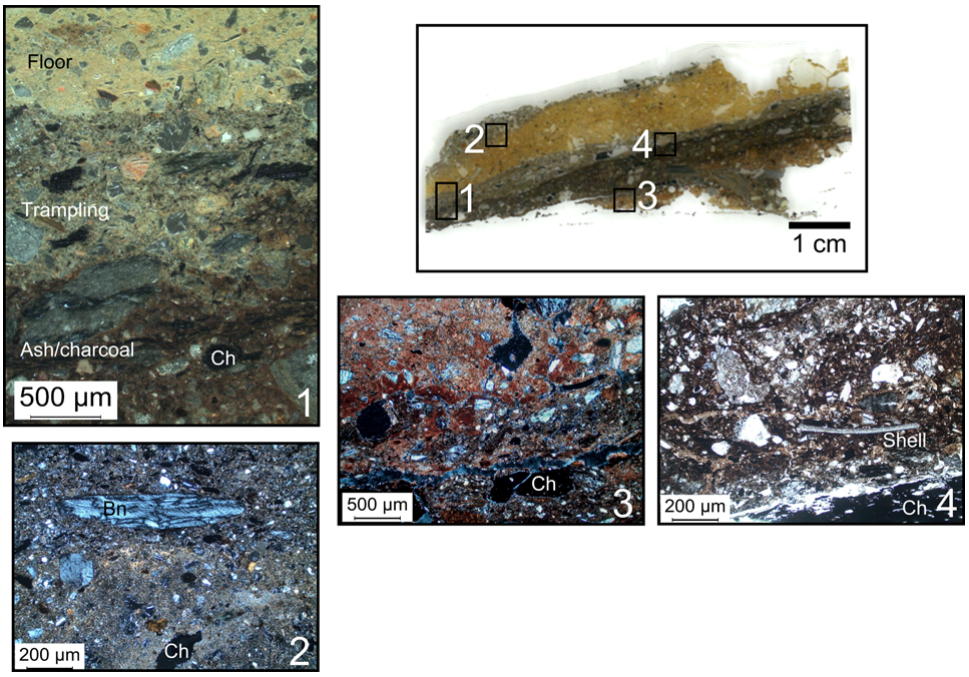

Figure 4.23. Photomicrographs of finely stratified occupation deposits identified in thin section (top right). Section through microstratigraphic layers showing ash/charcoal (DT1), trampling (DT5) and compact floor/surface (DT6) (OIL) (1); bone fragment in ash later (XPL) (2); charcoal (ch) and overlying burnt soil (XPL) (DT3) (3); and trampling later with parallel organic remains (PPL) (4). South facing section (Trench F), context F.096.

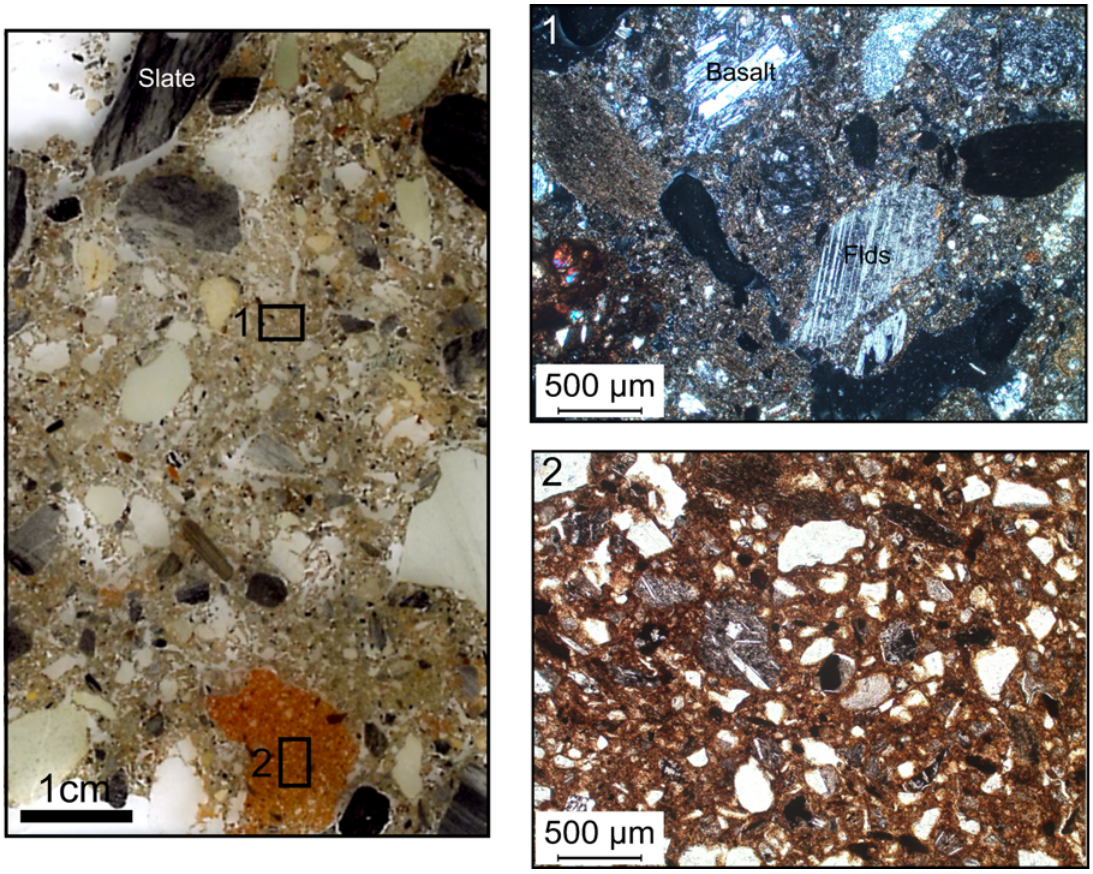

Figure 4.24. Photomicrographs of collapsed building material and reworked burnt soil aggregates identified in thin section (left) showing collapsed material containing soil aggregates and frequent rock fragment. Minerogenic-rich coarse and fine material showing complex mineralogy and vughy microstructure (DT4) (XPL) (1); and burnt soil aggregate showing relatively well-sorted inclusions of quartz minerals and basalt rock fragments(PPL) (2). South facing section (Trench F), context F.138.

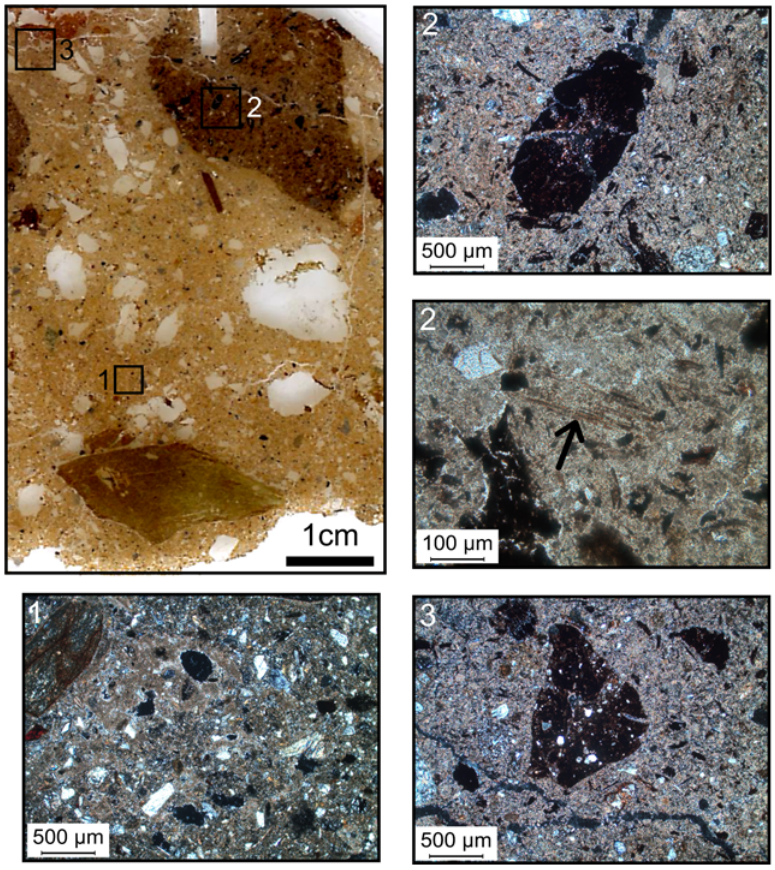

Figure 4.25. Photomicrographs of compacted occupation deposits with reworked carbonates, ashes and rock fragments identified in thin section (top left). Carbonates and frequent rock and mineral inclusions (DT2) (XPL) (1); reworked ash and charcoal aggregate containing grass phytoliths and seeds in the ashy matrix (DT1) (top: XPL, bottom: PPL) (2); and a fragment of a burnt soil aggregate found in ash deposit (XPL)(3). South facing section (Trench F), context F.129

4.2 Case study 2: Large-scale canals in the Mil Steppe, Azerbaijan

4.2.1 Introduction

The Mil Steppe is located in modern Azerbaijan in the Lesser Caucasus (Fig. 4.1). It is an extension of the Mughan Steppe, located to the east of the Lower Karabakh hills. The region is dominated by two major river systems which flow through the lowland regions, the Kura and the Araxes, which join and flow into the Caspian Sea. The '*Ancient Kura Research Project*' (2010 - present), aims to explore ancient landscapes of early sedentism covering the Neolithic to the Bronze Age (Helwing *et al.* 2012; Ricci *et al.* 2012), in a landscape currently under threat by destructive modern agriculture and irrigation. As part of the research, intensive landscape survey - Mil Steppe Survey (MPS) - was developed to identify sites of all periods, including Late Antique and Medieval settlements that were also under threat (Ricci 2012).

The survey has identified several small mounds of 0.1 to 0.2 ha in size, broadly dated to the Late Antique and Medieval period that appear to be closely connected to Ören Qal'eh (ancient Baylaqan). This is an important Late Sasanian/Early Islamic fortification, with extensive large-scale irrigation networks. It was originally investigated during the 1950s and 1960s by the A. A. Lessen expedition and was later published by Ahmadov (1997). The dating evidence available from this early excavation is sparse, however, recent survey pottery resembled Sasanian assemblages found at Ultan Qalasi (Alizadeh 2011; Lawrence & Wilkinson 2017). Fortified urban centres such as Ören Qal'eh, Ultan Qalasi, Qala Tepe and Bərda formed a road network which followed the Lower Karabakh hills (Lawrence & Wilkinson 2017),but the date of these sites is hampered by the lack of excavation. Ören Qal'eh remains a highly prestigious heritage site and no further excavation has been allowed. As part of the *Persia and its Neighbours Project*, an archaeological investigation of the irrigation system located next to the fortified site of Ören Qal'eh provided a unique opportunity to understand the chronology and evolution of large-scale canals broadly dated to the Late Sasanian/Early Islamic period.

The following section will first introduce the physical and environmental background of the region, and then the excavation results of the canal system and geoarchaeological assessment will be provided.

4.2.2 Physical background

The overall geology of the Lesser Caucasus is dominated by volcanic basaltic, andesitic, trachytic, and doleritic rocks (Gudjabidze & Gamkrelidze 2003). However, the Kura

basin is geologically varied due to tectonic activity (Forte *et al.* 2010), exposing a range of volcanic and sedimentary rocks that have been eroded to form thick colluvial and alluvial deposits in the Kura basin (Von Suchodoletz *et al.* 2015). The region is characterised as a semi-arid environment dominated by saline-rich serosems (Ollivier *et al.* 2015), and takyrs (Lebedeva-Verba & Gerasimova 2010). Extensive yellowish brown reworked loess and alluvial silts are widespread in the Lower Karabakh (Bebermeier *et al.* 2010), which is virtually treeless and dominated by lowland steppe vegetation (Connor & Kvavadze 2014). To irrigate these lowlands, most of the water originates from groundwater sources (45%), while 35% originates from perennial rivers from the Lesser Caucasus in the summer, and only 2% comes from rainfall (Ollivier *et al.* 2015). The hydrological system has also been influenced by fluctuating Caspian Sea levels, particularly the lowlands of the Kura Delta.

Since the Late Pleistocene, periodic transgressions and regressions of the Caspian Sea has significantly changed the coastline over the last 4000 years (Mamedov 1997; Hoogendoorn *et al.* 2005; Abbasov & Mahmudov 2009). Despite the chronological uncertainties associated with early records, it is clear that the Caspian Sea level remains sensitive to climate change as water originates from a number of major river systems such as the Volga, Ural, Emba and Kura (Naderi Beni *et al.* 2013). The 'Derbend Regression' has been widely reported, occurred around 1400 yr BP, with a lowstand of -34 m coinciding with the period of Late Antiquity Hoogendoorn *et al.* (2005), that permitted accessibility and transport along the Caspian Sea coast during this period. During the last ∼1000 years, significant fluctuations occurred, which have been linked to climate change in the region. During the 'Medieval Climate Anomaly' (MCA), the Caspian sea level dropped, which then increased again as a response to the 'Little Ice Age' (LIA) (Kroonenberg *et al.* 2007). Earthquakes and volcanic eruptions have caused significant fluctuations of the Caspian Sea, resulting in flooding and collapse of irrigation systems (Abbasov & Mahmudov 2009), which would have had a similar impact on irrigation systems in the past.

4.2.3 Fieldwork methodology

Remote sensing and ground based survey enabled targeted excavation of a well-preserved section of the Ören Qal'eh canal system (Fig. 2.1). Due to its sheer scale, the canal was machine excavated. A large trench (ca. 2 x 25 x 2.3 m) was established to expose the canal fill and associated upcast bank. The northwest facing section of the canal was carefully cleaned to expose the various deposits. The section was recorded at 1:20 scale onto permatrace to show the thickness and extent of each context and the location of samples taken, as illustrated in Fig. 4.26. The section was photographed and the location of the canal section was linked with the wider topographic survey of the region (Ricci 2012). The main contexts uncovered were described using the description

methods outlined in Sec. 3.2.3. Two pottery sherds and two charcoal fragments were retrieved from the canal fill, these were bagged, labelled and located onto the sections for identification and dating purposes.

4.2.4 Excavation results and geoarchaeological assessment

The following section will provide a description of the main phases of canal formation. Five main phases were identified (in chronological order): 1) natural alluvial deposits, 2) old ground surface, 3) construction bank, 4) upcast clean-out deposits, and 5) abandonment fills. Due to the complexity and significant reworking of deposits, the micromorphological analysis was combined in the field sedimentary descriptions.

Phase 1: Natural alluvium

The natural alluvium consisted of alternating fine sand, silt and silty clay and was olive gray (5Y4/2) and yellowish brown (10YR5/4) in colour and contained grit and occasional pebble inclusions, suggesting alternating fluvial energies (Allen 2012). Microscopically, the natural alluvium had a vesicular microstructure (Fig. 4.27; A), which forms as a result of water saturation and subsequent drying (Courty *et al.* 1989). Towards the top of the thin section (M6), the microstructure of this deposit showed frequent horizontal planes and platy crusts (Fig. 4.27; B), suggesting a reduction in porosity. These voids can form during a period of exposure, and similar features have been identified in tilled alluvial soils, furrows and rill channels (Pagliai *et al.* 1995; Pagliai & Stoops 2010). The overall sorting changed towards the top of the slide, where the alluvium mainly consists of poorly structured sands with frequent eroded silty clay relic aggregates, suggesting rapid erosion and deposition. Eroded clay aggregates are also commonly found in intertidal sediments (Reineck & Singh 1980). These poorly structured fine sands also contained multiple vertical microfractures suggesting that these sediments were compacted by overlying sediments (Phillips 2006).

Phase 2: Old ground surface

The old ground surface (OGS) was described in the field as a compact dark yellowish brown (10YR4/4) silty clay deposit. The boundary between the OGS and the upcast mound was sharp. The OGS appeared to have been reworking towards the centre of the canal. The micromorphological analysis of the OGS highlighted a number of features that were not visible in the field. The lowermost part of the OGS captured in the vertical thin section (M2) had a subangular blocky microstructure and frequent vesicles suggests that this deposit formed in wet conditions (Kovda & Mermut 2010)

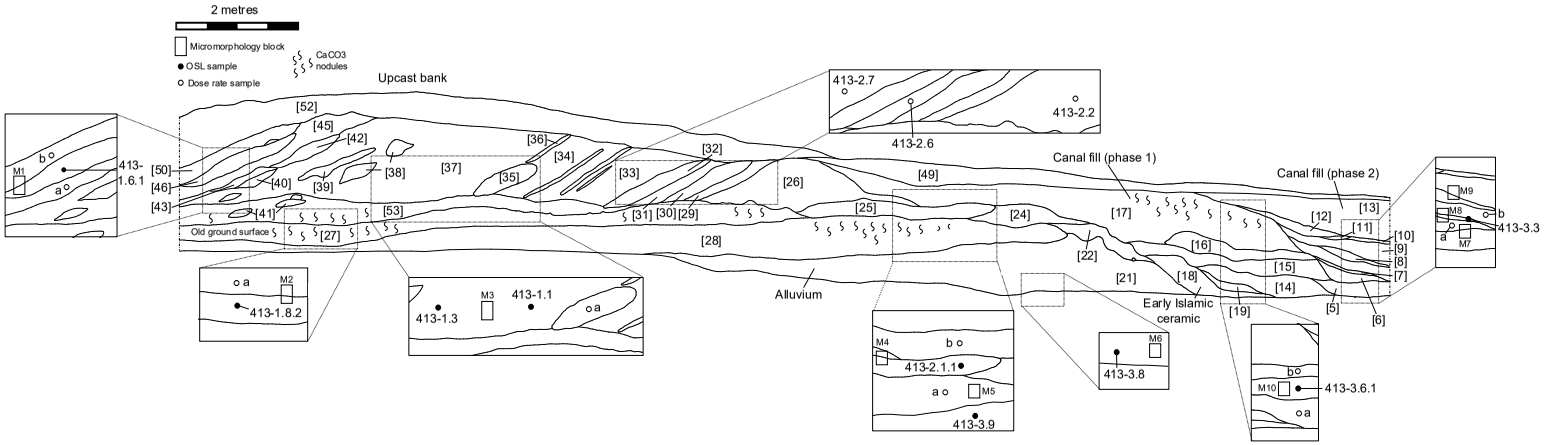

Figure 4.26. Ören Qal'eh canal stratigraphic profile (northwest facing). Boxes provide details of the deposits sampled for micromorphology (squares) and OSL (closed circles), and additional environmental samples (open circles).

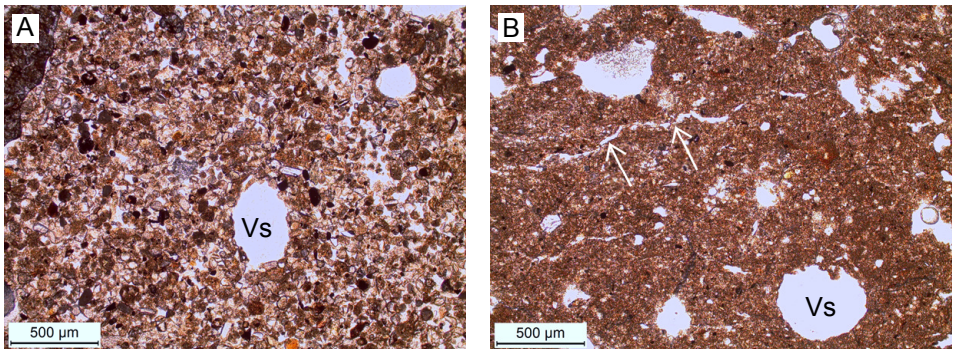

Figure 4.27. Thin section (M6) of natural alluvial sands and silts. Photomicrographs show: well-sorted fine sands with vesicular microstructure (Vs) (A); and moderately sorted sandy silt with vesicle (Vs) and planar voids (indicated by arrows) (PPL) (B). Northwest facing section through canal, micromorphological sample M6.

(Fig. 4.28; A). Frequent channels, modified planar voids and frequent ellipsoidal organo-mineral earthworm excrements were observed, suggesting significant biological activity (Kooistra & Pulleman 2010). The coarse component mainly included moderately well-sorted quartz, feldspar, and fragments of basalt and granite rock inclusions. Point-counting of coarse and fine-grained quartz/feldspar identified in the transition from the OGS to the upcast mound revealed that quartz was more abundant (Fig. 4.29; A). Although this was not applied routinely for all thin-sections analysed, the variability observed from the OGS to the mound revealed subtle variations to be identified in deposits that had not been significantly disturbed. Pedogenic features included frequent Fe and Mn oxide nodules indicative of alternating wetting and drying processes (Kovda & Mermut 2010). Dusty clay coatings were also identified suggesting disturbance (Kühn *et al.* 2010a), possibly related to anthropogenic mound construction processes.

The top of the OGS had a granular microstructure with frequent horizontal planes and surface crusts (4.28; C). Surface crusts are layered deposits formed by the settling of clay particles after a period of flooding, as observed in saline soils widely found in Central Asia (Mees & Singer 2006). These features were then disturbed and fragmented due to drying, shrinking and fragmentation caused by *in situ* pedogenic gypsum crystal growth. Dense infillings of lenticular gypsum were frequent at the transition between the OGS and the start of upcast mound formation, which caused significant disturbance creating a distinct crumb microstructure (Fig 4.28; C). The frequency of quartz also decreased towards the top of the OGS (Fig. 4.29; B).

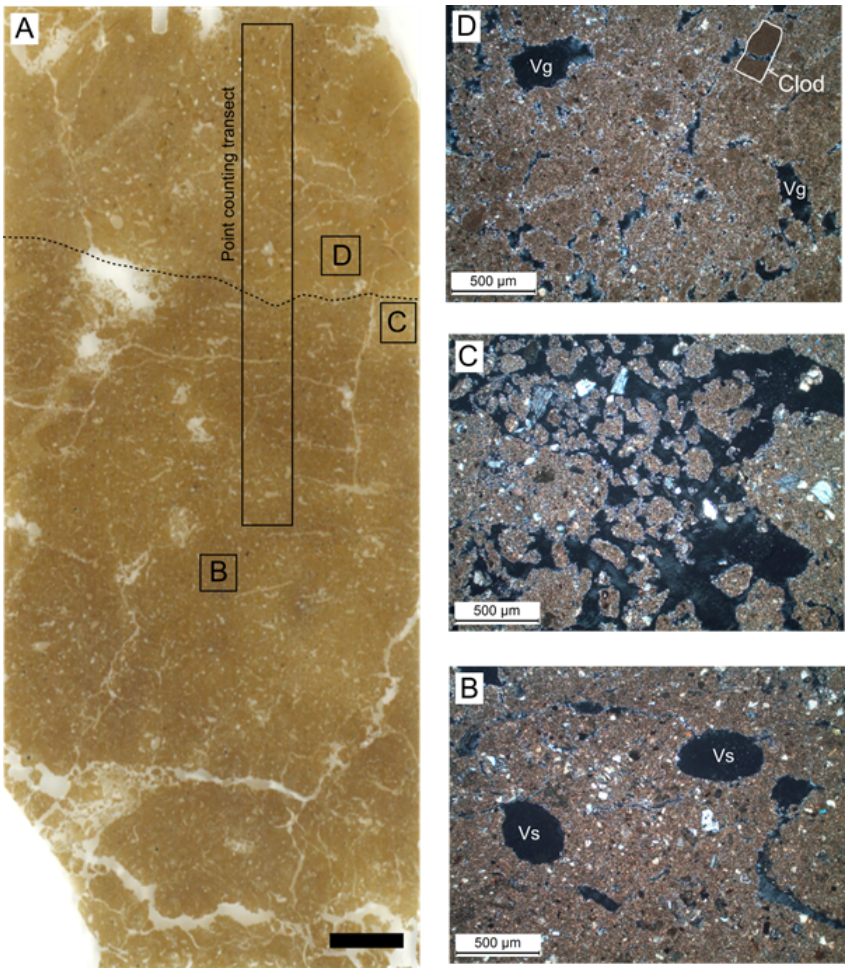

Figure 4.28. Thin section (M2) taken through the transition from the old ground surface and the construction mound deposits (A) (scale bar = 1 cm). Photomicrographs show: vesicular microstructure with wind-blown quartz (XPL) (B), crumb microstructure and occasional coarse-grains of quartz and feldspar (XPL) (C), and Vughy microstructure found in upcast mound deposits with frequent angular clay aggregates (XPL) (D). Northfacing section through canal, micromorphological sample M2.

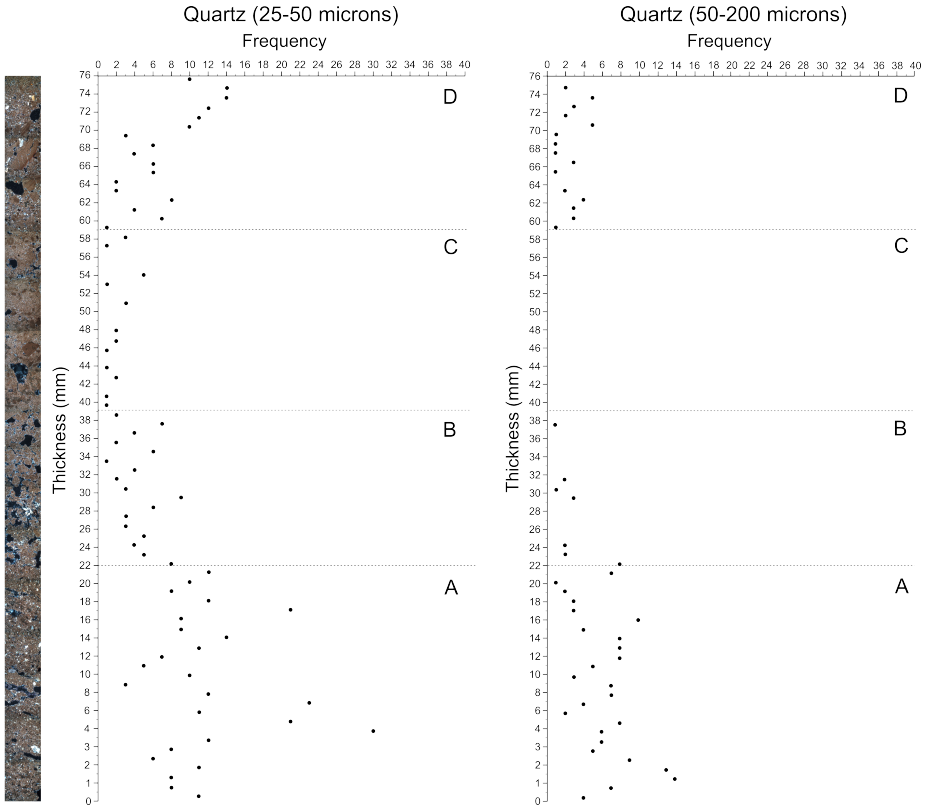

Figure 4.29. Point-count analysis of quartz and feldspar through a transect through the old ground surface to the upcast mound as indicated in Fig. 4.28. Within the two separate deposits, four subunits were seen in thin section: A) old ground surface with frequent fine and coarse sand inclusions, B) transition from old ground surface to mound, C) the construction mound deposit, and D) loess mixed with upcast deposits.

Phase 3: Bank construction

The mound construction deposit consists of reworked silty clay alluvium. It was described as a compact moderately-sorted yellowish brown (10YR5/4) silty clay deposit. Micromorphological analysis of the construction deposits revealed that is was composed of a well-sorted fine silt with frequent clay aggregate inclusions (Fig. 4.28; D). This deposit had frequent star-shaped vughs and chambered voids, which suggested rapid deposition and collapse of void structure during the construction of the mound. Coarse grained quartz/feldspar was virtually absent in the original construction mound deposit, and only occasional fine-grained quartz was found (Fig. 4.29; C). The microstructure of the mound deposits was dominated by a subangular blocky microstructure towards the top of the deposit, with frequent large vughs and a dense mass of poorly sorted coarse-grained quartz, as observed in the point-counting analysis (Fig. 4.29; D). Reworked and fragmented silty clay crusts were frequent, with an internal striated b-fabric that is typically found in transported sediment (Mücher *et al.* 2010).

Phase 4: Upcast deposits

The upcast deposits were described as loose, poorly sorted greyish brown (10YR5/2) silty clay deposits. Frequent rootlets, shell and carbonate nodules were also noted. At the microstratigraphic scale, these deposits were heterogeneous and contained a mixture of aggregates originated from different sources, ranging from large fragments of silty clay crusts, calcareous marl aggregates, and aggregates of poorly sorted sand and silt (Fig. 4.30; A). The upcast had a distinct crumb microstructure (Fig. 4.30; B and D) and contained frequent gypsum nodules and individual lenticular crystals (Fig. 4.30; E). The deposits also had variable quantities of wind-blown quartz (loess) that had entered via fissures and voids within the crumb microstructure.

Phase 5: Canal fill (abandonment)

Primary Fill. The canal appeared to have been re-cut at least once, as indicated by the two phases of fill. The primary fill was described as a compact moderately to well sorted silty clay brown (10YR4/3) sediment, with occasional grit inclusions. The borehole enabled the edge of the original canal to be traced below and beyond the limits of excavation (see further details in Appendix C). The fill consisted of unstructured well-sorted clay intercalated with lenses of well-sorted sand with occasional pebbles (1 cm in size).

Micromorphologically, these sediments had a massive structure with frequent angular channels and planes (Fig. 4.31; A). The degree of pedality varied from well to weakly developed peds. A mixture of voids were found in these deposits, ranging from vesicles, vughs, channels and chambers (Fig. 4.31; B to E), and some voids had been altered

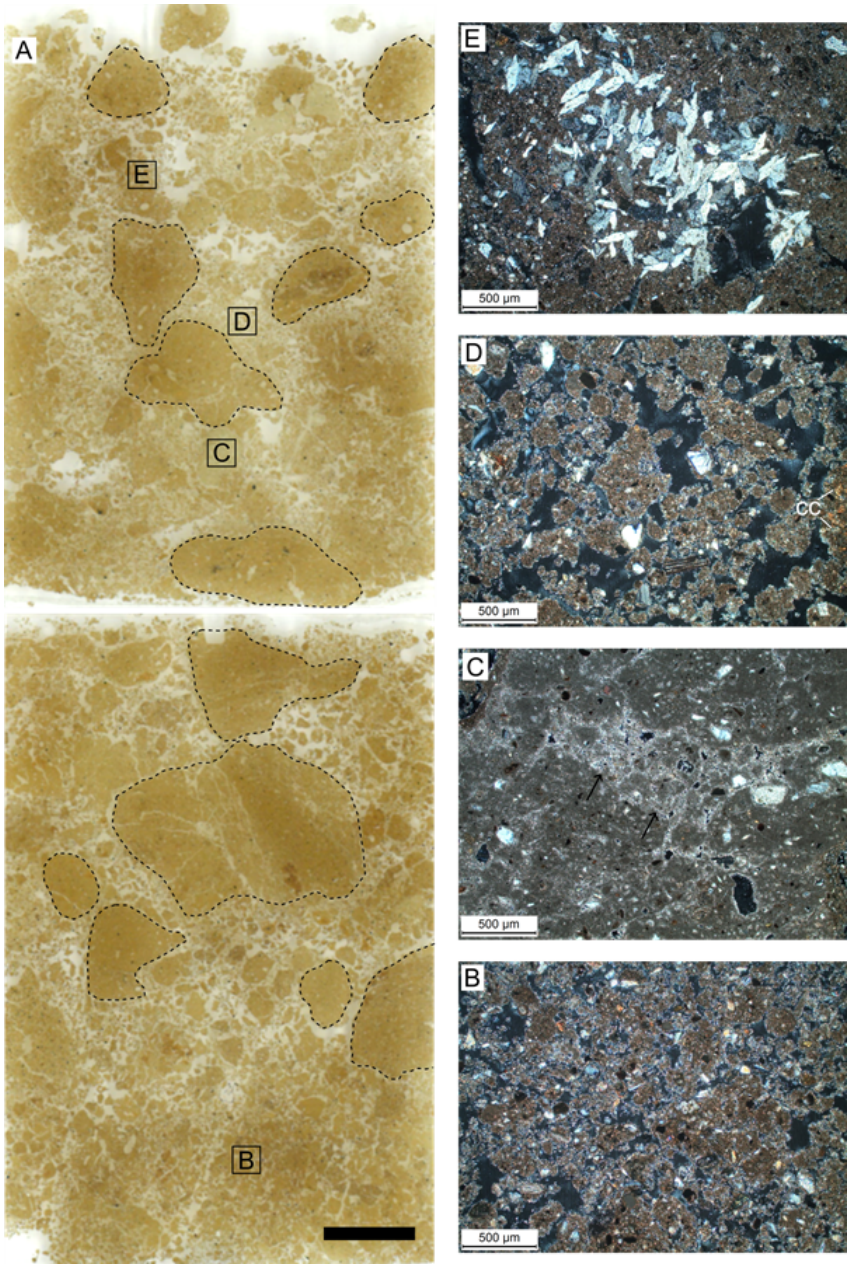

Figure 4.30. Thin section (M1) of upcast deposits showing individual silty clay clods within a loose matrix (scale bar = 1 cm) (A). Photomicrographs show: linked and coated related distribution of silty clay pellets with organic matter, coarse grained quartz, mica and calcite (XPL) (B); carbonate-rich marl aggregates with coarse-grained quartz with a loose porphyritic related distribution and occasional chambers and vughs, arrows indicate areas of carbonate depletion (XPL) (C); loose crumb microstructure with occasional quartz and feldspar minerals, and fragmented limpid clay coatings (CC) (XPL) (D); pedogenic gypsum with well-formed lenticular crystals in a sandy silt clod (XPL) (D). Northwest facing canal section, micromorphological sample M1.

due to biological activity and compaction. A number of channels showed infillings of alternating fine silt and clay or poorly sorted sandy silts, indicative of earthworm activity (Kooistra & Pulleman 2010). The coarse mineralogical component consisted of well-rounded quartz and occasional feldspars that showed moderate weathering and dissolution features. The related distribution was described as loose porphyric, where the minerals were embedded within the fine silty clay deposit.

This deposit contained abundant redoximorphic features, which form in association with wetness that resulted in the reduction and oxidation of Fe and Mn during water saturation (Lindbo *et al.* 2010; 129), most likely created by variable groundwater levels as a result of modern irrigation. Features identified include: Fe oxide coatings, hypercoatings and quasicoatings around voids (Fig. 4.31; B to F), resembling features commonly found it saturated sediments, e.g. terrace paddy soils (Lee *et al.* 2014) and irrigated subtropical soils (Huang *et al.* 2008). Reduction features were also present, creating patches of light speckled micritic $CaCO_3$ within the matrix and coatings of voids (Fig. 4.31; F and D). These pedogenic carbonate features were formed by a number of processes, such as dissolution, translocation and variable precipitation that commonly occur in regions dominated by calcareous soils (Khormali *et al.* 2006).

Secondary Fill. The secondary fills had frequent alternating clay and fine sand lenses. The fine well-sorted fine sand was a dark olive brown (2.5Y3/3) in colour, and the compact subangular blocky clay was a dark reddish brown (2.5YR3/3) colour. The canal fills reflected alternating environments, ranging from short fluvial episodes, as indicated by thin lenses of alluvium, intercalated with aeolian sand reflecting drying-up of the canal.

Two fine sand aeolian layers recorded in thin-section M8 had a loose porphyric structure containing a mixture of minerals and reworked clay aggregates, and frequent vesicles and planes were found (Fig. 4.32; D). The presence of vesicular voids suggest trapped air during rapid deposition into the canal, and is a common feature in many desert soils which have dried rapidly (Gerasimova & Lebedeva-Verba 2010). The coarse component contained abundant minerals of mica and various heavy minerals, which showed internal layering. Organic particles were also abundant within the fine sand. Overlying this layer was a thin layer of clay that had a subangular blocky microstructure and was dominated by planes, chambers and occasional vesicles. The fine component showed internal grading with a banded distribution (Fig. 4.32; C), suggesting low fluvial depositional energies. The uppermost boundary was sharp and wavy suggesting partial erosion by the deposition of fine sand directly above, this sand partly filled the drying cracks within the clay layer. The formation of clay crusts resembles those that typically form on the takyr plains found in other regions of Central Asia (Lebedeva-Verba & Gerasimova 2010). After multiple phases of aeolian deposition in the channel, low energy

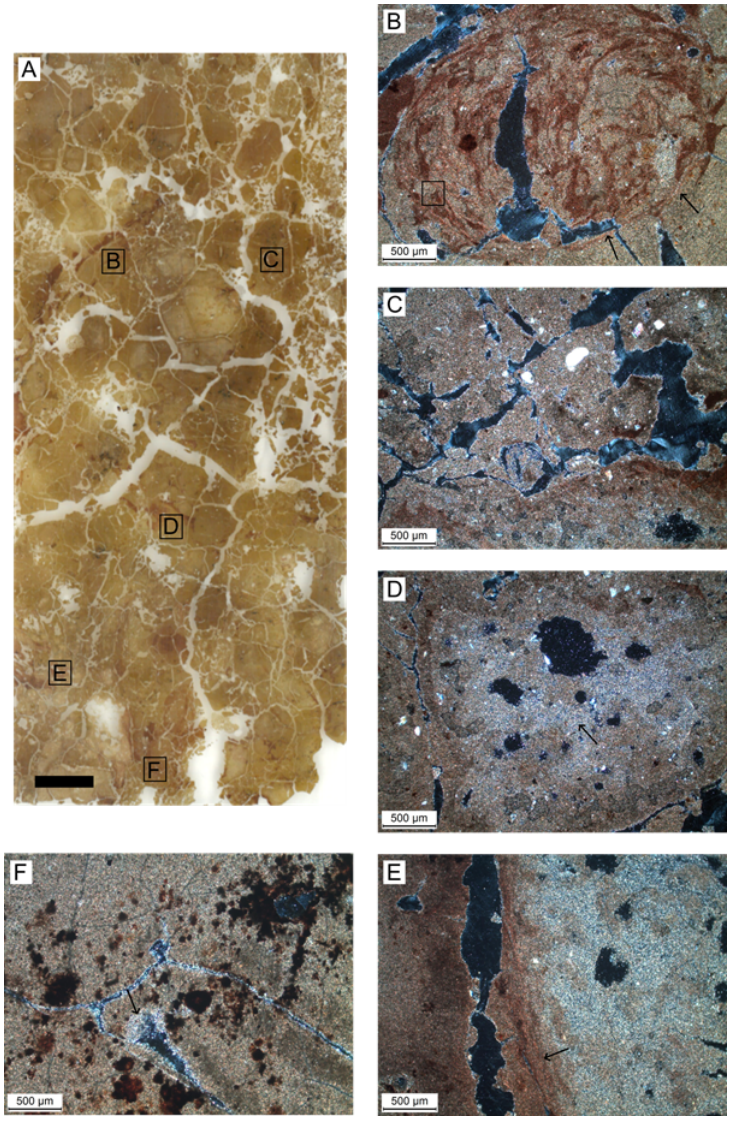

Figure 4.31. Thin section (M10) of primary canal fill deposits showing angular blocky microstructure with developed peds (scale bar = 1 cm). Photomicrographs show: B) Deformation structure of clay aggregate that was redeposited when wet showing rotational internal banding (arrows) (XPL). C) Silty clay with occasional wind-blown sand grains with complex vughs and chambers (XPL). D) Silty clay with vughs, wind-blown sand and carbonate dissolution (XPL). E) Intrusive redoximorphic feature showing Fe hypercoatings and quasicoatings along a linear channel and carbonate depletion features with vughs and channels (XPL). F) Dendritic Fe nodules surrounding vesicles and channel voids, voids show micritic carbonate coatings (arrow) (XPL). Northwest facing section through canal, micromorphological sample M10.

fluvial environments return, with banded structure. The erosion and incorporation of frequent large clay aggregates, aeolian sand, and coarse mineral inclusions (Fig. 4.32; B) suggests local erosion of the exposed canal banks during the abandonment phase. These fills were later reworked by earthworms, roots and carbonate deposits.

Summary

The complex and variable microstratigraphy of the canal deposits demonstrates the importance of a multi-method geoarchaeological approach. In the field, deposits appeared to be relatively similar, silty clay alluvium deposited by low fluvial energies intercalated by fine-sand deposited by aeolian deposition. The micromorphological analysis enabled subtle differences between the natural alluvium, OGS, bank construction and canal fills to be determines. The main differences being, the variable quantities of coarse-grained quartz, the frequency of feldspar, dissolution of grains, void space, mixing and reworking of deposits by natural processes at different phases of the canal.

Implications for OSL dating The complex canal stratigraphy required the sampling of many different deposits to build a chronostratigraphic framework. Samples were obtained from deposits that were considered to have undergone sufficient exposure during deposition in order to reset the signal in coarse grains of quartz. Furthermore, many deposits showed some degree of disturbance, particularly within the banks as grains could migrate between deposits via fissures and planes formed by natural disturbance (gypsum formation and bioturbation). Furthermore, the variable quantities of feldspar and the preservation of the internal structure of grains due to dissolution processes has implications for sample processing, particularly within the natural alluvial deposits where feldspars were dominant.

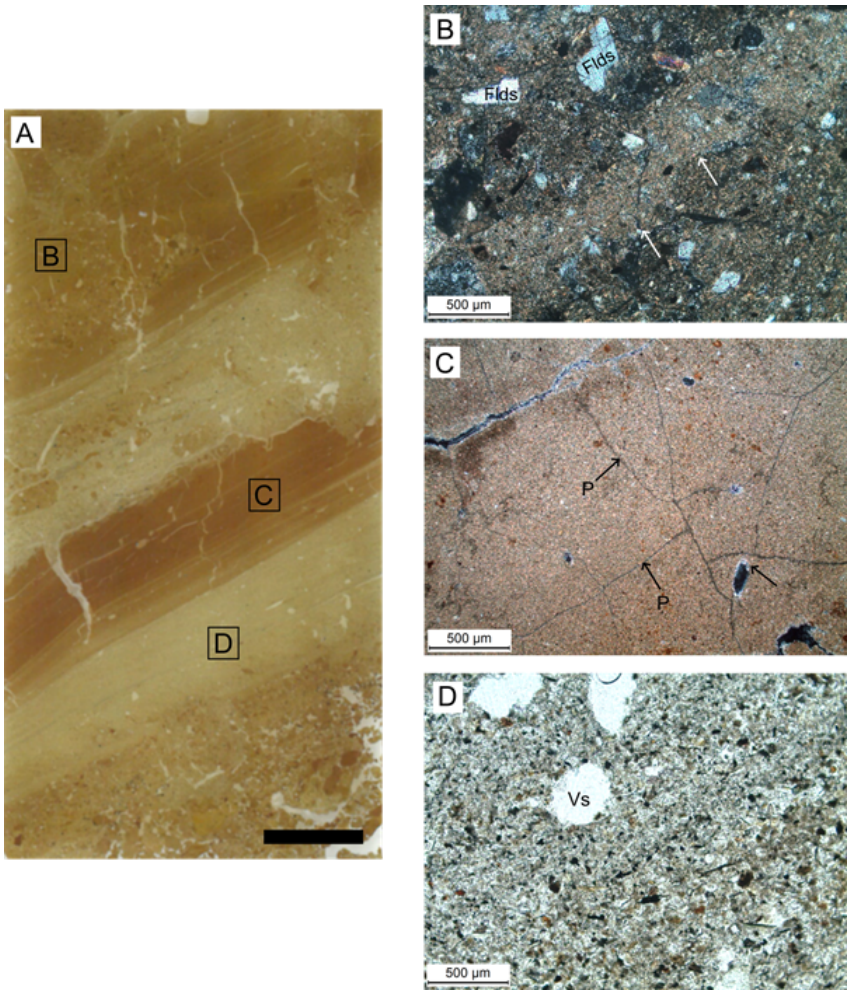

Figure 4.32. Thin section (M8) through secondary canal fill showing alternating layers of fine sand and clay (scale bar = 1 cm) (A). Photomicrographs of key features: porphyric banded related distribution with coarse grained feldspar and wind-blown quartz (XPL) (B); massive angular microstructure with frequent planes and occasional vesicles with micritic carbonate coatings, Fe mottling also present (XPL) (C); banded fluvial fine sand with frequent heavy minerals, linear organic material, mica and quartz and feldspar, and occasional vesicles (PPL) (D).

4.3 Case study 3: Gorgān Plain, Northeast Iran

4.3.1 Introduction

As introduced in Chapter 1, the Gorgān Plain is an example of a highly militarised Sasanian landscape, consisting of extensive ditches, walls, forts and canals (Sauer *et al.* 2013). During the '*Gorgān Wall Project*', conducted between 2005 and 2009, numerous and well-preserved irrigation networks were found within the lowland plain (Wilkinson *et al.* 2013). This project was further expanded as part of the *Persia and its Neighbours Project*, with the aim of understanding urban expansion and settlement patterns at the frontier.

4.3.2 Physical background

The Gorgān Plain is located in the south-eastern corner of the Caspian Sea, between the Ālborz Mountains to the south, and the dry steppe to the north (Fig. 4.33). The Gorgān River currently flows west across the southern section of the Gorgān Plain, but in the past, the river course had changed significantly, as indicated by numerous palaeochannels found in the lowland areas (Wilkinson *et al.* 2013; 30). The Gorgān River originates from the Kopeh Dagh, a mountainous area of limestone rich geology (Berberian & King 1981), while several tributaries that originate from the Ālborz Mountains. Sediments derived from the latter consist of coarse material originating from metamorphic rocks, sandstones, quartzites, and dolomites (*ibid.*). Sediments sourced from these two geologically different regions, combined with extensive lacustrine and fluvial sediments deposited in the delta of the Caspian Sea, which provide the main sediment source for loess and soil formation (Kehl 2010). The soils on the plain are dominated by aridisols, which evolve into brown and chestnut soils in the uplands (Khormali *et al.* 2012). The mean precipitation also varies with altitude, at the modern city of Gorgān it is ca. 600 mm, which then rapidly drops to 200 mm in the northern steppe (Kehl *et al.* 2005).

The northern Iranian loess deposits vary from ca. 30 m on the foothills of the Ālborz Mountains and reach a maximum of ca. 60 m in the loess plateau in the steppe (Khormali & Kehl 2011). The loess forms a distinct geomorphological feature of the Gorgān Plain and is dissected by the Gorgān and Sari Su Rivers. Due to its extensive nature, the loess deposits have been extensively investigated in the region, as these provide important pedo-sedimentary archives for Quaternary climate change, particularly the transition from the Last Glacial Maximum (LGM) to the start of the Holocene (Kehl *et al.* 2005; Frechen *et al.* 2009; Karimi *et al.* 2009; Kehl 2010; Karimi *et al.* 2013; Lauer *et al.* 2017). Alternating loess and palaeosol sequences provide direct proxies for alternating phases of increased dust accumulation during cold and arid conditions, intercalated by warmer

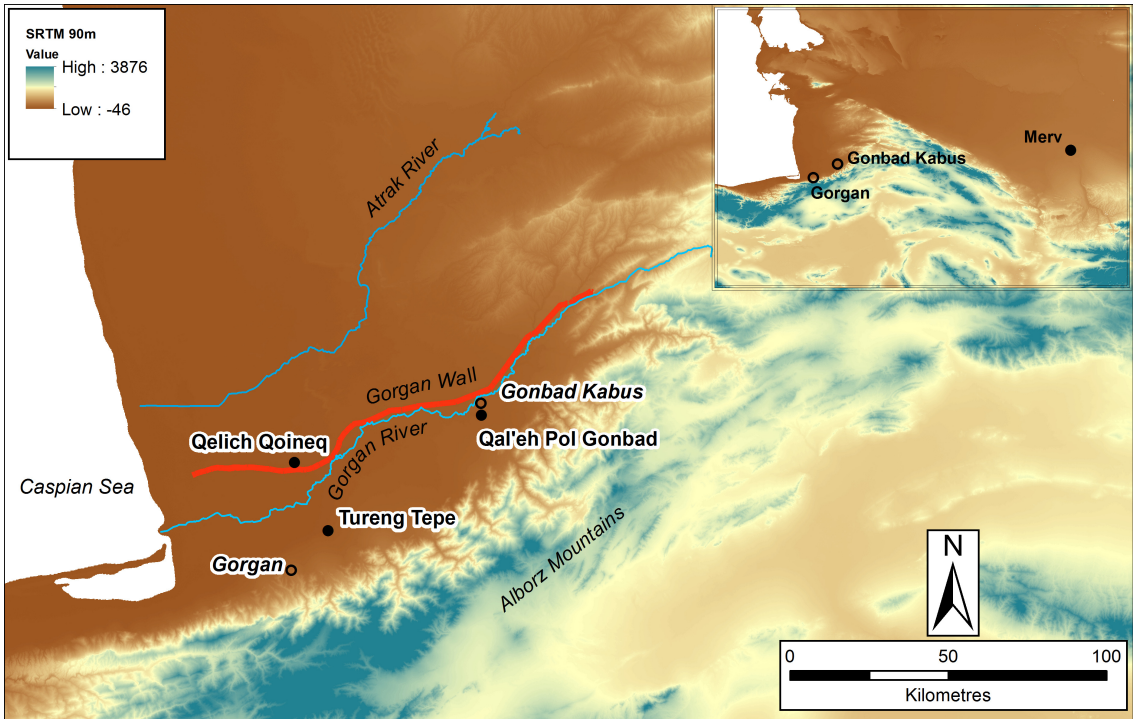

Figure 4.33. Map showing the Gorgān Plain and the main sites and features mentioned in text. Background SRTM (90m) courtesy of the U.S. Geological Survey.

and humid conditions enabling soil formation and landscape stability. These pedo-sedimentary archives have also been correlated with other palaeoenvironmental evidence for the region covering the LGM (Djamali *et al.* 2008). Holocene climate variability has also been observed in pollen cores from the Gorgān Plain. Dry phases were identified at ca. 5.9 and ca. 3.9 ka, and wet phases at ca. 2.7 and 0.7 ka (Shumilovskikh *et al.* 2016). The latter wet phase falls within the chronological period covering Late Antiquity, which correlate with other climate records covering this period in other regions of the Near East and the Mediterranean (see Sec. 1.1.2).

4.3.3 Excavation results

Within the context of the Sasanian frontiers, further expansion meant that several new urban centres and military campaign bases were established. One of the main sites investigated as part of the *Persia and its Neighbours Project*, Qal'eh Pol Gonbad, a site located in the Gorgān Plain (Fig. 4.34), was excavated. Surface pottery collected from the area of the site indicated a broad chronology ranging from the Sasanian to the Early Islamic period. The site is one of the largest rectilinear compound bases found on

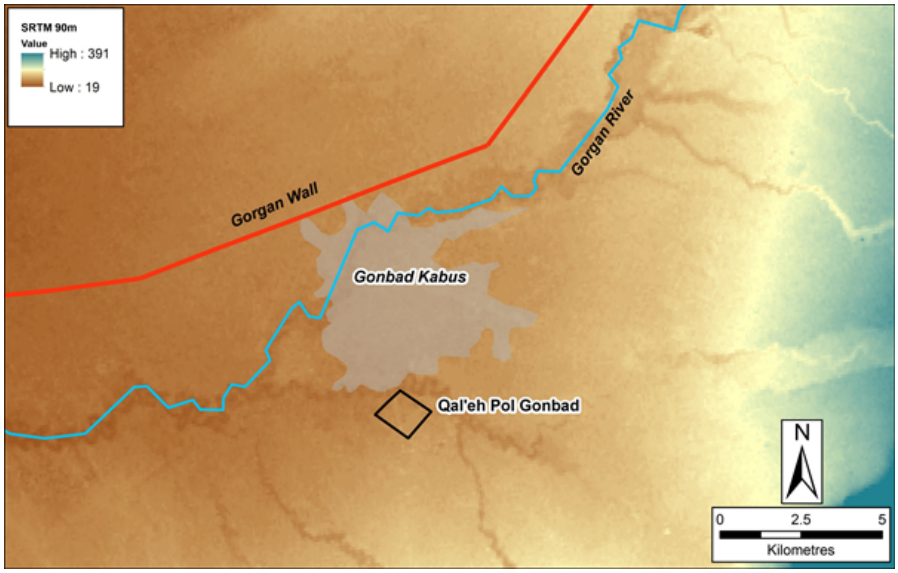

Figure 4.34. Map showing the location of Qal'eh Pol Gonbad in relation to the modern city of Gonbad Kabus and the Gorgān Wall. Background SRTM (90m) courtesy of the U.S. Geological Survey.

the plain and was strategically placed on a major river crossing, making the base easily accessible by the rivers (Sauer *et al.* 2013). The large military base was also occupied by many soldiers requiring a regular supply of water that was supplied by the nearby Chai Chai River via a raised canal (*ibid.*). The aim of the archaeological investigations conducted in 2014 was to gain a better understanding of the chronology of the site and its associated defensive moat.

In 2014 a ca. 30 m long step-trench was machine excavated through the moat to uncover the top four meters of stratigraphy to be exposed for recording and sampling (Fig. 4.35). The alluvial sediments that formed the fill of the ditch were mainly composed of alternating silty clay with lenses of fine sand. Five phases of recutting were recorded in the profile of the ditch (See Appendix E). Within the lowest fills of the ditch, bricks of Sasanian and Medieval periods were recovered, which appeared to been washed into the ditch from surrounding areas, but provided a broad indication of the periods of activity occurring in and around the immediate area. Only one sample was fully processed from the fill, and the results of the assessment are provided in Appendix E. During the 2015 season, additional samples were obtained from the old ground surface, rammed earth, rampart and collapsed deposits that formed the mound, as illustrated in Fig. 4.36.

Figure 4.35. Trench A excavated through the extensive alluvial fills (indicated by arrows) and the associated mound. (Photograph courtesy of Eberhard Sauer).

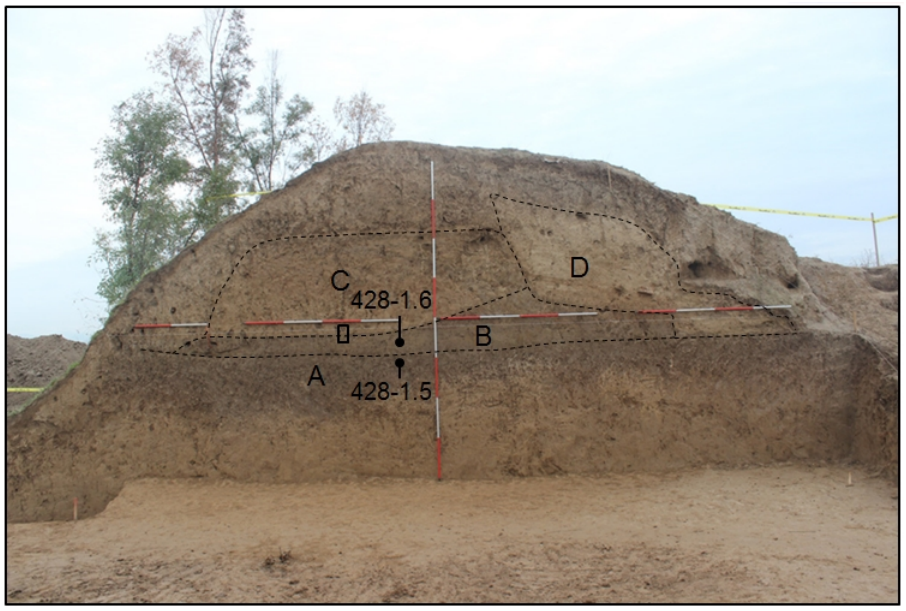

Figure 4.36. Section showing the mound and deposits uncovered: A) old ground surface,B) rammed earth, C) rampart, and D) collapse construction material mixed with loess. The closed circles indicate the locations of OSL tube samples (428-1.5 and 428-1.6), and the open box marks the location of micromorphological block sample taken. (Photograph courtesy of Eberhard Sauer).

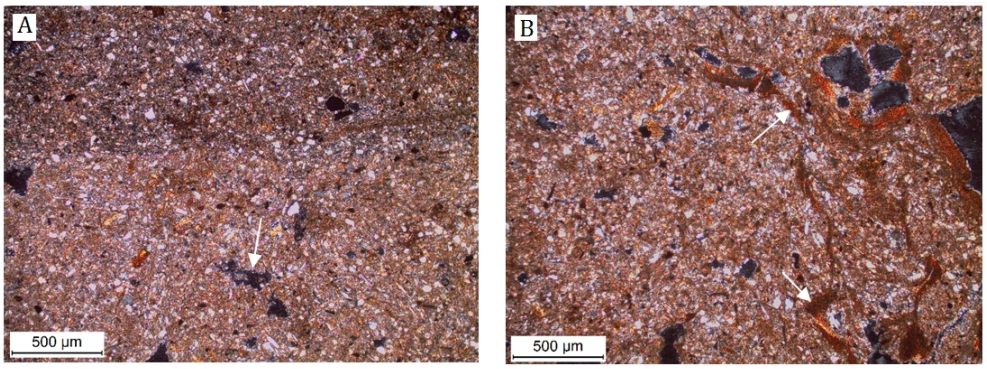

Figure 4.37. Photomicrographs taken of the mound deposits. The transition from the rammed earth to rampart showing moderately well-sorted loess, mica and occasional organic remains, arrow indicates collapsed vughs (XPL) (A); microstructure of the rammed earth deposit showing frequent vesicles, vughs, channels and dusty clay coatings around voids (indicated by arrows) (XPL) (B). Samples obtained from the mound associated with the moat, micromorphological sample taken from the transition from the rammed earth to the earthern rampart.

4.3.4 Summary of the OSL testing and micromorphological analysis

Three OSL samples were processes, two from the mound feature (samples 428-1.5 and 418-1.6) (Fig. 4.36), and one from the moat fill (sample 418-1.4) (Appendix E, Fig. E.1). The sample tested from the fill produced a small yield of coarse grained quartz, but only a small number of aliquots (n = 9) had sufficient signals to obtain D_e values. The results obtained are provided in Appendix E. No coarse grained quartz was obtained from the mound samples (428-1.5 and 418-1.6). Micromorphological thin sections of the mound deposits showed that the deposits were mainly dominated by fine-grained loess (20-50 μm). Other features and characteristics noted were the frequency of vughs and vesicle voids (Fig. 4.37; A) and dusty clay coatings (Fig. 4.37; B), suggesting disturbance of the mound. Due to the lack of sufficiently sensitised quartz (both fine and coarse-grain fraction) following sample pre-treatment, and the difficultly in obtaining a sufficient number of aliquots to run the full OSL analysis, no further processing was undertaken on these samples.

4.4 Case study 4: Fulayj Fort, Batinah coast, Oman

4.4.1 Introduction

Evidence for Sasanian military expansion in the Arabian Peninsula remains limited. It has been suggested that the region was only occasionally of interest during the 4th century AD (the expansion period) (Bosworth 1983; 15-16; Potts 1990). More recently, Sasanian-period evidence, e.g. diagnostic pottery, has been identified at several sites in the south-eastern provinces. Some of the sites that have been excavated that contained Late pre-Islamic artefacts include Mleiha, Masafi (Benoist *et al.* 2003; Mouton 2009), Kush, Khatt, Fujairah, and Dibba (U.A.E) and Sohar, Fulayj, and Rustaq in Oman (De Cardi *et al.* 1975; Wilkinson 1977; Kennet 1997) (Fig. 4.38).

The '*Saham Survey Project*' ,undertaken in 2012 (Al-Jahwari *et al.* 2014), first identified a small fortified site, the Fulayj Fort, which was later excavated as part of the *Persia and its Neighbours Project*.

Fulayj is a small fortified site located on a shallow limestone plateau outcrop 30 km south of the modern city of Sohar on the Batinah coast of Oman. Two field seasons in 2015 and 2016 involved excavations at the fort, combined with landscape survey and small-scale excavation of surface water-channels. The fort itself measured ca. 30 m x 30 m with ca. 2.65 m thick walls and four u-shaped corner towers. The foundations comprised of carefully shaped basalt stones held together with lime mortar. Inside the fort, excavations revealed that the upper levels of the fort were constructed of mudbrick, along with internal mudbrick structures to form individual living quarters. Radiocarbon dating combined with a well-constrained ceramic sequence identified four main phases of occupation of the fort, which are defined in Table 4.11.

The landscape surveys identified a series of water-related features (cisterns, water tanks, surface channels, revetments, and falaj shafts), within the immediate vicinity of Fulayj Fort. A number of shallow mounds containing reddened soil with extensive scatters of lime and fired ceramic material were also identified on the ground. These were later interpreted as remnants of lime kilns. Satellite imagery was of poor resolution for the area, requiring more extensive ground-based survey and mapping. On the ground, landscape features were difficult to trace and were often discontinuous, suggesting partial destruction or re-use of stone in later periods. Their chronological relationship was difficult to resolve on the ground, requiring further excavation and sampling to recover diagnostic artefacts and samples for absolute dating methods.

4.4.2 Physical background

The Hajar Mountain range forms the main geomorphological feature of the Oman Peninsula, which formed during the Palaeocene to Miocene tectonic collision of the Asian and

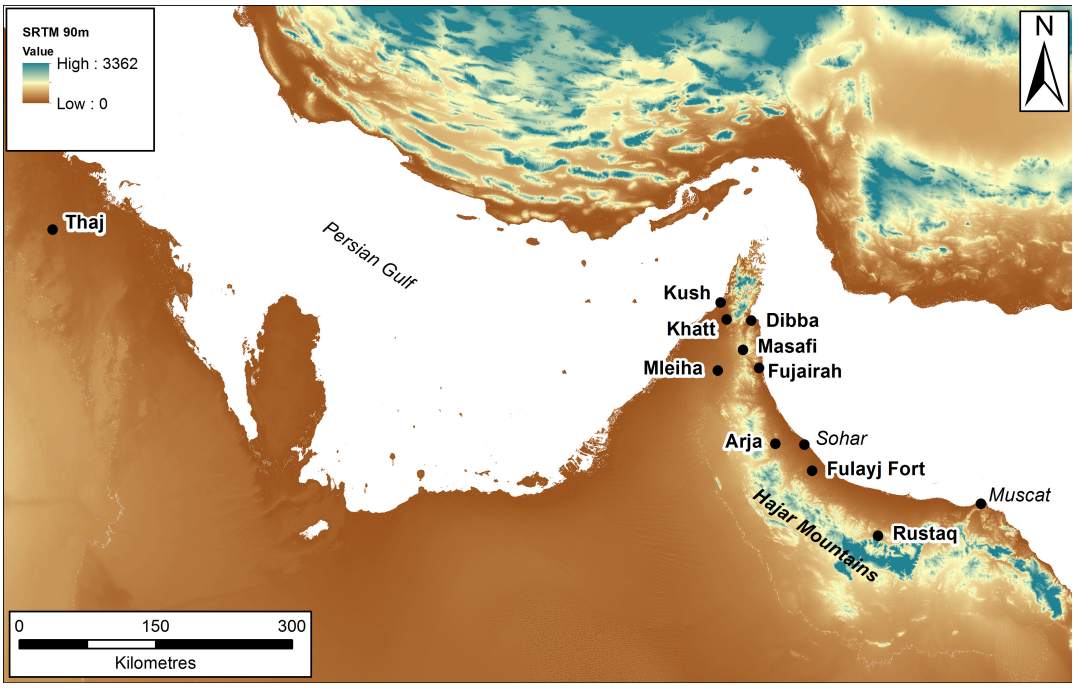

Figure 4.38. Map of the Arabian Peninsula showing the main sites mentioned in text. Background SRTM elevation data courtesy of the U.S. Geological Survey.

Phase	Period	Chronology
4	Late Islamic	10^{th}-15^{th} centuries AD
3	Early Islamic	7^{th}-9^{th} centuries AD
2	Sasanian	Early 5^{th}- mid 6^{th} centuries AD
1	Iron Age	1300 - 300 BC

Table 4.11. Occupation phases for Fulayj Fort

Arabian Plates (Parker & Goudie 2008). In the north, the mountains are dominated by limestone geology, whereas to the south metaporphic and igneous rocks occur. These are widely referred to as the Ophiolite Suite (*ibid.*). The landscapes surrounding the mountains consist of dunes, desert loess, alluvial fans, lakes, oases, wadi terraces, *sabkhas* and raised shorelines (*ibid.*). Many of these features provide records for Quaternary climate change for the region. These sedimentary archives record micro-regional climatic and environmental fluctuations (Fleitmann *et al.* 2003), that are not always detected in speleothems which cover extensive chronological time-scales but only reveal very broad changes. Late Holocene climate change is affected by the position of the inter-tropical convergence zone (ITCZ) and the influence of the Indian Ocean Monsoon (IOM) and the westerlies (*ibid.*). Extensive evidence for Late Holocene remobilisation of ancient desert dune systems is now widely recognised (Preusser *et al.* 2002; 2005). The lack of local palaeoenvironmental records, however, make it difficult to reconstruct the environmental conditions during the Late Holocene. Furthermore, more recently, archaeobotanical remains recovered from the excavation at Fulayj Fort have revealed that wood resources were exploited from upland areas, suggesting that the immediate areas surrounding the fort were harsh and lacked vegetation. Exposed ground would have enhanced surface erosion during periods of aridification and increased windiness in the region.

4.4.3 Excavation methodology

Landscape survey of the immediate area surrounding the fort identified several small surface channels (Fig. 4.39). The most well preserved channels were targeted for excavation and sampling. Each trench was hand excavated. Trenches I, J, L, M, and O were ca. 2 x 0.50 m, Trench K was ca. 3.5 x 1 m, and Trench L was ca. 3 x 1 m. The depth of each trench depended on the extent of the channel structures and associated deposits. All trenches were located using a digital GPS. Each trench was first cleaned of loose stones and photographed prior to excavation, and context descriptions followed those outlined in Section 3.2.3. All finds that were recovered from the archaeological contexts were bagged, labelled with individual find numbers and given context numbers. All sediment excavated was sieved through a coarse 1 mm mesh to ensure complete recovery of diagnostic artefacts. OSL sampling involved inserting a black PVC tube ca. 20 cm long with a ca. 1.5 cm diameter. A smaller diameter tube was used for contexts less than 20 cm thick. Combined with this, micromorphological blocks of unconsolidated sediments were taken from the channel fill and surrounding sediment for routine characterisation.

Figure 4.39. Map showing the location of surface channel features surrounding Fulayj Fort, Oman. The blue lines show the extent of channels visible on the ground (image © 2018 DigitalGlobe).

4.4.4 Excavation results

Trench I

This channel was clearly visible on the ground located on the edge of the limestone outcrop just north of the fort (Fig. 4.39) and was ca. 30 cm wide as illustrated in Fig. 4.40. The surface channel was located on-top of a carbonate-rich colluvial deposit (I.011), described as very compact pale brown (10YR6/3) silty sand. It was exposed on the north side of the trench along with an *in situ* basalt bedrock stone. Above this was an uneven layer of colluvial deposits containing silt lenses, frequent pebbles and calcareous nodules (I.005). This was cut into to form a surface consisting of rounded cobbles for the channel wall construction. Between the channel walls, the basal deposits consisted of a poorly sorted sandy gravel packing layer (I.003). The channel was lined with a layer of fragmented poorly fired ceramic material (I.007), overlying a thin layer of course sands and gravels (I.008). The fill of the channel consisted of moderately sorted light yellowish brown (10YR6/4) sandy silt deposits with occasional pebble inclusions and lenses of coarse sand (I.003). Surrounding the channel walls was a fine silty sand light brownish grey sediment, which accumulated post-construction (I.004). Covering the channel was a layer of loose stones and light brownish grey (10YR6/4) sandy silts (I.001). One abraded diagnostic ceramic fragment was recovered from a fill (I.009)

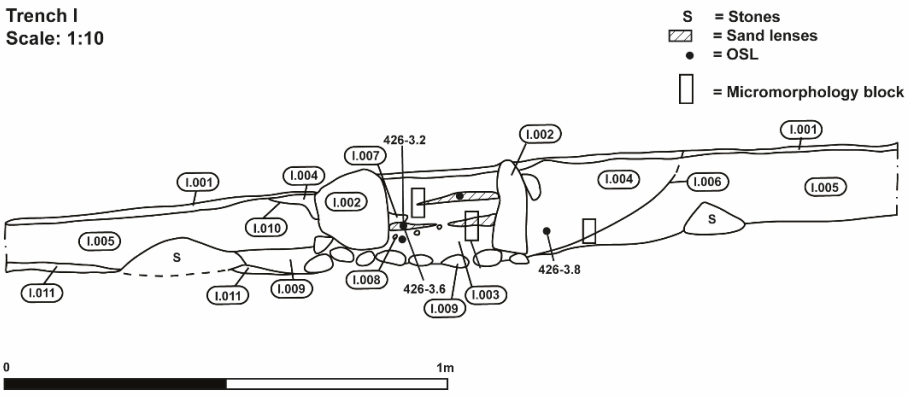

Figure 4.40. Stratigraphic section of Trench I showing the extent of contexts excavated (labelled as I.005), and location of OSL samples (426-3.2, 426-3.6 and 426-3.8) and micromorphology block samples (M1, M2 and M3). East facing section.

surrounding wall (I.002). This was identified as an Indian cooking pot dated to the Sasanian period (5^{th} - 6^{th} centuries AD).

Five OSL samples were collected from different phases of the channel construction. Sample 426-3.6 was taken from context I.008, sample 426-3.2 was obtained from the ceramic channel lining (I.007) and sample 426-3.8 was taken from deposits I.004 that accumulated behind the wall. Two additional samples were obtained but these were not processed due to time constraints.

Trench J

On the ground, this channel was considered to have been a continuation of that uncovered in Trench I, as it appeared to run in a similar orientation along the slope as seen in Fig. 4.39. Excavation confirmed that the channel was of different construction techniques as illustrated in Fig. 4.41, and did not form a continuation of the channel uncovered in Trench I. The channel was located in a small depression near a water cistern and an abandoned Late Islamic settlement. The underlying deposit was a well-sorted yellowish brown (10YR5/4) sandy silt alluvium (J.003). The walls of the channel were directly placed on this deposit, and no cuts were found. The walls of the channel were made of rounded wadi cobbles and angular worked basalt stones. The wall was filled with a loose brown (10YR5/3) sandy silt deposit (J.004) with frequent charcoal fragments, molluscs (sp. *melanoides tebrulata*), ash remains and pottery fragments, which were likely to be reworked anthropogenic deposits from the abandonment settlement. Covering the channel and associated deposits was the modern surface that was a loose yellowish brown (10YR5/4) sandy silt deposit (J.001) with frequent wadi stones and

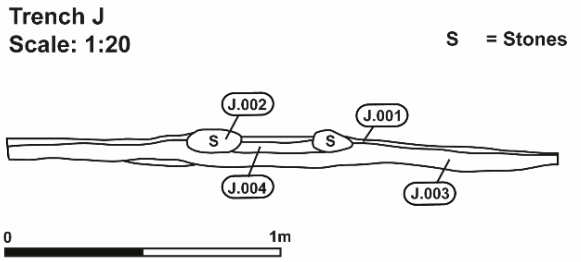

Figure 4.41. Stratigraphic section of Trench J showing the extent of contexts excavated. North facing section.

mollusc remains. Two sherds recovered from the channel fill were broadly dated to the Iron Age.

Trench K

This channel, which meandered along the slopes located to the southwest of the fort (Fig. 4.39), was approximately 1.7 m wide (Fig. 4.42). The two walls appeared to have been constructed in two separate phases. The underlying deposit was similar to that uncovered in Trench I, a moderately compact carbonate-rich pale brown (10YR 6/3) silty sand (K.018) and contained frequent pebble inclusions and Fe nodules. Overlying this was a poorly sorted sand and gravel deposit in which the feature was constructed. The first phase of construction consisted of large angular basalt stones and large wadi cobbles, approximately 40 x 20 x 30 cm in size. This formed a revetment which captured runoff from the slopes to the west. Within the fill were multiple lenses of poorly sorted yellowish brown (10YR5/4) sandy silts containing frequent pottery fragments. These deposits were partially disturbed during the construction of the second wall most likely built to channel a smaller volume of water. This wall consisted of large to medium-sized wadi stones, with the largest being ca. 30 x 20 x 10 cm in size, and the smallest ca. 15 x 50 x 10 cm in size. The stones were not as large or as deeply set as those used to construct the original revetment wall. The deposits in between the two walls consisted of moderately sorted yellowish brown (10YR5/4) sands and silts. Sediments uncovered outside of the walls were deposited more recently. On the east side of the channel, the sediments alternated between poorly-sorted sands and gravels to well-sorted sandy silts yellowish brown (10YR5/8) in colour, reflecting changes in fluvial depositional energies. Intercalated with the silt deposits was a series of coarse sand lenses suggesting mild flooding events. Two sherds of pottery were also recovered from this deposit. All of the pottery from this trench was Iron Age in date, which most probably originated from the Iron Age site located nearby and was subsequently transported downslope during the rainy seasons.

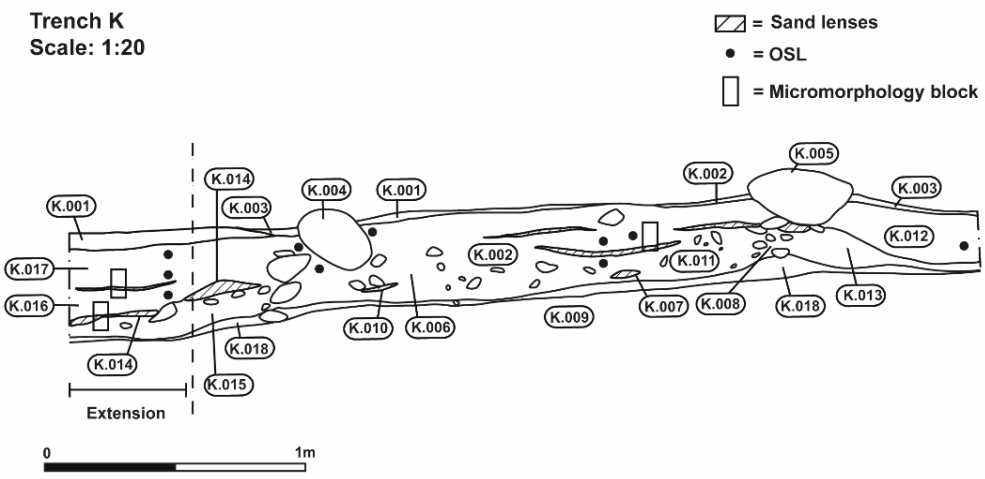

Figure 4.42. Stratigraphic section of Trench K showing the extent of contexts excavated, and location of OSL samples (unprocessed) and micromorphology samples (M1, M2, M3). Northeast facing section.

Trench L

This trench was excavated through the same channel as Trench K to confirm the full extent of deposits and features found at different locations in the southern part of the channel. This trench was not fully excavated because of the frequent large stones and lack of suitable contexts for OSL and environmental sampling. The excavation confirmed that the large revetment wall found in Trench K continued south; however, no evidence for a second wall was found. This confirmed that this system was mainly used as a revetment, and only more recently was it narrowed to form a channel to supply water to the lime processing areas.

Trench M

This channel was relatively short and may have been partially destroyed by the nearby wadi during flooding (Fig. 4.43). The underlying deposit was a loose greyish brown (10YR5/2) alluvial silty sand deposit. Overlying this was a stone wall which comprised of rounded and angular basalt stones, which were ca. 15 x 10 x 15 cm in size, and were tightly packed together. The second channel was consisted of an angular basalt stone, worked limestone and degraded ceramic material. The latter could be part of the poorly-fired ceramic lining used for the stone wall which had subsequently degraded. The fill of the channel consisted of a loose greyish brown (10YR5/2) sandy silt deposit with frequent pebble inclusions and degraded ceramic.

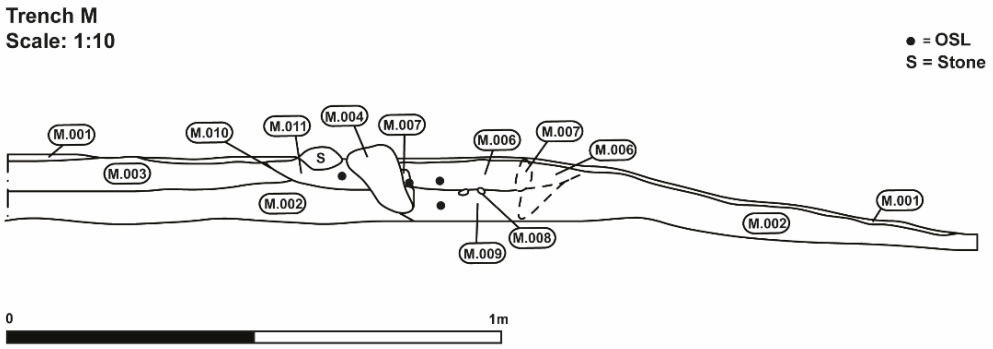

Figure 4.43. Stratigraphic section of Trench M showing the extent of contexts excavated, and location of OSL samples (unprocessed). West facing section.

Trench O

This trench was excavated through the main channel to understand different construction materials used to repair the channel walls (Fig. 4.44). The original wall was built from rectangular rounded wadi cobbles similar to those uncovered in Trench M. The wall was deposited in a well-sorted yellowish brown (10YR5/4) wind-blown sediment. The largest of the stones used in the wall construction were ca. 30 x 10 x 15 cm in size. The other side of the channel consisted of reused highly fired ceramic material (ca. 30 x 20 x 5 cm in size). This section of the channel wall was supported by frequent angular basalt stones packed behind it. Filling the channel was a compact well-sorted yellowish brown (10YR5/4) sandy silt with reworked clay aggregates. Overlying this was a silty clay grey ashy deposit approximately 2 cm thick, and a compact moderately sorted pebble lens. Ceramic material was then placed on top of the pebble layer. Overlying the ceramic material was a yellowish brown (10YR5/4) sandy silt fill containing frequent fragments of ceramic material and mollusc remains.

Summary

Small-scale excavations at Trench I and J were established to determine if the two channel sections identified during the landscape survey were of the same feature, as the full extend of the channel was not clearly visible on the surface. Excavation confirmed that this structure was of two different phases. Trench I revealed a channel with worked stone walls cut into the slope. This channel was constructed on a levelling surface and lined with a loosely fired orange ceramic material with frequent gravel inclusions, ideal for preventing water loss by sediment percolation. Surface runoff was the most likely source of water to feed the channel. The direction of flow was not easy to determine from the modern day surface but most likely flowed from fields located at slightly higher

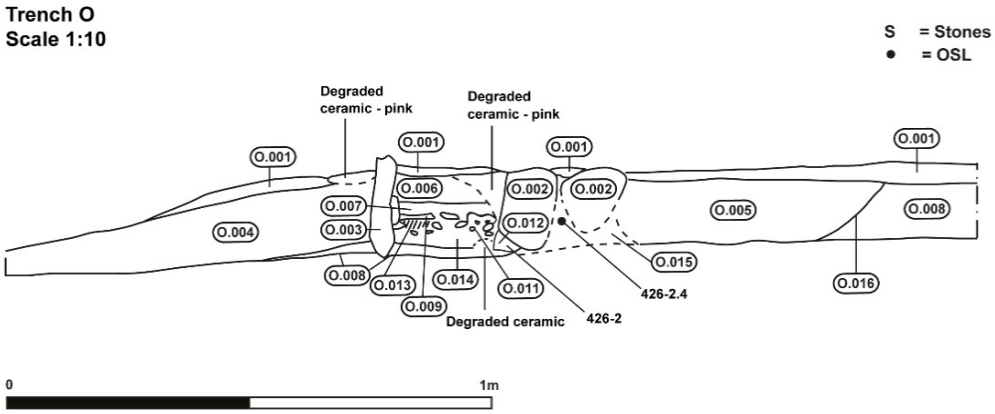

Figure 4.44. Stratigraphic section of Trench O showing the extent of contexts excavated and location of OSL samples. East facing section.

levels enabling water to flow through the field's downslope with gravity. Unfortunately, the fertile area to the north of the site had been significantly altered and so the original surface topography is no longer obvious. The most likely explanation is that there was a natural decrease in gradient towards the east where the modern way wadi occurs and where other groundwater sources end, suggesting that surface water was channelled along the slope into the alluvial plains to the north. Trench J confirmed that this section of the channel was not associated with that near the fort. Instead, this was a separate channel feature which consisted of two simple stone lines with no cuts or channel lining placed onto the sediment. This simple structure suggests that it may have been constructed to control groundwater associated with a nearby cistern.

Trench K was excavated to determine the relationship of this long channel system with the nearby lime kiln industrial areas south-east of the fort. This part of the channel had two distinct phases. The first phase consisted of large basalt stones placed on the East side of a gentle slope to act as a dam to channel water from the South. The modern surface appeared to have a subtle depression and accumulation of silts suggesting that this was an endpoint for surface runoff water from the West. This appeared to form a paleochannel-like feature which may have joined the wall constructed to channel the water from the South. At some point in time, the stone revetment was narrowed by constructing a second wall on the West side to form a narrow channel approximately 1 m wide. This second wall was subsequently undermined as some stones had been disturbed and evidence for rebuilding could be seen by the re-use of worked stones possibly originating from the nearby Late Islamic settlement. The preservation of the original channel sediments was poor as there was an abundance of coarse sands and gravels that had been washed into and against the original wall. This suggests that this system was most likely self-cleaning. Silts preserved behind the original channel wall

may have the best potential for dating using OSL and recovered ceramics are more likely to be linked to the time of construction.

Finally, the third channel feature closest to the wadi consisted of two phases of construction. The first was built from wadi cobbles to make a neat and substantial wall, which was later repaired using ceramics originating from the lime kiln area nearby. Interestingly, a similar ceramic lining material to that uncovered in Trench I was found in Trench O during the second repair phase. Furthermore, a nearby ceramic and stone-lined basin were found which could have been used for storing water brought by the channel for industrial activities such as lime burning. The surviving section of this channel appeared to be very short and narrow suggesting that it was not constructed to channel large volumes of water like that observed at Trench K, but instead, was used to channel water from the nearby wadi during the wet seasons. The following section provides a basic micromorphological characterisation of some of the main deposit types uncovered during the channel excavations.

4.4.5 Micromorphological assessment

Micromorphological analysis was undertaken on four thin sections from profiles uncovered in Trench I and Trench K, these were relatively shallow deposits and were generally poorly sorted and friable in nature. Three main deposit types (DT) were identified in thin sections. These comprised of poorly sorted sandy silts (DT1), coarse sands and gravels (DT2), and carbonate colluvial deposits (DT3).

Sandy silt alluvium (DT1)

This deposit type indicated periods of enhanced fluvial activity at the site and was present in all thin sections examined. It had a dominant close fine enaulic *c/f* distribution. The groundmass was dominated by a stipple-specked *b*-fabric. Microcharcoal and reworked soil aggregates were also found in small proportions. The minerogenic component mainly consisted of Fe nodules, pyroxenes, pedogenic carbonate, and occasional coarse-grained quartz. Thin lenses of silt forming microcrusts and aggregate cappings were common, and intercalations suggesting changes in fluvial activity (Kühn *et al.* 2010a) (Fig. 4.45; C). Carbonate micritic coatings and void infillings were present, suggesting dissolution and reprecipitation of pedogenic carbonates during wet and dry periods (Lindbo *et al.* 2010; Khormali & Kehl 2011). Linear channels and planar voids were common. The remains of poorly degraded roots were frequent (Fig. 4.45; D), and some were partially or completely mineralised. Complete replacement of organic matter in root cells by minerals forming rhizoliths, are common in many arid regions with calcareous bedrock (Klappa 1980).

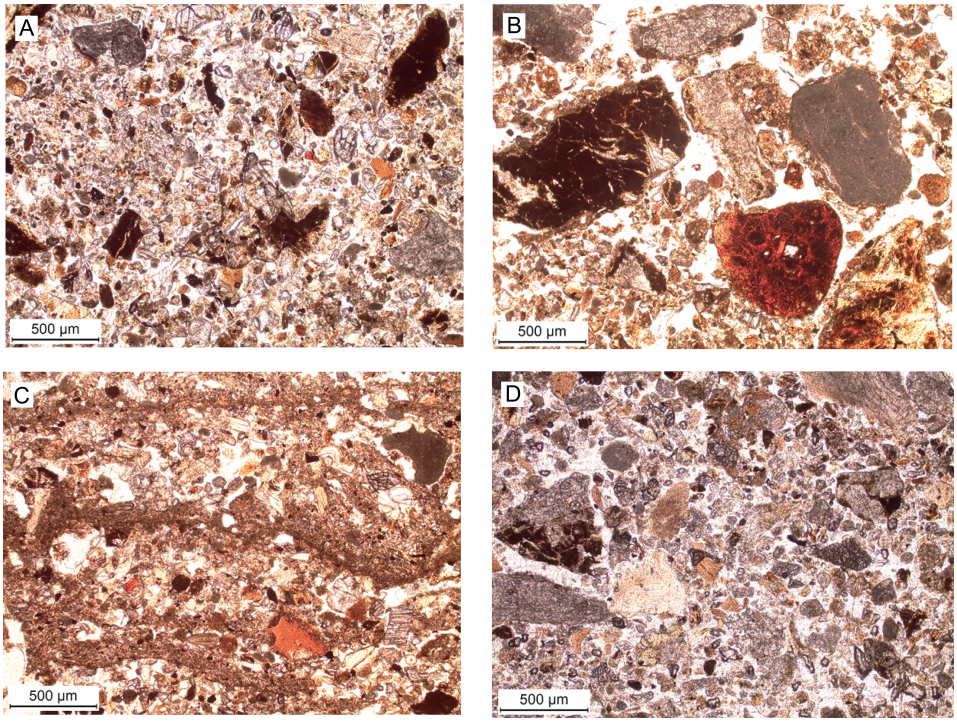

Figure 4.45. Photomicrographs of the various deposit types identified in thin sections. Sandy silt deposit (A) (Trench I, thin section M2); coarse sands and gravels (B) (Trench I, thin section M1); silt intercalations (cappings) in fine sand lenses (C) (Trench K, thin section M2); and colluvial deposits with abundant carbonates (D) (Trench I, thin section M3) (PPL).

Coarse sand and gravel alluvium (DT2)

This deposit was characterised by gefuric *c/f* related distribution with granostriated and concentrated stipple-speckled *b*-fabric surrounding aggregates (Fig. 4.45; B) These lenses were ca. 1 cm thick. The deposit was poorly sorted and contained a variety of coarse components: rock aggregates, heavy minerals, and pedogenic carbonates that were between 150-250 μm and rounded, suggesting long fluvial transport distances. Some post-depositional disturbance occurred resulting in the mixing of coarse sands with fine sands and silts. Occasional fining-upwards from coarse to fine was found in the channel (Trench I), suggesting a gradual reduction in fluvial energies.

Colluvium (DT3)

This deposit was characterised by its dominant single grain microstructure, monic *c/f* related distribution and undifferentiated grano-striated *b*-fabric, and coarse inclussions ranged between 50-100 μm in size (Fig. 4.45; D). This deposit was dominated by reworked carbonate aggregates and quartz. The quartz appeared as a secondary component that infilled voids, suggesting aeolian origin.

Summary

The mineralogical and aggregate inclusions present within the three deposit types reflect the sediment origins. The dominant component being fluvially reworked igneous pebbles originating from the ophiolite complex that form the Hajar Mountains (Parker & Goudie 2008). Furthermore, heavy minerals such as pyroxenes were present in abundance, suggesting that sediments originated from the weathering of volcanic material (Sedov *et al.* 2010; 2011) that originated from the mountainous regions. These sediments were transported via wadis from the foothills to form alluvial deposits on the lowland floodplain. Aeolian derived carbonates and quartz were frequent in all thin-sections examined. The exact source of this windblown material is difficult to trace without further geochemical analysis. It is possible that sediment found within the channel features sampled, originated from local sources, such as alluvium, coastal dunes or *sabkahs* (Pease *et al.* 1999). More distant sources of aeolian deposits may have originated from the remobilisation of the Wahiba sands (*ibid.*), located to the southeast of Oman.

Implications for luminescence dating

The micromorphological analysis enabled the identification of subtle variations between individual archaeological contexts that were not clearly visible in the field. The highly deflated landscape - as observed in the field - and the presence of coarse sand and gravel lenses, implies that fine sediments can be easily remobilised in such landscapes. Unless

preserved under ancient walls or other permanent site or landscape feature, sediments can be completely removed from the geoarchaeological archive. Due to the shallow nature of these deposits, significant reworking and disturbance was found, particularly the deposition of colluvial deposits built up behind and within channel walls. Aeolian quartz was found in abundance in the archaeological contexts uncovered, suggesting the potential for sediments to have been fully reset during sunlight exposure.

Chapter 5
Luminescence dating applications

5.1 Introduction: An outline of issues

As discussed in Chapter 4, a range of archaeological sites set in distinctively different landscapes were examined in this study, each with a differing set of sedimentary compositions. The combination of mineralogical complexity and anthropogenic modification of sediments strongly influenced the selection of both the mineral type for luminescence measurements and the choice of the experimental techniques that were applied. Two primary experimental issues that arose at each site included: a) the selection of the optimal type of mineral for a particular context, and b) the complexity of the sedimentary environment within which a sample is situated, both of which dictated the extent to which OSL dating approaches could be applied. With regards to the distribution of radionuclides within a sedimentary matrix, for example, which affects the assessment of the dose rate, a careful consideration of the various components of the sediment and other external variables is required. The experimental approaches applied in this study were adjusted to suit the particular site conditions. The degree to which the above issues affected the application of luminescence in each of the regions studied, and the extent of any previous luminescence work are briefly outlined in the following section.

5.1.1 Georgia

The application of OSL dating to archaeological sites and landscapes in the Caucasus region has been limited, being restricted to late Pleistocene-early Holocene fluvial sands and gravels (Von Suchodoletz *et al.* 2016), loess deposits (Pánek *et al.* 2012) and Palaeolithic cave sediments (Pinhasi *et al.* 2008). These applications gave no clear characterisation of the luminescence signals that might be obtained with samples from archaeological contexts similar to those included in this study. In the case of Late Antique and Medieval sites, such in the upland regions of the Central Caucasus, for example, little had been known until recently of the basic composition of sediments and soils. Intensively terraced landscapes have been found in the Kislovodsk Basin, North

Caucasus (Korobov & Borisov 2013), but no attempt at dating sediments using OSL has been applied. In the Dariali Gorge, the sediments sampled for dating measurements were derived from the erosion of local bedrock (folded sandstones, granites and rhyolites) and potentially included aeolian deposits from high winds which tunnel through the narrow gorge. Overall, the sediments from this region are dominated by components of volcanic and plutonic origin.

At Dariali Fort, the sedimentary deposits were further modified by a range of anthropogenic processes (e.g. mixing, dumping, trampling and heating) and the extensive occupational deposits were heavily modified and disturbed by sediments originating from a basalt outcrop. The complex burial history of sediment deposits resulted in heterogeneous strata, containing many inclusions, such as rock and heavy mineral inclusions, carbonates, hearth debris (charcoal and siliceous aggregates) and heated sediments. The latter provides an opportunity for minerals to be sensitised further through the process of heating. In the case of the agricultural terraces (DPS-6 and DPS-9), sediment formed by erosional slope processes progressively aggraded behind revetment walls, enabled the good potential for exposure of sediments to sunlight prior to burial, although within a relatively short timescale (ca. 10 years). Exposure to sunlight may have been highly variable, and the use of quartz in luminescence measurements, rather than feldspar, has been preferred in this study, with the application of OSL techniques with single grain resolution being a necessary requirement. Where quartz is one amongst a complex set of minerals, particularly sodium feldspars, issues related to the extraction of a pure quartz extract arise. Therefore it will be important to check for any residual feldspar grains after chemical and physical preparation methods. Furthermore, a check for feldspar signals will also be required in samples where residual feldspars remain.

5.1.2 Azerbaijan

In the semi-arid lowland plains of Caucasus, the sediments originated from volcanic sources found in the Southern Caucasus (Gudjabidze & Gamkrelidze 2003). The mound deposits associated with large-scale canal irrigation systems running next to the ancient city of Ören Qal'eh, located in the Mil Steppe, were typically composed of large 'clods', bioturbated and reworked alluvium and loess deposits and were assumed to have been partially zeroed. In these arid regions, 'lumpy' strata containing abundant carbonate material can complicate the evaluation of the radiation dose-rate. Below the primary canal deposits, the fluvial sediments present are, on the basis of previous luminescence studies of fluvial systems (e.g. Rittenour 2008), expected not to have been thoroughly exposed to daylight before burial, and contained a wide range of feldspars, including both sodic and potassic variants. Similar to the samples from Georgia, systematic checks for residual feldspar signals will be important to isolate those signals solely from quartz.

5.1.3 Iran

In the Gorgān plain, sediment that entered the floodplain derived from many sources: 1) the weathering of Precambrian metamorphic rocks, sandstones, quartzites, limestones and dolomites that form the Ālborz mountain range (Tchalenko *et al.* 1974), 2) the loess plateau (e.g. Karimi *et al.* 2009, and 3) sediment transported westwards over the Caspian Sea (e.g. Beaumont 1972). Previous analysis of samples taken from various archaeological deposits, including canal upcast banks, contained virtually no coarse-grained quartz and had very weak luminescence sensitivity to radiation dose (Schwenninger & Fattahi 2013). To circumvent this problem found in other regions of Iran, measurement procedures employing the fine grain 'polymineral' fractions of loess (Frechen *et al.* 2009) and coarse grain feldspar applied to qanat mounds (Fattahi 2015). Such issues were expected to be encountered within the moat at Qal'eh Pol Gonbad, where the sediment fill and mound predominantly comprised of fine silt and clay and reworked loess.

5.1.4 Oman

Fulayj Fort is located on the Arabian Peninsula, between the Hajar Mountains and the Bhatinah Coast. The site is located on a shallow plateau of ultrabasic igneous rock connected with the wider Ophiolite geological complex. Limestone and dolomitic limestone occur in the surrounding areas of the site and OSL dating studies applied to alluvial fan deposits (Fuchs *et al.* 2007), have similar characteristics to those found in the Central Caucasus, such as heterogeneity and low-quartz yield. Although wind-blown deposits are widespread, their high carbonate content has given rise to issues related to the assessment of dose-rate (Preusser *et al.* 2002; Zander *et al.* 2007). Only one example of OSL dating applied to channel irrigation structures in Oman has been reported (Desruelles *et al.* 2016). However, no detailed characterisation of the luminescence characteristics were provided in these studies. The samples obtained from the small surface channel systems surrounding Fulayj Fort were variable; some contexts contained fired materials and plaster used to line the channels. The sediments captured behind, between and within the fill of channel walls were deposited by fluvial and aeolian processes.

The following section provides a broad overview of the OSL dating technique, its methodological developments and the application of coarse-grained quartz to different depositional contexts. Table 5.1 provides the geological source and depositional contexts for samples obtained from the various regions explored in this research.

Sample number	Location	Site	Geological source	Archaeological deposit type
400-1	Dariali Gorge, Georgia	Dariali Fort	M/V/P	Mi
400-3		Dariali Fort	M/V/P	Mi
412-9.1		Tsdo-DPS-6	V/P/S	CL
412-15.3.1		Dariali Fort	M/V/P	O
412-15.2.1		Dariali Fort	M/V/P	C
412-15.1.1		Dariali Fort	M/V/P	PL
412-17.2		Qobi-DPS-9	V/P/S	CL
413-1.1	Mil Steppe, Azerbaijan	Ören Qal'eh	V/M/S	U
413-1.3		Ören Qal'eh	V/M/S	U
413-1.6.1		Ören Qal'eh	V/M/S	U
413-1.7.1		Ören Qal'eh	V/M/S	U
413-1.8.1		Ören Qal'eh	V/M/S	OGS
413-1.8.2		Ören Qal'eh	V/M/S	PL
413-2.1.1		Ören Qal'eh	V/M/S	U
413-2.2		Ören Qal'eh	V/M/S	U
413-3.3		Ören Qal'eh	V/M/S	CF
413-3.6.1		Ören Qal'eh	V/M/S	U
413-3.8		Ören Qal'eh	V/M/S	NA
426-2.2	Batinah Plain, Oman	Fuleyj	P	CL
426-2.4		Fuleyj	P	WF
426-3.2		Fuleyj	P	CL
426-3.6		Fuleyj	P	CL
426-3.7		Fuleyj	P	CF
426-3.8		Fuleyj	P	WF
418-1.1	Gorgān Plain, Northeast Iran	Qal'eh Gonbad	S	CF
418-1.4		Qal'eh Gonbad	S	CF
428-1.5		Qal'eh Gonbad	S	OGS
428-1.6		Qal'eh Gonbad	S	PL

Table 5.1. Summary of samples analysed in this research. Geological source: M = metamorphic, V = volcanic, S = sedimentary, P = plutonic. Archaeological deposit type: Mi = midden, O = occupation, C = collapse, PL = packing layer, CL = colluvium, U = upcast, OGS = old ground surface, C = construction, CF = canal fill, NA = natural alluvium, QU = qanat upcast, WF = wind-blown fill

5.2 Sample preparation

Firstly, the samples collected from the various regions and archaeological contexts were processed under low-energy subdued red light conditions. This was to prevent accidental bleaching of the OSL signal. Sub-samples of sediment were carefully excavated from tube and/or sediment blocks, taking care to prevent disturbance and mixing.

Two sub-samples were collected: 25 g of sediment for the OSL analysis and 25 g of sediment for dosimetry. Both sub-samples were dried at 30-40°C for 48 hours. Once dry, the OSL sub-sample was sieved through 355, 200, 150 and 90 μm mesh. A small quantity of sieved material was then visually examined under a binocular microscope in order to assess the following:

- The identity of organic material or clay coatings
- The frequency of quartz minerals in each fraction
- The robustness of quartz minerals after HF treatment by applying pressure to individual grains
- The occurrence of any residual feldspar grains

A basic visual examination enabled each sample to be assessed to determine the types of density separation and chemical treatment required to refine the sample prior to OSL testing.

5.2.1 Chemical treatment

Once the appropriate fraction had been selected, the sub-sample was wet-sieved and washed with industrial methylated spirits (IMS), acetone and then ultrasonicated to clean and disaggregate the sample. The samples were then treated with dilute hydrochloric acid (HCl) (17%) to remove carbonates, dried and then chemically etched using hydrofluoric acid (HF) (40%) for 45 minutes to remove other more resistant mineral components, but also to remove the outer alpha dosed layer of quartz grains. This is important as alpha irradiation can penetrate up to 30 μm and HF etching reduces the alpha dose rate to a negligible level. Finally, all samples were then treated with 30% hydrochloric acid (HCl) to for 45 minutes to remove precipitates from the HF treatment.

In a number of samples, HF resistant feldspars were found in large quantities, even after full chemical treatment. For those samples containing significant proportions of feldspars, heavy liquid separated and HF treatment was repeated. A simple grinding procedure using a mortar and pestle followed by sieving helped to purify the chemically treated samples and the removal of residual feldspar.

OSL sample	Location	Landscape feature
412-9.1	Georgia	Terrace
412-17.2	Georgia	Terrace
400-3	Georgia	Occupation deposits
400-1	Georgia	Occupation deposits
412-15.3.1	Georgia	Occupation deposits
412-15.2.1	Georgia	Occupation deposits
412-15.1.1	Georgia	Occupation deposits
413-1.1	Azerbaijan	Canal
413-1.3	Azerbaijan	Canal
413-1.6.1	Azerbaijan	Canal
413-1.8.1	Azerbaijan	Canal
413-2.1.1	Azerbaijan	Canal
413-3.3	Azerbaijan	Canal
413-3.6.1	Azerbaijan	Canal
413-3.8	Azerbaijan	Canal
426-2.2	Oman	Channel
426-2.4	Oman	Channel
426-3.2	Oman	Channel
426-3.6	Oman	Channel
426-3.8	Oman	Channel

Table 5.2. OSL samples with suitable characteristics for full analysis.

5.2.2 Density separation

Separation was achieved using prepared sodium polytungstate (SPT). The first stage of separation was carried out to separate clay, K- and Na- feldspars ($<$2.60 g cm^3) from quartz, plagioclase feldspar and other heavy minerals ($>$2.60 g cm^3). Material that sank was retained and separated again to extract pure quartz ($<$2.75 g cm^3) from heavy minerals, such as zircon ($>$2.75 g cm^3). To ensure full separation of minerals, the vials were centrifuged for 1 minute at each stage. However, initial testing and visual examination of separated sample extracts showed that not all minerals completely separate according to densities given in the published literature. This procedure had to be repeated for nearly all samples from Azerbaijan. Variable quartz densities could be caused by mineral shape, the presence of external mineral growths and the presence of voids created from weathering.

The following section will provide the technical background of the OSL procedure applied to coarse-grained quartz from each sample (Table 5.2).

5.3 Optically Stimulated Luminescence (OSL)

5.3.1 Introduction

Luminescence dating is a trapped charge dating method (Aitken 1985), which is based on the energy band model where electrons are moved and stored within traps at different energy levels between the conduction and valence band (Aitken 1985; Chen & McKeever 1997) (Fig. 5.10). The luminescence dating technique involves two methods for measuring energy trapped within crystalline materials such as quartz and feldspar. This can be achieved by heated during measurement, referred to as thermoluminescence (TL), and by exposure to artificial light, which is termed optically stimulated luminescence (OSL) (Huntley *et al.* 1985; Aitken 1998). Optical dating methods utilise the OSL signal from quartz (Smith *et al.* 1986) and feldspar (Godfrey-Smith *et al.* 1988) when stimulated with visible blue light. Alternatively, infrared stimulated luminescence (IRSL) (Hütt *et al.* 1988) is used to obtain signals from feldspar when stimulated with infrared light. The measurement protocol employed in optical dating is determined by the mineral of choice and grain size. The single aliquot regenerative (SAR) protocol (Murray & Wintle 2000; 2003) is now widely employed and has significantly improved the precision and reliability of the OSL dating technique. For this protocol to perform correctly, it is assumed that trapped electrons within the mineral grains have been effectively removed by exposure to light (also referred to as 'zeroing') during transportation. Effective zeroing is typical for sediments transported by aeolian processes, and these are classified as 'well-bleached' sediments (Duller 2008a). Once the mineral grains have been deposited and buried, the amount of energy stored within the mineral grain equates to the duration of burial in which they have been exposed to ionising radiation from the surrounding sedimentary medium. Alternatively, sediments deposited by fluvial, colluvial or anthropogenic processes, zeroing is less effective, and a residual signal is likely to remain in the mineral grains measured, these are termed 'poorly bleached' sediments (*ibid.*) (Fig. 5.1). To overcome issues related to partial bleaching, small aliquots or single-grain methods are employed (*ibid.*) (See Sec. 5.6.2).

5.3.2 Age determination

To determine an OSL age, the natural luminescence signal and the determination of the burial dose rate for each sample is first required (Aitken 1985). The equivalent dose (D_e) is the amount of energy stored within the mineral grain since last exposure to daylight and is measured in Grays (Gy). This is divided by the environmental dose rate (D_r), which is the total amount of ionising radiation delivered to the sample of around several milligray per year (mGy/a). Ionising radiation comes from the radioactive decay of uranium, thorium and potassium and a small proportion from cosmic rays (see Sec. 5.11).

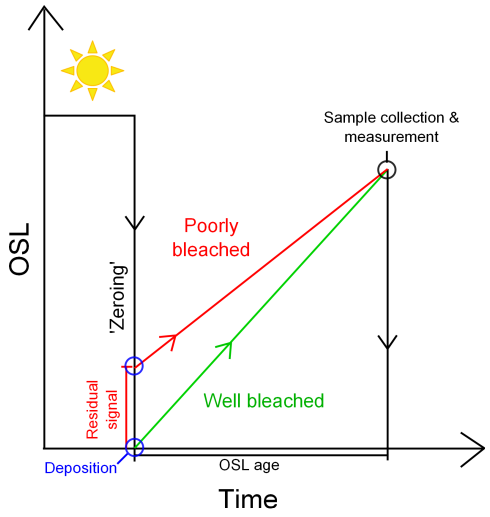

Figure 5.1. Schematic representation of the process of luminescence dating of sediments.

An OSL age is determined using the following equation;

$$\text{Burial age (years)} = \frac{\text{Equivalent dose } D_e \text{ (Gy)}}{\text{Dose rate } D_r \text{ (Gy year}^{-1}\text{)}} \tag{5.1}$$

5.4 Instrumentation

One major step in luminescence dating and the routine application of the SAR procedure was the development of semi-automated readers. In this research, a TL-DA-12 reader was used which includes a heating facility for TL measurements and a light stimulation facility for OSL measurements. In this research small-aliquots were used. Grains were mounted onto a 10mm diameter stainless-steel disc and attached with silicone oil (Silkospray). Each disc was then placed onto a 24-disc carousel which holds each disc in place during repeated heating, stimulation and luminescence was measured. A 24-disc carousel was used to ensure irradiation 'cross-talk' between adjacent discs on the carousel (Fig. 5.2). Each disc was lifted and heated by the heater plate and then stimulated with a light source to excite electrons from traps in the crystal lattice. Luminescence measurements on quartz were performed at elevated temperatures (usually 125°C) and stimulated with intense light. For OSL measurements, blue light (LED: 470±30 nm) was used to stimulate luminescence emission. For IRSL measurements, IR emitting LEDs (880±80 nm) provide the stimulation source to the sample are used (Bøtter-Jensen 1997; Bøtter-Jensen *et al.* 2003a) (Fig. 5.3). A conventional bialkali EMI 9635 QB photomultiplier tube (PMT) was used in a 'photon counting' mode (Bøtter-

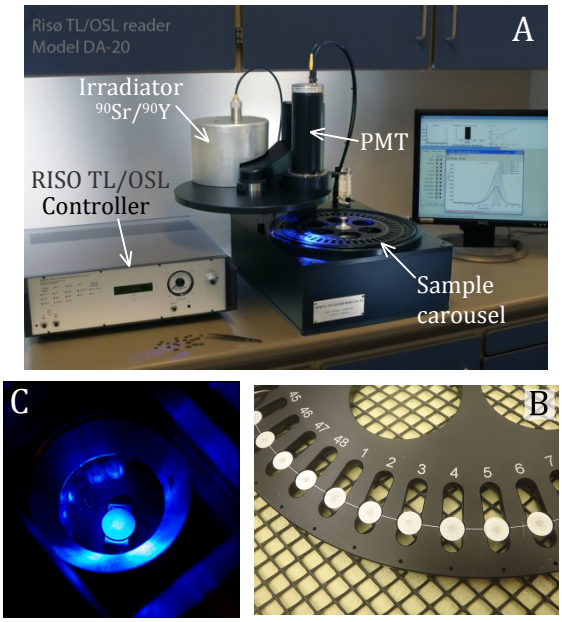

Figure 5.2. A) Shows the main components of a RISØ reader, including the 90S/90Y beta irradiator, photomultiplier tube (PMT), carousel and controller. B) Close-up of a 48-disc carousel containing samples. C) Image of stainless steel sample shown located on the heater plate and under blue light stimulation. (Source: Guide to "The Risø TL/OSL Reader" DTU, 2015)

Jensen 1997), to detect the luminescence and was positioned directly above the sample in order to collect as much light as possible.

5.4.1 Detection filters

Detection filters are used to detect the luminescence emission and discriminate against any scattered light from the stimulated source from reaching the PMT. The Hoya U-340 filter placed in front of the PMT tube transmits light in the ultraviolet (UV) region (Fig. 5.5). A Schott BG-39 filter was used for βTLD measurements as it covers a broad bandwidth covering blue-green transmission ranges required for detection of TL peaks of calcium fluoride (discussed in Sec. 5.12.5).

5.4.2 Optical stimulation modes

The reader was used in a continuous wave (CW) mode to measure CW-OSL and linearly modulated OSL (LM-OSL) (Fig. 5.6). The intensity and form of the CW-OSL decay curve stored trapped charge and the route of transfer charge from the traps to recombination centers. An LM-OSL signal is generated when the intensity of the stimulation,

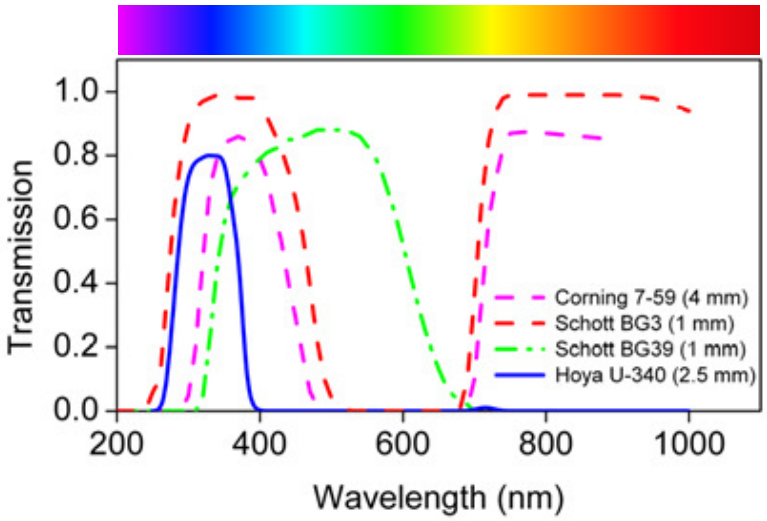

Figure 5.3. The emission spectra of blue and IR LEDs used in the Risø reader combined with the transmission curve of the Hoya U-340 filter and also a blue filter pack (not used). (Source: Guide to "The Risø TL/OSL Reader" DTU, 2015: 15).

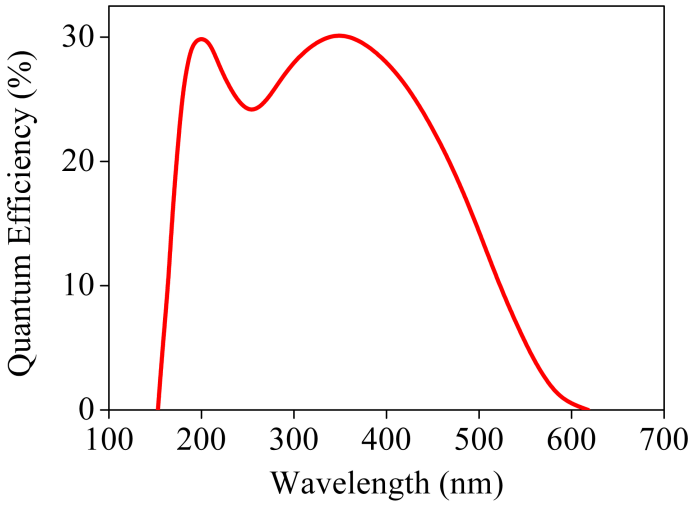

Figure 5.4. Quantum efficiency of the bialkali EMI 9235 QB photomultiplier tube (Source: Guide to "The Risø TL/OSL Reader" DTU, 2015: 7).

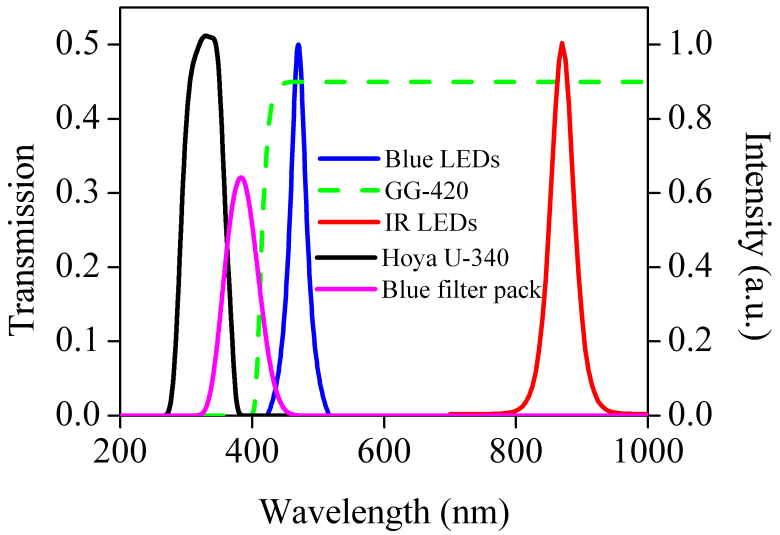

Figure 5.5. Different filter packs used for filtering light within a particular energy window used in the RISO system. Corning 7-59 and Schott BG3 (not used). (Adapted from Guide to "The Risø TL/OSL Reader" DTU, 2015: 7).

light is increased in a linear manner, from zero to maximum power (Bulur 1996). This is used to allow the identification of different OSL signal components, in particular the fast component commonly used in the OSL dating procedure. The LM-OSL decay signal appears as a series of peaks, each representing different components present within a crystalline material.

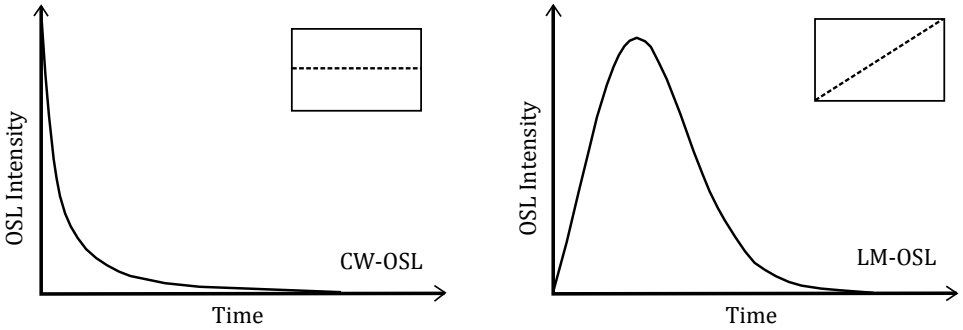

Figure 5.6. Optical stimulation modes used in experiments.

5.4.3 Beta irradiation

The Risø reader was equipped with a radiation source containing a ^{90}Sr ^{90}Y (Beta-41) source. The dose rate from the source was calculated using quartz (90-150 μm) irradiated with gamma radiation at a secondary standards laboratory (Göksu *et al.* 1995).

5.4.4 Residual signals

Prior to measurement, each sample disc was subjected to a routine background signal check. Discs were cleaned with dichloromethane (DCM) and ultrasonicated to remove any additional residues arising from previous use. Each disc is irradiated ($\sim$4 Gy), pre-heated at 220°C, and stimulated with blue light to test for a residual optically stimulated signal.

5.4.5 Data acquisition

The reader system is controlled using Minisys Windows programme (version 3.15) (Markey *et al.* 1997). The sequence of measurements steps applied was written in the i.c. SEQUENCE Editor, version 2.02 (Duller 2001). Prior to running the sequence, the blue LED counts and PMT dark counts were measured as a function of high voltage (HV), these counts were monitored to optimise the signal-to-noise ratio. These were usually between 40-60 counts per second (cps); any higher and the HV and blue LEDs were reset, and the sequence was restarted. Once a sequence of measurements was complete, the data were extracted using i.c. VIEWER software (Duller 2001) and manually transferred into Excel spreadsheets with Monte-Carlo macros.

5.4.6 Spatially resolved luminescence signals

Imaging systems such as charged coupled devices (CCD cameras) (Duller *et al.* 1997; 1999; Greilich *et al.* 2002) and laser scanners (Bailiff & Mikhailik 2003; Bailiff 2006) have been developed to perform spatially resolve D_e determinations coarse-grained quartz in the fired material, similarly Greilich *et al.* (2002) obtained D_e determinations from granite slices. The scanning system developed by Bailiff & Mikhailik (2003) has been successfully used for identifying bright grains (Bailiff 2006; Bailiff *et al.* 2015), and the recovery of D_e values from a specific grain from brick slices, however, complexities arise when individual grains are split. More recently, the developments of a highly sensitive charge couple devices and electron multiplier (EMCCDs) has enabled true single-grain dose distributions to be determined from a multiple-grain aliquot (Greilich *et al.* 2002; Greilich & Wagner 2006; Clark-Balzan & Schwenninger 2012). Thus the potential for *in situ* grains to be measured in their original contexts may enable the microdosimetry

variability of surrounding material to be accounted for. However, this is one area that still needs to be developed further, but is currently underway (e.g. Rufer & Preusser 2009).

5.4.7 OSL scanning: grain-count procedure

Spatially resolved OSL measurements of each disc was undertaken using an OSL scanner system similar to that described in Bailiff & Mikhailik (2003). Only aliquots that had passed the acceptance criteria following SAR procedure were scanned (see Table 5.4). The distribution of OSL was obtained within an area of 1000 μm X 1000 μm using a step-size of 125 μm. The optical stimulation bean was angled at the disc surface after passing through a shutter, optical filter and a lens. Each disc was moved under the angles beam path in a stepwise order. A pulsed green laser ($\sim$530nm) was used and each laser pulse was collected using a configuration outlined in Bailiff & Mikhailik (2003). The luminescence was detected using an EMI9635QA PMT. The x-y data output was manually transferred to an Excel spread sheet in order to visualise the OSL data as both 2D (Fig. 5.7) and 3D (Fig. 5.8) plots, this enabled individual areas of bright luminescence on an aliquot to be identified. This also enabled grains emitting luminescence to be spatially resolved. By counting the number of brightly emitting grains within a disc, it was possible to separate aliquots with 1, 2, 3, 4 dominant grains from those composed of multiple low intensity grains. The classification of grain-counts for each aliquot was as follows: 1 dominant grain = 1BG, 1 dominant, 1 minor = 1BG, 2 minor = 2BG, and 3 minor = 3BG (Fig. 5.9).

Grain-count classification enables a better assessment of D_e for individual samples and aids the interpretation of complex D_e distributions from samples containing a complex suite of luminescence characteristics. In relatively young samples ($<$1000 years) affected by partial bleaching, single dominant grains had larger D_e values of $\sim$11 Gy, while lower D_e values originated from aliquots composed of 3 bright grains (Fig. 5.9).

5.5 Luminescence theory

5.5.1 Introduction

The process of electron charge transfer within a mineral grain follows the energy band model (Aitken 1985; Chen & McKeever 1997)(Fig. 5.10), which consists of two energy levels, the valence band (VB) and the conduction band (CB). In between these energy levels is the 'forbidden gap', where there are a series of electron traps and defects that occur at different depths. In general, the deeper the trap the greater the thermal stability, requiring more energetic light to remove charge from the traps. A defect occurs

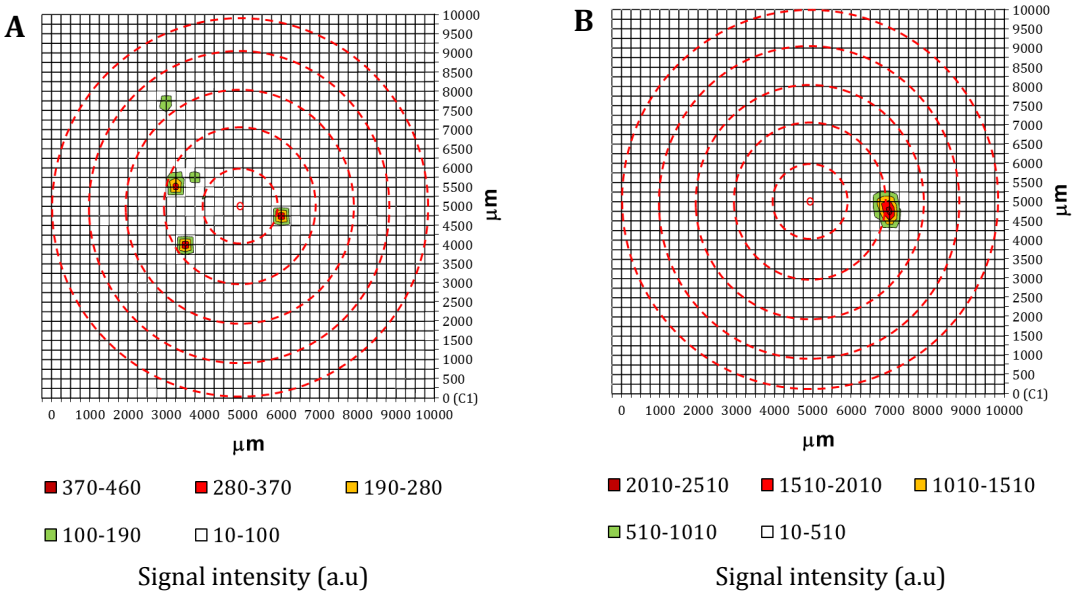

Figure 5.7. Contour plot of OSL distribution across two aliquots. Three dominant, two minor grains (A), and one dominant bright grain (B).

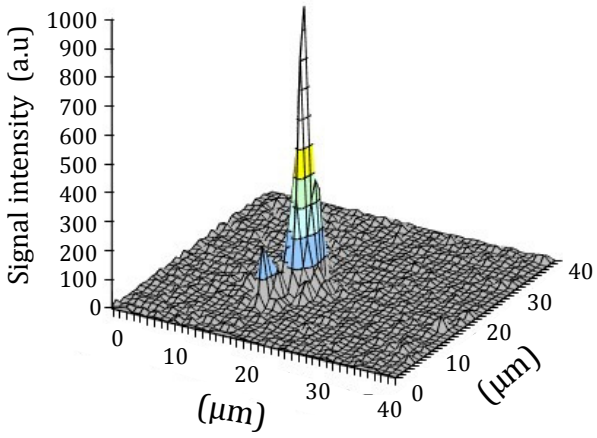

Figure 5.8. 3D plot showing the variability in signal intensity across a single aliquot, this example shows one dominant grain.

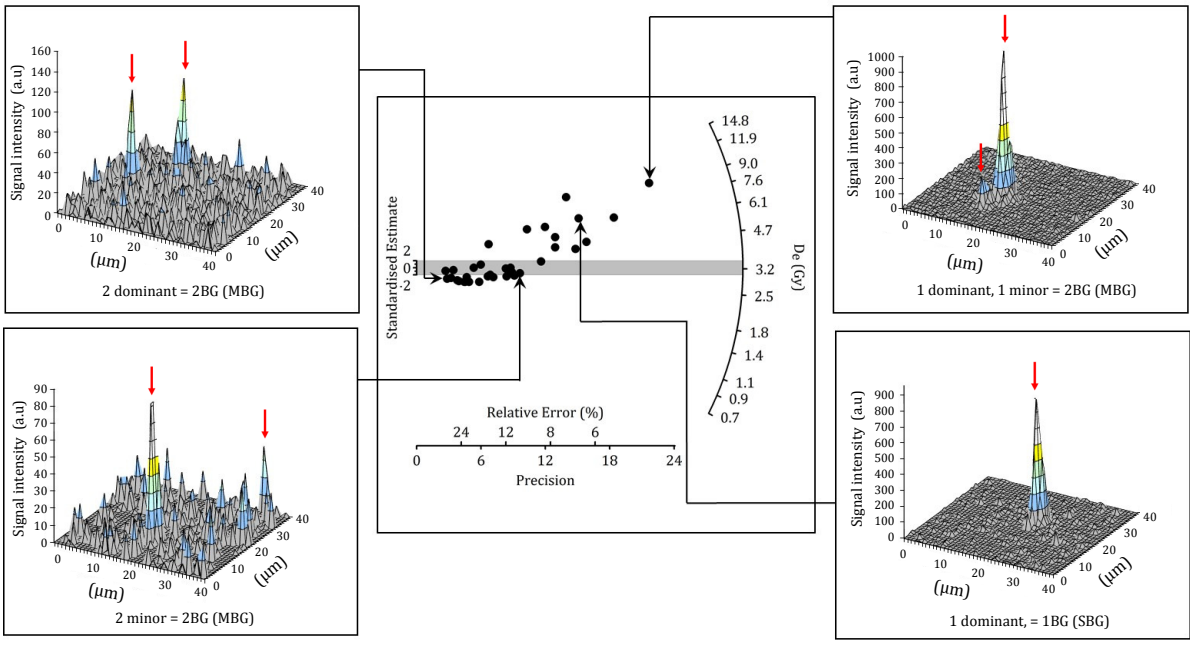

Figure 5.9. Radial plots showing spatially resolved grains and their effects on D_e distributions for sample 412-9.1.

when an atom is ionised and an electron is removed from the atomic structure to create an 'unstable' hole. Holes can be filled or recombined when stimulated by heat or light to form luminescence centres, which emit light photons in the form of luminescence signals.

The process of electron transfer and storage can also be complicated by two other processes; photo transfer TL, also referred to as PTTL (Bailiff *et al.* 1977; Bertucci *et al.* 2011) and thermal quenching (Curie 1960; Wintle 1975). PTTL is the TL from shallow traps caused by the transfer of charge from deeper traps (Chen & McKeever 1997; 230). This is particularly common in thermally unstable quartz (Preusser *et al.* 2009). The mechanisms and source of this transfer are complex, and some of the signals from quartz measured cannot be explained using a simple 'one-trap model' (Chen & McKeever 1997). Two contrasting hypotheses that have been proposed, which include the double-transfer and single-transfer models (Aitken & Smith 1988; Aitken 1998; Adamiec *et al.* 2008). The double-transfer model could explain the transfer signal observed at higher preheats, as heating can cause redistribution of signals from the trap responsible for the fast component and a refuge trap (Wang *et al.* 2006), which is a type of recuperation or 'charge trafficking' commonly observed in quartz (Aitken & Smith 1988). Recuperated signals are caused by signals originating from unstable shallow traps (Jain *et al.* 2003; Li & Li 2006; Steffen *et al.* 2009), requiring high temperature thermal treatments to remove unstable signals.

One particular luminescence characteristic commonly observed is the decrease in sensitivity during repeated heating, bleaching and irradiation. A decrease maybe related to the presence of non-radiative centres within the structure of certain quartz grains measured in this sample. Zimmerman (1971) proposed that heating can move electrons between the valence band and these non-radiative centres, which do not produce a detectable OSL signal.

5.5.2 Quartz characteristics: TL and OSL

The discovery of OSL signals from more than one defect in the crystal is a result of varying sensitivities to light, thermal stability and dose response (Singarayer & Bailey 2003). The fast component is related to traps responsible for TL peaks between 150-400°C, for example the 325°C (Aitken 1985; Spooner 1994; Kitis *et al.* 2010) (Aitken 1985; Spooner 1994; Kitis et al., 2010) and 375°C TL peaks (Aitken 1985). These are the peaks that are used to concentrate the stable fast component (Murray & Wintle 2000; 2003).

One persistent problem found in many geomorphological and archaeological contexts is the widespread occurrence of unsuitable luminescence characteristics found in quartz. These are discussed in detail in Preusser *et al.* (2009) and Wintle & Adamiec (2017). The main problems that have been encountered in OSL dating include: 1) sensitivity changes, 2) thermal transfer, 3) stability of OSL and TL signals, 4) fading of luminescence signals,

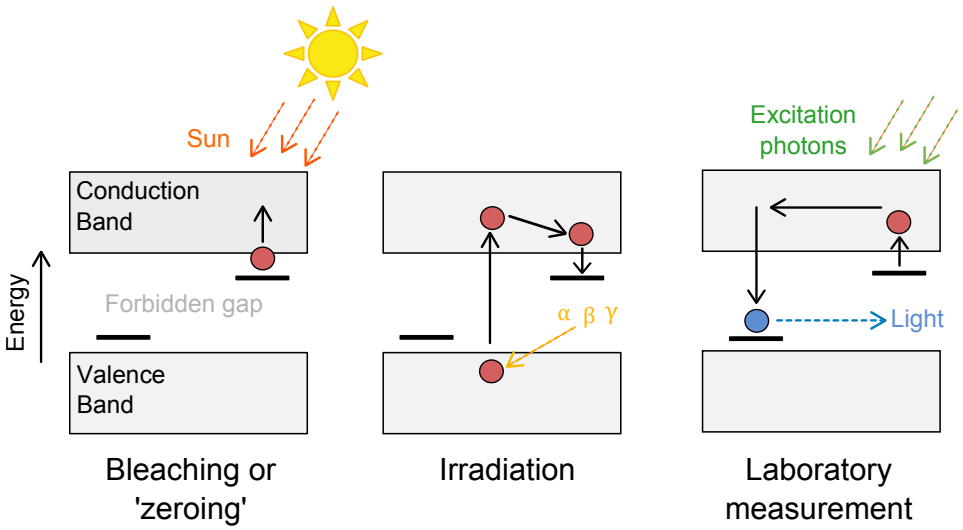

Figure 5.10. Energy band model (adapted from Aitken 1985; 44). Bleaching stage (left): ionising radiation of the crystal pushes electrons into the conduction band, leaving behind 'holes' in the valence band. Irradiation stage (middle): electrons are trapped at defects in the crystal. Laboratory measurement (right): crystal is stimulated by heat or light to release electrons, which then recombine in the holes at luminescence centres.

5) inadequate bleaching, and 6) low saturation doses (Stokes *et al.* 2000).

Many of these issues are common in geologically young regions e.g. the Himalayas or the European Alps (Preusser *et al.* 2006; Lukas *et al.* 2007; Steffen *et al.* 2009) and in regions where sediments are sourced from volcanic geology (Fattahi & Stokes 2003; Tsukamoto *et al.* 2003; Tokuyasu *et al.* 2010). Furthermore, sediments that have undergone limited cycles of erosion and transport (Duller 1994; 2006), or were deposited within the last 2000 years Rhodes & Pownall 1994; Murray 1996), have also shown to display complex signal characteristics. Sediments with low luminescence intensities have high signal-to-noise ratios, leading to imprecise D_e values. Furthermore, quartz derived from volcanic sources have also displayed anomalous fading, which causes significant age underestimation (Bonde *et al.* 2001; Tsukamoto *et al.* 2007). Feldspar inclusions found in quartz can also add additional complications (Wallinga *et al.* 2002).

The slow component has shown to have a higher dose saturation level but low thermal stability compared to the fast and medium components (Bailey 2000; Singarayer *et al.* 2000; Jain *et al.* 2003), as discovered through experimental measurements made at temperatures between 200-350°C (Kitis *et al.* 2007). Until recently, the slow and medium components were avoided due to their instability, but in cases where these signals dominate, ages based on such signals have shown to cause age inaccuracies (e.g. Choi *et al.* 2003). Such characteristics are typical for sediments deposited within short distances from its original source where the slow and medium component signals are

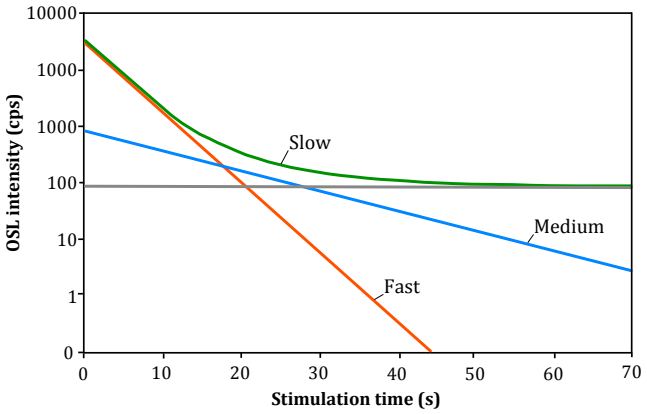

Figure 5.11. OSL decay components found in natural quartz presented on a logarithmic scale. Red = fast component, blue = medium component, green = slow component, grey = the sum of all signals. Adapted from Bailey *et al.* 1997.

likely to dominate. Unstable characteristics are also prominent in volcanic quartz due to issues of recuperation (Tsukamoto *et al.* 2003).

5.5.3 The OSL component

Smith & Rhodes (1994) found that the OSL dates from quartz were the sum of three signal components. Bailey *et al.* (1997) later confirmed that these signals derived from three specific traps in the crystal lattice, these were broadly classified as 'fast', 'medium' and 'slow' components (Fig. 5.11). Each component has a different photoionisation cross-section (σ) (Jain *et al.* 2003; Singarayer & Bailey 2004) (Table 5.3), giving rise to different bleaching rates (Bailey *et al.* 2003).

Assuming first-order kinetics, Bulur (2000) described these three components as follows:

$$L(t) = n_0\, b\, exp(-bt) \tag{5.2}$$

The signal intensity $L(t)$ is the number of trapped electrons n_0 , b is the decay of luminescence proportional to the detrapping probability of the photoionising cross section (σ) and I_0 is stimulation light intensity ($b = \sigma I_0$).

Visual examination of the CW-OSL decay curves of quartz and feldspar enable quick identification of feldspar contamination in samples as they each have distinct characteristic decays curves (Duller 2003).However, identification of different decay components can be problematic in the case of small aliquots that can contain many grains emitting weak OSL. If samples that contain very bright individual grains, LM-OSL measurements can be used for identifying different decay components.

Jain *et al.* 2003			Singarayer and Bailey 2003		
Component	σ/cm^2	Relative σ	Component	σ/cm^2	Relative σ
Ultrafast	$2.9\text{x}10^{-6}$	13	Ultrafast	$7.0\text{x}10^{-16}$	28
Fast	$(2.32\pm0.16)\text{x}10^{-17}$	1	Fast	$(2.5\pm)\text{x}10^{-18}$	1
Medium	$(5.59\pm0.44)\text{x}10^{-18}$	0.2	Medium	$(5.9\pm)\text{x}10^{-18}$	0.2
Slow 1	$(1.33\pm0.26)\text{x}10^{-18}$	0.06	-	-	-
Slow 2	$(2.08\pm0.46)\text{x}10^{-19}$	0.01	S_1	$(2.1\pm0.5)\text{x}10^{-19}$	0.01
Slow 3	$(2.06\pm0.16)\text{x}10^{-20}$	0.001	S_2	$(1.2\pm0.2)\text{x}10^{-20}$	0.001
Slow 4	$(2.76\pm0.17)\text{x}10^{-21}$	0.0001	S_3	$(1.9\pm2.9)\text{x}10^{-21}$	0.0001

Table 5.3. OSL decay components present in quartz (after Jain *et al.* 2003; Singarayer & Bailey 2003). σ: CW-OSL photon ionisation cross-section.

5.5.4 Linearly modulated OSL (LM-OSL)

LM-OSL measurements made using blue light (470 nm) at 125°C have revealed that quartz could contain up to seven different components. They were classified as ultrafast, fast, medium, slow 1, slow 2 (S_1), slow 3 (S_2) and slow 4 (S_3) (Jain *et al.* 2003; Singarayer & Bailey 2003) (Table 5.3) (Fig. 5.12). The slow 3 component corresponds to the Slow 2 component identified by Singarayer & Bailey (2004), and showed low thermal stability with a lifetime of ∼1 ka (Jain *et al.* 2003). However, the signal stability of the medium component has yet to be fully characterised. Further discussion of the signal lifetimes is provided in Sec. 5.5.5.

The fast component advocated for accurate D_e values (Murray & Wintle 2003) can be isolated by transformation of CW-OSL curves (Bulur 2000; Kuhns *et al.* 2000; Poolton *et al.* 2003; Singarayer & Bailey 2004; Choi *et al.* 2006; Kitis *et al.* 2007; Kiyak *et al.* 2007). To avoid issues of normalisation of LM-OSL curves, Bulur (2000) developed a method for deconvolution CW photoionising cross sections into LM-OSL curves, known as 'pseudo' LM-OSL (Fig. 5.13), which can provide a more accurate measured of the components present.

CW-OSL curves can be transformed into LM curves using the following additional parameters following Bulur (2000):

$$u = \sqrt{2tP} \tag{5.3}$$

where u is units of seconds and P is the measurement period. By combining Eqs. 5.2 and 5.3, and multiplying by u/P, the following is obtained:

$$I(u) = n_0 \frac{b}{P} u \, exp\left\{-\frac{b}{2P}u^2\right\} \tag{5.4}$$

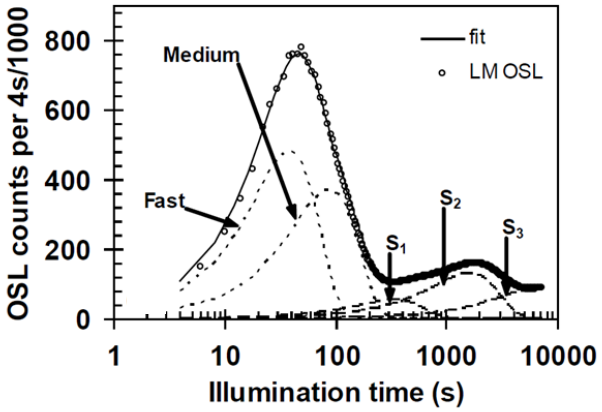

Figure 5.12. An example of LM-OSL plots showing the various components found in quartz (Singarayer & Bailey 2003).

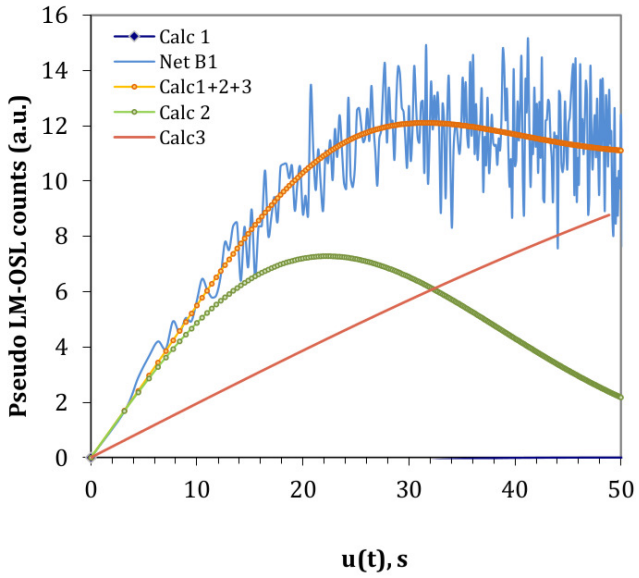

Figure 5.13. An example of a 'pseudo' LM-OSL transformation of CW data performed on a small aliquot from sample 412-9.1 containing a single bright quartz grain. This particular aliquot is dominated by the medium component.

5.5.5 Lifetimes of OSL decay components

Prior to undertaking equivalent dose measurements, a measure of the thermal stability of the signal is required to ensure that the mineral grains can be used for dating of sediments deposited within the time-frame of interest. A lifetime can be measured by calculating the difference in TL signal loss measured directly after irradiation and then re-measured after a period of storage (usually between 0 - 1000 s). Assuming first-order kinetic, i.e. signals unaffected by anomalous fading, a lifetime (τ) can be calculated as follows:

$$\tau = s^{-1} exp(E/kT) \tag{5.5}$$

where s (sec^{-1}) is the frequency, E (eV) is the trap depth, T is the absolute temperature, and k is Boltzmann's constant (at 17°C, $kT = 0.025$ eV).

In this study, isothermal decay measurements were carried out to define the trap depth (E) and frequency (s) following procedures similar to those outlined in Murray & Wintle (1999).

Initial tests were undertaken to determine the mean lifetimes of quartz from the various regions. First results have shown that the lifetime is stable over archaeological timescales required for the samples obtained (Bailiff, Pers. comm. 2017). The measured parameters and estimates of the mean lifetime for various samples is provided in Appendix D, Table D.1.

5.6 Measurement of equivalent dose

5.6.1 Development of the single aliquot regeneration (SAR) procedure

An alternative approach is the regeneration method and added dose developed by Mejdahl & Bøtter-Jensen (1994) and similar procedures developed for the pre-dose technique (Haskell & Bailiff 1985). This enabled correction for sensitivity changes but assumed that the D_e value was the same for every aliquot measured, but was mainly applied to heated archaeological contexts containing feldspars (Galloway 1996) and quartz (Murray *et al.* 1997). The development of a very early single-aliquot approach for sediments removed the need for normalisation(Duller 1991; 1995), however, reduction in trapped charge energy and sensitivity change between aliquots was observed. To overcome this, changes in the the 110°C TL peak found in quartz were 'monitored' in order to detect sensitivity change that typically occurs during repeated preheating and irradiation (Murray & Roberts 1997; Roberts *et al.* 1997; Murray & Roberts 1998). The inclusion of a test-dose measurement and a preheat applied after each OSL measurement was later introduced

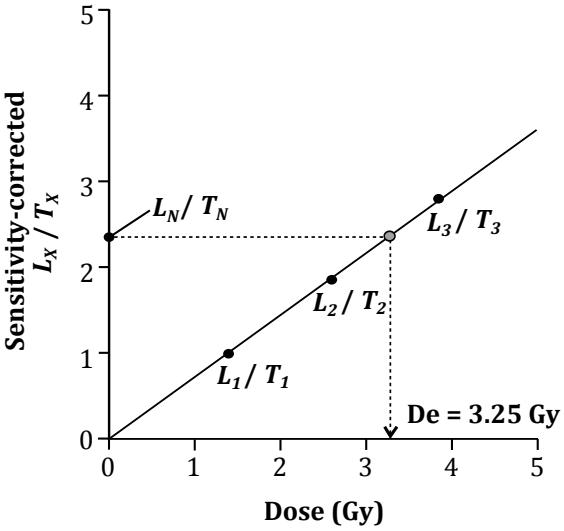

Figure 5.14. Dose response curve using the standard SAR procedure (Table 5.4).

(Wintle 1997), which significantly improved the accuracy and precision of D_e determination. The preheat is now an important step in the procedure as it removes any unstable signals from shallow traps.

Following on from this early work, the single-aliquot regeneration (SAR) protocol was proposed and is now the preferred method for determining the D_e for quartz (Murray & Wintle 2000; 2003). This standard procedure involves measuring a pair of signals, each followed by a preheat between 180-240°C; the natural signal in quartz (L_X) and its response to a test-dose (T_X), these are used to calculate the corrected-signals L_X/T_X. The value of the equivalent dose D_e, is determined by projecting from the corrected signal (L_N/T_N) where it intercepts the dose response curve defined by a series of regenerated doses (L_1/T_1, L_2/T_2, L_3/T_3...) (Fig. 5.14). When the D_e is larger than the highest regenerated dose applied, the aliquot is excluded from the analysis as grains reach saturation, which is referred to as the process where all available traps become filled, and so an estimate of D_e cannot be made. For all OSL measurements, the error in the background-corrected OSL signal is calculated. Of the various approaches that have been used to assess the error on D_e values, the Monte Carlo procedure (Duller 2007) is considered to be the most statistically robust.

Stage	Treatment	Description	Signal
1	TL + OSL	Natural ($NOSL_1$) / Screening test	
2	$50\beta s$TL + OSL	Natural ($NOSL_2$)	L_N
3	$25\beta s$; TL + OSL	PHM	T_N
4	$50\beta s$; TL + OSL	Sensitivity check	L_1
5	$25\beta s$; TL + OSL	PHM	T_1
6	$100\beta s$; TL + OSL	Sensitivity check	L_3
7	$25\beta s$; TL + OSL	PHM	T_3
8	$50\beta s$; TL + OSL	Sensitivity check	L_2
9	$25\beta s$; TL + OSL	PHM	T_2
10	$50\beta s$; TL + IR + OSL	IR recycling ratio	
11	$50\beta s$; TL + OSL		
12	$300\beta s$; TL	Scan	

Table 5.4. Modified SAR procedure used for small-aliquots.

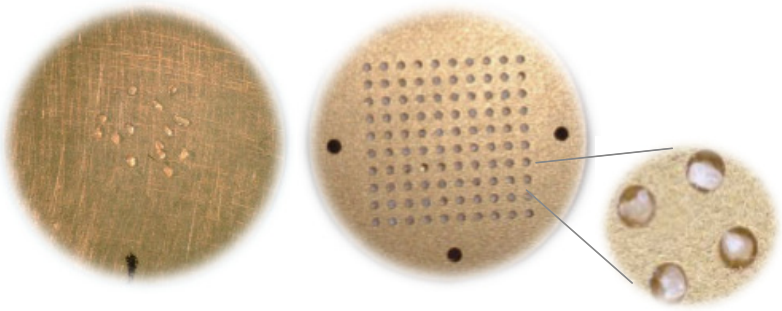

Figure 5.15. Left: Small-aliquot made up of 15 grains of quartz deposited in the centre of the aliquot to ensure even beta radiation of the aliquot surface. Right: Single-grain aliquot drilled with 100 holes to fit individual grains (adapted from Jacobs & Roberts 2007).

5.6.2 Single-grain and small-aliquot analysis

Development of single-grain readers enables the measurement of many individual grains. One of the main advantages of the single-grain (SG) approach is that a large number of measurements that can be made in a single run - 1000 grains can be measured in 24 hours from ten aliquots containing 100 holes (Fig. 5.15) ((Feathers 2003)). SG analysis also enables the accurate characterisation of luminescence signals from individual grains (Jacobs & Roberts 2007; Duller 2008b). Nevertheless, multiple grains measured from an aliquot can have very different characteristics, which can make the analysis of signal characteristics complex and often difficult to interpret. In situations where quartz grains have different bleaching histories, luminescence characteristics and the presence of residual feldspars, the SG approach is advantageous.

The SG approach requires a large number of measurements to assess D_e distributions. This is because the occurrence of individual bright grains can be only a few percentage of the overall grain population in a sample (Duller & Murray 2000). Most grains of quartz emit little or no signal above background (McCoy *et al.* 2000), requiring many D_e values in order to identify well-bleached grains amongst a population of partially-bleached grains. The overdisperion of a SG D_e distribution is usually larger than a distribution measured from a series of a small-aliquots.

In well-bleached depositional contexts, where grains are drawn from a homogeneous sediment source, small-aliquot approaches (Fig. 5.15) are suitable for SAR D_e measurements. This is because it is likely that there is very little external variability between individual grains. The size of an aliquot can also be adjusted depending on the concentration of bright grains (Duller 2008a), enabling any external variability to be average out (Arnold & Roberts 2009). Alternatively, individual grains can be handpicked and measured individually using standard RISØ machines, and contaminants can also be isolated, but this approach is often laborious and time-consuming.

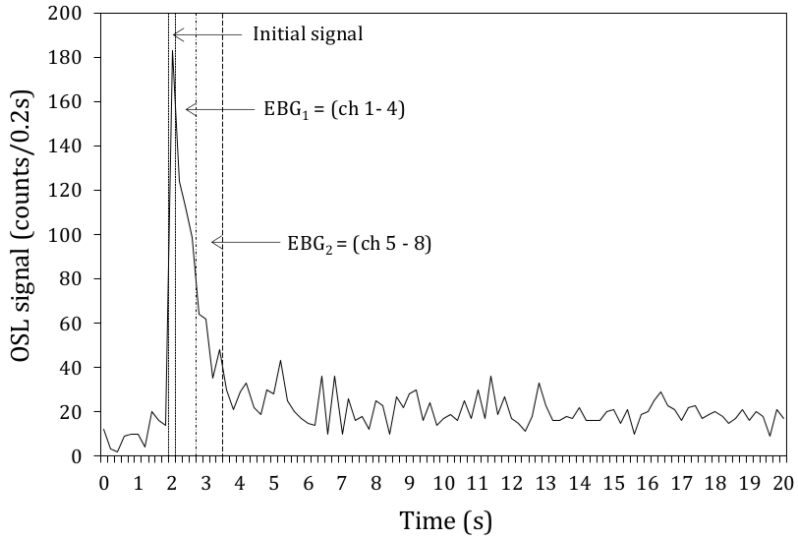

Figure 5.16. Example OSL decay curve showing the channels used to calculate the early background subtraction.

5.6.3 Early and late background subtraction signals

The selection of OSL signal intervals used in the the estimation of dose can be varied (Cunningham & Wallinga 2010). Firstly, late background subtraction (LBG) procedure as included in the modified SAR procedure outlined in Table 5.4, derives from the slow component and instrument background, and varies from aliquot-to-aliquot depending on their individual characteristics (Li 2007). This approach is particularly problematic when luminescence signal intensities from individual quartz grains are weak. Alternatively, the early background (EBG) procedure subtracts the signal immediately following the initial decay curve signal to increase the proportion of signal measured associated with the fast component (Fig. 5.16). This approach has shown to remove unstable medium components (Ballarini *et al.* 2007; Cunningham & Wallinga 2010) and reduces signals influenced by feldspar contamination (Wallinga *et al.* 2002), as feldspars display decays slower than most quartz.

5.6.4 Modified SAR procedure

A modified SAR procedure outlined in Table 5.4 was used in this research. This procedure is based on the standard procedure described in Murray & Wintle (2000; 2003) but includes an additional preheat monitor step (PHM) (Bailiff *et al.* 2015). D_e values obtained using this modified SAR can be calculated using the following equation:

$$R_N = \frac{I_N - I_{BG}}{I_{BG}} \tag{5.6}$$

where the ratio (R_N) of the integrated signal intensity (I_N) to the background (I_{BG}) (channels 1-4; 800 ms) was less than one. The PHM employed an EBG to detect thermal-transfer of OSL signal.

This value can then be compared with the one obtained by the one obtained with EBG subtraction (Ballarini *et al.* 2007), where the EBG is calculated as follows:

$$\mathrm{EBG} = \frac{\mathrm{EBG}_1}{\mathrm{EBG}_2} \tag{5.7}$$

where EBG_1 is the sum of the signals from channels 1 to 4, and EBG_2 is the sum of channels 5 to 8 as illustrated in Fig. 5.17.

5.6.5 The fast ratio

Detailed component fitting to detect the fast decay components in a sample is not always feasible in routine dating. However, the approach of Madsen *et al.* (2009) subdivided a continuous wave (CW) OSL decay curve into three parts; fast (L_1) forming the first 0.8 s, the medium (L_2) (4.96 - 9.60 s), and the slow component (L_3) (32.16 - 40.00 s). They define the fast ratio (FR) derived from these three components.

$$\text{Fast Ratio} = \frac{L_1 - L_2}{L_2 - L_3} \tag{5.8}$$

This was further developed by Durcan & Duller (2011) to enable rapid characterisation of CW-OSL curves. Using CW- and LM-OSL stimulations of various quartz dominated samples from different depositional contexts and locations. It was found that the threshold FR value of 20 defined the fast component, which equates to more than 90% of the overall signal originating from this component Durcan & Duller (*ibid.*). In this research, the FR value was used as a criteria for assessing the strength of the fast component in a measured CW-OSL decay curve.

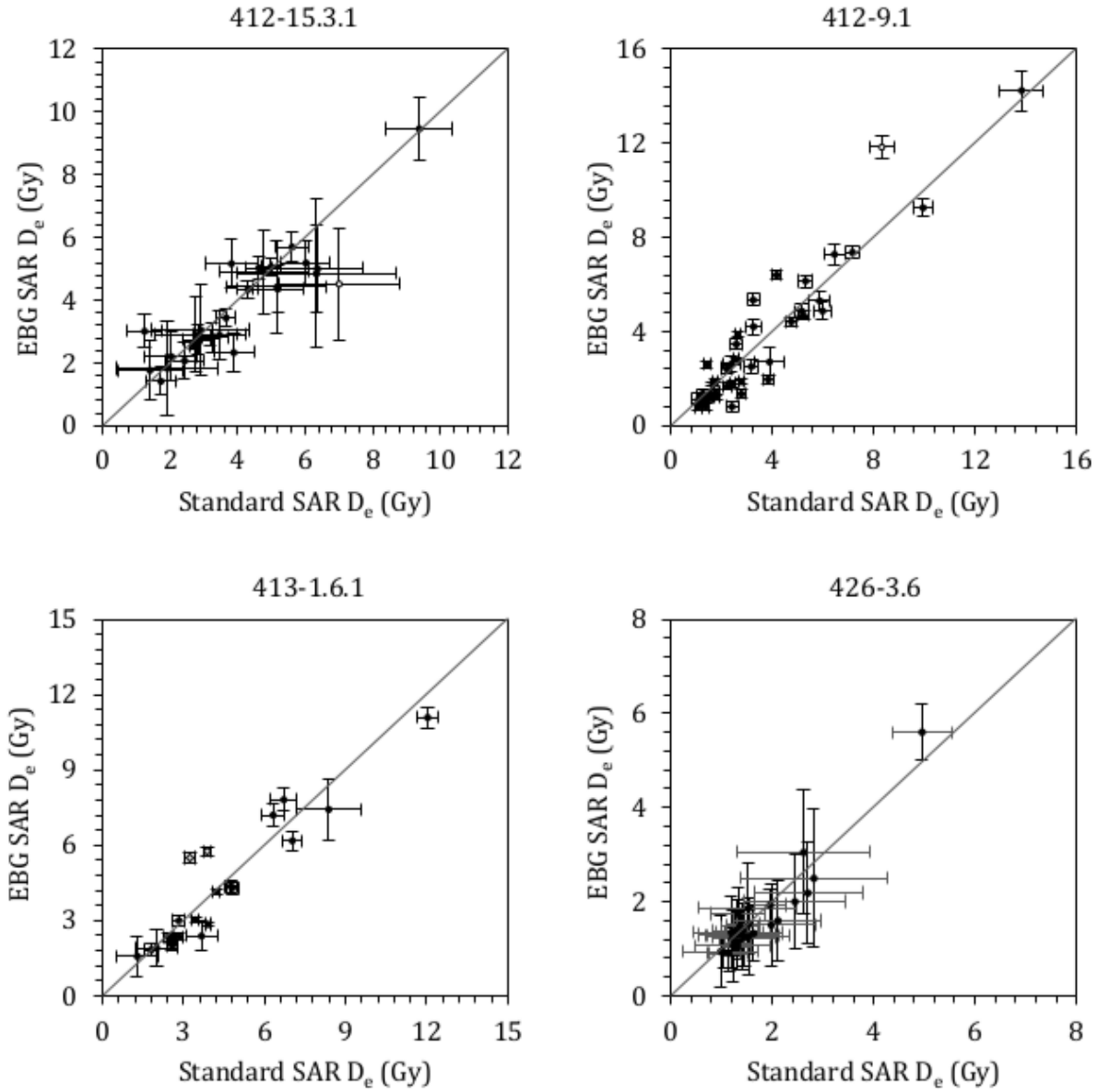

Figure 5.17. Correlation between D_e values obtained using the modified SAR and the EBG-SAR procedures for four different samples.

5.7 Suitability of quartz

A series of routine checks were applied to determine the suitability of the quartz for application of the SAR procedure. This was to ensure that only the most reliable D_e values were used to construct a D_e distribution from which an age model could be applied.

5.7.1 Luminescence screening

Prior to undertaking D_e measurements, the natural signal of a small aliquot was first measured. Signals which were greater than 100 counts were measured using the full SAR procedure. An aliquot with signal intensity with an R_N ratio greater than 5 was considered to be be sufficiently bright. The natural signal intensity can be defined as follows:

$$R_N = \frac{I_N - I_{BG}}{I_{BG}} \tag{5.9}$$

where the ratio (R_N) of integrated signal intensity (I_N) (channels 1-4) to the background (I_{BG}) (channels 1-4; 800 ms), was less than 1.

5.7.2 SAR dose recovery experiment

As the name implies, the dose recovery SAR measurement procedure (Table 5.5) checks that the applied dose D_a can be successfully recovered following resetting of the sample in the laboratory (Murray & Roberts 1998). In this study, preheat temperatures of 180°C, 200°C and 220°C were generally applied to construct a plateau test using small aliquots of quartz grains between 90-150 μm. The ratio between D_e and D_a should be close to the value of 1 (Fig. 5.18). Preheat temperatures made at temperatures lower than 180°C may lead to the retention of unstable charge, and temperatures above 280°C can lead to significant thermal erosion of the OSL signal combined with strong sensitisation effects. Therefore, it is important to select a suitable preheat temperature prior to undertaking SAR measurement.

The recycling ratio in the dose recovery experiment was also used to check the consistency of the SAR procedure. The dose recovery experiment was also used to estimate an intrinsic uncertainty (σ_i) in the determination of D_e, and this was derived from the standard deviation of the values of D_a obtained for the given preheat temperature. This was to ensure that 'between aliquot' variation was taken into account for the standard errors calculated for each aliquot.

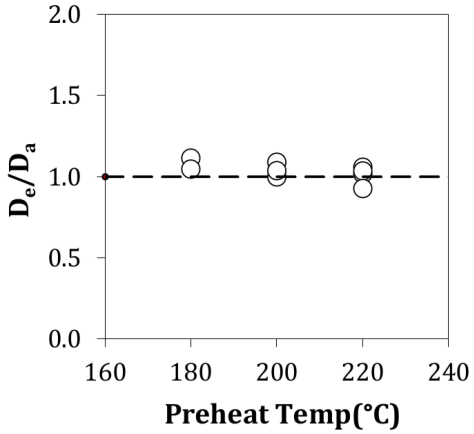

Figure 5.18. Dose-recovery preheat plateau for a sampled from Oman (426-3.2) showing the D_e/D_a ratios. Applied dose was 4.56 Gy.

Stage	Treatment	Description	Signal
1	TL + OSL	OSL screening	
2	$50\beta s$TL + OSL	Zeroing	
3	$50\beta s$TL + OSL	Applied dose	L_N
4	$25\beta s$; TL + OSL	PHM	T_N
5	$50\beta s$; TL + OSL	Sensitivity check	L_1
6	$25\beta s$; TL + OSL	PHM	T_1
7	$100\beta s$; TL + OSL	Sensitivity check	L_3
8	$25\beta s$; TL + OSL	PHM	T_3
9	$50\beta s$; TL + OSL	Sensitivity check	L_2
10	$25\beta s$; TL + OSL	PHM	T_2
11	$50\beta s$; TL + IR + OSL	IR recycling ratio	
12	$50\beta s$; TL + OSL		
13	$300\beta s$; TL	Scan	

Table 5.5. Dose recovery SAR procedure.

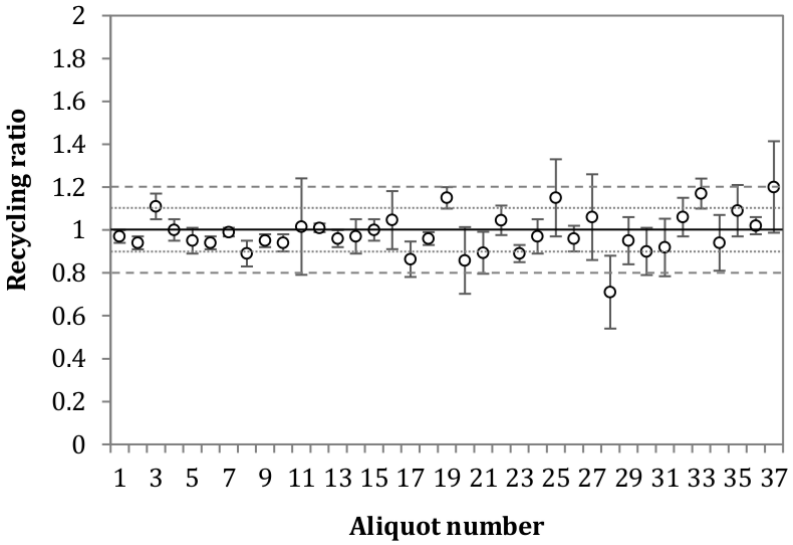

Figure 5.19. Scatter plot showing values of the recycling ratio measured with aliquots of a sample from Georgia (412-15.2.1), showing ±10 and 20% limits.

5.7.3 The recycling ratio (RR)

To check that the corrections for sensitivity change in the SAR procedure was successful in the samples tested, the response to the lowest regeneration dose applied at the start and the end of the procedure were compared. This is referred to as the recycling ratio (RR). The ratio is expected to be 1.0 and a ±10% tolerance is widely used (Murray & Wintle 2000) (Fig. 5.19).

5.7.4 Grain counts

Firstly, all aliquots were scanned (Sec. 5.4.7) after SAR measurement in order to determine the number of bright grains contributing to the measured OSL signal. Aliquots were then grouped according to the number of dominant bright grains detected, where single bright grain aliquots are referred to as (SBG), and aliquots with 2-4 bright grains are referred to as multiple grain aliquots (MBG). Aliquots with multiple low-intensity grains contributing to the signal were excluded from the analysis.

5.7.5 IRSL response

A visual examination of the OSL decay curve and the IRSL signals measured during the SAR procedure were used to identify the presence of any feldspar contamination. IRSL signals exceeding 100 counts were excluded from the analysis.

5.8 Equivalent dose evaluation

5.8.1 Overdispersion

Overdispersion (OD) can be defined as the additional scatter in data that cannot be explained by uncertainties of individual D_e values (Galbraith 2005). In a D_e distribution, OD occurs as a result of a combination of internal (e.g. Thomsen *et al.* 2003) and external factors such as beta dose-rate variability (e.g. Nathan *et al.* 2003). These factors are discussed further in the following sections.

A typical well-bleached sample with D_e values derived from single grains that have received the same radiation dose (e.g. complete bleaching) and have remained undisturbed (Galbraith 2005). The OD of a well-bleached sample, for example, an aeolian dune sand, has shown to be 20 percent or less (Olley *et al.* 2004). However, not all aeolian sediments reported have low OD values. Lomax *et al.* (2007) found that some samples had an OD of 75%, suggesting that variations in beta dose-rate was one likely cause for the variability observed. In poorly bleached samples, such as those deposited by fluvial processes, or mixed deposits from an archaeological deposit, the OD of a D_e distribution is generally larger (Fig. 5.21). Therefore, it is important to evaluate D_e distributions and the percentage of OD within a sample to ensure that appropriate age models are applied. This can be achieved visually using various plots, and also numerically by employing the central dose model (CDM) to obtain the weighted mean D_e.

5.8.2 Visualisation of equivalent dose distributions

Distributions of D_e can be plotted in various ways to assess the OD of a sample to help guide the type of age model that can be applied. Ideally, different plots should be used to visualise the same data set. The two plots used to display D_e distributions in this research includes the kernel density estimate plot and the radial plot. These are discussed further below.

5.8.3 Kernel density estimate plot

The kernel density estimate (KDE) plot is similar to that of a histogram. It enables the shape of the distribution to be observed (Galbraith 2010). One advantage of the KDE plot is that it displays relative frequencies as a continuous curve and is useful for displaying small sample sizes (*ibid.*). In this research, this plot was used to characterise the shape of D_e values. An example of a KDE plot from a large dataset of single-grain D_e values from a poorly-bleached aeolian sample from Olley *et al.* (2004) is provided in Fig. 5.20.

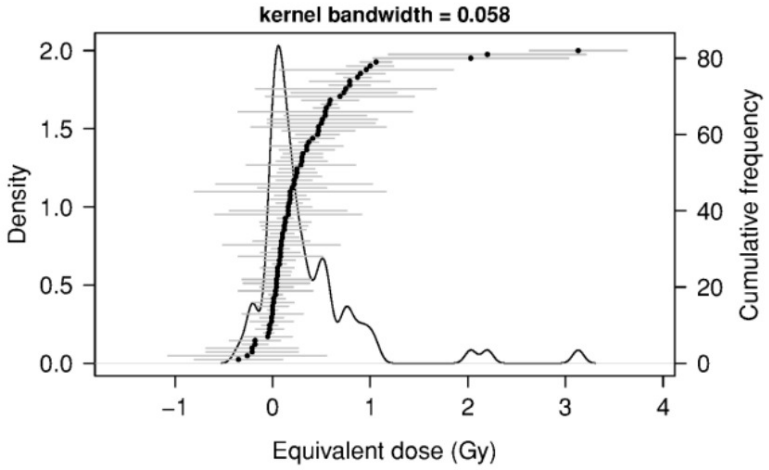

Figure 5.20. An example of a kernel density plot of single-grain data from an aeolian sediment (adapted from Galbraith 2011, data from Olley *et al.* 2004)

.

5.8.4 Radial plot

Radial plots are now the most widely used plots as they are a visual aid for the spread and statistical consistency of individual D_e values within a sample, and these are plotted as a function of precision (Galbraith 1990). The radial plot enables a rapid evaluation of the overdispersion of D_e values in a sample (Fig. 5.21). On the right is the radial line showing the various D_e values present in the sample, the line is drawn from the left to the right which intercepts the arc which gives the D_e value depending on the model applied, assuming that a 95% confidence interval of the data within $\pm 2\sigma$ of the mean. This approach enables the variability in precision to be easily interpreted - D_e values located further to the right are more precise. In this research, RadialPlotter software (Vermeesch 2009) was used for visual display D_e values as it enables a rapid tool for characterising a sample.

5.9 Luminescence age models

All statistical models must be considered within the broader context of each sample. The mode of deposition, bleaching and post-depositional disturbance are the main characteristics which need to be assessed prior to applying a particular model. The following section will provide an overview of the models widely used to estimate D_e.

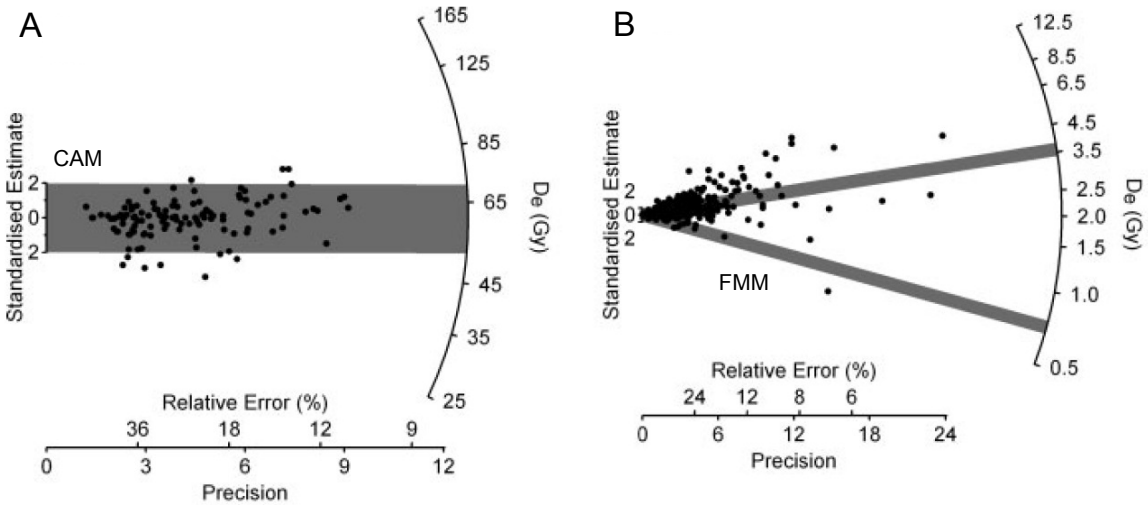

Figure 5.21. Example of two radial plots showing a well-bleached sample (grey indicates CAM or CDM model) (left) and a poorly-bleached sample (right) (grey indicates two components of an FMM model) (adapted from Jacobs & Roberts 2007).

5.9.1 Central Dose Model (CDM)

The central dose model (CDM) takes into account any overdispersion when determining the weighted mean and the standard error of a sample (Galbraith *et al.* 1999; Galbraith 2005) It is applied to sediments that have been deposited by a single event and have been well-bleached. A well-bleached deposit tends to have a gaussian distribution of the weighted average D_e value. This model takes into account the uncertainty of each D_e value. In well-bleached deposits, the percentage of OD is generally small. In this research, the acronym CDM is used to refer to the central age model (CAM).

5.9.2 Minimum Dose Model (MDM)

In contexts where sediments have been incompletely bleached, only a small proportion of the lower D_e values are considered to be fully bleached at the time of burial. For such depositional contexts, the minimum dose model (MAM) is appropriate (Galbraith 2005). This model assumes that the minimum D_e population in a sample has been fully bleached at deposition, and this can be achieved using the 3 or 4-parameter MDM. The success of each depends on the overall distribution, which can be evaluated by skewness and c/c_{crit} values (Arnold & Roberts 2009). Furthermore, the MDM-3 has shown to give better recovery for samples with few D_e estimates (Bailey & Arnold 2006). The application of the MDM model also requires an estimate of the relevant parameters, termed σ_b. An estimate of σ_b is important in order to consider how much

variation there is between aliquots, which arises due to poor bleaching, sediment mixing or dose rate variation (Galbraith 2005). This can be calculated using the standard error calculated using the CDM from a well-bleached sample (*ibid.*). Arnold & Roberts (2009) reported that OD values of 10 and 20 (%) was sufficient to take into account the variation between aliquots that is likely to occur in sediments deposited in a variety of different depositional environments. In this research, the MAM is referred to as the minimum dose model (MDM).

5.9.3 Internal-External Uncertainty approach (IEU)

The Internal-External Uncertainty (IEU) approach by (Thomsen *et al.* 2003; 2007) was developed for poorly-bleached samples and is used to identify the lowest D_e population, assuming that corresponding grains were well-bleached at deposition. This approach is a useful tool for testing for internal and external errors in a large single grain D_e dataset. Internal uncertainty is caused by statistical errors and instrument reproducibility etc. (Thomsen *et al.* 2007), while extrinsic uncertainties are caused by partial resetting of luminescence signals, spatial distribution of radioelements (Brennan 2006; Mayya *et al.* 2006) and sediment mixing (Bateman *et al.* 2003; 2007a).

The IEU approach is widely used for single-grain datasets in order to identify grains to include in the estimate the mean value of D_e. An estimate of the standard error is used to measure the 'internal' and 'external' uncertainty (Topping 1972). The external (e) standard error of the weighted mean can be calculated using the following equation provided in Thomsen *et al.* (2003)

$$\alpha_e = \frac{\sum_{i=1}^{n}(\chi_i - \chi_b)^2/\sigma_i^2}{(n-1)\sum_{i=1}^{n} 1/\sigma_i^2} \tag{5.10}$$

Where α is the standard error, χ_i are the individual D_e estimates, χ_b is the weighted average, σ_i is the individual standard error of the D_e value χ_i, and n is the total number of measurements. The first estimate, α_e, includes both the individual estimates of uncertainty σ_i, and deviation from the weighted mean $(\chi_i - \chi_b)$.

The internal (i) standard error is calculated as follows:

$$\alpha_i = \frac{1}{\sum_{i=1}^{n} 1/\sigma_i^2} \tag{5.11}$$

When this model was applied to a set of data from a poorly-bleached sample from a canal fill in Azerbaijan, the discrepancy between the D_e estimates calculated using the CDM and the IEU approach was found (Fig. 5.22). The IEU D_e (3.92±0.21 Gy) was slightly larger than the CDM D_e estimate (3.27±0.18 Gy), taking into account the internal and external errors. However, this approach is only useful where there are many single-grain D_e estimates.

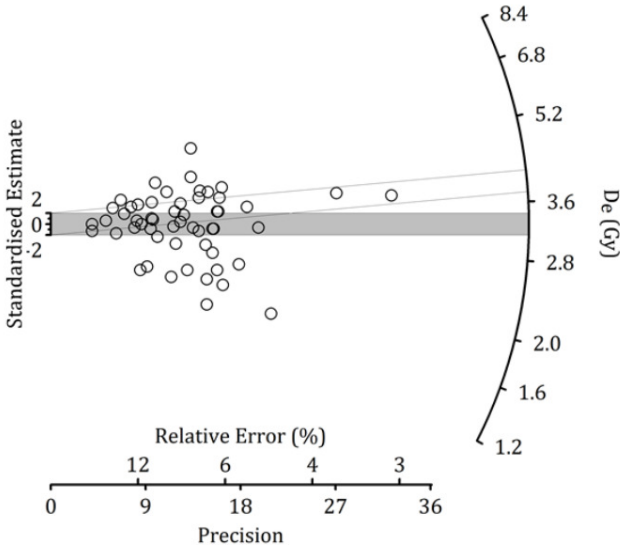

Figure 5.22. D_e distribution with CDM (grey bar) compared with the IEU approach (Thomsen *et al.* 2003; 2007) (open bar).

5.9.4 Finite Mixture Model (FMM)

The finite mixture model (FMM) was developed for heterogeneous samples where the mean, minimum and maximum D_e estimates do not relate to the burial age of the sample (Galbraith 1990; Roberts *et al.* 2000; Galbraith 2005). The FMM takes into account the standard deviation and overdispersion of each component present. The overdispersion and component number (also referred to as K) is required to determine the suitability of each FMM component within a D_e population (Roberts *et al.* 2000; Bateman *et al.* 2007b; David *et al.* 2007; Jacobs *et al.* 2008). This model provides an estimate of the number of D_e components and their relative proportion (%) of each component present in the sample. Furthermore, this age model is best suited for single-grain data, as multi-grain aliquots are affected by averaging out of the dose across the aliquot disc (Arnold & Roberts 2009). However, this model has received criticism for sampling biases as the number of dose components present in a distribution can be overestimated (Titterington 1990). Additional steps have been employed to improve this model. Firstly, David *et al.* (2007) stated that two values should be specified when applying this model: a) the overdispersion parameter for each component, and b) to define the number of expected components in a sample. However, such information is not always available from the site sampled, for example, well- bleached samples are very rarely found within the same area, and assuming a 20% OD threshold (Olley *et al.* 2004), may not be representative of the sample. Alternatively, Galbraith (2005) proposed two statistical measures, a) the maximum log likelihood (L_{lik}), and b) Bayes Information Criterion (BIC). The BIC

value can be defined as follows;

$$\mathrm{BIC} = 2L_{lik} + (2K_{n-1}1n(n)) \tag{5.12}$$

where L_{lik} is the maximum log-likelihood estimate for each FMM fit and n is the number of D_e values. The lowest BIC score gives an indication of which K value (or component) to generate the best parameterisation of the FMM. Although this model has been applied to disturbed contexts, such as cave deposits (e.g. Jacobs *et al.* 2008), the multiple components identified by the model may also reflect partial bleaching of sediments and it needs to be carefully considered before it can be routinely applied. Therefore, an assessment of the depositional process, bleaching and burial history of the contexts are fully understood prior to applying the FMM.

5.10 Data analysis

D_e values were first manually entered into Excel spreadsheets with macros to measure D_e uncertainties using Monte Carlo fitting procedures (written by Bailiff (2014), pers. comm.). In the second stage of analysis, accepted values of D_e were first examined using radial plots to visually assess the overall distribution prior to applying routine statistical models. Radial plots were generated using RadialPlotter 4.7 software developed by Vermeesch (2009), and KDE plots were generated using the R - 'Luminescence' package (Kreutzer *et al.* 2017). The CDM and MDM (Galbraith *et al.* 1999) were applied to the D_e datasets using the 'Luminescence' package in R-Studio (Version 1.0.136). A student t-Test of significant difference (Ward & Wilson 1978), was also performed in 'R'. The skewness values were calculated for each D_e distribution (SBG, MBG and Combined), following Galbraith (2010) and Galbraith & Roberts (2012), using the 'numOSL' R package (Peng *et al.* 2013).

5.11 Natural radioactivity

This section will provide a brief overview to some of the radiation characteristics relevant to luminescence dating. Unlike radiocarbon, where the half-life is comparable to the age of the sample, in luminescence dating, the radioactivity of the parent isotopes uranium (^{235}U and ^{238}U), thorium (^{232}Th) and potassium (^{40}K) are 'long-lived' and go beyond the age range of an archaeological sample (Aitken 1985; 62) (Tables 5.6, 5.7 and 5.8). Four types of radiation are relevant to luminescence dating and they are alpha particles, beta particles, gamma rays and cosmic radiation. It is the decay of the parent isotopes in the uranium and thorium by alpha decay and beta decay which form daughter isotopes, assuming secular equilibrium (Aitken 1985; 253; Ivanovich & Harmon 1992;

Dominant decay	Element	Half-life	Gamma energy (keV)
	^{238}U	4.47x10^{9} y	-
α	^{234}Th	24.1 d	63
β	^{234}Pa	1.18 m	-
β	^{234}U	2.48x10^{5} y	-
α	^{230}Th	7.52x10^{4} y	68
α	^{226}Ra	1602 y	186
α	^{222}Rn	3.83 d	-
α	^{218}Po	3.05 min	-
α	^{218}At	2 s	-
β	^{214}Pb	26.8 min	37, 352, 295
β	^{214}Bi	19.7 min	609, 1120, 1765, 2204
β	^{214}Po	1.64x10^{-4} s	-
α	^{210}Ti	1.32 min	-
β	^{210}Pb	$\sim$22 y	-
β	^{210}Bi	5.02 d	-
β	^{210}Po	138 d	-
β	^{206}Pb	Stable	-

Table 5.6. Summary of the uranium decay series (Ivanovich 1992; 21). Notes: Beta and gamma radiation are introduced when pure uranium decays to form daughters ^{234}Th and ^{234}Pa. Energies associated with radioactive elements measured using high resolution gamma spectrometry to calculate specific activities used in this study to quantify the uranium content of a sample.

8). Cosmic radiation originates from outer space and is composed of a 'soft' and 'hard' component. The 'soft' component is absorbed by the top 50 cm of sediment overburden, and the 'hard' component is affected by the geographical position (longitude, latitude and altitude).

5.11.1 Secular equilibrium

In luminescence dating, it is assumed that the creation of daughter isotopes in a closed systems occurs under secular equilibrium conditions, i.e. the activity of the daughter is equal to that of the parent. In many sedimentary environments, however, an open system is likely to occur, where the removal or introduction of one of the daughters can occur as a result of different depositional processes and post-depositional alterations in the sedimentary environment (Gascoyne 1992; 53). Detection of disequilibrium is important in order to make an accurate assessment of the dose rate.

Dominant decay	Element	Half-life	Gamma energy (keV)
	^{232}Th	1.39x10^{1}0 y	-
α	^{228}Ra	5.75 y	-
β	^{228}Ac	6.13 h	338, 463, 270, 911, 969
β	^{228}Th	1.91 y	-
α	^{224}Ra	3.64 d	-
α	^{220}Rn	55.6 s	-
α	^{216}Po	0.15 s	-
α	^{212}Pb	10.64 h	239, 300
β	^{212}Bi	60.5 m	727
β	^{212}Po	3.04x10^{-7} s	-
α	^{208}Ti	3.1 min	2615, 583, 861
β	^{208}Pb	Stable	-

Table 5.7. Summary of the thorium decay series (Ivanovich 1992; 26). Notes: Beta and gamma radiation are introduced when thorium decays to form daughters ^{228}Ra and ^{228}Ac. Energies associated with radioactive elements measured using high resolution gamma spectrometry to calculate specific activities used in this study to quantify the thorium content of a sample.

Dominant decay	Element	Half-life	Gamma energy (keV)
	^{40}K	1.25x10^{9} y	1461
β	^{40}Ar	Stable	-
γ	^{40}Ca	Stable	-

Table 5.8. Summary of the potassium decay series (Aitken 1985; 62).

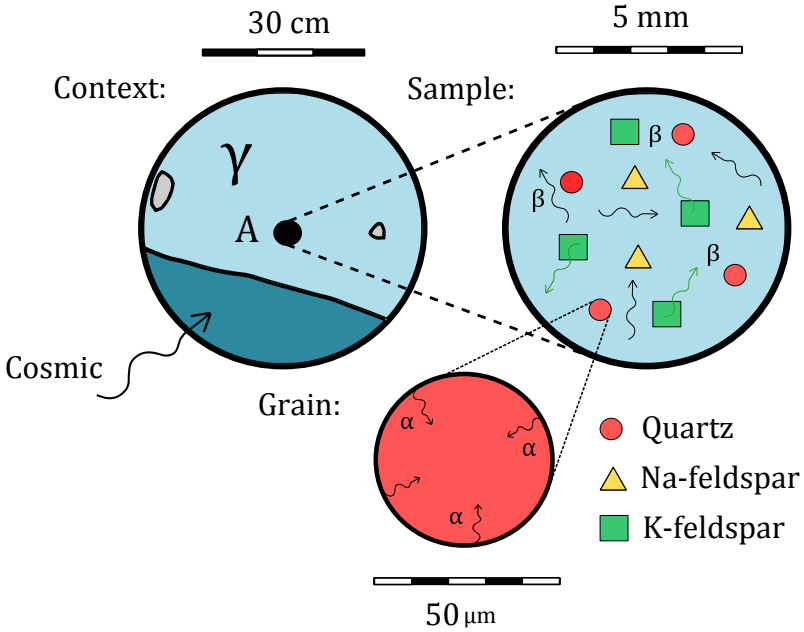

Figure 5.23. Schematic illustration showing a sampled location (A) and the immediate areas influenced by α, β, γ and cosmic radiation. Individual grains are influenced by alpha radiation, which only penetrates the outer 10-20 μm rim of the grain that is removed by HF etching.

5.12 Dose rate determination

5.12.1 Introduction

The influence of the four main types of radiation occurring at various scales within a sampled location is summarised in Fig. 5.23. At an individual grain level, the effects of alpha particles is highly localised and penetrates the outer 10 μm rim of an individual quartz grain. The influence of beta particles occurs on a slightly larger scale (a few millimetres), which originate from the surrounding matrix and non-quartz grains, that have shown to cause beta dose-rate variability (Murray & Roberts 1997; Vandenberghe *et al.* 2003; Kalchgruber *et al.* 2003; Mayya *et al.* 2006). Gamma rays can penetrate the sediments within ca. 30 cm radius of the sampled location (Fig. 5.23). Therefore, the various levels of complexity in the natural radioactive environment requires a careful calculation of the dose-rate. The dose rate ($\dot{D}$) was calculated for coarse-grained quartz where the alpha dosed layers were assumed to have been evenly removed by HF etching following Aitken (1985). Dose rate ($\dot{D}$) can be defined as:

$$\dot{D} = \dot{D}_{\beta} + \dot{D}_{\gamma} + \dot{D}_{cos} \tag{5.13}$$

5.12.2 Dose rate: individual grain

The internal dose rate of quartz is insignificant as alpha efficiency is low (Aitken 1985; 1998). Trace quantities of radioelements within the grains needs to be taken into account, as inclusions can introduce additional Th and U heterogeneity (Vandenberghe *et al.* 2003). As such, the variability that can be found between samples means that a direct measure of the internal dose rate for grains from each sample is not always practical. In the Luminescence Research Laboratory at Durham University, a standard value of 0.035 mGy a^{-1} was applied.

In terms of the external dose rate, only alpha activity is relevant, as beta particles and gamma rays are much larger than the size of grains used in coarse-grain OSL dating (Fig. 5.23). In coarse-grain dating, which includes grain-sizes 90-150 μm and 150-200 μm, the variability in alpha radiation is avoided by the removal of the outer 10-20 μm of the grain that is most likely affected by alpha radiation (Bell 1979; 1980). Mejdahl (1979) and Brennan (2003) calculated attenuation factors for quartz within a homogeneous matrix, where all quartz grains are of the same size and shape e.g. aeolian sand dunes. However, in many archaeological contexts, this is rarely encountered. More recently, characterisation of sediment samples enabled any spatial variability in dose rate of heterogeneous sediments to be accounted for (Rufer & Preusser 2009)(Rufer and Presser 2009). Furthermore, statistical modelling of grain density and voids now currently under developed, but has yet to be applied routinely in OSL dating(Guérin & Mercier 2012; Martin *et al.* 2015).

Despite the natural variabilities, the attenuation factor calculated for etched grains by Brennan (2003) was applied in this study. For grains with ø100 μm diameter, the value of 0.92±0.03 was used for the 90-150 μm fraction, and for grains with ø200 μm diameter, the value of 0.86±0.03 was used for the 150-200 μm fraction (*ibid.*).

5.12.3 Dose-rate: individual sample

The calculation of the dose rate from a sediment sample is complex. The infinate matrix concept (Aitken 1985) is based on a homogeneous matrix where the rate of emitted energy per unit mass and the unit time equates to the rate of absorbed dose of an individual grain (Guérin & Mercier 2012). To measure the dose rate of an infinate matrix, a measure of the radioisotopes, radioelements and half-life is required (*ibid.*). In this study, correction factors were applied to concentrations of radioelements in the U and Th decay-chains, including K, following Guérin *et al.* (2011).

The presence of moisture in sediment pore spaces can have a significant effect on the dose rate to grains, as water dilutes radioelements and absorbs radiation (Aitken 1985). Due to the difference in energy absorption coefficients between water and sediment for beta and gamma radiation, a correction factor is applied (Guérin *et al.* 2011).

More recently, β attenuation of quartz recovered from a calcareous medium has shown to be lower (1.19 - 1.20) than originally proposed (Nathan & Mauz 2008). Furthermore, Guérin & Mercier (2012) addressed the effect of moisture on gamma dose rate, where β attenuation was dependent on the packing geometry of grains e.g. grain/pore size arrangement to consider when dating moist sediments, as beta radiation emitting from grains such as feldspar (as illustrated in Fig. 5.23) travels through pores filled with water where energy is deposited before reaching a grain, thus an underestimation in gamma dose rate is likely to occur if assuming a homogeneous infinate matrix Zimmerman (1971). Despite this, the packing geometry is negligible, particularly in sediments that have been naturally or anthropogenically reworked, as this is difficult to reconstruct Zimmerman (1971). Nevertheless, this raises the importance of sediments characterisation in order to identify components that are likely to cause beta heterogeneity, as this is considered to be an important extrinsic factor for obtaining more precise OSL dates in complex sediments (Nathan *et al.* 2003; Mayya *et al.* 2006).

In this research, a fixed volume of wet sediment was first weighed, dried at 24°C for 48 hours, and then re-weighed. The calculated water content (W) was given a ±5% measurement error (Aitken 1985; 1998; 43) and this was calculated as follows:

$$\mathrm{W} = \frac{\text{wet weight } (g)}{\text{dry weight } (g)} \tag{5.14}$$

To take into account the effects of moisture content on dose rate, the following equation was used to obtain a water corrected dose rate ($\dot{D}_w$) for each sample (after Aitken 1985):

$$\dot{D}_w = \frac{\dot{D}_d}{1 + XWF} \tag{5.15}$$

where $\dot{D}_d$ is the dose in a medium when dry, X is the correction factor that takes into account the different energy absorption coefficients between water and the matrix (Guérin *et al.* 2011), W is the saturation water content, and F is the fraction of pore space occupied by water.

5.12.4 High resolution gamma spectrometry

The concentration of radioelements from the U and Th decay-chain, including K, was obtained from a dry sub-sample. Firstly, 25 g of the sediment was sealed and measured after 3 days and after one month of storage using a high resolution gamma ray spectrometer. A Canberra high purity germanium coaxial detector (GR2018) with a Be window was used. The spectrometer was regularly calibrated using silica-rich sands that contained certified concentrations of lithogenic radionuclides provided by the New

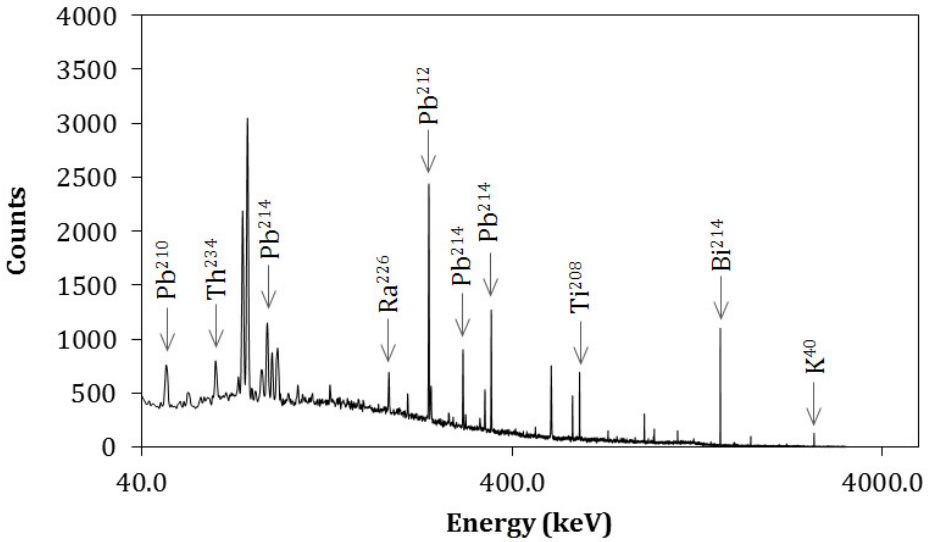

Figure 5.24. Example of high-resolution gamma spectrum for sample 413-2.2 with identification of main radioisotope peaks used to calculate U, Th and K activities.

Brunswich Laboratories. This method enables the energies (keV) of a radioactive isotope decay to be identified (Fig. 5.24). Specific peaks are used to quantify the activities (Bq Kg^{-1}) for U, Th and K, and the specific energy peaks used are provided in Tables 5.6, 5.7 and 5.8.

The specific activity of uranium was calculated by taking the average of the activities obtained from ^{234}Th, ^{226}Ra, ^{214}Pb and ^{214}Bi, and then multiplied by one. As for thorium, the average of the activities of ^{228}Ac, ^{212}Bi, ^{212}Pb and ^{208}Ti were used.

5.12.5 Beta thermoluminescence dosimetry (βTLD)

Beta dose-rate was directly measured using the βTLD technique (Bailiff 1982; 1980). This technique employs $CaFi_2$ dosimeters encapsulated in a silicone resin. A 1 cm^3 acrylic container with a thin (~0.18 mm thick) plastic window held 1 g of sediment. The plastic window absorbs alpha particles preventing their detection by the sensitive phosphor dosimeter below. The dosimeter was placed inside a lead safe and stored for a minimum of one week. The TL emissions are measured by heating the aliquot at 400°C in a nitrogen (N_2) atmosphere. The equivalent dose was determined using a regenerative procedure. The beta dose rate at the centre of the sample matrix was obtained by applying a conversion factor determined for each measurement unit in a calibration experiment outlined in Bailiff (1982). This method measures the average dose rate from particles from sources within the volume of sediment stored. The advantage of this

method is that it performs a direct measure of beta dose rate and also employs smaller samples (∼2 g) than that used in HRGS, providing a means of assessing beta dose rate variability within the bulk sample. The standard error was calculated by taking the squared root of the standard deviation of the dose rate, which was calculated from 4 or 5 dosimeters depending on the sample.

5.12.6 Cosmic rays

Another aspect of dose rate assessment is the contribution of cosmic ray radiation to the total dose rate. Cosmic rays contributed only a small proportion (5-8%) to the overall dose rate in the samples analysed in this research. Cosmic ray dose rate ($\dot{D}_{cos}$) for each sample was calculated by obtaining geomagnetic latitude values (degrees °), height (km), density (cm^3), depth below ground level (BGL) (cm), and mass (x) (hg cm^{-2}). F, J and H values were extracted from Prescott & Hutton (1988), which synthesised modern-day cosmic ray data originally presented in Prescott & Stephan (1982). Firstly, D_0 (Gy ka^{-1}) was calculated as follows:

$$\dot{D}_0 = 0.21exp(-0.07x + 0.0005x^2) \tag{5.16}$$

A second part of the equation was later modified to take into account samples positioned at depths larger than 70 hg cm^{-2}, this was calculated as follows:

$$\dot{D}_{cos} = \frac{\dot{D}_0}{F + Jexp\left(\frac{h}{H}\right)} \tag{5.17}$$

Cosmic $\dot{D}$ variability is particularly important for near-surface samples. For example, those obtained from channel features in Oman were positioned within the top 10-20 cm below the modern ground surface, where the $\dot{D}_{cos}$ values ranged from 0.23 to 0.27 mGy a^{-1}. In comparison, a sample obtained from 2.12 cm BGL from the canal in Azerbaijan, had a significantly lower cosmic dose rate of 0.16±0.02 mGy a^{-1}. The influence of sample depth and cosmic dose rate received by illustrated in Fig. 5.25.

5.13 Gamma dose rate

The gamma dose rate ($\dot{D}_\gamma$) for each sample location was calculated using a spreadsheet model (Bailiff & Tooley 2000) that employs geometry coefficients provided in Aitken (1985) (Appendix H) and allows calculation of gamma dose rate due to the sampled and adjacent contexts. The thickness of each context could be adjusted according to the stratigraphic sequence of interest, along with the moisture content and sediment density. This model was applied either as static mode, each layer was rapidly established,

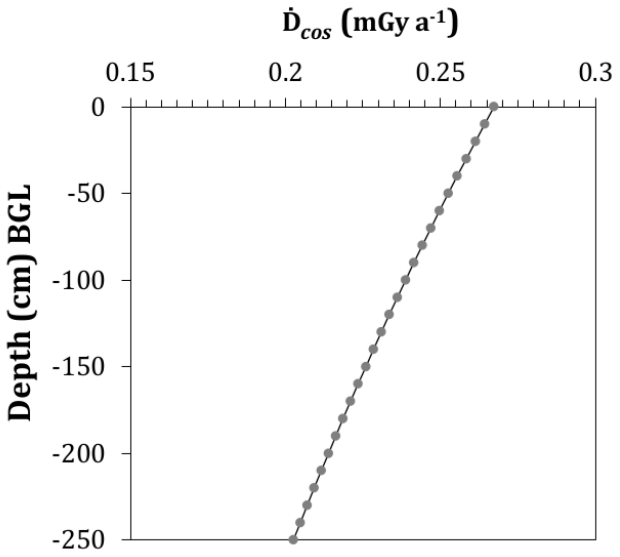

Figure 5.25. Calculated cosmic dose rate for sample 412.9.1 from Georgia, located 1735 m (a.s.l).

or dynamic mode whether the layers aggraded over a long period of time. Fig. 5.26 provides a schematic summary of various stages of deposition which were employed in the model.

5.14 OSL age and error calculations

The OSL age is calculated using Eq. 5.1, (Sec. 5.3.2).The D_e estimate is divided by the total dose rate. The total uncertainty of the age is calculated using two methods. Type A error is calculated using the standard uncertainty obtained by repeated observations of both random and systematic measurement. Type B error, also referred to as $\pm\sigma$b is calculated at the 68% confidence level (1σ) in quadrature (Aitken 1985). All OSL dates are reported with both errors.

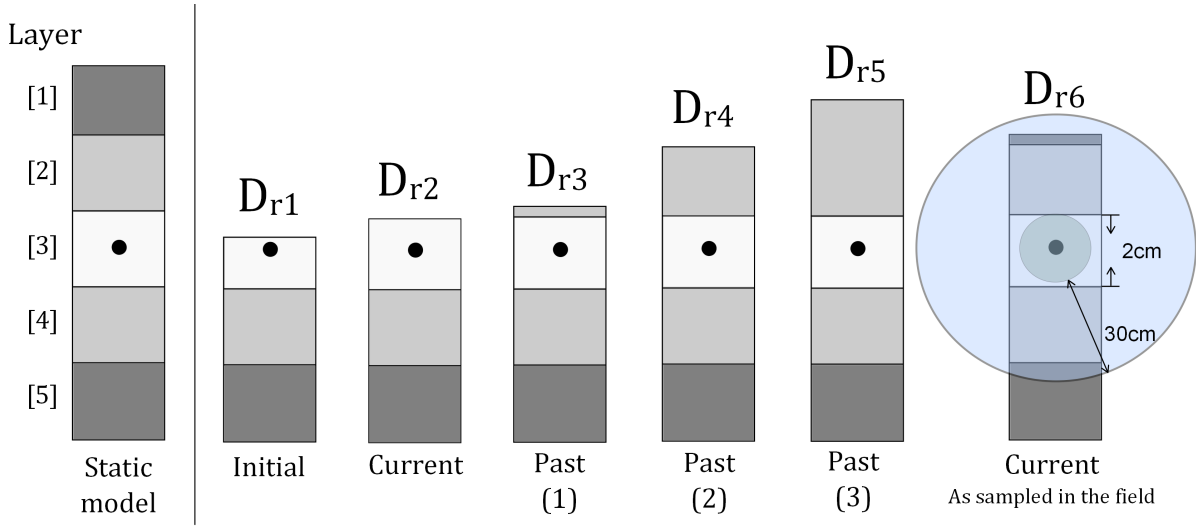

Figure 5.26. A schematic diagram to illustrate the model applied to vertically aggrading terrace deposit from Georgia. $\dot{D}_1$ is the first stage, assuming a minimum thickness of 2 cm for the deposit sampled for dating (layer 4), taking into account contributions from underlying deposits (layers 5 and 6). The second stage, $\dot{D}_2$ is the current thickness of the deposit. The initiation of overburden (layer 3), was then included ($\dot{D}_3$), assuming both a minimum thickness of 2 cm and a maximum thickness ($\dot{D}_4$), when the $\dot{D}$ contributing to the sample reaches a limit. The final stage of the model is the current thickness of initial overburden (layer 3) and the second phase of overburden (layer 2).

Chapter 6
OSL dating applications

6.1 Case study 1 (a): Luminescence dating applied to terrace basal deposits (Georgia)

6.1.1 Initial OSL testing

The following section provides details of the initial characterisation of sediments from the basal terrace deposits and occupation deposits uncovered in Trench F at Dariali Fort. This was a necessary first step as the luminescence characteristics of quartz from this region was unknown prior to fieldwork. Firstly, ca. 50 small aliquots (i.e. 1-20 grains) of HF-etched grains were screened to obtain a sufficient number of aliquots with measurable natural OSL signals for each sample. Each aliquot containing coarse grains (90-150 μm) was preheated (180/220°C, 10 s), irradiated (~5 Gy), and then stimulated with blue LEDs (90% full power) for 20 s at a sample measurement temperature of 125°C. To check for the presence of feldspars, each aliquot was stimulated for 70 s at 125°C with IR LEDs. The natural OSL decay curves obtained were visually examined and grouped into three categories according to signal intensity and decay curve form:

1. 'Dim' aliquots, with predominantly weakly emitting quartz grains, where the ratio (R_N) of integrated signal intensity (I_N) to the background (I_{BG}) (channels 1-4; 800 ms), was less than 1. R_N can be defined as:

$$R_N = \frac{I_N - I_{BG}}{I_{BG}} \tag{6.1}$$

2. Bright aliquots, with one or more brightly emitting quartz grain had an R_N value greater than 1.

3. Contaminated aliquots, where OSL emission from HF-resistant feldspars was detected, with an IR response greater than 100 counts.

Site	% 'Dim'	% Bright	% IR dominant
DPS-6	71	27	2
DPS-8	64	27	9
DPS-9	81	12	7
DPS-10	29	35	36
Dariali Fort	67	15	18

Table 6.1. Aliquot categorisation of natural OSL signals from initial testing (50 aiquots per sample).

6.1.2 SEM and EDX analysis

Further characterisation of sub-samples of grains was analysed using an SEM with an attached EDXRF probe (Sec. 3.6). High-resolution SEM backscatter images (Fig. 6.1) revealed that quartz grains appeared as both rounded and angular forms, suggesting different modes of deposition. A close-up image of one quartz grain showed irregular parallel surface abrasion textures (Fig. 6.1, A), suggesting recent mechanical weathering processes (Vos *et al.* 2014). Visual examination under a microscope with the transmitted light of a small sub-sample of coarse grains (200-355 μm), revealed a rich mineralogical assemblage. Electron microprobe analysis (EDX) generated a spectrum of elements present in individual grains. The spectral details of minerals analysed were compared to published spectra of common rock-forming minerals (Severin 2004). Quartz was the most dominant mineral present, clinopyroxenes, rutile, amphiboles, plagioclase and orthoclase feldspars, Fe-rich rock fragments and clay aggregates were present in relatively small quantities in the sediment mixture, all of which suggest an immature sedimentary history of metamorphic origin (MacKenzie & Guilford 2014). A mixture of mineral grains with well-formed crystals showing limited mechanical and chemical weathering, suggests an immature sedimentary history.

Table 6.1 provides a summary of the initial OSL and SEM tests for four terrace samples and one sample from Dariali Fort. The sample preparation procedures (Sec. 5.2) were sufficient to produce quartz dominant extracts in all but two samples. In DPS-9, sediments had a large proportion of 'dim' signals (81%), and at DPS-10, feldspars were the most dominant mineral, comprising 36% of the overall dataset. Further measurement of these two samples was not performed due to the relatively high abundance of feldspars and very low quartz yields. Sediments from Dariali Fort had a complex mixture of 'dim' and bright quartz and feldspar dominated signals, with the latter mainly concentrated in one sample (412-15.2.1).

Although 'dim' quartz was prevalent in all samples from the region, samples from DPS-8 and DPS-6 were selected for dating measurements because of the relatively better yields of bright quartz grains and the lower yield of HF-resistant feldspars. This was confirmed by high resolution SEM-EDX of treated mineral extracts from each sample. At each site, the terrace stratigraphy was well-preserved and the basal layers from

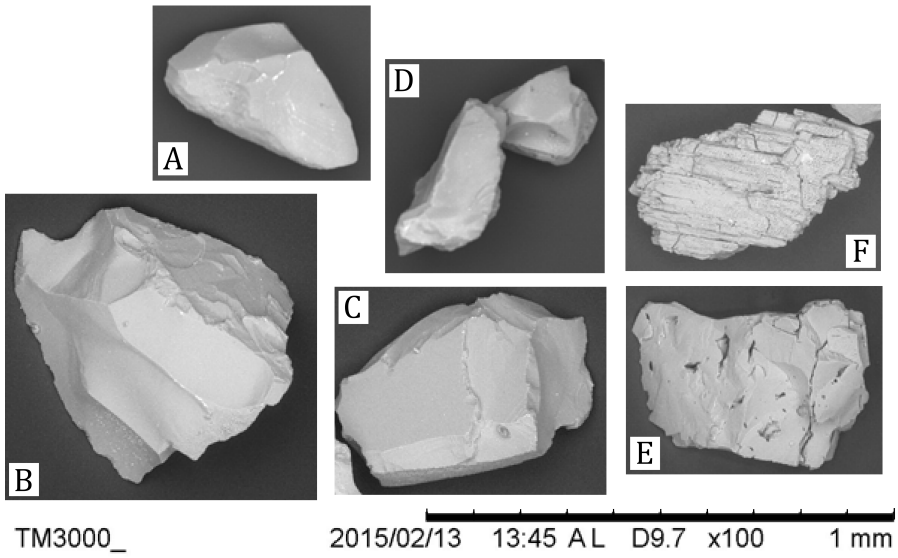

Figure 6.1. SEM backscatter images of various quartz grains (A-E) and a residual feldspar grain (F).

which these samples were taken had not been affected by modern disturbance. The following section will discuss in more detail the measurements performed with the two basal samples from sections DPS-6 and DPS-8, referred to by their laboratory sample numbers, 412-9.1 (or 9.1 for short) (Fig. 4.6) and 412-17.2 (17.2), respectively (Fig. 4.9). Firstly the luminescence characteristics and signal analysis will be presented, followed by the determination of equivalent dose D_e, dose rate (Sec. 5.12), and the age calculation (Sec. 5.3.2), for both samples. The results from the archaeological excavation at Dariali Fort are presented separately (Sec. 6.2).

6.1.3 Luminescence characteristics

The occurrence of a high proportion of 'dim' aliquots obtained from the basal terrace deposits, combined with the likelihood that the quartz grains were partially reset before deposition, indicated that it would be necessary to produce a large dataset (30-40) of D_e values and apply a minimum dose model. In these circumstances, a principal concern is whether a sufficient number of aliquots containing individual quartz grains producing OSL signals that are resolved above the background signal can be obtained. The OSL scanning stage (Sec. 5.4.7) performed following the completion of the SAR procedure, enabled the number of grains contributing to the spatially integrated OSL detected by the PMT to be counted.

6.1.4 OSL signal analysis

In both samples, the relatively few individual bright quartz grains made it impractical to deconvolute the decay curves (e.g. Bulur 2000) at levels of dose comparable to that used in the SAR procedure. The signal-to-background ratios of the natural OSL signals (R_N), and the Fast Ratio (Sec. 5.6.5) (FR) for each accepted D_e measurement was used to characterise the two samples. The two groups comprised single bright grain (SBG) and multiple bright grain (MBG) aliquots, where the latter contained 2-5 bright grains. The values of R_N and FR obtained with SBG and MBG aliquots are plotted as histograms (Fig. 6.2. The SBG aliquots provide the best opportunity for characterisation, as the influence of other grains with potentially very different characteristics is avoided. The MBG characteristics are also included in the analysis to compare with the SBG aliquot data.

The histograms displaying the frequency of R_N and FR values for the SBG and MBG aliquots from both samples show a positive skewness, which reflects signal intensities that are mostly concentrated within a low range (R_N=1-8). Sample 9.1 in particular, had 40% of the SBG aliquots within the range R_N=5-6, and 27% within the range R_N=3-4, only two SBG aliquots had significantly high R_N values (17-18, and >70 R_N). The MBG aliquots produced the largest proportion of signals within the range R_N=3-4 (46%) and 13% in the ranges of R_N=5-6 and R_N=0-2. This sample also had a small proportion of SBG and MBG aliquots containing significantly brighter grains (R_N>10). In total, six aliquots were measured at the higher preheat (PH) temperature (220°C), no difference was observed in the frequency of R_N and FR values. The aliquots from sample 17.2 produced generally low OSL intensities; for the SBG aliquots, 57% were in the ranges R_N=3-4, 43% in R_N=0-1, and 29% R_N=5-6. A similar pattern was observed with the MBG aliquots. Due to the low signal intensities, the detection of individual bright grains in the OSL scans was difficult to resolve, as the signal characterisation was based on a relatively small number of SBG aliquots (n=14).

Sample 17.2 produced SBG aliquots with half the values within the 1-2 FR range, and a similar pattern was found for the MBG aliquots (29%). Most MBG aliquots were in the 0 to 1 range (45%), and this was slightly lower in the SBG aliquots (36%). The highest FR value was ∼12 in the MBG aliquots, and no aliquots with FR values exceeding 20 were present. These values indicate that the quartz OSL for sample 17.2 is dominated by a medium decay component (Fig. 6.3).

6.1.5 Sensitivity change

Differing behaviour of sensitivity change, measured as the response to the monitor dose during the SAR measurement procedure, was observed in a number of aliquots from both samples, although these changes are taken into account for in the SAR procedure.

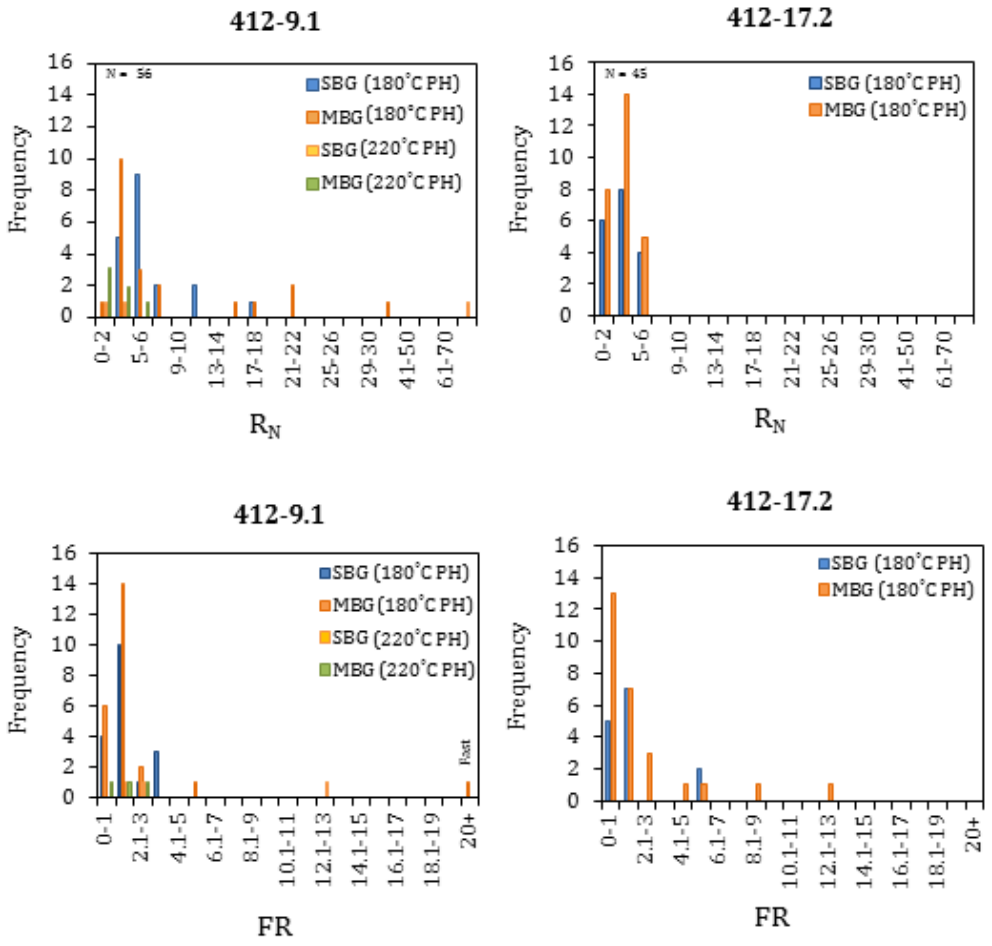

Figure 6.2. Histograms showing the R_N and FR values for SBG and MBG aliquots for sample 412-9.1 (n = 46) and sample 412-17.2 (n = 45), measured using 180°C and 220°C pre-heats for both basal samples.

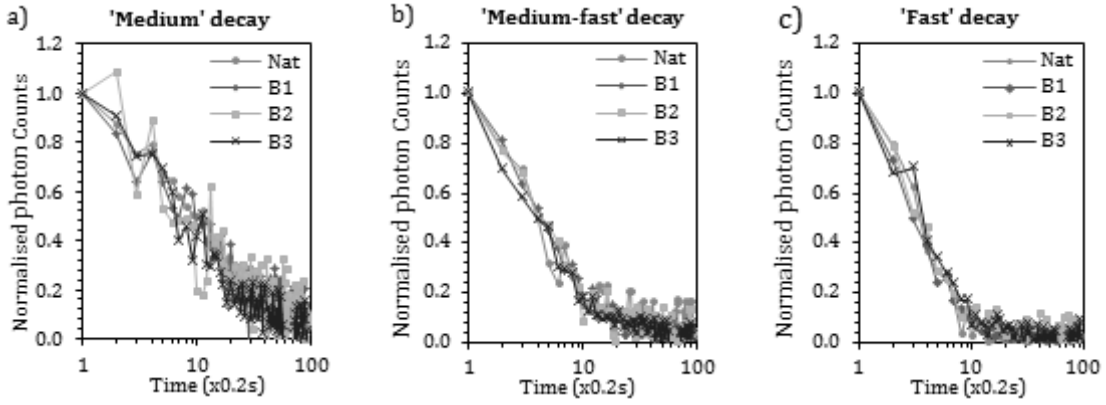

Figure 6.3. Examples of the three main types of OSL decay signals found in quartz extracted from the terrace basal deposits. The 'medium' (a) and 'medium-fast' decays (b) were the most common, and only a few aliquots with a dominant 'fast' decay (c) were detected. The 'Nat' decay refers to the natural OSL signal present, and the B1-3 decays are the background corrected laboratory beta-induced OSL signals measured during the SAR procedure.

A gradual decrease in OSL sensitivity was seen in a number of aliquots from sample 9.1 (Fig. 6.4; a), and a drop in the signal after IRSL stimulation was observed in several aliquots (Fig. 6.4; c). Increases and decreases in sensitivity during the SAR procedure have also been reported elsewhere (Armitage *et al.* 2000), and is known to be caused by repeated heating and irradiation during measurement as part of the SAR procedure (Jungner & Bøtter-Jensen 1994).

6.1.6 Thermal transfer

As illustrated in Fig. 6.5, the OSL decay curve measured following a 220°C preheat shows the effect of thermal transfer and that this can be avoided by selecting a lower preheat. Although the early background subtraction accounts for this effect, lower preheats were selected to the generation of this signal.

6.1.7 Discussion

The intensities of the natural OSL signals obtained with quartz from the two basal samples varied significantly. Microscopic observations revealed that sample 9.1 had a relatively heterogeneous mixture of quartz, as reflected in the range of R_N and FR values. The OSL sensitivity of quartz extracts was generally weak, preventing quantitative deconvolution of decay curves at relevant levels of dose (1 or 2 Gy). Used as a proxy for decay characterisation, the FR values indicated that a dominant medium-fast decay was prevalent in sample 9.1.

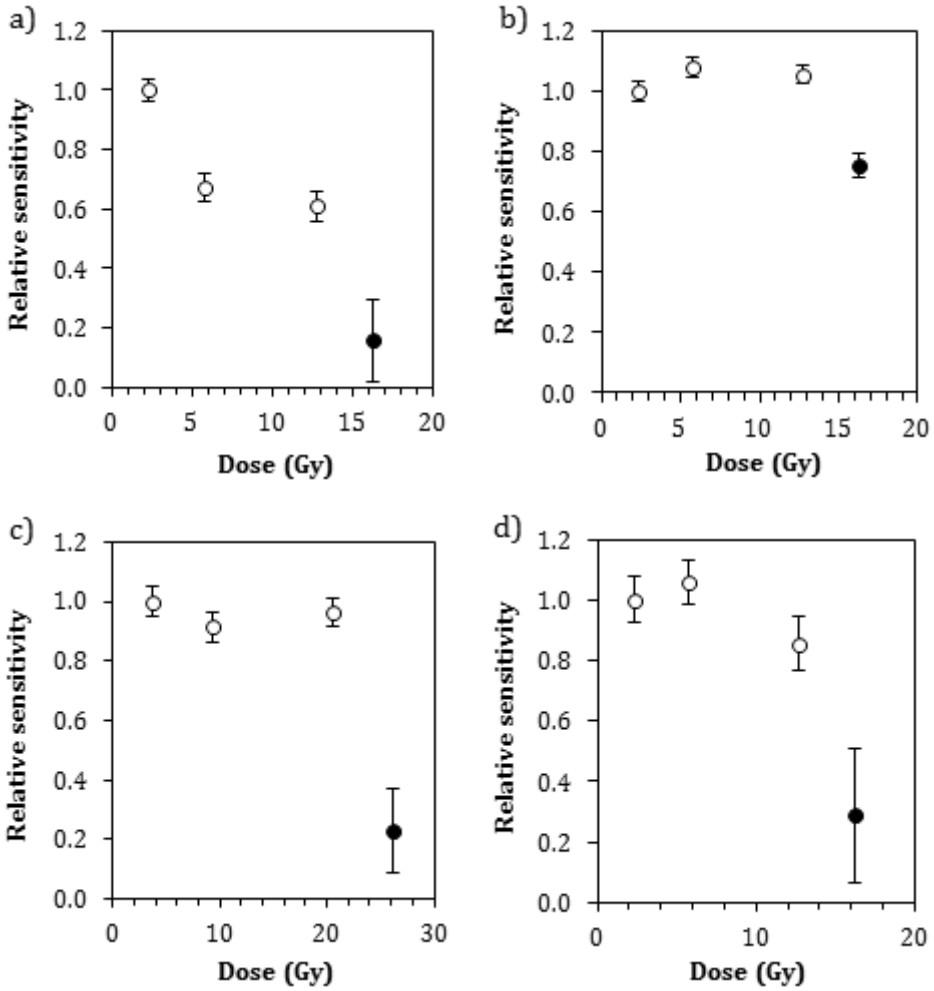

Figure 6.4. Common types of sensitivity change (as reflected in the change of the response to a monitor dose) observed during the SAR measurement procedure found in quartz from the basal terrace deposits (sample 9.1). a) A progressive reduction in sensitivity in the SAR sequence (open marker) and a reduction in signal after IR stimulation (closed marker). b) A slight reduction in sensitivity was observed. Examples of quartz grains from Sample 17.2, showed only a slight change in sensitivity during the SAR sequence similar to c) and d) for sample 9.1.

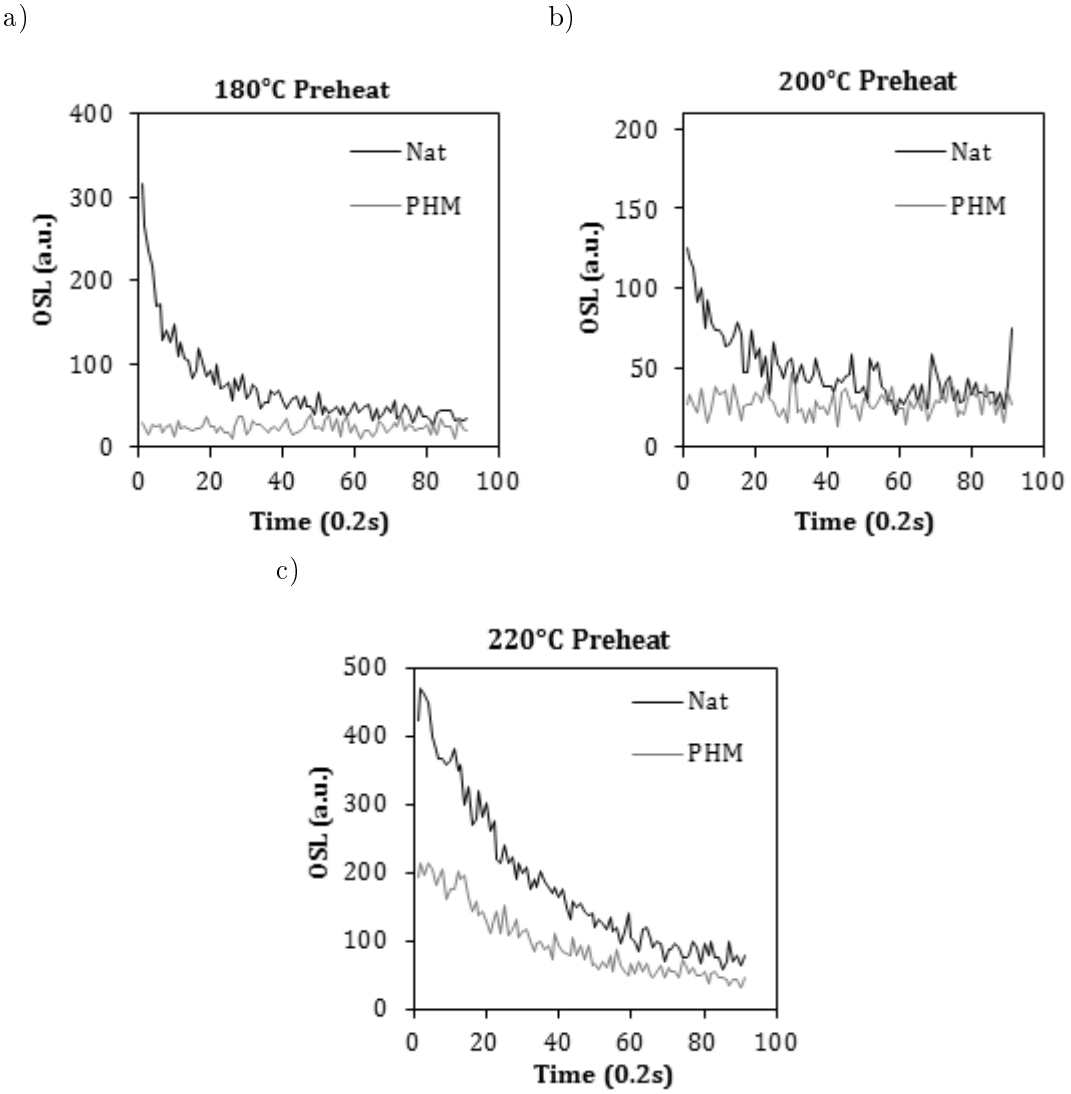

Figure 6.5. Effects of different preheat temperatures on OSL signals in sample 9.1 of three different aliquots. The pre-heat for 180°C, 200°C and 220°C measured for 5°C s^{-1}; 10 s hold. The 'Nat' decay curve is the natural OSL signal, and the PHM is the pre-heat monitor OSL signal.

OSL signal characteristics have been linked to both the geological source of sedimentary quartz grains (Zheng *et al.* 2009; Sawakuchi *et al.* 2011) and depositional and post-depositional sedimentary processes (Bateman *et al.* 2003). Quartz originating from metamorphic sources have been shown to have higher OSL sensitivities (Sawakuchi *et al.* 2011), however, different thermal histories can affect the type of signal observed after beta irradiation (Preusser *et al.* 2006). The OSL sensitivity has also been shown to be linked to depositional processes in both fluvial (Pietsch *et al.* 2008; Fitzsimmons *et al.* 2010) and colluvial deposits (Eriksson *et al.* 2000; Fuchs *et al.* 2010), and also in deposits that have undergone pedoturbation (Bateman *et al.* 2003; Bush & Feathers 2003). Through the repeated erosion and exposure of grains, high sensitivity of a small proportion of the grains measured in 9.1, reflects repeated cycles of sediment remobilisation, related to both anthropogenic (e.g. middening) and natural (e.g. erosion) processes.

Aliquots measured from sample 17.2 produced a large proportion of low- intensity OSL signals with both a 'medium' and 'medium-fast' decays being the most dominant signal. In a number of aliquots, some sensitivity change was also observed between irradiation cycles. The R_N and FR values were consistently low, suggesting that the quartz in this sample had also undergone similar depositional histories. Preusser *et al.* (2006) reported low luminescence intensities, thermal transfer and poor SAR performance caused by poor recycling behaviour, which did not enable reliable correction for sensitivity changes. Furthermore, in similar depositional contexts found in Southern Peru, low OSL intensity quartz and thermally unstable medium decay dominated (Steffen *et al.* 2009). Such complex quartz characteristics were argued to be related to the short sedimentary history commonly found in some mountainous regions. However, not all sediments deposited in similar settings are problematic to date (Fuchs *et al.* 2007).

6.1.8 Dose recovery experiment

A summary of the results of the dose recovery experiments is given in Table 6.2. The ratio of the evaluated equivalent dose (D_e) to the known applied beta dose (D_a) is expected to be 1, and the values of this ratio (D_e/D_a) using three preheat temperatures (180, 200 and 220°C), and these data, together with the values of recycling ratio, are also plotted in Fig. 6.6. The recycling ratio, D_e/D_a ratio and the intrinsic uncertainty (σ_i) values presented are calculated as an average of the number of aliquots measured for each preheat temperature.

It can be seen for the three preheat temperatures used for sample 9.1, the recovery ratio was relatively close to 1 in all three cases; 1.08±0.06, 1.09±0.05 and 0.96±0.06 (Fig. 6.6; a). The standard errors were generally small and the recycling ratios showed relatively low scatter. The SAR procedure accounted for any sensitivity change observed at different preheats (Fig. 6.6; b). The 180°C preheat was selected as the most appropriate preheat temperature for sample 9.1.

Sample	Applied dose (Gy)	Number of aliquots	Preheat (°C) 10 s	Recycling ratio (RR)	Ratio D_e/D_a	OD σ_i(%)
412-9.1	3.76	3	220	1.03±0.06	0.96±0.13	13
	4.68	4	200	1.09±0.05	1.03±0.08	8
	3.76	4	180	1.08±0.06	1.07±0.07	7
412-17.2	2.81	4	220	1.09±0.15	1.01±0.12	12
	2.81	5	200	1.15±0.11	1.05±0.03	3
	2.81	3	180	1.23±0.06	0.97±0.05	5

Table 6.2. Dose recovery results for terrace basal samples.

Sample 17.2 exhibited relatively low scatter in the values of the ratio D_e/D_a (Fig. 6.6; c), with 180°C and 200°C preheat providing the closest agreement with the expected value of 1. However, correction for sensitivity change monitored by the recycling ratio showed significant scatter that increased with preheat temperature, the average recycling ratios for 180°C, 200°C and 220°C were 1.23±0.06, 1.15±0.11, and 1.09±0.15, respectively (Fig. 6.6; d). On the basis of these mixed characteristics, the experimental data indicated that a preheat temperature of 180°C was the most appropriate for both samples, avoiding issues of thermal transfer and providing less attenuation of the signal by the preheat treatment.

6.1.9 D_e measurements: Acceptance criteria

Of the aliquots tested from samples 9.1 and 17.2, only 46/184 and 45/225 passed the acceptance criteria. From the SAR results obtained for samples 9.1 and 17.2, 35 and 27 accepted values of D_e were obtained, respectively, together with the number of aliquots rejected on the basis of each of the acceptance criteria. A summary of the accepted and rejected D_e values is provided in Table 6.3

The recycling ratios (RR) of accepted aliquots for samples 9.1 and 17.2 respectively, were 1.02±0.03 (13% OD), and 1.04±0.02 (8% OD) (Fig. 6.7), indicating satisfactory behaviour. Poor recycling was a significant problem with both samples, as was found in results of the dose recovery experiments, and a number of aliquots (17.2) were rejected due to large uncertainties associated with values of D_e close to 0 (∼0-1 Gy).

6.1.10 Accepted aliquots

The recycling ratios (RR) provides a check for the method of dose calculation and the monitor response. Due to the general weakness of the signals, the RR rejection limit normally set at ±10% of 1 (Murray & Wintle 2000; 2003) was increased to ±20%. A summary of the aliquots rejected from the analysis is listed in Table 6.3. The numbers of aliquots accepted were 35 in sample 9.1 and 28 in 17.2.

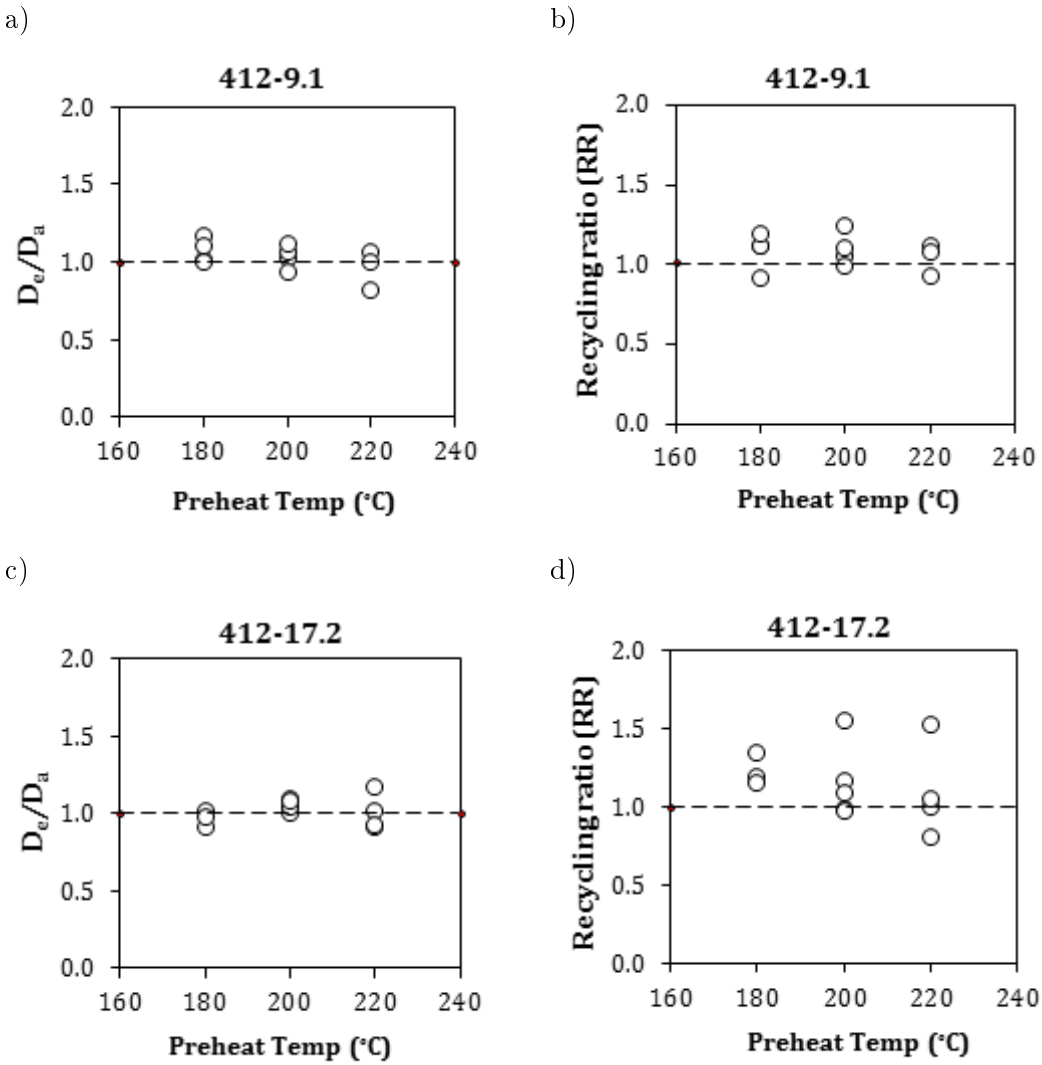

Figure 6.6. Dose recovery and recycling ratio scatter plots for samples 9.1 and 17.2

	Sample	
	412.9.1	412-17.2
Overall summary:		
Aliquots tested	184	225
Average aliquot size (grains)	15	25
Aliquots for SAR measurement	46	45
Accepted D_e	35	28
Rejected aliquots:		
D_e uncertainity	2	14
Saturated	1	0
Recycling ratio	8	1
IR response	0	0
Multiple low intensity grains	1	1

Table 6.3. SAR summary.

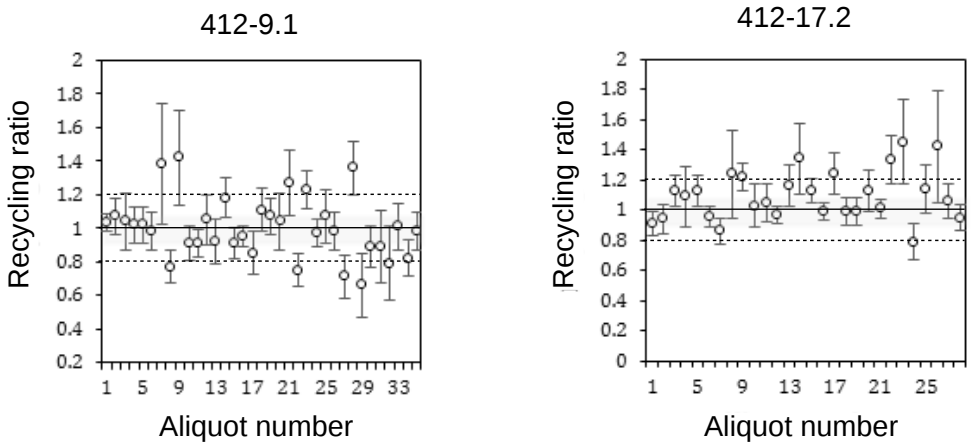

Figure 6.7. Plots showing recycling ratios and standard errors for accepted D_e values. The solid black line indicates the expected ratio of 1, and the dashed lines indicate the ±20% rejection limit for this ratio, pre-heat temperature for both samples was 180°C.

Sample	1BG	2BG	3BG	>3BG
412-9.1	16	5	6	7
412-17.2	9	5	7	6

Table 6.4. Aliquot OSL scanning result summary. 1BG = a single dominant bright grain, 2BG = two bright grains, 3BG = three bright grains, >3BG = more than three bright grains.

6.1.11 D_e distributions

The D_e values were grouped according to assigned bright grain count (Table 6.4). Accepted D_e values and their uncertainties, including the aliquot type and the number of bright grains contributing to MBG aliquots, are provided at the end of this case study (see Table 6.10). The dispersion of the accepted D_e values was first visually assessed using a radial plot and numerically evaluated as the overdispersion (OD) using the CDM to calculate the weighted mean value of D_e (Fig. 6.8). The values of OD for the SBG aliquots are large for both samples, 412-9.1 (74%) and 412-17.2, (54%), and the broad spread in D_e values and the associated large OD, suggests that a high proportion of grains had not been fully optically reset before deposition. The recycling ratios for each accepted D_e value (Fig. 6.7), shows moderate scatter, and those with large errors show that for some aliquots the statistical fluctuation in the value of the ratio is high. A visual assessment of accepted D_e values as both kernel density estimate (KDE) plots and radial plots, enables the identification of a relatively well-bleached population of grains in which an appropriate age model is applied.

The kernel density estimate (KDE) plots of the D_e values obtained with SBG aliquots indicate a component in the D_e distribution for sample 9.1 that appears to be well-bleached, whereas, for sample 17.2, a comparable component was not clearly defined due to the relatively few SBG D_e values (n=9). The KDE plots of D_e values obtained with the MBG aliquots (as indicated in red) appear to provide better definition of a group of aliquots with relatively well-bleached grains. In the case of sample 17.2, the lower dose peak in the KDE plot is similar to that found in 9.1, is consistent with the SBG D_e data (as indicated in black). While a slight reduction in OD is observed for the D_e values from SBG to MBG aliquots for sample 9.1, as expected on the basis of grain averaging effects, there is no comparable change in 17.2. These comparative data sets suggest that the SBG and MBG D_e values could potentially be analysed as a combined dataset.

The positive skewness values (Table 6.5), when compared with published skewness critical values (c/c_{crit}) (Bailey & Arnold 2006; Arnold & Roberts 2009; Bailiff *et al.* 2015), and the mode of deposition of both samples, indicate that the application of a minimum dose model (MDM) is appropriate to calculate the mean value of D_e in both samples. Micromorphological analysis of these basal contexts (Sec. 4.1.6), indicated

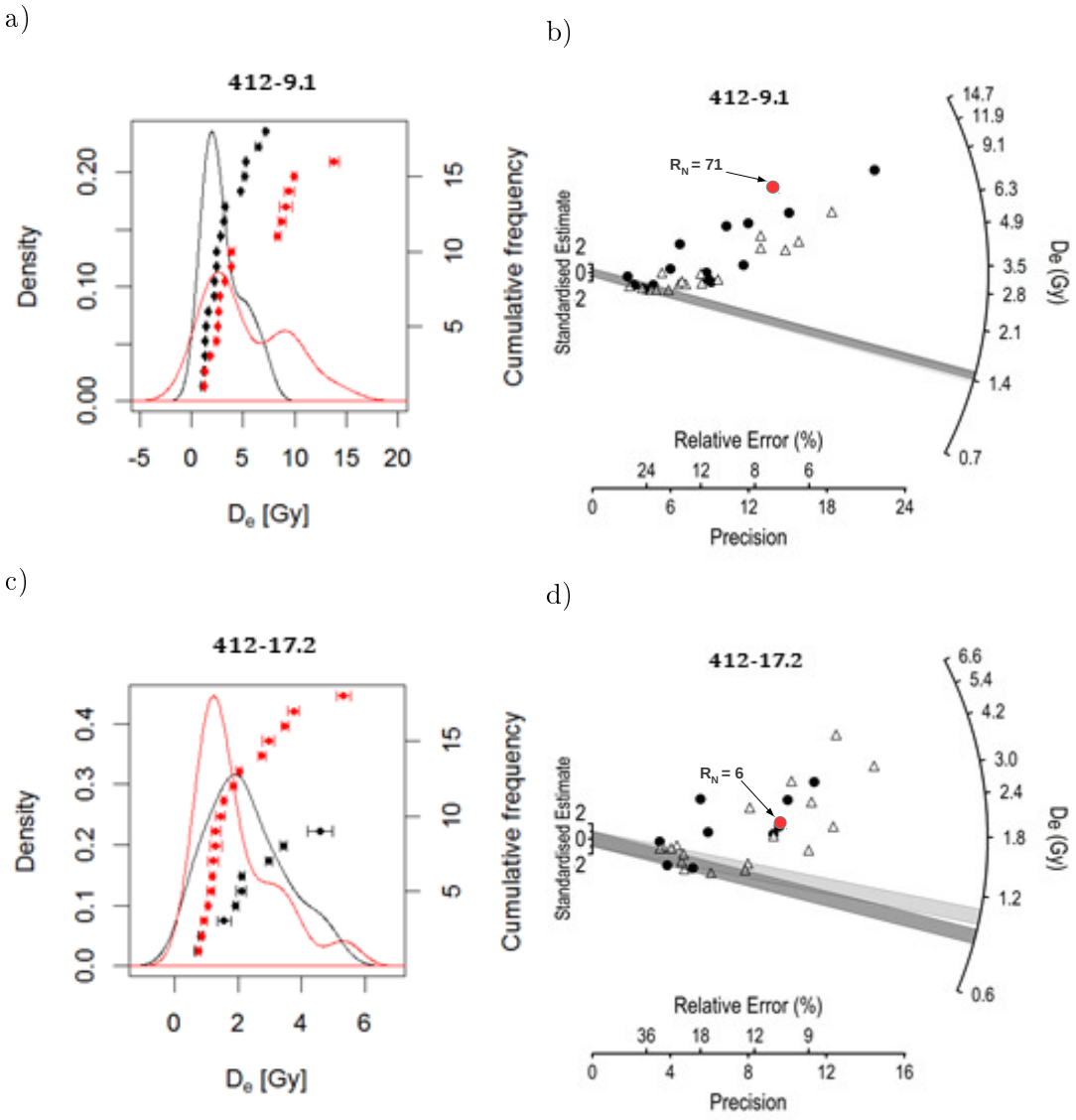

Figure 6.8. KDE plots of accepted D_e values (a and c). Black = SBG, Red = MBG, and radial plots of accepted D_e values (b and d). Closed circles = SBG, open triangles = MBG. The shaded regions indicate the D_e values (2σ uncertainty ranges) obtained when the MDM-3 was applied to SBG and MBG D_e values. Examples of SBG aliquots with large natural signals (R_N) are also indicated in red.

Sample	Aliquot type	n	CDM (Gy)	OD (%)	Skewness	t-test results*	
						t-value	p-value
412-9.1	SBG	16	2.63±0.36	57±10	1.39±0.58	1.66	0.12
	MBG	19	4.08±0.76	74±13	0.82±0.61		
	Combined	35	3.30±0.39	68±09	2.21±0.41		
412-17.2	SBG	9	1.97±0.37	54±14	0.50±0.82	0.74	0.47
	MBG	18	1.68±0.22	60±10	2.04±0.56		
	Combined	27	1.77±0.19	54±08	1.61±0.47		

Table 6.5. D_e distribution characteristics. *95% confidence interval.

Sample	Aliquot type	MDM-3 (Gy)
412-9.1	SBG	1.47±0.35
	MBG	1.42±0.25
	Combined	1.53±0.31
412-17.2	SBG	0.91±0.28
	MBG	1.05±0.18
	Combined	0.98±0.16

Table 6.6. Results of the minimum dose model (MDM-3) applied to D_e distributions

the absence of post-depositional mixing and support the assumption that the minimum dose group identified by the MDM is associated with a primary depositional process. Using the MDM, the weighted mean values of D_e were calculated separately for SBG and MBG D_e datasets. The difference in mean values of D_e was tested and found not to be statistically significant using Ward and Wilson's (1978) t-test (Table 6.6). Based on the outcome of this statistical test, both sets of D_e values were combined to take advantage of the larger dataset and improved precision. The computational procedure for MDM-3 (logged $\pm 2\sigma$) (Sec. 5.9.2), was applied to the combined D_e data dataset (Table 6.6), where the standard error assigned to each value of D_e was obtained by combining the uncertainty produced by applying a Monte Carlo (MC) fitting procedure (Sec. 5.10) to the dose-response curve and an intrinsic uncertainty (σ_i), derived from the dose-recovery experiments (Table 6.2).

6.1.12 Dose rate assessment

The dose rate was measured using a combination of high-resolution gamma spectrometry (HRGS) (Sec. 5.12.4) and the βTLD technique (Sec. 5.12.5). The specific activities of the lithogenic radionuclides (Bq kg^{-1}) and the isotopic ratios ^{210}Pb/^{226}Ra and ^{210}Pb/^{av}U are presented in Table 6.7; the samples were measured using HRGS for three days. The ratios of these activities enable an assessment of secular equilibrium within the

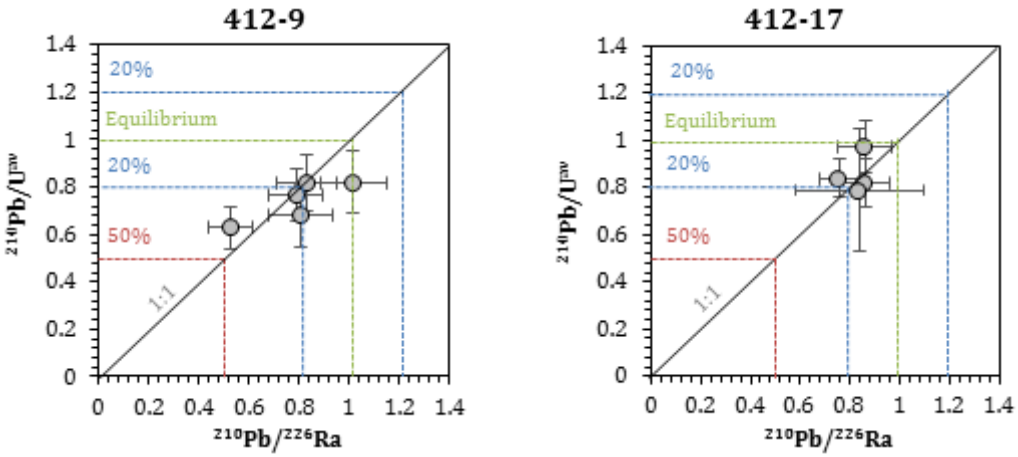

Figure 6.9. Plots of ^{210}Pb/^{av}U and ^{210}Pb/^{226}Ra ratios for samples from both sampled sequences.

	Isotope activities (Bq/kg^{-1})			Isotope ratios	
Sample/context	^{238}U	^{232}Th	^{40}K	^{210}Pb/^{av}U	^{210}Pb/^{226}Ra
412-9.3 [C.002]	31.5±2.0	41.8±3.5	493.6±8.2	0.79±0.1	0.77±0.1
412-9.2 [C.003]	32.4±2.0	37.5±3.4	456.5±7.7	0.81±0.1	0.68±0.1
412-9.1 [C.004]	28.0±2.0	41.5±3.5	384.3±7.2	0.83±0.1	0.82±0.1
412-9 [rock]	27.8±1.5	36.1±2.6	372.8±5.9	1.02±0.1	0.82±0.1
412-9 [C.005]	27.9±1.7	39.5±3.0	343.0±6.2	0.53±0.1	0.63±0.1
412-17.1 [C.002]	29.3±2.0	37.2±3.3	418.3±7.3	0.86±0.1	0.82±0.1
412-17.2 [C.004]	34.3±1.7	43.3±2.9	553.8±7.4	0.76±0.1	0.84±0.1
412-17 [C.005]	33.4±1.8	34.5±3.0	375.8±6.6	0.86±0.1	0.82±0.1
412-17 [C.006]	41.1±5.8	45.1±2.3	514.7±4.2	0.84±0.3	0.79±0.2

Table 6.7. Summary of radioactive isotope activities and ratios measured as an infinite medium of a point absorber.

^{238}U/^{235}U and ^{232}Th decay series. In situations where disequilibria are pronounced (>50% difference in the ratios), greater uncertainty in the dose rate is introduced. Figs. 6.9 and 6.10 display these ratios, where the dashed green line represents the conditions of secular equilibrium, and the effect of 20% and 50% of disequilibria is also indicated.

6.1.13 Observed secular equilibrium conditions

The specific activities of radionuclides within the ^{238}U decay chain, pre and post ^{222}Rn activities were examined. In all samples from sections 412-9 and 412-17, a decrease in activity at the end of the series was observed. Specific activities for ^{214}Pb and ^{214}Bi (half-life <30 minutes) showed little change, suggesting that this deficit, as indicated

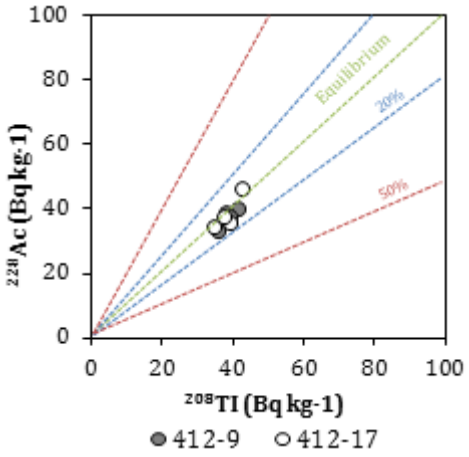

Figure 6.10. Scatter plot of ^{228}Ac vs ^{208}Ti activities in the ^{232}Th series in samples from both stratigraphic sequences.

by the ^{210}Pb/^{av}U ratios (Fig. 6.9), originated from the long-term loss in ^{214}Po. Only a small loss in Rn was detected in the ^{238}U chain. The maximum influence on the overall dose rate of the lowermost sample was estimated to be 3%. In the ^{232}Th decay chain, the activities of ^{228}Ac/^{208}Ti in all samples were in equilibrium (Fig. 6.10).

6.1.14 Beta dose-rate

The occurrence of clay translocation features and Fe/Mn nodules found in micromorphological thin sections (Sec. 4.1.6), was detected using bulk moisture/organic content and magnetic susceptibility techniques, and these post-depositional features occurred throughout the sequence, suggesting that redistribution of isotopes (e.g. radium) due to translocation of fine clays, may have occurred. Furthermore, weathering of pumice fragments and feldspar grains was observed, and such alterations of K-rich coarse inclusions are likely to cause *in situ* alterations of the beta dose-rate in localised areas. Considering the localised variability observed at the sub-mm scale, beta heterogeneity is likely to have a moderate effect on the measured beta dose-rate.

A direct measurement of beta dose-rate was performed using the βTLD technique using a sample size of ∼1.6 g (Sec. 5.12.5). Although this technique cannot provide resolution on a sub-mm scale that is sufficient to identify beta dose rate heterogeneity at the level of individual grains, by employing smaller volumes of the measurement sample, it provides a more sensitive probe of variation compared with laboratory-based high-resolution gamma spectrometry, where the sample size is ∼25 g.

The measured values of the beta dose rate are given in Table 6.8. These values were compared with those calculated using published conversion factors (Guérin *et al.* 2011)

Sample	$\dot{D}_\beta$±s.e.* (mGy a^{-1})	$\dot{D}_\gamma$±s.e. (mGy a^{-1})	$\dot{D}_{cos}$±s.e. (mGy a^{-1})	$\dot{D}_{tot}$±s.e. (mGy a^{-1})
412-9.1	1.39±0.01	0.81±0.01	0.23±0.003	2.47±0.05
412-17.2	2.49±0.01	1.06±0.01	0.24±0.003	3.81±0.08

Table 6.8. Dose rate summary. * Attenuation factor applied: 0.913 (after Brennan 2003).

and the specific activities determined with larger samples by gamma spectrometry. A slight discrepancy was observed between the values of beta dose rate using the two techniques for 17.2, where the average beta dose rate was 3.19±0.14 mGy a^{-1} and the beta dose rate calculated using the gamma spectrometry values was significantly lower (2.18±0.39 mGy a^{-1}) (ratio: 1.74±0.02). The same material was sieved to concentrate the fine fraction (<90 μm), and measured using βTLD. The measured dose rate of the fine fraction was 14% lower (2.78±0.18 mGy a^{-1}), suggesting that there is a grain size effect. This variability is potentially related to the sediment heterogeneity found in the coarse and fine component, particularly the presence of fine particles of higher radioactivity closer to the dose meter used in βTLD measurement, as observed in the sedimentary thin section as Fe enriched clays.

6.1.15 Cosmic ray dose-rate

The cosmic ray dose rate at each sample location was calculated following Prescott & Hutton (1995). The sample depth; 1.30 m BGL (sample 9.1) and 1.16 m BGL (sample 17.2), geographical position; 42°N 44°E, 130 km (9.1), 42°N 44°E, 160 km (17.2), and density of the sediment overburden; 1.62 g cm^{-3} and 1.63 g cm^{-3} generated cosmic dose rate values of 0.23 mGy a^{-1} and 0.24 mg a^{-1} for samples 9.1 and 17.2, respectively. The calculated cosmic dose rates formed a relatively small contribution to the overall total dose rate (6-8%) received by the grains.

6.1.16 Gamma dose rate

The multilayer gamma dose rate model (Sec. 5.13, Fig. 5.26) was used to assess the influence of gamma dose rate contributions to each sample from the sediments below and those deposited above. Fig. 6.11 shows the influence of the contexts contributing gamma dose rate to the OSL sample, $\dot{D}^s_\gamma$. The model was applied to assess the variation in dose rate with the thickness of overburden, developed with time using approximate dates for the terraces (9.1; 300 years and 17.2; 600 years), and assuming a rapid aggradation rate (ca. 10 years). The model consisted of six stages of deposition (Fig. 5.26). The sediment surrounding 9.1, context 4, contributed 73% (0.75 mGy a^{-1}) of the total gamma dose rate, 14% (0.15 mGy a^{-1}) originating from contexts deposited above and 11% from rock

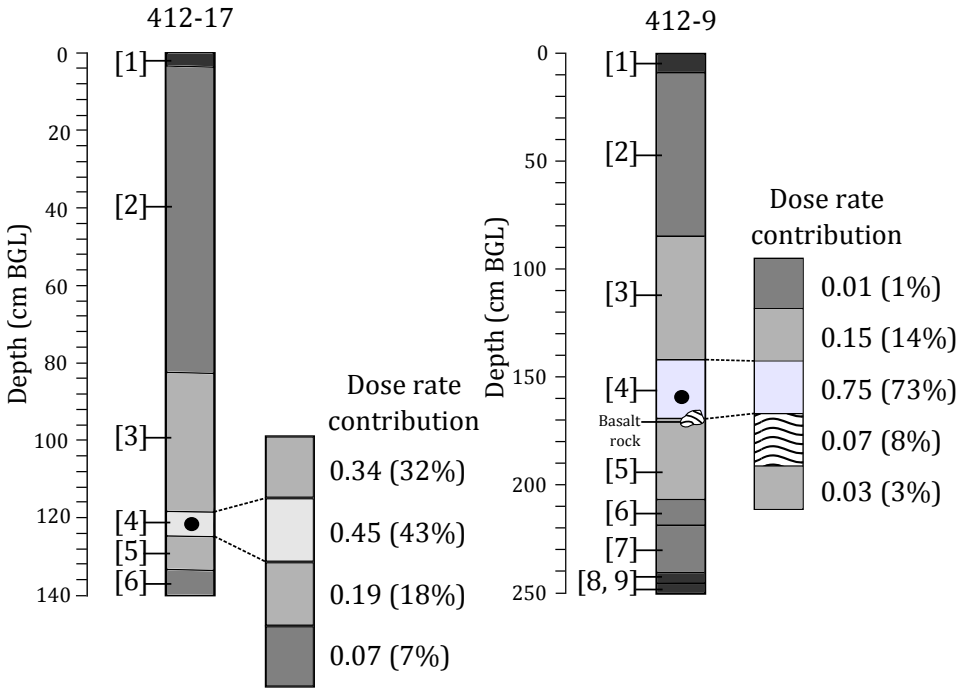

Figure 6.11. Stratigraphic diagram of contexts showing a breakdown of the modelled $\dot{D}$ for the two OSL samples indicated as closed circles. The contributions from the surrounding contexts given in both mGy a^{-1} and % of the gamma dose-rate contributing to the OSL sample.

and sediment below. Nearly half of the total dose rate (43%, 0.46 mGy a^{-1}) received by 17.2 came from context 4, 32% (0.34 mGy a^{-1}) from overlying contexts and 18%; 0.19 mGy a^{-1} from immediately below the sample. A complete breakdown of the modelled dose rate is illustrated in Fig. 6.11. The radioactivity of the rock was not significantly different to that of the surrounding sediment. The dose rate for both samples showed little change during different stages of the model applied; 412-17.2 (0.71-0.83 mGy a^{-1}) and 412-9.1 (0.79-0.88 mGy a^{-1}). Based on these observations, the modelled dose rate for gamma, assuming a static configuration, was incorporated in the age calculation. The modelled dose rate was corrected for the average moisture content, using the percentage values stated above and their uncertainties (5% measurement error).

Sample	Burial age (before 2016)	OSL age* (AD)	$\pm\sigma_a$	$\pm\sigma_b$
412-9.1	567	1450	115	119
412-17.2	259	1755	42	44

Table 6.9. OSL age determinations for the two basal terrace samples. σ_a = Type A; σ_b = Type B (after ISO 8601:2004). * rounded t o the nearest 5 years.

6.1.17 Age determinations

The OSL ages calculated using Eq. 5.1 (Sec. 5.3.2) are calendar years (BC/AD) and include two error terms ($\pm\sigma_a$ and $\pm\sigma_b$) (Sec. 5.14). The burial age is expressed as years before 2016 (Table 6.9).

412-9.1			412-17.2		
D_e(Gy)	±s.e. (1σ)	GC	D_e(Gy)	±s.e. (1σ)	GC
1.26	0.11	SBG	0.71	0.18	SBG
1.3	0.26	SBG	0.82	0.14	SBG
1.79	0.13	SBG	1.55	0.43	SBG
2.38	0.34	SBG	1.91	0.16	SBG
2.56	0.09	SBG	2.09	0.32	SBG
2.63	0.12	SBG	2.12	0.16	SBG
2.77	0.17	SBG	2.96	0.21	SBG
3.25	0.25	SBG	3.43	0.18	SBG
3.84	0.20	SBG	4.60	0.79	SBG
3.89	0.59	SBG	0.75	0.16	MBG(3)
8.33	0.48	SBG	0.84	0.14	MBG(4)
8.74	0.68	SBG	0.91	0.20	MBG(2)
9.12	1.26	SBG	1.03	0.13	MBG(4)
9.47	0.88	SBG	1.13	0.24	MBG(3)
9.95	0.38	SBG	1.17	0.15	MBG(4)
13.83	0.85	SBG	1.21	0.35	MBG(2)
1.08	0.26	MBG(2)	1.29	0.36	MBG(2)
1.25	0.20	MBG(5)	1.29	0.32	MBG(4)
1.35	0.14	MBG(3)	1.43	0.33	MBG(3)
1.36	0.14	MBG(4)	1.54	0.14	MBG(3)
1.42	0.13	MBG(3)	1.85	0.20	MBG(2)
1.64	0.08	MBG(2)	2.03	0.16	MBG(2)
2.21	0.19	MBG(2)	2.75	0.24	MBG(3)
2.22	0.16	MBG(5)	2.96	0.37	MBG(4)
2.41	0.24	MBG(6)	3.47	0.24	MBG(4)
2.43	0.13	MBG(3)	3.75	0.37	MBG(3)
2.79	0.12	MBG(4)	5.33	0.43	MBG(3)
3.16	0.27	MBG(3)			
3.26	0.33	MBG(4)			
4.75	0.18	MBG(2)			
5.16	0.30	MBG(3)			
5.23	0.20	MBG(4)			
6.45	0.43	MBG(3)			
7.16	0.29	MBG(2)			

Table 6.10. Accepted D_e values with uncertainties and grain count (GC) for samples 9.1 and 17.2. SBG: Single bright grain aliquots; MBG: multiple bright grain aliquots. The number of bright grains is indicated in brackets.

6.2 Case study 1 (b): Luminescence dating applied to Dariali Fort (Georgia)

6.2.1 Luminescence characteristics

In this section, OSL dating techniques were applied to occupation deposits at Dariali Fort, Trench F. The sediments were sampled to enable comparisons of the OSL dates with other dating evidence (radiocarbon and archaeomagnetic dating). The full radiocarbon chronostratigraphy is provided in Fig. B.1 in Appendix B. The Initial OSL characterisation of samples recovered from Dariali Fort were summarised in Sec. 6.1.1. Quartz grains recovered from the sediments at the fort originated from many different sources (bedrock quartz and degraded architectural building material). Opportunities for bleaching of mineral grains were limited to phases of anthropogenic sediment remobilisation ranging from the chaotic dumping of midden deposits (F.122, and F.037) to the collapse of building materials (F.129 and F.138). These deposits were intercalated by finely stratified deposits consisting of floors, trampled deposits and heated sediments (F.096), where the grains were likely to have been fully reset. The locations of the OSL samples are illustrated in Fig. 4.2.

6.2.2 OSL signal analysis

The signal intensity (R_N) and fast ratio (FR) histograms show a positive skewness (Figs. 6.12 and 6.13). The R_N and FR values for the SBG aliquots provide the best opportunity for characterisation. The results from the MBG aliquots are also provided for comparison.

The majority of R_N values measured from the SBG and MBG aliquots measured were within the low R_N range 0-10 in all samples. Samples 3.1 and 1.1 had a broad range of signal intensities, but a dominance of low signal intensities were found. A small proportion of aliquots from samples 400-3, 3.1 and 1.1 had R_N signals greater than 30. Overall, the grains extracted from these samples had low signal intensities and the preheat temperatures applied (180°C and 220°C) showed no effect on the distribution of R_N values.

The FR provides a proxy for the amount of stable 'fast' signal contributing to the overall luminescence signal. The FR ratios for sample 400-3 were within the low range (1.1-2 FR), 50% of the SBG aliquots and 44% of the MBG aliquots, respectively. One outlier with high FR values within the 17-18 range was present in the MBG aliquots. The SBG aliquots measured from sample 400-1 were concentrated within the low FR range (0-4). A similar pattern was observed in the MBG aliquots and two were within the higher ranges (12.1-13 and 16.1-17). Samples 3.1, 2.1, and 1.1 had a broad range

of FR values, the SBG aliquots were within the 0-4 FR range. The MBG aliquots were also concentrated within this range and a number of aliquots from sample 3.1 and 1.1 had FR values exceeding 20. The FR values suggest that the 'medium-fast' signal is the most dominant in all samples, and only a small proportion of grains had 'fast' signals.

6.2.3 Sensitivity change

In a number of SBG aliquots (n=8), only a subtle decrease in sensitivity change was observed (Fig. 6.14; a). Some sensitivity change was associated with a dominant 'slow-medium' decay (Fig. 6.15; c), where a greater decrease in sensitivity occurred between repeated beta doses (Fig 6.14; b). In a small number of aliquots, an 'ultrafast' decay form was present. This type of signal showed a significant shift from a 'slow-medium' decay observed in the natural, and after laboratory beta irradiation, an 'ultrafast' decay was observed (Fig. 6.15; a). Aliquots showing such sensitivity change are considered to be unreliable and are rejected. Some SBG aliquots of sample 3.1, showed an increased sensitivity (Fig. 6.14; c) which was associated with a relatively fast decay (Fig. 6.15; b).

6.2.4 Summary

The variability in the intensities of the natural OSL signals obtained from quartz recovered from the occupation deposits suggests a mixture of quartz grains with different luminescence characteristics. Samples 400-3 and 400-1 contained quartz that was mainly dominated by low signal intensities, making the detection of quartz grains with sufficiently bright signals difficult to identify (Fig. 6.16). The brighter SBG aliquot signals showed relatively similar characteristics based on the range R_N and FR values found. Both samples contained relatively bright signals associated with a 'medium' decay, and occasional 'medium-fast' decays, as detected in two MBG aliquots in 400-3.

The quartz characteristics found in the finely stratified deposits (3.1, 2.1 and 1.1) showed a mixture of R_N and FR values. Samples 3.1 and 1.1 in particular, had SBG aliquots with a broad range of signal intensities. Only a small number of quartz dominant signals could be isolated in sample 2.1 due to the dominance of HF resistant feldspars, although a number of aliquots with quartz dominant signals produced relatively strong luminescence signals. The FR values indicated that a dominant 'medium-fast' decay was prevalent in all three samples. The broad range of FR values for samples 3.1 and 1.1, suggests a mixture of signal characteristics, with some aliquots showing complex 'ultrafast' and 'slow-medium' decays.

The detection of 'ultrafast' decays has implications for accurately estimating D_e as it has shown to cause significant underestimation in the OSL age calculation (Jain *et al.* 2008; Steffen *et al.* 2009). This characteristic of quartz occurs when electrons are

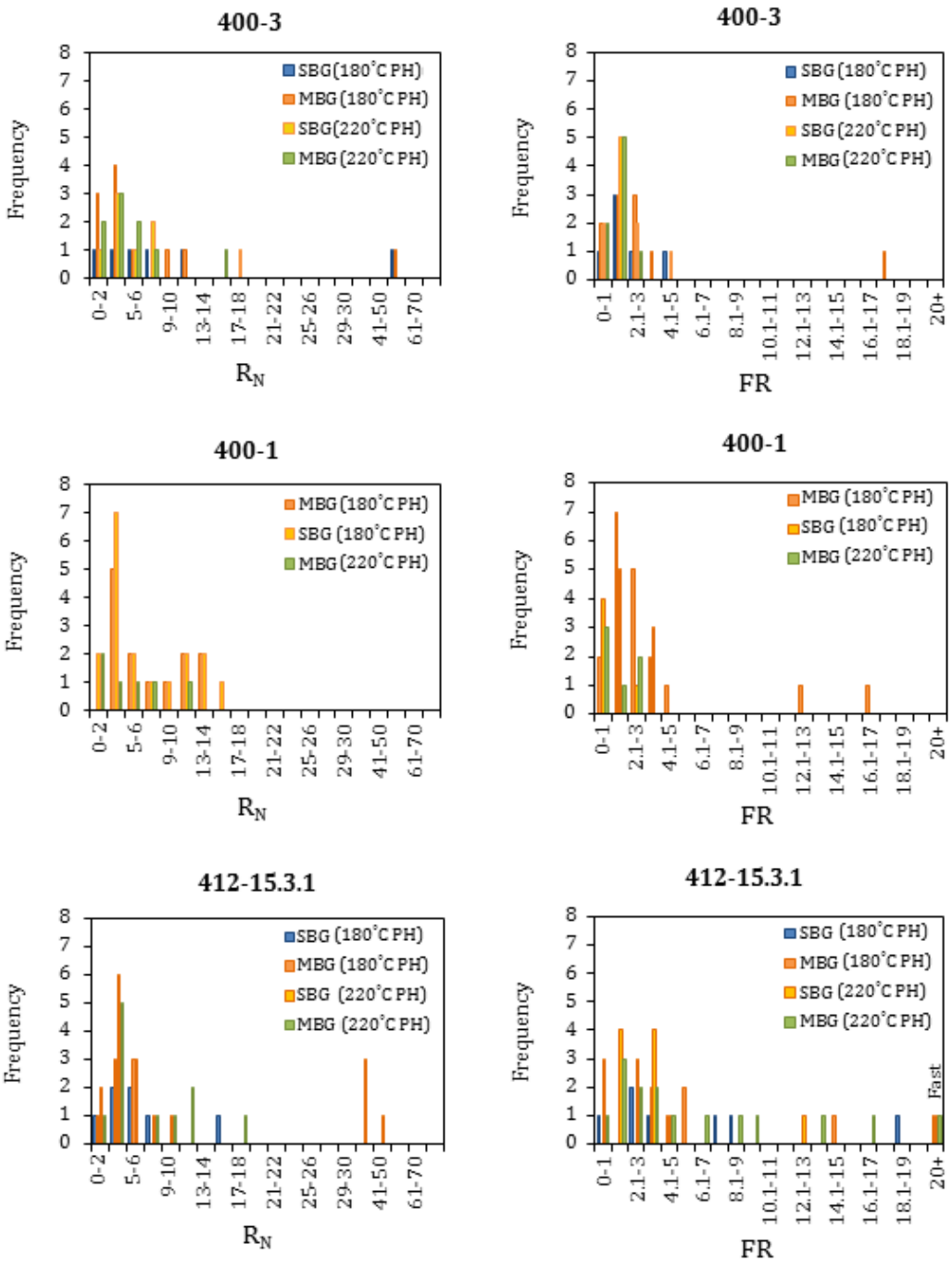

Figure 6.12. Histograms of R_N and FR ratio values for three samples from the occupation deposits uncovered. The number of aliquots for each sample is: 400-3 (n = 34), 400-1 (n = 36), 412-15.3.1 (n = 42).

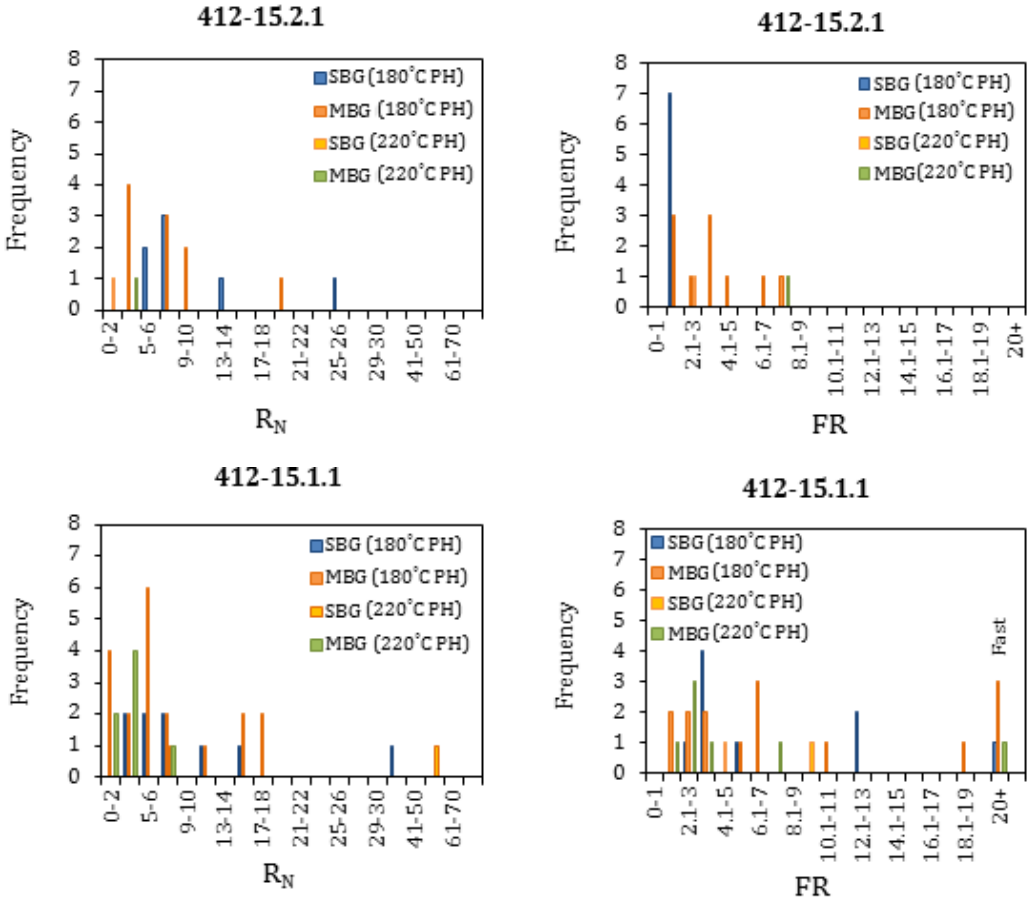

Figure 6.13. Histograms of R_N and FR ratio values for two samples from the occupation deposits uncovered. The number of aliquots for each sample is: 412.15.2.1 (n = 45), 412-15.1.1 (n = 41).

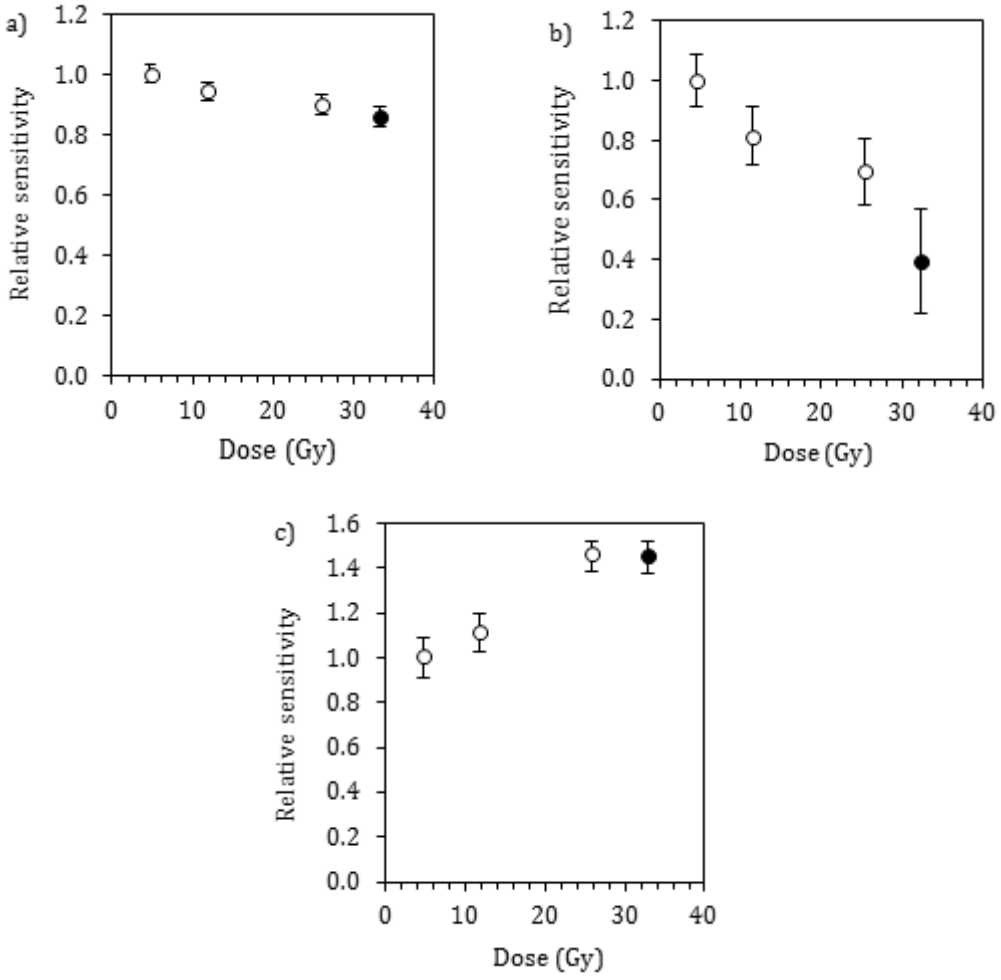

Figure 6.14. Examples of the three main types of sensitivity change observed in some aliquots. a) A gradual reduction in sensitivity in the SAR sequence; b) a significant reduction in sensitivity and statistical fluctuation was observed; and c) an increase in sensitivity during repeated beta irradiation.

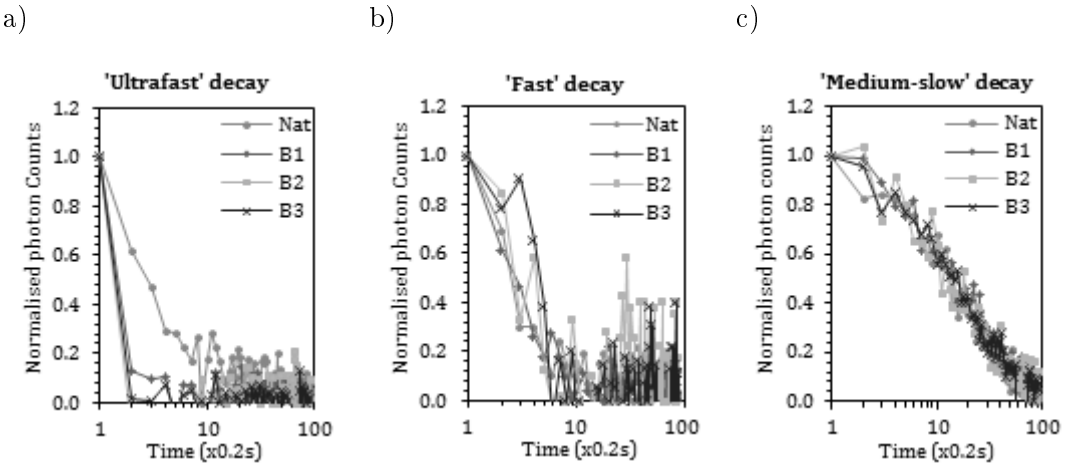

Figure 6.15. Examples of the three main types of OSL decay signals found in quartz extracted from the occupation deposits. The 'Ultrafast' (a), 'Fast' (b) and 'Medium-slow' decay (c) were detected. The 'Nat' decay refers to the natural OSL signal present, and the B1-3 decays are the background corrected laboratory beta-induced OSL signals measured during the SAR procedure.

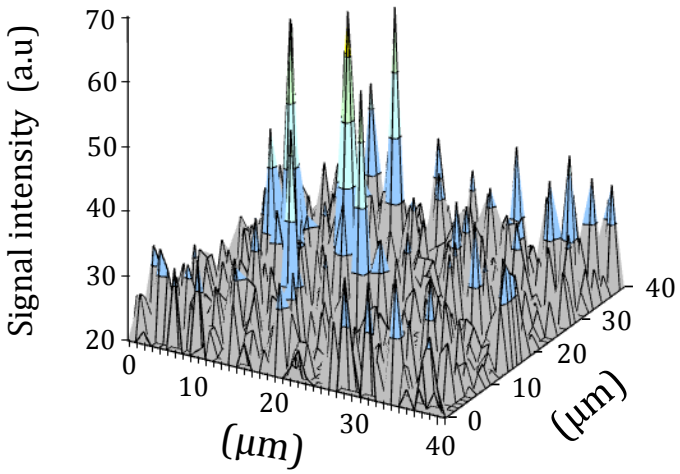

Figure 6.16. 3D plot displaying the signal intensities from a scanned aliquot obtained from sample 400-1 showing multiple low intensity grains.

	Sample				
	400-3	400-1	412-15.3.1	412-15.2.1	412-15.1.1
Overall summary:					
Aliquots tested	270	216	123	45	138
Average aliquot size (grains)	20	30	15	15	25
Aliquots for SAR measurement	34	36	42	45	41
Accepted D_e	31	34	29	15	21
Rejected aliquots:					
D_e uncertainity	0	0	1	1	5
Saturated	3	1	4	9	8
Recycling ratio	0	0	1	0	2
IR response	0	0	2	3	0
Unstable signals	0	0	3	7	5

Table 6.11. SAR summary.

released from shallow unstable traps (Jain *et al.* 2008). One way to resolve such unstable components requires high temperature preheats (>220°C) to prevent retrapping of electrons from the fast component traps into the unstable ultrafast shallow traps (*ibid.*). The presence of 'medium' and 'slow-medium' decays have already been addressed in Sec. 6.1.4. The occurrence of these signals may relate to the geological source of quartz as discussed in Sec. 6.1.7. Due to their unstable signals, aliquots displaying such signals were rejected (Table 6.11).

6.2.5 Dose recovery experiment

The dose recovery experiments were performed with samples 400-1, 3.1 and 1.1 due to the better yield of sufficiently bright quartz grains. The values of the evaluated equivalent dose (D_e) and the D_e/D_a ratio using three preheat temperatures (180, 200 and 220°C) and the RR are given in Table 6.12 and plotted in Fig. 6.17.

Of the three preheat temperatures used for sample 400-1, only the 180°C recovered dose ratio was close to 1 (1.00±0.05). Significant scatter was observed at higher preheat temperatures, and a progressive overestimation of D_a. The average recovery ratio for 180°C and 200°C preheats applied to 3.1 were closest to 1; 1.14±0.19 and 0.98±0.07 respectively. Preheat temperature had little effect on the recovery ratio in sample 1.1, as demonstrated by the plateau seen in the D_e/D_a values. Similar scatter was observed in the recycling ratio values for the D_e values between all three preheats applied, although the scatter appears to decrease with increasing temperature. Overall, 180°C preheat was considered to be best compromise for all samples.

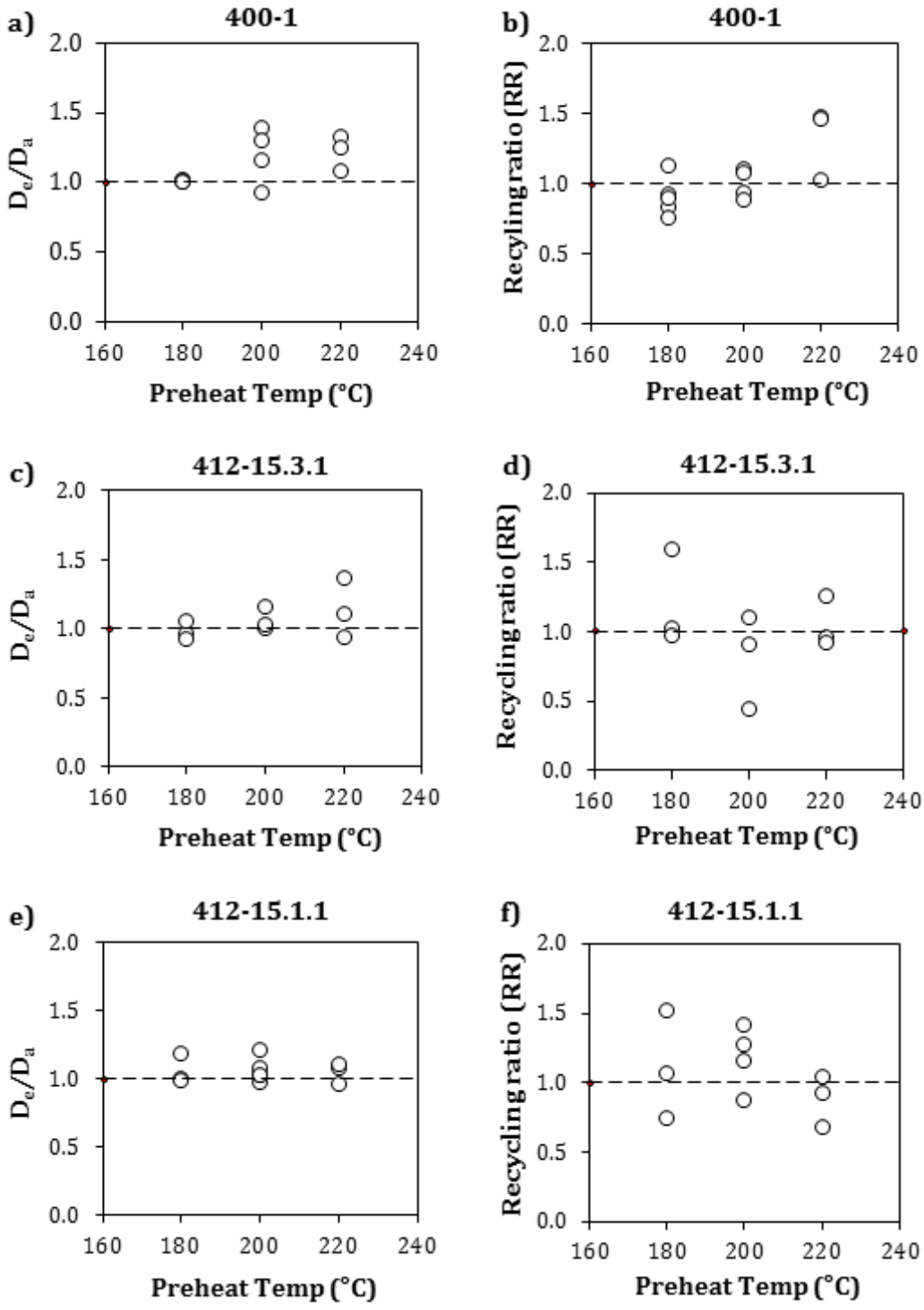

Figure 6.17. Dose recovery and recycling ratio scatter plots for samples 400-1, 412-15.3.1 and 412-15.1.1.

Sample	Applied dose (Gy)	Number of aliquots	Preheat (°C) 10 s	Recycling ratio (RR)	Ratio D_e/D_a	OD σ_i(%)
		4	220	1.26±0.12	1.18±0.09	9
400-1	4.84	5	200	0.92±0.07	1.13±0.13	12
		6	180	0.94±0.06	1.00±0.05	5
		3	220	0.75±0.06	1.14±0.19	19
412-15.3.1	9.00	3	200	1.06±0.21	1.06±0.08	8
		3	180	0.85±0.02	0.98±0.07	7
		3	220	0.97±0.12	1.07±0.12	12
412-15.1.1	7.04	4	200	1.18±0.11	1.23±0.06	6
		3	180	1.10±0.22	1.02±0.03	3

Table 6.12. Dose recovery results for the occupation deposits.

6.2.6 D_e measurements: Acceptance criteria

The number of aliquots tested and those that had a sufficient natural signal (R_N>1) varied between samples. Samples 400-3 and 400-1 produced a large proportion of low-intensity signals, and therefore a large number of grains were measured. In total, 31/270 and 35/216 SAR measurements were made on these two samples respectively. The screening of a large number of small aliquots and the rejection of variable natural signals observed within the first decay curve measured, improved the yield of accepted D_e values, which were 31 and 35, respectively. Only a small number were rejected due to saturated signals. The OSL signals from the underlying finely stratified occupation deposits was significantly brighter but contained a number of aliquots with poor luminescence characteristics; large uncertainties (>30%), saturation, poor recycling, IR sensitivity and unstable signals arising from 'slow-medium' and 'ultrafast' decays. The number of SAR measurements for each sample includes: 42/123 (sample 3.1), 45/45 (sample 2.1) and 41/138 (sample 1.1), of these aliquots measured, 30, 16 and 21 were accepted. Aliquots with unstable 'medium-slow' and 'ultrafast' signals were removed, as this signal can cause an underestimation of D_e (Jain *et al.* 2003). A small proportion of aliquots were also removed due to IR sensitivity, which can lead to D_e underestimation (e.g. Spooner *et al.* 2001). A summary of the accepted and rejected D_e values are provided in Table 6.11.

6.2.7 Accepted aliquots

A summary of the accepted D_e values and their grain counts are provided in Tables 6.13 and 6.14. The average recycling ratios and standard errors of accepted aliquots for the samples measured were; 400-1: 1.02±0.02 (1σ) (8.2% OD), 400-3: 1.07±00.02 (1σ) (5% OD), 412-15.3.1: 0.98±00.01 (1σ) (0% OD), 412-15.2.1: 1.00±00.01 (1σ) (0% OD),

Sample	1BG	2BG	3BG	>3BG
400-3	15	10	4	2
400-1	16	3	2	13
412-15.3.1	16	2	11	0
412-15.2.1	7	1	4	3
412-15.1.1	4	3	8	6

Table 6.13. Aliquot OSL scanning result summary. 1BG = a single dominant bright grain, 2BG = two bright grains, 3BG = three bright grains, >3BG = more than three bright grains.

Sample	Aliquot type	n	CDM (Gy)	OD (%)	Skewness	T-test results*	
						T-value	P-value
400-3	SBG	15	4.63±0.61	45±09	2.01±0.63	1.26	0.22
	MBG	16	6.34±0.75	44±08	-0.78±1.23		
	Combined	31	5.48±0.49	47±06	1.37±0.44		
400-1	SBG	16	6.03±1.00	65±11	0.50±0.61	0.79	0.43
	MBG	18	8.33±1.31	66±11	1.20±0.58		
	Combined	34	7.20±0.84	65±08	1.28±0.42		
412-15.3.1	SBG	16	4.22±0.57	46±09	-0.54±0.59	0.53	0.60
	MBG	13	3.85±0.31	27±06	4.77±0.61		
	Combined	29	4.03±0.31	39±06	5.24±0.45		
412-15.2.1	SBG	7	7.71±1.83	27±85	-0.28±0.93	0.35	0.73
	MBG	8	5.53±0.53	29±48	0.51±0.87		
	Combined	15	6.27±0.54	34±11	0.13±0.61		
412-15.1.1	SBG	4	13.77±3.29	71±17	0.23±0.82	0.63	0.53
	MBG	17	7.27±0.51	23±05	-0.35±0.66		
	Combined	21	8.34±1.05	63±09	1.40±0.48		

Table 6.14. D_e distribution characteristics. *95% confidence interval.

412-15.1.1: 1.03±00.03 (1σ) 6.2%, indicating that the SAR procedure was successfully performed. The recycling ratios of accepted D_e values are presented in Fig. 6.18.

6.2.8 D_e distributions

The D_e values were grouped according to the assigned bright grain count (Table 6.13). Accepted D_e values and their uncertainties, including the aliquot type and the number of bright grains contributing to MBG aliquots, are provided at the end of this case study (see Tables 6.18 and 6.19). The dispersion of the accepted D_e values was first visually assessed using a radial plot and numerically evaluated using a measure of overdispersion (OD) using the CDM to calculate the weighted mean value of D_e (Figs. 6.19 to 6.21). The values of OD for the SBG aliquots for all samples were varied: 400-3 (45%), 400-1

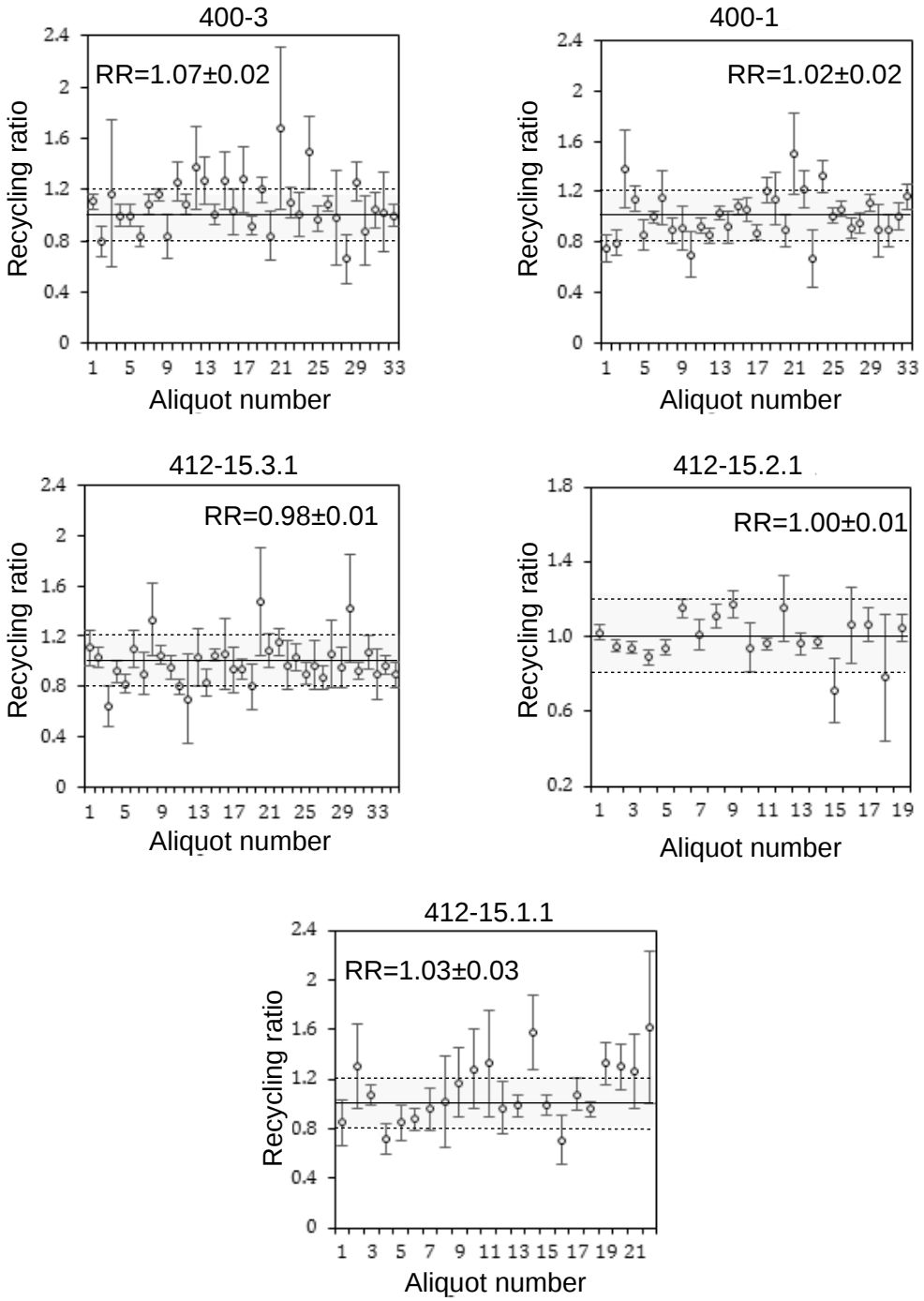

Figure 6.18. Plots showing the recycling ratios for accepted D_e values. The solid black line indicates the expected ratio of 1, and the dashed lines indicate the ±20% rejection limit for this ratio.

(65%), 3.1 (49%), 2.1 (27%) and 1.1 (71%). The broad spread in D_e values and the associated large OD, suggest that a high proportion of grains had not been fully optically reset prior to deposition. The recycling ratios for each accepted D_e value (Fig. 6.18) shows moderate scatter. A visual assessment of accepted D_e values as both KDE and radial plots enabled the identification of the relatively well-bleached population of grains in which an appropriate age model could be applied. Due to the small sample size, a T-test was applied to both the SBG and MBG values, in all five samples, the difference in the mean D_e values were considered to be insignificant, and these two datasets were therefore combined to estimate D_e.

The KDE plots for samples 400-3 and 400-1 (Fig. 6.19; a and b) show that there are subtle differences in the SBG and MBG D_e distributions. The SBG (indicated in black) indicate a lower dose population in sample 400-3. This suggests that the MBG aliquots are affected by aliquot averaging effects. The radial plots for both samples clearly shows the broad range of D_e values present, including one outlier with a very small standard error in sample 400-1. The positive skewness values (Table 6.14) and the relatively rapid deposition of both samples indicate that the application of a minimum dose model (MDM) is the most appropriate to calculate the mean value of D_e in both samples. Due to the limited number of SBG aliquots and the low signal intensities, the MBG aliquots were also included in the model.

The SBG and MBG D_e distributions for sample 3.1 are very similar, but with a single value of a higher dose (∼13 Gy) present in the SBG aliquots. Although OD of 20% has been proposed for the upper limit for well-bleached sediments (Olley *et al.* 2004), this sample was considered to be well-bleached according to the skewness value close to the critical value of 0. Considering that the SBG aliquots were overdispersed by 46% σ_b, a well-bleached component could be identified by the KDE plot with a narrow peak at ∼4 Gy. Based on these observations, the CDM model was applied to the SBG and MBG aliquot distributions. Three aliquots of low doses (∼1-2 Gy) were sensitive to IR stimulation and these were removed from the distribution.

The distributions of the two underlying samples, 2.1 and 1.1, were difficult to define as they were affected by low quartz yields (2.1) and low-intensity quartz signals (1.1). The SBG dataset was relatively small (n=7 and n=4), and a reliable measure of OD for these samples would require a much larger SBG dataset. The KDE plots of the SBG and MBG distributions for 2.1 differed, as the MBG distribution had a broad peak at ∼4 Gy and the SBG distribution was dominated by higher dose D_e values (∼9 Gy). The most appropriate age model was judged to be the MDM. Finally, sample 1.1, contained very few sufficiently bright SBG aliquots, but the KDE plot indicates a peak at ∼7 Gy. The MBG aliquots had a very broad range of D_e values, and the peak at ∼3 Gy suggests potential averaging effects of multiple low-intensity grains contributing to D_e (Fig. 6.22). The MDM was also applied to this sample.

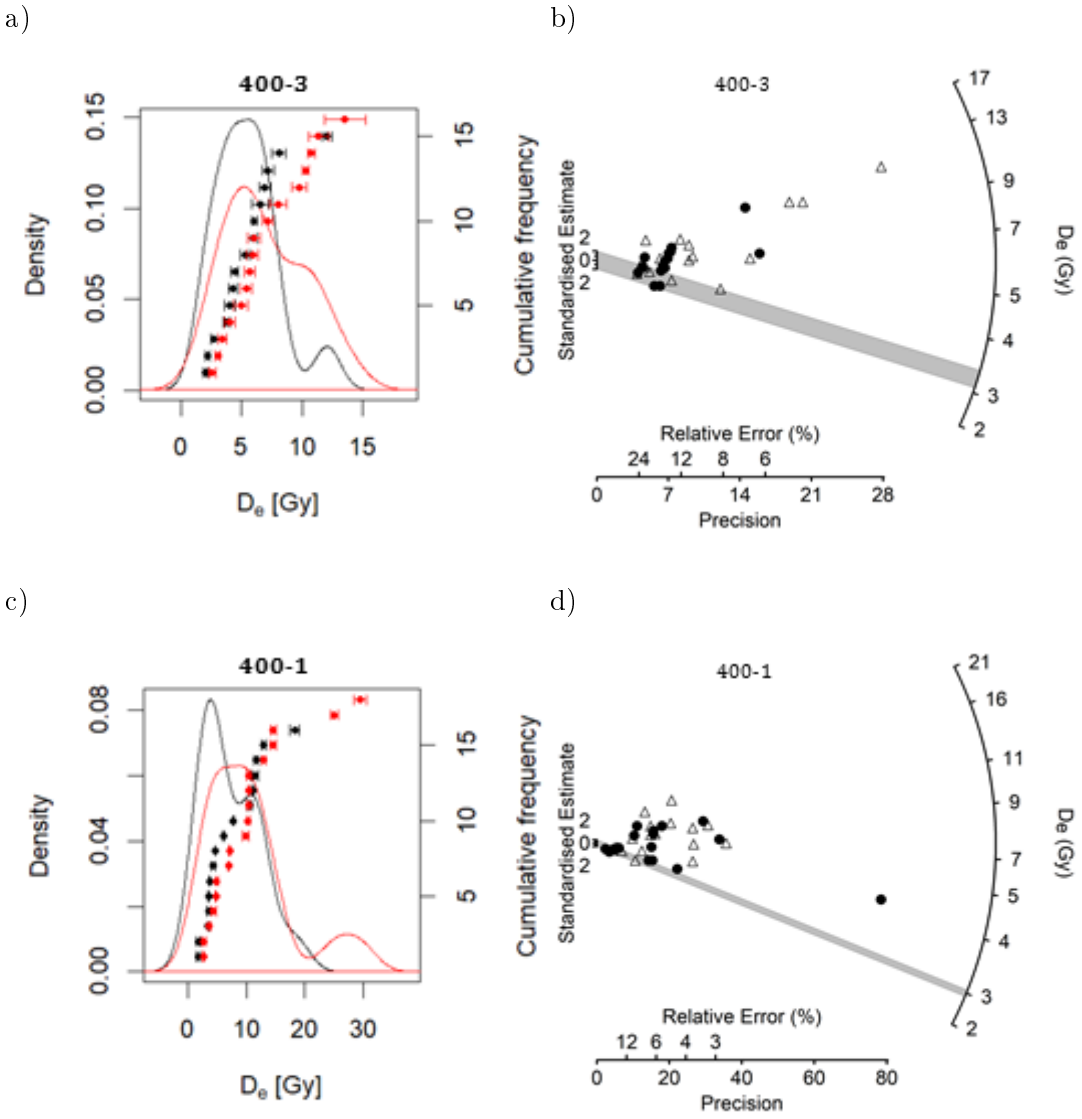

Figure 6.19. KDE plots of accepted D_e values (a and c). Black = SBG, Red = MBG, and radial plots of accepted D_e values (b and d). Closed circles = SBG, open triangles = MBG. The shaded regions indicate the D_e values (2σ uncertainty ranges) obtained when the MDM-3 was applied to SBG and MBG D_e values.

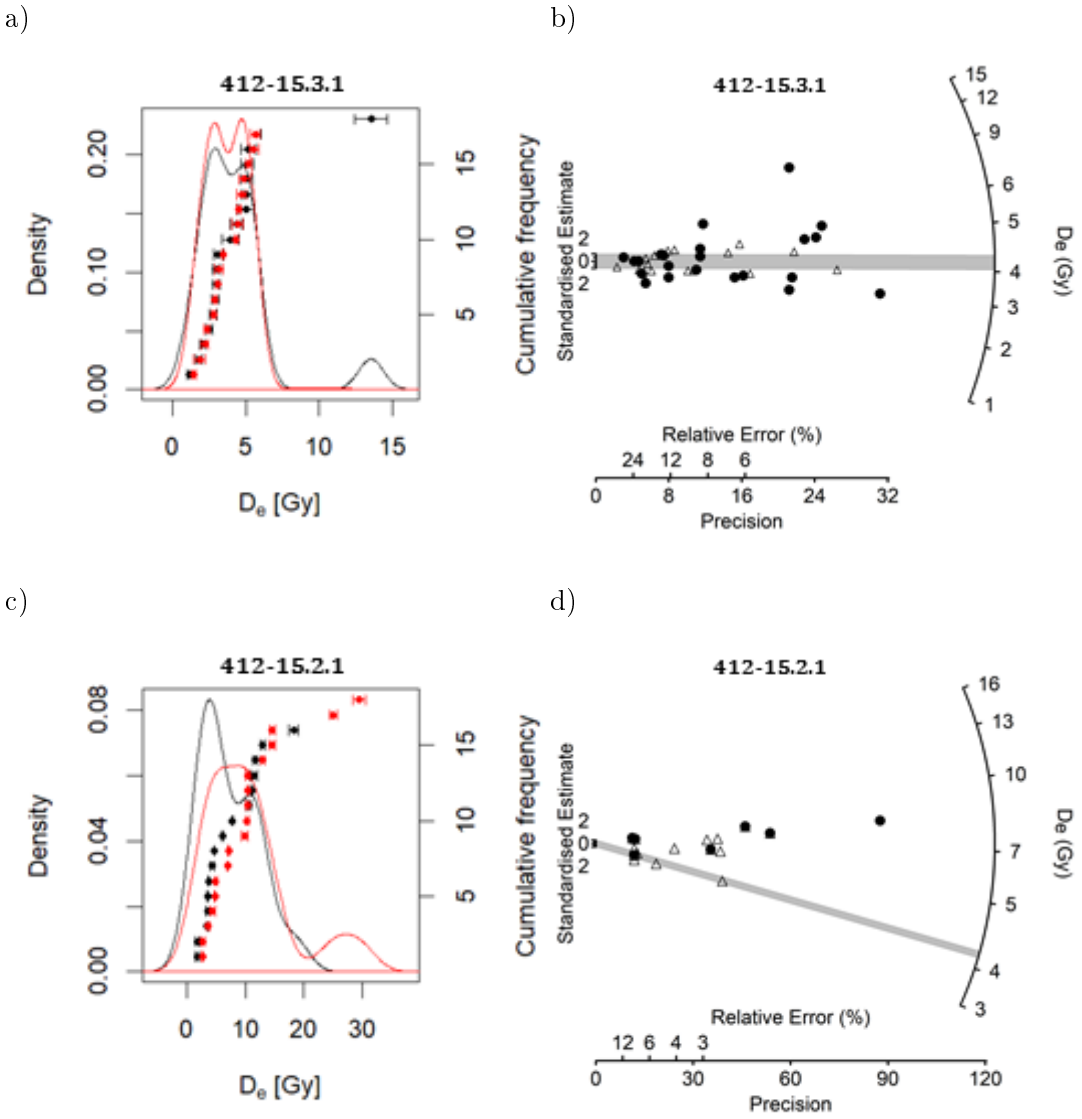

Figure 6.20. KDE plots of accepted D_e values (a and c). Black = SBG, Red = MBG, and radial plots of accepted D_e values (b and d). Closed circles = SBG, open triangles = MBG. The shaded regions indicate the D_e values (2σ uncertainty ranges) obtained when the MDM-3 was applied to SBG and MBG D_e values.

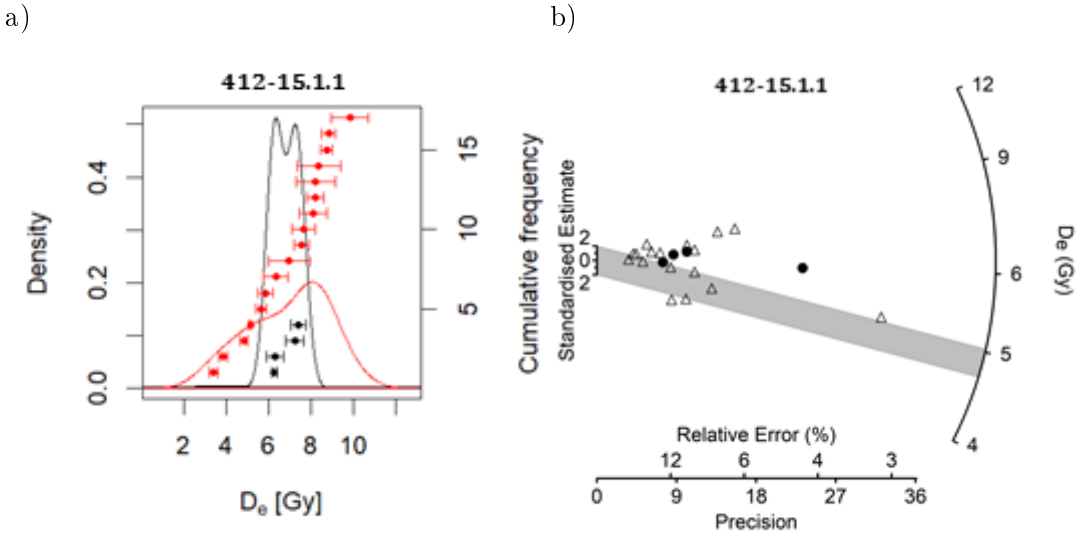

Figure 6.21. KDE plots of accepted D_e values (a). Black = SBG, Red = MBG, and radial plots of accepted D_e values (b). Closed circles = SBG, open triangles = MBG. The shaded regions indicate the D_e values (2σ uncertainty ranges) obtained when the MDM-3 was applied to SBG and MBG D_e values.

6.2.9 Dose rate assessment

The specific activities of the lithogenic radionuclides (Bq kg^{-1}) and the isotopic ratios ^{210}Pb/^{226}Ra and ^{210}Pb/^{av}U are presented in Table 6.15. The ratios of these activities enable an assessment of secular equilibrium within the ^{238}U/^{235}U and ^{232}Th decay series. In situations where disequilibria are pronounced (>50% difference in the ratios), greater uncertainty in the dose rate is introduced. Fig 6.23 illustrates the variability observed in these ratios, where the green dashed line represents the conditions of secular equilibrium, and the effect of 20% and 50% of disequilibria is also indicated.

6.2.10 Observed secular equilibrium conditions

The specific activities of radionuclides within the ^{238}U decay chain, pre and post ^{220}Rn activities were examined. In all samples measured, a decrease in activity at the end of the series was observed. A reduction in ^{222}Rn originated from the long-term loss in ^{214}Po towards the end of the ^{238}U chain was observed, which was also detected in the terrace basal samples (Sec. 6.1.13). The effect on the dose rate was estimated to be minimal. The ^{232}Th decay chain, the activities of ^{228}Ac/^{208}Ti in all samples were in equilibrium (Fig. 6.23; b).

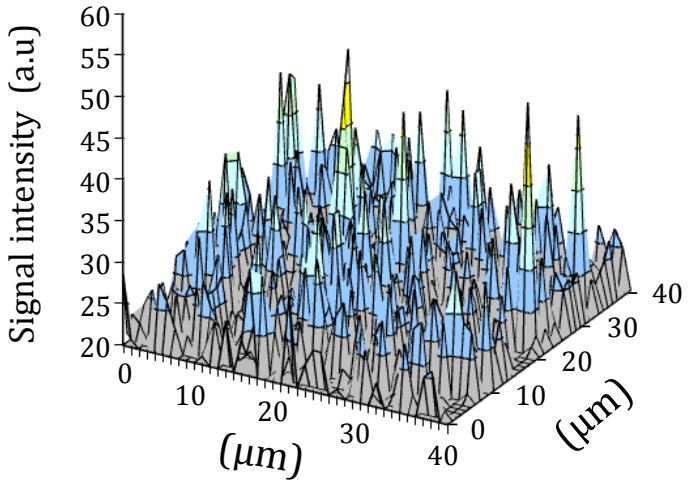

Figure 6.22. 3D plot displaying the signal intensities from a scanned aliquot obtained from sample 412-15.1.1 showing multiple low intensity grains.

	Isotope activities (Bq/kg^{-1})			Isotope ratios	
Sample/context	^{238}U	^{232}Th	^{40}K	$^{210}Pb/^{av}U$	$^{210}Pb/^{226}Ra$
400-3 [F.022]	36.7±1.9	47.6±3.3	562.7±7.9	0.88±0.1	0.81±0.1
400-1 [F.037]	35.9±1.9	43.4±3.3	527.3±7.8	0.86±0.1	0.83±0.1
412-15.3.1 [F.096]	39.3±1.9	42.9±3.2	572.5±8.0	0.91±0.1	0.81±0.1
412-15.2.1 [F.138]	31.2±1.7	38.3±2.8	536.3±7.3	0.93±0.1	0.86±0.1
412-15.1.1 [F.129]	38.7±1.9	38.7±3.3	624.8±8.4	0.76±0.1	0.84±0.1

Table 6.15. Summary of radioactive isotope activities and ratios measured as an infinite medium of a point absorber.

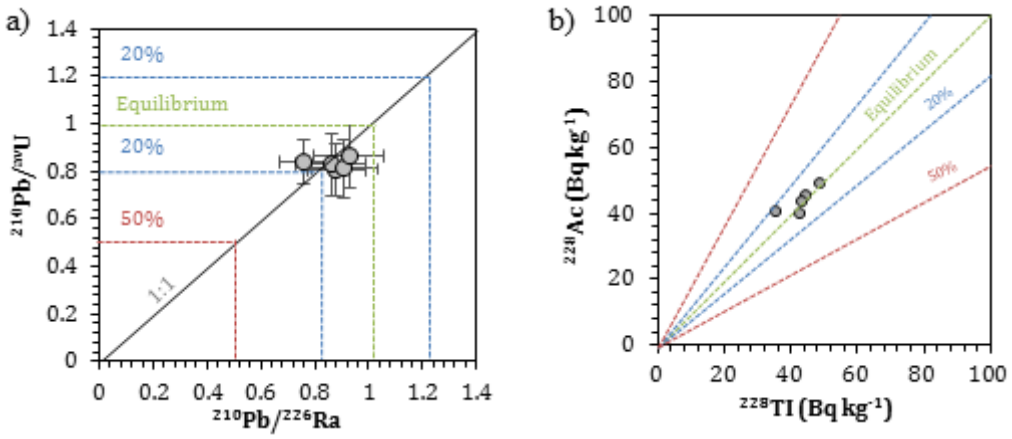

Figure 6.23. Assessment of current secular disequilibria in occupation deposits. a) Plots of ^{210}Pb/^{av}U and ^{210}Pb/^{226}Ra ratios. b) Scatter plot of ^{228}Ac vs ^{208}Ti activities in the ^{232}Th series.

Sample	$\dot{D}_\beta$±s.e.* (mGy a^{-1})	$\dot{D}_\gamma$±s.e. (mGy a^{-1})	$\dot{D}_{cos}$±s.e. (mGy a^{-1})	$\dot{D}_{tot}$±s.e. (mGy a^{-1})
400-3	2.05±0.04	1.03±0.02	0.23±0.02	3.34±0.07
400-1	1.74±0.03	1.22±0.02	0.22±0.02	3.22±0.06
412-15.3.1	1.90±0.04	1.22±0.03	0.21±0.02	3.36±0.07
412-15.2.1	1.74±0.04	1.10±0.02	0.21±0.02	3.08±0.06
412-15.1.1	2.01±0.04	1.11±0.02	0.20±0.02	3.36±0.07

Table 6.16. Dose rate summary. * Attenuation factor applied: 0.913 (Brennan 2003).

6.2.11 Beta dose rate

The values of the beta dose rate measured using βTLD are provided in Table 6.16 and these can be compared with the beta dose rate calculated ($\dot{D}_\beta$). The specific activities were determined with larger samples (25 g) by gamma spectrometry. The beta dose rate values obtained using the two methods are in agreement (Fig. 6.24), suggesting that beta dose rate is relatively homogeneous within the sedimentary matrix.

6.2.12 Cosmic ray dose rate

The cosmic ray dose rate at each sample location was calculated following Prescott & Hutton (1995), taking into consideration the geographical position, 42°N; 44°E, 148 km, average density of the sediment overburden (1.61 g cm^{-3}) and the sample depths below ground level, starting with the uppermost sample (400-3) located 138 cm (BGL) and the lowest sample (1.1) at 247 cm (BGL). The calculated cosmic dose rates ranged from

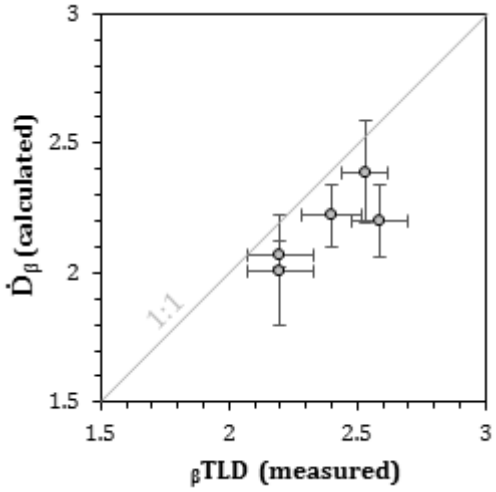

Figure 6.24. Scatter plot to compare the $\dot{D}_\beta$ and the βTLD dose rates for the five occupation deposits.

0.20 to 0.23 mg a^{-1} (Table 6.16), therefore making a relatively small contribution to the overall total dose rate of 6 to 7%.

6.2.13 Gamma dose rate

An examination of the stratigraphy (Fig. 4.2) had indicated that midden deposits (contexts F.122 and F.037) had been deposited within the building as a result of rapid dumping. Only the lower finely stratified contexts (F.096, F.138, and F.129) were deposited horizontally. The multilayer gamma dose rate model (Sec. 5.13); was applied to assess the influence of gamma dose rate contributions to each sample from contexts above and below. Due to the complex nature of the depositional processes, the model was only used to determine the contributions from surrounding deposits. For samples 400-3 and 400-1, the gamma dose rate was calculated using just two bulk contexts, F.122 and F.037, respectively. These two contexts also contained lenses of ash and charcoal intercalated with distinct layers of concentrated ceramic and animal bone. Therefore, the U, Th and K concentrations are likely to vary between these contexts, requiring a much high resolution sampling strategy (every 10 cm intervals). Furthermore, considering the uneven deposition of context F.037, as clearly illustrated in the section drawing (Fig. 4.2), approximately 30 cm was deposited directly above the sampled locations of the underlying finely stratified deposits. Over half of the dose rate of the underlying sediments originated from the sampled context, and 17 to 31% of the measured gamma dose rate came from contexts immediately above and below the OSL samples (Fig. 6.25). The deposit underlying F.129, was considered to be relatively similar in composition, and so the dose rate contribution was negligible.

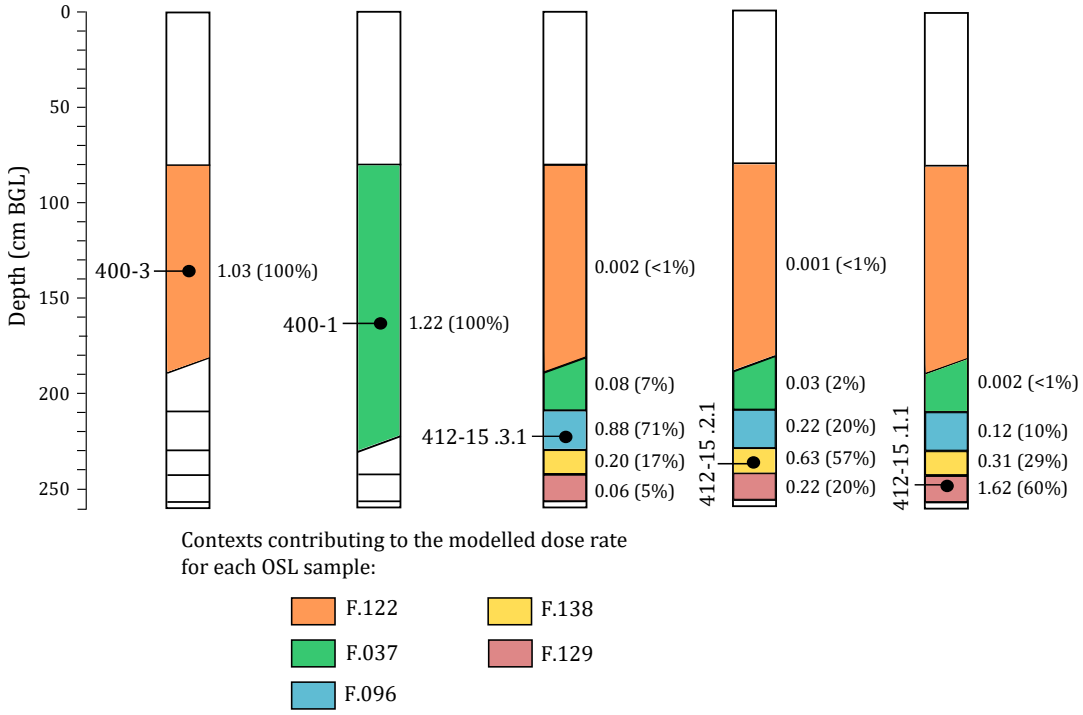

Figure 6.25. Stratigraphic diagram of contexts showing the dose-rate contributions from the surrounding contexts given in both mGy a^{-1} and % of the total gamma dose-rate contributing to the OSL sample. The numbers on the left of each stratigraphic column are related to the following context numbers: 1) F.122, 2) F.037, 3) F.096, 4) F.138 and 5) F.129.

6.2.14 Age determinations

The OSL ages calculated using the age equation 5.1 (Sec. 5.3.2) are calendar years (BC/AD) and include two error terms ($\pm\sigma_a$ and $\pm\sigma_b$) (Sec. 5.14). These ages are then converted to calendar dates before 2016 (Table 6.17).

Sample	Burial age (before 2016)	OSL age* (AD)	$\pm\sigma_a$	$\pm\sigma_b$
400-3	904	1110	145	154
400-11	926	1090	129	138
412-15.3.1	1240	775	98	120
412-15.2.1	1462	550	181	198
412-15.1.1	1426	590	142	163

Table 6.17. OSL age determinations for the occupation deposits at Dariali Fort (Trench F). σ_a = Type A; σ_b = Type B (after ISO 8601:2004). * rounded to the nearest 5 years.

400-3			400-1		
D_e(Gy)	±s.e. (1σ)	GC	D_e(Gy)	±s.e. (1σ)	GC
2.02	0.36	SBG	1.72	0.47	SBG
2.16	0.35	SBG	1.76	0.69	SBG
2.73	0.67	SBG	3.48	0.24	SBG
3.74	0.59	SBG	3.52	0.71	SBG
3.98	0.87	SBG	3.56	0.16	SBG
4.27	0.64	SBG	3.72	0.24	SBG
4.40	0.68	SBG	4.24	0.69	SBG
5.27	0.79	SBG	4.70	0.06	SBG
5.88	0.85	SBG	6.11	0.40	SBG
6.04	0.38	SBG	7.80	0.23	SBG
6.50	1.38	SBG	10.64	0.68	SBG
6.91	0.98	SBG	11.21	0.38	SBG
7.16	0.99	SBG	11.49	1.09	SBG
8.08	1.10	SBG	11.68	0.75	SBG
12.06	0.83	SBG	12.87	0.71	SBG
2.56	0.65	MBG(3)	18.28	1.62	SBG
3.01	0.41	MBG(2)	2.65	0.25	MBG(4)
3.27	0.27	MBG(4)	2.66	0.62	MBG(5)
3.39	0.66	MBG(2)	3.64	0.53	MBG(5)
3.98	0.85	MBG(2)	4.40	0.82	MBG(6)
4.94	1.12	MBG(4)	4.77	0.18	MBG(4)
5.38	0.60	MBG(2)	4.93	0.39	MBG(4)
5.68	0.38	MBG(3)	6.94	0.26	MBG(5)
5.91	0.95	MBG(2)	7.14	0.20	MBG(4)
6.00	0.64	MBG(3)	9.86	1.00	MBG(3)
8.03	0.89	MBG(2)	10.33	0.39	MBG(4)
9.78	1.20	MBG(2)	10.35	0.64	MBG(2)
10.28	0.51	MBG(2)	10.42	0.34	MBG(4)
10.75	0.57	MBG(3)	10.43	0.70	MBG(5)
11.37	0.41	MBG(2)	12.92	0.63	MBG(3)
13.54	2.81	MBG(2)	14.54	0.98	MBG(2)
			14.64	0.98	MBG(2)
			25.01	1.21	MBG(5)
			29.48	2.21	MBG(5)

Table 6.18. Accepted D_e values with uncertainties and grain count (GC) for samples 400-3 and 400-1. SBG: Single bright grain aliquots; MBG: multiple bright grain aliquots. The number of bright grains is indicated in brackets.

412-15.3.1			412-15.2.1			412-15.1.1		
D_e(Gy)	±s.e. (1σ)	GC	D_e(Gy)	±s.e. (1σ)	GC	D_e(Gy)	±s.e. (1σ)	GC
2.07	0.30	SBG	4.00	0.34	SBG	6.27	0.27	SBG
2.75	0.55	SBG	6.56	0.18	SBG	6.31	0.84	SBG
2.80	0.54	SBG	8.20	0.15	SBG	7.24	0.83	SBG
2.98	0.34	SBG	8.56	0.10	SBG	7.41	0.73	SBG
3.01	0.26	SBG	9.09	0.20	SBG	3.40	0.40	MBG(3)
3.94	1.11	SBG	9.60	0.78	SBG	3.84	0.38	MBG(3)
3.96	1.19	SBG	9.94	0.87	SBG	4.83	0.37	MBG(2)
4.36	0.91	SBG	3.28	0.28	MBG(2)	5.13	0.16	MBG(4)
4.85	1.13	SBG	3.81	0.20	MBG(4)	5.64	0.51	MBG(3)
5.03	0.42	SBG	4.16	0.11	MBG(4)	5.87	0.70	MBG(5)
5.06	0.98	SBG	4.59	0.36	MBG(4)	6.33	1.20	MBG(3)
5.17	1.08	SBG	5.57	0.47	MBG(3)	6.97	1.93	MBG(3)
5.53	2.05	SBG	6.41	0.26	MBG(3)	7.55	0.68	MBG(2)
5.70	0.46	SBG	6.44	0.17	MBG(3)	7.66	1.07	MBG(6)
9.46	1.04	SBG	7.86	0.23	MBG(3)	8.11	1.30	MBG(4)
13.55	0.64	SBG				8.19	0.80	MBG(3)
2.20	0.46	MBG(3)				8.23	1.85	MBG(6)
2.34	0.38	MBG(3)				8.38	2.04	MBG(3)
2.82	0.28	MBG(3)				8.74	0.56	MBG(2)
2.90	0.27	MBG(3)				8.85	0.65	MBG(3)
3.05	0.18	MBG(3)				9.85	1.74	MBG(6)
3.18	0.56	MBG(3)						
4.34	0.20	MBG(2)						
4.42	0.80	MBG(3)						
4.51	0.31	MBG(3)						
4.73	0.64	MBG(3)						
4.90	0.76	MBG(2)						
5.19	0.33	MBG(3)						
5.56	0.64	MBG(3)						

Table 6.19. Accepted D_e values with uncertainties and grain count (GC) for samples 412-15.3.1, 412-15.2.1 and 412-15.1.1. SBG: Single bright grain aliquots; MBG: multiple bright grain aliquots. The number of bright grains is indicated in brackets.

6.3 Case study 2: Luminescence dating applied to a large-scale canal (Mil Steppe, Azerbaijan)

6.3.1 Luminescence characteristics

The following section presents the results from the application of OSL dating to sediments associated with a large canal system. Four main deposit types were explored, alluvial sediments deposited by fluvial processes, an old ground surface formed by the *in situ* pedogenesis, anthropogenically reworked alluvial upcast deposits, and canal infill deposited (Fig. 4.26). The sediments are relatively similar in composition and mineralogy but deposited under very different conditions. Quartz and feldspar (sodic and potassic) were the most abundant minerals found in the sediments sampled. High resolution CL imagining (Sec. 3.6.2) indicated that quartz came from two main sources: alluvial deposits from the Lesser Caucasus mountain range, and aeolian deposits originating from loess in the Transcaspian region. The CL colours varied from red and dark blue in colour (Fig. 6.26). Quartz appeared as both angular and rounded forms (Fig. 6.27; C and E) suggesting variable transport distances, and grains deposited by aeolian processes were typically well-rounded. Feldspars were found in relative abundance in the alluvial deposits (Fig. 6.27; A, B and D). However, the frequency of feldspar grains appeared to reduce in the upcast deposits due to post-depositional dissolution, as observed in both the micromorphological thin sections (Sec. 4.2.4) and reflected in low IRSL signal intensities (Sec. 6.3.3).

A number of samples were screened to identify those with dominant quartz signals, of those tested, nine samples were measured in detail, 413-1.1, 1.3, 1.6.1, 1.8.2, 2.1.1, 3.3, 3.6.1, and 3.8, and their specific locations within the canal sequence are illustrated in Fig. 4.26. The following section provides the OSL dating results for these samples.

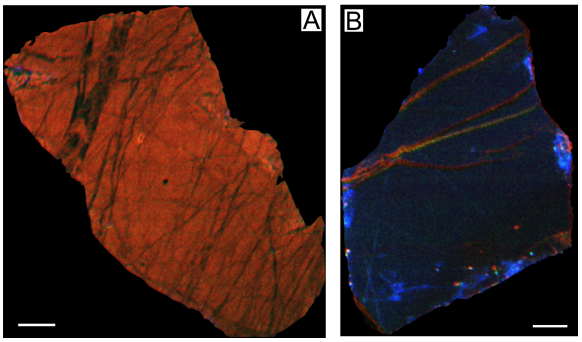

Figure 6.26. Cathodoluminescence images of two quartz grains showing volcanic red quartz (A), and low intensity dark blue (B). Scale = 20 μm.

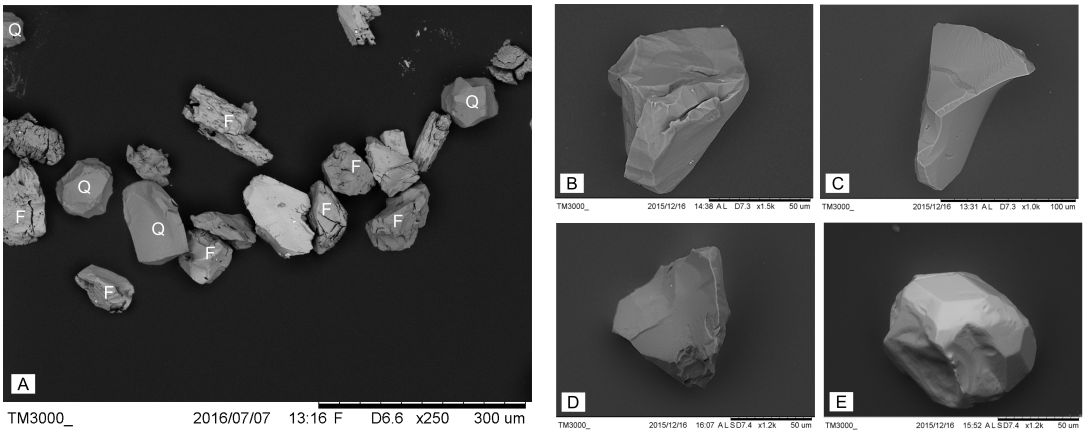

Figure 6.27. High-resolution SEM backscatter images of quartz and feldspar grains recovered from the canal deposits. A) A mixture of quartz and heavily HF etched feldspar grains (413-3.8), B-D) angular to sub-angular feldspar grains (413-2.2), and E) rounded quartz grains (413-1.6.1).

6.3.2 OSL signal analysis

Quartz OSL signals from nine samples are presented in Figs. 6.28, 6.29 and 6.30, which include the FR and R_N ratios from the SBG and MBG aliquots. Three samples in total (1.7.1, 1.8.2 and 3.3) were affected by low quartz yields and low signal intensities (natural OSL signals <100 counts). OSL signals from 1.1, 1.3, 1.6.1, 2.1.1, 3.6.1 and 3.8 are discussed in detail as the larger dataset enables a more reliable characterisation of the signals present in the quartz from the sediments sampled.

The samples contained a significant proportion of grains with relatively low luminescence signal intensities (R_N), and so a large number of aliquots were screened to identify those with the most suitable characteristics. Most of the R_N ratios for the SBG and MBG aliquots from sample 1.1 were within the 0 to 8 R_N range, with two MBG aliquots in the high range (17 to 22). The R_N signals for the SBG aliquots from sample 1.3 were broadly distributed between the R_N ranges 2 to 16, and three aliquots between 23 and 30 R_N. The R_N values for the MBG aliquots were also broadly distributed (1 to 18 R_N) but most were concentrated (63%) in the 3 to 6 range. Over half (56%) of the SBG aliquots measured in sample 1.6.1 had R_N values within the range of 3 to 6 R_N ,and 42% of the MBG aliquots were in the 0 to 2 R_N range. Most of the SBG aliquots in 2.1.1 were concentrated in the 3 to 12 R_N range, with two aliquots in the high range (17 to 18). A broad spread in R_N values were present in the MBG aliquots. In sample 3.6.1, nearly half (48%) of the R_N values measured were concentrated in the low range (1 to 2), and 26% of the MBG aliquots were also in the low R_N range (1 to 3). Half of the SBG aliquot R_N values were in the 5 to 12 range and 26% in the high range (30 to 50). A broad range of R_N values were observed in the MBG aliquots, again, most

(85%) were concentrated in the 1 to 12 R_N range.

Sample 1.1 revealed a broad spread in FR values in nearly all ranges in both the SBG and MBG aliquots. The FR frequencies for sample 1.3 showed a positive skewness, with majority of the FR for the SBG aliquots were in the low range 1.1 to 2, and one in the higher range (+20). A similar frequency distribution was observed in the MBG aliquots, and also two MBG aliquots in the high range. The SBG aliquots from sample 1.6.1 were concentrated in the 1.1 to 2 FR range (48%) and one in the 9.1 to 10 FR range. A broad spread in FR values was observed in the MBG aliquots and one within the 16.1 to 17 FR range. The second upcast sample, 2.1.1 had 38% of the SBG aliquots in the 2.1 to 3 FR range, similarly the MBG aliquots were also concentrated between 0 to 4 FR ratios and only one within the higher range 12.8 to 18. Sample 3.6.1 revealed that 38% of the values from the SBG aliquots were in the 3-7 FR range, and two from the 19 to 20 and 20+ range. The R_N signals from the underlying natural alluvial deposit sampled as 3.8 contained nearly half (47%) of the SBG aliquots in the low FR range (1.1 to 2), and most were between 0-4 FR. Similar proportions were observed in the MBG aliquots, 76% were within the 0-4 FR range, and one aliquot in the high FR range (16.1 to 17).

The R_N and FR values for the three remaining samples (1.7.1, 1.8.2 and 3.3) revealed that the R_N signals measured from the few aliquots obtained were within the low range (0 to 6), and a broad distribution of FR values was found in all three samples.

6.3.3 IRSL signal

The IRSL signal was measured after stimulation for 70 s at 125°C with IR LEDs. Examples of the IRSL signals obtained from a selection of aliquots from the four phases of the canal are provided in Fig. 6.31. It was observed that no IRSL signal was present in the old ground surface or the construction deposits (Fig. 6.31; a). Only a small IRSL signal was observed within the clean-out deposits which formed the main component of the upcast banks associated with the canal (Fig. 6.31; c and d). Some aliquots of sample extracted from the alluvial deposits and canal fills contained a number produced a relatively strong IRSL signals (Fig. 6.31; b). In most samples, excluding 3.6.1 and 3.8, the presence of residual feldspars was avoided using small aliquots, and those with dominant IRSL signals identified in screening tests (Sec. 5.7.5), were not measured using the full SAR measurement. For samples 2.1.1 and 3.8, it was necessary to perform HLS twice and apply careful abrasion to the mineral extracts to break up any fragile feldspar grains remaining.

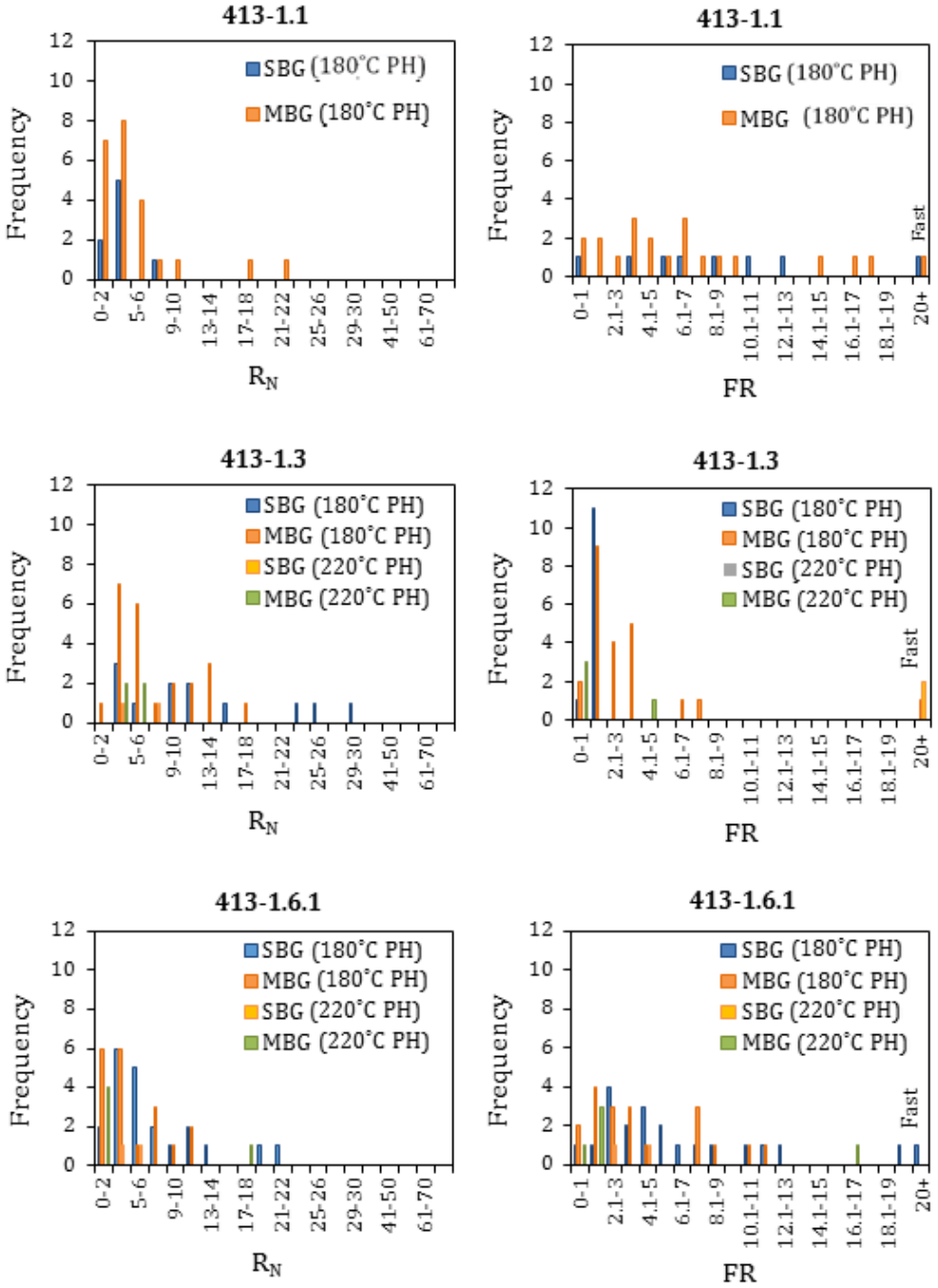

Figure 6.28. Histograms to show the fast ratio and R_N of SBG and MBG aliquots for samples 1.1 (n = 29), 1.3 (n = 41) and 1.6.1 (n = 47).

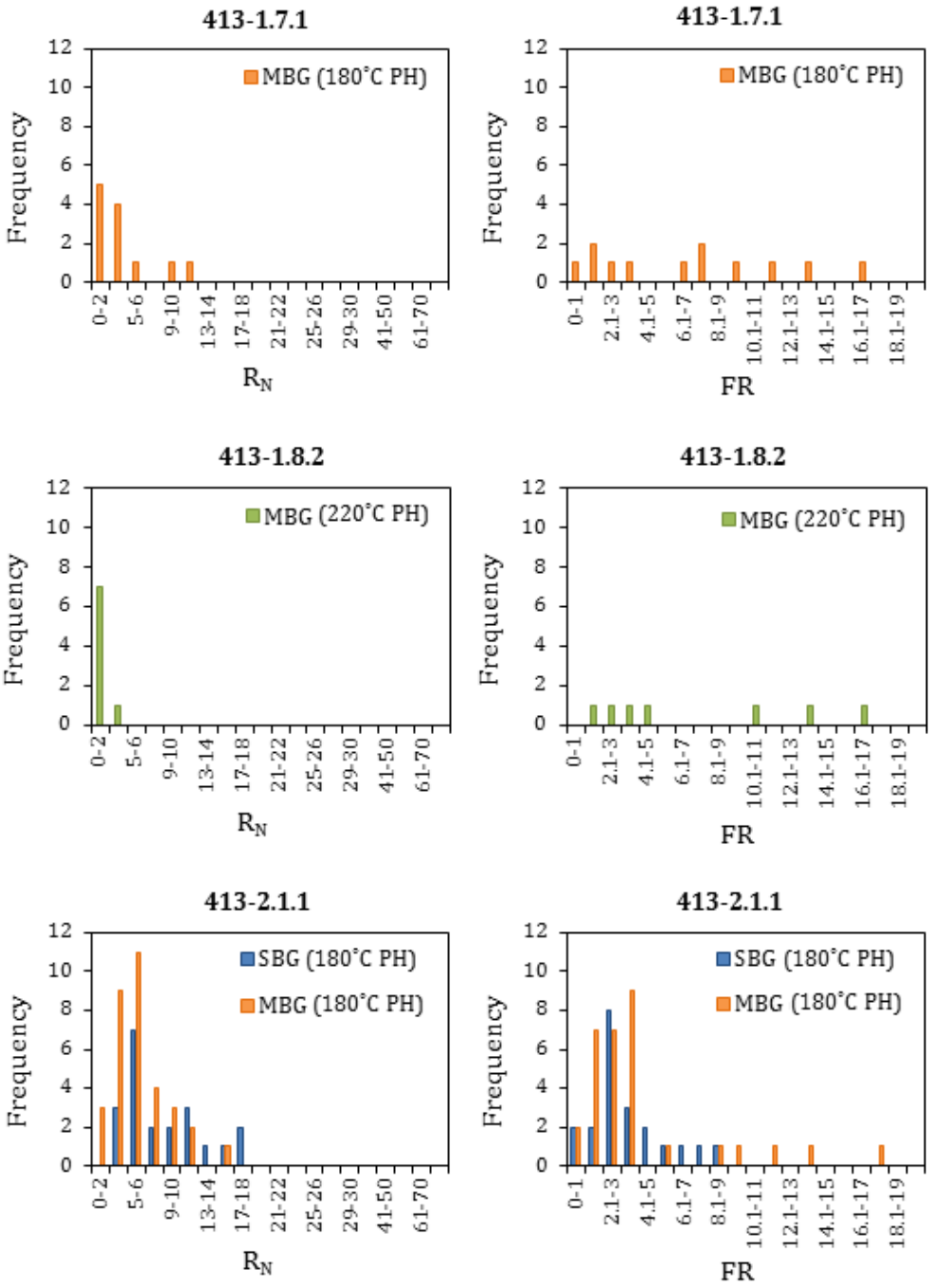

Figure 6.29. Histograms to show the fast ratio and R_N of SBG and MBG aliquots for samples 1.7.1 (n = 11), 1.8.2 (n = 11) and 2.1.1 (n = 54).

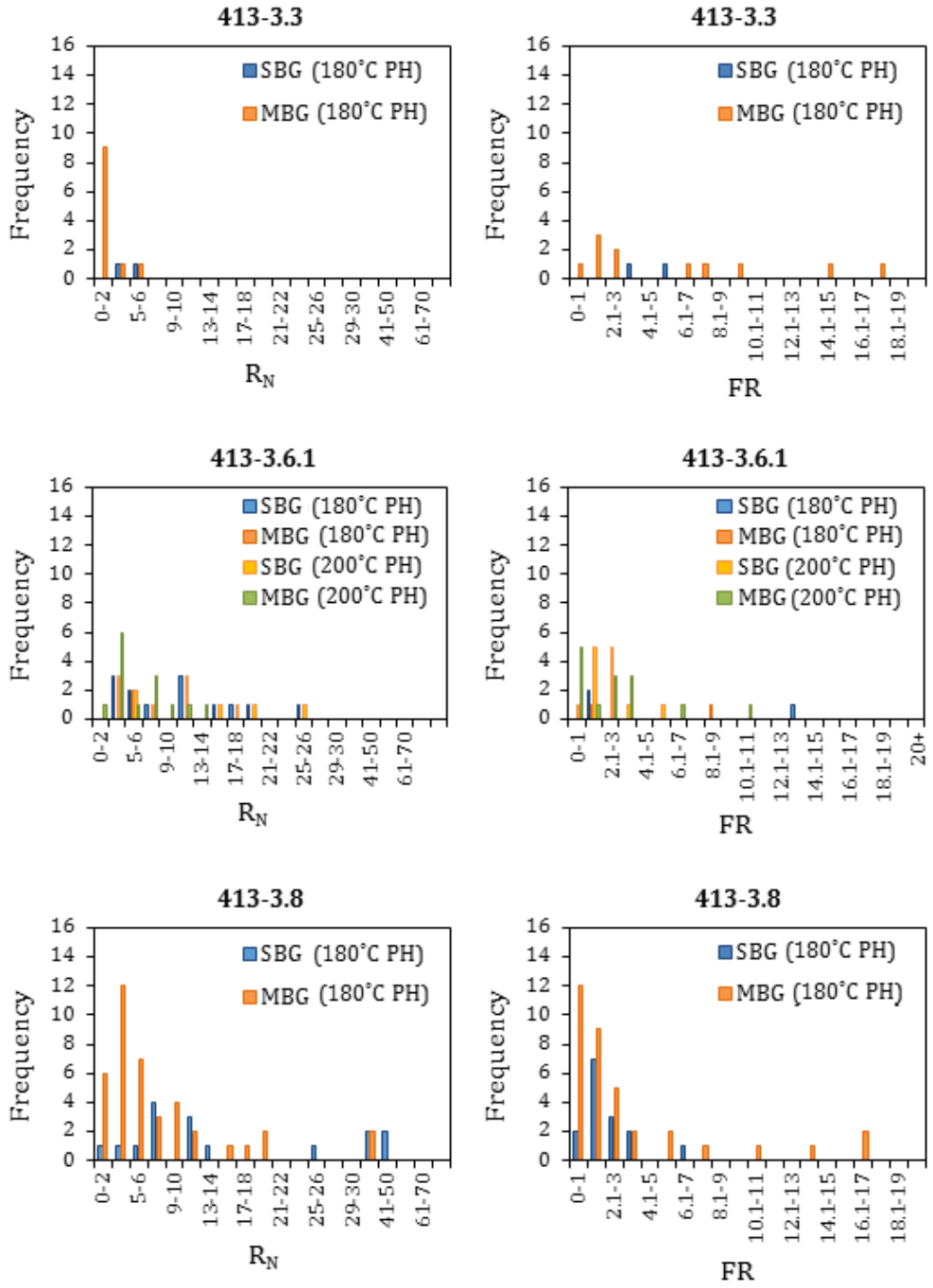

Figure 6.30. Histograms to show the fast ratio and R_N of SBG and MBG aliquots in samples 3.3 (n = 13), 3.6.1 (n = 32) and 3.8 (n = 27).

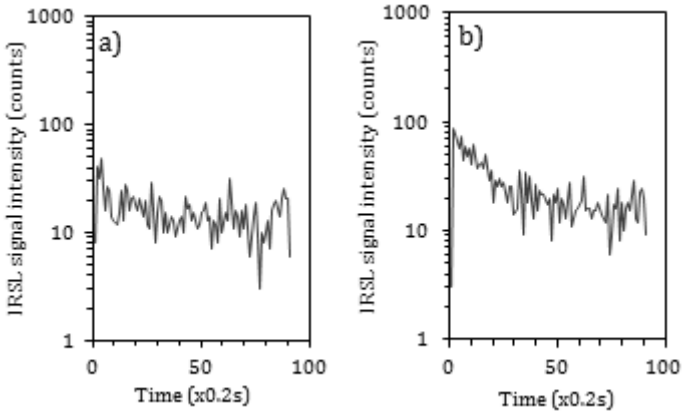

Figure 6.31. IRSL signals measured as part of the final stage of the SAR procedure. a) No signal was observed in the old ground surface. b) A low IRSL signal detected in the upcast deposits.

6.3.4 Sensitivity change

The sensitivity of OSL signals have shown to increase with increasing fluvial recycling (Pietsch *et al.* 2008). Highly sensitised grains are those that have undergone repeated recycling and are ideal for the SAR procedure. Therefore, alluvial sediments which make up the deposits within the canal was thought to contain quartz with relatively stable signals and any sensitivity change could be easily accounted for. A large number of aliquots were screened to concentrate those with sufficiently bright signals to be fully measured. However, in a number of aliquots, sensitivity change was observed during repeated beta irradiation. Sensitivity change during different repeated beta irradiation doses (Fig. 6.32; a) and statistical fluctuation was found in a number of aliquots (Fig. 6.32; a, d and f). Little change in sensitivity was observed in a number of aliquots, particularly those with dominant fast decays (Fig. 6.32; b), and a medium decay was observed when little sensitivity change occurred but a drop in sensitivity after IR stimulation was found (Fig. 6.32; a). An example of an increase in sensitivity before a drop after IR stimulation was observed (Fig. 6.32; e) and this showed a switch from a fast decay to a medium decay after the second beta irradiation cycle. Similar shifts in signals were observed in aliquots with significant statistical fluctuation were also identified, where a change from a 'fast' decay as measured in the natural signal which then changed to a medium decay after beta irradiation (Fig. 6.33).

6.3.5 Summary

High-resolution CL and SEM analysis revealed that quartz originated from two potential sources, and a significant proportion of these grains were dominated by red CL emissions

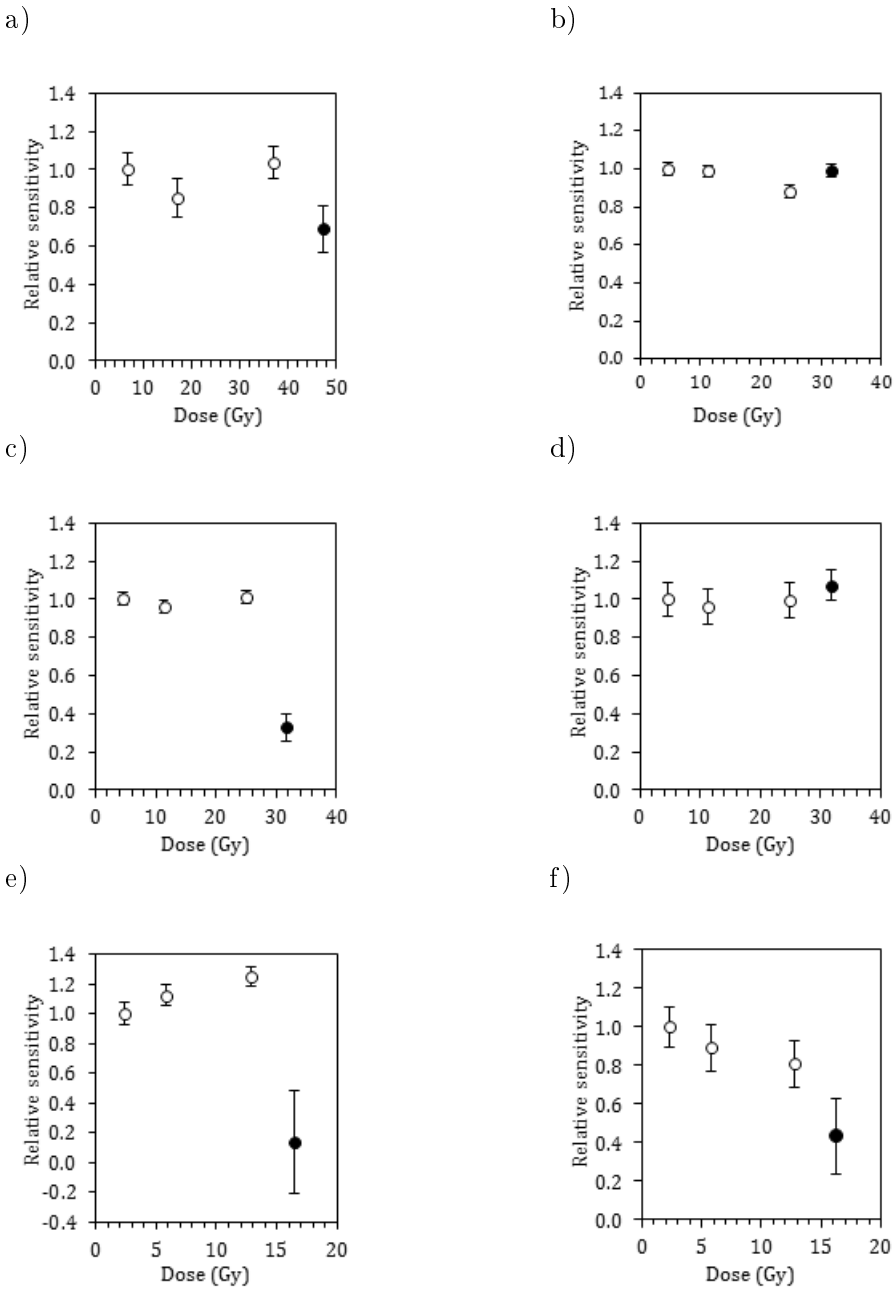

Figure 6.32. Common types of sensitivity change observed during the SAR measurement procedure found in quartz extracted from the canal deposits. a) Significant fluctuation in sensitivity, b) relatively stable signal with minor reduction in the sensitivity in OSL signal after the three beta irradiation, c) no sensitivity change until a drop is observed after IR stimulation (closed marker), d) relatively little sensitivity change but significant statistical fluctuation between beta irradiation cycles, e) an increase in sensitivity and a sudden decrease after IR stimulation, and f) a gradual decrease in sensitivity and significant statistical fluctuation.

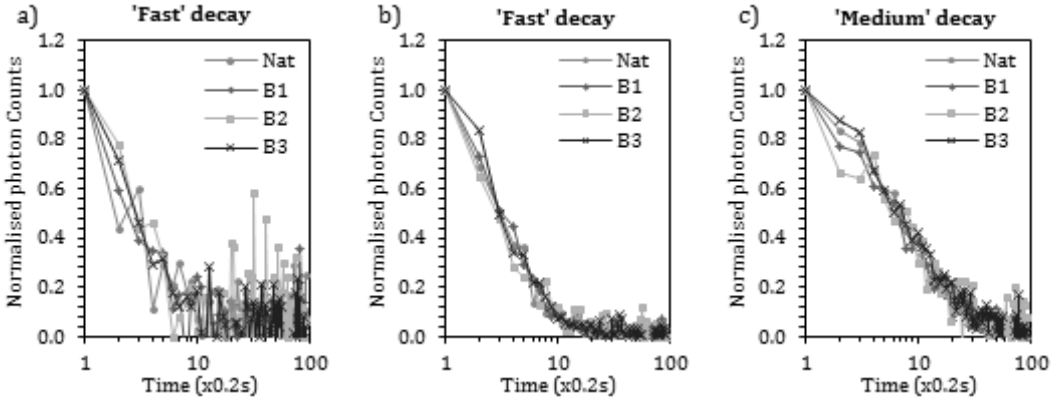

Figure 6.33. Examples of the OSL decay signals found in quartz extracted from the occupation deposits. The 'Fast' (a and b) and 'Medium' decay (c) were detected. The 'Nat' decay refers to the natural OSL signal present, and the B1-3 decays are the background corrected laboratory beta-induced OSL signals measured during the SAR procedure.

typically found in volcanic quartz. Similar to the samples measured in terrace and occupation deposits in Georgia, this type of volcanic quartz goes undetected using the standard filter combination and PMT tubes used for quartz dominated by UV/blue emissions. In a number of samples, residual feldspars were prevalent but were avoided using small-aliquots of 15-20 grains. The use of screening procedure was necessary to identify aliquots with sufficiently bright quartz OSL because of the general weak signals. The proportion of SBG aliquots with dominant fast decay components were limited to only a few aliquots in samples 1.3, 1.1, and 1.6.1 and most were dominated by a 'medium' decay. These signals are considered to be unstable and can result in an underestimation of D_e.

6.3.6 Dose recovery experiment

A large number of aliquots were tested to obtain a sufficient number of aliquots suitable for the dose recovery experiment with samples 1.3, 1.6.1, 2.1.1, 3.6.1 and 3.8. The results of the dose recovery for sample 1.3 were applied to sample 1.1, and those measured for sample 3.6.1 were applied to samples 1.8.2 and 3.3, respectively. The values of D_e and the D_e/D_a ratio using three preheat temperatures (180°C, 200°C and 220°C), and the recycling ratio (RR) are given in Table 6.20 and are plotted in Figs. 6.34 and 6.35.

Sample 1.3: The 180 and 220°C preheats provided the closest agreement with the expected value of 1, but significant scatter in the D_e/D_a ratio was found at 200°C. The average recycling ratios for the 180°C and 220°C were 1.07±0.03, and 1.02±0.08, suggest that either the 180°C or the 220°C preheats could be used with this sample.

Sample 1.6.1: Although the values of the D_e/D_a ratio was relatively close to 1

at all three preheat temperatures, the recycling ratios showed significant scatter with increasing preheat temperature, and the preferred preheat for this sample was 180°C, but also the 200°C preheat was also suitable.

Sample 2.1.1: All three preheat temperatures produced significant scatter in the D_e/D_a ratio values for all three temperatures, although it was slightly less using 180°C preheat. However, the D_e/D_a ratio values were systematically lower than the required value of 1, with the 180°C preheat being closest to the value (0.89±0.10). The average recycling ratios, revealed that the 220°C preheat showed the least scatter but exceeded the expected value of 1. The average recycling ratios for 180°C, 200°C and 220°C preheats were 1.20±0.20, 0.92±0.22 and 1.14±0.05, respectively. Hence, while the 180°C preheat was able to recover the dose it was at a compromise of relatively poor recycling. Despite this it was the chosen preheat temperature for this sample.

Sample 3.6.1 exhibited significant scatter in the values of the ratio D_e/D_a with increasing temperature. All preheat temperatures were able to recover the dose effectively. The average recycling ratio for 180°C, 200°C and 220°C was 0.96±0.05, 0.97±0.01 and 1.12±0.04, respectively. Of these preheats applied, the 200°C preheat was selected for SAR measurement.

Sample 3.8: The average values of D_e/D_a ratio obtained using the 180°C and 200°C preheats overlapped with the required value of 1, although the average recycling ratios for the preheat was less than 1 (0.87±0.04) it was selected as the preferred preheat temperature over the 200°C preheat because of the significant difference in D_e/D_a values obtained at this temperature.

6.3.7 D_e measurements: Acceptance criteria

A screening procedure was applied to identify aliquots that had a sufficient natural signal (>1 R_N). In order to obtain a statistically significant D_e dataset, (between 20 and 30), required the testing of a minimum of 150 aliquots. Table 6.21, provides a full summary of the aliquots that were accepted and rejected. The large number of aliquots rejected based on the presence of unstable signals, are those with D_e values that are dominated by 'slow' or 'medium-slow' decays, which were frequent in samples 2.1.1 and 3.8. As discussed in Sec. 5.5.2, these signals can lead to an underestimation of D_e. A significant number of aliquots were rejected for poor recycling (>30% of 1) in samples 1.1, 1.3, 1.6.1 and 3.8.

6.3.8 Accepted aliquots

The average recycling ratios for aliquots producing accepted D_e values are summarised in Table 6.22 and Figs. 6.36 and 6.37. Satisfactory behaviour for the SAR procedure was obtained in all but one sample (1.8.2). Due to the limited number of sufficiently

Sample	Applied dose (Gy)	Number of aliquots	Preheat (°C) 10 s	Recycling ratio (RR)	Ratio D_e/D_a	OD σ_i(%)
		4	220	0.86±0.07	0.99±0.03	3
413-1.3	4.67	6	200	1.02±0.08	1.16±0.16	16
		5	180	1.07±0.03	1.09±0.03	3
		3	220	1.28±0.39	0.95±0.10	10
413-1.6.1	4.52	4	200	1.19±0.13	0.95±0.09	9
		3	180	0.99±0.03	0.97±0.07	7
		3	220	1.14±0.05	0.72±0.39	39
413-2.1.1	4.52	3	200	0.92±0.22	0.82±0.32	32
		3	180	1.20±0.20	0.89±0.10	10
		3	220	0.96±0.05	1.02±0.05	5
413-3.6.1	2.35	3	200	0.97±0.01	0.92±0.02	2
		3	180	1.12±0.04	1.09±0.05	5
		4	220	1.24±0.14	1.14±0.07	7
413-3.8	4.53	5	200	0.98±0.06	1.09±0.20	20
		5	180	0.87±0.04	1.07±0.12	12

Table 6.20. Dose recovery results.

	Sample (413)								
	1.1	1.3	1.6.1	1.7.1	1.8.2	2.1.1	3.3	3.6.1	3.8
Overall summary:									
Aliquots tested	220	250	158	70	150	200	120	192	224
Average aliquot size (grains)	30	20	15	20	30	20	20	15	15
Aliquots for SAR measurement	29	41	47	11	10	54	13	32	56
Accepted D_e	19	25	34	3	7	27	8	17	17
Rejected aliquots:									
D_e uncertainity	6	1	5	5	3	0	5	0	6
Saturated	2	0	0	0	0	0	0	0	1
Recycling ratio	9	10	9	7	0	5	1	6	14
IR response	0	1	1	0	0	0	0	3	4
Unstable signals	3	6	6	3	0	13	0	2	11

Table 6.21. Summary of accepted and rejected aliquots.

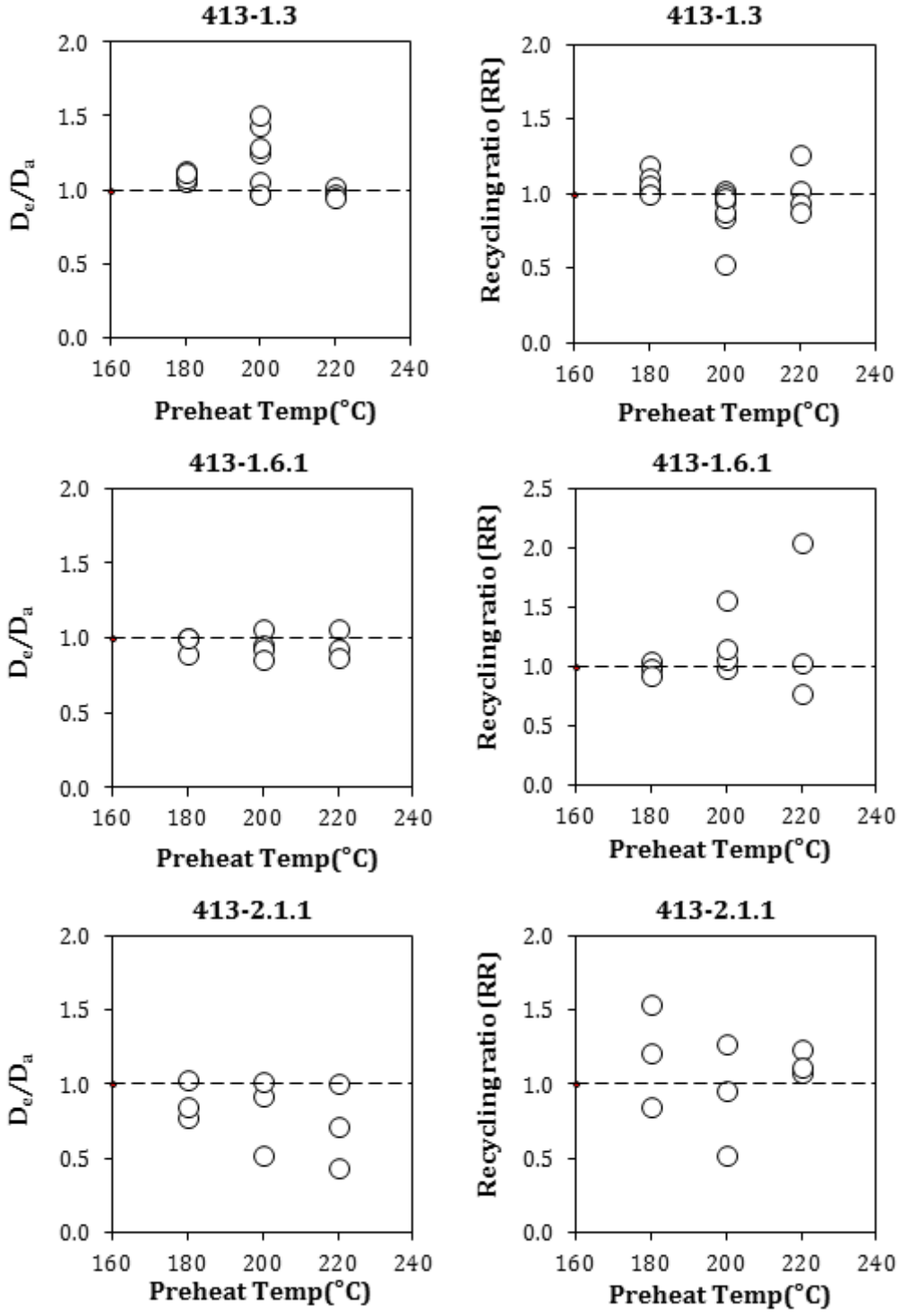

Figure 6.34. Dose recovery and recycling ratio scatter plots for samples 1.3, 1.6.1 and 2.1.1

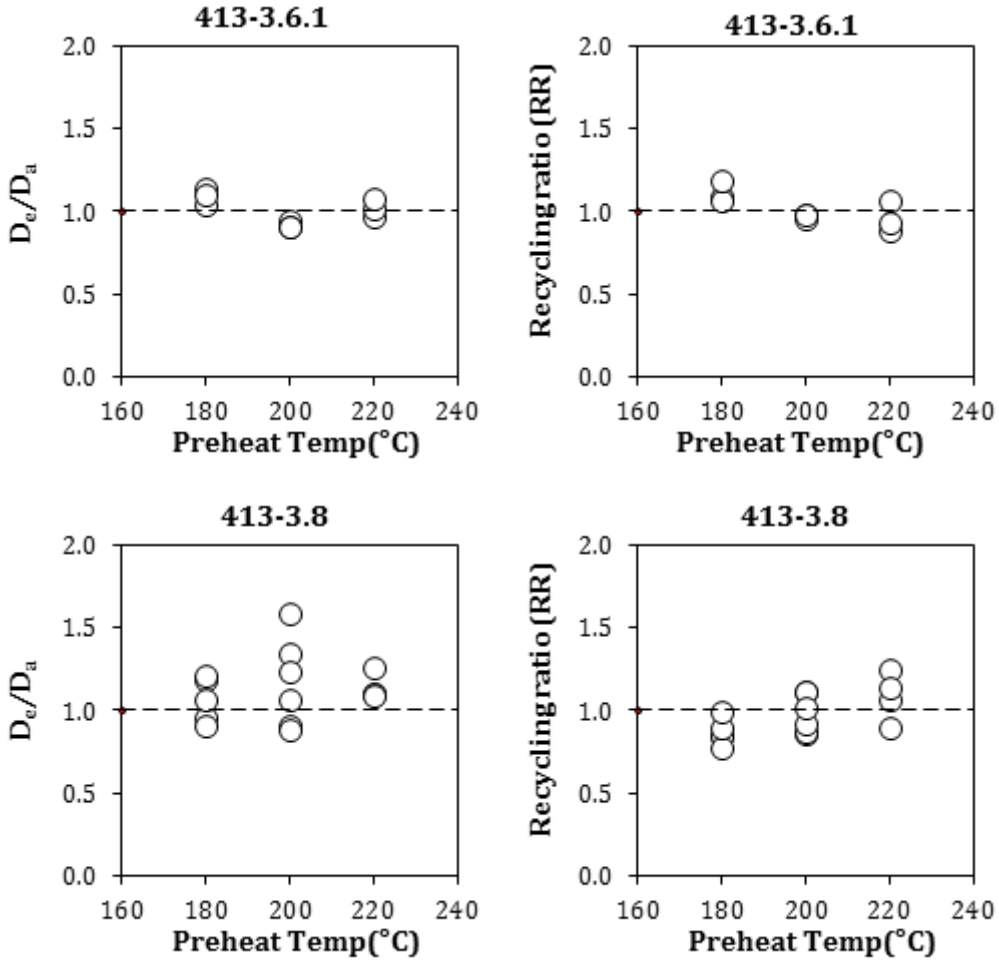

Figure 6.35. Dose recovery and recycling ratio scatter plots for samples 3.6.1 and 3.8

Sample	Recycling ratio	OD (%)
413-1.1	0.99±0.05	0
413-1.3	1.05±0.03	6.1
413-1.6.1	1.00±0.02	7.4
413-1.8.2	1.04±0.15	18
413-2.1.1	1.01±0.02	4.3
413-3.6.1	0.99±0.02	3.3
413-3.3	1.03±0.05	6.8
413-3.8	1.00±0.01	1.1

Table 6.22. Average recycling ratio and overdisperion of accepted D_e values.

bright quartz grains recovered from this sample, the margin of acceptable recycling was ±30%.

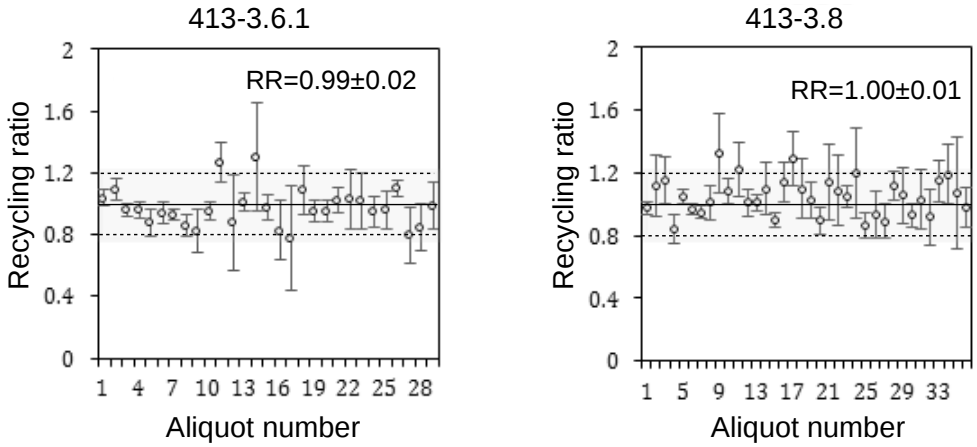

Figure 6.37. Plots of recycling ratios and standard errors for accepted D_e values, the preheat applied was 180°C. The solid black line indicates the expected value of 1, and the dashed lines indicate the ±20% rejection limit for this ratio.

6.3.9 D_e distributions

Each accepted D_e value was grouped according to grain count (Table 6.23), their values plotted separately for the SBG and MBG aliquots (2 to 4 bright grains), and the results presented as radial and KDE plots. Accepted D_e values and their uncertainties, including the aliquot type and the number of bright grains contributing to MBG aliquots, are provided at the end of this case study (see Tables 6.29, 6.30 and 6.31). Only MBG aliquots were obtained from sample 1.8.2 and only two SBG aliquots were obtained from sample 3.3, and were therefore grouped together as a combined (SBG and MBG)

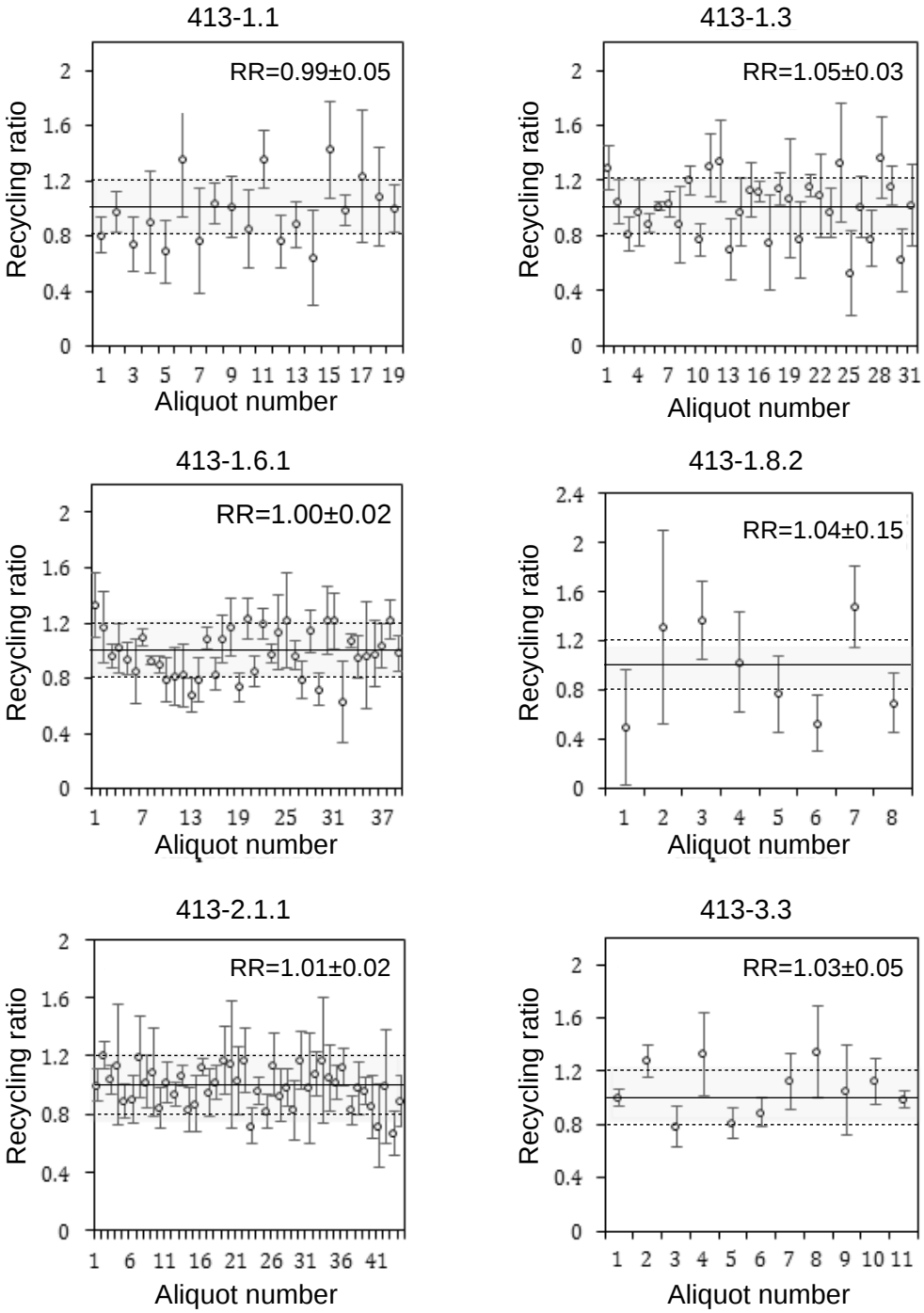

Figure 6.36. Plots of recycling ratios and standard errors for accepted D_e values, the preheat applied was 180°C. The solid black line indicates the expected value of 1, and the dashed lines indicate the ±20% rejection limit for this ratio.

dataset. The overdispersion (OD) was calculated using the CDM with samples where there was a sufficient number of SBG aliquots. Sample 1.6.1 had the largest number of SBG aliquots (n=18) where the luminescence signals meant that the detection of single bright drains was difficult to resolve using the small-aliquot approach, and hence the calculation of the OD is problematic. In such cases, the SBG and MBG D_e values were combined to obtain an estimate of the OD. A summary of the D_e distribution characteristics is provided in Table 6.24.

Where D_e datasets were based on relatively small proportion of SBG aliquots (samples 1.1, 1.3, 1.6.1, 2.1.1, 3.6.1 and 3.8), a test of significant difference (student t-Test) was applied to the SBG and MBG groups of D_e values calculated for the SBG and the MBG aliquots using the chosen models defined previously. In these cases, no significant difference was found between the two datasets and so the D_e values were combined to estimate the weighted mean value of D_e. As discussed in Sec. 6.1.11, σ_i values were folded into the original uncertainty values calculated using the Monte Carlo (MC) fitting procedure, to overcome issues related to averaging effects observed in multi-grain aliquots (Arnold *et al.* 2012).

Sample 1.3 was the most widely overdispersed (90%), followed by sample 3.6.1 (68%). Three samples, 1.1, 1.6.1 and 3.8 were overdispersed by 46%. Although no SBG aliquots were obtained from sample 1.8.2 and only a few from sample 3.3, significant overdispersion was observed in both samples, 72% (MBG aliquots) and 87% (Combined aliquots), respectively. Considering the large overdispersion and the calculated skewness values, which exceeded the critical value of 0, therefore that the minimum dose model was the most appropriate for the D_e distributions for each of these samples. The minimum dose population was thus considered to be the relatively well-bleached component, and this component was well-defined in the KDE plots for samples 1.6.1 and 3.6.1, but was difficult to define in samples 1.1, 1.3 and 3.8 (Figs. 6.38 to 6.41). The relatively few D_e measurements for 1.8.2 and 3.3 were not sufficient to make a detailed assessment of the D_e distributions, and these samples would benefit from more D_e measurements to reduce the uncertainty in the mean D_e value calculated using the MDM.

Although sample 2.1.1 had been expected to be partially bleached, on the basis of micromorphological thin section analysis, evidence for bioturbation and disturbance was found. The finalised dataset had a small overdispersion of 22% and the skewness values close to the critical value of 0 (-0.05) (Table 6.24). In this case the CDM was applied to the SBG and MBG D_e values.

6.3.10 Dose rate assessment

Table 6.42 provides the details of the specific activities of the lithogenic radionuclides (Bq kg^{-1}) and the isotopic ratios ^{210}Pb/^{226}Ra and ^{210}Pb/^{av}U measured for the OSL samples. An additional five samples (413-2.2, 2.6, 2.7, 3.5, and 3.9) were measured to

Sample	1BG	2BG	3BG	>3BG
413-1.1	7	4	2	6
413-1.3	8	3	6	8
413-1.6.1	18	4	4	7
413-1.7.1	0	1	1	9
413-1.8.2	0	1	0	6
413-2.1.1	9	3	10	5
413-3.3	2	0	1	5
413-3.6.1	9	4	2	2
413-3.8	8	2	10	7

Table 6.23. Aliquot OSL scanning result summary. 1BG = a single dominant bright grain, 2BG = two bright grains, 3BG = three bright grains, >3BG = more than three bright grains.

Sample	Aliquot type	n	CDM (Gy)	OD (%)	Skewness	t-test results*	
						T-value	P-value
413-1.1	SBG	7	16.48±2.96	46±08	0.67±0.93	0.99	0.34
	MBG	12	14.63±1.81	41±09	1.93±0.72		
	Combined	19	15.29±0.49	43±08	1.61±0.56		
413-1.3	SBG	8	10.61±3.44	90±23	0.12±0.87	1.40	0.17
	MBG	17	10.02±1.57	64±11	0.49±0.59		
	Combined	25	7.20±0.84	71±10	0.41±0.49		
413-1.6.1	SBG	18	4.00±0.45	46±08	2.64±0.58	1.18	0.24
	MBG	18	5.56±0.75	56±10	1.86±0.58		
	Combined	34	4.67±0.45	54±07	2.24±0.42		
413-1.8.2	MBG	7	6.87±1.93	71±20	1.11±0.93	-	-
13-2.1.1	SBG	9	3.65±0.28	22±06	-0.05±0.82	1.21	0.24
	MBG	18	4.12±0.27	26±05	0.68±0.58		
	Combined	27	3.93±0.21	26±04	0.64±0.47		
413-3.3	Combined	8	2.55±0.80	87±23	2.71±0.87	-	-
413-3.6.1	SBG	9	3.48±0.80	68±16	1.88±0.82	0.60	0.56
	MBG	8	3.17±0.45	39±10	1.71±0.87		
	Combined	17	3.29±0.44	54±10	1.84±0.59		
413-3.8	SBG	8	12.29±2.00	46±12	0.95±0.87	1.10	0.28
	MBG	20	10.18±1.14	49±08	0.96±0.55		
	Combined	28	10.79±1.01	49±07	1.37±0.46		

Table 6.24. D_e distribution characteristics. *95% confidence interval.

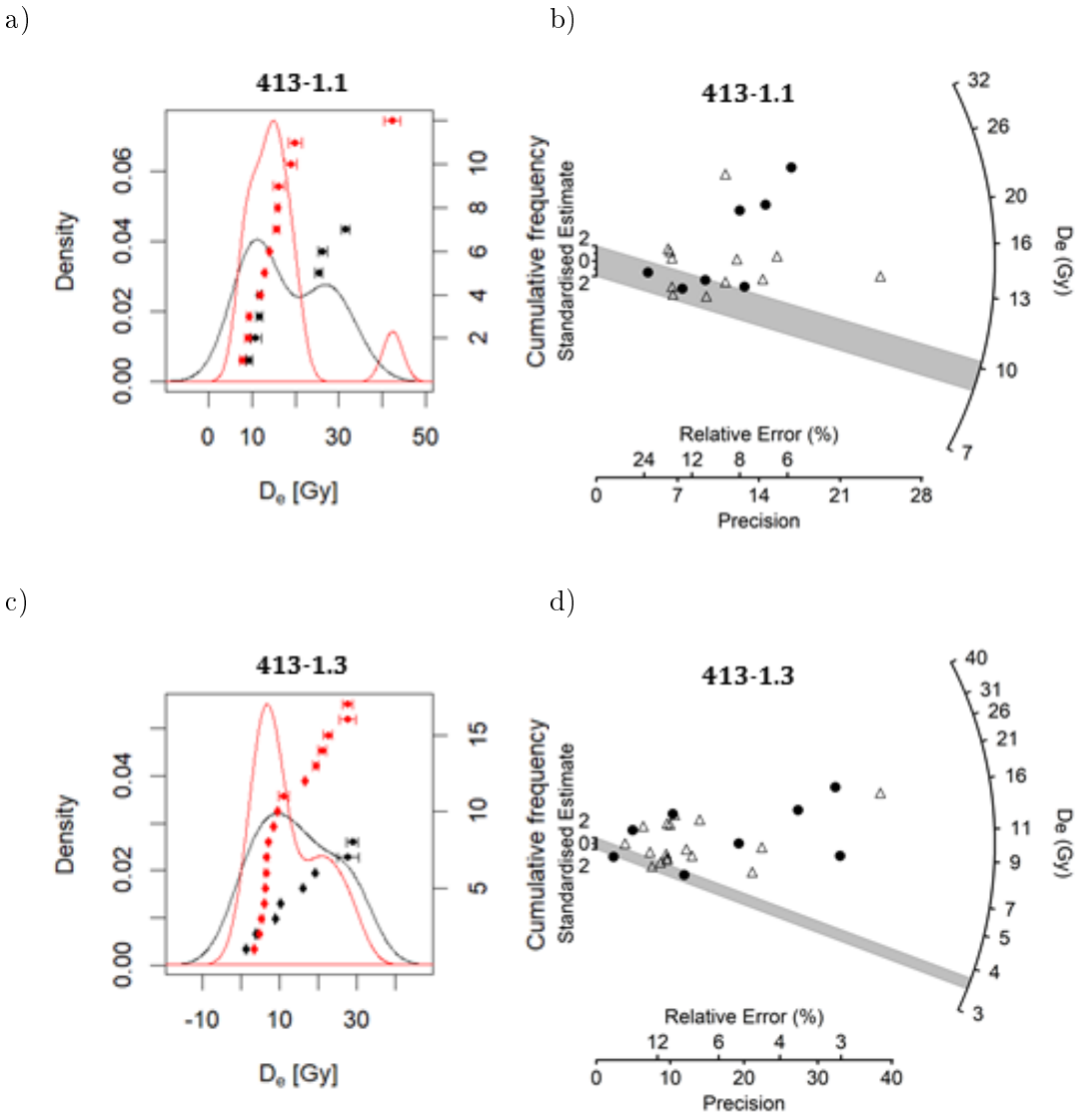

Figure 6.38. Samples 1.1, and 1.3. KDE plots of accepted D_e values (a and c). Black = SBG, Red = MBG, and radial plots of accepted D_e values (b and d). Closed circles = SBG, open triangles = MBG. The shaded regions indicate the D_e values (2σ uncertainty ranges) obtained when the MDM-3 was applied to SBG and MBG D_e values.The 'R Luminescence' package was used to run the models in R studio (version 1.0.136) (Kreutzer *et al.* 2012).

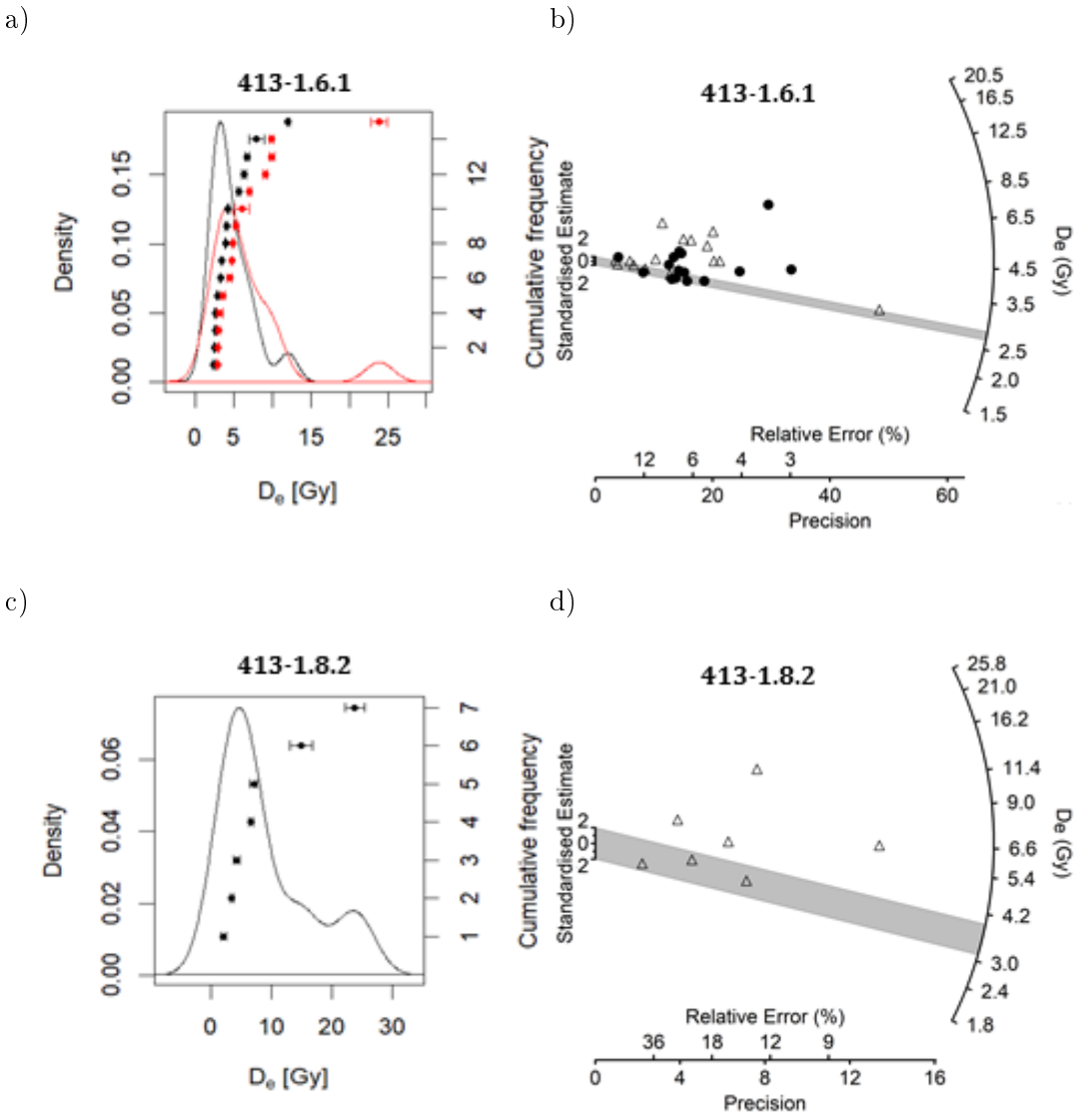

Figure 6.39. Samples 1.6.1 and 1.8.2. KDE plots of accepted D_e values (a and c). Black = SBG, Red = MBG, and radial plots of accepted D_e values (b and d). Closed circles = SBG, open triangles = MBG. The shaded regions indicate the D_e values (2σ uncertainty ranges) obtained when the MDM-3 was applied to SBG and MBG D_e values.The 'R Luminescence' package was used to run the models in R studio (version 1.0.136) (Kreutzer *et al.* 2012).

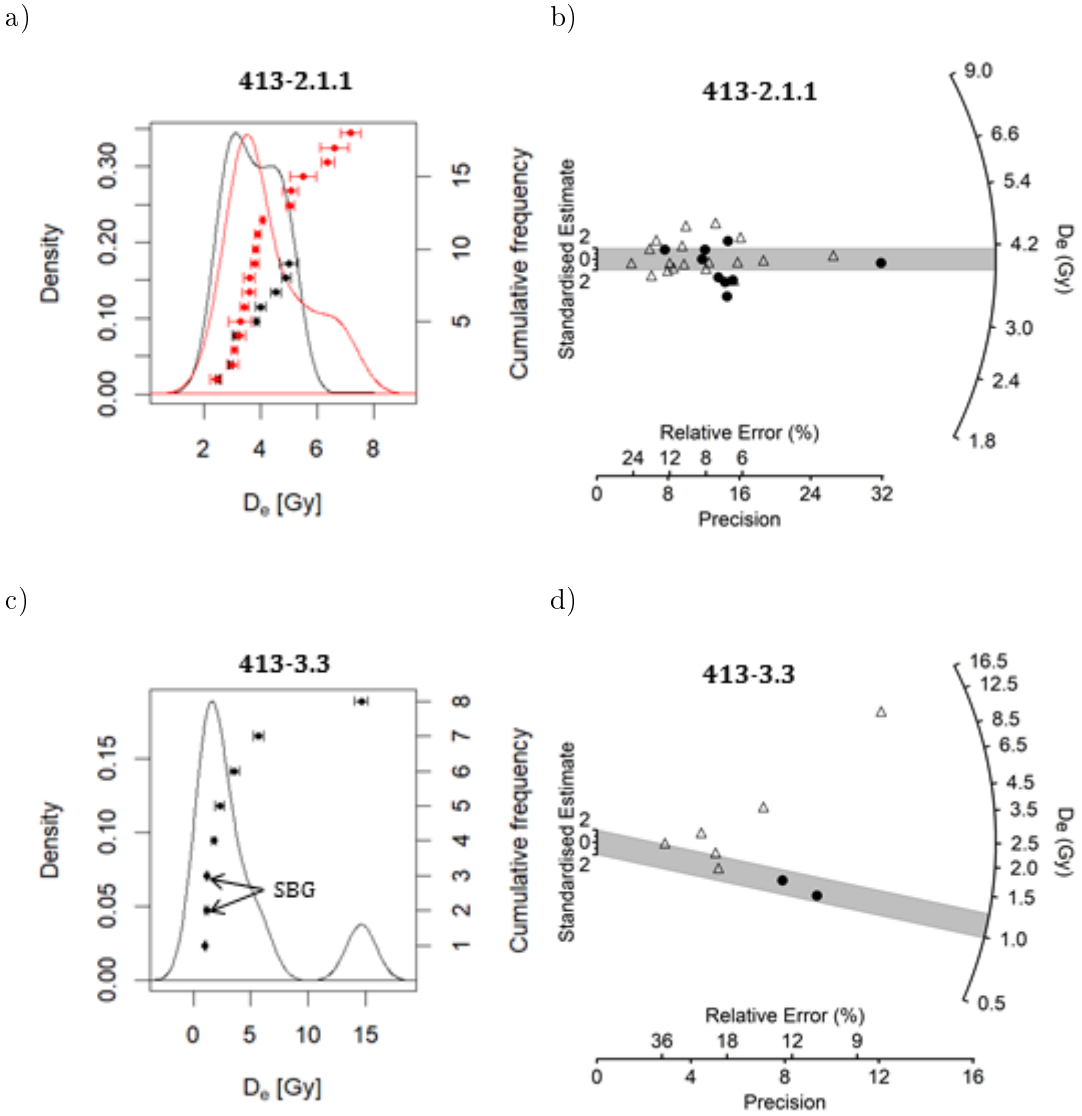

Figure 6.40. Samples 2.1.1 and 3.3. KDE plots of accepted D_e values (a and c). Black = SBG, Red = MBG, and radial plots of accepted D_e values (b and d). Closed circles = SBG, open triangles = MBG. The shaded regions indicate the D_e values (2σ uncertainty ranges) obtained when the MDM-3 was applied to SBG and MBG D_e values.

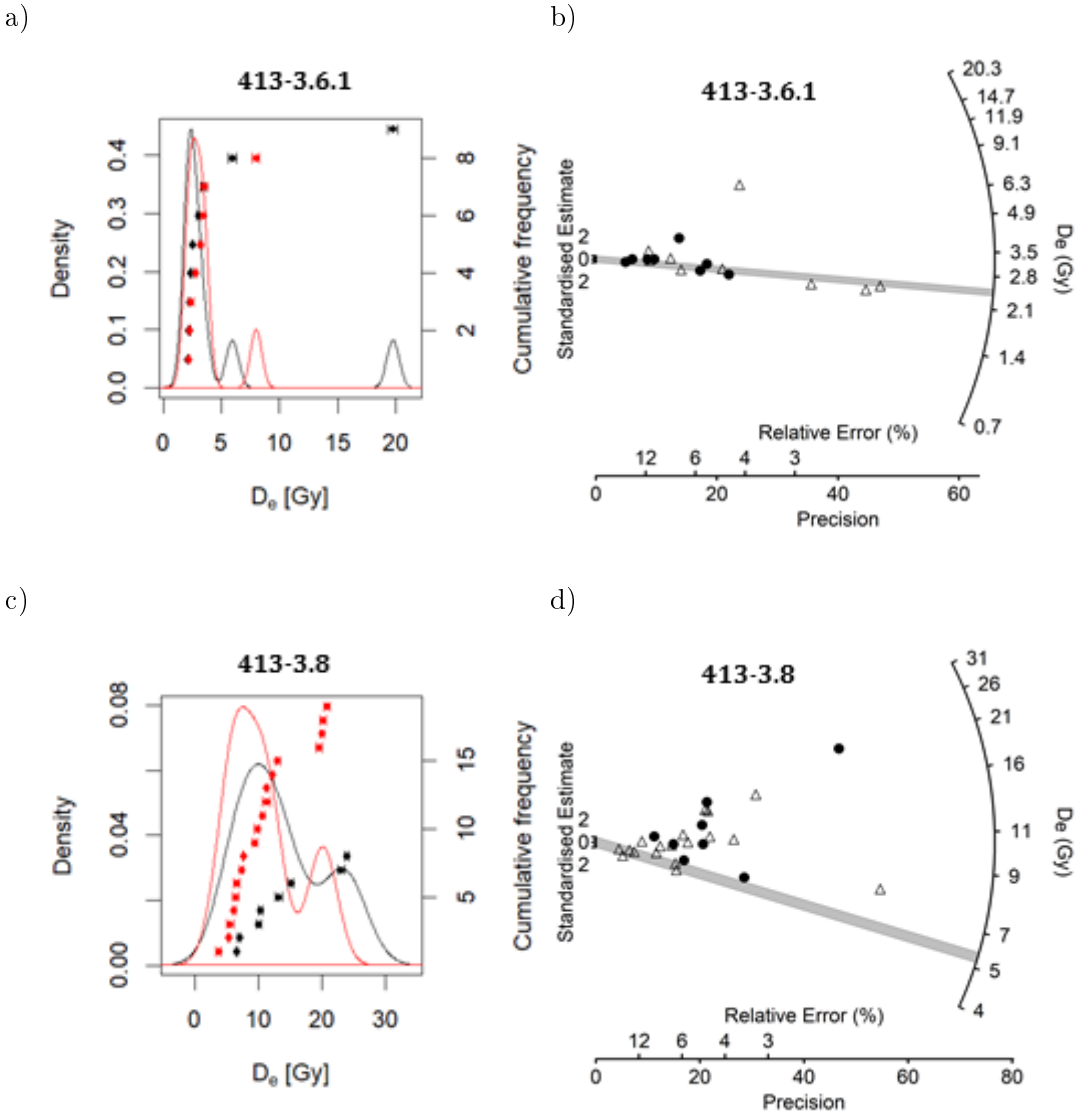

Figure 6.41. Samples 3.6.1 and 3.8. KDE plots of accepted D_e values (a and c). Black = SBG, Red = MBG, and radial plots of accepted D_e values (b and d). Closed circles = SBG, open triangles = MBG. The shaded regions indicate the D_e values (2σ uncertainty ranges) obtained when the MDM-3 was applied to SBG and MBG D_e values.

Sample	Isotope activities (Bq/kg^{-1}) ^{238}U	^{232}Th	^{40}K	Isotope ratios ^{210}Pb/^{av}U	^{210}Pb/^{226}Ra
413-1.1	32.4±1.9	37.5±3.4	456.5±7.7	0.80±0.1	0.80±0.1
413-1.3	36.7±1.9	31.3±3.1	548.5±7.9	0.80±0.1	0.80±0.1
413-1.6.1	35.3±1.8	30.1±3.0	488.5±7.4	0.76±0.1	0.78±0.1
413-1.8.2	33.7±4.8	32.3±3.0	466.9±7.3	1.00±0.1	0.99±0.2
413-2.1.1	37.2±5.4	39.9±3.4	629.3±8.8	0.93±0.1	0.88±0.2
413-3.3	25.4±4.6	26.6±2.9	436.1±7.0	1.08±0.2	0.96±0.2
413-3.6.1	40.1±5.0	34.9±3.1	522.4±7.7	0.77±0.1	0.75±0.1
413-3.8	35.1±5.0	36.8±3.1	560.6±8.0	0.96±0.1	0.91±0.2
413-2.2	30.0±4.8	30.8±3.0	531.3±7.7	1.17±0.2	1.01±0.2
413-2.6	29.9±4.7	28.1±2.9	428.7±7.0	0.81±0.1	0.82±0.2
413-2.7	33.5±5.0	35.8±3.1	577.1±8.0	0.93±0.1	0.86±0.2
413-3.5	31.7±4.8	30.2±3.0	502.5±7.6	0.94±0.1	0.86±0.2
413-3.9	36.5±4.9	34.4±3.1	560.5±7.9	0.91±0.1	0.84±0.1

Table 6.25. Summary of radioactive isotope activities and ratios measured as an infinite medium point absorber. Samples in bold were fully processed for OSL dating.

model the dose rate received above and below the OSL sample. The ratios of these activities enable an assessment of secular equilibrium within the ^{238}U/^{235}U and ^{232}Th decay series. In situations where disequilibria are pronounced (>50% difference in the ratios), greater uncertainty in the dose rate is introduced. Fig. 6.42 illustrates the variability observed in these ratios, where the green dashed line represents the conditions of secular equilibrium, and the effect of 20% and 50% of disequilibria is also indicated.

No significant disequilibria was observed in the samples measured as indicated by the uncertainties of ±0.2, the values are not significantly different. Sample 1.8.2 was within equilibria and originated from the old ground surface that had undergone no anthropogenic alterations. A slight increase (8 to 13%) in the ratios was found in two samples (3.3 and 2.2). Both samples originated from deposits that were formed by fluvial processes. A slight reduction (between 4 and 9%) in the ratios was observed in samples 2.1.1, 2.7, 3.5, 3.7 and 3.9. These originated from alluvial deposits and upcast deposits. The greatest reduction (19 to 22% in the ^{210}Pb/^{226}Ra and ^{210}Pb/^{av}U ratios was observed in samples 1.1, 1.3, 1.6.1, 2.6 and 3.6.1, which were deposited by anthropogenic processes and affected by post-depositional disturbance (e.g. bioturbation).

6.3.11 Observed secular equilibrium conditions

The specific activities of radionuclides within the ^{238}U decay chain, pre and post ^{220}Rn activities were examined. In samples 1.1, 1.6.1 and 3.6.1, which originated from the construction and upcast deposits, showed a decrease in activity at the end of the series

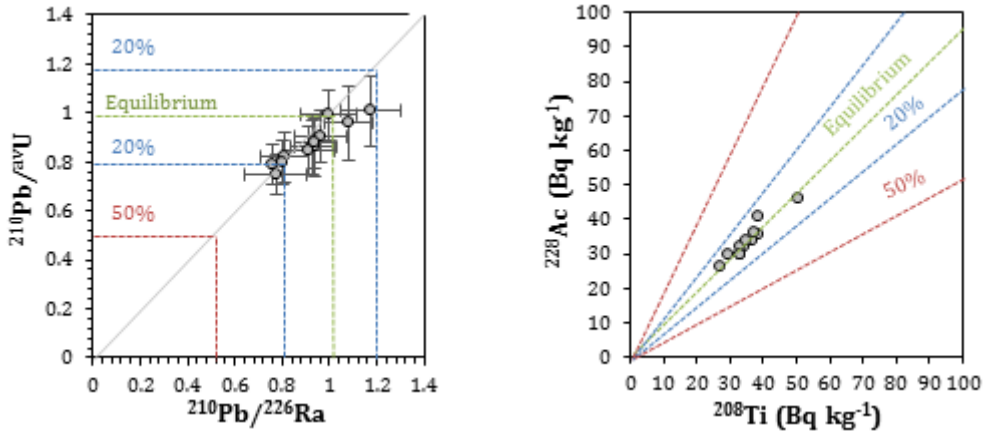

Figure 6.42. Assessment of secular disequilibria in occupation deposits. a) Plots of ^{210}Pb/^{av}U and ^{210}Pb/^{226}Ra ratios. b) Scatter plot of ^{228}Ac vs ^{208}Ti activities in the ^{232}Th series.

originated from the long-term loss in ^{214}Po. This had minimal effect on the dose rate in the samples measured, this loss was approximately 6 to 7% in the three samples. The ^{228}Ac/^{208}Ti activities measured in the ^{232}Th decay chain were in equilibrium (Fig. 6.42).

6.3.12 Beta dose rate

The measured values of the beta dose rate are provided in Table 6.26 specific activities determined with larger samples by gamma spectrometry were used to calculate the beta dose rate. A direct measurement of beta dose-rate was also performed using the βTLD technique. A discrepancy in the dry beta dose rate was found between the two methods (Fig. 6.43, Table 6.27), and this was evaluated using the following equation:

$$\dot{D}_\beta \, ratio = \frac{\dot{D}_\beta^\gamma}{\dot{D}_\beta^{\beta TLD}} \tag{6.2}$$

The difference of ±28 and ±23 was found between the two methods for samples 3.3 and 1.8.2, suggesting that beta-dose was relatively heterogeneous within these two samples. This was confirmed in the micromorphological assessment of the contexts sampled. The presence of calcium carbonate nodules, aggregates of marl, gypsum, Fe/Mn nodules and coatings, and feldspars were found, which have variable geochemical properties and can introduce beta-dose heterogeneity (Olley *et al.* 1997; Mayya *et al.* 2006; Nathan & Mauz 2008).

Sample	Depth BGL (m)	$\dot{D}_\beta$±s.e.* (mGy a^{-1})	$\dot{D}_\gamma$±s.e. (mGy a^{-1})	$\dot{D}_{cos}$±s.e. (mGy a^{-1})	$\dot{D}_{tot}$±s.e. (mGy a^{-1})
413-1.1	1.49	1.95±0.04	1.04±0.02	0.17±0.02	3.20±0.06
413-1.3	1.51	1.02±0.02	1.10±0.02	0.17±0.02	2.34±0.05
413-1.6.1	1.22	1.36±0.03	1.03±0.02	0.18±0.02	2.62±0.05
413-1.8.2	2.12	2.02±0.04	1.08±0.02	0.16±0.02	3.31±0.07
413-2.1.1	0.80	1.74±0.04	1.24±0.03	0.19±0.02	3.18±0.06
413-3.3	1.40	1.55±0.03	0.92±0.02	0.18±0.02	2.67±0.05
413-3.6.1	1.25	1.86±0.04	1.12±0.02	0.18±0.02	3.20±0.07
413-3.8	1.83	1.53±0.03	1.16±0.02	0.17±0.02	2.91±0.06

Table 6.26. Dose rate summary for the eight OSL samples that were successfully dated. * Attenuation factor applied: 0.913 (after Brennan 2003).

Sample	$\dot{D}_\beta$ ratios
413-1.1	0.89 ±0.02
413-1.3	0.90 ±0.01
413-1.6.1	1.13 ±0.01
413-1.8.2	0.77 ±0.03
413-2.1.1	1.12 ±0.01
413-3.3	1.28 ±0.01
413-3.6.1	0.87 ±0.01
413-3.8	1.06 ±0.01

Table 6.27. Ratios between the $\dot{D}_\beta$ values calculated using gamma spectrometry and βTLD.

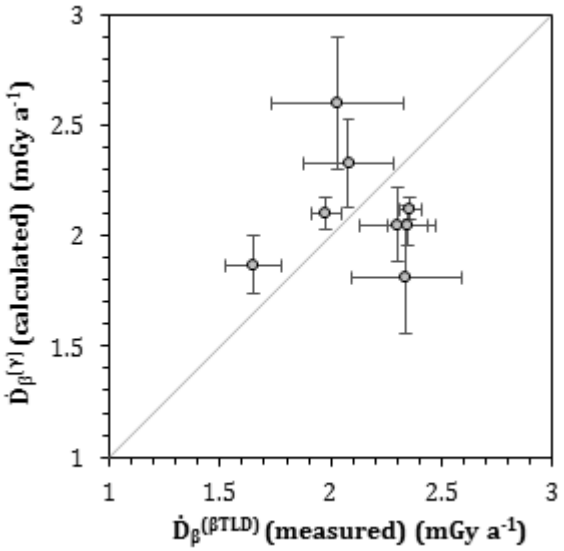

Figure 6.43. Plot of $\dot{D}_\beta$ values and uncertainties calculated using gamma spectrometry ($\dot{D}_\beta^{\gamma}$), and those directly measured using the βTLD technique ($\dot{D}_\beta^{\beta TLD}$).

6.3.13 Cosmic dose rate

The depth of samples below the modern ground level (BGL) measured in meters and the calculated cosmic dose rates are summarised in Table 6.26. The geographical position; 39°N 47°E and 80 km above sea level and average density of the sediment overburden (1.72 g cm^{-3}) was used to calculate the cosmic ray dose rate at each sample location (F, J and H values) following Prescott & Hutton (1995). The calculated cosmic dose rate formed a relatively small contribution to the overall total dose rate (6-8%) received by the grains.

6.3.14 Gamma dose rate

The section cut through the canal (Fig. 4.26) exposed a highly complex set of deposits. They appeared to be relatively similar in both texture, colour and sorting during field excavation, however the micromorphological analysis revealed that the microstructure varied between the different phases. The stratigraphic relationship between deposits also varied depending on the rate and direction of aggradation. The alluvial deposits, old ground surface and canal fills aggraded vertically, whereas the construction and clean-out upcast deposits aggraded laterally in a random manor. The upcast mounds were originally much larger and pronounced, but with time, they were truncated and

Sample	Burial age (before 2016)	OSL age* (BC/AD)	$\pm\sigma_a$	$\pm\sigma_b$
413-1.1	3013	-1000	426	454
413-1.3	1606	410	245	405
413-1.6.1	1015	1010	101	113
413-1.8.2	1094	920	159	169
413-2.1.1	1245	770	68	93
413-3.3	419	1600	75	79
413-3.6.1	767	1250	46	63
413-3.8	1972	50	217	245

Table 6.28. OSL age determinations for the canal deposits. σ_a = Type A; σ_b = Type B (after ISO 8601:2004). * rounded to the nearest 5 years.

disturbed, leaving only a small proportion of the original mound structure preserved 1m below the modern ground level. Due to the post-depositional alterations, the multilayer gamma dose rate model (Sec. 5.13) was applied to assess the influence of gamma dose rate contributions to each sample from contexts above and below or either side in laterally deposited sediments. Considering the variability in the microstructure, correction for the moisture content (%) measured for each sample was applied, which includes: 7% (samples 1.1, 1.3, 1.6.1), 9% (samples 1.8.2 and 2.1.1), 14% (sample 3.6.1), 15% (sample 3.8), and 16% (sample 3.3).

6.3.15 Age determinations

The OSL ages calculated using Eq. 5.1 (Sec. 5.3.2) are calendar years (BC/AD) before 2016 and each is provided with two error terms ($\pm\sigma_a$ and $\pm\sigma_b$) (Sec. 5.14) in Table 6.28.

413-1.1			413-1.3			413-1.6.1		
D_e(Gy)	±s.e. (1σ)	GC	D_e(Gy)	±s.e. (1σ)	GC	D_e(Gy)	±s.e. (1σ)	GC
9.37	1.26	SBG	1.34	0.55	SBG	2.35	0.29	SBG
10.83	2.41	SBG	3.87	0.32	SBG	2.43	0.18	SBG
11.66	1.24	SBG	8.90	0.27	SBG	2.57	0.16	SBG
11.74	0.92	SBG	10.39	0.54	SBG	2.58	0.19	SBG
23.01	1.08	SBG	15.96	0.58	SBG	2.83	0.15	SBG
23.88	0.51	SBG	19.27	0.60	SBG	3.24	0.21	SBG
25.42	1.74	SBG	27.74	5.53	SBG	3.45	0.24	SBG
26.24	2.12	SBG	28.88	2.77	SBG	3.89	0.16	SBG
31.65	1.88	SBG	3.39	0.45	MBG(3)	4.03	0.32	SBG
7.81	1.18	MBG(5)	4.63	0.53	MBG(4)	4.22	0.13	SBG
9.16	1.40	MBG(6)	5.38	0.56	MBG(4)	5.61	0.42	SBG
9.29	0.98	MBG(2)	6.00	0.62	MBG(3)	6.31	0.43	SBG
11.83	1.06	MBG(2)	6.22	0.29	MBG(2)	6.71	0.46	SBG
12.96	0.90	MBG(3)	6.50	0.90	MBG(6)	7.94	1.30	SBG
14.05	0.57	MBG(3)	6.68	0.70	MBG(3)	12.03	0.41	SBG
15.66	1.29	MBG(4)	7.22	0.56	MBG(3)	2.83	0.22	MBG(4)
15.95	1.02	MBG(2)	8.45	0.69	MBG(3)	2.93	0.06	MBG(3)
16.22	2.48	MBG(2)	9.54	0.43	MBG(5)	2.99	0.35	MBG(2)
18.92	2.97	MBG(4)	11.06	2.81	MBG(2)	3.14	0.83	MBG(2)
19.97	3.23	MBG(5)	16.65	0.43	MBG(4)	3.51	0.54	MBG(5)
42.38	3.80	MBG(6)	19.38	1.39	MBG(5)	4.43	0.74	MBG(7)
			21.03	2.10	MBG(4)	4.75	0.22	MBG(4)
			22.52	2.35	MBG(3)	4.81	0.24	MBG(3)
			27.59	4.34	MBG(2)	5.32	0.51	MBG(3)
			27.73	2.59	MBG(6)	6.05	1.76	MBG(6)
						7.03	0.37	MBG(3)
						9.06	0.55	MBG(6)
						9.90	0.66	MBG(2)
						9.91	0.49	MBG(5)
						23.90	2.09	MBG(2)

Table 6.29. Accepted D_e values with uncertainties and grain count (GC) for samples 413-1.1, 413-1.3 and 413-1.6.1. SBG: Single bright grain aliquots; MBG: multiple bright grain aliquots. The number of bright grains is indicated in brackets.

413-1.8.2			413-2.1.1			413-3.3		
D_e(Gy)	±s.e. (1σ)	GC	D_e(Gy)	±s.e. (1σ)	GC	D_e(Gy)	±s.e. (1σ)	GC
2.19	0.96	MBG(5)	2.51	0.17	SBG	1.02	0.11	SBG
3.50	0.49	MBG(2)	2.95	0.21	SBG	1.17	0.15	SBG
4.29	0.94	MBG(5)	3.07	0.20	SBG	1.15	0.22	MBG(4)
6.69	0.51	MBG(6)	3.10	0.23	SBG	1.82	0.36	MBG(5)
7.14	1.14	MBG(7)	3.87	0.12	SBG	2.30	0.79	MBG(5)
14.99	3.85	MBG(5)	4.00	0.34	SBG	3.60	0.81	MBG(3)
23.86	3.13	MBG(5)	4.34	0.64	SBG	5.68	0.80	MBG(4)
			4.54	0.37	SBG	14.64	1.21	MBG(5)
			4.91	0.33	SBG			
			5.00	0.65	SBG			
			2.43	0.39	MBG(5)			
			3.02	0.38	MBG(3)			
			3.09	0.20	MBG(3)			
			3.27	0.38	MBG(4)			
			3.28	0.83	MBG(3)			
			3.44	0.28	MBG(2)			
			3.60	0.44	MBG(5)			
			3.60	0.37	MBG(3)			
			3.79	0.30	MBG(5)			
			3.83	0.24	MBG(3)			
			3.91	0.21	MBG(3)			
			4.07	0.15	MBG(3)			
			5.04	0.31	MBG(3)			
			5.07	0.53	MBG(3)			
			5.51	0.93	MBG(2)			
			6.38	0.48	MBG(4)			
			6.61	0.99	MBG(2)			
			7.19	0.72	MBG(3)			

Table 6.30. Accepted D_e values with uncertainties and grain count (GC) for samples 413-1.8.2, 413-2.1.1 and 413-3.3. SBG: Single bright grain aliquots; MBG: multiple bright grain aliquots. The number of bright grains is indicated in brackets.

413-3.6.1			413-3.8		
D_e(Gy)	±s.e. (1σ)	GC	D_e(Gy)	±s.e. (1σ)	GC
2.13	0.15	SBG	6.55	0.23	SBG
2.19	0.06	SBG	6.97	0.41	SBG
2.23	0.05	SBG	10.07	0.67	SBG
2.37	0.05	SBG	10.31	0.50	SBG
2.51	0.12	SBG	13.18	1.16	SBG
3.02	0.34	SBG	15.08	0.73	SBG
3.47	0.28	SBG	23.01	1.08	SBG
5.94	0.68	SBG	23.88	0.51	SBG
19.74	0.83	SBG	3.72	0.70	MBG(5)
2.20	0.10	MBG(2)	5.28	0.34	MBG(2)
2.25	0.13	MBG(3)	5.56	1.22	MBG(6)
2.37	0.47	MBG(2)	6.17	0.40	MBG(3)
2.77	0.15	MBG(3)	6.40	0.86	MBG(4)
3.18	0.33	MBG(2)	6.62	1.00	MBG(3)
3.43	0.40	MBG(2)	7.35	0.63	MBG(2)
3.54	0.59	MBG(4)	7.64	0.14	MBG(3)
7.98	0.58	MBG(5)	9.44	0.76	MBG(3)
			9.78	0.67	MBG(5)
			10.63	0.60	MBG(3)
			11.25	1.27	MBG(6)
			11.30	0.43	MBG(3)
			12.14	0.55	MBG(3)
			12.99	0.77	MBG(3)
			19.50	0.90	MBG(4)
			20.03	0.65	MBG(5)
			20.15	0.96	MBG(3)
			20.81	0.98	MBG(3)

Table 6.31. Accepted D_e values with uncertainties and grain count (GC) for samples 413-3.6.1 and 413-3.8. SBG: Single bright grain aliquots; MBG: multiple bright grain aliquots. The number of bright grains is indicated in brackets.

6.4 Case study 4: Luminescence dating applied to surface channels (Batinah Coast, Oman)

6.4.1 Luminescence characteristics

This section provides the OSL dating results applied to surface channels located near a Sasanian/Early Islamic fortification on the Batinah Coast, Oman. The location of samples obtained from Trench I and O is illustrated in Figs. 4.40 and 4.44, respectively.

The natural deposits were carbonate-rich and contained frequent mollusc inclusions. Frequent inclusions of ophiolite pebbles were also found in the channel sediments, suggesting that they were transported to the area by active wadis from the Oman Mountains. This was also supported by high-resolution CL and SEM examination revealed that quartz grains were from volcanic, plutonic, metamorphic and hydrothermal sources (Table 3.2, Sec. 3.6.2). Some of the samples were tested, had poor quartz yields, and the OSL analysis was focused on samples recovered from Trench I and O, which produced bright luminescence signals from quartz. Considering the abundance of quartz in the samples used in the OSL analysis, a small proportion of the quartz had ideal luminescence characteristics, suggesting that the grains had been eroded from distant sources and were transported by aeolian processes and deposited within the channel (Sec. 4.4.5). Five OSL samples were fully processed from this site: 426-2.2 (referred to in text as 2.2) and 426-2.4 (2.4) from Trench O, and samples 426-3.2 (3.2), 426-3.6 (3.6) and 426-3.8 (3.8) from Trench I.

6.4.2 OSL signal analysis

The OSL characteristics, which includes the signal-to-background ratios (R_N) and the fast-ratio (FR), from samples with quartz with sufficiently strong luminesce signals are presented in Figs. 6.44 and 6.45. The FR values for sample 2.2 showed a broad spread (1 - 60) with four aliquots with FR values greater than 20. Sample 2.4 displayed a negative skewness, with 50% of the SBG aliquots having FR values greater than 20; the MBG aliquots (38%) had a similar range of FR values. For sample 3.2, the SBG and MBG aliquots displayed a bimodal distribution of FR values, with 31% between a FR range 4 - 5, and 31% greater than 20. Sample 3.6 produced a high proportion of SBG aliquots with FR values between 0 to 4 (71%), and some MBG aliquots had high FR values (10 - 19). A broad spread in FR values was obtained for the SBG aliquots from sample 3.8, ranging in value from 2 to 20. Overall, the signals measured with SBG aliquots, indicate that most of the quartz is dominated by a 'fast' decaying signal, and only sample 3.6 produced OSL signals that were dominated by a 'medium-fast' signal. The R_N ratios obtained with the SBG and MBG aliquots for sample 2.2 showed a broad

range (0.1 to 28) of R_N values, with 75% concentrated between 0.1 and 6 R_N. Similarly, a broad range of R_N values were found in sample 2.4, ranging from 0 to 26 R_N, with 56% of the SBG and MBG aliquots concentrated between 0.1 to 6 R_N. For the second channel sampled, sample 3.2 showed similar R_N distributions for both the SBG and MBG aliquots. For the SBG aliquots, 23% were in the 0.1 to 2 R_N range, and 54% were within the range of 3 to 4. Most R_N ratios for the SBG aliquots from sample 2.4 were concentrated between the range of 0 and 8 R_N, with over half (52%) in the lowest range 0.1 to 2 R_N, and occasional in the slightly higher R_N ranges. For sample 3.8, a broad range of R_N ratios (0.1 to 8 R_N) were found, and 50% were concentrated in the 2 to 4 R_N range. Only one SBG aliquot was in the higher R_N range (21 to 22). Most R_N values of single-bright grains were concentrated between 0.1 to 8 ranges, suggesting that the aliquots were dominated by bright luminescence signals.

6.4.3 Sensitivity change

Two samples were obtained from fired materials used to line the channels, sample 2.2, was effectively fired and therefore quartz had been sensitised. Sample 3.2 contained a number of grains with variable sensitisation, from a strong increase after repeated beta irradiation cycles (Fig 6.46; a), and those that showed only a slight increase in sensitivity (Fig. 6.46; c). Most quartz grains from this site showed increased sensitisation during the SAR procedure (Fig. 6.46; b). Overall, no unstable signal (e.g. slow decaying signals) were found in the aliquots measured, implying that the quartz from these deposits had ideal characteristics for the procedure outlined in Sec. 5.6.1, Table 5.4, and that the signal was dominated by a fast decay component (Fig. 6.47).

6.4.4 Dose recovery experiment

A summary of the results of the dose recovery experiments applied to the five samples is given in Table 6.32. The ratio of the evaluated equivalent dose (D_e) to the known applied beta dose (D_a) is expected to be 1. The values of the ratio (D_e/D_a) using three preheat temperatures (180, 200 and 220°C), together with the values of recycling ratio, are given in Table 6.32 and plotted in Figs. 6.48 and 6.49.

All three preheat measurements for sample 2.2, 180, 200 and 220°C, produced D_e/D_a recovered dose ratio values close to 1, 1.04±0.03, 1.08±0.04, and 1.02±0.10, respectively. Preheat temperatures of 200 and 220°C were considered to be the most suitable for this sample. For sample 2.4, the D_e/D_a ratios for 180°C and 220°C preheats were closest to 1, however, the recycling ratio for 200°C was closest to 1 (0.98±0.04), and moderate scatter was found in the other temperatures applied. For this sample, all three preheat temperatures were deemed to be appropriate for this sample, however the 200°C preheat was able to recover the signal and correct for sensitivity change more effectively.

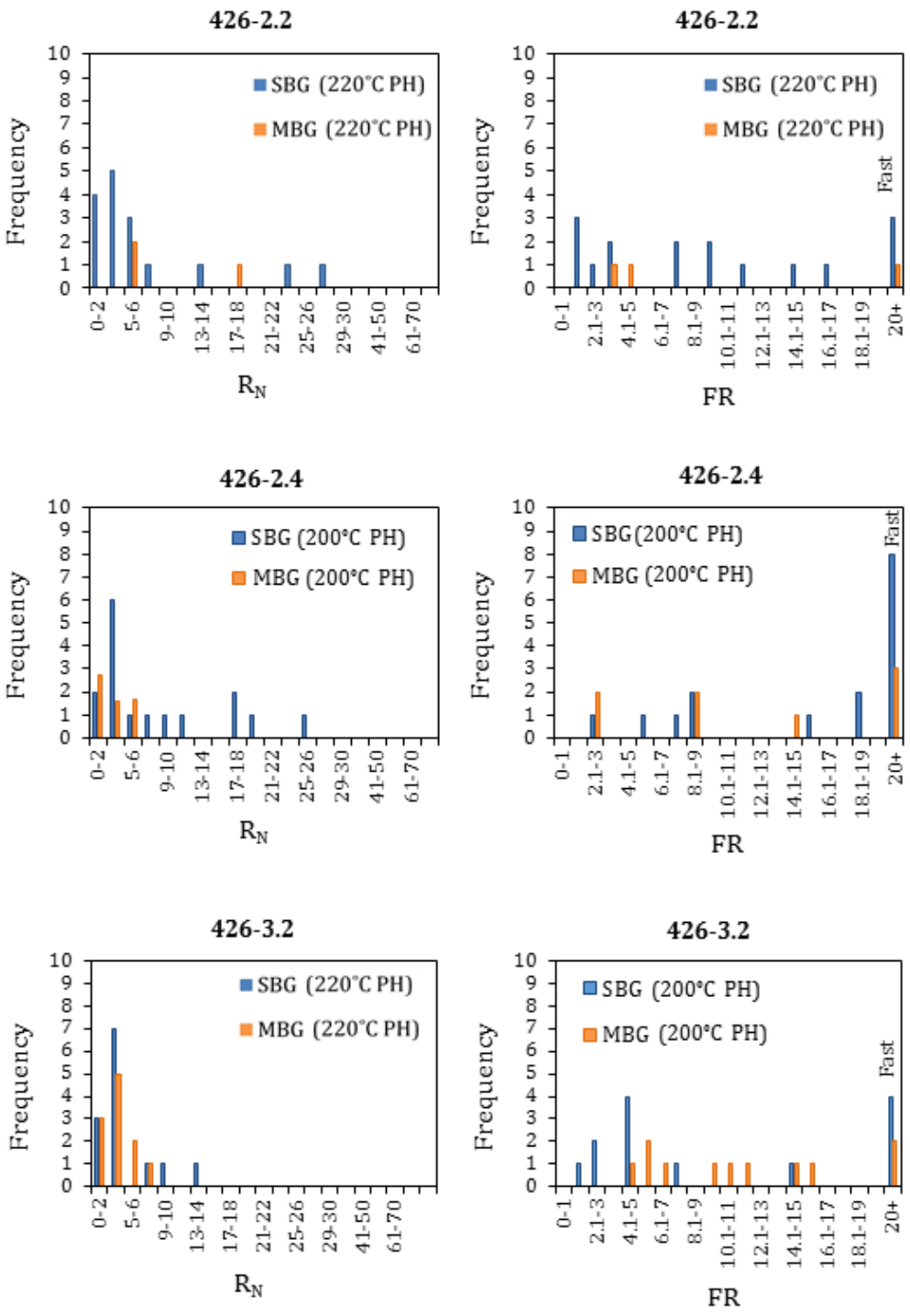

Figure 6.44. Histograms to show the distributions of SBG and MBG aliquot R_N and FR ratios for samples 426-2.2 (n = 19), 426-2.4 (n = 18) and 426-3.2 (n = 24).

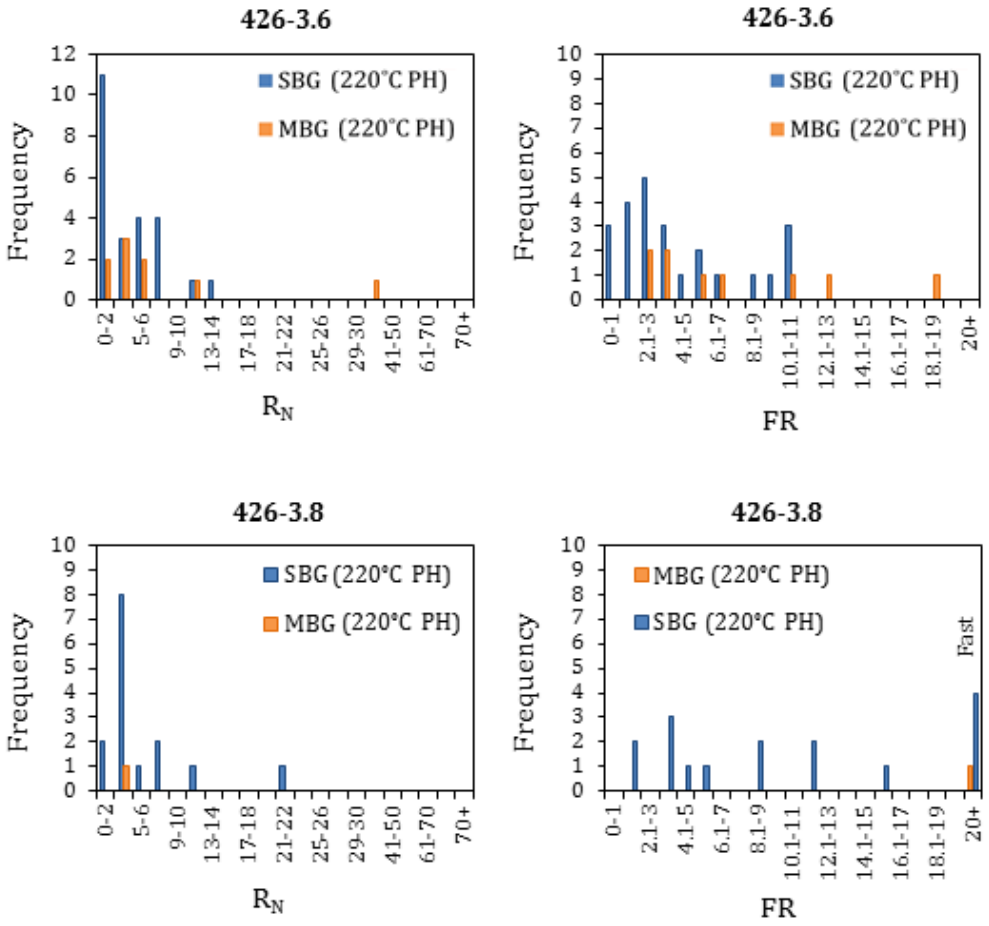

Figure 6.45. Histograms to show the distributions of SBG and MBG aliquot R_N and FR ratios for samples 426-3.6 (n = 33) and 426-3.8 (n = 16).

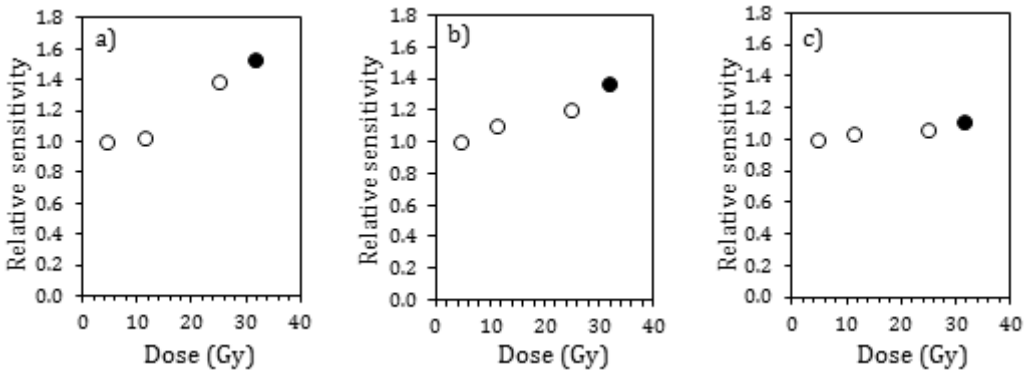

Figure 6.46. Sensitivity changes observed in three different samples during the SAR procedure. a) Increase in sensitivity in fired material (sample 2.2). b) Increase in sensitivity in non-fired sediments (sample 3.2). c) Slight sensitivity change in a grain from sample 3.2.

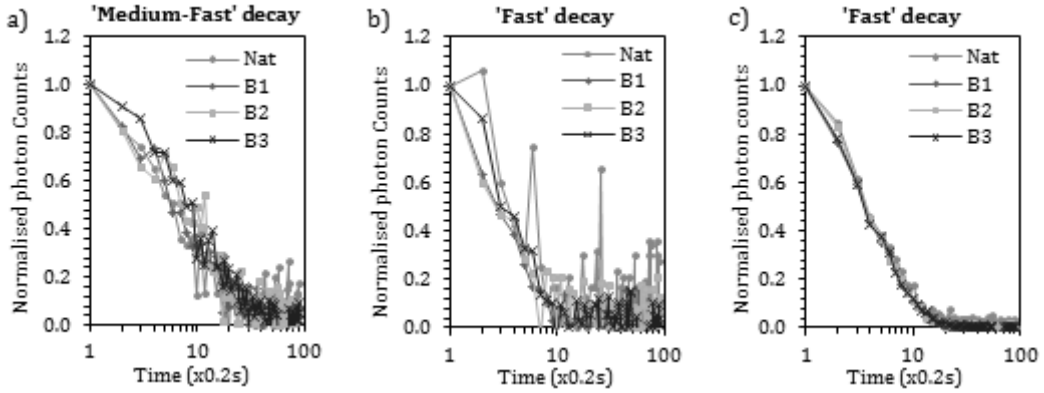

Figure 6.47. Fast decay curves observed in SBG aliquots. a) 'Medium-fast' decay. b) 'Fast' decay with statistical fluctuation observed in the natural signal. c) 'Fast' decay with aliquots producing stronger OSL emissions of the natural signal or between beta irradiation cycles.

Sample	Applied dose (Gy)	Number of aliquots	Preheat (°C) 10 s	Recycling ratio (RR)	Ratio D_e/D_a	OD σ_i(%)
		4	220	1.04 ±0.03	0.99±0.03	3
426-2.2	4.51	5	200	1.08 ±0.05	1.05±0.08	8
		3	180	1.02 ±0.10	1.18±0.10	10
		3	220	1.10 ±0.07	0.96±0.03	5
426-2.4	4.51	3	200	0.98 ±0.04	1.18±0.16	16
		3	180	1.05 ±0.03	1.02±0.05	5
		3	220	0.99 ±0.10	1.02±0.05	5
426-3.2	4.56	3	200	1.10 ±0.04	0.92±0.02	2
		3	180	1.08 ±0.05	1.09±0.05	5
		3	220	1.02 ±0.04	1.01±0.09	9
426-3.6	4.56	3	200	1.03 ±0.01	1.02±0.06	6
		6	180	0.99 ±0.04	1.02±0.09	9
		4	220	1.06 ±0.05	1.14±0.07	7
426-3.8	4.53	5	200	1.01 ±0.06	1.09±0.20	20
		5	180	0.99 ±0.07	1.07±0.12	12

Table 6.32. Dose recovery results.

Sample 3.2 showed good dose recovery for all three preheat temperatures applied. The recycling ratio for D_a showed a slight overestimation at both 180°C and 200°C preheat temperatures (1.08±0.05, and 1.10±0.04), and an underestimation at 220°C in nearly all aliquots was found except in one measured aliquot, the average recycling ratio was 0.99±0.10. For this sample, the 200°C was selected. The D_e/D_a ratio for sample 3.6 revealed that the SAR procedure was successful at recovering the dose using all three preheat temperatures. The recycling ratios for all preheats were close to 1, 1.02±0.04 (180°C), 1.03±0.01 (200°C), and 1.03±0.01 (220°C). Based on these observations, all three preheats were considered appropriate, but the 220°C was selected as less scatter was observed in D_a. The three preheats for sample 3.8, had recovered dose ratios close to 1, 1.10±0.12 (180°C), 0.99±0.08 (200°C), and 1.06±0.11 (220°C). The 180°C showed a slight overestimation of D_a and some scatter was observed in the recycling ratios (1.01±0.06). Either the 200 or 220°C preheats were considered to be the most suitable for this sample.

6.4.5 D_e measurements: Acceptance criteria

Table 6.33 provides a summary of the outcomes of testing aliquots with which accepted and rejected values of D_e were obtained. The natural signal intensity of 50 to 160 aliquots from the samples collected from the two channels were tested. Of the aliquots

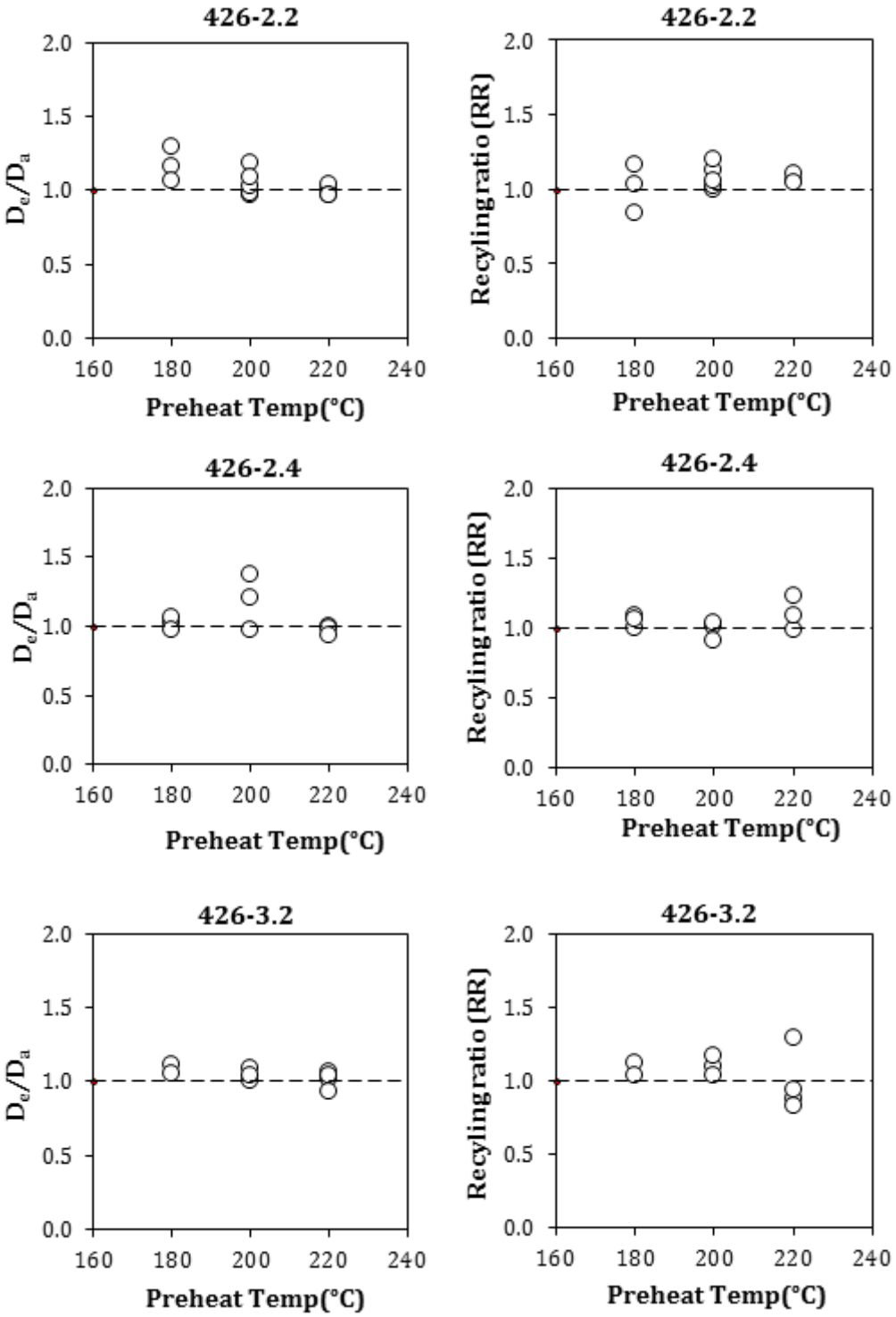

Figure 6.48. Plots of D_e/D_a and RR obtained from the dose recovery experiments for samples 2.2, 2.4 and 3.2.

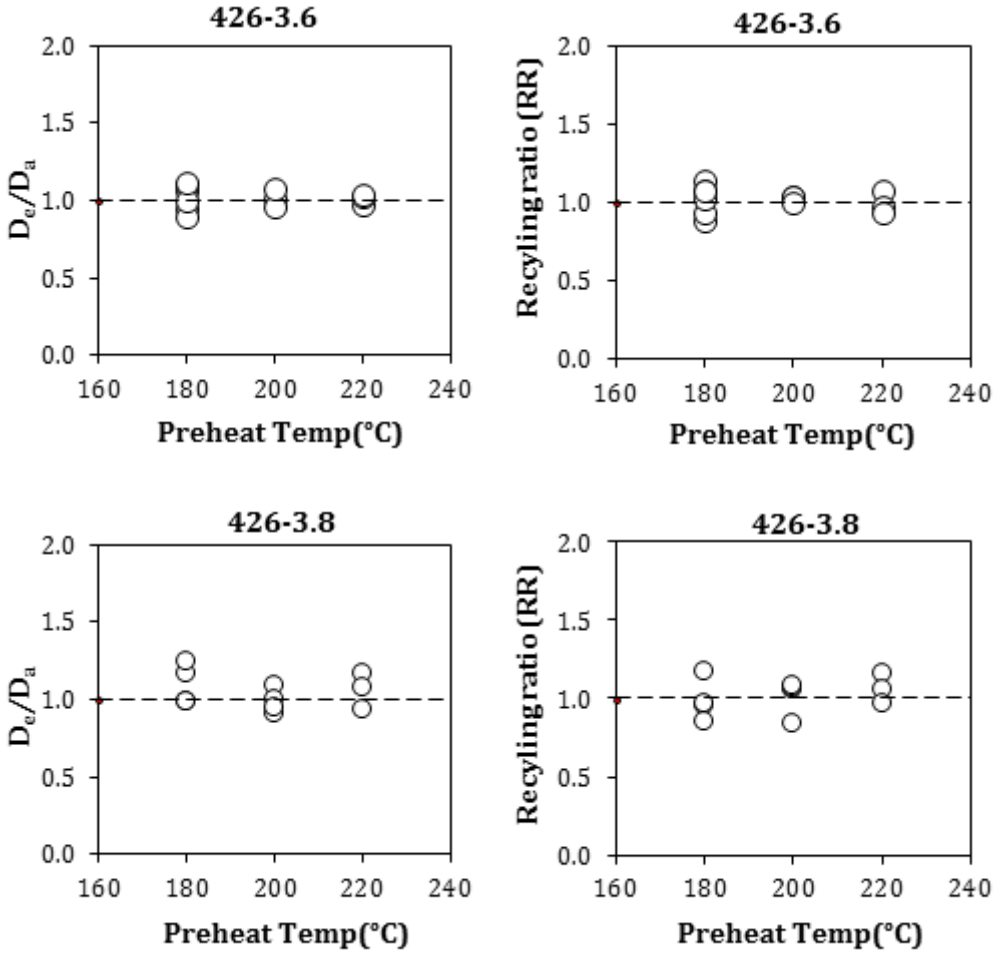

Figure 6.49. Plots of D_e/D_a and RR obtained from the dose recovery experiments for samples 3.6 and 3.8.

	Sample				
	426-2.2	426-2.4	426-3.2	426-3.6	426-3.8
Overall summary:					
Aliquots tested	50	120	90	130	160
Average aliquot size (grains)	15	15	15	20	20
Aliquots for SAR measurement	19	18	24	33	16
Accepted D_e	14	11	11	16	11
Rejected aliquots:					
D_e uncertainity	3	6	8	14	0
Saturated	0	0	0	0	1
Recycling ratio	0	1	1	5	1
IR response	0	0	0	0	0
Unstable signals	0	0	0	0	0

Table 6.33. SAR summary.

Sample	1BG	2BG	3BG	>3BG
426-2.2	11	1	2	0
426-2.4	11	9	2	1
426-3.2	5	1	1	5
426-3.6	10	2	1	3
426-3.8	11	0	0	0

Table 6.34. Aliquot OSL scanning result summary of samples from site 426. 1BG = a single dominant bright grain, 2BG = two bright grains, 3BG = three bright grains, >3BG = more than three bright grains.

with sufficiently bright quartz signals, 84% of aliquots measured from sample 2.2 were accepted, 61% from sample 2.4, 63% from sample 3.2, 55% from sample 3.6 and 81% from sample 3.8. The main cause for rejection was D_e uncertainty, and contained only a small yield of individual bright grains (Sec. 6.4.2), and had very poor recycling ratios, however no aliquots contained residual feldspars and most aliquots were dominated by stable quartz signals. The OSL scanning results of the accepted aliquots revealed that bright grains were easily detected using the procedure outlined in Sec. 5.4.7 (Fig. 6.50). A full summary of the grain-counts is provided in Table 6.34.

6.4.6 Accepted aliquots

The average recycling ratio for each sample is provided in Table 6.35, together with the individual recycling ratios, which are plotted in Fig. 6.51. The average value of RR are in agreement with unity, with overdispersions ranging from 0 to 4.6%. Hence quartz recovered from these samples had good characteristics for the SAR procedure.

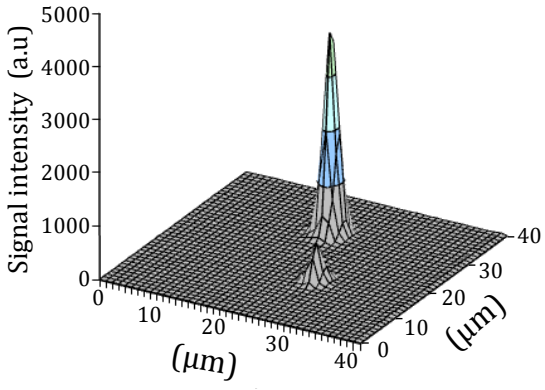

Figure 6.50. 3D plot of scanned aliquot containing a single-dominant bright grain from sample 2.2.

Sample	Recycling ratio	OD (%)
426-2.2	1.00±0.02	3
426-2.4	0.98±0.01	1.7
426-3.2	1.02±0.02	0
426-3.6	1.04±0.02	4.6
426-3.8	1.02±0.02	4.2

Table 6.35. Average recycling ratio and overdisperion of accepted D_e values. The preheat temperature applied for each sample was: 200°C for 3.2 and 3.2 and 220°C for 2.2, 2.4 and 3.8.

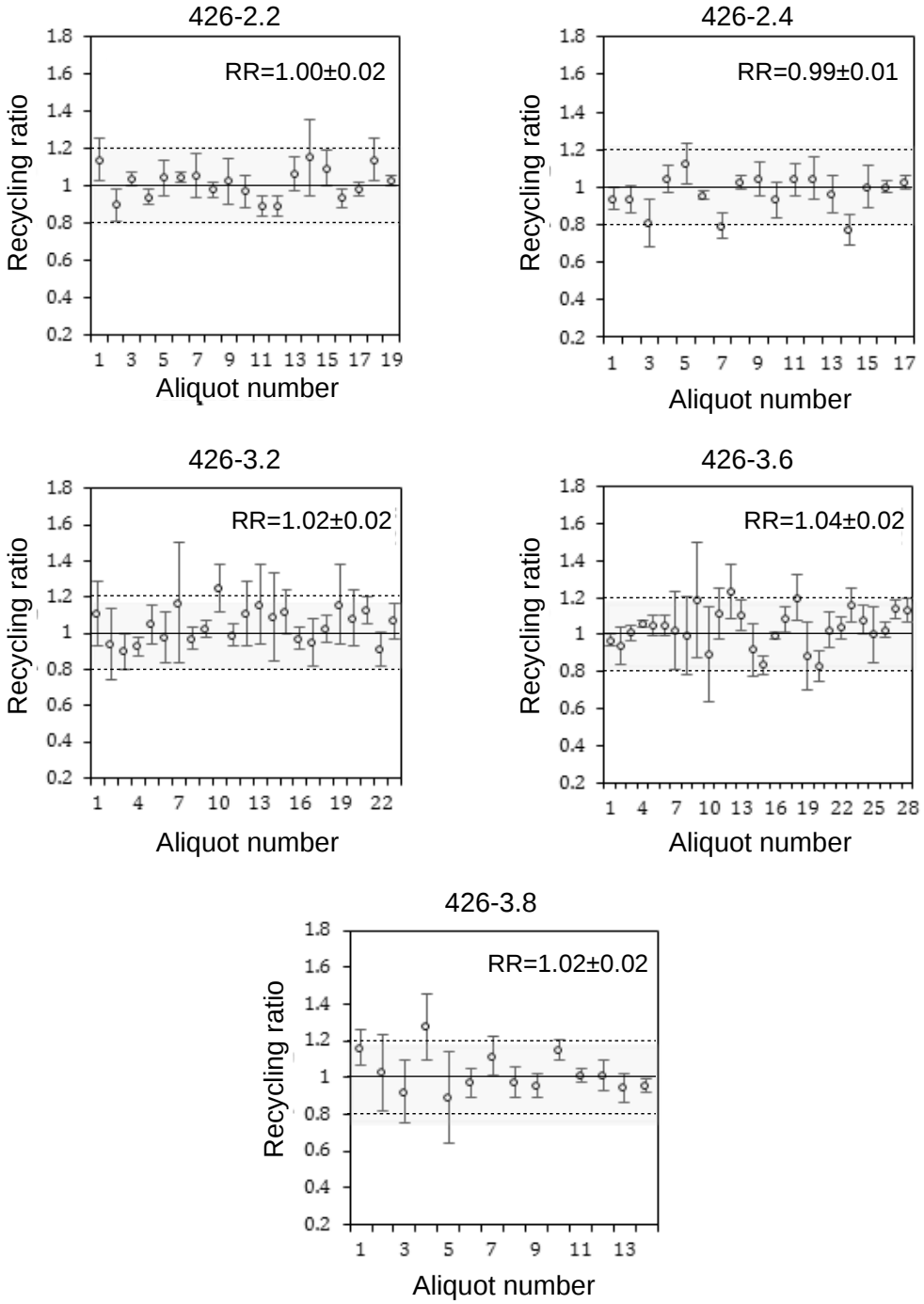

Figure 6.51. Plots showing recycling ratios and standard errors for accepted D_e values. The solid black line indicates the expected ratio of 1, and the dashed lines indicate the ±20% rejection limit applied.

6.4.7 D_e distributions

A summary of the D_e distribution characteristics is provided in Table 6.36. Accepted D_e values and their uncertainties, including the aliquot type and the number of bright grains contributing to MBG aliquots, are provided at the end of this case study (see Tables 6.40 and 6.41). This includes a measure of the overdispersion calculated using the CDM applied to the SBG and MBG aliquots. The results of the t-test applied to test for a significant difference between the SBG and MBG datasets are also provided, to assess whether the two datasets could be combined. The skewness values were also calculated to measure normality of the distributions, particularly for D_e values dominated by single-bright grains.

A measure of overdispersion and the visual assessment of D_e values using the Radial Plotter software indicated that generally the grains had been sufficiently reset, enabling the CDM to be applied. However, all samples contained a few with outlying D_e values, and these are attributed to the shallow nature of the samples, where some intrusive grains entered the deposits by post-depositional processes such as surface runoff or anthropogenic disturbance. The numbers of intrusive grains excluded from the analysis of D_e, were as follows: 2.2 (n=1), 2.4 (n=1), 3.2 (n=3), 3.6 (n=1), and 3.8 (n=2).

The finalised D_e dataset for each sample are presented as KDE and radial plots (Figs. 6.52 to 6.54). Most of the D_e distributions are dominated by aliquots containing single bright grains. The MBG and SBG aliquots show similar peaks in D_e values observed in the KDE plots for most samples. However, the peak defined by the SBG aliquot D_e values differs to that defined by the MBG aliquots in sample 3.6, suggesting aliquot averaging effects, and the combination of signals from low signal intensity grains, resulted in a shift in the D_e peak to higher values of dose. The CDM D_e estimate for the SBG aliquot was used to calculate the burial age of this sample. In all other samples, the MBG aliquots were included in the analysis of D_e based on the absence of significant different between the weighted mean values of D_e calculated individually with the two sets of data (SBG and MBG).

6.4.8 Dose rate assessment

The specific activities of the lithogenic radionuclides (Bq kg^{-1}) and the isotopic ratios ^{210}Pb/^{226}Ra and ^{210}Pb/^{av}U are presented in Table 6.37. The ^{238}U activities were slightly higher in the ceramic material used to line the channel compared with the activities of the surrounding natural sediment. The ratios of these activities enable an assessment of secular equilibrium within the ^{238}U/^{235}U and ^{232}Th decay series (Fig. 6.55). Overall, all samples were relatively low in activity, and therefore defining the peaks within the ^{238}U/^{235}U and ^{232}Th decay series was difficult, and the uncertainties associated with the calculated activities are relatively large. However, no significant disequilibrium was

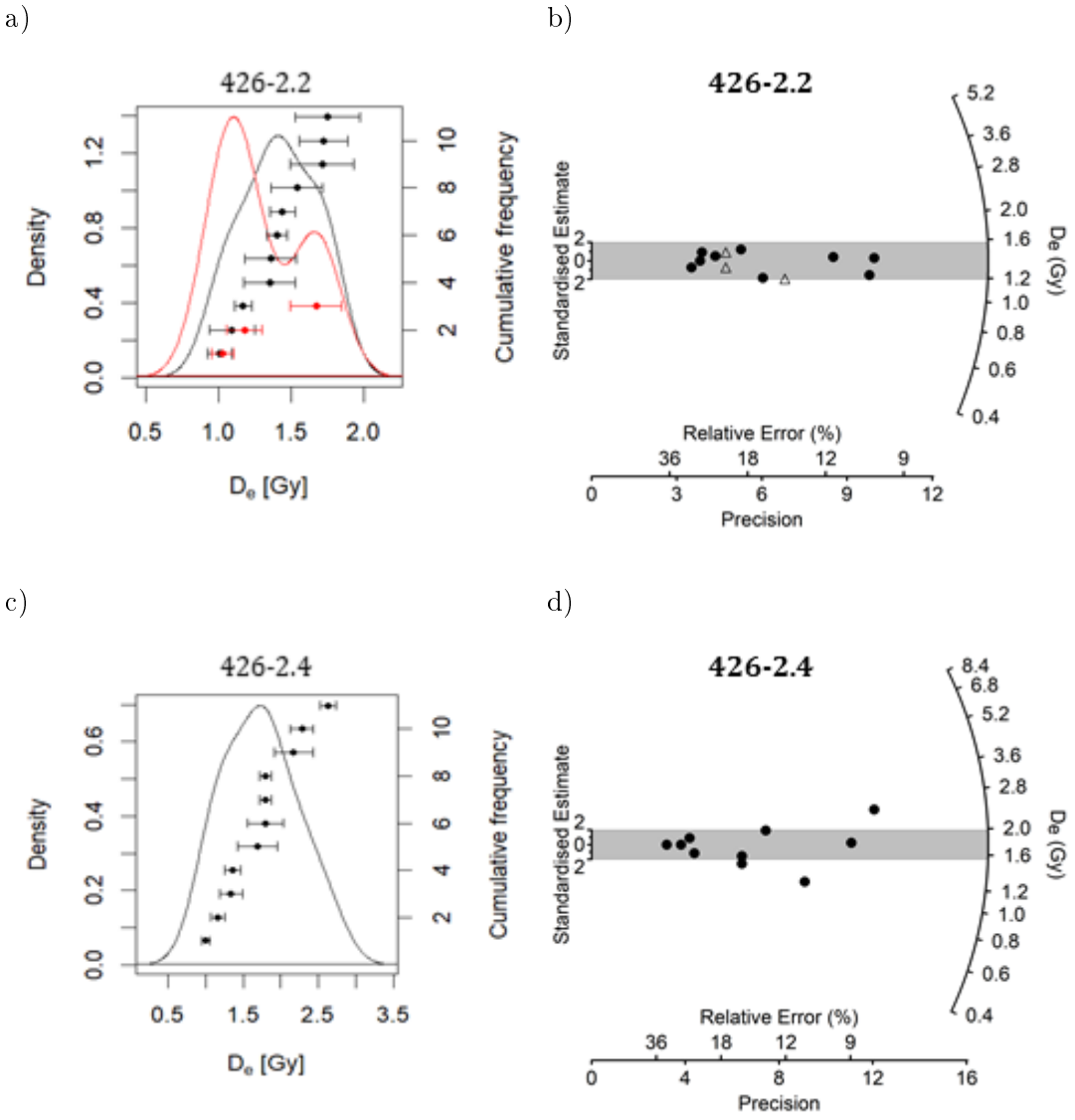

Figure 6.52. KDE plots of accepted D_e values (a and c). Black = SBG, Red = MBG, and radial plots of accepted D_e values (b and d). Closed circles = SBG, open triangles = MBG. The shaded regions indicate the D_e values (2σ uncertainty ranges) obtained when the MDM-3 was applied to SBG and MBG D_e values.

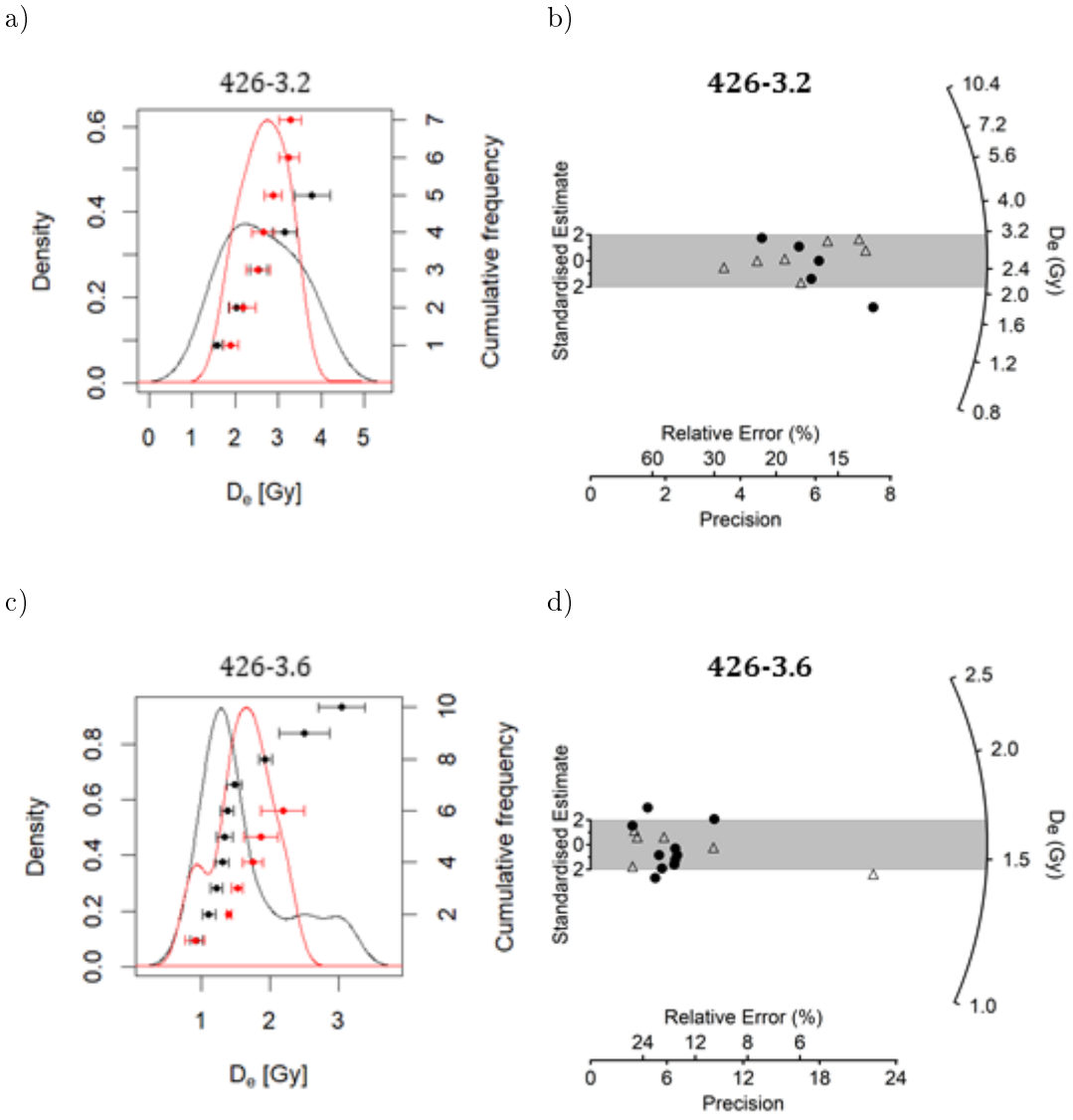

Figure 6.53. KDE plots of accepted D_e values (a and c). Black = SBG, Red = MBG, and radial plots of accepted D_e values (b and d). Closed circles = SBG, open triangles = MBG. The shaded regions indicate the D_e values (2σ uncertainty ranges) obtained when the MDM-3 was applied to SBG and MBG D_e values.

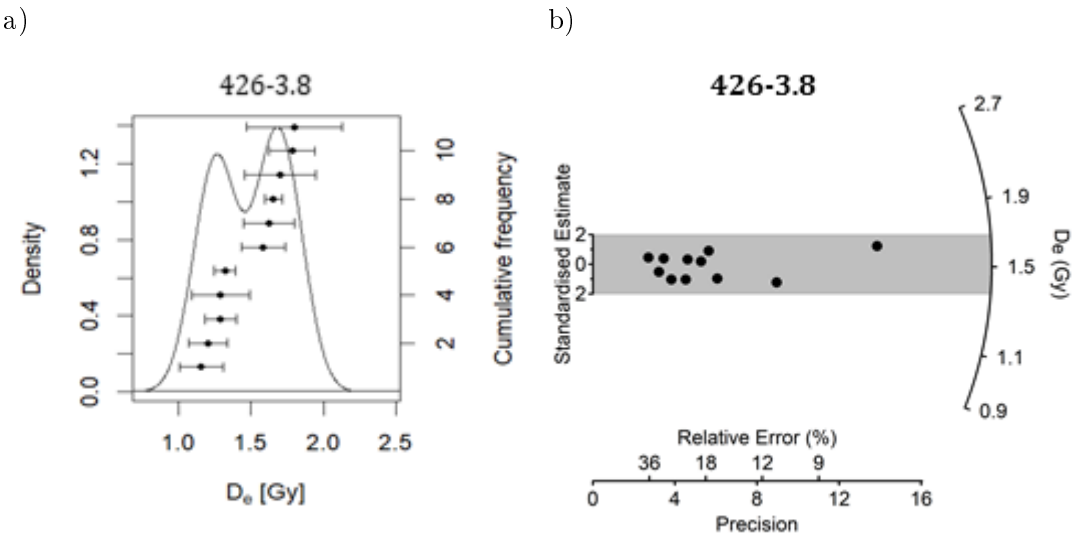

Figure 6.54. KDE plots of accepted D_e values (a and c). Black = SBG, Red = MBG, and radial plots of accepted D_e values (b and d). Closed circles = SBG, open triangles = MBG. The shaded regions indicate the D_e values (2σ uncertainty ranges) obtained when the MDM-3 was applied to SBG and MBG D_e values.

Sample	Aliquot type	n	CDM (Gy)	OD (%)	Skewness	t-test results*	
						t-value	p-value
	SBG	11	1.35±0.07	**1.87±23**	-0.25±0.74		
426-2.2	MBG	3	1.21±0.14	-	-	1.04	0.32
	Combined	14	1.36±0.08	11±10	-0.03±0.66		
426-2.4	SBG	11	1.67±0.16	27±08	0.52±0.74	-	-
	SBG	5	2.43±0.34	**26±34**	-0.06±1.10		
426-3.2	MBG	7	2.74±0.20	7±12	-0.01±0.93	0.84	0.42
	Combined	11	2.56±0.20	16±09	0.17±0.74		
	SBG	10	1.48±0.14	25±08	0.65±0.78		
426-3.6	MBG	6	1.44±0.07	-	-0.14±1.00	0.22	0.83
	Combined	16	1.57±0.11	13±10	0.98±0.61		
426-3.8	SBG	11	1.51±0.07	3±12	-0.05±0.74	-	-

Table 6.36. D_e distribution characteristics. *95% confidence interval. OD values in bold have large uncertainties and are considered to be unreliable. Therefore, the OD of SBG aliquots for samples 2.4 and 3.6 provide the best estimate (25 to 27%).

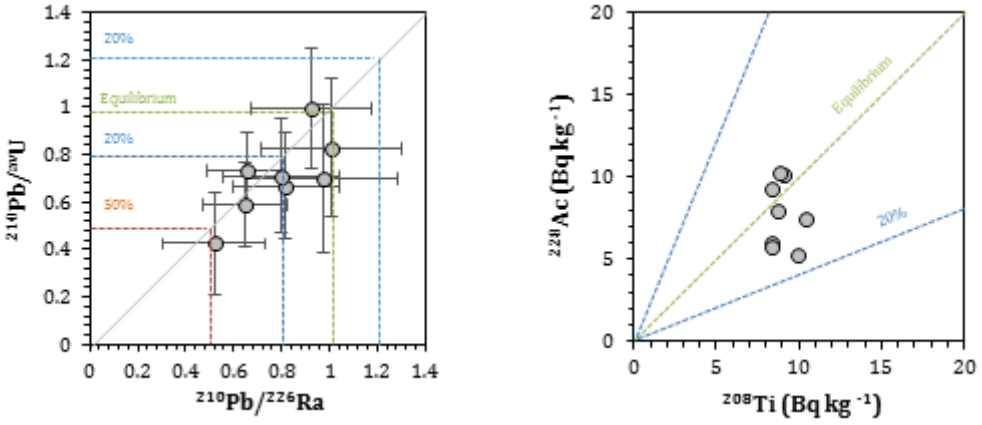

Figure 6.55. Assessment of secular disequilibria in occupation deposits. a) Plots of ^{210}Pb/^{av}U and ^{210}Pb/^{226}Ra ratios, and b) Scatter plot of ^{228}Ac vs ^{208}Ti ctivities in the ^{232}2Th series.

	Isotope activities (Bq/kg^{-1})			Isotope ratios	
Sample/context	^{238}U	^{232}Th	^{40}K	^{210}Pb/^{av}U	^{210}Pb/^{226}Ra
426-2.2 [0.013]	14.6±1.5	10.0±2.5	184.1±4.8	0.65±0.2	0.59±0.2
426-2.4 [0.015]	12.1±1.5	11.0±2.6	229.2±5.3	0.80±0.2	0.71±0.2
426-2.5 [0.011]	11.8±3.9	9.9±2.5	204.0±5.0	1.01±0.3	0.83±0.3
426-3.2 [L007]	16.2±3.7	10.5±2.4	153.7±4.3	0.65±0.2	0.56±0.2
426-3.6 [L008]	11.7±1.5	8.3±2.5	169.4±4.7	0.93±0.3	0.87±0.2
426-3.8 [L004]	12.3±3.9	10.2±2.5	171.6±4.6	0.52±0.2	0.42±0.2
426-3.5 [L008]	12.5±3.8	7.8±2.5	157.9±4.5	0.97±0.3	0.70±0.3
426-3.7 [L008]	14.5±4.0	9.7±2.6	186.4±4.8	0.82±0.2	0.67±0.2

Table 6.37. Summary of radioactive isotope activities and ratios measured as an infinite medium of a point absorber.

indicated.

Sample 3.8 was obtained from a deposit rich in carbonate material, where a small proportion of Rn loss within the U decay series was detected. Despite this, this loss is expected to have a minimal effect on the measured dose rate.

6.4.9 Beta dose rate

The results of the βTLD measurements indicated to be relatively homogeneous in terms of radionuclide distribution. Sample 3.6 contained a significant proportion of coarse sand grains and pebble inclusions used to form the foundations for the channel, but had been accounted for in the βTLD measurements. The ceramic material (sample 3.2)

Sample	Depth BGL (m)	$\dot{D}_{\beta}$±s.e.* (mGy a^{-1})	$\dot{D}_{\gamma}$±s.e. (mGy a^{-1})	$\dot{D}_{cos}$±s.e. (mGy a^{-1})	$\dot{D}_{tot}$±s.e. (mGy a^{-1})
426-2.2	0.05	1.81±0.04	0.22±0.01	0.27±0.02	2.32±0.06
426-2.4	0.08	1.55±0.04	0.25±0.01	0.25±0.02	2.09±0.05
426-3.2	0.19	2.26±0.06	0.19±0.02	0.25±0.02	2.72±0.07
426-3.6	0.23	2.81±0.07	0.19±0.01	0.23±0.02	3.27±0.09
426-3.8	0.16	1.97±0.05	0.25±0.01	0.24±0.02	2.50±0.06

Table 6.38. Dose rate summary for the five OSL samples that were successfully dated. * Attenuation factor applied: 0.913 (after Brennan 2003).

contained abundant Fe-rich rock aggregates. Overall, the beta dose-rate formed the greatest proportion of the total dose rate in the channel samples. The measured beta dose rate for each sample is provided in Table 6.38.

6.4.10 Cosmic dose rate

The depth of samples below the modern ground level (BGL) measured in meters and the calculated cosmic dose rates are summarised in Table 6.38. The geographical position of the samples were 24°N; 56°E, the channels uncovered in Trench O and Trench I was located 69 and 72 m above sea level, respectively. The assumed average density of the sediment overburden was 1.63 g cm^{-3} and this was used along with the geographical positioning data to calculate the cosmic ray dose rate at each sample location following Prescott & Hutton (1995) for the relatively shallow deposits uncovered in the channels excavated, the calculated cosmic dose rate contributed 7 to 10% to the overall total dose rate in the samples measured.

6.4.11 Gamma dose rate

The surface channels were relatively shallow and very little sediment was preserved (Figs. 4.40 and 4.44). One additional sample was measured from Trench O (sample 2.5), and two from Trench I (samples 3.5 and 3.7). The average moisture content for the samples was 10%. Overall, the gamma dose rates ranged between 0.187 and 0.247 mGy a-1, forming only a small proportion of the total dose rate.

6.4.12 Age determinations

The ages for the five channel deposits are calculated in both calendar years (AD/BC) before 2016 and OSL dates, each one provided with two error terms ($\pm\sigma_a$ and $\pm\sigma_b$). The results are presented in Table 6.39.

Sample	Burial age (before 2016)	OSL age* (AD)	$\pm\sigma_a$	$\pm\sigma_b$
426-2.2	632	1385	45	59
426-2.4	608	1410	57	65
426-3.2	934	1080	70	92
426-3.6	477	1540	36	47
426-3.8	605	1410	32	48

Table 6.39. OSL age determinations for the surface channel deposits. σ_a = Type A; σ_b = Type B (after ISO 8601:2004). * rounded t o the nearest 5 years.

426-2.2			426-2.4			426-3.2		
D_e(Gy)	±s.e. (1σ)	GC	D_e(Gy)	±s.e. (1σ)	GC	D_e(Gy)	±s.e. (1σ)	GC
1.01	0.17	SBG	1.00	0.11	SBG	1.59	0.21	SBG
1.10	0.31	SBG	1.16	0.18	SBG	2.02	0.34	SBG
1.17	0.12	SBG	1.34	0.30	SBG	2.55	0.42	SBG
1.35	0.35	SBG	1.36	0.21	SBG	3.15	0.57	SBG
1.36	0.36	SBG	1.69	0.53	SBG	3.79	0.83	SBG
1.41	0.14	SBG	1.80	0.47	SBG	1.90	0.34	MBG(4)
1.44	0.17	SBG	1.80	0.16	SBG	2.18	0.61	MBG(2)
1.54	0.35	SBG	1.80	0.16	SBG	2.53	0.57	MBG(6)
1.72	0.44	SBG	2.17	0.52	SBG	2.66	0.51	MBG(5)
1.72	0.33	SBG	2.28	0.31	SBG	2.88	0.39	MBG(3)
1.75	0.45	SBG	2.63	0.22	SBG	3.26	0.45	MBG(5)
1.03	0.15	MBG(2)				3.28	0.52	MBG(4)
1.18	0.25	MBG(3)						
1.67	0.35	MBG(3)						

Table 6.40. Accepted D_e values with uncertainties and grain count (GC) for samples 426-2.2, 426-2.4 and 426-3.2. SBG: Single bright grain aliquots; MBG: multiple bright grain aliquots. The number of bright grains is indicated in brackets.

412-9.1			412-17.2		
D_e(Gy)	±s.e. (1σ)	GC	D_e(Gy)	±s.e. (1σ)	GC
0.91	0.18	SBG	1.16	0.30	SBG
1.10	0.20	SBG	1.21	0.27	SBG
1.22	0.18	SBG	1.29	0.21	SBG
1.30	0.19	SBG	1.29	0.40	SBG
1.33	0.25	SBG	1.32	0.15	SBG
1.37	0.20	SBG	1.59	0.30	SBG
1.48	0.22	SBG	1.63	0.35	SBG
1.93	0.20	SBG	1.65	0.12	SBG
2.49	0.74	SBG	1.70	0.49	SBG
3.05	0.68	SBG	1.78	0.31	SBG
0.90	0.27	MBG(5)	1.80	0.66	SBG
1.40	0.06	MBG(6)			
1.52	0.16	MBG(2)			
1.74	0.30	MBG(5)			
1.86	0.50	MBG(2)			
2.19	0.64	MBG(3)			

Table 6.41. Accepted D_e values with uncertainties and grain count (GC) for samples 426-3.6 and 426-3.8. SBG: Single bright grain aliquots; MBG: multiple bright grain aliquots. The number of bright grains is indicated in brackets.

6.5 Summary

This section provides a summary of the signal characteristics and the overdispersion found in the samples, outlining the methodological advancements in applying OSL dating procedures to irrigation and field systems.

6.5.1 Signal characteristics

The quartz signals from these samples were significantly varied, reflecting the complex geology of the Caucasus. Although a fast decay was found in a number of aliquots measured, the medium and slow components were prevalent in nearly all of the samples tested. The slow component is commonly found in sediments originating from volcanic sources (e.g. Tsukamoto *et al.* 2003), or in sediments that have undergone limited bleaching cycles (Preusser *et al.* 2009; Steffen *et al.* 2009), where signals have shown significant thermal instability. Considering the signal complexities encountered in a number of samples from this region, samples obtained from the field systems agreed with historical maps, and when compared with calibrated radiocarbon dates from archaeological contexts obtained from the same sampled locations, the OSL dates were in relatively good agreement.

The percentage of SBG aliquots with fast decay signals was higher in samples from Oman (e.g. 426-2.4). However, the medium component was also prevalent in most of the samples. The estimation of D_e values applied to SBG aliquots with dominant fast decays showed no difference to the value of D_e calculated for those with a dominant medium component, thus justifying that the medium component found in quartz may not be unstable in all regions as widely reported (Steffen *et al.* 2009; Trauerstein *et al.* 2017). The application of the EBG SAR procedure has been widely used where fast, medium and slow signals are difficult to separate (Ballarini *et al.* 2007; Cunningham & Wallinga 2009). However, in most of the SBG aliquots tested in this research, the medium/slow components were dominant, and so no difference was observed between the standard SAR and the EBG D_e estimates.

6.5.2 Overdispersion

Small-aliquots were employed to concentrate signals from individual bright grains and to avoid contamination from multiple bright grains. However, this was not always possible where dim quartz was dominant, requiring slightly larger aliquots (∼30 grains). A measure of overdispersion (OD) was used to quantify: a) level of bleaching, b) disturbance, and c) variability in beta irradiation received by individual grains. The OD of samples obtained from agricultural field systems ranged between 54 to 74%; these were affected by partial-bleaching. While occupation deposits varied significantly between 27 to 71%, which was caused by a mixture of quartz signal heterogeneity and partial-bleaching, in one sample, intrusive grains could be excluded, thus reducing the OD to 27%. Similar complexities were observed in canal deposits, the broad spread in OD (22 to 68%), which reflects the variable depositional and post-depositional processes affecting the sediments. In such complex situations, the application of a finite mixture model (FMM) could not be justified, as it was difficult to ascertain the number of components present due to the complex signal characteristics. To obtain an accurate estimate of D_e using the FMM, an independent estimate of dispersion parameter is required, ideally from a well-bleached undisturbed deposit. All of the archaeological contexts examined in the Caucasus, partial bleaching and bioturbation was prevalent. Alternatively, a measure of a modern 'zero dose' sample could be used as an independent estimate of dispersion (Roberts *et al.* 1999), particularly if single-grain analysis is available. This would enable a rapid determination of the dispersion parameter of a well-bleached sample, and to analyse only stable signals - fast components - originating from individual grains.

The small-aliquot approach employed in this research was sufficient to isolate D_e values from SBG aliquots. To provide an accurate estimate of OD, particularly for partially bleached contexts such as canals, a true measure of OD could only be obtained from aliquots with single bright grains in order to avoid averaging effects of signals originating from multiple grains (Arnold & Roberts 2009). The recovery of SBG aliquots in sam-

ples dominated by low luminescence signals from quartz was particularly challenging, especially in regions where quartz signal characteristics were highly variable, requiring many number of aliquots to be tested. In nearly all samples measured using the SAR procedure, the OD could be evaluated using the SBG D_e dataset. For the Oman samples which were relatively well-bleach, the OD values were between 25 to 27%, and therefore the small-aliquot approach was reliable.

Chapter 7
Discussion

7.1 Introduction

The *Persia and its Neighbours Project* took a period-specific approach to investigate the impacts of the Sasanian Empire on the wider landscaped within the frontier regions. By utilising this extensive landscape dataset, this research project targeted the most optimal sites for sampling, as mentioned in the aims and objectives introduced at the beginning of this thesis. The following discussion will focus on areas where OSL dating and geoarchaeology were employed, drawing on the results from Georgia, Azerbaijan and Oman.

7.2 Landscape archaeology in the frontiers

7.2.1 To identify landscape features with well-preserved contexts within the frontier regions.

As mentioned above, the wider landscape study was used to identify suitable sites for excavation and sampling, employing a two-stage approach. Firstly, the identification of irrigation features, and agricultural field systems, that were within close proximity to sites with known Sasanian occupation. Secondly, settlement and landscape data were utilised to focus on specific sites with the best preservation potential for accessing contexts related to the construction and maintenance events. This methodology was adapted slightly for each region investigated, which was dictated by accessibility and scale of the landscape features found.

Georgia

In upland regions of the Greater Caucasus in Georgia (Chapter 4), numerous fields, agricultural terrace systems and isolated hilltop sites were clearly visible in Google

Earth™ imagery. The spatial relationship between various sites of known dates and specific landscape features was difficult to resolve on the ground due to the lack of visible surface artefacts and access to relevant historical sources prior to fieldwork. Besides, the resolution of satellite imagery for the region was generally poor due to the rough terrain requiring intensive ground based field survey and small-scale excavation. Several small-scale excavations meant that many samples from a range of locations were screened to identify the most suitable sites to focus the OSL analysis. The second stage of fieldwork involved both small excavations of field systems and cleaning of exposed sections. Those positioned at isolated outcrops at higher altitudes were generally well preserved. The results from Georgia highlighted the significant variability in the OSL properties of quartz that can be found within a relatively small catchment area.

Azerbaijan

Two types of irrigation systems were identified in the alluvial plains of the Mil Steppe, Azerbaijan, including the qanat and earthen canal systems. The relatively flat terrain of this region meant that canals and upcast banks could be easily identified, both in satellite imagery and on the ground, but are now subjected to systematic destruction by modern irrigation. Primary and secondary canals are defined by large upcast banks on either side, but taphonomic alterations have meant that banks have become heavily eroded and disturbed. Large canal systems were challenging to excavate, requiring large-scale excavation of both the fill and upcast banks. Large stratigraphic sections gave an insight into the stratigraphic complexity of different phases of canal evolution, and raised interesting questions regarding the processes involved in their construction and maintenance. Unlike coring, which has been one approach used to study canals (Bishop *et al.* 2004), large profiles can reveal the full extent of a deposit, including the identification of disturbance.

Oman

In Oman, a variety of water management features were identified, ranging from qanats or *falaj*, field walls/revetments, and surface channels, all of which were relatively visible on the ground surface. The visibility of these features in satellite imagery was generally poor due to their small size, requiring intensive ground-based survey. The field survey successfully identified a complex network of channels. Unlike the large-scale canal systems found in the lowlands of the northern frontiers, the channels were relatively shallow, and so small-scale excavation was sufficient to completely uncover the channel deposits. Similar to the approach undertaken in the survey in the Dariali Gorge, a series of channels were excavated and sampled, enabling a focus upon those with the best luminescence characteristics.

7.2.2 Summary

The broad landscape approach of the *Persia and its Neighbours Project* enabled many research areas to be investigated to identify the best sites for sampling. Unfortunately, in nearly all cases, poor preservation, accessibility and time-constraints were some of the issues that were encountered in the field. To further integrate landscape survey with geoarchaeology and the various dating methods now widely available, a systematic survey is first required in areas where these logistical issues do not occur. As these areas investigated are relatively new, our understanding of the settlement patterns, land use and chronology remains limited to only a few key areas. Further investigation of these regions is therefore required to build up a larger data set in order to test this two-stage methodology.

7.2.3 Future developments

To improve sampling strategies in the field, geoarchaeological methods combined with portable OSL readers would enable rapid characterisation of the luminescence characteristics of sediments and soils in the field. This would be particularly useful when working in various landscapes to enable more targeted sampling strategies, particularly for identifying parts of a stratigraphic sequence that had been sufficiently reset (Sanderson *et al.* 2003; Sanderson & Murphy 2010; Kinnaird *et al.* 2017). In regions where the luminescence characteristics are suitable for the SAR procedure, e.g. fast decays, D_e values calculated using a standardised growth curve (SGC) have shown to be in good agreement with D_e values calculated using the standard SAR procedure for quartz from different regions (Roberts & Duller 2004), demonstrating that rapid D_e assessment can significantly reduce instrument time.

7.3 Sample characteristics

7.3.1 To characterise the sediments sampled in order to place the OSL dates within their stratigraphic context.

Georgia

Firstly, the macroscale approach highlighted the need to obtain a basic understanding of the local geomorphology of the region, in order to rapidly assess the stratigraphic integrity of the features investigated. In general , sites located on high plateaus were well-preserved, while those located on the colluvial fans in the valley were disturbed. On the microstratigraphic level, clay translocation features were identified in both stratigraphic profiles investigated, which were not visible in the field. Bioturbation was also prevalent

in both sequences, but was mainly concentrated in the organic A-soil horizons. The basal deposits were the least affected by bioturbation, and these were the deposits that were investigated further in the OSL analysis.

The occupation deposits uncovered at Dariali Fort were complex, and was further demonstrated in the micromorphological analysis. These deposits were disturbed and heavily modified by anthropogenic and natural agencies. In such cases, the successful application of the OSL dating was depended on obtaining samples from contexts that had remained undisturbed. By sub-sampling from micromorphological blocks, areas of disturbance could be avoided, and targeted high-resolution sampling of burnt sediment horizons was made possible.

In both depositional contexts; natural colluvial deposits and anthropogenic deposition, thin-sections enabled the *in situ* examination of quartz in its original context. Micromorphology and CL analysis combined, revealed the variability in quartz found in the region, which also provided insights into the potential complexity of the luminescence signals likely to be found in the samples obtained.This level of characterisation can also be used to target samples with quartz originating from one geological source that produces quartz with suitable luminescence characteristics, e.g. sandstone.

Azerbaijan

The construction of large canals requires the removal of large volumes of alluvial silts to form a canal. The construction event created large upcast banks which helped to preserve the structural integrity of the canal. Its repeated use required frequent dredging to remove silt to ensure the effective flow of water through the canal. Cleaning and maintenance resulted in the further build-up of the upcast banks, before eventual abandonment. These large banks provide a record of the anthropogenic processes involved in their construction. The geoarchaeological assessment provided insights into the complexities of these deposits, enabling various stages of the canal evolution to be reconstructed, as illustrated in Fig. 7.1. The microstratigraphic observations revealed that these different phases of canal construction, maintenance and abandonment created many types of microstructural, pedogenic and post-depositional features, which were altered by bioturbation.

The main phases that were identified can be summarised as follows:

Stage 1 - Pre-canal: natural alluvium (possible flooding event).

Stage 2 - Canal construction: cutting and bank construction.

Stage 3 - Aggradation and canal silting

Stage 4 - Canal maintenance: anthopogenic removal of silts and clays.

Stage 5 - Canal maintenance: anthropogenic removal of silts and clays. Erosion and deflation of canal bank.

Stage 6 - Canal abandonment: erosion and deflation of canal banks.

Stage 7 - Canal infill (primary): aggradation and erosion of banks. Aeolian sediment input.

Stage 8 - Canal infill (secondary): aggradation and erosion of banks. Aeolian sediment input.

Firstly, like the samples obtained from Georgia, deposits were mineralogically diverse. In the context of canals, quartz was deposited by a range of processes, aeolian, fluvial and colluvial, which were subsequently modified by bioturbation processes. These different processes create different resetting mechanisms of the quartz, which introduced further variability into the luminescence characteristics at the single-grain level. The frequency of quartz/feldspar grain-sizes was particularly varied within the canal. For example, the transition from the old ground surface to the bank revealed that the frequency of quartz and feldspar varied considerably within a very small area (ca. 8 cm vertical transect). This suggests that the conventional sampling strategies employed in OSL dating, e.g. tube-sampling, may not always provide the best resolution for such complex stratigraphy. Similar to the occupation deposits investigated in Georgia, sub-samples from micromorphology blocks enabled more targeted sampling, however, the internal variability of upcast deposits was too complex to isolate quartz that had been sufficiently reset.

Furthermore, canals and alluvial deposits were significantly bioturbated, as they provide the ideal conditions for earthworms and plant growth. Arid environments with saline soils commonly found in Central Asia, are rich in salts and pedogenic gypsum. The formation of these minerals significantly disturb and disaggregate the sediments within the banks and upcast deposits. Where gypsum was concentrated, significant disturbance of deposits resulting in the vertical movement of grains through the profile, can complicate the OSL analysis (Bateman *et al.* 2003; 2007a). Fortunately, micromorphology can be used to rapidly identify contexts that were bioturbated and disturbed, which was not easily identifiable in the field. In contexts where bioturbation was unavoidable, intrusive grains could be excluded from the analysis, and this is where the micromorphological assessment was most useful.

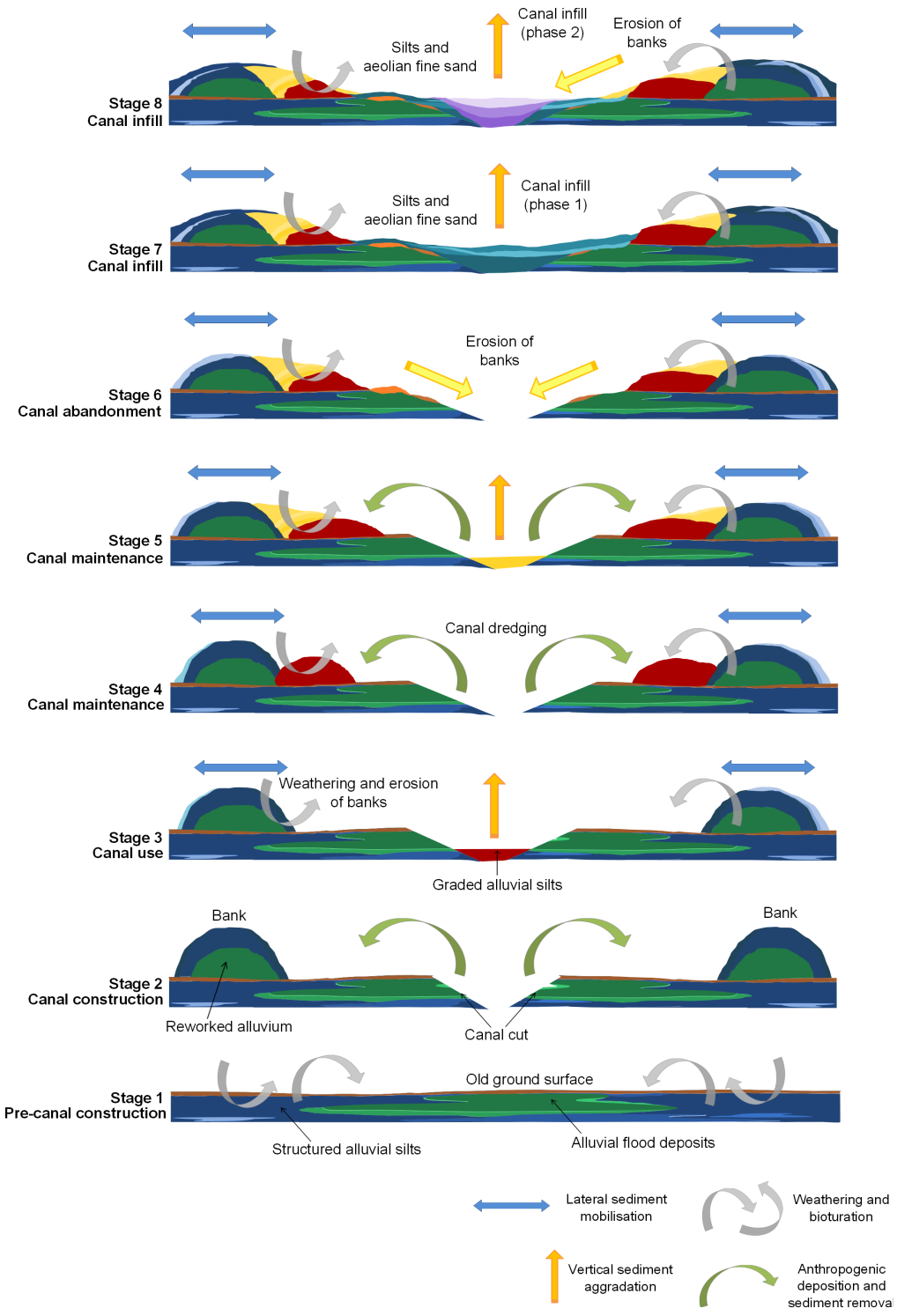

Figure 7.1. Stratigraphic model of Ören Qal'eh canal.

Oman

The Batinah coastal plain of Oman was formed by the accumulation of alluvial sediments deposited by wadi systems originating from the mountains. Another mode of deposition that actively shaped the landscape was aeolian processes which cause both the removal and redeposition of sediments. The contexts sampled originated from features that were relatively shallow and remained partially visible of the modern surface. The sediments that were deposited within the channels reflected the local limestone geology, as indicated by the frequent carbonate inclusions. Frequent rock inclusions originating from volcanic and metamorphic sources were also found within the contexts, indicating that sediments originated from the mountains regions. Aeolian sediments were common in the area, formed by the erosion of local sediment traps (e.g. alluvial deposits and *sabkahs*) that were deposited locally within the contexts investigated. No post-depositional features were found in the micromorphological thin-sections, most likely due to the arid and relatively stable environment during deposition. Pedogenic carbonates were abundant in the contexts found, but careful attention in the calculation of dose rate confirmed that these sediments remained as 'closed systems' e.g. unaffected by post-depositional alteration, and so no significant disequilibria in the U and Th decay series was observed.

7.3.2 Summary

This research employed a multi-method approach, employing a) a basic characterisation of key depositional processes, b) identification of mineralogical components, and c) the micromorphological analysis of contexts sampled to provide *in situ* characterisation to inform the OSL analysis. *In situ* characterisation was particularly important for the evaluation of dose rate for the sampled contexts.

7.3.3 Future developments

Post-depositional alterations

Repeated wetting and drying cycles resulted in the formation of a number of post-depositional features: gypsum, Fe nodules, $CaCO_3$ nodules and micritic coatings, and clay coatings, all of which were identified in the different contexts investigated. Post-depositional alterations introduced additional complex chemical interactions into the soil and sedimentary environment, potentially resulting in localised variations in beta dose-rate. The combined method of high resolution gamma spectrometry (HRGS) and the βTLD technique was employed in this study, enabling a careful consideration of potential dose-rate variability. The latter was particularly useful for assessing the beta heterogeneity on a mm scale, particularly in contexts where clay translocation features

were present. To further understand the dose-rate variability, further *in situ* examination and quantification of U, Th and K of sediment and soil slices is required.

Microstructure

The type and percentage of voids present in the various contexts sampled raised questions related to the accurate quantification of bulk density and moisture content. Further investigation of the void area would provide a more detailed estimation of the bulk density, which would require high-resolution image analysis to accurately quantify the area of voids present on a sample-by-sample basis.

Mineralogy

The combination of SEM and CL enabled rapid characterisation of the frequency of quartz and the formation and post-depositional histories of these minerals to be determined. However, these methods required disaggregation for chemical and physical treatment of the samples to isolate the quartz. *In situ* analysis would provide the spatial relationship of brightly emitting grains of different sizes to be analysed within their original stratigraphic position. Techniques such as autoradiography would enable the detection of 'coldspots' and 'hotspots' caused by the concentration of carbonates and K-rich minerals and clays within the sedimentary matrix (Rufer & Preusser 2009). Such images would help to inform high-resolution sampling strategies of impregnated sediment blocks for OSL dating. High-resolution sampling was not employed in any of the contexts investigated in this research, however, a reduction in sample tube diameter (1.5 cm), significantly reduced the overdispersion of D_e values in small channels sampled in Oman. Therefore, if these two approaches could be combined, i.e. small cores from impregnated blocks, it would help to target areas unaffected by bioturbation and disturbance that is difficult to identify in the field.

7.4 Suitability of quartz

7.4.1 To determine the suitability of coarse-grained quartz recovered from the sampled contexts for applying the conventional SAR dating procedure.

The *Persia and its Neighbours Project* enabled the testing of samples obtained from many geographical regions, Georgia, Azerbaijan, Northeast Iran and Oman. Prior to undertaking full analysis using the SAR procedure, coarse-grained quartz from the various archaeological contexts were examined. At the single-grain level, quartz appeared

to have highly variable sensitivities and signal characteristics, that could be related to the geological source of quartz and its formation histories (Preusser *et al.* 2009), and also the deposition processes at play (Duller 2008a). In order for the SAR procedure to perform correctly, a fast decaying OSL signal is usually desirable (Murray & Wintle 2000; 2003). Luminescence characterisation of samples with sufficiently bright signals included the fast ratio (FR) - calculated using the CW-OSL curves - and the natural background ratio (R_N). These characteristics revealed that in most samples, a complex mixture of signals were present at an individual grain level. The likelihood for homogeneous signals (e.g. signals composed on one component) from coarse-grained quartz is rarely encountered in nature, and only in wind-blown sediments is it possible to find grains with similar characteristics. The samples analysed from Oman are an example where the SAR procedure was most successful, as the fast decaying component was the most dominant signal. A minor aeolian component was also found in some of the samples from the canal in Azerbaijan, but were mixed with grains with undesirable characteristics.

Future developments: Feldspar dating

Feldspars are well known for exhibiting anomalous fading (Wintle 1973), and have been shown to have slow resetting of signals (Godfrey-Smith *et al.* 1988), variable fading rates (Lamothe & Auclair 1997), and are thermally unstable (Wallinga *et al.* 2000; Preusser 2003; Blair *et al.* 2005). The development of feldspar dating in regions where quartz characteristics are unsuitable would require detailed characterisation of the different emissions from feldspars, as found in the CL analysis, the feldspars from these regions were variable. Feldspars would also require high-resolution geochemical characterisation for internal ^{40}K content and assessment of fading and thermal stability of individual grains. The internal dose rate of individual feldspar grains also varies significantly, and so OD is likely to be very broad and could only be accounted for using single-grain analysis. Whether feldspars would be able to provide a more accurate estimation of D_e for archaeological timescales between ca. 500 to 2000 years remains questionable, considering that poor bleaching and bioturbation was prevalent in all of the contexts investigated. Fattahi (2015) applied single-grain feldspar to anthropogenic mounds associated with qanats in Iran and found that only a small number of D_e values were able to define the minimum dose population within a poorly-bleached sample. Furthermore, small-aliquots of quartz were also applied to the same sampled contexts, producing similar D_e estimates, suggesting that small-aliquots of quartz is sufficient to accurately measure D_e in poorly-bleached context. Despite these complexities, further development in OSL dating by utilising signals from feldspars where quartz characteristics are not ideal, routine characterisation of feldspars combined with single-grain analysis is required. This would enable grain-to-grain variability between feldspars to be accounted

for. Alternatively, the multi-elevated-temperature post-IR IRSL (MET-pIRIR) protocol (Li & Li 2011) has demonstrated that at elevated temperatures, anomalous fading was found to be negligible. This is one alternative protocol that could be tested on samples dominated by well-formed k-feldspar.

7.5 Chronostratigraphy

7.5.1 A chronostratigraphic sequence for ancient landscape features will be developed and the OSL dates will be considered within their wider chronological context.

The following sections will discuss the OSL dates of the irrigation and agricultural systems explored in Georgia, Azerbaijan and Oman within the regional chronological framework (Fig. 7.2).

Occupation and control of the Caucasus

A small number of OSL dates was obtained from key phases of occupation at Dariali Fort (Table 7.1) and from two well-preserved field systems located to the south of the fort (Table 7.2). The OSL dates from Dariali Fort revealed a broad period of occupation, ranging from the 6^{th} - 12^{th} centuries AD, which reflects the complex socio-political history of the region. Numerous political units were actively involved in the establishment of the Central Caucasus as a major frontier, demarcating the boundaries between the Russia Steppe and the Near East. The Khazars (4^{th} - 9^{th} centuries AD) were a group of pastoral nomads that dominated the Russian steppe for many centuries (Noonan 1999; 500). However, this was a politically unstable region to defend and permanently occupy. Three phases of instability have been widely reported: 1) 3^{rd} - 6^{th} centuries AD; incursions by the Byzantine and Sasanian Empires; 2) Between 650 and 750 AD a series of Arab-Khazar internal wars, and 3) the first of the Mongol invasions in the 7^{th} century AD (Masson 1996; Howard-Johnston 2007) (see Chapter 1). Repeated invasions further weakened the Khazar Khagan state and by the 9^{th} century AD and Khazaria began to fragment, resulting in a significant settlement shift into upland areas of the Caucasus.

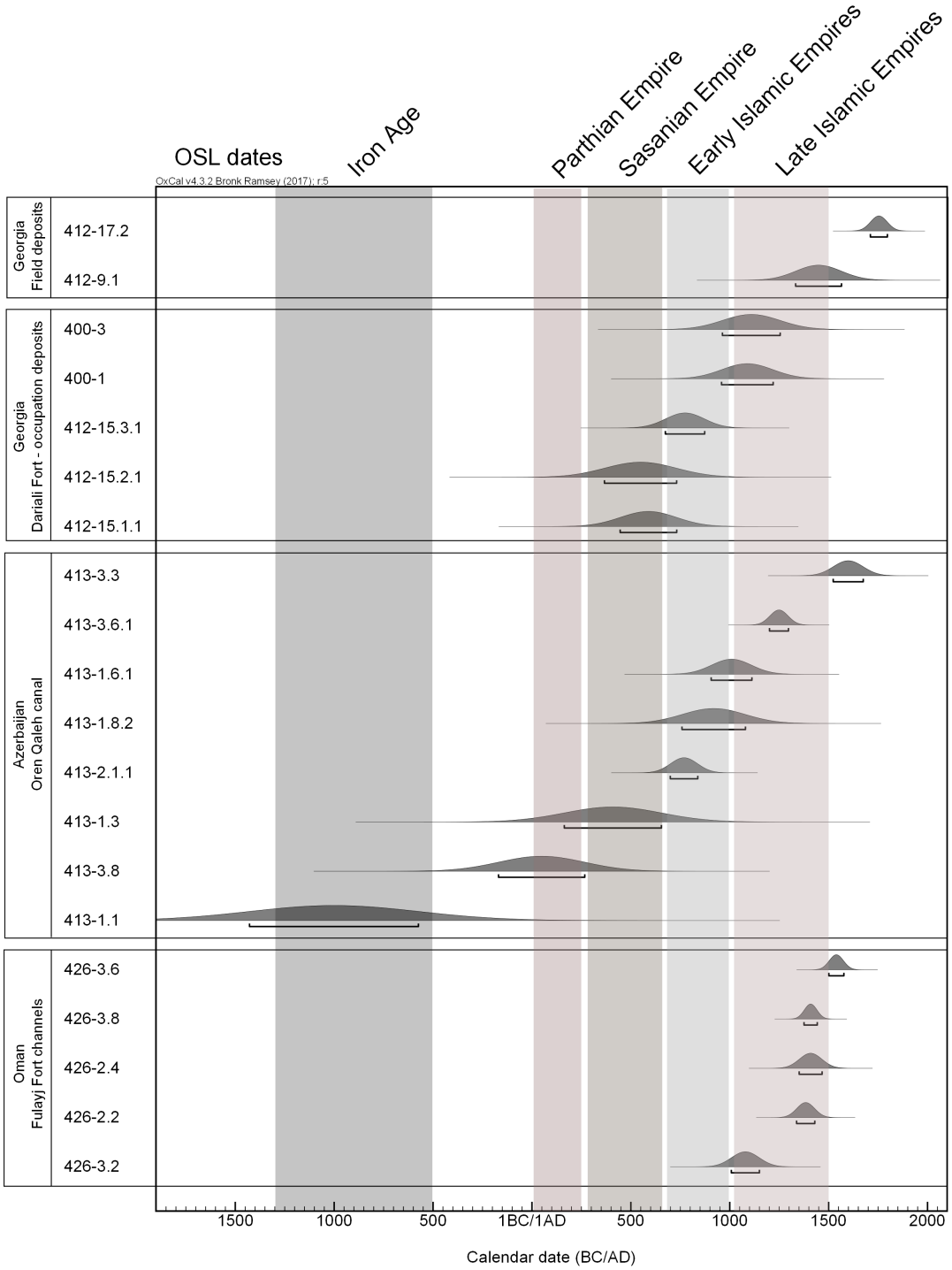

Figure 7.2. Summary diagram showing OSL dates with σ_b uncertainties displayed as Gaussian distributions with 2σ range indicated. Plotted using OxCal v4.3.2 ; r5. N.B. The Early and Late Islamic periods equates to the Steppe Empires in the Caucasus.

Sample	OSL date (BC/AD)	$\pm\sigma_a$
412-9.1	1450	115
412-17.2	1755	40

Table 7.2. OSL dates for the basal field deposits.

Sample	OSL date (AD)	$\pm\sigma_a$
400-3	1110	145
400-1	1090	130
412-15.3.1	775	100
412-15.2.1	550	180
412-15.1.1	590	140

Table 7.1. OSL dates for the occupation deposits, Dariali Fort, Georgia.

The wider landscape investigations involved the stratigraphic investigations of two field systems. At the modern village of Tsdo, numerous defensive walls and structures were visible and extensive terrace and field systems were preserved. Excavation of a terrace yielded reworked fragmentary pottery recovered from the fills which ranged from the 8^{th} to the 10^{th} centuries AD. Underlying the fill deposits, an OSL date (412-9.1) obtained from the basal deposits gave a date range from 1335 to 1565 AD. The OSL date corresponded with Early Medieval terracing also found in the Kislovodsk Basin located on the foothills of the North Caucasus (Arzhantseva *et al.* 2001; 120, Korobov & Borisov 2013). These terraces along with those build in the Dariali Gorge may have been constructed as a response to significant landscape degradation or volcanic activity occurring between the 8^{th} to 10^{th} centuries AD, as indicated by an intense period of occupation found at Dariali Fort (Sauer *et al.* 2015). An OSL date (412-17.2) from a second field system further south of Tsdo was dated to the 18^{th} century AD. Although this date indicates a much more recent occupation of the gorge, it suggests that hilltop locations were still occupied until relatively recently, maybe as a result of sheep herding and access to pastureland, which was the main economic driver until the fall of the Soviet Union (Hanauer *et al.* 2017).

The construction of extensive stone walled and earthen terraces would have required the input from small-scale communities to construct extensive walls and risers to improve the land. A similar process of terrace construction was found in the uplands of the southern Levant, where extensive terracing were constructed near a large Iron Age settlement, where local-communities could be easily employed to build the terraces (Hopkins 1985; 185, 266). Earthen terraces on the other hand, formed by natural slope aggradation, requiring minimal human input and was effective in managing landscapes that were sparsely populated (Wilkinson 1977; Wilkinson *et al.* 2013; 186). To fully

understand the social aspects of terrace construction would require further investigation of many numbers of terraces that can be accurately dated and directly associated with settlements of known date.

Adaptation to unstable landscapes The Dariali Gorge formed part of a natural frontier between the Russian Steppe and the Middle and Near East (Kohl 1988). The Caucasus provides a unique insight into the role of local elites that were successful at securing and protecting a region that had important trade and exchange networks connecting the high mountain passes with the lowland plains. Local elites were able to successfully deter the incisions of large powerful empires from the southeast and southwest of the Caucasus for many centuries. Although there is significant evidence for confrontation and warfare from other political units of the lowland plains (Chapter 1), it was likely that there were periods of peace and stability. The upland regions were important for providing natural resources such as raw materials, wood and spring water, despite its unstable landscape characteristics, and the lowland regions would have provided cereals and accessibility to pasture land during the winder seasons when the Caucasus were inaccessible. The management of the natural resources in the uplands would have required a low impact approach, as these areas are sensitive to climatic and anthropogenic landscape degradation (e.g. overgrazing or deforestation), leading to erosion and destabilisation. Furthermore, upland areas were, and still remain, vulnerable to landslides, rock falls and avalanches (Pánek *et al.* 2012). Attempts to prevent landslides and manage erosion is clear from the abundance of terraces found. The terraces, which reflects long-term adaptation to unstable landscape, enabling small polities to be relatively self-sufficient in extreme marginal environments.

Large-scale canal systems as archives for socio-economic complexity in multi-period landscapes.

The canal system that was explored close to Ören Qal'eh in the Mil Steppe, Azerbaijan, provided a unique opportunity to investigate the chronology and understanding of the complex depositional histories involved in the formation of canals and associated upcast banks. The results of the OSL dating applied to the different phases of the canal (Fig. 4.26) revealed a broad chronology, suggesting a repeated and long use of the canal. Due to the complex chronostratigraphy obtained from different phases of the canal, the OSL dates provided in Table 7.3, will be discussed in relation to the wider landscape context and regional chronology.

Sample	OSL date (BC/AD)	$\pm\sigma_a$
413-1.1	-1000	425
413-1.3	410	245
413-1.6.1	1010	100
413-1.8.2	920	160
413-2.1.1	770	70
413-3.3	1600	75
413-3.6.1	1250	45
413-3.8	50	215

Table 7.3. OSL dates for the canal.

Pre-Sasanian landscape investment

An OSL date (413-1.1) obtained from the construction phase of the bank ranged from 1425-574 BC, broadly within the range of the Iron Age period, which consists of three sub-periods (I, II and III), from 800 BC - AD 400. Although this date may relate to a deposit that had not been reset during the construction of the canal in the Sasanian period, as indicated by the second OSL date obtained from the same context (165-655 AD), the date suggests that these sediments had been bleached in the Iron Age. The construction phase contained a mixture of deposits originating from the natural alluvium and deposits reset in Late Antiquity. Furthermore recent landscape survey data from the Mil Steppe (Ricci 2012), suggested that the region was intensively occupied in the Iron Age as substantial pottery indicated peaks in settlement density in the region. This deposit may reflect wider landscape modifications resulting in increased riverbed silting and eventual flooding.

The Iron Age period represents the first major settlement dispersal occurring over many large areas, enabling settlements to establish in previously unoccupied regions (Wilkinson *et al.* 2013; 134). In many untouched regions of the Middle East and Central Asia, a unique set of ecological niches specific to the region enabled a complex socio-political system to evolve. The Iron Age was originally considered to be a period dominated by a mobile cattle-breeding economies, during a period of enhanced humidity (Djamali *et al.* 2009). Now there is an expanding quantity of evidence for Iron Age occupation in previously uninhabited areas, such as the semiarid deserts of Central Asia. Evidence has been reported in Central Iran (Fahimi 2010), Dehestan (Lecomte 2007), Uzbekistan (Stride *et al.* 2009), Kazakhstan (Kohl *et al.* 1984) and Turkmenistan Azerbaijan (Ricci 2012), and at sites found in the northeast of Iran (Sauer *et al.* 2013). However, chronological uncertainties remain due to a combination of landscape survey biases, excavation and poorly constrained ceramic typologies (Chapter 2, Sec. 2.2). One other possibility could be linked to a major flooding event at the time of the Iron Age (5^{th} century BC) where the Caspian Sea was 3 m higher than present day level (South

Caspian river mouth configuration under human impact and sea level fluctuations; Lahijani *et al.* 2009; 67), resulting in the formation of small islands of occupation which may have caused significant gaps in settlement densities for this period.

Considering these chronological issues, there appears to be significant evidence for occupation of marginal environments prior to the arrival of the Parthian and Sasanian Empires. Indirect evidence for irrigation infrastructure comes from an increase in barley pollen in palaeoenvironmental archives from Lake Almalou in Northwest Iran dated to the 6th century BC (Djamali *et al.* 2009) (Fig. 7.3), which corresponds to the rise of the Achaemenid Empire in the region. Such data should also be treated with caution, as tree pollen can travel long distances, and/or dominate the record if located near the lake. Further, investigations into local archaeobotanical remains from secure archaeological contexts would enhance our understanding of the agricultural economy during these key transition periods.

Renewed landscapes

It is unclear what the environment was like prior to the implementation of large-scale irrigation in the lowland plains. Palaeoenvironmental records have shown that this was a time of landscape degradation (e.g. overgrazing) prior to the Sasanian Period in the Northwest (Djamali *et al.* 2009) and Northeast Iran (Shumilovskikh *et al.* 2016). Irrigation was then introduced to expanding agricultural land, a tree cultivation phase (e.g. walnut, chestnut and grapevine) was identified (Fig. 7.3), which began much earlier in the Parthian period and was further expanded under the Sasanian Empire (Djamali *et al.* 2009; Leroy *et al.* 2013; Talebi *et al.* 2016; Shumilovskikh *et al.* 2016). An OSL date (413-3.8) obtained from the lowermost alluvial deposit produced a Parthian/early Sasanian date (170 BC - 230 AD). Whether this deposit relates to an early irrigation system that had failed, or was formed by natural flooding, remains unclear. Thus requiring more extensive geoarchaeological investigations of the surrounding areas to determine major depositional events. Despite this, the evidence available from the canal suggests that any sudden landscape intensification may have triggered short term flooding events in the lowland plain, but could have also been triggered by more regional climatic events in the Kura Basin (Naderi Beni *et al.* 2013). Climate and environmental change have caused intensive flooding in the Kura River Basin in modern times, as silts enter the riverbed via three sources: during periods of high Caspian Sea levels, intensive rainfall, and snowmelt from the mountains (Abbasov & Mahmudov 2009). Other drivers relate to anthropogenic impacts on the modern landscape such as land use modification, deforestation and erosion (*ibid.*), both local climate and anthropogenic factors would have also influenced flooding of the Kura River in the past. Excavations at Ultan Qalasi in the Mughan Steppe in Azerbaijan recovered a radiocarbon date that indicated a mid-5th century AD date obtained from the lowermost levels of the mudbrick foundations

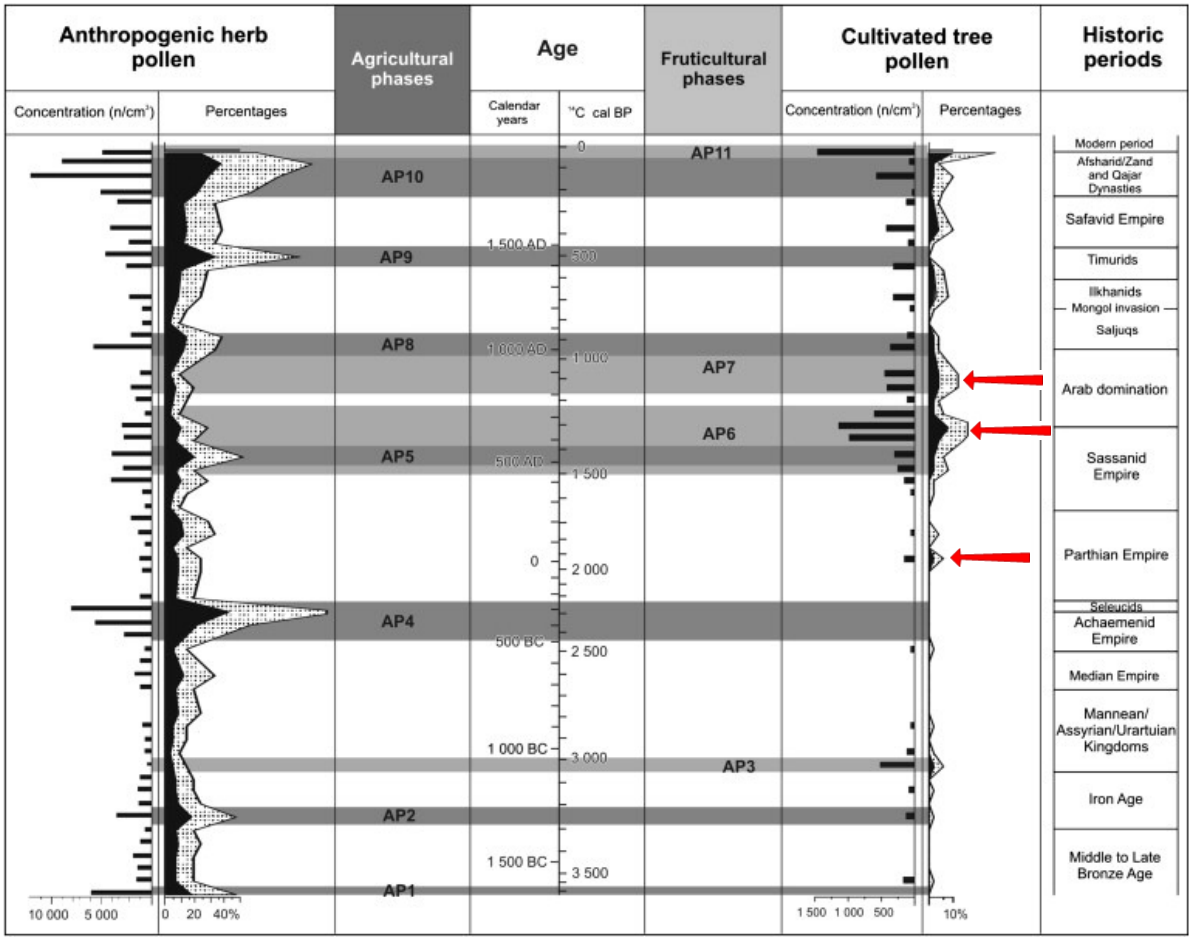

Figure 7.3. Palaeoenvironmental records from Lake Almalou, NW Iran, showing key phases of increased cultivated tree pollen (adapted from Djamali *et al.* 2009; Fig. 5). The location of the core is illustrated in Fig. 7.4.

(Alizadeh 2011). Overlying these deposits were extensive fluvial sand deposits that were indicative of a major avulsion event of the nearby Aras River, supporting that this region of Azerbaijan was prone to flooding in the past.

From state to local investment in the landscape

The canal was constructed broadly from 165 to 655 AD (OSL sample: 413-1.3), which corresponds to the Late Sasanian/Early Islamic period, and was subsequently maintained into the Middle Islamic period (7^{th} - 10^{th} centuries AD) (OSL samples: 413-1.6.1, 413-1.8.2, 413-2.1.1). The canals were also highly sensitive to climate change, as observed in modern irrigation networks in the region (Abbasov & Mahmudov 2009). In the 5^{th} century AD, the Caspian Sea was at a low stand (Karpychev 2001; Hoogendoorn *et al.* 2005; Lahijani *et al.* 2009), enabling the construction of extensive walls, banks and canal systems on the Gorgān Plain (Wilkinson *et al.* 2013; 35), and this period of stability also enabled the construction of numerous forts and canal systems in the Mil and Mughan Steppe of Azerbaijan. However, by the 10^{th} Century AD, the Caspian Sea experienced multiple high-stands (Kroonenberg *et al.* 2007; Naderi Beni *et al.* 2013), which caused river avulsions in different lowlands deltas around the Caspian, e.g. Kura and Gorgān River, which are intricately connected to the wider Caspian hydrological system (Fig. 7.4).

The three OSL dates obtained from the upcast revealed that the canal system was continuously used and maintained for a significant period of time, most likely as a result of increased precipitation and decreased evaporation of the Caspian Sea (Kroonenberg *et al.* 2007). In parts of the canal upcast, frequent pollen and fragments of reeds observed in thin section supports the idea that the local environment had become wetter, requiring more frequent cleaning to ensure enough water could be diverted through the canal. This was also evident in the stratigraphic section as extensive tipping layers were found in the upcast banks, suggesting that the canal had been repeatedly cleaned.

Although this is a period when the steppe was dominated by a pastoral economy, due to the expansion of grassland due to increased humidity widely reported for this period (Büntgen *et al.* 2011), Kurdish and Turkish nomadic groups most likely coexisted with local sedentary farmers, as illustrated by the extensive evidence for nomadic settlement at the northern frontiers (Alizadeh & Ur 2007; Stride *et al.* 2009). The continued reuse of the canal suggests that after the demise of the Sasanian Empire, local elites were able to take control of the old systems and continued to benefit from them. Mobile groups most likely continued to benefit from these as they required regular access to water and pastureland for livestock. Increasing evidence for the reuse of Sasanian canals into the Early Islamic period has also been found at Ultan Qalasi in the Mughan Steppe, Azerbaijan (Alizadeh *et al.* 2004), and also the major canal systems that ran through Sultan Kala, a major Early Islamic city established at Merv (Williams 2007), all of which

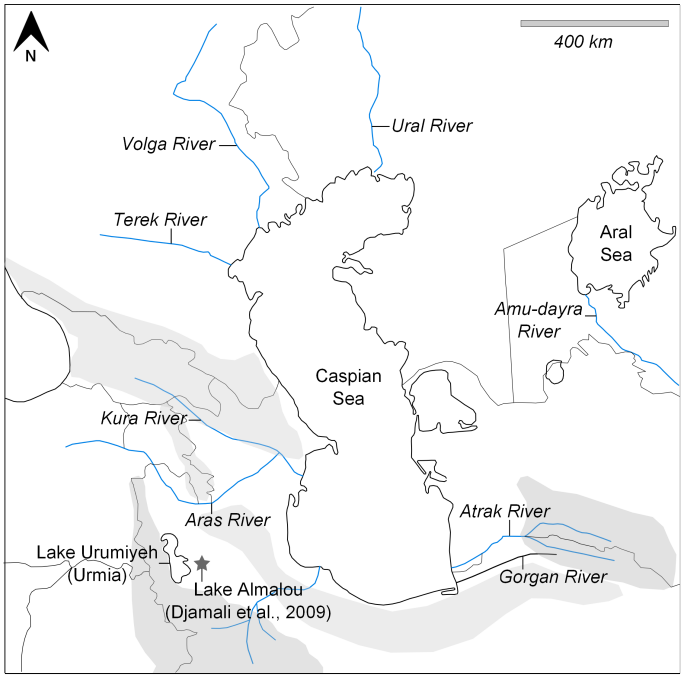

Figure 7.4. Transcaspian hydrological system showing the main river networks that supply water to the Caspian Sea. Shaded regions indicate highland regions. (Adapted from Naderi Beni *et al.* 2013).

had Islamic names (Kennedy 1999). However, further investigation into the chronology of these systems is required to enable cross-correlation between irrigation systems found in different regions.

In conclusion, the canal system located within close proximity to Ören Qal'eh, Azerbaijan, shows clear evidence for continued re-use into the Early Islamic period, suggesting that irrigation was important for the economy even after the demise of the Sasanian Empire, ensuring the continuation of trade, exchange and movement continued across the steppe. This evidence also has broader implications for the way in which we understand the fall of empires. It has been suggested that the LALIA was a major trigger for the the collapse of the Sasanian Empire (Büntgen *et al.* 2016). However, the chronostraigraphic evidence from the canal suggests that climate change was not necessarily the trigger for the empire's ultimate decline. Instead, the evidence suggests that the Sasanians were able to adapt to changing climate and local environmental conditions in the Transcaspian region. Canal sediments are ideal proxies for understanding landscape change linked to control and power. The continued use of the canal also suggests that the shift in political power was most probably a gradual process, rather than an abrupt change such as those commonly linked to societal collapse (Diamond 2005). Therefore, social, political and economic aspects linked to irrigation and agriculture most probably

continued in regions that were already effectively managed and remained productive, despite the continuous risks associated with aggricultural intensification during this period.

Canal destruction and political instability

The final phase of major landscape change recorded in the canal system comes from the extensive fill deposits associated with destruction/abandonment events. Two OSL dates were obtained, one was from the 13th century AD (OSL sample: 413-3.6.1). The first phase of canal fill showed evidence for significant reworking of the canal bank that appeared to be mixed with deposits that were fluvially deposited, suggesting a return to wet conditions resulting in the erosion of the canal banks. Whether the canal was abandoned during major depopulation of the steppe, or the destruction of local elites during mass invasions of the steppe in the 13th century AD by the Mongols (Fletcher 1986), is difficult to answer from one sedimentary sequence. Significant avulsions of the Amu-Darya, which runs through the desert plains of Turkmenistan into Uzbekistan, also occurred in the 13th century AD (Boroffka *et al.* 2006; Oberhänsli *et al.* 2007). This was supported by salinity proxy records (diatoms) which revealed increased freshwater input into the Aral Sea in 1220 AD due to river avulsions of the Amu-Darya River (Austin *et al.* 2007; Boomer *et al.* 2009). The destruction of major dams resulting in significant hydrological change of the Amu-Dayra was linked to the Mongol invasion, and is likely to be one cause for flooding events observed in the canal sequence in the Mil Steppe.

Although the Mongols were renowned for causing large-scale destruction and disruption during a series of raids in the 13th century AD (Oberhänsli *et al.* 2007), our understanding of the scale of destruction remains unclear without further excavation. It is likely that the initial raids were highly destructive on the landscape (Clarke *et al.* 2005), but after a period of stability, settlements were under direct control by taxation regimes (Christian 2018; 37). In summary, canal sequences can provide indirect evidence for the destructive and in destructive effects of the Mongols in the wider landscape, as the disruption of the local socio-political system meant that canals were no longer maintained.

Eventually the region regained stability between 1491 and 1736 AD during the Safavid dynasty (Bosworth 1989). The second OSL date obtained from phase two was dated to the 16th and 17th Centuries AD (OSL sample: 413-3.3). Alternating phases of drying and wetting were identified, suggesting that the landscape had become increasingly arid and less favorable for irrigation, resulting in the eventual abandonment of the canal system. This is supported by variations in Caspian Sea levels, low-stands during the 'Medieval Climate Anomaly' (MCA) and high-stands during the Little Ice Age (LIA) (Kroonenberg *et al.* 2007; Naderi Beni *et al.* 2013), which would have had a significant impact on the wider hydrological regime of the Transcaspian region, and

thus a direct effect on local irrigation networks.

Summary

In summary, large-scale canal systems provide a long record for human-environment interactions in marginal environments. The OSL dates enabled key phases of anthropogenic activity to be identified, and that canals provide a proxy for socio-political complexity in the steppe region. The results revealed a long and complex history, suggesting that canals were modeled on top of old irrigation systems that were continuously reused, altered and adapted to suit the changing environments and hydrology.

Furthermore, the long period of canal use raises important questions regarding the chronological resolution of nearby sites used to date landscape features by association. To further develop multiscale methodologies, the systematic excavation of sites, combined with absolute dating and the recovery of *in situ* diagnostic artefacts, would significantly improve our understanding of the size and scale of occupation and landscape investment in regions that have been intensively occupied.

Water-control features at Fulayj, Oman

The deflated landscape of the Batinah Coast of Oman introduced a different set of methodological challenges, here landscape features were on a much smaller scale and were well-preserved on the ground surface. Archaeological investigations at Fulayj Fort provided a well-constrained chronostratigraphic sequence, that enabled four main phases of occupation to be identified that could be used to link landscape features with key phases of activity, these include; Iron Age (1300-300 BC); Sasanian (early 5^{th} - mid 6^{th} centuries AD); Early Islamic (9^{th} - 13^{th} centuries AD); and a Late Islamic phase (17^{th} - 19^{th} centuries AD). Considering its relatively small scale, the fort was intensively occupied, particularly from the Late Sasanian to the Early Islamic period. A wider landscape survey combined with small-scale excavation revealed a complex network of surface channels, *falaj* (or qanats), and fields, however, their chronology and relationship to the fort was difficult to ascertain from the ground. The OSL dating results for the channels are provided in Table 7.4. The pottery retrieved from the deposits associated with the channel construction and abandonment fill were broadly Iron Age in date. However, the OSL dates obtained from the channels were significantly more recent and were contemporary in date (1350 - 1470 AD) (OSL samples: 426-2.3 -3.8). This has implications for dating methodologies applied to channels, supporting that relative chronologies should be considered within their depositional contexts and that in most cases, artefacts are reworked from older deposits and used in the construction of surface channels. Both channels were lined with waterproof plaster. An OSL date (426-2.2) from plaster obtained from one of the channels was contemporary with the construction date

Sample	OSL date (AD)	$\pm\sigma_a$
426-2.2	1385	45
426-2.4	1410	55
426-3.2	1080	70
426-3.6	1540	35
426-3.8	1410	30

Table 7.4. OSL dates for the water-control features, Fulayj Fort, Oman.

(1340 - 1430 AD), and the ceramic material used in the second channel was significantly older (1010 - 1150 AD) (426-3.2), suggesting the reuse of residual ceramic to reinforce the channel.

The chronological significance of these dates suggests that the channels were constructed during the fourth phase of occupation of the fort during the Late Islamic period (15^{th} and 16^{th} centuries AD). Small-scale camps and pits excavated into Sasanian/Early Islamic levels suggests that the fort had changed function. In earlier periods, it was primarily used for defense and trade, and a relatively small garrison could be supplied with resources from the coast. The lack of evidence for irrigation infrastructure constructed during the Sasanian period may also relate to a hyperarid event, as indicated in speleothem records (Fleitmann *et al.* 2003; 2007), where conditions were less favorable for agricultural intensification. After the abandonment phase between the late 6^{th} - 7^{th} centuries AD, the fort went into disrepair and any small-scale farming systems were subsequently abandoned.

The fort and surrounding area did not appear to be intensively occupied again until the Early Islamic period. This sudden reoccupation of the site may link with a wider mining settlement network such as that found at Arja, an Early Islamic settlement located close to copper resources (Costa & Wilkinson 1987; 93). This evidence suggests there was a possible shift in occupation to other settlement areas on the Batinah Coast to exploit other available natural resources during this period. As the region is rich in natural resources, these would have provided alternative resources for overland trade with other neighbouring polities. Evidence for lime processing in the immediate areas of the fort suggests that this area may have provided important natural resources for the construction of monumental architecture and water infrastructure, thus requiring water-control features required to supply sufficient amounts of water to slacking lime.

The OSL dates obtained from the small surface channels produced mid-Islamic dates, which may correspond to the lime burning activities found at the site. As found at Arja, similar channels were constructed to divert water from a nearby wadis to copper mines (*ibid.*). This supports the idea that water-control was not exclusively used for agricultural activities, but comprised a complex network of surface channels, tanks and water mills used to divert water to limestone processing areas. Lime production along with

other natural resources were important economic resources, enabling trade and exchange to develop within the Arab Kingdoms of Arabia. The construction of large fortified settlements, ports and irrigation networks found in connection with large settlements such as those in Yemen (Gibson & Wilkinson 1995; Weiss & Gerlach 2009) and in the North Eastern provinces of Arabia (Mouton 2009) demonstrates that the socio-political economy was able to function on a local scale, and for maintaining close contact and negotiations between regional groups in the Early Islamic period (Ulrich 2011).

Human adaptation to arid environments

One interesting outcome of the chronostratigraphic investigations undertaken at the fort has raised important questions regarding the role of water, industrial activities and climate in regions less suitable for agricultural intensification. There appears to be increasing evidence for social complexity and the use of lime in arid environments in various regions of the Near and Middle East, Arabia and the Mediterranean (Karkanas 2007; Goren & Goring-Morris 2008; Weiss & Gerlach 2009; Itkin *et al.* 2016), and that it was frequently used to make irrigation channels and water pools water-tight in areas which receive very little precipitation to ensure that no water was lost (Weiss & Gerlach 2009; Hadas 2012). One of the detrimental effects of lime production is the sheer volume of fuel required to burn carbonate-bearing rock (limestone) and water to slake lime (Dix 1982), which can be limited in arid environments. With regards to the channels found surrounding the fort, the construction of the water-control features did not require a large labour force, but instead, required significant labour to source sufficient volumes of fuel to burn raw limestone. This industrial process would have ultimately caused significant landscape degradation (Miller 1990; 71). The widespread occurrence of wind-blown sand found in both the channel deposits and within various contexts uncovered at the fort, suggests localised landscape and environmental degradation. Charred plant remains from early Islamic levels within the fort revealed a predominance of drought tolerant trees such as Acacia, along with various low-lying shrubs. Charcoal remains of various wood species indicated that wood originated from the foothills and mountains, suggesting that the coastal plain lacked suitable wood resources for fuel. From the early Islamic period, it is likely that the local environment was dry with very little vegetation cover, however, further investigations are required to fully understand the local environmental conditions in the region.

The predominance of a wind-blown component within the early Islamic layers of the fort and within channel deposits dated to the 15th century AD, also supports this being a period of aridity. Sediments are easily remobilised on the plain where there is only sparse vegetation, creating a deflated landscape similar to that found today. The increase in wind-blown sediment may also indicate regional environment and climate change. Recently published climate change records covering the last 2000 years have

revealed distinct shifts in aridity and precipitation affecting regions closely connected to the Gulf of Oman. Between the 9th and 15th centuries AD, this period was affected by the MCA, as indicated by desert and semi-desert plant taxa and an increase in sedimentation into the sea. During the LIA, 13th to 15th centuries AD, a shift in desert vegetation to grassland was observed in the pollen records, suggesting slightly wetter conditions, which coincides with the archaeological data at Fulayj Fort from Phase 4. The construction of the two channels during the 15th century AD may reflect this transition from dry to wetter conditions, resulting in a reactivation of wadi systems and an increasing need for surface runoff.

Summary

In summary, the landscape surrounding the fort represents a landscape palimpsest, where small-scale agriculture and industrial activities occurred simultaneously. These two landscape components were difficult to separate on the ground, and could only be resolved through absolute dating, which could place these features within the regional chronology in order to relate the site within the wider Batinah Plain. Further survey, excavation and sampling would enhance our understanding of the complex but well-preserved archaeological landscape.

7.5.2 Future developments

The OSL dates obtained in this study has enable certain landscape features to be placed within their wider archaeological context, confirming that this is an invaluable technique for dating complex landscape structures, particularly in contexts where material short lived organic remains have been reworked or were absent. However, in order to understand the scale and extent of irrigation and landscape intensification within a particular time period, multiple features and irrigation structures need to be examined, particularly in regions where wind-blown sediment is prevalent. OSL analysis combined with microstratigraphic analysis can also provide not only details regarding natural and anthropogenic site-formation processes, but also reveal subtle variations in local environmental change. During this research, it become increasingly obvious that there is a general lack of detailed local and regional palaeoenvironmental records available covering the last 2000 years within the regions investigated. Those that are currently available, are generally disconnected from the archaeological record, resulting in inaccuracies regarding the timing and extent of climate variability and its impact on societies in the past. In order to understand the role of irrigation and landscape management practices, it is important to be aware of the local environmental conditions. Furthermore, the sites and landscapes used in this study have revealed a methodological gap with regards to the integration of environmental archaeology applied to off-site and on-site analysis.

Therefore, future methodological developments for understanding landscape features located in marginal environments would benefit from the integration of ethnoarchaeology, phytolith studies (particularly in arid environments where archaeobotanical remains are generally poorly preserved), and hydrological modelling.

Chapter 8
Summary and conclusions

The overarching aim of this thesis was to develop luminescence and geoarchaeological methods applied to ancient landscape features identified in the arid and semi-arid environments of the northern and southern frontier regions of the Sasanian Empire. An overview of the social, political, military and religious aspects of the Sasanian Empire was provided in Chapter 1. This was necessary to set the research context, as the varied landscapes and environments encountered during the expansion period introduced further complexities into how landscapes were utilised. Chapter 2 introduced the physical and environmental background of the various types of landscape features identified in the field and the main dating methods widely employed were reviewed. The two most widely employed methods in landscape archaeology are: 'dating by association' and diagnostic artefacts recovered from the ground surface. Radiocarbon dating of organic remains is a common method for dating fields and terrace systems, but a number of studies have shown that ^{14}C dates can show a chronological reversing as a result of the erosion and redeposition of reworked organic remains from upslope. This is also problematic for diagnostic artefacts, however, the variability in the assemblage and level of abrasion can provide some insights as to how much sediment reworking occurred prior to deposition. Alternatively, OSL dating is another method employed in other regions for dating channels, canals, qanats and also terraces, but the success was variable depending on the geology, sediment source and also the site-formation processes. These three issues were addressed further in Chapter 3 which provided the background and methodological approach. As addressed in Chapter 2, very few studies have combined OSL dating with geoarchaeology, particularly micromorphological analysis, which is essential to place absolute dates within their stratigraphic context. This was the approach taken in this research, particularly for the identification of bioturbation and sample heterogeneity. The latter is important for the successful and routine application of OSL dating to archaeological contexts, which are generally composed of many natural and anthropogenic components, making the assessment and interpretation of luminescence results highly complex. A geoarchaeological assessment was provided for the landscape features investigated in the various regions presented in Chapter 4, and this was an

essential first step prior to undertaking the full luminescence dating procedure. In the following section a summary of the main findings will be provided for each case study explored.

In the Dariali Gorge, Georgia, the upland alpine landscape was mainly dominated by terracing constructed as a response to slope instability and the demand for more pasturland. In most cases, the terraces were well preserved at higher altitudes than those lower down near the floodplain. Two different terraces were investigated, one that formed gradually and another that formed more rapidly in an area that was intensively occupied. Further to the north, the fortified settlement of Dariali Fort was intensively occupied, as demonstrated by the deep and complex stratigraphy. The radiocarbon chronology from this site demonstrated that the site was re-occupied on several occasions, suggesting that it was strategically important for a long period of time. Whether this military investment at fortified sites was more important than the agricultural economy, was unclear without absolute dating to determine the chronological connection between sites and nearby landscape features such as terraces.

The Mil Steppe in Azerbaijan was very different in terms of the landscape geomorphology, hydrology and climate, which enabled complex a network of irrigation system to be established. In this area, several fortified sites were constructed along with several primary and secondary canals that could be easily identified in satellite imagery. The landscape resembled that found in the Gorgān Plain, northeast Iran, however, no extensive walls were constructed suggesting that landscape investment was mainly focused on agricultural intensification. The geoarchaeological assessment of the canal system revealed a complex stratigraphy that reflected the repeated use of the canal. Although nearby fortified sites provided a relative chronology for the canal that could be broadly dated to Late Antiquity, the deposits uncovered in the canal provided an opportunity to obtain high-resolution chronologies for different phases of the canal. Such details are not always clear on the ground, requiring the excavation to expose the underlying stratigraphy. The geoarchaeological assessment revealed that canal banks were highly complex, consisting of minerals reflecting different sediment sources and depositional histories. Furthermore, bioturbation and post-depositional disturbance was prevalent, emphasising the need to undertake a detailed geoarchaeological assessment of deposits at the microscale to select deposits most suitable for OSL dating.

Fulayj Fort on the Batinah coast of Oman was much smaller in scale compared to those located in the northern frontiers. Within the immediate area of the fort, several small channels were identified and two of these were sampled in detail. Furthermore, the chronological relationship between the fort and the channels was not clear on the ground, requiring the need for OSL dating to be applied where no organic material was found. The geoarchaeological assessment of the deposits enabled the main components to be identified that were not visible in the field. The relatively shallow nature of the deposits had implications for the preservation of the original stratigraphy, as flash

flooding and wind-erosion was prevalent. Despite this, micromorphology confirmed that the deposits below the surface were secure. Overall, the deposits in the areas were composed of carbonate-rich colluvial deposits mixed with reworked alluvium eroded from nearby sources and later deposited by aeolian processes. The identification of the aeolian component was important as well-bleached samples are generally considered to be less complex, which is important to assess prior to undertaking full OSL analysis.

In summary, the different environment and landscape features investigated in the four case studies dictated the geoarchaeological methods that could be employed. For canals, micromorphology was the most important method for identifying subtle differences between the main phases of reworked alluvial deposits uncovered in the canal. While in the context of terraces where stratigraphy was deposited vertically, bulk sedimentary techniques were sufficient to identify any variability with depth. However, in the context of channels where deposits were relatively shallow, micromorphology revealed that the sediments across the area that were captured between and behind channel walls were relatively similar (carbonate-rich with aeolian quartz). Therefore, in such situations, a detailed study of the deposits from a well-preserved channel is sufficient to assess the site-formation processes and identify any heterogeneity that may occur in other nearby channels.

The variability in the deposits uncovered in the four regions set the scene for the luminescence background presented in Chapter 5. OSL dating applied to colluvial, aeolian, fluvial and anthropogenic deposits can give variable results depending on the frequency of well-bleached quartz grains present. These different scenarios were explored further in this chapter, including a review of the procedures applied to deposits that had been poorly-bleached, especially for deposits from canals and terraces, and also for well-bleached deposits, such as aeolian quartz that found in the surface channels in Oman. For the deposits that yielded sufficient quartz, a chronostratigraphy was devised to connect the landscape features to the broader chronological context of the specific region.

One of the major findings of the OSL dating was the broad chronology that was obtained. Although the study covered vast geographical areas, and that the case studies provided targeted opportunities to determine a better chronological resolution to those widely used in landscape archaeology, the dates revealed that Sasanian landscape investment was not uniform or continuous. Only in the canal system in Azerbaijan did a firm Sasanian chronology come to light, and even in this case, most of the dates post-dated the Sasanian period, suggesting a much longer period of use. This result also has major implications for the way in which agricultural and irrigated landscapes are interpreted, especially for understanding the socio-political system attached to a particular canal network, as this example demonstrated that the canal was continued to be maintained beyond the time of Sasanian control. Therefore, these deposits provide useful achieves for socio-political change over the longue durée.

Terraces and surface channels also yielded Early and Late Medieval dates suggesting that there was no requirement for landscape modification to enhance agriculture during the Sasanian occupation. Instead, investment in maintaining trade links was considered more important in these regions. Alternatively, the dates may also reflect taphonomic biases towards the later periods of landscape occupation. Terraced landscapes are renowned for being remodelled according to the changing climate and hydrology of a region, requiring the removal of ancient collapsed terrace walls and the levelling of the land by the redistribution of large volumes of sediment on a slope.

In summary, this thesis demonstrates that the combined geoarchaeological and luminescence dating method can be successfully employed in regions where there are well-preserved landscape features. There are two main methodological themes this thesis has contributed to. Firstly, geoarchaeological investigation of landscape features enabled a detailed understanding of the human-environment interactions that can occur at a particular point in time. This has implications for landscape archaeology and the need for linking geoarchaeological archives with large site datasets. Secondly, in terms of OSL dating applications, the canal study was the first of its kind to combine micromorphology and OSL dating to a large-scale canal. With regards to developing this method for terraces and channels in areas where they are abundant, a large number of OSL dates would help to identify when shifts in landscape activity occurred. Due to time constraints, only a small number of dates were obtained in this research. Furthermore, there is potential for this combined approach to be applied to a number of terraces and channels that were identified in the landscape surveys undertaken in Georgia and Oman, and this is one area of research that could be developed further in the future.

The following section will summarise the key findings from this thesis under two main methodological themes; landscape archaeology and OSL dating applications.

1. **Landscape archaeology**

    - Variability in site preservation and visibility in the archaeological record can cause sampling biases. Landscape features with well-defined features, e.g. canal banks, are more highly visible, compared with features that are small and ephemeral, e.g. channels and field systems, requiring more intensive ground-based survey;
    - Systematic sampling strategies are difficult to implement in certain regions, and so procedures have to be adapted according to access, preservation and the stratigraphic integrity of the features identified in satellite imagery and landscape survey;
    - An understanding of the microstratigraphy is vital for sediment characterisation prior to applying routine OSL dating procedures. This is a necessary

step in order to take into account factors that may influence the evaluation of equivalent dose and also the dose-rate;

- The broad range of OSL dates obtained revealed that irrigation systems found in association with Sasanian sites cannot be reliably dated 'by association' or from surface artefacts alone, a method widely used in landscape archaeology to rapidly define the main chronological phases on the ground. Unfortunately, the OSL characteristics found in the regions investigated made the OSL dating procedure difficult and time consuming. However, in regions where a fast decay component was common, a large number of dates combined with geoarchaeological analysis is required to fully understand the chronology of complex landscapes that have been intensively utilised and altered in the past.

2. **OSL dating applications**

- The OSL sensitivity of coarse-grained quartz was significantly variable within the five regions explored. Of these regions, landscape features sampled in Georgia, Azerbaijan and Oman yielded quartz with sufficiently bright signals to evaluate the equivalent dose (D_e);
- The poor-bleaching characteristics of the contexts sampled required the testing of many aliquots to obtain a sufficient D_e dataset, thus limiting the number of OSL dates that could be obtained in this study;
- The OSL decay characteristics of quartz aliquots revealed a systematic predominance of the medium/slow decay components in samples from the Caucasus region. This may be linked to limited bleaching cycles of sediments originated from mountainous regions where quartz is derived from a mixture of sources, as revealed through CL analysis. The fast decay component was prevalent in samples obtained from channel systems in Oman, where quartz had been sufficiently sensitised during aeolian transportation;
- The initial testing of the mean lifetimes of quartz revealed that the OSL decay components originated from sufficiently stable traps - covering the chronological time periods required in this research. The OSL dates obtained from samples with dominant medium components were supported by the radiocarbon evidence obtained from the same contexts sampled at Dariali Fort.

Bibliography

Abbasov, R. & R. Mahmudov (2009). Analysis of non climatic origins of floods in the downstream part of the Kura River, Azerbaijan. *Natural hazards,* 50, 235.

Abudu, S., S. Y. Cevik, S. Bawazir, J. P. King, & C. Chunliang (2011). Vitality of ancient karez systems in arid lands: a case study in Turpan region of China. *Water History,* 3, 213.

Acabado, S. (2009). A Bayesian approach to dating agricultural terraces: a case from the Philippines. *Antiquity,* 83, 801.

Adamiec, G., R. M. Bailey, X. L. Wang, & A. G. Wintle (2008). The mechanism of thermally transferred optically stimulated luminescence in quartz. *Journal of Physics D: Applied Physics,* 41, 135503.

Adams, R. M. (1965). *Land behind Baghdad: A History of Settlement on the Diyala Plain.* Chicago: University of Chicago Press.

Adams, R. M. (1970). Tell Abū Sarīfa: A Sassanian - Islamic Ceramic Sequence from South Central Iraq. *Ars Orientalis,* 8, 87.

Adams, R. M. (1981). *Heartland of cities. Surveys of Ancient Settlement and Land Use on the Central Floodplain of the Euphrates.* Chicago: University of Chicago Press.

Adams, R. M. (2006). Intensified large-scale irrigation as an aspect of imperial policy: strategies of statecraft on the late Sasanian Mesopotamia plain. In: *Agricultural strategies.* Ed. by J. Marcus & C. Stanish. Cotsen Institute of Archaeology, UCLA, 17.

Ahmadov, Q. (1997). *Qadim Beylaqan.* Baku: Azerbaijan Dovlat Nashriyati.

Aitken, M. J. (1985). *Thermoluminescence Dating.* Academic Press, London.

Aitken, M. J. (1998). *An Introduction to Optical Dating: The Dating of Quaternary Sediments by the Use of Photon-stimulated Luminescence.* Oxford University Press.

Aitken, M. J. & B. W. Smith (1988). Optical dating: Recuperation after bleaching. *Quaternary Science Reviews,* 7, 387.

Al-Jahwari, N. S., W. S. Al-Muzini, & N. M. Al-Aghbari (2014). Results of the first season of archaeological survey 2010-2011 in Al-Fulayj area at Saham, Sultanate of Oman [in Arabic]. *Journal of Humanity Studies,* 12, 75.

Al-Tikriti, W. Y. (2002). The south-east Arabian origin of the falaj system. *Proceedings of the Seminar for Arabian Studies,* 32, 117.

Alizadeh, A., N. Kouchoukos, A. M. Bauer, T. J. Wilkinson, & M. Mashkour (2004). Human-Environment Interactions on the Upper Khuzestan Plains, Southwest Iran. Recent Investigations. *Paléorient,* 30, 69.

Alizadeh, K. (2011). Ultan Qalasi: A Fortified Site in the Sasanian Borderlands (Mughan Steppe, Iranian Azerbaijan). *Iran,* 49, 55.

Alizadeh, K. & J. A. Ur (2007). Formation and destruction of pastoral and irrigation landscapes on the Mughan Steppe, north-western Iran. *Antiquity,* 81, 148.

Allen, J. (2012). *Principles of physical sedimentology.* Springer Science & Business Media.

Andó, S., E. Garzanti, M. Padoan, & M. Limonta (2012). Corrosion of heavy minerals during weathering and diagenesis: A catalog for optical analysis. *Sedimentary Geology,* 280, 165.

Armitage, S., G. Duller, & A. Wintle (2000). Quartz from southern Africa: sensitivity changes as a result of thermal pretreatment. *Radiation Measurements,* 32, 571.

Arnold, L. & R. Roberts (2009). Stochastic modelling of multi-grain equivalent dose (D_e) distributions: Implications for OSL dating of sediment mixtures. *Quaternary Geochronology,* 4, 204.

Arnold, L., M. Demuro, & M. N. Ruiz (2012). Empirical insights into multi-grain averaging effects from 'pseudo' single-grain OSL measurements. *Radiation Measurements,* 47, 652.

Arzhantseva, I. A., I. Turova, M. Bronnikova, & E. Zazovskaya (2001). Alan settlements of the first millennium in the Kislovodsk basin. In: *One land, many landscapes. Papers from a session held at the European Association of Archaeologists Fifth Annual Meeting in Bournemouth 1999 (BAR); 987.* Ed. by T. Darvill & M Gojda. Oxford: Archaeopress, 115.

Augustsson, C. & A. Reker (2012). Cathodolumenescence spectra of quartz as provenance indicators revisited. *Journal of Sedimentary Research,* 82, 559.

Austin, P., A. Mackay, O. Palagushkina, & M. Leng (2007). A high-resolution diatom-inferred palaeoconductivity and lake level record of the Aral Sea for the last 1600Â yr. *Quaternary Research,* 67, 383.

Avni, G., N. Porat, & Y. Avni (2013). Byzantine-Early Islamic agricultural systems in the Negev Highlands: Stages of development as interpreted through OSL dating. *Journal of Field Archaeology,* 38, 332.

Avni, Y., N. Porat, & G. Avni (2012). Pre-farming environment and OSL chronology in the Negev Highlands, Israel. *Journal of Arid Environments* 86, 12.

Bailey, R. M. (2000). The slow component of quartz optically stimulated luminescence. *Radiation Measurements,* 32, 233.

Bailey, R. M. & L. J. Arnold (2006). Statistical modelling of single grain quartz D_e distributions and an assessment of procedures for estimating burial dose. *Quaternary Science Reviews,* 25, 2475.

Bailey, R. M., B. W. Smith, & E. J. Rhodes (1997). Partial bleaching and the decay form characteristics of quartz OSL. *Radiation Measurements,* 27, 123.

Bailey, R. M., J. S. Singarayer, S. Ward, & S. Stokes (2003). Identification of partial resetting using D_e as a function of illumination time. *Radiation Measurements,* 37, 511.

Bailiff, I. K. (2006). Development of single grain OSL dating of ceramic materials: Spatially resolved measurement of absorbed dose. *Radiation Measurements* 41, 744.

Bailiff, I. K. & V. Mikhailik (2003). Spatially-resolved measurement of optically stimulated luminescence and time-resolved luminescence. *Radiation Measurements,* 37, 151.

Bailiff, I. K. & M. J. Tooley (2000). Luminescence dating of fine-grain Holocene sediments from a coastal setting. *Geological Society, London, Special Publications,* 166, 55.

Bailiff, I. K., S. Bowman, S. Mobbs, & M. J. Aitken (1977). The phototransfer technique and its use in thermoluminescence dating. *Journal of Electrostatics,* 3, 269.

Bailiff, I. K., C. Gerrard, A. Gutiérrez, L. Snape-Kennedy, & K. Wilkinson (2015). Luminescence dating of irrigation systems: Application to a qanat in Aragón, Spain. *Quaternary Geochronology,* 30, 452.

Bailiff, I. (1982). Beta-TLD apparatus for small samples. In: *PACT*. Vol. 6, 72–76.

Ball, D. F. (1964). Loss-on-ignition as an estimate of organic matter and organic carbon in non-calcareous soils. *Journal of Soil Science,* 15, 84.

Ballarini, M., J. Wallinga, A. Wintle, & A. Bos (2007). A modified SAR protocol for optical dating of individual grains from young quartz samples. *Radiation Measurements,* 42, 360.

Banaji, J. (2002). *Agrarian Change in Late Antiquity: Gold, Labour, and Aristocratic Dominance: Gold, Labour, and Aristocratic Dominance*. Oxford University Press.

Banerjea, R. Y., M. Bell, W. Matthews, & A. Brown (2015). Applications of micromorphology to understanding activity areas and site formation processes in experimental hut floors. *Archaeological and Anthropological Sciences,* 7, 89.

Banning, E. B. (2002). *Archaeological survey*. Springer Science & Business Media.

Barker, G., D. Gilbertson, & D. J Mattingly (2007). *Archaeology and Desertification: the Wadi Faynan Landscape Survey, southern Jordan*. Oxbow Books, Oxford.

Bateman, M. D., C. D. Frederick, M. K. Jaiswal, & A. K. Singhvi (2003). Investigations into the potential effects of pedoturbation on luminescence dating. *Quaternary Science Reviews,* 22, 1169.

Bateman, M. D., C. H. Boulter, A. S. Carr, C. D. Frederick, D. Peter, & M. Wilder (2007a). Detecting post-depositional sediment disturbance in sandy deposits using optical luminescence. *Quaternary Geochronology,* 2, 57.

Bateman, M. D., C. H. Boulter, A. S. Carr, C. D. Frederick, D. Peter, & M. Wilder (2007b). Detecting post-depositional sediment disturbance in sandy deposits using optical luminescence. *Quaternary Geochronology,* 2, 57.

Beaudoin, A. (2003). A comparison of two methods for estimating the organic content of sediments. *Journal of Paleolimnology,* 29, 387.

Beaumont, P. (1971). Qanat systems in Iran. *Hydrological Sciences Journal,* 16, 39.

Beaumont, P. (1972). Alluvial fans along the foothills of the Elburz Mountains, Iran. *Palaeogeography, Palaeoclimatology, Palaeoecology,* 12, 251.

Beaumont, P., M. E. Bonine, & K. S. McLachlan (1989). *Qanat, Kariz, and Khattara: traditional water systems in the Middle East and North Africa.* Wisbech, Cambridgeshire, MENAS Press.

Bebermeier, W, F Schlütz, & A Goren (2010). Ancient and modern landscape along the Qaracay and Masavera valleys-first results. *Ancient Kura* 2011, 145.

Beckers, B., J. Berking, & B. Schütt (2013). Ancient water harvesting methods in the drylands of the Mediterranean and Western Asia. *Journal for Ancient Studies,* 2, 145.

Bell, W. T. (1979). Attenuation factors for the absorbed radiation dose in quartz inclusions for thermoluminescence dating. *Ancient TL,* 8, 12.

Bell, W. T. (1980). Alpha dose attenuation in quartz grains for thermoluminescence dating. *Ancient TL,* 12, 8.

Benoist, A., M. Mouton, & J. Schiettecatte (2003). The artefacts from the fort at Mleiha: distribution, origins, trade and dating. In: *Proceedings of the Seminar for Arabian Studies.* Archaeopress, 59.

Berberian, M. & G. C. P. King (1981). Towards a paleogeography and tectonic evolution of Iran. *Canadian Journal of Earth Sciences,* 18, 210.

Berger, G. W., T. K. Henderson, D. Banerjee, & N. F. L. (2004). Photonic dating of prehistoric irrigation canals at Phoenix, Arizona, USA. *Geoarchaeology,* 19, 1.

Berger, G. W., P. Stephen, & W. Chris (2009). Single and multigrain quartz-luminescence dating of irrigation-channel features in Santa Fe, New Mexico. *Geoarchaeology,* 24, 383.

Berger, J.-F., J.-P. Bravard, L. Purdue, A. Benoist, M. Mouton, & F. Braemer (2012). Rivers of the Hadramawt watershed (Yemen) during the Holocene: Clues of late functioning. *Quaternary International,* 266, 142.

Bertucci, M., I. Veronese, & M. Cantone (2011). Photo-transferred thermoluminescence from deep traps in quartz. *Radiation Measurements* 46, 588.

Bevan, A., J. Conolly, S. Colledge, C. Frederick, C. Palmer, R. Siddall, & A. Stellatou (2013). The Long-Term Ecology of Agricultural Terraces and Enclosed Fields from Antikythera, Greece. *Human Ecology,* 41, 255.

Bevan, A. & J. Conolly (2011). Terraced fields and Mediterranean landscape structure: An analytical case study from Antikythera, Greece. *Ecological Modelling,* 222, 1303.

Bintliff, J. & A. Snodgrass (1988). Off-Site Pottery Distributions: A Regional and Interregional Perspective. *Current Anthropology,* 29, 506.

Bishop, P., D. C. W. Sanderson, & M. T. Stark (2004). OSL and radiocarbon dating of a pre-Angkorian canal in the Mekong delta, southern Cambodia. *Journal of Archaeological Science,* 31, 319.

Blair, M., E. Yukihara, & S. McKeever (2005). Experiences with single-aliquot OSL procedures using coarse-grain feldspars. *Radiation Measurements,* 39, 361.

Blott, S. J. & P Kenneth (2006). Particle size distribution analysis of sand-sized particles by laser diffraction: an experimental investigation of instrument sensitivity and the effects of particle shape. *Sedimentology,* 53, 671.

Boggs, S. & D. Krinsley (2006). *Application of cathodoluminescence imaging to the study of sedimentary rocks*. Cambridge University Press.

Bonde, A., A. Murray, & W. L. Friedrich (2001). Santorini: Luminescence dating of a volcanic province using quartz? *Quaternary Science Reviews,* 20, 789.

Boomer, I., B. Wünnemann, A. W. Mackay, P. Austin, P. Sorrel, C. Reinhardt, D. Keyser, F. Guichard, & M. Fontugne (2009). Advances in understanding the late Holocene history of the Aral Sea region. *Quaternary International,* 194, 79.

Boroffka, N. (2010). Archaeology and Its Relevance to Climate and Water Level Changes: A Review. In: *The Aral Sea Environment*. Ed. by A. G. Kostianoy & A. N. Kosarev. Springer Berlin Heidelberg, 283.

Boroffka, N., O. Hedi, S. Philippe, D. Francois, R. Christian, W. Bernd, A. Kamildzhan, B. Sergey, R. Kamildzhan, S. Nasbirgen, S. Timur, K. S. K., & R. Ursula (2006). Archaeology and climate: Settlement and lake-level changes at the Aral Sea. *Geoarchaeology,* 21, 721.

Bosworth, C. (1989). *Azerbaijan iv. Islamic History to 1941*. Ed. by E. Yarshater. Vol. 3. Bibliotheca Persica Press, 224–231.

Bosworth, C. E. (1983). Iran and the Arabs before Islam. In: *The Cambridge History of Iran*. Ed. by E. Yarshater. Cambridge University Press, 593–612.

Bosworth, C. E. (1999). *History of al-Tabari Vol. 5, The: The Sasanids, the Byzantines, the Lakhmids, and Yemen*. SUNY Press.

Bøtter-Jensen, L. (1997). Luminescence techniques: instrumentation and methods. *Radiation Measurements,* 27, 749.

Bøtter-Jensen, L., C. Andersen, G. Duller, & A. Murray (2003a). Developments in radiation, stimulation and observation facilities in luminescence measurements. *Radiation Measurements,* 37, 535.

Bøtter-Jensen, L., S. W. McKeever, & A. G. Wintle (2003b). *Optically stimulated luminescence dosimetry.* Elsevier.

Boucharlat, R. & O Lecomte (1987). Fouilles de Tureng Tepe sous la direction de Jean Deshayes 1. *Les periodes sassanides et islamiques, Paris,*

Bouchaud, C., M. Tengberg, & P. Dal Prà (2011). Cotton cultivation and textile production in the Arabian Peninsula during antiquity; the evidence from Madâ'in Sâlih (Saudi Arabia) and Qal'at al-Bahrain (Bahrain). *Vegetation History and Archaeobotany,* 20, 405.

Boyer, P., N. Roberts, & D. Baird (2006). Holocene environment and settlement on the Çarşamba alluvial fan, south-central Turkey: Integrating geoarchaeology and archaeological field survey. *Geoarchaeology,* 21, 675.

Brennan, B. J. (2003). Beta doses to spherical grains. *Radiation Measurements,* 37, 299.

Brennan, B. J. (2006). Variation of the alpha dose rate to grains in heterogeneous sediments. *Radiation Measurements,* 41, 1026.

Brown, A. G. (1997). *Alluvial geoarchaeology: floodplain archaeology and environmental change.* Cambridge University Press.

Bruins, H. J. (2012). Ancient desert agriculture in the Negev and climate-zone boundary changes during average, wet and drought years. *Journal of Arid Environments,* 86, 28.

Bruins, H. J. & G. Ore (2009). Runoff from loess or bedrock? Hillslope geoarchaeology of ancient runoff farming systems at Horvat Haluqim and Har Eldad in the central Negev Desert. *Israel Journal of Earth Sciences,* 57, 231.

Bulliet, R. W. (2009). *Cotton, climate, and camels in early Islamic Iran: a moment in world history.* Columbia University Press.

Bullock, P., N. Fedoroff, A. Jongerius, G. Stoops, & T. Tursina (1985). *Handbook for soil thin section description.* Waine Research.

Bulur, E. (1996). An alternative technique for optically stimulated luminescence (OSL) experiment. *Radiation Measurements,* 26, 701.

Bulur, E. (2000). A simple transformation for converting CW-OSL curves to LM-OSL curves. *Radiation Measurements,* 32, 141.

Büntgen, U. & N. Di Cosmo (2016). Climatic and environmental aspects of the Mongol withdrawal from Hungary in 1242 CE. *Scientific Reports,* 6, 25606.

Büntgen, U., W. Tegel, K. Nicolussi, M. McCormick, D. Frank, V. Trouet, J. O. Kaplan, F. Herzig, K. U. Heussner, H. Wanner, J. Luterbacher, & J. Esper (2011). 2500 Years of European Climate Variability and Human Susceptibility. *Science,* 331, 578.

Büntgen, U., V. S. Myglan, F. C. Ljungqvist, M. McCormick, N. Di Cosmo, M. Sigl, J. Jungclaus, S. Wagner, P. J. Krusic, J. Esper, J. O. Kaplan, M. A. C. De Vaan, J. Luterbacher, L. Wacker, W. Tegel, & A. V. Kirdyanov (2016). Cooling and societal change during the Late Antique Little Ice Age from 536 to around 660 AD. *Nature Geoscience,* 9, 231.

Bush, D. & J. Feathers (2003). Application of OSL single-aliquot and single-grain dating to quartz from anthropogenic soil profiles in the SE United States. *Quaternary Science Reviews,* 22, 1153.

Butzer, K. W. (1982). *Archaeology as human ecology: method and theory for a contextual approach.* Cambridge University Press.

Butzer, K. W. (2008). Challenges for a cross-disciplinary geoarchaeology: The intersection between environmental history and geomorphology. *Geomorphology,* 101, 402.

Butzer, K. W. (2012). Collapse, environment, and society. *Proceedings of the National Academy of Sciences,* 109, 3632.

Cameron, A. (2015). *The Mediterranean world in late Antiquity: AD 395-700.* Routledge.

Canepa, M. P. (2010). Technologies of Memory in Early Sasanian Iran: Achaemenid Sites and Sasanian Identity. *American Journal of Archaeology,* 114, 563.

Canti, M. (2001). What is Geoarchaeology? Re-Examining the Relationship Between Archaeology and Earth Science. In: *Environmental Archaeology: Meaning and Purpose.* Ed. by U. Albarella. Springer, 103.

Chen, R. & S. W. McKeever (1997). *Theory of Thermoluminescence and Related Phenomena.* World Scientific Publishing Co. Pte. Ltd.

Choi, J. H., A. S. Murray, C. S. Cheong, D. G. Hong, & H. W. Chang (2003). The resolution of stratigraphic inconsistency in the luminescence ages of marine terrace sediments from Korea. *Quaternary Science Reviews* 22, 1201.

Choi, J. H., G. Duller, & A. Wintle (2006). Analysis of quartz LM-OSL curves. *Ancient TL,* 24, 9.

Choksy, J. K. (1987). Zoroastrians in Muslim Iran: selected problems of coexistence and interaction during the early medieval period. *Iranian Studies,* 20, 17.

Christensen, P. (1993). *The Decline of Iranshahr: Irrigation and Environments in the History of the Middle East, 500 BC to AD 1500.* Museum Tusculanum Press.

Christian, D. (2018). *A History of Russia, Central Asia and Mongolia, Volume II: Inner Eurasia from the Mongol Empire to Today, 1260-2000.* John Wiley & Sons.

Clark-Balzan, L. & J.-L. Schwenninger (2012). First steps toward spatially resolved OSL dating with electron multiplying charge-coupled devices (EMCCDs): System design and image analysis. *Radiation Measurements,* 47, 797.

Clark, R. J. & I. K. Bailiff (1998). Fast time-resolved luminescence emission spectroscopy in some feldspars. *Radiation Measurements,* 29, 553.

Clarke, D., R. Sala, J.-M. Deom, & E. Meseth (2005). Reconstructing irrigation at Otrar Oasis, Kazakhstan, AD 800r-1700. *Irrigation and Drainage,* 54, 375.

Clarke, M. L., H. M. Rendell, L. Sanchez-Muñoz, & J. Garcia-Guinea (1997). A comparison of luminescence spectra and structural composition of perthitic feldspars. *Radiation Measurements,* 27, 137.

Connor, S. E. & E. V. Kvavadze (2009). Modelling late Quaternary changes in plant distribution, vegetation and climate using pollen data from Georgia, Caucasus. *Journal of Biogeography,* 36, 529.

Connor, S. E. & E. V. Kvavadze (2014). Environmental context of the Kura-Araxes culture. *Paléorient,* 40, 11.

Connor, S. E., I. Thomas, & E. V. Kvavadze (2007). A 5600-yr history of changing vegetation, sea levels and human impacts from the Black Sea coast of Georgia. *The Holocene,* 17, 25.

Costa, P. M. & T. J. Wilkinson (1987). The hinterland of Sohar: Archaeological surveys and excavations within the region of an Omani seafaring city. *Journal of Oman Studies,* 9, 1.

Costa, P. M. (1983). Notes on traditional hydraulics and agriculture in Oman. *World Archaeology,* 14, 273.

Coulter, L. S. (1994). Series Product Manual. *Coulter Corporation, Miami, FL,*

Courty, M. A., P. Goldberg, & R. Macphail (1989). *Soils and micromorphology in archaeology.* Cambridge, UK,

Cullen, H. M., P. B. deMenocal, S. Hemming, G. Hemming, F. H. Brown, T. Guilderson, & F. Sirocko (2000). Climate change and the collapse of the Akkadian empire: Evidence from the deep sea. *Geology,* 28, 379.

Cumberland, S. A., G. Douglas, K. Grice, & J. W. Moreau (2016). Uranium mobility in organic matter-rich sediments: A review of geological and geochemical processes. *Earth-Science Reviews,* 159, 160.

Cunningham, A. C. & J. Wallinga (2009). Optically stimulated luminescence dating of young quartz using the fast component. *Radiation Measurements,* 44, 423.

Cunningham, A. C. & J. Wallinga (2010). Selection of integration time intervals for quartz OSL decay curves. *Quaternary Geochronology,* 5, 657.

Curie, D (1960). *Luminescence in crystals.* New York, Wiley.

Daryaee, T. (2003). The Persian Gulf in Late Antiquity. *Journal of World History,* 14, 1.

Daryaee, T. (2009). *Sasanian Persia : the rise and fall of an empire.* London; New York, I.B. Tauris : In association with the Iran Heritage Foundation.

Daryaee, T. (2010). Bazaars, Merchants, and Trade in Late Antique Iran. *Comparative Studies of South Asia, Africa and the Middle East,* 30, 401.

Daryaee, T. & K. Rezakhani (2016). Sasanian Empire. In: *The Encyclopedia of Empire.* American Cancer Society, 1–8.

David, B., R. G. Roberts, J. Magee, J. Mialanes, C. Turney, M. Bird, C. White, L. K. Fifield, & J. Tibby (2007). Sediment mixing at Nonda Rock: investigations of stratigraphic integrity at an early archaeological site in northern Australia and implications for the human colonisation of the continent. *Journal of Quaternary Science,* 22, 449.

Davidovich, U., N. Porat, Y. Gadot, Y. Avni, & O. Lipschits (2012). Archaeological investigations and OSL dating of terraces at Ramat Rahel, Israel. *Journal of Field Archaeology,* 37, 192.

De Cardi, B., C. Vita-Finzi, & A. Coles (1975). Archaeological Survey in Northern Oman, 1972. *East and West,* 25, 9.

De Klerk, P., A. Haberl, A. Kaffke, M. Krebs, I. Matchutadze, M. Minke, J. Schulz, & H. Joosten (2009). Vegetation history and environmental development since ca 6000 cal yr BP in and around Ispani 2 (Kolkheti lowlands, Georgia). *Quaternary Science Reviews,* 28, 890.

Deák, J., A. Gebhardt, H. Lewis, M. R. Usai, & H. Lee (2017). *Soils disturbed by vegetation clearance and tillage*, 233.

Dearing, J. (1994). Using the Bartington MS2 system. In: *Environmental magnetic susceptibility.* Kenilworth, Chi. Publ.

Decker, M. J. (2009). Plants and progress: rethinking the Islamic agricultural revolution. *Journal of World History,* 20, 187.

Decker, M. J. (2017). Approaches to the environmental history of Late Antiquity, part 1: The rise of Islam. *History Compass,* 15.

Deer, W. A., R. A. Howie, W. S. Wise, & J. Zussman (1963). *Rock-forming minerals. Vol. 4B, Framework silicates: silica minerals, feldspathoides and the zeolites.* Geological Society.

Desruelles, S., E. Fouache, W. Eddargach, C. Cammas, J. Wattez, T. Beuzen-Waller, C. Martin, M. Tengberg, C. Cable, C. Thornton, & A. Murray (2016). Evidence for early irrigation at Bat (Wadi Sharsah, northwestern Oman) before the advent of farming villages. *Quaternary Science Reviews,* 150, 42.

Diamond, J. (2005). *Collapse: How societies choose to fail or succeed.* Penguin.

Dietrich, R. V. & B. J. Skinner (1979). *Rocks and rock minerals.* John Wiley & Sons, Inc.

Dignas, B. & E. Winter (2007). *Rome and Persia in late antiquity: neighbours and rivals.* Cambridge University Press.

Dix, B. (1982). The manufacture of lime and its uses in the western Roman provinces. *Oxford Journal of Archaeology,* 331.

Djamali, M., J.-L. de Beaulieu, M. Shah-hosseini, V. Andrieu-Ponel, P. Ponel, A. Amini, H. Akhani, S. A. Leroy, L. Stevens, H. Lahijani, & S. Brewer (2008). A late Pleistocene long pollen record from Lake Urmia, NW Iran. *Quaternary Research,* 69, 413.

Djamali, M., J.-L. de Beaulieu, V. Andrieu-Ponel, M. Berberian, N. F. Miller, E. Gandouin, H. Lahijani, M. Shahr-Hosseini, P. Ponel, M. Salimian, & F. Guiter (2009). A late Holocene pollen record from Lake Almalou in NW Iran: evidence for changing land-use in relation to some historical events during the last 3700 years. *Journal of Archaeological Science,* 36, 1364.

Djamali, M., P. Ponel, V. Andrieu-Ponel, J.-L. de Beaulieu, F. Guibal, N. F. Miller, E. Ramezani, M. Berberian, H. Lahijani, & R. Lak (2010). Notes on Arboricultural and Agricultural Practices in Ancient Iran based on New Pollen Evidence. *Paléorient,* 36, 175.

Downing, T. E. & M. Gibson (1974). *Irrigation's Impact on Society.* University of Arizona Press, Tucson.

Duller, G. A. T. (1991). Equivalent dose determination using single aliquots. *International Journal of Radiation Applications and Instrumentation. Part D. Nuclear Tracks and Radiation Measurements,* 18, 371.

Duller, G. A. T. (1994). Luminescence dating of poorly bleached sediments from Scotland. *Quaternary Science Reviews,* 13, 521.

Duller, G. A. T. (1995). Luminescence dating using single aliquots: Methods and applications. *Radiation Measurements,* 24, 217.

Duller, G. A. T. (2003). Distinguishing quartz and feldspar in single grain luminescence measurements. *Radiation Measurements,* 37, 161.

Duller, G. A. T. (2006). Single grain optical dating of glacigenic deposits. *Quaternary Geochronology,* 1, 296.

Duller, G. A. T. (2007). Assessing the error on equivalent dose estimates derived from single aliquot regenerative dose measurements. *Ancient TL,* 25, 15.

Duller, G. A. T. (2008a). Single-grain optical dating of Quaternary sediments: why aliquot size matters in luminescence dating. *Boreas,* 37, 589.

Duller, G. A. T. (2008b). *Luminescence Dating: guidelines on using luminescence dating in archaeology.* English Heritage.

Duller, G. A. T. & L. Bøtter-Jensen (1997). Optically stimulated luminescence emission spectra from feldspars as a function of sample temperature. *Radiation Measurements,* 27, 145.

Duller, G. A. T. & A. S. Murray (2000). Luminescence dating of sediments using individual mineral grains. *Geologos,* 5.

Duller, G. A. T., L. Bøtter-Jensen, & B. G. Markey (1997). A luminescence imaging system based on a CCD camera. *Radiation Measurements,* 27, 91.

Duller, G. A. T., L. Bøtter-Jensen, P. Kohsiek, & A. Murray (1999). A High-Sensitivity Optically Stimulated Luminescence Scanning System for Measurement of Single Sand-Sized Grains. *Radiation Protection Dosimetry,* 84, 325.

Durcan, J. A. & G. A. Duller (2011). The fast ratio: a rapid measure for testing the dominance of the fast component in the initial OSL signal from quartz. *Radiation Measurements,* 46, 1065.

Eastwood, W. J., N. Roberts, & H. F. Lamb (1998). Palaeoecological and archaeological evidence for human occupance in southwest Turkey: the Beyşehir occupation phase. *Anatolian Studies,* 48, 69.

Ehrich, R. W. (1992). *Chronologies in old world archaeology.* University of Chicago Press.

English, P. W. (1968). The Origin and Spread of Qanats in the Old World. *Proceedings of the American Philosophical Society,* 112, 170.

Eriksson, M. G., J. M. Olley, & R. W. Payton (2000). Soil erosion history in central Tanzania based on OSL dating of colluvial and alluvial hillslope deposits. *Geomorphology,* 36, 107.

Evans, M. & F. Heller (2003). *Environmental magnetism: principles and applications of enviromagnetics*. Academic press.

Fahimi, H. (2010). An Iron Age fortress in central Iran: archaeological investigations in Shamshirgah, Qom, 2005. Preliminary report. In: *Proceedings of the 6th International Congress on the Archaeology of the Ancient Near East*. Vol. 5, 165–83.

Fattahi, M. (2015). OSL dating of the Miam Qanat (KĀRIZ) system in NE Iran. *Journal of Archaeological Science,* 59, 54.

Fattahi, M. & S. Stokes (2003). Dating volcanic and related sediments by luminescence methods: a review. *Earth-Science Reviews,* 62, 229.

Fattahi, M., A. Aqazadeh, R. T. Walker, M. Talebian, R. A. Sloan, & M. M. Khatib (2011). Investigation on the Potential of OSL for Dating Qanat in the Dasht-e Bayaz Region of Northeastern Iran Using the SAR Protocol for Quartz. *Journal of Seismology and Earthquake Engineering,* 13, 65.

Feathers, J. K. (2003). Use of luminescence dating in archaeology. *Measurement Science and Technology,* 14, 1493.

Fei, J., J. Zhou, & Y. Hou (2007). Circa a.d. 626 volcanic eruption, climatic cooling, and the collapse of the Eastern Turkic Empire. *Climatic Change,* 81, 469.

Finch, A. A. & J. Klein (1999). The causes and petrological significance of cathodoluminescence emissions from alkali feldspars. *Contributions to Mineralogy and Petrology* 135, 234.

Fitzsimmons, K. E., E. J. Rhodes, & T. T. Barrows (2010). OSL dating of southeast Australian quartz: A preliminary assessment of luminescence characteristics and behaviour. *Quaternary Geochronology,* 5. 12th International Conference on Luminescence and Electron Spin Resonance Dating (LED 2008), 91.

Fleitmann, D., S. J. Burns, M. Mudelsee, U. Neff, J. Kramers, A. Mangini, & A. Matter (2003). Holocene Forcing of the Indian Monsoon Recorded in a Stalagmite from Southern Oman. *Science,* 300, 1737.

Fleitmann, D., S. J. Burns, A. Mangini, M. Mudelsee, J. Kramers, I. Villa, U. Neff, A. A. Al-Subbary, A. Buettner, D. Hippler, & A. Matter (2007). Holocene ITCZ and Indian monsoon dynamics recorded in stalagmites from Oman and Yemen (Socotra). *Quaternary Science Reviews,* 26, 170.

Fletcher, J. (1986). The Mongols: Ecological and Social Perspectives. *Harvard Journal of Asiatic Studies,* 46, 11.

Forte, A. M., E. Cowgill, T. Bernardin, O. Kreylos, & B. Hamann (2010). Late Cenozoic deformation of the Kura fold-thrust belt, southern Greater Caucasus. *GSA Bulletin,* 122, 465.

Frechen, M., M. Kehl, C. Rolf, R. Sarvati, & A. Skowronek (2009). Loess chronology of the Caspian Lowland in Northern Iran. *Quaternary International,* 198, 220.

Frederick, C. D. & A. Krahtopoulou (2000). Deconstructing agricultural terraces: examining the influence of construction method on stratigraphy, dating and archaeological visibility. In: *Landscape and land use in postglacial Greece.* Ed. by P. Halstead & C. Frederick. Sheffield Academic Press, 79–94.

French, C. A. I. (2003). *Geoarchaeology in action: studies in soil micromorphology and landscape evolution.* Psychology Press.

French, C. A. I. & T. M. Whitelaw (1999). Soil erosion, agricultural terracing and site formation processes at Markiani, Amorgos, Greece: The micromorphological perspective. *Geoarchaeology,* 14, 151.

Frye, R. N. (1983). The political history of Iran under the Sasanians. In: *The Cambridge History of Iran.* Ed. by W. B. Fisher. Cambridge University Press, 116–180.

Frye, R. N. (1987). Feudalism in Iran. *Jerusalem Studies in Arabic and Islam,* 9, 14.

Fuchs, M., C. Woda, & A. Bürkert (2007). Chronostratigraphy of a sediment record from the Hajar mountain range in north Oman: Implications for optical dating of insufficiently bleached sediments. *Quaternary Geochronology,* 2, 202.

Fuchs, M., M. Fischer, & R. Reverman (2010). Colluvial and alluvial sediment archives temporally resolved by OSL dating: Implications for reconstructing soil erosion. *Quaternary Geochronology,* 5, 269.

Fuks, D., O. Ackermann, A. Ayalon, M. Bar-Matthews, G. Bar-Oz, Y. Levi, A. M. Maeir, E. Weiss, T. Zilberman, & Z. Safrai (2017). Dust clouds, climate change and coins: consiliences of palaeoclimate and economy in the Late Antique southern Levant. *Levant* 49, 205.

Galbraith, R. F. (1990). The radial plot: Graphical assessment of spread in ages. *International Journal of Radiation Applications and Instrumentation. Part D. Nuclear Tracks and Radiation Measurements,* 17, 207.

Galbraith, R. F. (2005). *Statistics for fission track analysis.* CRC Press.

Galbraith, R. F. (2010). On plotting OSL equivalent doses. *Ancient TL,* 28, 1.

Galbraith, R. F. (2011). Some comments arising from Berger (2010). *Ancient TL,* 29, 41.

Galbraith, R. F. & R. G. Roberts (2012). Statistical aspects of equivalent dose and error calculation and display in OSL dating: An overview and some recommendations. *Quaternary Geochronology,* 11, 1.

Galbraith, R. F., R. G. Roberts, G. M. Laslett, & H. Y. andJ. M. Olley (1999). Optical dating of single and multiple grains of quartz from Jinmium rock shelter, Northern Australia: Part I, experimental design and statistical models. *Archaeometry,* 41, 339.

Galiatsatos, N. (2009). The Shift from Film to Digital Product: Focus on CORONA Imagery. *Photogrammetrie - Fernerkundung - Geoinformation,* 2009, 251.

Galloway, R. B. (1996). Equivalent dose determination using only one sample: Alternative analysis of data obtained from infrared stimulation of feldspars. *Radiation Measurements,* 26, 103.

Gascoyne, M. (1992). Geochemistry of the actinides and their daughters. In: *Uranium-series disequilibrium: applications to earth, marine, and environmental sciences. 2. ed.* Ed. by M. Ivanovich & R. S. Harmon. Clarendon Press, 34–61.

Gerasimova, M. & M. Lebedeva-Verba (2010). Topsoils - Mollic, Takyric and Yermic Horizons. In: *Interpretation of Micromorphological Features of Soils and Regoliths.* Ed. by G. Stoops, V. Marcelino, & F. Mees. Elsevier, 351 –368.

Gibson, M. & T. J. Wilkinson (1995). The Dhamār Plain, Yemen: A preliminary study of the archaeological landscape. *Proceedings of the Seminar for Arabian Studies,* 25, 159.

Gilliland, K., I. A. Simpson, W. P. Adderley, C. I. Burbidge, A. J. Cresswell, D. C. W. Sanderson, R. A. E. Coningham, M. Manuel, K. Strickland, P. Gunawardhana, & G. Adikari (2013). The dry tank: development and disuse of water management infrastructure in the Anuradhapura hinterland, Sri Lanka. *Journal of Archaeological Science,* 40, 1012.

Gillmore, G. K., R. A. E. Coningham, H. Fazeli, R. L. Young, M. Magshoudi, C. M. Batt, & G. Rushworth (2009). Irrigation on the Tehran Plain, Iran: Tepe Pardis - The site of a possible Neolithic irrigation feature? *CATENA,* 78, 285.

Glick, T. F. (1970). *Irrigation and society in medieval Valencia.* Belknap, Cambridge.

Godfrey-Smith, D. I., D. J. Huntley, & W.-H. Chen (1988). Optical dating studies of quartz and feldspar sediment extracts. *Quaternary Science Reviews,* 7, 373.

Göksu, H. Y., I. K. Bailiff, L. Bøtter-Jensen, L. Brodski, G. Hütt, & D. Stoneham (1995). Interlaboratory beta source calibration using TL and OSL on natural quartz. *Radiation Measurements,* 24, 479.

Goldberg, P. & R. I. Macphail (2003). Short contribution: Strategies and techniques in collecting micromorphology samples. *Geoarchaeology,* 18, 571.

Goldberg, P. & R. I. Macphail (2006). *Practical and Theoretical Geoarchaeology.* Blacwell Science Ltd, Oxford, USA.

Goren, Y. & A. N. Goring-Morris (2008). Early pyrotechnology in the Near East: Experimental lime-plaster production at the Pre-Pottery Neolithic B site of Kfar HaHoresh, Israel. *Geoarchaeology,* 23, 779.

Götze, J. & W. Zimmerle (2000). *Quartz and silica as guide to provenance in sediments and sedimentary rocks.* Schweizerbart Science Publishers.

Götze, J., M. R. Krbetschek, D. Habermann, & D. Wolf (2000). High-Resolution Cathodoluminescence Studies of Feldspar Minerals. In: *Cathodoluminescence in Geosciences.*

Ed. by M. Pagel, V. Barbin, P. Blanc, & D. Ohnenstetter. Springer Berlin Heidelberg, 245–270.

Götze, J., M. Plötze, & D. Habermann (2001). Origin, spectral characteristics and practical applications of the cathodoluminescence (CL) of quartz – a review. *Mineralogy and Petrology,* 71, 225.

Götze, J., M. Plötze, T. Graupner, D. K. Hallbauer, & C. J. Bray (2004). Trace element incorporation into quartz: A combined study by ICP-MS, electron spin resonance, cathodoluminescence, capillary ion analysis, and gas chromatography. *Geochimica et Cosmochimica Acta,* 68, 3741.

Götze, J., M. Plötze, & T. Trautmann (2005). Structure and luminescence characteristics of quartz from pegmatites. *American Mineralogist,* 90, 13.

Götze, J., Y. Pan, M. Stevens-Kalceff, U. Kempe, & A. Müller (2015). Origin and significance of the yellow cathodoluminescence (CL) of quartz. *American Mineralogist,* 100, 1469.

Grattan, J. (2006). Aspects of Armageddon: An exploration of the role of volcanic eruptions in human history and civilization. *Quaternary International,* 151, 10.

Greilich, S. & G. A. Wagner (2006). Development of a spatially resolved dating technique using HR-OSL. *Radiation Measurements,* 41, 738.

Greilich, S., U. A. Glasmacher, & G. A. Wagner (2002). Spatially resolved detection of luminescence: a unique tool for archaeochronometry. *Naturwissenschaften,* 89, 371.

Grove, A. T. & O. Rackham (2001). *The nature of Mediterranean Europe: an ecological history.* Yale University Press.

Gudjabidze, G. & I. Gamkrelidze (2003). Geological map of Georgia, 1:500.000. *Georgian State Department of Geology and National Oil Company Saqnavtobi, Tbilisi,*

Guérin, G. & N. Mercier (2012). Preliminary insight into dose deposition processes in sedimentary media on a scale of single grains: Monte Carlo modelling of the effect of water on the gamma dose rate. *Radiation Measurements,* 47, 541.

Guérin, G., N. Mercier, & G. Adamiec (2011). Dose-rate conversion factors: update. *Ancient TL,* 29, 5.

Hadas, G. (2012). Ancient agricultural irrigation systems in the oasis of Ein Gedi, Dead Sea, Israel. *Journal of Arid Environments,* 86, 75.

Haiman, M. (2012). Dating the agricultural terraces in the southern Levantine deserts–The spatial-contextual argument. *Journal of Arid Environments,* 86, 43.

Hanauer, T., C. Pohlenz, B. Kalandadze, T. Urushadze, & P. Felix-Henningsen (2017). Soil distribution and soil properties in the subalpine region of Kazbegi; Greater Caucasus; Georgia: Soil quality rating of agricultural soils. *Annals of Agrarian Science,* 15, 1.

Harrower, M. J. (2008). Hydrology, Ideology, and the Origins of Irrigation in Ancient Southwest Arabia. *Current Anthropology,* 49, 497.

Haskell, E. H. & I. K. Bailiff (1985). Diagnostic and corrective procedures for TL analysis using the pre-dose technique. *Nuclear Tracks and Radiation Measurements (1982),* 10, 503.

Heiri, O., A. F. Lotter, & G. Lemcke (2001). Loss on ignition as a method for estimating organic and carbonate content in sediments: reproducibility and comparability of results. *Journal of Paleolimnology,* 25, 101.

Helwing, B., T. Aliyev, & A. Ricci (2012). Mounds and settlements in the lower Qarabakh-Mil Plain, Azerbaijan. In: *Tells: Social and Environmental space*. Ed. by R. Hofmann, F.-K. Moetz, & J. Müller. Proceedings of the International Workshop "Socio-Environmental Dynamics over the Last 12,000 Years: The Creation of Landscapes II (14th-18th March 2011)" in Kiel (Volume 3), 67–77.

Herrmann, G. (1997). A Central Asian city on the Silk Road: ancient and medieval Merv. *Archaeology International,* 1, 32.

Heyvaert, V. M., J. Walstra, P. Verkinderen, H. J. Weerts, & B. Ooghe (2012). The role of human interference on the channel shifting of the Karkheh River in the Lower Khuzestan plain (Mesopotamia, SW Iran). *Quaternary International,* 251. LAC 2010: 1st international conference on Landscape Archaeology, 52.

Holliday, V. T. (2004). *Soils in archaeological research*. Oxford University Press.

Honeychurch, W. (2014). Alternative Complexities: The Archaeology of Pastoral Nomadic States. *Journal of Archaeological Research,* 22, 277.

Hoogendoorn, R. M., J. F. Boels, S. B. Kroonenberg, M. D. Simmons, E. Aliyeva, A. D. Babazadeh, & D. Huseynov (2005). Development of the Kura delta, Azerbaijan; a record of Holocene Caspian sea-level changes. *Marine Geology,* 222-223, 359.

Hopkins, D. C. (1985). *The Highlands of Canaan: Agriculture Life in the Early Iron Age*. Sheffield: Almond Press.

Hourani, A. (2013). *A history of the Arab peoples: Updated edition*. Faber & Faber.

Howard-Johnston, J. (1995). The two great powers in late antiquity: A comparison. *The Byzantine and Early Islamic Near East,* 3, 157.

Howard-Johnston, J. (2006). *East Rome, Sasanian Persia and the end of antiquity: historiographical and historical studies*. Ashgate Publishing, Ltd.

Howard-Johnston, J. (2007). Byzantine sources for Khazar history. In: *The World of the Khazars*. Ed. by P. Golden, H. Ben-Shammai, & A. Roná-Tas. Brill, 163 –194.

Howard-Johnston, J. (2010). The Sasanian's Strategic Dilemma. In: *Commutatio et Contentio: Studies in the Late Roman, Sasanian and Early Islamic Near East*. Ed. by H. Börm & J. Wiesehöfer. Düsseldorf:Wellem-Verl., 37–70.

Hritz, C. (2010). Tracing Settlement Patterns and Channel Systems in Southern Mesopotamia Using Remote Sensing. *Journal of Field Archaeology,* 35, 184.

Hu, N., X. Li, L. Luo, & L. Zhang (2017). Ancient irrigation canals mapped from corona imageries and their implications in juyan oasis along the silk road. *Journal of Field Archaeology,* 9, 1283.

Hu, W., J. Zhang, & Y. Liu (2012). The qanats of Xinjiang: historical development, characteristics and modern implications for environmental protection. *Journal of Arid Land,* 4, 211.

Huang, L., J. Hong, W. Tan, H. Hu, F. Liu, & M. Wang (2008). Characteristics of micromorphology and element distribution of iron-manganese cutans in typical soils of subtropical China. *Geoderma,* 146, 40.

Huckleberry, G. & T. Rittenour (2014). Combining radiocarbon and single-grain optically stimulated luminescence methods to accurately date pre-ceramic irrigation canals, Tucson, Arizona. *Journal of Archaeological Science,* 41, 156.

Hunt, R. C. (1988). Size and the structure of authority in canal irrigation systems. *Journal of Anthropological Research,* 44, 335.

Hunt, R. C. & E. Hunt (1976). Canal Irrigation and Local Social Organization. *Current Anthropology,* 17, 389.

Huntley, D. J., D. I. Godfrey-Smith, & M. L. W. Thewalt (1985). Optical dating of sediments. *Nature* 313, 105.

Huntley, D. J., D. I. Godfrey-Smith, & E. H. Haskell (1991). Light-induced emission spectra from some quartz and feldspars. *International Journal of Radiation Applications and Instrumentation. Part D. Nuclear Tracks and Radiation Measurements* 18, 127.

Hütt, G., I. Jaek, & J. Tchonka (1988). Optical dating: K-feldspars optical response stimulation spectra. *Quaternary Science Reviews,* 7, 381.

Itkin, D., H. Goldfus, & H. C. Monger (2016). Human induced calcretisation in anthropogenic soils and sediments: Field observations and micromorphology in a Mediterranean climatic zone, Israel. *CATENA,* 146, 48.

Itonishvili, V. D. (1953). Agriculture in Khevi (in Georgian). In: *Collection of scientific works of students, VI.* Tbilisi, 187–212.

Itonishvili, V. D. (1971). *Daily life of the family in Mtiuletia-Gudamakars (in Georgian).*

Ivanovich, M. & R. S. Harmon (1992). *Uranium-series disequilibrium: applications to earth, marine, and environmental sciences.* Oxford UniversityPress, New York.

Izdebski, A., J. Pickett, N. Roberts, & T. Waliszewski (2016). The environmental, archaeological and historical evidence for regional climatic changes and their societal impacts in the Eastern Mediterranean in Late Antiquity. *Quaternary Science Reviews,* 136, 189.

Jacobs, Z. & R. G. Roberts (2007). Advances in optically stimulated luminescence dating of individual grains of quartz from archeological deposits. *Evolutionary Anthropology: Issues, News, and Reviews,* 16, 210.

Jacobs, Z., A. G. Wintle, G. A. T. Duller, R. G. Roberts, & L. Wadley (2008). New ages for the post-Howiesons Poort, late and final Middle Stone Age at Sibudu, South Africa. *Journal of Archaeological Science,* 35, 1790.

Jacobsen, T. (1958). Summary of a report by the Diyala Basin Archaeological Project, June 1 1957 to June 1 1958. *Sumer,* 14, 79.

Jain, M., A. S. Murray, & L. Bøtter-Jensen (2003). Characterisation of blue-light stimulated luminescence components in different quartz samples: implications for dose measurement. *Radiation Measurements,* 37, 441.

Jain, M., J. H. Choi, & P. J. Thomas (2008). The ultrafast OSL component in quartz: Origins and implications. *Radiation Measurements,* 43, 709.

Johnson, S. F. (2012). *The Oxford Handbook of Late Antiquity.* Oxford University Press.

Jones, A. P., M. E. Tucker, & J. Hart (1999). *The description & analysis of quaternary stratigraphic field sections.* Quaternary Research Association.

Jungner, H. & L. Bøtter-Jensen (1994). Study of sensitivity change of OSL signals from quartz and feldspars as a function of preheat temperature. *Radiation Measurements,* 23, 621.

Kalceff, M. A. S. & M. R. Phillips (1995). Cathodoluminescence microcharacterization of the defect structure of quartz. *Physical Review B,* 52, 3122.

Kalchgruber, R., M. Fuchs, A. S. Murray, & G. A. Wagner (2003). Evaluating dose-rate distributions in natural sediments using α-Al_2O_3:C grains. *Radiation Measurements* 37, 293.

Kamash, Z. (2012). Irrigation technology, society and environment in the Roman Near East. *Journal of Arid Environments,* 86, 65.

Karimi, A., H. Khademi, M. Kehl, & A. Jalalian (2009). Distribution, lithology and provenance of peridesert loess deposits in northeastern Iran. *Geoderma,* 148, 241.

Karimi, A., H. Khademi, & S. Ayoubi (2013). Magnetic susceptibility and morphological characteristics of a loessr-paleosol sequence in northeastern Iran. *CATENA,* 101, 56.

Karimian, H. (2015). Cities and social order in Sasanian Iran – the archaeological potential. *Antiquity,* 84, 453.

Karkanas, P. (2007). Identification of lime plaster in prehistory using petrographic methods: A review and reconsideration of the data on the basis of experimental and case studies. *Geoarchaeology,* 22, 775.

Karpychev, Y. A. (2001). Variations in the Caspian Sea Level in the Historic Epoch. *Water Resources,* 28, 1.

Kehl, M. (2010). *Quaternary loesses, loess-like sediments, soils and climate change in Iran.* Gebrüder Borntraeger Verlagsbuchhandlung.

Kehl, M., M. Frechen, & A. Skowronek (2005). Paleosols derived from loess and loess-like sediments in the Basin of Persepolis, Southern Iran. *Quaternary International,* 140-141, 135.

Kelly, W. W. (1983). Concepts in the Anthropological Study of Irrigation. *American Anthropologist,* 85, 880.

Kennedy, H. (1999). Medieval Merv: an historical overview. In: *Monuments of Merv: traditional buildings of the Karakum*. Ed. by G. Hermann. Society of Antiquaries of London, 25–44.

Kennedy, H. (2007). *The great Arab conquests: How the spread of Islam changed the world we live in*. Da Capo Press.

Kennet, D. (1997). Kush: a Sasanian and Islamic-period archaeological tell in Ras al-Khaimah (U.A.E.) *Arabian Archaeology and Epigraphy,* 8, 284.

Kennet, D. (2004). *Sasanian and Islamic pottery from Ras al-Khaimah (eBook version): classification, chronology and analysis of trade in the Western Indian Ocean*. Archaeopress.

Kennet, D. (2007). The decline of eastern Arabia in the Sasanian period. *Arabian Archaeology and Epigraphy,* 18, 86.

Khokhlova, O. S., I. S. Kovalevskaya, & S. A. Oleynik (2001). Records of climatic changes in the carbonate profiles of Russian Chernozems. *CATENA,* 43, 203.

Khokhlova, O. S., A. M. Kouznetsova, & A. A. Khokhlov (2009). Transformation pathway of carbonate pedofeatures based on their micromorhology and carbon isotope data in the Northern Caucasus region, Russia. *Journal of Mountain Science,* 6, 139.

Khormali, F. & M. Kehl (2011). Micromorphology and development of loess-derived surface and buried soils along a precipitation gradient in Northern Iran. *Quaternary International,* 234, 109.

Khormali, F., A. Abtahi, & G. Stoops (2006). Micromorphology of calcitic features in highly calcareous soils of Fars Province, Southern Iran. *Geoderma,* 132, 31.

Khormali, F., S. Ghergherechi, M. Kehl, & S. Ayoubi (2012). Soil formation in loess-derived soils along a subhumid to humid climate gradient, Northeastern Iran. *Geoderma,* 179-180, 113.

Kinnaird, T., J. Bolòs, A. Turner, & S. Turner (2017). Optically-stimulated luminescence profiling and dating of historic agricultural terraces in Catalonia (Spain). *Journal of Archaeological Science,* 78, 66.

Kitis, G., G. S. Polymeris, & N. G. Kiyak (2007). Component-resolved thermal stability and recuperation study of the LM-OSL curves of four sedimentary quartz samples. *Radiation Measurements,* 42, 1273.

Kitis, G., N. Kiyak, G. S. Polymeris, & N. C. Tsirliganis (2010). The correlation of fast OSL component with the TL peak at 325°C in quartz of various origins. *Journal of Luminescence,* 130, 298.

Kiyak, N. G., G. S. Polymeris, & G. Kitis (2007). Component resolved OSL dose response and sensitization of various sedimentary quartz samples. *Radiation Measurements,* 42, 144.

Klappa, C. F. (1980). Rhizoliths in terrestrial carbonates: classification, recognition, genesis and significance. *Sedimentology,* 27, 613.

Kohl, P. L. (1988). The Northern "Frontier" of the Ancient Near East: Transcaucasia and Central Asia Compared. *American Journal of Archaeology,* 92, 591.

Kohl, P. L., H. P. Francfort, & J. C. Gardin (1984). *Central Asia palaeolithic beginnings to the Iron Age.* Vol. 14. Éditions Recherche sur les civilisations.

Kooistra, M. J. & M. M. Pulleman (2010). Features Related to Faunal Activity. In: *Interpretation of Micromorphological Features of Soils and Regoliths.* Ed. by G. Stoops, V. Marcelino, & F. Mees. Elsevier, 397 –418.

Korobov, D. & A. V. Borisov (2013). The origins of terraced field agriculture in the Caucasus: new discoveries in the Kislovodsk basin. *Antiquity,* 87, 1086.

Kovda, I. & A. R. Mermut (2010). Vertic Features. In: *Interpretation of Micromorphological Features of Soils and Regoliths.* Ed. by G. Stoops, V. Marcelino, & F. Mees. Elsevier, 109 –127.

Krahtopoulou, A. & C. Frederick (2008). The stratigraphic implications of long-term terrace agriculture in dynamic landscapes: Polycyclic terracing from Kythera Island, Greece. *Geoarchaeology,* 23, 550.

Krbetschek, M. R., J. Götze, A. Dietrich, & T. Trautmann (1997). Spectral information from minerals relevant for luminescence dating. *Radiation Measurements,* 27, 695.

Kreutzer, S., C. Schmidt, M. C. Fuchs, M. Dietze, M. Fischer, & M. Fuchs (2012). Introducing an R package for luminescence dating analysis. *Ancient TL,* 30, 1.

Kreutzer, S., M. Dietze, C. Burow, M. C. Fuchs, C. Schmidt, M. Fischer, J. Friedrich, N. Mercier, R. K. Smedley, & C. Christophe (2017). Package 'Luminescence'.

Kroetsch, D. & C. Wang (2008). Particle size distribution. In: *Soil sampling and methods of analysis, Second Edition.* Ed. by M. R. Carter & E. G. Gregorich. Boca Raton: CRC Press.

Kroonenberg, S. B., G. M. Abdurakhmanov, E. N. Badyukova, K. van der Borg, A. Kalashnikov, N. S. Kasimov, G. I. Rychagov, A. A. Svitoch, H. B. Vonhof, & F. P. Wesselingh (2007). Solar-forced 2600 BP and Little Ice Age highstands of the Caspian Sea. *Quaternary International,* 173-174, 137.

Kubiëna, W. L. (1948). *Entwicklungslehre des bodens.* Springer-Verlag.

Kubiëna, W. L. (1953). *The soils of Europe.* Thomas Murby And Company: London.

Kühn, P., J. Aguilar, & R. Miedema (2010a). Textural Pedofeatures and Related Horizons. In: *Interpretation of Micromorphological Features of Soils and Regoliths.* Ed. by G. Stoops, V. Marcelino, & F. Mees. Elsevier, 217 –250.

Kühn, P., D. Pietsch, & I. Gerlach (2010b). Archaeopedological analyses around a Neolithic hearth and the beginning of Sabaean irrigation in the oasis of Ma'rib (Ramlat as-Sab'atayn, Yemen). *Journal of Archaeological Science,* 37, 1305.

Kühn, P., E. Lehndorff, & M. Fuchs (2017). Lateglacial to Holocene pedogenesis and formation of colluvial deposits in a loess landscape of Central Europe (Wetterau, Germany). *CATENA,* 154, 118.

Kuhns, C. K., N. A. Larsen, & S. W. S. McKeever (2000). Characteristics of LM-OSL from several different types of quartz. *Radiation Measurements,* 32, 413.

Laessøe, J. (1951). The Irrigation System at Ulhu, 8th Century B.C. *Journal of Cuneiform Studies,* 5, 21.

Lahijani, H. A. K., V. Tavakoli, & A. H. Amini. South Caspian river mouth configuration under human impact and sea level fluctuations.

Lahijani, H. A. K., H. Rahimpour-Bonab, V. Tavakoli, & M. Hosseindoost (2009). Evidence for late Holocene highstands in Central Guilan-East Mazanderan, South Caspian coast, Iran. *Quaternary International,* 197, 55.

Lamothe, M. & M. Auclair (1997). Assessing the datability of young sediments by IRSL using an intrinsic laboratory protocol. *Radiation Measurements,* 27, 107.

Lane, K. (2016). Puquios and Aqueducts in the Central Andes of South America. In: *Underground Aqueducts Handbook*. Ed. by A. N. Angelakis, E. Chiotis, S. Eslamian, & H. Weingartner. CRC press, 465–472.

Lang, A. & S. Hönscheidt (1999). Age and source of colluvial sediments at Vaihingen–Enz, Germany. *CATENA,* 38, 89.

Lang, A. & S. Nolte (1999). The chronology of Holocene alluvial sediments from the Wetterau, Germany, provided by optical and 14C dating. *The Holocene,* 9, 207.

Lauer, T., M. Frechen, S. Vlaminck, M. Kehl, E. Lehndorff, A. Shahriari, & F. Khormali (2017). Luminescence-chronology of the loess palaeosol sequence Toshan, Northern Iran – A highly resolved climate archive for the last glacial-interglacial cycle. *Quaternary International,* 429, 3.

Lavrushin, V. Y., V. N. Kuleshov, & O. E. Kikvadze (2006). Travertines of the northern Caucasus. *Lithology and Mineral Resources,* 41, 137.

Lawrence, D. & T. Wilkinson (2017). The northern and western borderlands of the Sasanian Empire: contextualizing the Roman/Byzantine and Sasanian frontier. In: *Sasanian Persia: Between Rome and the Steppes of Eurasia*. Ed. by E. B. Sauer. Edinburgh University Press.

Lebedeva-Verba, M. P. & M. I. Gerasimova (2010). Micromorphology of takyrs and the desert "papyrus" of Southwestern Turkmenia. *Eurasian Soil Science,* 43, 1220.

Lecomte, O. (2007). Gorgan and Dehistan: the north-east frontier of the Iranian empire. In: *After Alexander: Central Asia Before Islam*. Ed. by J. Cribb & G. Herrmann. Oxford University Press, British Academy, 295–312.

Lee, H., C. French, & R. I. Macphail (2014). Microscopic Examination of Ancient and Modern Irrigated Paddy Soils in South Korea, with Special Reference to the Formation of Silty Clay Concentration Features. *Geoarchaeology,* 29, 326.

Leroy, S. A. G., A. A. Kakroodi, S. Kroonenberg, H. K. Lahijani, H. Alimohammadian, & A. Nigarov (2013). Holocene vegetation history and sea level changes in the SE corner of the Caspian Sea: relevance to SW Asia climate. *Quaternary Science Reviews,* 70, 28.

Lewis, D. W. & D. McConchie (1994). Textures. In: *Analytical sedimentology*. Springer Science & Business Media.

Li, B. (2007). A note on estimating the error when subtracting background counts from weak OSL signals. *Ancient TL,* 25, 9.

Li, B. & S.-H. Li (2006). Comparison of D_e estimates using the fast component and the medium component of quartz OSL. *Radiation Measurements,* 41, 125.

Li, B. & S.-H. Li (2011). Luminescence dating of K-feldspar from sediments: A protocol without anomalous fading correction. *Quaternary Geochronology,* 5, 468.

Lieu, S. N. (1986). Captives, refugees and exiles: A study of cross-frontier civilian movements and contacts between Rome and Persia from Valerian to Jovian. In: *The defense of the Roman and Byzantine East. Proceedings of a Colloquium held at the University of Sheffield in April*, 475–505.

Lightfoot, D. R. (1996). Syrian qanat Romani: history, ecology, abandonment. *Journal of Arid Environments,* 33, 321.

Lightfoot, D. R. (1997). Qanats in the Levant: Hydraulic Technology at the Periphery of Early Empires. *Technology and Culture,* 38, 432.

Lightfoot, D. R. (2000). The Origin and Diffusion of Qanats in Arabia: New Evidence from the northern and southern Peninsula. *The Geographical Journal,* 166, 215.

Lightfoot, K. G. & A. Martinez (1995). Frontiers and Boundaries in Archaeological Perspective. *Annual Review of Anthropology,* 24, 471.

Lindbo, D. L., M. H. Stolt, & M. J. Vepraskas (2010). Redoximorphic Features. In: *Interpretation of Micromorphological Features of Soils and Regoliths*. Ed. by G. Stoops, V. Marcelino, & F. Mees. Elsevier, 129 –147.

Lisa, L., P. Lisy, M. Chadima, P. Čejchan, A. Bajer, V. Cilek, L. Sukova, & P. Schnabl (2012). Microfacies description linked to the magnetic and non-magnetic proxy as a promising environmental tool: Case study from alluvial deposits of the Nile river. *Quaternary International,* 266, 25.

Lomax, J., A. Hilgers, C. R. Twidale, J. A. Bourne, & U. Radtke (2007). Treatment of broad palaeodose distributions in OSL dating of dune sands from the western Murray Basin, South Australia. *Quaternary Geochronology,* 2, 51.

Lukas, S., J. Q. Spencer, R. A. Robinson, & D. I. Benn (2007). Problems associated with luminescence dating of Late Quaternary glacial sediments in the NW Scottish Highlands. *Quaternary Geochronology,* 2, 243.

MacKenzie, W. S. & C Guilford (2014). *Atlas of the Rock-Forming Minerals in Thin Section*. Routledge.

Madsen, A. T., G. A. T. Duller, J. P. Donnelly, H. M. Roberts, & A. G. Wintle (2009). A chronology of hurricane landfalls at Little Sippewissett Marsh, Massachusetts, USA, using optical dating. *Geomorphology,* 109, 36.

Magee, P. (1998). Settlement patterns, polities and regional complexity in the Southeast Arabian Iron Age. *Paléorient,* 24, 49.

Magee, P. (2005). The chronology and environmental background of Iron Age settlement in Southeastern Iran and the question of the origin of the Qanat irrigation system. *Iranica Antiqua,* 40, 217.

Maher, B. A., A. Alekseev, & T. Alekseeva (2002). Variation of soil magnetism across the Russian steppe: its significance for use of soil magnetism as a palaeorainfall proxy. *Quaternary Science Reviews,* 21, 1571.

Maher, B. A., A. Alekseev, & T. Alekseeva (2003). Magnetic mineralogy of soils across the Russian Steppe: climatic dependence of pedogenic magnetite formation. *Palaeogeography, Palaeoclimatology, Palaeoecology,* 201, 321.

Malatesta, L. C., S. Castelltort, S. Mantellini, V. Picotti, I. Hajdas, G. Simpson, A. E. Berdimuradov, M. Tosi, & S. D. Willett (2012). Dating the Irrigation System of the Samarkand Oasis: A Geoarchaeological Study. *Radiocarbon,* 54, 91.

Mamedov, A. V. (1997). The Late Pleistocene-Holocene history of the Caspian Sea. *Quaternary International,* 41-42, 161.

Mange, M. A. & H. Maurer (2012). *Heavy minerals in colour*. Springer Science & Business Media.

Marcus, J. & C. Stanish (2006). *Agricultural strategies*. Los Angeles: Cotsen Institute, University of California.

Markey, B. G., L. Bøtter-Jensen, & G. A. T. Duller (1997). A new flexible system for measuring thermally and optically stimulated luminescence. *Radiation Measurements,* 27, 83.

Martin, L., N. Mercier, S. Incerti, Y. Lefrais, C. Pecheyran, G. Guérin, M. Jarry, L. Bruxelles, F. Bon, & C. Pallier (2015). Dosimetric study of sediments at the beta dose rate scale: Characterization and modelization with the DosiVox software. *Radiation Measurements,* 81, 134.

Masson, V. M. (1996). *History of Civilizations of Central Asia: The crossroads of civilizations, AD 250 to 750*. UNESCO.

Matter, A. & K. Ramseyer (1985). Cathodoluminescence Microscopy as a Tool for Provenance Studies of Sandstones. In: *Provenance of Arenites*. Ed. by G. G. Zuffa. Springer Netherlands, 191–211.

Matthews, W., C. A. I. French, T. Lawrence, D. F. Cutler, & M. K. Jones (1997). Microstratigraphic traces of site formation processes and human activities. *World Archaeology,* 29, 281.

Mayya, Y. S., P. Morthekai, M. K. Murari, & A. K. Singhvi (2006). Towards quantifying beta microdosimetric effects in single-grain quartz dose distribution. *Radiation Measurements,* 41, 1032.

McCormick, M., U. Büntgen, M. A. Cane, E. R. Cook, K. Harper, P. Huybers, T. Litt, S. W. Manning, P. A. Mayewski, A. F. M. More, K. Nicolussi, & W. Tegel (2012). Climate Change during and after the Roman Empire: Reconstructing the Past from Scientific and Historical Evidence. *The Journal of Interdisciplinary History,* 43, 169.

McCoy, D. G, J. R. Prescott, & R. J. Nation (2000). Some aspects of single-grain luminescence dating. *Radiation Measurements,* 32, 859.

McMichael, A. J. (2012). Insights from past millennia into climatic impacts on human health and survival. *Proceedings of the National Academy of Sciences,* 109, 4730.

Mees, F. & A. Singer (2006). Surface crusts on soils/sediments of the southern Aral Sea basin, Uzbekistan. *Geoderma,* 136, 152.

Mejdahl, V. (1979). Thermoluminescence dating: Beta-dose attenuation in quartz grains. *Archaeometry,* 21, 61.

Mejdahl, V. & L. Bøtter-Jensen (1994). Luminescence dating of archaeological materials using a new technique based on single aliquot measurements. *Quaternary Science Reviews,* 13, 551.

Milek, K. B. (2012). Floor formation processes and the interpretation of site activity areas: An ethnoarchaeological study of turf buildings at Thverá, northeast Iceland. *Journal of Anthropological Archaeology,* 31, 119.

Miller, N. F. (1990). Clearing land for farmland and fuel: Archaeobotanical studies of the ancient Near East. In: *Economy and Settlement in the Near East.* Ed. by N. F. Miller. MASCA Research Papers in Science and Archaeology, 71–78.

MoLAS (1994). *Archaeological Site Manual, 3rd edition.* Museum of London.

Morony, M. (1994). Land use and settlement patterns in late Sasanian and early Islamic Iraq. In: *he Byzantine and Early Islamic Near East II. Land Use and Settlement Patterns.* Darwin Press, Princeton, 221–229.

Morony, M. (2004). Economic Boundaries? Late Antiquity and Early Islam. *Journal of the Economic and Social History of the Orient,* 47, 166.

Mouton, M. (2009). The settlement patterns of north-eastern and south-eastern Arabia in late antiquity. *Arabian Archaeology and Epigraphy,* 20, 185.

Mücher, H., H. van Steijn, & F. Kwaad (2010). Colluvial and Mass Wasting Deposits. In: *Interpretation of Micromorphological Features of Soils and Regoliths.* Ed. by G. Stoops, V. Marcelino, & F. Mees. Elsevier, 37 –48.

Mullins, C. E. (1977). Magnetic susceptibility of the soil and its significance in soil science – a review. *Journal of Soil Science,* 28, 223.

Munsell, C. C. (1954). *Charts, Munsell Soil Color.* Vol. 2. Inc., Baltimore.

Murphy, C. P. (1986). *Thin section preparation of soils and sediments.* AB Academic Publishers.

Murray, A. S. (1996). Developments in optically stimulated luminescence and phototransferred thermoluminescence dating of young sediments: Application to a 2000-year sequence of flood deposits. *Geochimica et Cosmochimica Acta,* 60, 565.

Murray, A. S. & R. G. Roberts (1997). Determining the burial time of single grains of quartz using optically stimulated luminescence. *Earth and Planetary Science Letters,* 152, 163.

Murray, A. S. & R. G. Roberts (1998). Measurement of the equivalent dose in quartz using a regenerative-dose single-aliquot protocol. *Radiation Measurements,* 29, 503.

Murray, A. S. & A. G. Wintle (1999). Isothermal decay of optically stimulated luminescence in quartz. *Radiation Measurements,* 30, 119.

Murray, A. S. & A. G. Wintle (2000). Luminescence dating of quartz using an improved single-aliquot regenerative-dose protocol. *Radiation Measurements,* 32, 57.

Murray, A. S. & A. G. Wintle (2003). The single aliquot regenerative dose protocol: potential for improvements in reliability. *Radiation Measurements,* 37, 377.

Murray, A. S., R. G. Roberts, & A. G. Wintle (1997). Equivalent dose measurement using a single aliquot of quartz. *Radiation Measurements,* 27, 171.

Naderi Beni, A., H. Lahijani, R. Mousavi Harami, K. Arpe, S. A. G. Leroy, N. Marriner, M. Berberian, V. Andrieu-Ponel, M. Djamali, A. Mahboubi, & P. J. Reimer (2013). Caspian Sea level changes during the last millennium: historical and geological evidences from the south Caspian Sea. *Climate of the Past,* 9, 1645.

Nakhutsrishvili, G. (2012). *The vegetation of Georgia (South Caucasus).* Springer Science & Business Media.

Nathan, R. P. & B. Mauz (2008). On the dose-rate estimate of carbonate-rich sediments for trapped charge dating. *Radiation Measurements,* 43, 14.

Nathan, R. P., P. Thomas, M. Jain, A. S. Murray, & E. J. Rhodes (2003). Environmental dose rate heterogeneity of beta radiation and its implications for luminescence dating: Monte Carlo modelling and experimental validation. *Radiation Measurements,* 37, 305.

Neely, J. A. (1974). Sasanian and Early Islamic Water-Control and Irrigation Systems on the Deh Luran Plain, Iran. In: *rrigation's Impact on Society.* Ed. by T. E. Downing & M. Gibson. University of Arizona Press, Tucson, 21 –42.

Neely, J. A. (2016). Parthian and Sasanian Settlement Patterns on the Deh Luran Plain, Khuzistan Province, Southwestern Iran. *Iranica Antiqua,* 51, 235.

Neely, J. A. & H. T. Wright (1994). *Early settlement and irrigation on the Deh Luran plain: village and early state societies in southwestern Iran.* University of Michigan, Museum of Anthropology.

Neer, W., W. Wouters, & M. Mouton (2013). Evidence of sun-dried fish at Mleiha (S.-E. Arabia) in antiquity. *Arabian Archaeology and Epigraphy,* 24, 224.

Nesse, W. D. (2009). *Introduction to Optical Mineralogy.* Oxford Univeristy Press.

Newson, P., G. Barker, P. Daly, D. Mattingly, & D. Gilbertson (2007). The wadi Faynan field systems. In: *he Wadi Faynan Landscape Survey, Southern Jordan.* Ed. by G. Barker & D. Mattingly. Oxbow.

Nokandeh, J., E. W. Sauer, H. O. Rekavandi, T. Wilkinson, G. A. Abbasi, J.-L. Schweninger, M. Mahmoudi, D. Parker, M. Fattahi, L. S. Usher-Wilson, M. Ershadi, J. Ratcliffe, & R. Gale (2006). Linear Barriers of Northern Iran: The Great Wall of Gorgan and the Wall of Tammishe. *Iran,* 44, 121.

Noonan, T. S. (1999). European Russia c.500-c.1050. In: *The New Cambridge Medieval History: Volume 3, c.900-c.1024*. Cambridge University Press.

Oberhänsli, H., N. Boroffka, P. Sorrel, & S. Krivonogov (2007). Climate variability during the past 2,000Â years and past economic and irrigation activities in the Aral Sea basin. *Irrigation and Drainage Systems,* 21, 167.

Oldfield, F. & J. Crowther (2007). Establishing fire incidence in temperate soils using magnetic measurements. *Palaeogeography, Palaeoclimatology, Palaeoecology,* 249, 362.

Olley, J. M., R. G. Roberts, & A. S. Murray (1997). Disequilibria in the uranium decay series in sedimentary deposits at Allen's cave, nullarbor plain, Australia: Implications for dose rate determinations. *Radiation Measurements,* 27, 433.

Olley, J. M., T. Pietsch, & R. G. Roberts (2004). Optical dating of Holocene sediments from a variety of geomorphic settings using single grains of quartz. *Geomorphology,* 60, 337.

Ollivier, V., M. Fontugne, & B. Lyonnet (2015). Geomorphic response and 14C chronology of base-level changes induced by Late Quaternary Caspian Sea mobility (middle Kura Valley, Azerbaijan). *Geomorphology,* 230, 109.

Pagliai, M. & G. Stoops (2010). Physical and Biological Surface Crusts and Seals. In: *Interpretation of Micromorphological Features of Soils and Regoliths*. Ed. by G. Stoops, V. Marcelino, & F. Mees. Elsevier, 419 –440.

Pagliai, M., M. Raglione, T. Panini, M. Maletta, & M. La Marca (1995). The structure of two alluvial soils in Italy after 10 years of conventional and minimum tillage. *Soil and Tillage Research,* 34, 209.

Pánek, T., K. Šilhán, J. Hradeckỳ, A. Strom, V. Smolková, & O. Zerkal (2012). A megalandslide in the Northern Caucasus foredeep (Uspenskoye, Russia): Geomorphology, possible mechanism and age constraints. *Geomorphology,* 177-178, 144.

Parker, A. G. & A. S. Goudie (2008). Geomorphological and palaeoenvironmental investigations in the southeastern Arabian Gulf region and the implication for the archaeology of the region. *Geomorphology,* 101, 458.

Payne, R. (2013). Cosmology and the Expansion of the Iranian Empire, 502–628 ce. *Past & Present,* 220, 3.

Payne, R. (2014). The Reinvention of Iran: The Sasanian Empire and the Huns. In: *The Cambridge Companion to the Age of Attila*. Ed. by M. Maas. Cambridge University Pres, 282–299.

Payne, R. (2017). Territorializing Iran in Late Antiquity: Autocracy, Aristocracy, and the Infrastructure of Empire. In: *Ancient States and Infrastructural Power: Europe, Asia, and America*. Ed. by A. Clifford & S. Richardson. University of Pennsylvania Press, 179–217.

Pease, P. P., G. D. Bierly, V. P. Tchakerian, & N. W. Tindale (1999). Mineralogical characterization and transport pathways of dune sand using Landsat TM data, Wahiba Sand Sea, Sultanate of Oman. *Geomorphology,* 29, 235.

Peng, J., Z. Dong, F. Han, H. Long, & X. Liu (2013). R package numOSL: numeric routines for optically stimulated luminescence dating. *Ancient TL,* 31, 41.

Peters, C., M. J. Church, & C. Mitchell (2001). Investigation of fire ash residues using mineral magnetism. *Archaeological Prospection,* 8, 227.

Phillips, E. (2006). Micromorphology of a debris flow deposit: evidence of basal shearing, hydrofracturing, liquefaction and rotational deformation during emplacement. *Quaternary Science Reviews,* 25, 720.

Pietsch, T. J., J. M. Olley, & G. C. Nanson (2008). Fluvial transport as a natural luminescence sensitiser of quartz. *Quaternary Geochronology,* 3, 365.

Pinhasi, R., B. Gasparian, K. Wilkinson, R. Bailey, G. Bar-Oz, A. Bruch, C. Chataigner, D. Hoffmann, R. Hovsepyan, S. Nahapetyan, A. Pike, D. Schreve, & M. Stephens (2008). Hovk 1 and the Middle and Upper Paleolithic of Armenia: a preliminary framework. *Journal of Human Evolution,* 55, 803.

Poole, I. (2014). Analysis of charcoalified wood samples recovered in 2014 from the Caucasian Gates, Georgia (Unpublished report).

Poolton, N. R. J., L. Bøtter-Jensen, C. E. Andersen, M. Jain, A. S. Murray, A. E. R. Malins, & F. M. Quinn (2003). Measuring modulated luminescence using non-modulated stimulation: ramping the sample period. *Radiation Measurements,* 37, 639.

Potts, D. T. (1990). *The Arabian gulf in antiquity: From Alexander the Great to the coming of Islam.* Vol. 2. Oxford.

Potts, D. T. (1992). *The Arabian Gulf in Antiquity.* Clarendon Press.

Powers, M. C. (1953). A new roundness scale for sedimentary particles. *Journal of Sedimentary Research,* 23, 117.

Prescott, J. R. & J. T. Hutton (1988). Cosmic ray and gamma ray dosimetry for TL and ESR. *International Journal of Radiation Applications and Instrumentation. Part D. Nuclear Tracks and Radiation Measurements,* 14, 223.

Prescott, J. R. & J. T. Hutton (1995). Environmental dose rates and radioactive disequilibrium from some Australian luminescence dating sites. *Quaternary Science Reviews,* 14, 439.

Prescott, J. R. & L. G. Stephan (1982). The contribution of cosmic radiation to the environmental dose for thermoluminescence dating. Latitude, altitude and depth dependences. In: *PACT.* Vol. 6, 17–25.

Preusser, F. (2003). IRSL dating of K-rich feldspars using the SAR protocol: comparison with independent age control. *Ancient TL,* 21, 17.

Preusser, F., D. Radies, & A. Matter (2002). A 160,000-Year Record of Dune Development and Atmospheric Circulation in Southern Arabia. *Science,* 296, 2018.

Preusser, F., D. Radies, F. Driehorst, & A. Matter (2005). Late Quaternary history of the coastal Wahiba Sands, Sultanate of Oman. *Journal of Quaternary Science,* 20, 395.

Preusser, F., K. Ramseyer, & C. Schlüchter (2006). Characterisation of low OSL intensity quartz from the New Zealand Alps. *Radiation Measurements,* 41, 871.

Preusser, F., M. L. Chithambo, T. Götte, M. Martini, K. Ramseyer, E. J. Sendezera, G. J. Susino, & A. G. Wintle (2009). Quartz as a natural luminescence dosimeter. *Earth-Science Reviews,* 97, 184.

Purdue, L., W. Miles, K. Woodson, A. Darling, & J.-F. Berger (2010). Micromorphological study of irrigation canal sediments: Landscape evolution and hydraulic management in the middle Gila River valley (Phoenix Basin, Arizona) during the Hohokam occupation. *Quaternary International,* 216, 129.

Puschnigg, G. (2010). *Ceramics of the Merv Oasis: recycling the city.* Routledge.

Pye, K. (1995). The nature, origin and accumulation of loess. *Quaternary Science Reviews,* 14, 653.

Ramseyer, K. & J. Mullis (1990). Factors influencing short-lived blue cathodoluminescence of alpha-quartz. *American Mineralogist,* 75, 791.

Rapp, G. R. & C. L. Hill (2006). *Geoarchaeology: the earth-science approach to archaeological interpretation.* Yale University Press.

Reineck, H.-E. & I. B. Singh (1980). *Depositional sedimentary environments: with reference to terrigenous clastics.* Springer Science & Business Media.

Reinhold, S. & D. S. Korobov (2007). The Kislovodsk basin in the North Caucasian piedmonts-archaeology and GIS studies in a mountain cultural landscape. *Preistoria Alpina,* 42, 183.

Rekavandi, H. O., E. W. Sauer, T. Wilkinson, E. S. Tamak, R. Ainslie, M. Mahmoudi, S. Griffiths, M. Ershadi, J. J. V. Rensburg, M. Fattahi, J. Ratcliffe, J. Nokandeh, A. Nazifi, R. Thomas, R. Gale, & B. Hoffmann (2007). An Imperial Frontier of the Sasanian Empire: Further Fieldwork at the Great Wall of Gorgan. *Iran,* 45, 95.

Rekavandi, H. O., E. W. Sauer, T. Wilkinson, G. A. Abbasi, S. Priestman, E. S. Tamak, R. Ainslie, M. Mahmoudi, N. Galiatsatos, K. Roustai, J. J. V. Rensburg, M. Ershadi, E. MacDonald, M. Fattahi, C. Oatley, B. Shabani, J. Ratcliffe, & L. S. Usher-Wilson (2008). Sasanian Walls, Hinterland Fortresses and Abandoned Ancient Irrigated Landscapes: The 2007 Season on the Great Wall of Gorgan and the Wall of Tammishe. *Iran,* 46, 151.

Rendell, H. M. & M. L. Clarke (1997). Thermoluminescence, radioluminescence and cathodoluminescence spectra of alkali feldspars. *Radiation Measurementsi,* 27, 263.

Rhodes, E. J. & L. Pownall (1994). Zeroing of the OSL signal in quartz from young glaciofluvial sediments. *Radiation Measurements,* 23, 581.

Rhodes, E. J., C. B. Ramsey, Z. Outram, C. Batt, L. Willis, S. Dockrill, & J. Bond (2003). Bayesian methods applied to the interpretation of multiple OSL dates: high

precision sediment ages from Old Scatness Broch excavations, Shetland Isles. *Quaternary Science Reviews,* 22, 1231.

Ricci, A. (2012). Archaeological landscape studies: The Mil-Karabakh Plain and the Kvemo Kartli Survey Projects: a preliminary account of the first two field seasons (2010-11), in Ancient Kura 2010-2011. *The first two seasons of joint fieldwork in the Southern Caucasus ,* AMIT.

Ricci, A., B. Helwing, & T. Aliyev (2012). The Neolithic on the Move: High Resolution Settlement Dynamics Investigations and Their Impact on Archaeological Landscape Studies in Southwest Azerbaijan. *eTopoi. Journal for Ancient Studies,* 3, 369.

Rittenour, T. M. (2008). Luminescence dating of fluvial deposits: applications to geomorphic, palaeoseismic and archaeological research. *Boreas,* 37, 613.

Roberts, H. M. & G. A. T. Duller (2004). Standardised growth curves for optical dating of sediment using multiple-grain aliquots. *Radiation Measurements,* 38, 241.

Roberts, N., W. J. Eastwood, C. Kuzucuoğlu, G. Fiorentino, & V. Caracuta (2011). Climatic, vegetation and cultural change in the eastern Mediterranean during the mid-Holocene environmental transition. *The Holocene,* 21, 147.

Roberts, R. G., G. Walsh, A. Murray, J. Olley, R. Jones, M. Morwood, C. Tuniz, E. Lawson, M. Macphail, D. Bowdery, *et al.* (1997). Luminescence dating of rock art and past environments using mud-wasp nests in northern Australia. *Nature,* 387, 696.

Roberts, R. G., R. F. Galbraith, J. M. Olley, H. Yoshida, & G. M. Laslett (1999). Optical dating of single and multiple grains of quartz from Jinmium rock shelter, northern Australia: Part II, results and implications. *Archaeometry,* 41, 365.

Roberts, R. G., R. F. Galbraith, H. Yoshida, G. M. Laslett, & J. M. Olley (2000). Distinguishing dose populations in sediment mixtures: a test of single-grain optical dating procedures using mixtures of laboratory-dosed quartz. *Radiation Measurements,* 32, 459.

Roque, C., P. Guibert, M. Duttine, E. Vartanian, R. Chapoulie, & F. Bechtel (2004). Dependence of luminescence characteristics of irradiated quartz with the thermal treatment and consequences for TL dating. *Geochronometria,* 23, 1.

Rufer, D. & F. Preusser (2009). Potential of Autoradiography to Detect Spatially Resolved Radiation Patterns in the Context of Trapped Charge Dating. *Geochronometria,* 34, 1.

Sadori, L., C. Giraudi, A. Masi, M. Magny, E. Ortu, G. Zanchetta, & A. Izdebski (2016). Climate, environment and society in southern Italy during the last 2000 years. A review of the environmental, historical and archaeological evidence. *Quaternary Science Reviews,* 136, 173.

Sallares, R. (2002). *Malaria and Rome: a history of malaria in ancient Italy.* Oxford University Press.

Sanderson, D. C. W. & S. Murphy (2010). Using simple portable OSL measurements and laboratory characterisation to help understand complex and heterogeneous sediment sequences for luminescence dating. *Quaternary Geochronology,* 5, 299.

Sanderson, D. C. W., P. Bishop, M. Stark, & J. Spencer (2003). Luminescence dating of anthropogenically reset canal sediments from Angkor Borei, Mekong Delta, Cambodia. *Quaternary Science Reviews,* 22, 1111.

Sanderson, D. C. W., P. Bishop, M. Stark, S. Alexander, & D. Penny (2007). Luminescence dating of canal sediments from Angkor Borei, Mekong Delta, Southern Cambodia. *Quaternary Geochronology,* 2, 322.

Sauer, E. W. (2017). *Sasanian Persia: Between Rome and the Steppes of Eurasia.* Edinburgh University Press.

Sauer, E. W., H. Omrani Rekavandi, T. J. Wilkinson, & J Nokandeh (2013). *Persia's Imperial Power in Late Antiquity: The Great Wall of Gorgan and Frontier Landscapes of Sasanian Iran.* Oxbow Books, Oxford.

Sauer, E. W., K. Pitskhelauri, K. Hopper, A. Tiliakou, C. Pickard, D. Lawrence, A. Diana, E. Kranioti, & C. Shupe (2015). Northern outpost of the Caliphate: maintaining military forces in a hostile environment (the Dariali Gorge in the Central Caucasus in Georgia). *Antiquity,* 89, 885.

Sawakuchi, A. O., M. W. Blair, R. DeWitt, F. M. Faleiros, T. Hyppolito, & C. C. F. Guedes (2011). Thermal history versus sedimentary history: OSL sensitivity of quartz grains extracted from rocks and sediments. *Quaternary Geochronology,* 6, 261.

Schiffer, M. B. (1986). Radiocarbon dating and the "old wood" problem: the case of the Hohokam chronology. *Journal of Archaeological Science,* 13, 13.

Schiffer, M. B. (1987). *Formation processes of the archaeological record.* University of New Mexico Press.

Schwenninger, J. L. & M. Fattahi (2013). OSL Dating. In: *Persia's Imperial Power in Late Antiquity: The Great Wall of Gorgan and Frontier Landscapes of Sasanian Iran.* Ed. by E. W. Sauer, H. Omrani Rekavandi, T. J. Wilkinson, & J Nokandeh. Oxbow Books, Oxford.

Sedov, S., E. Solleiro-Rebolledo, & J. E. Gama-Castro (2003). Andosol to Luvisol evolution in Central Mexico: timing, mechanisms and environmental setting. *CATENA,* 54, 495.

Sedov, S., G. Stoops, & S. Shoba (2010). Regoliths and Soils on Volcanic Ash. In: *Interpretation of Micromorphological Features of Soils and Regoliths.* Ed. by G. Stoops, V. Marcelino, & F. Mees. Elsevier, 275.

Sedov, S., O. S. Khokhlova, & A. M. Kuznetsova (2011). Polygenesis of volcanic paleosols in Armenia and Mexico: Micromorphological records of climate variations in the quaternary period. *Eurasian Soil Science,* 44, 766.

Severin, K. P. (2004). *Energy dispersive spectrometry of common rock forming minerals.* Springer.

Seyedolali, A., D. H. Krinsley, S. Boggs Jr, P. F. O'Hara, H. Dypvik, & G. G. Goles (1997). Provenance interpretation of quartz by scanning electron microscope cathodoluminescence fabric analysis. *Geology,* 25, 787.

Shumilovskikh, L. S., K. Hopper, M. Djamali, P. Ponel, F. Demory, F. Rostek, K. Tachikawa, F. Bittmann, A. Golyeva, F. Guibal, B. Talon, L.-C. Wang, M. Nezamabadi, E. Bard, H. Lahijani, J. Nokandeh, H. O. Rekavandi, J.-L. de Beaulieu, E. Sauer, & V. Andrieu-Ponel (2016). Landscape evolution and agro-sylvo-pastoral activities on the Gorgan Plain (NE Iran) in the last 6000 years. *The Holocene,* 26, 1676.

Sigl, M., M. Winstrup, J. R. McConnell, K. C. Welten, G. Plunkett, F. Ludlow, U. Büntgen, M. Caffee, N. Chellman, & D. Dahl-Jensen (2015). Timing and climate forcing of volcanic eruptions for the past 2,500 years. *Nature* 523, 543.

Simpson, S. J. (1996). From Tekrit to the Jaghjagh: Sasanian sites, settlement patterns and material culture in northern Mesopotamia. In: *Continuity and change in northern Mesopotamia from the Hellenistic to the early Islamic period.* Ed. by K. Bartl & S. Hauser. Berliner Beitrage zum Vorderen Orient, Berlin, 87–126.

Simpson, S. J. (2000). Mesopotamia in the Sasanian Period: Settlement patterns, arts and crafts. In: *Mesopotamia and Iran in the Parthian and Sasanian periods: Rejection and Revival c 238 BC-AD 642.* Ed. by J Curtis. London: British Museum, 57–80.

Simpson, S. J. (2014). Merv, an archaeological case-study from the northeastern frontier of the Sasanian Empire. *Journal of Ancient History,* 2, 116.

Singarayer, J. S. & R. M. Bailey (2003). Further investigations of the quartz optically stimulated luminescence components using linear modulation. *Radiation Measurements,* 37, 451.

Singarayer, J. S. & R. M. Bailey (2004). Component-resolved bleaching spectra of quartz optically stimulated luminescence: preliminary results and implications for dating. *Radiation Measurements,* 38, 111.

Singarayer, J. S, R. M Bailey, & E. J Rhodes (2000). Potential of the slow component of quartz OSL for age determination of sedimentary samples. *Radiation Measurements,* 32, 873.

Sinor, D. (1990). *The Cambridge history of early inner Asia.* Cambridge University Press.

Smith, B. W. & E. J. Rhodes (1994). Charge movements in quartz and their relevance to optical dating. *Radiation Measurements,* 23, 329.

Smith, B. W., M. J. Aitken, E. J. Rhodes, P. D. Robinson, & D. M. Geldard (1986). Optical Dating: Methodological Aspects. *Radiation Protection Dosimetry,* 17, 229.

Smith, M. L. (2005). Networks, Territories, and the Cartography of Ancient States. *Annals of the Association of American Geographers,* 95, 832.

Solomina, O., I. Bushueva, E. Dolgova, V. Jomelli, M. Alexandrin, V. Mikhalenko, & V. Matskovsky (2016). Glacier variations in the Northern Caucasus compared to

climatic reconstructions over the past millennium. *Global and Planetary Change,* 140, 28.

Spooner, N. A. (1994). On the optical dating signal from quartz. *Radiation Measurements,* 23, 593.

Spooner, N. A., J. M. Olley, D. G. Questiaux, & X. Y. Chen (2001). Optical dating of an aeolian deposit on the Murrumbidgee floodplain. *Quaternary Science Reviews,* 20, 835.

Stathakopoulos, D. C. (2017). *Famine and pestilence in the late Roman and early Byzantine empire: a systematic survey of subsistence crises and epidemics.* Routledge.

Steffen, D., F. Preusser, & F. Schlunegger (2009). OSL quartz age underestimation due to unstable signal components. *Quaternary Geochronology,* 4, 353.

Stokes, S., A. E. L Colls, M. Fattahi, & J. Rich (2000). Investigations of the performance of quartz single aliquot D_e determination procedures. *Radiation Measurements,* 32, 585.

Stoops, G. (2003). *Guidelines for analysis and description of soil and regolith thin sections.* Soil Science Society of America Inc.

Stoops, G., V. Marcelino, & F. Mees (2010). *Interpretation of micromorphological features of soils and regoliths.* Elsevier.

Stride, S., B. Rondelli, & S. Mantellini (2009). Canals versus horses: political power in the oasis of Samarkand. *World Archaeology,* 41, 73.

Talebi, T., E. Ramezani, M. Djamali, H. A. K. Lahijani, A. Naqinezhad, K. Alizadeh, & V. Andrieu-Ponel (2016). The Late-Holocene climate change, vegetation dynamics, lake-level changes and anthropogenic impacts in the Lake Urmia region, NW Iran. *Quaternary International,* 40.

Tchalenko, J. S., M. Berberian, H. Iranmanesh, M. Bailly, & M. Arsovsky (1974). Tectonic framework of the Tehran region. *Geological Survey of Iran, Report,* 29.

Thomsen, K. J., M. Jain, L. Bøtter-Jensen, A. S. Murray, & H. Jungner (2003). Variation with depth of dose distributions in single grains of quartz extracted from an irradiated concrete block. *Radiation Measurements,* 37, 315.

Thomsen, K. J., A. S. Murray, L. Bøtter-Jensen, & J. Kinahan (2007). Determination of burial dose in incompletely bleached fluvial samples using single grains of quartz. *Radiation Measurements,* 42, 370.

Tite, M. S. & C. Mullins (1971). Enhancement of the magnetic susceptibility of soils on archaeological sites. *Archaeometry,* 13, 209.

Titterington, D. M. (1990). Some recent research in the analysis of mixture distributions. *Statistics,* 21, 619.

Tokuyasu, K., K. Tanaka, S. Tsukamoto, & A. Murray (2010). The Characteristics of OSL Signal from Quartz Grains Extracted from Modern Sediments in Japan. *Geochronometria,* 37, 13.

Topping, J. (1972). *Errors of Observation and their Treatment.* Chapman & Hall, London.

Trauerstein, M., S. E. Lowick, F. Preusser, & H. Veit (2017). Testing the suitability of dim sedimentary quartz from northern Switzerland for OSL burial dose estimation. *Geochronometria,* 44, 66.

Tsukamoto, S., W. J. Rink, & T. Watanuki (2003). OSL of tephric loess and volcanic quartz in Japan and an alternative procedure for estimating D_e from a fast OSL component. *Radiation Measurements,* 37, 459.

Tsukamoto, S., A. S. Murray, S. Huot, T. Watanuki, P. M. Denby, & L. Bøtter-Jensen (2007). Luminescence property of volcanic quartz and the use of red isothermal TL for dating tephras. *Radiation Measurements,* 42, 190.

USDA, S. T. (1975). *Soil taxonomy: a basic system of soil classification for making and interpreting soil surveys.* US Department of Agriculture.

Ulrich, B. (2011). Oman and Bahrain in late antiquity: the Sasanians' Arabian periphery. *Proceedings of the Seminar for Arabian Studies,* 41, 377.

Ur, J. A. (2013). CORONA Satellite Imagery and Ancient Near Eastern Landscapes. In: *Mapping Archaeological Landscapes from Space.* Springer New York, 21–31.

Urushadze, T. F. (1999). Soils and the soil cover of Georgia as reflected in the journal Pochvovedenie. *Eurasian soil science,* 32, 141.

Vandenberghe, D., S. M. Hossain, F. De Corte, & P. Van den haute (2003). Investigations on the origin of the equivalent dose distribution in a Dutch coversand. *Radiation Measurements,* 37, 433.

Vermeesch, P. (2009). RadialPlotter: A Java application for fission track, luminescence and other radial plots. *Radiation Measurements,* 44, 409.

Volodicheva, N (2002). The Caucasus. In: *The physical geography of northern Eurasia.* Ed. by M. Shahgedanova. Oxford University Press.

Von Suchodoletz, H., M. Menz, P. Kühn, L. Sukhishvili, & D. Faust (2015). Fluvial sediments of the Algeti River in southeastern Georgia – An archive of Late Quaternary landscape activity and stability in the Transcaucasian region. *CATENA,* 130, 95.

Von Suchodoletz, H., A. Gärtner, S. Hoth, J. Umlauft, L. Sukhishvili, & D. Faust (2016). Late Pleistocene river migrations in response to thrust belt advance and sediment-flux steering – The Kura River (southern Caucasus). *Geomorphology,* 266, 53.

Vos, K., N. Vandenberghe, & J. Elsen (2014). Surface textural analysis of quartz grains by scanning electron microscopy (SEM): From sample preparation to environmental interpretation. *Earth-Science Reviews,* 128, 93.

Wallinga, J., A. S. Murray, & L. Bøtter-Jensen (2002). Measurement of the Dose in Quartz in the Presence of Feldspar Contamination. *Radiation Protection Dosimetry,* 101, 367.

Wallinga, J., A. Murray, & G. Duller (2000). Underestimation of equivalent dose in single-aliquot optical dating of feldspars caused by preheating. *Radiation Measurements,* 32, 691.

Wang, T., D. Surge, & K. J. Walker (2013). Seasonal climate change across the Roman Warm Period/Vandal Minimum transition using isotope sclerochronology in archaeological shells and otoliths, southwest Florida, USA. *Quaternary International,* 308-309, 230.

Wang, X. L., Y. C. Lu, & A. G. Wintle (2006). Recuperated OSL dating of fine-grained quartz in Chinese loess. *Quaternary Geochronology,* 1, 89.

Ward, G. K. & S. R. Wilson (1978). Procedures for comparing and combining radiocarbon age determinations: a critique. *Archaeometry,* 20, 19.

Watson, A. M. (1981). A Medieval Green Revolution: new crops and farming techniques in the early Islamic World. *The Islamic Middle East,* 700, 1900.

Weiss, C. & I. Gerlach (2009). Qadhat — a comparative study of ancient and new lime mortar from the Marib province/Yemen. *Archaeological and Anthropological Sciences,* 1, 87.

Wenke, R. J. (1975). Imperial investments and agricultural developments in Parthian and Sassanian Khuzestan: 150 BC to AD 640. *Mesopotamia Torino,* 10.31.

Wenke, R. J. (1987). Western Iran in the Partho-Sasanian period: the imperial transformation. In: *The Archaeology of Western Iran.* Ed. by K. Hole. United States of America: Smithsonian Institution, 251–281.

Whitehouse, D. (1971). Sīrāf: a Sasanian port. *Antiquity,* 45, 262.

Whitehouse, D. & A. Williamson (1973). Sasanian Maritime Trade. *Iran,* 11, 29.

Wilkinson, J. C. (1977). *Water and Tribal Settlement in South-East Arabia: A Study of the Aflāj of Oman.* Oxford University Press.

Wilkinson, K. N., A. R. Beck, & G. Philip (2006). Satellite imagery as a resource in the prospection for archaeological sites in central Syria. *Geoarchaeology,* 21, 735.

Wilkinson, T. J. (1982). The Definition of Ancient Manured Zones by Means of Extensive Sherd-Sampling Techniques. *Journal of Field Archaeology,* 9, 323.

Wilkinson, T. J. (1997). Holocene environments of the high plateau, Yemen. Recent geoarchaeological investigations. *Geoarchaeology,* 12, 833.

Wilkinson, T. J. (1998). Water and Human Settlement in the Balikh Valley, Syria: Investigations from 1992–1995. *Journal of Field Archaeology,* 25, 63.

Wilkinson, T. J. (2003). *Archaeological landscapes of the Near East.* University of Arizona Press.

Wilkinson, T. J. & L. Rayne (2010). Hydraulic landscapes and imperial power in the Near East. *Water History,* 2, 115.

Wilkinson, T. J., R. Boucharlat, M. W. Ertsen, G. Gillmore, D. Kennet, P. Magee, K. Rezakhani, & T. De Schacht (2012). From human niche construction to imperial power: long-term trends in ancient Iranian water systems. *Water History,* 4, 155.

Wilkinson, T. J., H. O. Rekavandi, K. Hopper, S. Priestman, K. Roustaei, & N. Galiatsatos (2013). The Landscapes of the Gorgān Wall. In: *Persia's Imperial Power in Late Antiquity: The Great Wall of Gorgan and Frontier Landscapes of Sasanian Iran*. Ed. by E. W. Sauer, H. Omrani Rekavandi, T. J. Wilkinson, & J Nokandeh. Oxbow Books, Oxford.

Williams, T. (2007). The city of Sultan Kala, Merv, Turkmenistan: communities, neighbourhoods and urban planning from the eighth to the thirteenth century. In: *Cities in the Pre-Modern Islamic World: The Urban Impact of Religion, State and Society*. Ed. by A. Benninson & A. Gascoine. Routledge, 42–62.

Williams, T. & P. Wordsworth (2010). Merv to the Oxus: a desert survey of routes and surviving archaeology. *Archaeology International,* 12, 27.

Wintle, A. G. (1973). Anomalous fading of thermo-luminescence in mineral samples. *Nature* 245, 143.

Wintle, A. G. (1975). Thermal Quenching of Thermoluminescence in Quartz. *Geophysical Journal of the Royal Astronomical Society* 41, 107.

Wintle, A. G. (1997). Luminescence dating: laboratory procedures and protocols. *Radiation Measurements,* 27, 769.

Wintle, A. G. & G Adamiec (2017). Optically stimulated luminescence signals from quartz: A review. *Radiation Measurements* , 98, 10.

Xoplaki, E., D. Fleitmann, J. Luterbacher, S. Wagner, J. F. Haldon, E. Zorita, I. Telelis, A. Toreti, & A. Izdebski (2016). The Medieval Climate Anomaly and Byzantium: A review of the evidence on climatic fluctuations, economic performance and societal change. *Quaternary Science Reviews,* 136, 229.

Zander, A., D. Degering, F. Preusser, H. U. Kasper, & H. Brückner (2007). Optically stimulated luminescence dating of sublittoral and intertidal sediments from Dubai, UAE: Radioactive disequilibria in the uranium decay series. *Quaternary Geochronology,* 2, 123.

Zheng, C. X., L. P. Zhou, & J. T. Qin (2009). Difference in luminescence sensitivity of coarse-grained quartz from deserts of northern China. *Radiation Measurements,* 44, 534.

Zimmerman, J (1971). The radiation-induced increase of the 100 C thermoluminescence sensitivity of fired quartz. *Journal of Physics C: Solid State Physics,* 4, 3265.

Zinkernagel, U. (1978). *Cathodoluminescence of quartz and its application to sandstone petrology*. Schweizerbart Science Publishers.

Appendix A
Bulk sedimentary techniques

A.1 Loss-on-ignition (LOI) and moisture content procedure, Geography Department, Durham University

1. Dry the crucibles to be used in the determination overnight in a drying oven at 105°C. Place in a desiccator to cool prior to weighing. Crucibles should always be removed individually to prevent them gaining mass (moisture). This and all subsequent masses should be taken and recorded to 4 decimal places, with data recorded against the crucible number which has been burned onto the porcelain - do not add other markings. This step gives crucible mass (A).

2. Add 3-5 g of the sediment to be determined into the pre-weighed crucible; weigh and record masses to 4 decimal places. This addition should be done in a timely manner in order to avoid bias as sediment can rapidly lose (or gain) mass to the atmosphere. This gives crucible plus wet sediment mass (B).

3. Dry the crucibles plus samples in a drying oven at 105°C for 24 hours. Place in a desiccator to cool prior to weighing and recording of masses. This gives crucible plus oven-dry sediment mass (C).

4. Place the crucibles plus samples into the cold muffle furnace, taking care to avoid 'cool spots' at the back and the front of the furnace. Ensure the furnace is set at the desired temperature (usually 550°C) and close the muffle door. Ensure the extractor fan above the furnaces has been turned on. NB Allowing the samples to be taken through the temperature range prevents sudden ignition of material which may 'spit', contaminating other samples and biasing results.

5. Using long-reach tongs, remove the crucibles from the furnace after 4 hours at 550°C. Using a glass desiccator, crucibles can be placed carefully inside and the

lid replaced.

6. After samples have cooled (about 45 minutes), weigh and record masses. NB As the cooling of the samples will have created a vacuum inside the desiccator, the bung should be removed carefully to prevent air rushing inside and disturbing the ash remaining in the crucibles and biasing results. This gives crucible plus ashed sediment mass (D).

Appendix B
Radiocarbon chronostratigraphy: Trench F, Dariali Fort, Georgia

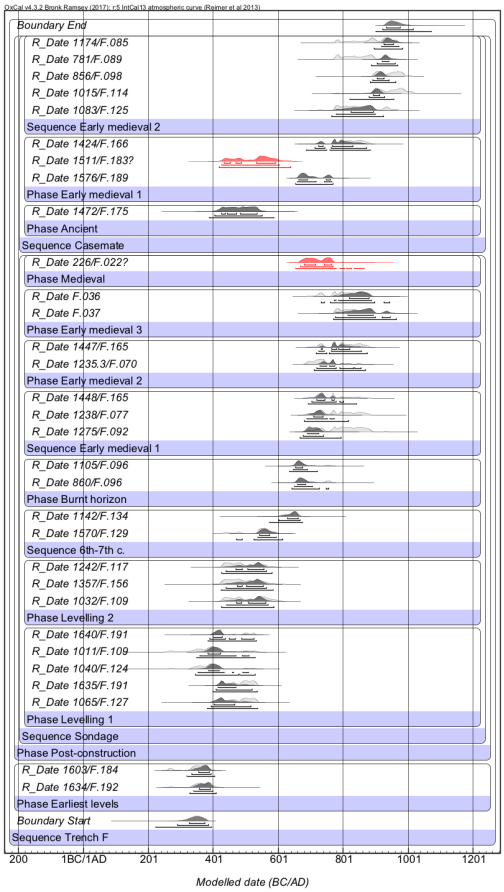

Figure B.1. Bayesian model of ^{14}C dates from Dariali Fort, Trench F. Data processed in OxCal v4.1 (Bronk Ramsey 2017) using the calibration dataset of Reimer et al., (2012). (Courtesy Eberhard Sauer).

Appendix C
Sedimentary descriptions: Ören Qal'eh canal, Azerbaijan

Context number	Munsell soil colour	Texture	Notes
5	Brown (10YR4/3)	Silty clay loam	Well formed peds, compact, well sorted
6	Brown (10YR4/3)	Silty clay	Compact, well sorted
7	Brown (10YR4/3)	Silty clay	Compact, well sorted
8	Dark greyish brown (10YR4/2)	Fine sand	Compact, well sorted
9	Dark greyish brown (10YR4/2)	Sandy clay	Compact, well sorted
10	Brown (7.5YR4/2)	Clay	Compact, well sorted
11	Weak red (2.5Y4/2)	Loamy sand	Compact, well sorted
12	Brown (10YR4/3)	Clay	Well formed peds, occ shell fragments, compact, well sorted
13	Brown (10YR4/3)	Clay	Compact, well sorted
14	Brown (10YR4/3)	Silty clay	Compact, well sorted
15	Dark greyish brown (10YR4/2)	Silty clay	Well formed peds, compact, well sorted
16	Brown (10YR4/3)	Silty loam	Compact, well sorted
17	Brown (10YR4/3)	Silty loam	Moderately compact, well sorted
18	Dark yellowish brown (10YR4/4)	Silty loam	Compact, well sorted
19	Dark yellowish brown (10YR4/4)	Silty clay	Compact, well sorted
21	Dark yellowish brown (10YR4/4)	Silty clay loam	Compact, well sorted
22	Dark yellowish brown (10YR4/4)	Silty clay	Compact, well sorted
23	Dark yellowish brown (10YR4/4)	Silty loam	$CaCO_3$ nodules (1-3 mm), compact, well sorted
24	Dark yellowish brown (10YR4/4)	Clay	Rootlets, compact, well sorted
25	Brown (10YR4/3)	Sandy loam	Compact, well sorted
26	Dark greyish brown (10YR4/2)	Clay	Compact, well sorted
27	Brown (10YR4/3)	Clay	Compact, well sorted
28	Brown (10YR4/3)	Clay	Compact, well sorted

Table C.1. Sediment description of the main contexts uncovered from the Ören Qal'eh canal.

Context number	Munsell soil colour	Texture	Notes
29	Brown (10YR4/3)	Clay	Occ shell and $CaCO_3$ nodules (<2 mm), compact, well sorted
30	Brown (10YR4/3)	Silty clay	Moderately compact and poorly sorted
31	Dark yellowish brown (10YR4/4)	Clay	Rootlets, $CaCO_3$ nodules (<2 mm), compact, well sorted
32	Brown (10YR4/3)	Silty clay	$CaCO_3$ nodules (1-2 mm), moderately compact and poorly sorted
33	Brown (10YR5/3)	Silty clay	$CaCO_3$ nodules (1-2 mm), moderately compact and poorly sorted
34	Dark yellowish brown (10YR4/4)	Silty clay	$CaCO_3$ nodules (1-2 mm), moderately compact and poorly sorted
35	Pale brown (10YR6/3)	Clay	$CaCO_3$ nodules (1-2 mm), compact and well sorted
36	Dark yellowish brown (10YR4/4)	Silty clay	Occ rootlets, $CaCO_3$ nodules (<1 mm), moderately compact and poorly sorted
37	Dark yellowish brown (10YR4/4)	Clay	Moderately compact, well sorted
38	Dark yellowish brown (10YR4/4)	Silty clay	Moderately compact, well sorted
39	Brown (10YR4/3)	Silty loam	Moderately compact, well sorted
40	Brown (10YR4/3)	Silty loam	Moderately compact, well sorted
42	Brown (10YR4/3)	Silty clay	$CaCO_3$ nodules, moderately compact, poorly sorted
43	Brown (10YR4/3)	Silty clay	Occ rootlets, clay pellets, moderately compact, poorly sorted
45	Brown (10YR4/3)	Silty clay	Clay pellets, moderately compact, poorly sorted
46	Brown (10YR4/3)	Silty clay	$CaCO_3$ nodules (1-2 mm), moderately compact, well sorted
50	Dark greyish brown (10YR4/2)	Silty clay	$CaCO_3$ nodules (1-2 mm), clay pellets, moderately compact and poorly sorted
52	Brown (10YR4/3)	Silty loam	Rootlets, $CaCO_3$ nodules (1-2 mm), moderately compact, poorly sorted

Table C.1. Sediment description of the main contexts uncovered from the Ören Qal'eh canal.

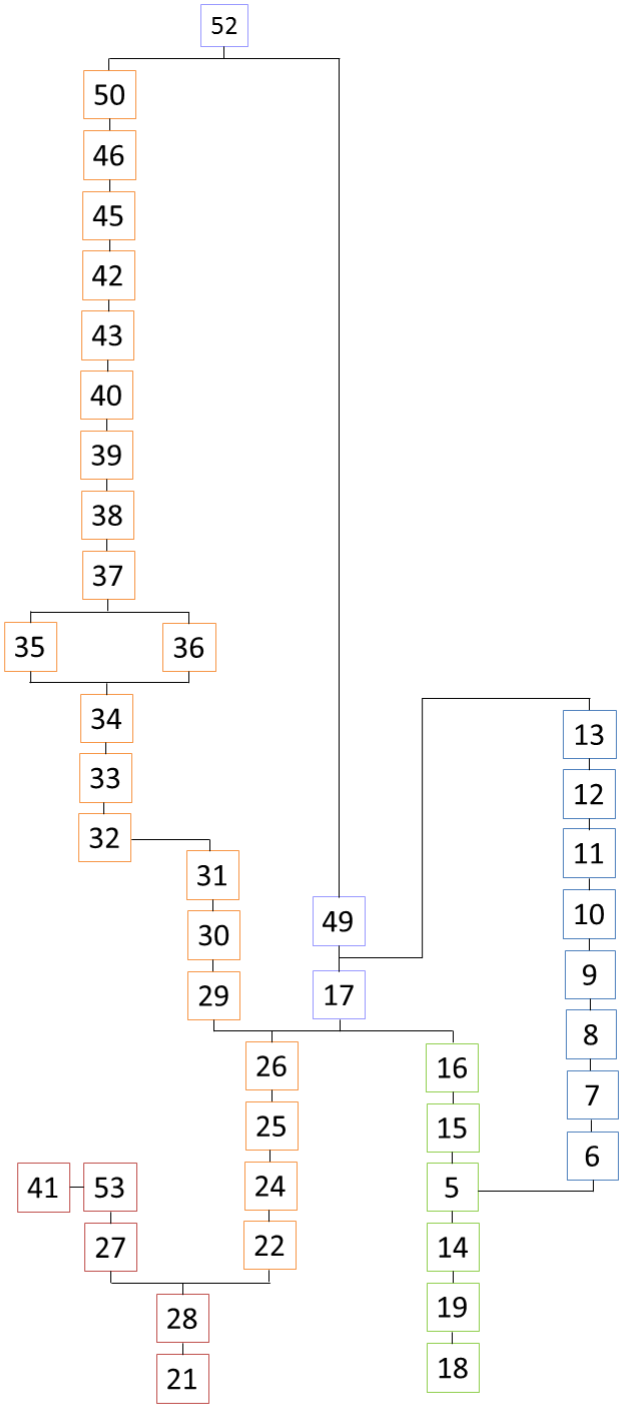

Figure C.1. Harris matrices for Ören Qal'eh.

Appendix D
Thermal stability measurements

Baikiff, IK (2017)

Results

The calculated values of E, S (as log10S) and the estimated mean lifetimes calculated for an average temperature of 15°C are summarised in Table D.1. With the exception of the samples from Dariali Fort (412-15), this initial study identifies trap depths in the range ca. 1.2-1.4 eV associated with the terrace samples (412-9.1 and 17.2) and canal upcast deposits (413-1.3.1 and 1.6.1). The Oman samples (426) exhibit differing characteristics, one (3.8) resembling the Georgian and Azeri quartz with an E value of ca 1.2 eV and the other (3.6 eV) with an E value of ca 1.8 eV and consequently significantly larger mean lifetime.

The generally weak OSL signals and the presence of a slow decay component in the 412-15 samples caused problems of signal reproducibility and further measurements are required for samples 15-1.1 and 15-3.1 at higher levels of dose to obtain better reproducibility when applying the EBG subtraction procedure. Although adequate signals were obtained with sample 412-15.2.1, the value of S appears to be anomalously low and the isothermal decay characteristics may contain more components that assumed, again requiring further investigation. A Monte Carlo simulation procedure was applied when fitting an exponential function to the Arrenhius plots to obtain estimates of uncertainty I n E and S, and the values of s.d. have been included to underline thepotential dispersion inherent in these calculations.

The predicted loss of charge associated with the measured OSL is calculated for a mean temperature of 15°C over the periods indicated in the table. In addition to a further investigation of the isothermal decay characteristics of the 412-15.1 samples using higher levels of dose, pseudo-LM-OSL decay data will be obtained to enable comparison with previously classified decay components of the quartz OSL decay curve (Bailey, 2000; Jain et al, 2003; Singarayer and Bailey, 2004).

Sample	Disc	IPH (°)	E (eV)	s.d. 1σ	s.e. 1σ	$\log_{10}$S	$\tau(a)$ 15° (a) (a)	s.d.	s.e.	Calc. loss at 15° for period (a) 500	1000	1500	2000
412-9.1	#1	200	1.22	0.2	0.03	9.25	2.53E+04	2.55E-04	3.47E-03	<1%	<1%	<1%	1%
412-17.2	#3	200	1.48	0.35	0.05	11.99	2.72E+06	3.46E-06	4.71E-05	<1%	<1%	<1%	<1%
412-15.2.1	#7	200	1.04	0.07	0.01	7.75	7.69E+02	3.09E+02	4.21E+02	48%	86%	100%	100%
413-1.3.1	#1	200	1.31	0.14	0.02	10.27	1.20E+05	6.06E+04	8.24E+03	<1%	1%	1%	2%
413-1.6.1	#5	200	1.37	0.31	0.04	10.51	4.70E+05	5.70E+05	7.76E+04	<1%	<1%	<1%	<1%
426-3.6	#2	180	1.81	0.12	0.02	14.26	9.80E+09	1.88E+09	2.56E+08	<1%	<1%	<1%	<1%
426-3.8	#5	180	1.23	0.10	0.01	9.32	4.47E+04	1.78E+04	2.42E+03	1%	2%	3%	4%

Table D.1. Summary of measured parameters and estimates of mean lifetime calculation.

Appendix E
OSL test results: Qal'el Pol Gonbad, Iran

Nsig/BG	SAR T4	± s.e.	% s.e.	RR	Uncert	GC
2.1	2.71	0.90	0.33	0.99	0.09	1d 2m
2.4	6.91	0.80	0.12	0.77	0.19	1d
3.1	14.12	1.73	0.12	0.91	0.34	1d 1m
1.7	2.85	1.09	0.38	1.04	0.10	1d
6.8	2.98	0.22	0.07	1.17	0.09	2d 2m
6.6	12.96	0.75	0.06	1.01	0.13	2d 1m
9.5	12.28	0.44	0.04	1.14	0.11	Multiple (>3d)
1.1	3.45	1.17	0.34	1.48	0.29	Multiple (>3d)
6.8	2.86	0.36	0.13	1.01	0.05	1d

Table E.1. D_e summary of aliquots with sufficient quartz signals from sample 418-1.4

	Isotope activities (Bq/kg^{-1})			Isotope ratios	
Sample	^{238}U	^{232}Th	^{40}K	^{210}Pb/^{av}U	^{210}Pb/^{226}Ra
418-1.4	40.4±5.12	40.4±5.1	551.9±7.2	0.92±0.1	0.82±0.1

Table E.2. Summary of radioactive isotope activities and ratios measured as an infinite medium of a point absorber (Sample 418-1.4).

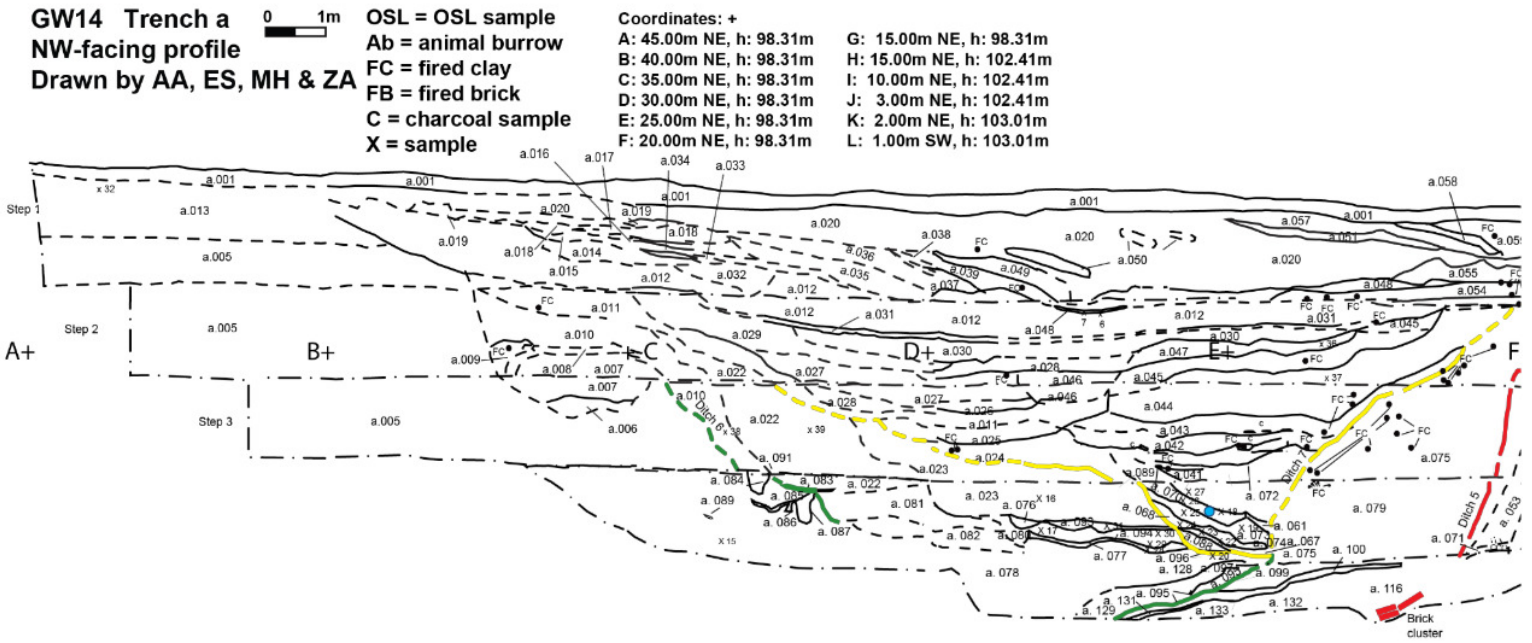

Figure E.1. Stratigraphic section of the moat fill, Qal'eh Pol Gonbad, Iran, showing the location of the OSL test sample (418-1.4) (blue circle).

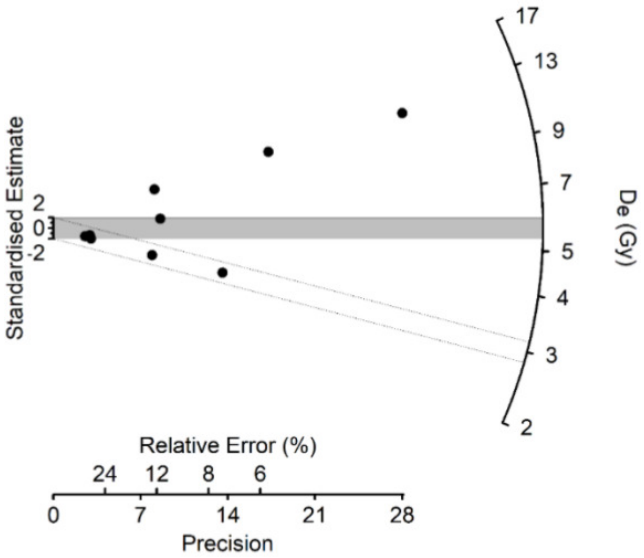

Figure E.2. Radial plot showing the D_e values presented in Table E.1 for sample 418-1.4. Grey region: central value 5.6±1.30 Gy.